Nuclear Fusion Programme Annual Report of the Association Forschungszentrum Karlsruhe/EURATOM

January 2004 - December 2004

Programm Kernfusion

Mai 2005

Forschungszentrum Karlsruhe

in der Helmholtz-Gemeinschaft

Wissenschaftliche Berichte

FZKA 7117
EUR 21526 EN

Nuclear Fusion Programme
Annual Report of the
Association Forschungszentrum Karlsruhe/
EURATOM
January 2004 - December 2004

compiled by W. Bahm
Programm Kernfusion

Introduction

Nuclear fusion represents a most promising option for a safe, sustainable energy source which can be made inherently safe and which, even with a substantial contribution to a future global energy supply will not meet resource limits and should not leave burdens for future generations. Fusion research therefore has to fully explore this option as to provide a complete basis of proven information whether energy production by fusion is technically feasible, ecologically tolerable and finally, economically meaningful.

The FZK fusion research programme is fully integrated in the European Fusion Programme which follows a road map towards commercial fusion energy. At present the so-called Fast Track is intensively discussed in Europe which would reduce the time span to commercial fusion power by ten years (Fig. 1). Three major elements of research and development are required in order to generate the know-how for the construction of a fusion power station DEMO/PROTO:

A base physics programme targeted to improve capabilities to simulate plasma confinement concepts while making use of existing experimental facilities.

A major facilities programme including ITER as the most important next step, IFMIF for the qualification of materials for DEMO and a component test facility.

A base technology programme comprising plasma support technologies such as superconducting magnets, fuelling systems, high heat flux components, remote maintenance, reactor relevant steady state plasma heating systems etc., and fusion power technologies such as breeding blankets, helium cooled divertor and tritium extraction systems.
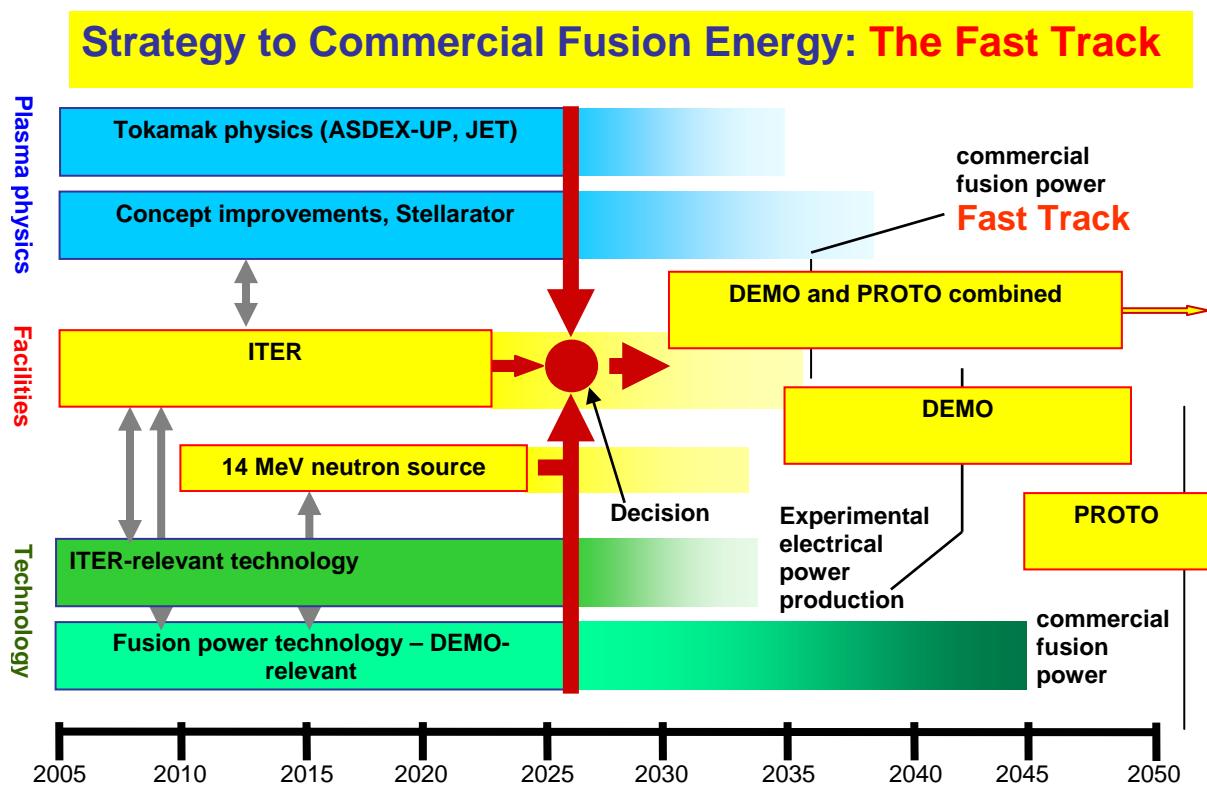
The activities of all the European fusion laboratories (known as EURATOM Associations) and industry are combined into one organisational structure via the European Fusion Development Agreement (EFDA). EFDA has a leader and two associate leaders (one for JET and one for fusion technology). It is guided by a steering committee, consisting of the heads of association laboratories, which has to approve the major strategy and annual work programmes as well as large contracts with industry or associations.

Within this framework FZK is developing key technologies in the areas of superconducting magnets, microwave heating systems (Electron-Cyclotron-Resonance-Heating, ECRH), the deuterium-tritium fuel cycle, He-cooled breeding blankets, a He-cooled divertor and structural materials as well as refractory metals for high heat flux applications including a major participation in the international IFMIF project. Furthermore investigations on plasma wall interactions and core and divertor modelling are carried out and a global plasma model is being developed.

The results from experimental activities such as the tests of high temperature superconducting current leads in the test facility TOSKA, the quasi-stationary gyrotron operation and the operation of fuel cycle subsystems and components with deuterium-tritium have already been utilised for the design work for ITER. In addition large progress has been made in the engineering design of test blanket modules for ITER.

With regard to DEMO design integration of blanket modules taking into account requirements of remotely controlled handling has been started and the conceptual design of a He-cooled divertor considering two alternatives of cooling the target plate has been elaborated. Both activities will serve as an input to the planned DEMO study.

The detailed design and construction of ITER components and subsystems needs to be supported by experiments such as prototype testing, validation of scale up factors and additional R&D. For this purpose a helium loop HELOKA is being planned which not only serves for experimental investigations but also as a pilot loop in view of the loops to be installed in ITER for the cooling of test blanket modules.

In order to efficiently manage these tasks a project-oriented approach is required involving a quality assured and quality controlled exploitation of R&D results. Subsequently the development of a quality control system has been started. This process shall result in the development of complete licensable components and systems. In a later phase support has to be provided to industrial partners who shall produce, assemble and finally install the components or systems into ITER, taking quality control and licensing aspects into account. However, the responsibility for the performance and the overall management of the procurement, installation and commissioning shall remain with the designers.

In order to meet this challenge, a project-oriented organisation structure is maintained in the FZK fusion programme by means of task forces in the areas Blanket/Divertor, Microwave Heating, Superconducting Magnets, Fuel Cycle and IFMIF (14 MeV neutron source). A task force which is responsible for a large component or subsystem to be delivered to ITER can be seen as a design and development division with a division head and several groups, each of them having a group leader. A team of design engineers supported by CAD constitutes the nucleus of each group in the task force. Besides the above-mentioned task forces materials research is oriented at engineering requirements.

About 220 professionals and technicians are involved in the fusion programme of the Association FZK-EURATOM with additional support of the technical departments.

Progress from January 2004 to December 2004 is reported here. More information is available from the programme management and from the responsible scientists. The website www.fzk.de/fusion offers further access to the fusion activities of FZK.

Contents   Page

Introduction

Page

Plasma Edge

EFDA/03-1080

Characterisation of Material Damage for EU W and CFC ITER Divertor Materials under Repetitive Plasma Energy Fluxes by Modelling and Experimental Validation

1. Introduction

Operation of the tokamak ITER in the ELMy H−mode at repetitive pulses of plasma irradiations with the divertor heat load Q ~ 1-3 MJ/m2 on the time scale τ ~ 0.3 ms, deteriorates armour performance. The main parts of the armour of vertical divertor will probably be covered by tungsten and also by CFC. This report describes joint numerical and experimental investigations of erosion mechanisms of CFC and tungsten targets carried out in FZK, TRINITI[1] and KIPT[2]. The CFC modelling uses the anisotropic thermomechanics code PEGASUS−3D and the surface melt motion code MEMOS−1.5D. Experiments aimed at validation of the codes are being carried out at the plasma gun facilities MK−200UG, QSPA-T and QSPA-Kh50 which produce the streams of hydrogen plasma with Q and τ of the values that enable to simulate the repetitive ELM loads expected in ITER. To produce the ELM relevant loads the experimental facilities decreased their power in comparison with previous disruption relevant regimes. Investigations of tungsten armour behaviour under the ITER ELM relevant heat loads and multiple pulse irradiations of tungsten samples as well as their surface analysis have been performed and the values of Q for the onset of melting (the tungsten melting threshold) obtained.

2. The experimental facilities and the codes engaged for the simulations

In the facility MK-200UG the plasma acceleration is due to the magnetic pressure applied to a plasma cloud that was previously produced between the coaxial electrodes of the accelerator. High pulse voltage rising between the electrodes induces a current through the plasma and thus a magnetic pressure gradient that accelerates the plasma cloud. The plasma gun of MK-200UG can produce only short pulses with the duration τ of 0.05 ms and the heat load Q up to 15 MJ/m^2, ion impact energies E_i up to 2.5 keV, and electron temperature T_e up to 300 eV, the target surface can be inclined under the angle of 20 degrees in respect to the guiding magnetic field up to 3 T.

The plasma accelerators QSPA-T and QSPA-Kh50 are the so-called Quasi-Stationary Plasma Accelerators. The plasma is propelled in crossed electric E and magnetic B fields by means of the E×B drift, which allows the generation of much longer pulses compared to MK-200UG. However, the large plasma conductivity prevents fast penetration of the fields into the stream. In a stationary regime this circumstance would limit E_i by a few tenths of eV, which is of no use for the ELM load simulation. Only at a pulsed regime the energy E_i increases but only up to 0.2 keV (τ = 0.25 ms in QSPA−Kh50 and 0.5 ms in QSPA-T). The electron temperature is not known, but one can reasonably assume a T_e of a few eV.

To numerically simulate the brittle destruction mechanisms, in PEGASUS-3D the matrix and the fibres of CFC structure are described by means of several millions of numerical cells of one-micrometer size. Some grains built of different groups of the cells are implemented to simulate more appropriately the graphite structure. Neighbour grains contact by means of mechanical- and heat conduction bonds. The complicated composition of CFC is modelled varying the involved material properties of the cells, which are the thermal conductivity, the coefficient of thermal expansion and the Young's modulus.

MEMOS$-$1.5D describes the process of surface melting in frame of the 'shallow water' model. The code was validated comparing the simulation results with the e-beam facilities JUDITH for beryllium and JEBIS for tungsten. The melt motion in MEMOS$-$1.5D is described taking into account the surface tension, viscosity of molten metal, and the radiative losses from the hot tungsten surface. The gradient of plasma pressure and the gradient of surface tension as well as the Lorentz force of the currents crossing the melt layer in strong magnetic field produce the melt acceleration along the divertor plate. A two-dimensional heat transport equation with two boundary conditions at the moving vapour-liquid- and liquid-solid interfaces describes the temperature inside the target. Temperature dependent thermophysical data are used.

3. Simulation of CFC brittle destruction under ITER ELM relevant loads

In CFC, plasma-induced erosion results not solely from the vaporization but also from macroscopic erosion mechanisms. The pulses of energetic plasma cause brittle destruction that arises because of the thermal stress shocks in the material volume, and the eroded material emits from the target as carbon grains.

CFC have been tested at MK-200UG and QSPA-T. The main objective of the experiments is longevity testing of carbon-fibre composites NS31 and NB31 by multiple (up to 250) plasma irradiations investigating the erosion rate and erosion mechanisms. At both facilities, the CFC targets have been irradiated by hydrogen plasma streams impacting target perpendicularly with nearly equal heat load $Q \approx 10$ MJ/m^2 but different plasma pulse durations. In these experiments the load is several times larger than Q anticipated for ITER ELMs however it seems that at the target surface Q is much closer to the ELM conditions due to the vapour shield effect.

From the measurements follows no notable difference in behaviour of NS31 and NB31. The erosion is rather small and limited to a few microns per shot. The erosion products are being emitted from the target surface mainly as small carbon particles of the sizes of 1 - 3 μm, but there are also large particles with the sizes of 50 – 150 μm.

Emission of large carbon debris results in formation of open cavities at the CFC surface which are formed mainly at the boundaries between the pitch fibres. (The pitch fibres are perpendicular to the face target surface, and the PAN fibres are parallel to the surface.) The PAN fibres erode faster than the pitch fibres. The wavy profile of exposed target surface is forming with the valleys at the positions of the PAN fibres and the ridges at the position of the pitch fibres.

During the first 50 – 70 shots at MK-200UG, the measured mass loss is mainly determined by the erosion of the PAN fibres. The pitch fibres damage is almost negligible and their contribution to the net erosion is rather small. Only after 70 - 100 shots, when the PAN fibres are eroded on the depth about 0.5 mm, the erosion of the pitch fibres becomes notable. The mass loss increases with the number of plasma exposures from 15 mg/shot up to 40 mg/shot after 200 shots. In average, the mass loss obtained at MK-200UG corresponds to 1 μm/shot.
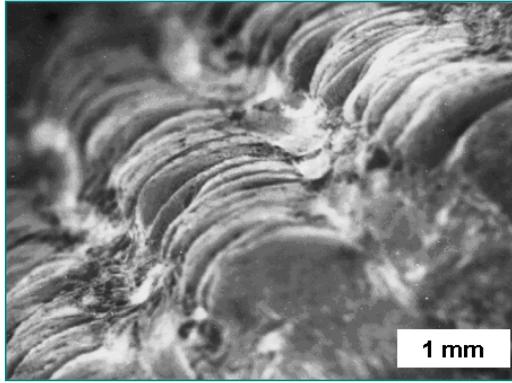
Fig. 1: CFC surface after 150 shots at QSPA-T.

The sample of NS31 tested at MK-200UG was further tested at QSPA–T assuming that the preliminary erosion obtained at the described experiments at MK–200UG will not influence the testing for much larger erosion effects. Indeed, after 250 shots at QSPA-T, the net erosion of CFC target became large enough to be seen by eyes. Fig. 1 shows the CFC sample after plasma testing. The overall CFC erosion corresponds to the average erosion rate about 12 μm/shot.

Because of considerable difference of the simulation conditions in the plasma guns MK-200UG and QSPA-T from the ITER impact, the results of the experimentally determined erosion mechanism should be extrapolated on the ITER ELM conditions, which can be done using the code PEGASUS-3D. Therefore special numerical simulations have been performed in order to validate the code.

Calculation of CFC erosion by PEGASUS-3D implies definition of the numerical sample, definition of heating conditions and then calculation of heat transport, thermostress and cracking in the sample. The numerical sample is a part of a cubic array of 200x200x200 cubic cells. The sample has a structure from fibres and matrix arranged similarly to NB31. The carbon fibres consist of the cubic cells with two anisotropy axes directed in axial and radial directions of the fibre. The matrix is simulated by small grains of the mean size of 2.5 μm that have random shapes with the anisotropy axes directed randomly for different grains.

The following heating scenario for comparison with the experiments has been calculated. From the start of the load the sample surface is heated by a constant heat flux till the time when the surface temperature reaches the carbon sublimation temperature. From then on the vaporisation of the carbon produces the vapour shield. The shielding of target surface is a self-adjusted process, which maintains the surface temperature very close to the sublimation temperature. In the experiments the vaporization erosion is much smaller than one micron, which enabled to neglect it in the simulation.
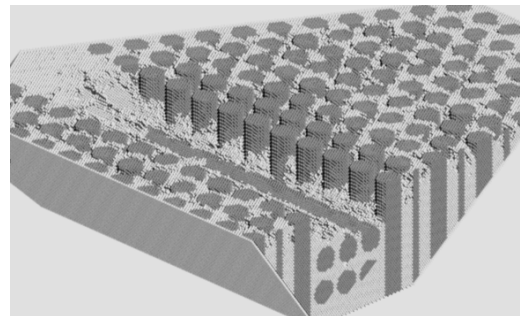
Fig. 2: Erosion of CFC NB31 simulated with PEGA-SUS-3D

The results of the numerical simulation for the plasma guns conditions are shown in Fig. 2. Most important fact is that the CFC erosion is qualitatively the same as it has been obtained in the experiments. Erosion of the PAN fibres (seen as a valley along the left side of the sample) is much larger than the erosion in the pitch fibres region at the right side.

4. Tungsten melting threshold experiments and validation of MEMOS-1.5D

The plasma-induced erosion of metallic targets depends mainly on the processes occurring in the melt layer which forms at the target surface under the action of hot plasma stream. However, recent experiments at MK-200UG and QSPA-Kh50 reported here concern the onset conditions of tungsten melting. The melting threshold energy has been studied aiming validation of MEMOS−1.5D.

At MK-200UG, a fast two-channel infrared pyrometer was used for online measurement of the tungsten surface temperature. The radiation was collected from the small target area of a size below 1 mm. The time resolution of the pyrometer is about 100 ns. The plasma energy

was measured at each plasma shot using a calorimeter attached to the target. The performed online measurements of tungsten surface temperature showed that tungsten melting starts at the plasma heat load above 0.3 MJ/m^2, at the shot duration about 0.05 ms.

To measure the plasma stream parameters at QSPA-Kh50 the calorimetric- and spectroscopic techniques have been used. The irradiated W targets were tested aiming toinvestigate melting onset. The samples are plates of EU trademark delivered by FZK of the sizes $5 \times 5 \times 1$ cm. One sample was exposed to a large number of shots impacting perpendicularly through a diaphragm. Special small markers were indented at the target surface for monitoring the surface and for measurements of melt thickness. Main results of 270 exposures in the regime with the plasma heat loads below but close to the melting threshold can be summarized as follows: The surface roughness is caused mainly by cracking. The main crack meshes of sizes of about 0.1 cm form after a few initial shots. For the regime with the triangular shape of the heat load the melting threshold was determined as 0.56 MJ/m^2, however, a large number of exposures resulted in a change of it down to 0.45 MJ/m^2 (after 150 exposures) which seems due to material modification and the development of bulk cracks parallel to the surface. The melt layer of the thickness below 1 µm was detected. A mass loss corresponding about 1.2 nm per pulse was obtained.

Another sample was exposed at QSPA-Kh50 to 250 pulses above the melting threshold at 0.62 MJ/m^2. The melt layer of the thickness larger than 5 µm and a considerable surface roughness due to both cracks and melt motion up to 80-100 µm was obtained. Molten material moves to the crack voids and the cracks become covered by melt however new cracks appear in places of the fused ones. Crumbling out of large material pieces of the sizes up to 400 µm was found. The pattern of fine cracks changes from pulse to pulse because of remelting in contrast to the pattern of large cracks, therefore the meshes of the large cracks are used in the microscopy analysis as reference objects. Firstly after several hundreds pulses the fine cracks become to be the main feature of the erosion pattern. The mass loss is 2, 3 and 5 times higher for first 100 pulses, next 100 pulses and next 50 pulses, respectively.
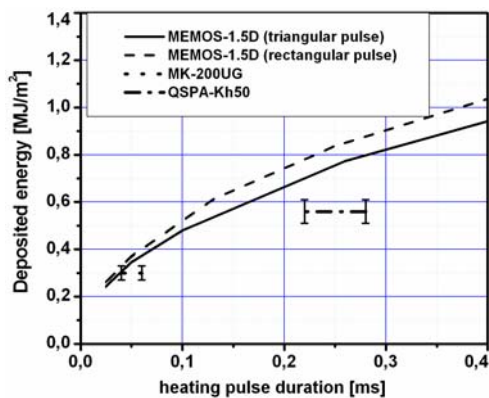
Fig.3: Comparison of experimental- and numerical W melting threshold.

For checking the experimental results on tungsten melting threshold obtained at MK-200UG and QSPA-Kh50 and aiming MEMOS-1.5D validation, the tungsten melting threshold was also calculated. In the calculations the triangle and rectangular shapes of the impinging plasma load in time are assumed, with the pulse durations covering the range 0.05-0.25 ms. Fig. 3 illustrates the experimental results mentioned and the numerical results obtained, with an uncertainty of 15-20% that is caused by the lack of accurate data for tungsten at the temperatures near the melting point. For MK−200UG there is a reasonable agreement, from which it is concluded that the measurements have been carried properly and the validation is successful. The substantial distinction of about 30% between QSPA−Kh50 and MEMOS-1.5D is not explained yet.

5. Conclusions

Both experimental and numerical simulations resulted in the same erosion pattern for the CFC NB31. The erosion rate of the PAN fibres is always much higher than that of the pitch fibres. Erosion of the pitch fibres occurs due to vaporization. From the results of the simulations the conclusion follows that for a significant improvement of performance of CFC at the ITER off-normal events the structure of CFC should have as less fibres parallel to the armour surface (e.g. weaving and needling fibres) as possible. From comparison of the simulation of PEGASUS−3D and the experiments at MK−200UG and QSPA-T it is concluded that the ex-

periment confirms the simulation concerning the development of the caverns and cracking CFC along the boundaries between vertical bunches and horizontal bunches of the fibres.

First investigations of tungsten armour behaviour under the ELM heat loads have been performed. The melting onset load Q_{min} = 0.3 MJ/m^2 at τ = 0.05 ms has been obtained at MK-200UG and 0.56 MJ/m^2 at τ = 0.25 ms at QSPA-Kh50, however after a large number of exposures (150) at QSPA-Kh50 the melt threshold decreased to 0.45 MJ/m^2. From the experiments at QSPA-Kh50 it is concluded that even after 200 exposures relevant to ITER ELMs the development of the numerous processes at the tungsten surface has not reached a quasi-stationary phase, and much more exposures are required. The tungsten melting threshold obtained in experiments on MK-200UG and QSPA-Kh50 is in a reasonable agreement with the calculations of MEMOS-1.5D, which justifies the application of the code for melt motion damage of tokamak tungsten armour.

Staff:

I.S. Landman
S.E. Pestchanyi
B.N. Bazylev

Literature:

[1] S. Pestchany, V. Safronov, I. Landman, Estimation of carbon fibre composites as ITER divertor armour, Journ. Nucl. Mat. 329-333 (2004) 697

[2] I.S. Landman, S.E. Pestchanyi, V.M. Safronov, B.N. Bazylev, I.E. Garkusha, "Material surface damage under high pulse loads typical for ELM bursts and disruptions in ITER", Physica Scripta, T111 (2004) 206

[3] I.S. Landman, B.N. Bazylev, I.E. Garkusha, A. Loarte, S.E. Pestchanyi, V.M. Safronov, "Simulation of tokamak armour erosion and plasma contamination at intense transient heat fluxes in ITER", Proc. 16 Int. Conf. on Plasma Surface Interaction, Portland, USA, May 2004

TW4-TPP-CARWMOD
Molecular Dynamics Simulations of Carbon and Tungsten Sputtering

1. Introduction

The objective of this task is to carry out molecular dynamics (MD) simulations of carbon and tungsten sputtering taking into account effects that may be important under ITER divertor plasma conditions. FZK is responsible for one part of the task: chemical erosion of tungsten under simultaneous bombardment of oxygen and deuterium for ITER relevant energy ranges. In 2004 the earlier developed MD code CADAC was generalized in the direction of realistic simulations: multi-body interactions between the atoms of the H-O-W system in question are implemented. However, this work is still under way and the validation is not yet done. Here Ref. [1] is shortly reproduced.

The oxygen atoms form molecular complexes O_xW_y at the tungsten surface that may sublimate at the high operation wall temperatures of $(0.5-1.5) \times 10^3$ K. The H-atoms retained near the surface can create volatile complexes H_xO_y, which would reduce the sublimation rate of O_xW_y. The impacting atoms also influence the surface processes, because they may destroy the complexes. To the date, available data for numerical simulations of such processes concern mostly pair-wise interatomic potentials. However, chemical effects of the atomic interactions and molecular organization of atoms cannot be analyzed in such restricted way. Chemical features erase from complicated electronic interactions among the many atoms. The quantum problem of their rigorous obtaining is hardly solved and tremendous number of needed computer operations hampers practical applications.

There are nevertheless various computationally efficient semi-heuristic models approximately describing molecular behaviour by means of 'effective' pair potentials that include multi-body forces. It seems that the model of Abell which incorporates the multi-body interactions by means of a modification factor at the attractive term of a pair-potential is most suitable for the problem. Therefore this art is exploited in CADAC. The approach accounts for the projectile- and target atoms including their mutual chemical behaviour.

The interaction is described using the atomic valences, which are usually being a well predictable parameter and comprise most important quantum features of molecular interactions. A heuristic valence concept introduced for the first time enables to analyze involved chemical reactions using quite transparent formulas. Some simple molecules built of H-, O- and W-atoms in vacuum, the cubical tungsten lattice and a single impurity atom near the W-lattice are analysed.

2. Effective interatomic potentials

In CADAC the potential energy of an *N*-atomic assembly is given by

$$V(\mathbf{r}_1, \mathbf{r}_2, ..., \mathbf{r}_N) = \sum_{1 \le i < j \le N} \left(V_{\text{rep}ij}(r_{ij}) + \alpha_{ij} V_{\text{attr}ij}(r_{ij}) \right) \tag{1}$$

Here $\mathbf{r}_i$ are the nuclear positions, $r_{ij} = |\mathbf{r}_i - \mathbf{r}_j|$ the interatomic distances, $V_{\text{rep}ij} > 0$ repulsive pair-potentials describing also high energy interactions, and $V_{\text{attr}ij} < 0$ the attractive exponential terms of the Morse potentials used in the code that are important in a low energy region where the chemical features develop. While calculating the interatomic force $-\partial V/\partial \mathbf{r}_i$ at $N \gg 1$, only j with $r_{ij} < r_{\max} = 6.32$ Å are considered in Eq.(1) and thus a small but most important fraction of $N(N-1)/2$ terms. The α-factors in Eq.(1) of different interactions are introduced as

$$\alpha_{ij} = 1 - \beta_{ij} \frac{\upsilon_i^{ij}(r_{ij}) - \upsilon_i}{\upsilon_{ni}} - \gamma_{ij} \frac{\upsilon_j^{ij}(r_{ij}) - \upsilon_j}{\upsilon_{nj}} \qquad (2)$$

The parameters υ_{ni} and υ_{nj} are conventional chemical valences of atomic kinds: $\upsilon_n = 1$ for H, 2 for O and 6 for W. The fitting parameters $\beta_{ij} > 0$ and $\gamma_{ij} > 0$ are introduced for each kind of interacting atomic pairs, with $\gamma_{ij} = \beta_{ij}$ for the partners of the same kind. The nominators in Eq.(2) are formed of the 'actual valences' introduced as follows.

The (actual) valence is a real variable $\upsilon > 0$ prescribed to an atom, to characterize, informally saying, its attraction for some other atoms. It relates with the number of valence electrons (or the holes of the atomic outer shell) the orbits of which span also neighbour atoms. For an isolated atom $\upsilon = \upsilon_n$ is valid, however valence conservation is not implied.

It is assumed that a pair (*ij*) 'spends' some equal amount $\Delta\upsilon_{ij}$ of the partner valences υ_i and υ_j for each other. If they spent the valence amount $\Delta\upsilon_{ij} > 0$, the valences of both partners correspondingly decrease and for other neighbours remains less of their valences. The $\Delta\upsilon_{ij}$ depends on υ_i, υ_j and r_{ij}. To describe the dependence on r_{ij}, a special 'spent function' $p_{ij}(r_{ij})$ is introduced, in this work as an exponent:

$$p_{ij}(r_{ij}) = p_{0ij} \exp\left(-\frac{r_{ij} - a_{ij}}{r_{pij}}\right) \qquad (3)$$

The Morse equilibrium distance a_{ij} and the fitting parameters r_{pij} and p_{0ij} depend on the atomic species, with p_{ij} negligible at $r_{ij} > r_{max}$. The proportionality of $\Delta\upsilon_{ij}$ on the minimum of υ_i and υ_j is assumed. Consequently, the equations that describe the actual valences take the form:

$$\upsilon_i = \upsilon_{ni} - \sum_{j \neq i} p_{ij}(r_{ij}) \min(\upsilon_i, \upsilon_j), \qquad i = 1..N, \ r_{ij} < r_{max} \qquad (4)$$

At $N = 2$ the solution to Eq.(4) is given by

$$\upsilon_i \equiv \upsilon_i^{ij} = \upsilon_{ni} - \frac{p_{ij}}{1 + p_{ij}} \min(\upsilon_{ni}, \upsilon_{nj}), \qquad \upsilon_j = \upsilon_j^{ij} = \upsilon_{nj} - \frac{p_{ij}}{1 + p_{ij}} \min(\upsilon_{ni}, \upsilon_{nj}) \qquad (5)$$

Hence, the terms $\upsilon_i^{ij}(r_{ij})$ and $\upsilon_j^{ij}(r_{ij})$ in Eq.(2) are the partners actual valences of the isolated pair (*ij*).

3. Simple molecules

Based on Eqs.(1)-(5) some configurations of a few H-, O-, and W-atoms are considered. The r_p is assumed to relate with the Morse bond strength k as $r_p = 1/k$, the equality $\gamma = \beta$ is assumed as well, and β and p_0 are chosen as follows, outgoing from most evident molecular effects.

For example, it is known that the molecules H_3 hardly exist in a rare hydrogen gas. This fact is used to find out reasonable β and p_0 requiring the repulsion to be larger than the attraction in equilateral triangle of three H-atoms. Due to the symmetry, all υ and $p = p_0 \exp(-kr)\exp(ka)$ are the same, with r the triangle side. From Eq.(4), $\upsilon = 1/(1 + 2p)$ follows, and from Eqs.(2) and (5), $\alpha = 1 - 2\beta f$, where the function $f(p) = p/((1+p)(1+2p))$. The range of monotonic increase of $f(p)$ is $0 < p < 1/\sqrt{2}$, and $p = 1/\sqrt{2}$ corresponds to a minimum of α; this minimum is chosen at the Morse equilibrium distance a. The parameter p_0 is thus equal to $1/\sqrt{2}$. For simple molecules this value is accepted as a reasonable estimation. In CADAC, $r_{pHH} = 0.49$ A is

valid and $\alpha(a)$ zeroes at $\beta \approx 3$, which provides the required repulsion. The minimum U_{H3} of the potential energy Eq.(1) $V_{H3}(r) = 3(V_{rep} + \alpha V_{attr})$ is calculated as $U_{H3} \approx -1.61$ eV at $\beta = 3$. This value is much higher than that of -8.51 eV obtained at $\beta = 0$, i.e. with the pure pair interactions. Therefore the H-atoms would pair rather than create H_3. It is worthwhile noting that the obtained figures need corrections after a required validation.
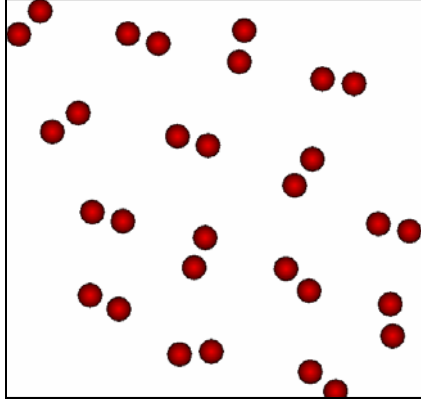
Fig. 1: A CADAC simulation for oxygen atoms moving in a plane (equilibrium state).

The similar problems were analysed for O_3, H_3O, H_8W and O_4W symmetrical configurations in order to adjust the parameters. Always the value of $\beta = 3$ was found to be acceptable. Fig. 1 demonstrates a gas of O-atoms in the thermodynamic equilibrium at 300 K simulated with CADAC. Having randomly started in one plane, the atoms form O_2-molecules and the molecules mutually repulse.

4. Interactions among W-atoms

For W-W interaction the consideration is carried out quite differently. In the wall erosion problem, tungsten is involved mainly as a solid body. Therefore instead isolated atomic pair the bulk W-lattice is chosen as the initial configuration for implementing the valence model. In CADAC the W-W-interaction in the bulk is described by a modified Morse pair potential which provides the bcc-lattice. The bulk W–W multi-body forces are implicitly included in this potential. Therefore for general application of Eq.(2) to W-W interactions the bulk actual valence υ_b replaced the pair-valences $\upsilon_i^{jj}(r)$ and $\upsilon_j^{jj}(r)$. The modified equation for the α-factors takes the form:

$$\alpha_{ij} = 1 + \beta \frac{\upsilon_i + \upsilon_j - 2\upsilon_b}{\upsilon_n} \qquad (\upsilon_n = 6) \qquad (6)$$

The $r_{pWW} = 0.75$ A is chosen. As to p_0, the value $1/\sqrt{2}$ deduced for isolated pair of H-atoms becomes not acceptable. A reasonable value of p_0 was estimated as $p_{0WW} = 0.1$. Estimation of β is based on fitting to the tungsten cohesive energy $E_{coh}^{W} = 9$ eV, and $\beta \approx 1$ was obtained.

5. Single O- and H-atom at the W-surface

One atom (O or H) at the [0,0,1] surface of bcc-W-lattice is considered. A thin tungsten film with two free boundaries is simulated in a box with periodic boundary conditions. As the W-W-interaction forces upon the presurface atoms are initially not compensated in the ideal lattice, in the course of MD calculation the film becomes thinner and relaxes to a new equilibrium state in which the atomic positions and the valences were then fixed. Fig. 2 demonstrates the actual valences in the film. They are obtained smaller by about 30% than those estimated for the ideal lattice. An O- (or H-) atom was eventually created near the surface and its potential energy minimized varying its position.
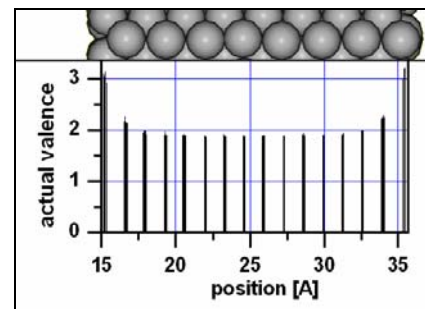
Fig. 2: Cross-section of a tungsten film and actual valences of W-atoms in the corresponding [1,0,0] planes.

At $\beta_{OW} = \gamma_{OW} = 3$, a repulsive interaction between the impurity atom and the lattice was stated, because some α_{OW}-factors became negative. As in reality the O-atoms can accommodate at the W-surface, it was decided to change the parameter γ_{OW} down to the value of $\gamma_{OW} = 1$, thus correcting the previous attempt to estimate it. At $\beta_{OW} = 3$ and $\gamma_{OW} = 1$, the pre-

surface minimum potential -1.17 eV is obtained. The same analysis for H-atoms resulted in -0.32 eV. These figures are quite realistic compared to that early obtained without accounting for the chemical features as -56 eV for H- and -35 eV for O-impurity.

6. Conclusions

A computationally efficient model for molecular- and solid body interactions is suggested in which pair-wise interatomic potentials are combined with atomic valences. Analysis of configurations formed of H-, O- and W-atoms showed their relevance to real molecular structures. It seems that the available fitting parameters can be effectively exploited for validation. This work presents an initial stage of the analysis based on the valence approach at which the involved parameters have been groped. The validation by experimental data is not done up to now therefore optimal values are not yet obtained.

Staff:

I.S. Landman

Literature:

[1] I.S. Landman, "Simulation of multi-atomic interactions in H-O-W system with the MD code CADAC", Proc. 23rd Symposium on Fusion Technology, Venice, Italy, 2004

TW3-TPP-DISELM
Modeling of ELM-induced Plasma Contamination and Disruption W-Macrobrush Damage in ITER Relevant Scenarios

1. Introduction

In this report, theoretical investigations carried out in FZK-IHM in 2004 for the ITER tokamak armor damages after transient events such as ELMs or disruptions and the consequent impurity propagation in SOL are described. Any intense transient process results in a complicated self-consistent plasma wall interaction. The armour erosion occurs mainly due to melt motion and evaporation. The eroded material propagates along the magnetic field lines in SOL intensively reradiating energy of the pedestal plasma, which is dangerous because it can cause collapse of the confinement. The computational tool applied for direct calculation of wall loads and plasma processes is the two-dimensional (2D) RMHD (radiation-magneto-hydrodynamics) code FOREV−2D applied for ITER relevant simulations in SOL. For simulation of the damage to tungsten surfaces the incompressible fluid dynamics code MEMOS-1.5D is applied.

2. Simulation of SOL plasma with FOREV-2D

The code FOREV-2D models the hot plasma lost across the separatrix into SOL during a transient event, its propagation towards the wall and impact on the armor, accounting for a self-consistent evaporation, ionization of carbon-, tungsten- and beryllium atoms, the radiation transport in the contaminated plasma and backward propagation of the erosion products into SOL. At the loads relevant to the main ITER regime in ELMy H−mode the structure of the DT−plasma flux is important and it should be calculated accurately. Therefore the detailed geometry of the ITER magnetic field and elaborated description of the plasma have recently been implemented in FOREV−2D [1], including the toroidal magnetic field with single poloidal field null and one divertor, the whole SOL, inner- and outer divertor plates as well as the ion fluids of D, T, He, He^+ and all charge states of the light impurities such as C or Be.

In 2004 the main development of FOREV-2D concerned the implementation of radiation transport in the toroidal geometry [2]. Former forward-reverse technique based on rectangular meshes has been adjusted to curvilinear coordinates and arbitrary skewed tetragonal meshes. Then the heating of both divertor armour plates and their vaporization followed by expansion of carbon vapour into SOL was calculated for off-normal operation regimes relevant to the tokamaks ITER and JET.

Radiation transport due to impurities is a complex nonlinear problem. For reliable simulation of the radiation cooling, numerical results have to be verified by some experiments on the existing tokamaks. Therefore JET relevant calculations for a giant ELM of ~1 MJ size have been performed. In the ELM scenario the hot plasma losses from the pedestal region through the separatrix with a rate determined by the specified deposition energy Q and the duration τ of the ELM. It is assumed that the lost plasma appears then in SOL having an exponential density profile with some maximum density at the separatrix. The hot plasma propagates towards the CFC divertor armor legs, heats them and causes vaporization at their surfaces. The carbon vapor propagates backwards finally filling the whole SOL.

According to the simulation, the main contribution to the radiation flux arises from a few strong carbon lines. For adequate simulation of line radiation the opacity data of FOREV have been upgraded to better resolve their line shapes. The radiation at the main lines centre is obtained to be substantially reabsorbed which deforms the line profiles (see Fig. 1). The numerical results are compared with the available experimental data. Simulation of ELMs in JET resulted in a reasonable agreement with measured total cooling rate of 20 MW, but the

calculated cooling rate of 35-50 MW obtained in the simulation is strongly dependent on the ELM scenario.

Several simulations of type I ELMs in ITER at $Q = 1$-3 MJ/m^2 and $\tau = 0.1$-0.5 ms revealed that there are two different regimes of radiative cooling. The first can be characterized by low carbon plasma temperature less than 6 eV and high cooling rate, when all the heating power from the pedestal plasma is dissipated by radiation and the impurity temperature keeps low. In this regime the radiative cooling rate can be comparable with the ITER fusion power of 0.5 GW. The second regime occurs when the carbon density is low. The heating power becomes to be sufficient to overcome the radiation barrier. In this case the carbon plasma temperature increases up to 40-50 eV and the radiative cooling becomes 2-3 orders of magnitude lower than that in the first regime. The carbon impurity absorbs about 1 keV per carbon atom, spending the energy for ionization. A typical radiation flux distribution calculated at the first wall is shown in Fig. 2 corresponding to a time moment when the carbon plasma is distributed almost uniformly along the separatrix in SOL and in the divertor legs. The maximal radiation heat load is on the dome and adjoining parts of divertor most filled with the radiative impurity. A smaller peak of the radiation flux is seen at the top of the main chamber, where the plasma thickness is rather large due to a divergence of the poloidal magnetic field.
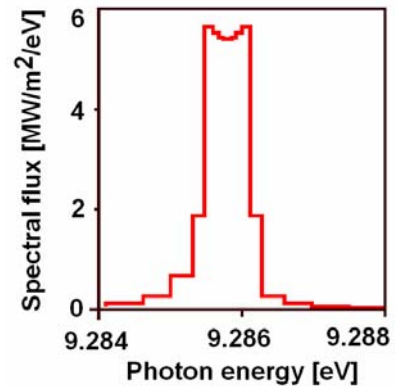
Fig. 1.: Spectral radiation flux in vicinity of a strong line.
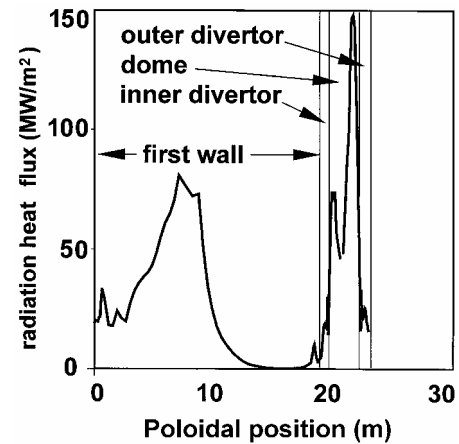
Fig. 2: Radiation load onto ITER vessel walls (results of FOREV-2D)

3. Melting of W-brush's surfaces

The main disadvantage of bulk tungsten armor is surface cracking under the high heat loads typical for intense transient events with $Q > 1$ MJ/m^2 and $\tau > 0.1$ ms. One possibility to mitigate the surface cracking is the tungsten macrobrush armor (W-brush). For the disruptions the most important mechanisms of metallic armor damage are surface melting and melt splashing. Single giant ELMs also result in melting and evaporation, and in the vapor shield which generates the motion of the melt layer due to pressure gradient along the target surface. However, because of a rather short time of ELMs and moderate velocities of melt motion the melt splashing seems to be negligible.

The melt layer erosion of the W-brush armor under the heat loads caused by single and multiple transient events was numerically investigated using the code MEMOS-1.5D in assumption of the flat melt surfaces [3]. The melt motion is described in the "shallow water" approximation, with the surface tension, viscosity of molten metal, and the radiative losses from the hot surface taken into account. The plasma pressure gradient along the divertor plate, the gradient of surface tension and the Lorentz force cause the melt acceleration. A two-dimensional heat transport equation with two boundary conditions at the moving vapor-liquid- and liquid-solid interfaces describes the temperature inside the target. Temperature dependent thermophysical data are used.
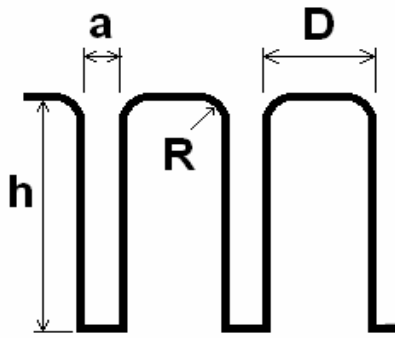
Fig. 3: Macro-brush target schematically.

To take into account the main features of the macro-brush geometry the code MEMOS has been upgraded [4]. For avoiding sharp brush edges (see Fig. 3) it is assumed that their shape is an arc with a radius R of about 1 mm. For the macrobrush target a continuous surface consisting of a sequence of top-brush sections, the circular segments, the lateral-brush sections, and the gap-bottom sections is implemented. A non-uniform curvilinear orthogonal numerical grid (x,z) with the coordinate x along the surface and the coordinate z directed inside the target fits the whole surface. It is assumed that the melt moves always along the surface without separation from the melt bottom and without droplet formation, including the arc segments between the tops of W-brushes and their lateral surfaces. The value of the melt velocity is assumed constant at the edge arcs where the centrifugal force appears. The tangential friction force appearing due to the momentum transfer from inclined plasma stream dumped onto the target surface is included. Distributions of the heat load and the plasma pressure at all macrobrush elements are recalculated taking into account the geometric features of the target and plasma shield. The heat loads at the lateral surfaces are determined by the radiation from the shielding layer.

The first validation of the code is performed against experiments on W-macrobrush target erosion under repetitive plasma loads for the heat load at the plasma gun facility QSPA. A castellated tungsten target consisting of separate elements of sizes D of 10x10x3 mm^3 with separation gaps of the width $a = 0.3$ mm was exposed to repetitive pulses of heat loads of $Q \sim 1.5$ MJ/m^2 and $\tau \sim 0.5$ ms with inclined plasma impact under the inclination angle of 20 deg. The experimental profile was obtained to be well reproduced by the numerical simulations.

Several scenarios for single giant ELMs and single moderate disruptions have been simulated. The W-macrobrush armour is assumed to consist of separate elements of sizes $D = 1$ cm, $R = 0.5$ mm, $a = 0.3$, 0.5 and 1 mm. In the test simulations the Lorentz force is omitted. Erosions of the macrobrush target and the bulk tungsten target are compared under the same heat load conditions. A giant ELM load with $Q = 3.5$ MJ/m^2 and $\tau = 0.5$ ms taken as the ITER reference scenario is modelled. The first disruption scenario corresponds to the mitigated disruption with $Q = 6$ MJ/m^2 and $\tau = 2$ ms. The second scenario corresponds to $Q = 15$ MJ/m^2 and $\tau = 5$ ms. The heat loads and plasma pressure distributions at the bulk tungsten target were calculated with FOREV-2D. In both scenarios the same peak energy flux at the target of 3 GW/m^2 was obtained.
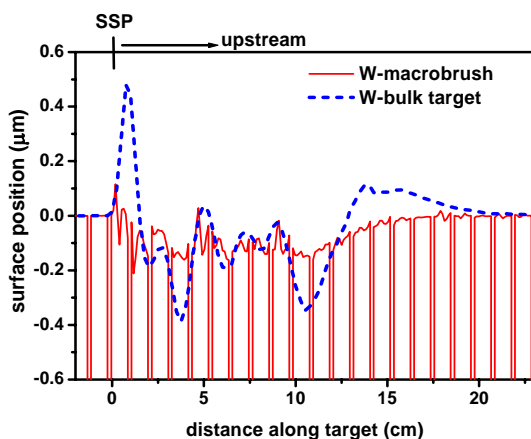
Fig. 4: Erosion of W-brush armour with a = 1 mm in comparison with that of bulk target (Q = 3.5 MJ/m^2, τ = 0.5 ms).

The MEMOS simulations of W-macrobrush armor damage under a single ELM and moderate disruptions demonstrated that radiation heat loads at the lateral surfaces of the W−brushe are not sufficient for melting; the surface temperature at the top-brush- and arc segments coincides with that calculated for the bulk target. The W-brushes melt depth correlates well with that of the bulk target both for ELMs and disruptions. Plasma pressure gradient causes the melt motion with the melt velocity along the bulk target about 0.6 – 1 m/s whereas velocity of melt motion along the top-brush segments does not exceed 0.1 m/s for both ELMs and disruptions. Because of the rather small surface temperature

at the lateral surface, the penetration of melted material into the gaps is negligible. The small sizes of W-brush faces prevent the violent melt motion and decrease the melt erosion of W-brush armor. In case of giant ELMs surface roughness of the W-brush drops to 0.1 µm (see Fig. 4.) which is small compared to that 0.5 µm of the bulk target. For the giant ELMs the final erosion profile of the W-brush armor becomes comparable with the evaporation profile. In the case of moderate disruption the surface roughness increases up to 0.5 µm for the first scenario and up to 2.0 µm for the second one, which is due to much longer duration of the melt motion, remaining still much less than it is obtained for the bulk target (where the surface roughness of 1.2 µm and of 5 µm respectively was obtained). For the moderate disruptions the final erosion profile of the W-brush armor slightly exceeds the evaporation profile.

5. Conclusions

In the radiation transport calculations for carbon impurity, the line radiation dominates. It is to note that the data for line shapes need further improvements, which demands significant effort for producing new opacities. Other experimental facilities could be used for simulation, for instance, the TEXTOR tokamak. Plasma diffusion in the pedestal and SOL should be taken into account in order to better estimate the density of carbon impurity in SOL and in the pedestal. For further validation of the code the measurements of the radiative cooling rate, of the amount of vaporized carbon and the electron temperature in the JET tokamak during ELMs with the time resolution of ~10 μs are necessary.

First validation of the code MEMOS-1.5D performed against experiments on W-macrobrush target erosion under repetitive plasma loads was successful. Numerical simulations demonstrated that for giant ELMs the W-macrobrush structure prevents violent melt motion: The velocity of melt motion drops more than for 3 times in comparison with the bulk armor and the final erosion of the W-brush elements significantly decreases. Further development of MEMOS is necessary, to take into account the real shape of brush elements for more accurate simulation of repetitive transient events. The validation of the code against surface temperature measurements at the plasma gun facility QSPA-T could be useful.

Staff:

I.S. Landman
S.E. Pestchanyi
B.N. Bazylev

Literature:

[1] S.E. Pestchanyi, I.S. Landman, H. Würz, "Hot plasma contamination in ELMs by divertor material", 30th EPS Conference on Contr. Fusion and Plasma Phys. St. Petersburg, 7-11 July 2003 ECA Vol. 27A, P-2.164 (compact disk)

[2] S. Pestchanyi, B. Bazylev and I. Landman, "Radiation losses from ITER SOL due to divertor material plasma", 31st EPS Conference on Plasma Phys. London, 28 June - 2 July 2004 ECA Vol.**28G**, P-1.135 (2004), avail. online: http://130.246.71.128/pdf/P1_135.pdf

[3] B. Bazylev, G.Janeschitz, I. Landman, S. Pestchanyi, "Erosion of tungsten armor after multiple intense transient events in ITER", Proc. 16 Int. Conf. on Plasma Surface Interaction, Portland, USA, 2004, to be published

[4] B.N. Bazylev, G.Janeschitz, I.S. Landman, S.E. Pestchanyi, "Erosion of macrobrush tungsten armor after multiple intense transient events in ITER". Proc. 23rd Symposium on Fusion Technology, Venice, Italy, 2004

TW4-TPP-TRIDEP
Studies of Hydrocarbon Formation and Redepostion in ITER Relevant Divertor Chamber Conditions

Carbon-based materials are preferably used in current fusion devices and are also intended to be used in ITER. On the other hand, the production of thick amorphous hydrocarbon films cause a significant problem, particularly because of the danger of tritium accumulation in such layers. A better understanding of the basic mechanisms leading to such layers and the identification of methods to avoid them are therefore highly desired. Carefully designed experiments as well as modelling calculations have been performed at the Humboldt University in Berlin for this purpose. The plasma generator PSI-2 offers the possibility to conduct such investigations aiming at the analysis of decomposition, transport and deposition of hydrocarbon molecules. To this end defined amounts of CH_4 (methane) and C_2H_4 (ethene) were blown into stationary plasmas. The thickness of the deposited layers on a collector (outside the plasma column) was measured in situ for different plasma conditions and gases and for different collector temperatures. ERO-code modelling with three different sets of atomic data were used for comparison.

In a first study [1] we found large differences between experiment and modelling for hydrogen and deuterium discharges: The observed layers were up to a factor of 5 thicker than predicted by the modelling. This disagreement could be reduced considerably by using more recent values for the sticking coefficient of CH in the modelling (see Table 1) and applying the adequate density of the layers for evaluation of the experiments.

The experiments were conducted in the PSI-2 device, a high current arc discharge. Between a heated LaB_6 cathode and a hollow Mo anode a current produces the plasma, which is guided by a magnetic field of B ≈ 0.1 T into the target chamber which extends over a length of about 1.5 m. The radial profiles of electron density and temperature are determined by Langmuir probes and these profiles are included in the modelling. For argon and hydrogen discharges the typical electron temperatures are T_e = 4 … 8 eV for discharge currents of I = 50…300 A. On the other hand, the electron density shows a pronounced increase with current (Ar: n_e = 0.2 to $5 \cdot 10^{18}$ m^{-3}). The diameter of the plasma column is locally varying along the axis and in the range of 6 to 8 cm. In the middle of the target chamber a floating, temperature controlled flat collector is positioned in a distance of 6 cm to the plasma edge. Furthermore, it is equipped with an annular limiter (2 cm in height) that protects the collecting

Fig. 1: Film thickness vs. time for a low density discharge with C_2H_4 injection. The growth rates are seen to be independent of the position of injection (Nozzle: opposite to collector, Valve: remote from collector)

area from ion and electron bombardment. The film thickness is determined by illuminating the Si-wafer being attached to the collector with white light and recording the reflected spectra. The optical parameters of the a-C:H films, needed to determine the film thickness, were measured by ex situ ellipsometry. There are two possibilities for hydrocarbon injection: 1) opposite to the collector via a nozzle being located close to the plasma edge, and 2) remote from the collector via a valve being located on the same side but 40 cm upstream at a distance of 15 cm to the plasma.

During the last year we concentrated mainly on Ar plasmas for scanning a wide range of plasma parameters. Moreover, in hydrogen discharges the situation is more complicated due to the erosion of the a:CH films by atomic hydrogen. This erosion mechanism is not yet in-

cluded in the modelling since some important parameters, such as the flux density and energy of the hydrogen atoms, are very uncertain.

The mechanism of hydrocarbon decomposition can be described as follows: For low electron density only a very small fraction of the injected hydrocarbons is immediately disintegrated to species with high sticking probability. They form amorphous C:H films only near to the position of injection. The non-sticking particles are reflected one or more times at the wall before entering the plasma a second time. After a number of such cycles they are eventually converted into a well sticking particle which, in general, is deposited at the wall remote from the injection position. For the same conditions a relatively large fraction ($\approx$ 10%) of the particle input can be pumped off. Furthermore, we expect a fairly homogeneous film formation all over the inner walls of the chamber. Or, in other words, the film formation under low electron density conditions is not a local but rather a global process: deposition is independent of the position of injection. A typical example confirming this statement is shown in Fig. 1 for an argon plasma (n_e =2*10^{17}m^{-3}, T_e = 3 eV). The results can also reasonably be explained by estimating the growth rate for injection of 0.5 sccm C_2H_4 (1.35·10^{19} molecules per min) into the plasma. Finally all hydrocarbons stick on the wall of a cylinder of 1.2 m length and 0.2 m diameter (target chamber). This results in a deposition of 3.6·10^{15} C-atoms/(cm^2 min). For a soft film with a density of 1 g/cm^3 (equivalent to 5·10^{15} C-atoms/(nm*cm^2)) the averaged growth rate is thus estimated to be 0.72 nm/min., i.e. slightly larger than the experimentally determined growth rate in Fig. 1 which varies between 0.48 to 0.60 nm/min.
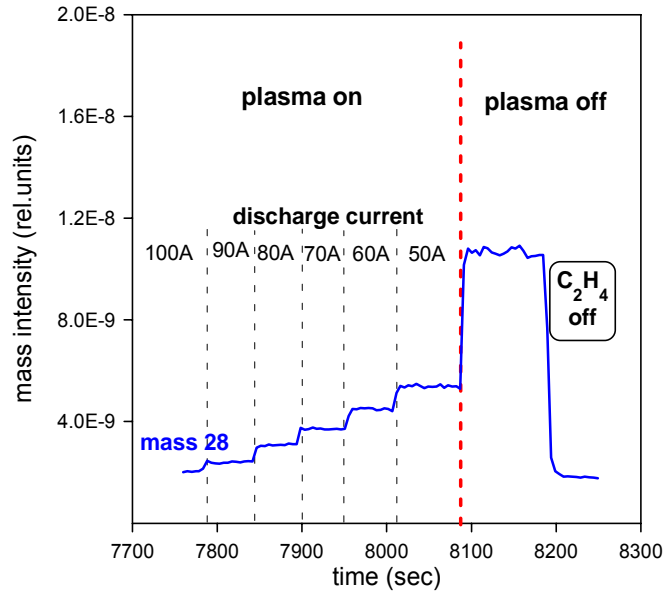
Fig. 2: Normalized mass spectrometer signal for ethene injection. Lowering the current (n_e) results in reduced disintegration of the molelules.
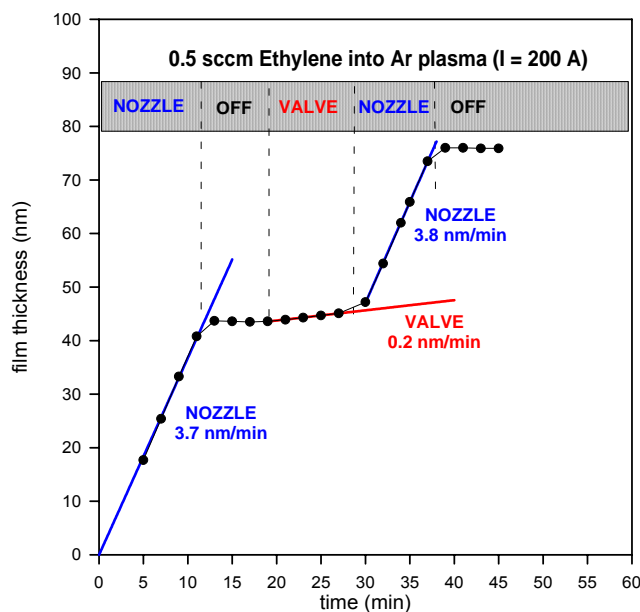
Fig. 3: Film thickness as a function of time for "nozzle" and "valve" injection into a high density plasma demonstrating the effect of local deposition.

The increasing probability of disintegration with electron density is demonstrated in Fig. 2.. Here the detected density of ethene (atomic mass number 28) is shown for the cases "with" and "without" Ar plasma when a constant ethene flux of 0.5 sccm is injected into the vessel. For 100 A discharge current we detect a relatively low C_2H_4 density (about 10 % of the value without plasma). Thereafter the discharge current is ramped down and we notice an increase in ethene density with decreasing current (i. e. decreasing electron density). When switching off the discharge, a further increase by a factor of 2.5 is to be noticed.

For higher electron densities (n_e > 10^{18}m^3) we expect a more local disintegration. Most of the injected hydrocarbons will be decomposed to high sticking

particles already during the first passage through the plasma. For such conditions the film growth rate depends strongly on the position of hydrocarbon injection. An example is given in Fig. 3 showing a significant difference (factor 18) in film growth rates for "nozzle" and "valve" injection into an argon discharge (n_e = 4.5*10^{18} m^{-3}, T_e = 5 eV).

Such a local deposition can be described very well by 3-D Monte Carlo code ERO [2]. For these conditions the mean free path length for the decomposition process is comparable or smaller than the characteristic dimensions used in the modelling. All processes like impact ionisation by electrons, dissociation, dissociative excitation, ionisation and recombination as well as charge exchange collisions are included in the modelling. As a result of modelling the numbers of the various particles impinging on the collector plate are obtained in a first step. Multiplying these numbers with the specific sticking coefficients and summing over all species yields the total number of hydrocarbons forming the a-C:H film. For a given input flux of CH$_4$ or C$_2$H$_4$ the growth rate of the film can thus be predicted and compared with the experimental values. All species of type C$_x$H$_y$ and C$_x$H$_y^+$ with x = 1, 2 and y = 1, 2,…6 are included in the calculations. The corresponding 22 species are listed in Tab.1. The label number assigned to them is used in Fig. 4 as abscissa. The graphs shown in this figure demonstrate that a wide spectrum of hydrocarbons is produced in the plasma that can hit the collector. However, only four species (#6: CH, #8: C, #16: C$_2$H$_3$, #20: C$_2$H) out of these do contribute to film formation. Quantitatively, for the injected flux of CH$_4$ an integral film growth of 1.9 nm/min is predicted. This value has to be compared with 3.7 nm/min found in the experiment (Fig. 3).

Table 1: Hydrocarbons and their sticking coefficients.

#	C$_x$H$_y$	Sticking
0	CH$_4$	0
1	CH$_4^+$	1
2	CH$_3$	0.001
3	CH$_3^+$	1
4	CH$_2$	0.026
5	CH$_2^+$	1
6	CH	0.26
7	CH$^+$	1
8	C	1
9	C$^+$	1
10	C$_2$H$_6$	0
11	C$_2$H$_6^+$	1
12	C$_2$H$_5$	0.01
13	C$_2$H$_5$+	1
14	C$_2$H$_4$	0
15	C$_2$H$_4^+$	1
16	C$_2$H$_3$	0.35
17	C$_2$H$_3^+$	1
18	C$_2$H$_2$	0
19	C$_2$H$_2^+$	1
20	C$_2$H	0.8
21	C$_2$H$^+$	1
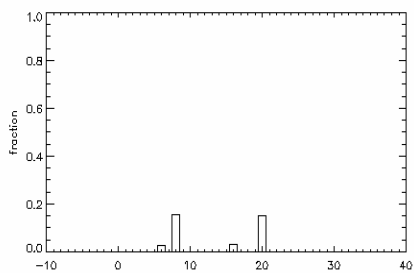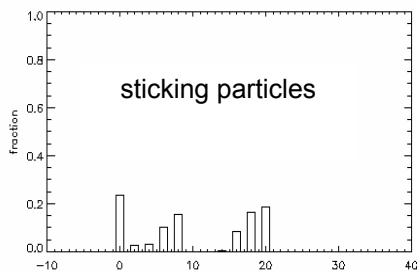
Fig. 4: Flux of impinging and sticking particles modelled by ERO for a 200 A discharge in argon.

The modelling results are thus in fair agreement with the experiments although modelling is becoming difficult and uncertain for the very low density range.

Staff:

W. Bohmeyer [2)]
D. Naujoks [2)]
G. Fussmann [1)]
A. Markin [3)]

1) Humboldt Universität zu Berlin, Institut für Physik
2) Association Euratom-Max-Planck Institut für Plasmaphysik, Germany
3) Institute of Physical Chemistry, Russian Academy of Sciences, Moscow, Russia

Literature:

[1] Bohmeyer,W., D. Naujoks, A. Markin, B. Koch, D. Schröder and G. Fussmann, *Transport and Deposition of Injected Hydrocarbons in Plasma Generator PSI-2*. Proc. of the 16th Int. Conf. on Plasma Surface Interaction, PSI-16, Maine, USA (2004), published in JNM

[2] Naujoks, D., Coster, D., Kastelewicz, H., Schneider, R., J. Nucl. Mater. 266-269 (1999) 360-364.

Divertor and Core Plasma Modelling for ITER

1. Introduction

The goal of the core and divertor plasma modelling program is the development, improve-ment, and application to ITER of a set of modelling codes which describe the ITER plasma from the core to the divertor plates in a coherent way so as to permit a consistent prediction of ITER plasma operating modes, operating windows, performance, and scenarios. Two separate codes are used for this purpose: the 2D coupled fluid-Monte Carlo code B2-EIRENE for two-dimensional modelling of the ITER divertor and scrape-off layer, and the ICPS model incorporated into the 1D ASTRA transport code for one-dimensional modelling of the ITER core and pedestal. The two codes communicate by means of scaling laws de-rived for the separatrix parameters from stand-alone runs of the codes. A variant of the model, which uses a simpler two-point model for the scrape-off and divertor plasma, is used to fit results from the experiments. Quantitative predictive modelling of ITER is done with the more complete model.

ITER performance modelling, crucial to establish the expected performance of ITER and to define the operating scenarios to obtain this performance, can be carried out only with such an integrated plasma model which describes in a coherent way the entire plasma from the centre via the pedestal and the scrape-off layer to the divertor plate. Our model has been developed in the framework of a quadripartite collaboration (FZ Karlsruhe, ITER International team, Hydro-Québec, Varennes, Québec, Canada, and INRS-EMT, Varennes, Québec, Canada), as described in previous Annual Reports.

The previous version of the model and the results obtained were described in the Annual Reports Sept. 2001-2002 and Sept. 2002-2003 and references therein, as well as in [1]. Ini-tial results obtained in 2004 were described in [1]. Advances in ITER 2D divertor modelling were described in [2], [3], with particular emphasis on scaling results with realistic carbon surfaces and variable erosion yields [2] and the consequences of the introduction of a more complete neutral model [3]. Advances in 1D modelling of the plasma core were described in [4], with particular emphasis on the modelling of improved H-modes. Work on ELM triggering, performed by the Lehigh University group in collaboration with us, was described in [5]. There were two presentations to the ITPA meetings in Lisbon [6], [7]. The work in [2] to [5] is also summarised in [8].

2. Divertor Plasma Modelling

As reported in the previous Annual Reports and [1], a major new initiative in two-dimensional modelling of the ITER divertor plasma has been the introduction of "realistic surfaces", i.e. metallic surfaces having realistic carbon deposition and erosion. An important extension of this work in 2004 has been ITER simulations with various values of the erosion yield of the redeposited carbon. As a result of these simulations, it has been found that the scaling of the transition point (near which the inner divertor plasma detaches) differed from the former metal or carbon wall cases. All the results can be described in terms of a normalised pres-sure $\mu = \left(\Gamma_{\#} / S_{\#} \right) P_{\#}^{-0.87} f_{f}^{-0.8} f_{w}^{-1} q_{\#}^{-0.27}$, which now includes a factor f_{w} which depends on the erosion yield and the type of wall [2]. The older metal wall calculations were less realistic because they assumed that all the carbon incident on the metal walls was absorbed there but that the surface characteristics were unchanged and remained those of the metal wall. In contrast, the present calculations are more realistic since they maintain a metal wall with metal characteristics only in those areas for which the net erosion exceeds the net deposition (i.e. no net carbon is deposited), and the surfaces adopt the characteristics of the rede-posited carbon only in those areas where deposition exceeds erosion. Typical results of fit-ting the scaling relations to the simulations are illustrated in Fig. 1.
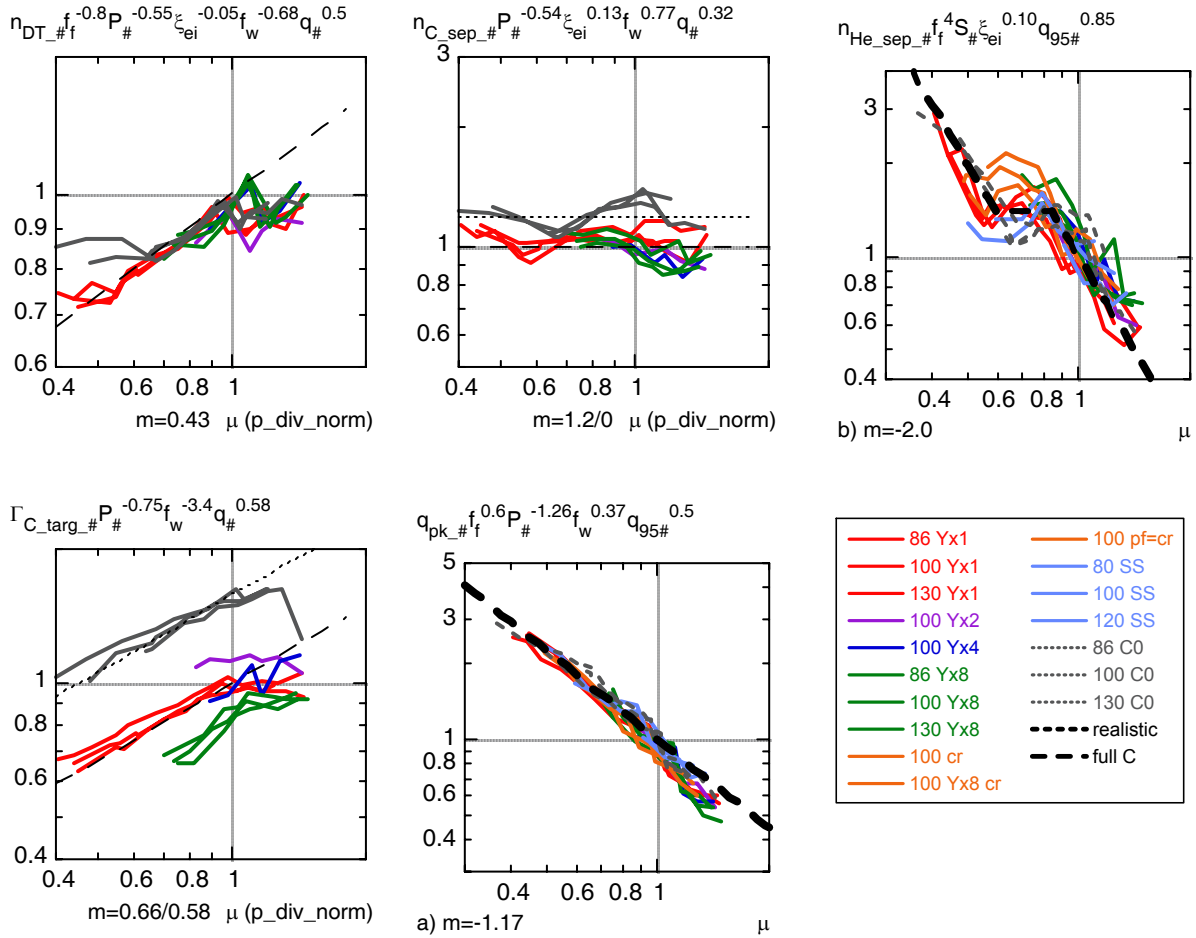
Fig. 1: Scaling of normalised DT, carbon and helium densities, carbon erosion flux and peak power to divertor plate with varying erosion yields, simple neutral model. Definitions and scalings in [2].

On the whole, as shown in [2], the parameters of full carbon walls and realistic surfaces follow the same scalings once the wall factor is introduced. The exception to this is the carbon density and the target erosion: because for full carbon walls the effective area which emits carbon is higher (surfaces which are net erosion surfaces in the realistic wall case emit more carbon than they receive in the full carbon wall case), at the same μ full carbon walls have 20% higher carbon content and 60% higher carbon erosion flux than the realistic wall cases, reflecting the carbon release in the erosion-dominated areas for that case. Note also the strong decrease in target erosion flux as erosion yield Y_{C_dep} increases (variation of the erosion flux as $f_w^{3.4}$). The helium-related quantities cannot be expressed as a simple power law, as Fig.1 shows. However, the results confirm that, for the reference case (realistic surfaces, $Y_{C\_dep} = 1$, inductive operation, 100 MW power from the core) at the highest divertor pressure ($\mu = 1$), helium pumping is relatively uncritical, i.e. the helium concentration at the separatrix is below 1% and the inward helium neutral flux is less than 1/3 of the helium production rate by fusion reactions of 0.64 Pa-m^3/s. Thus, new scalings have been developed [2] for the edge plasma parameters, unifying the data obtained with different carbon re-erosion properties and different connection lengths. These scalings form a new set of boundary conditions for the core models, allowing analysis of the operational space of ITER in a consistent way, for both the standard inductive and steady-state operation.

In further work described in [3], the neutral transport model for the ITER divertor is extended to include neutral-neutral collisions and molecular dynamics, particularly the ion conversion process (MAR) and elastic collisions of molecules with the plasma ions. This new model has

been applied to a limited number of cases at present. The most pronounced effect of these model extensions is a significant increase of the neutral pressure in the PFR for the same plasma parameters. A new factor f_{nn} (1 for the simple neutral model, 1.18 when only neutral-neutral collisions are included, 1.83 for the full neutral model) must be introduced in the normalised neutral pressure, which becomes $\mu = \left(\Gamma_{\#}/S_{\#}\right)P_{\#}^{-0.87}f_{f}^{-0.8}f_{w}^{-1}q_{\#}^{-0.27}f_{nn}^{-1}$. The results are illustrated in Fig. 2.
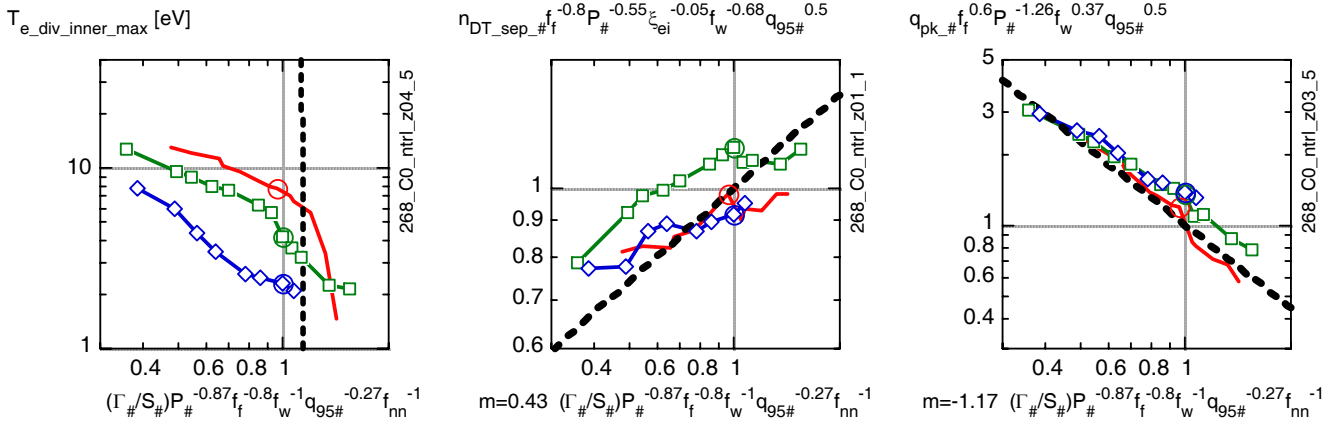
Fig. 2: Scaling of maximum temperature at the inner divertor, normalised DT density, and peak power to divertor plate with simple neutral model (circles), neutral-neutral collisions (squares) and full neutral model (lozenges). Definitions and scalings in [3].

These initial results indicate that (a) introduction of the molecular dynamics package leads to plasma detachment of the inner divertor at a higher neutral pressure, (b) the operational window of the ITER divertor retains the same width but shifts to higher neutral pressure in the PFR, and (c) the parameters of the interface to the core at the transition point remain approximately the same.

3. Core Plasma Modelling

As reported in previous Annual Reports and [1], the Integrated Core-Pedestal-SOL (ICPS) model has been continuously modified and improved, so that it now models core energy transport with the MMM95 transport coefficients, stabilized by a combination of ExB velocity flow shear and magnetic shear in order to obtain an edge pedestal. For ITER modelling, the boundary conditions (separatrix parameters) for the core model are self-consistently determined by scaling relationships, obtained from a database of B2-Eirene runs for the ITER SOL and divertor. The model also includes neoclassical accumulation of the carbon intrinsic impurity, with a separatrix density determined from B2-Eirene modelling.

In the present period, the model has been modified as follows. The shear correction to account for an X-point described previously has been removed, since comparison with detailed equilibrium calculations had shown the correction to be much smaller than had been derived analytically. The effect of this change on the results is minimal. ETG transport, which is not stabilized by flow shear, has been added to the electron channel, because the predicted pedestal electron temperatures were systematically higher than the AUG experimental values, whereas the ion temperatures already showed good agreement. Also, the beam particle source previously used was too small by a factor of almost two, and this is now corrected. With these improvements, good agreement is now obtained for both electron and ion pedestal temperatures in AUG (fig. 3).
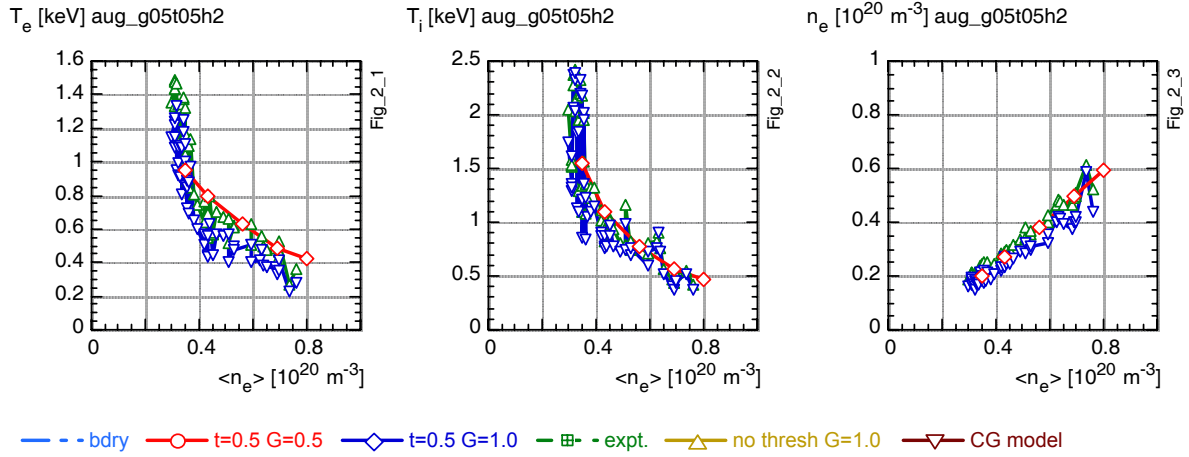
Fig. 3: Comparison of simulations (red lines and symbols) with experimental database for Asdex-UG for temperatures of electrons (left), ions (middle), and electron density (right).

The major emphasis has been placed on the development of a model for improved H-modes, specifically those characterized by low magnetic shear with central q close to but somewhat larger than unity. Such H-modes have been achieved in AUG with off-axis current drive by neutral beams and are considered promising candidates to obtain improved confinement in ITER. To model this operation, we postulate a turbulent transport reduction in regions for which the low order rational q surfaces are sparse. A "sparseness function" is therefore defined, depending on the q-profile but approximately machine-independent, whose value allows a good discrimination between normal and flat q-profiles. Below a threshold value, the turbulent transport is reduced by a given factor. The strength of the stabilization is adjusted so that the central temperatures and the H-factor improvement correspond to those obtained in AUG. The same model then replicates also the temperature increases and H-factor improvement observed for a similar type of discharge on JET.

The ITER simulation represents conditions for which the q profile is established and frozen in during rampup such that the resulting q profiles are similar to those obtained for AUG and JET. The total current is reduced to 12 MA, resulting in an edge q of ~4.5. The results are shown in Fig. 4 for an average density of ~90% of the Greenwald limit n_{GW}. When the stabilisation due to the sparseness of rational surfaces is applied, both electron and ion temperatures rise and the H factor increases by 20% (from H98y2 = 1.25 to 1.47), half of which is the direct result of the flattened q profile. The other half comes from the transport reduction by a factor of 5 in the flat q region. Despite the improved confinement demonstrated here, the fusion power does not increase with the transport reduction because anomalous particle transport in the model is proportional to turbulent energy transport. Neoclassical accumulation of carbon then results in fuel dilution and even reduces the alpha heating power density somewhat despite the increase in central temperature. The corresponding total fusion power goes from 260 MW with the normal profile to 210 MW (see. fig.4 - top row).

The carbon accumulation will probably be less severe than in the example above. Indeed, experiments indicate that both passive (e.g. fishbones) and active (e.g. central electron heating) methods are effective in limiting impurity accumulation. If passive or active mitigation is successful in maintaining the carbon profile similar to that obtained for the normal current profile case, the peak alpha heating power density increases (fig. 4). The corresponding total fusion power then rises from 260 MW to 436 MW (Q ~ 5 initially in this low-current case, rising to Q ~ 8.5 in the improved H-mode condition).
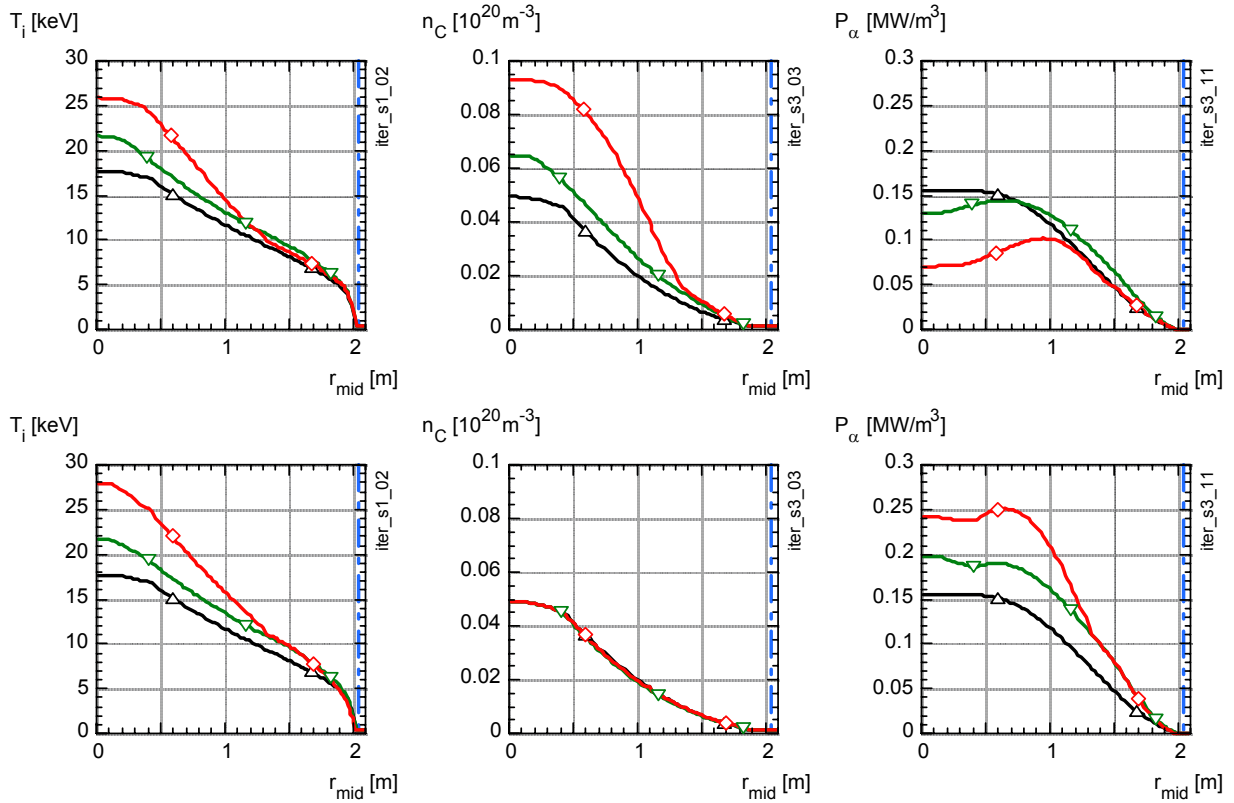
Fig. 4: Simulation for ITER parameters (B=5.3 T, I=12 MA) showing radial profiles of: ion temperature (left), carbon density (centre), and alpha heating power density (right). Top row without impurity accumulation mitigation, bottom row with very effective mitigation such that no accumulation occurs because of improved confinement. All profiles for same additional heating power: black - normal current profile, green - ~0 shear, red - ~0 shear with transport reduction of 1/5.

4. Perspectives

Work on divertor and core modelling for ITER is continuing, with particular emphasis on:

- In two-dimensional modelling of the ITER scrape-off and divertor plasma, application of the improved neutral model to a wider range of ITER parameters including variation of the input power and fuelling scheme, development of scaling relations for these conditions, implementation in the code of the Lyman alpha radiation transport in the divertor plasma, variations of ITER geometry and plasma position, and examination of existing simulations of ASDEX Upgrade and/or JET to generate scaling relations for these devices

- In one-dimensional modelling of the plasma core, detailed improvement and validation of the stabilization model including further development of the implementation of multi-mode transport, validation of the impurity accumulation and implementation of time-dependent impurity transport, extension of the impurity treatment, and application of the model to density limits, advanced operating modes, and improved H-mode scenarios for ITER.

Staff:

H. D. Pacher (INRS-EMT, Varennes, Québec, Canada)
G. W. Pacher (Hydro-Québec, Varennes, Québec, Canada)
A. S. Kukushkin (ITER International Team)
G. Janeschitz
I. Landman, S. Pestchanyi, with the collaboration of G. Pereverzev (IPP Garching).

Literature:

[1] Pacher H.D., Pacher G.W., in collaboration with ITER IT Garching, FZ Karlsruhe, Max-Planck-Institut für Plasmaphysik Garching, EFDA CSU Garching, "Divertor and core plasma modelling for ITER - Final Report June 2004", INRS Energie, Mat. et Télécom. Report, 2004, INRS-EMT-09-0604, July, 2004

[2] Kukushkin A.S., Pacher H.D., Coster D.P., Pacher G.W., Reiter D., "ITER divertor performance in conditions of carbon re-erosion", 16th Conf. on Plasma-Surface Interactions Portland, 2004

[3] Kukushkin, A. S., Pacher, H. D., Kotov, V., Reiter, D., Coster, D., Pacher, G. W., "Modelling Studies of ITER Divertor Plasma", Proc. 20th IAEA Fusion Energy Conf. Vilamoura, 2004, to be submitted to Nucl. Fusion

[4] Pacher G. W., Pacher, H. D. , Janeschitz G., Kukushkin A. S., Coster D., Pankin A., Pereverzev G., Voitsek-hovitch I., "Modelling of ITER Improved H-mode Operation with the Integrated Core Pedestal SOL Model", Proc. 20th IAEA Fusion Energy Conf. Vilamoura, 2004, , , Congrès, to be submitted to Nucl. Fusion,

[5] Pankin A.Y., Bateman G., Brennan D.P., Schnack D.D., Snyder P.B., Voitsekhovitch I., Kritz A.H., Janeschitz G., Kruger S., Onjun T., Pacher G.W., Pacher H.D., "ELM triggering conditions for the integrated modeling of H-mode plasmas", Proc. 20th ICPP International Congress on Plasma Physics, Nice, 2004 Transport", pres. to ITPA TG on Edge and Pedestal Physics, October 2003 (2002)

[6] Kukushkin A.S., Pacher H.D., "Critical Issues in SOL&Divertor Operation in ITER: Modelling-Assisted De-sign", presented to ITPA Topical Group on Divertor and SOL Physics, Lisbon, 2004

[7] Kukushkin A. S., Pacher H. D., Pacher G. W., Polevoi A.R., "Fuelling Requirements for ITER", presented to ITPA Topical Groups on Divertor and SOL Physics and Edge and Pedestal Physics, Lisbon, 2004

[8] Pacher H.D., Pacher G.W., in collaboration with ITER IT Garching, FZ Karlsruhe, Max-Planck-Institut für Plasmaphysik Garching, EFDA CSU Garching, "Divertor and core plasma modelling for ITER - Intermediate Report December 2004", INRS Energie, Mat. et Télécom. Report, 2004, INRS-EMT-012-1104, December, 2004, in preparation

Heating and Current Drive

TW3-TPHE-ECHULA
Physics Analysis, Prototyping and Beam Line Mock-up Tests for the ITER ECRH Upper Launcher

Subtask B: Launcher Structural Design Integration

Objectives

The ITER electron cyclotron heating and current drive (ECH&CD) system uses several upper port plug systems which are composed of the port plug ("launcher") attached to the port flange of the vacuum vessel (VV) and of an interspace plug ('mini-duct') inside the port duct connecting the VV to the cryostat/biological shield. Integral part of the systems is also the test cell for the launcher and the hot cell installations for maintenance and repair of the launcher satisfying remote handling (RH) requirements. The objective of this task is to ensure the integration of the upper port plug system into the ITER boundary conditions. In particular the structural elements are developed for integrating the EC-wave (mm- wave) beam line elements into the port plug.

Deliverable b.1
Basic elements of the upper launcher design activity

The launcher is composed of the blanket shield module (BSM), the millimetre wave (mm-wave) system integrated into internal shields, the port plug frame ('main structure'), the closure plate forming the boundary between the in-vessel part and the back section, and the connecting flange to the VV (cf. Fig.1). The BSM includes the first wall panel, shielding elements, and side walls attached to the mounting flange. In the BSM structure, penetrations for mm-wave beams and space for potential integration of the front mirrors are foreseen. The mm-wave system includes fixed and steering mirrors, waveguides and vacuum windows with their cooling channels. 'Dog-leg' structures for reducing neutron streaming along straight waveguide channels are preferably avoided to allow axial disassembly, which is potentially obstructed by inserted mitre bends.

Flange connection to VV   Port plug frame (main structure)   Blanket shield module (front shield)

Closure plate

Millimeter wave system   Internal shield
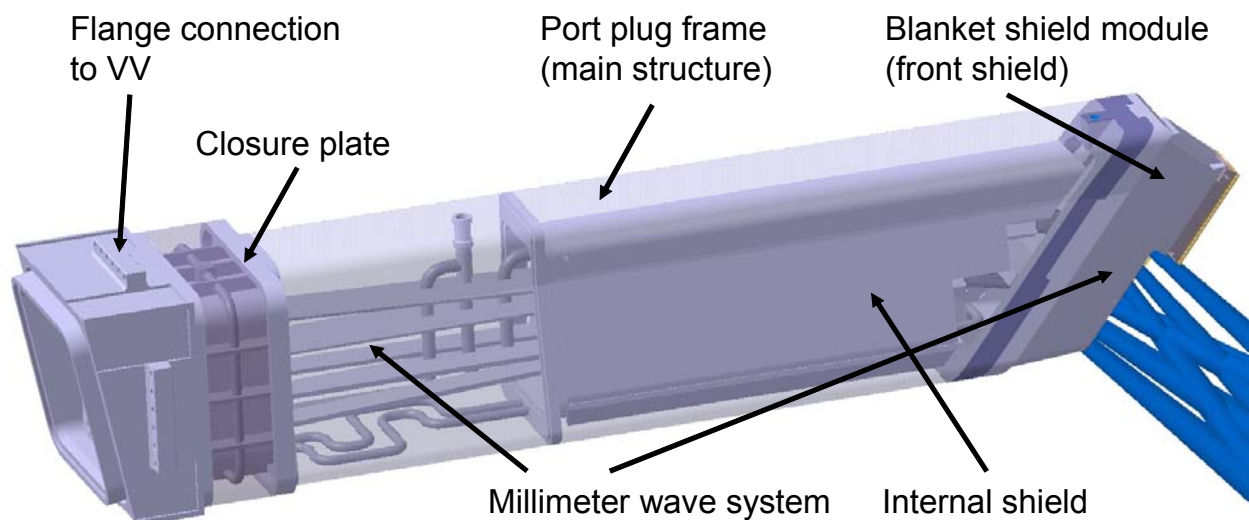
Fig. 1: Basic elements of the ITER ECRH Upper Launcher.

The CAD design activities are shared with the mm-wave engineering groups at FOM Rijnhuizen (NL) and CRPP Lausanne (CRPP). For the EU team, a documentation and a CAD design library was set up and is being maintained at FZK. The design is based on common structure and name conventions agreed for working models (in the form of CATIA

V5R12 products) stored at the design library. A reference model for the remote steering launcher was transferred to the ITER Design Office to be included at the working level.

Deliverable b.2
Perform mechanical, thermal and neutronics analysis on the Upper Launcher design

The aim of the deliverable is to determine the deflection of the port plug structure under external (especially electromagnetic) forces, to determine temperature and thermo-mechanical stress profiles in the front shield, and to quantify fast neutron fluxes along the wave guide structures and across the structural materials at the boundary of the port plug.

A preliminary mechanical analysis of the UPP launcher structure has been performed with the CATIA code. The geometrical model comprises the trapezoidal double-wall part of the main structure, that is fixed at the rear end and free to bend at the front end. The load cases studied include combined end loads typical for heavy disruption scenarios, unit end loads as forces and moments, distributed loads simulating the dead weight, and examples of special load conditions like internal pressure and thermal constraints. The results show good agreement with earlier estimates on launcher deflection under given electro-magnetic loads ranging up to about 10 mm at the front end. The maximum stresses in these pessimistic scenarios are tolerable.

Emphasis in thermo-mechanics was placed on the analysis of the front shield housing with ANSYS. It started with a simple unit cell model of the front panel and proceeded with a slice model, that represents the full width of the panel including the side walls, but at a quasi 2-dimensional simulation (cf. Fig. 2a,b). Meanwhile a complete 3-D ANSYS model of the front shield housing derived from the CATIA model is investigated (cf. Fig. 3). Stresses obtained so far under steady state conditions have not yet been evaluated firmly. Equivalent stress levels reach about 1.5 S_m in the beryllium zone, 0.9 S_m in the Cu-alloy zone, 1.5 S_m in the SS front tubes, and 1.3 S_m in the SS back plate. They are mainly of secondary type with peak values occurring very localised., so that the $3S_m$ criterion can likely be applied. Further studies, including transient situations, are in progress.

a)

b)
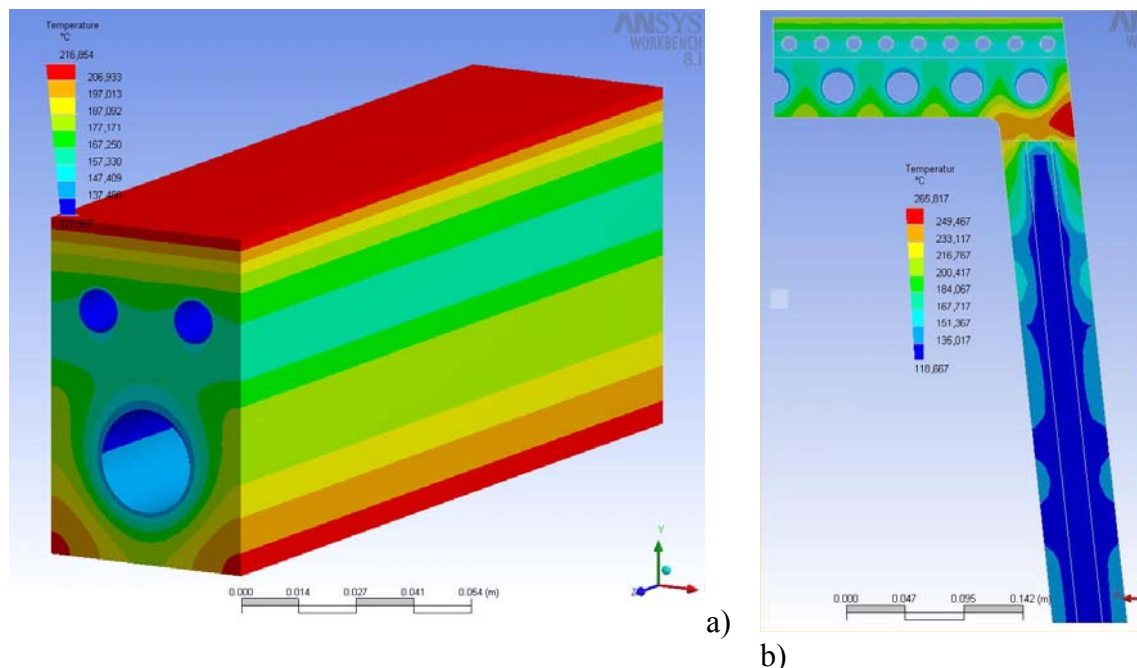
Fig. 2: Temperature distributions obtained for the housing of the blanket shield module by FEM analysis based on a simple unit cell (a) and a refined slice model (b).
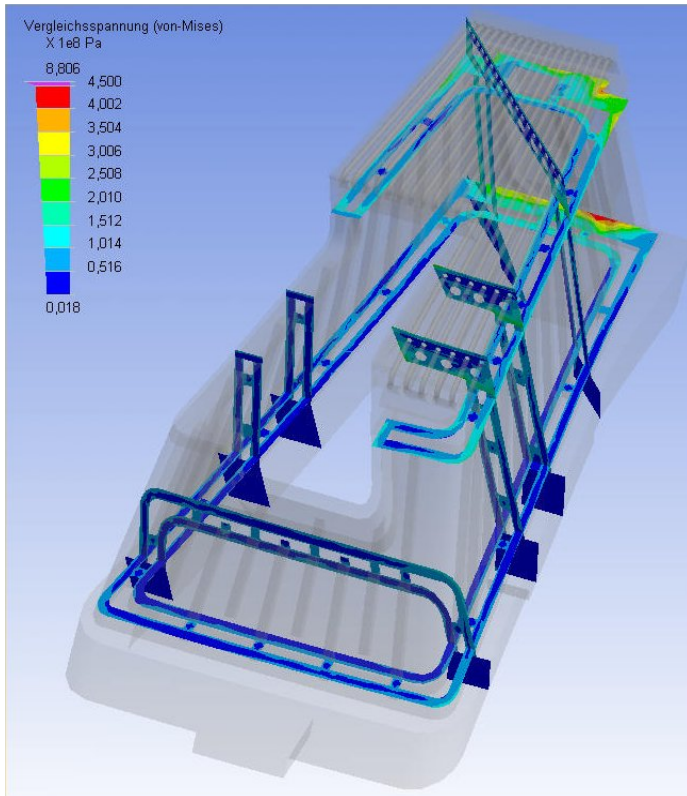
Fig. 3: Equivalent stress values simulated in different cuts using 3-dimensional model of the front shield housing.

The objectives of the neutronics analyses were (i) to assess the neutron streaming in the waveguide channels and show that the design limit for the radiation load to the CVD diamond window at the exit of waveguides can be met and (ii) to assess and optimize the shielding of the launching system to ensure the radiation loads to adjacent components such as the vacuum vessel (VV) are tolerable. The neutronics calculations have been performed with the Monte Carlo code MCNP [1]. A detailed three-dimensional (3D) geometry model of the ECW launcher system was generated from the underlying CAD model by an automated conversion (Fig. 4) and integrated into the upper port of the ITER MCNP model. The ECW launcher geometry with long (460 cm) and narrow (5 cm times 5 cm) waveguide channels necessitated the use of dedicated techniques for handling the neutron streaming. A two-step approach was applied to this end. First, a surface source was calculated at the entrance of the waveguide cannels using a full ITER torus sector model with reflective boundaries. This surface source was then used in the second run for calculating the neutron streaming trough the waveguide channels by using the point detector estimator [2].
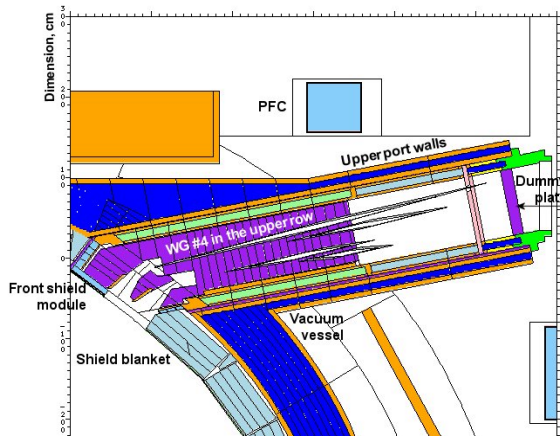
Fig. 4: MCNP model of the ITER upper port with the FF launcher integrated (radial-poloidal cross-section).
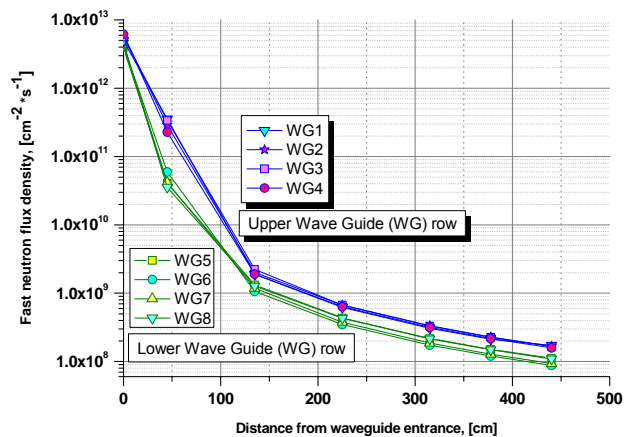
Fig. 5: Fast neutron flux profiles along the waveguides (FF launcher).

The limited focusing (LF) launcher with shield blocks in the front shield module showed a fast neutron flux attenuation from $(1.50 - 3.30)*10^{12}$ n*cm^{-2}*s^{-1} at the waveguide entrances to $(1.93 - 3.44)*10^{8}$ n*cm^{-2}*s^{-1} at the exits. With regard to fast neutron flux attenuation, the full focusing (FF) reference launcher model compares favourably with the LF launcher with filler blocks although there is a larger blanket opening, see Fig. 5 for the profiles along the waveguide channels. This is due to a less forward biased angular distribution of the neutrons entering the waveguide channels.

The calculations showed that the design limits for the fast fluence of 10^{20} m^{-2} at the CVD diamond window and the helium production rate in the VV (1 appm per year) can be safely met assuming an ITER operation of one full power year. It is noted that ITER will actually achieve no more than half a full power year over the scheduled lifetime of 20 years.

Deliverable b.3
Outline design of the neutron shielding elements for the Launcher, including the shielding blanket modules

The design work concentrated on detailing the front shield internals, i.e., the shield blocks and mirror attachments, and the necessary cooling piping. Also several approaches to the internal shield in the launcher main structure have been developed. The aim is to show a first consistent shield concept with all its space requirements and fixation means and to support the neutronics and thermo-mechanical analyses performed under Deliverable b.2 by providing appropriate CATIA models. Figure 6 gives a schematic overview of the launcher front end with its internals indicating the effort for maximum shielding performance, i.e., minimal openings for the beams.
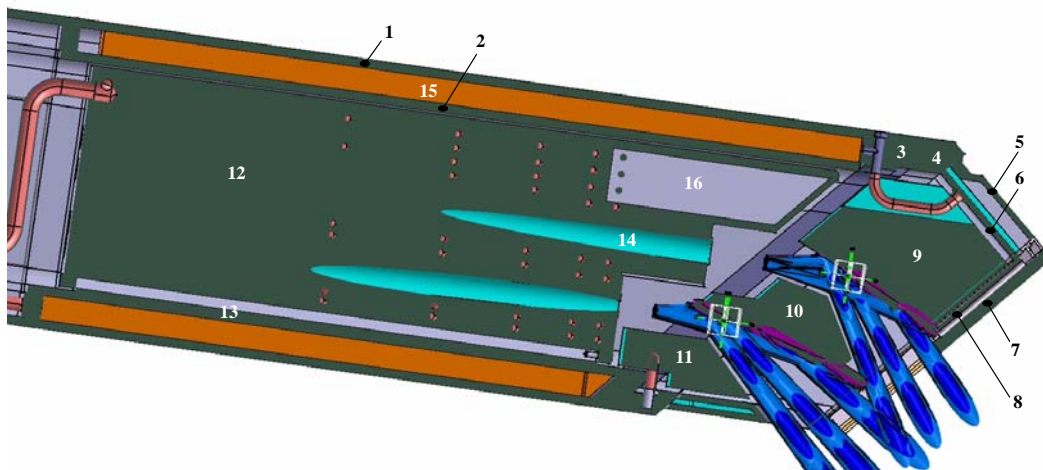
Legend:
1=Frame outer front ; 2=Frame inner front ; 3=Flange rear; 4=Flange front; 5=Front shield shell outer; 6=Front shield shell inner; 7=Front panel Cu & Be layers; 8=Front panel SS plate; 9=Shield front top; 10=Shield front middle; 11=Shield front bottom; 12=Shield internal; 13=Shield base plate; 14=Channels for wave guides; 15=Longitudinal ribs; 16=Shield tank (optional)

Fig. 6: Launcher front end with neutron shielding elements

The front shield houses two sets of fixed mirrors and must give way to the mm-wave beams. The rest of the volume is filled up with shielding material. Also cooling connections to and from the front shield as well as connections between the internals are incorporated. The two sets of mirrors have become extremely large, extending the front shield depth. Two variants of shield blocks have been outlined, the upper one as tank design with inserted steel plates to accommodate the desired water/steel fraction of 20/80, and the middle and bottom shields as solid blocks with machined cooling channels sealed by welded cover plates. Figure 7 illustrates the CATIA model of shield blocks, mirrors and pipes in the front shield with the front shield housing being masked out. The piping is designed as to provide a serial flow path from top to bottom (cf. Deliverable b.4). All of the front shield blocks are fixed to the front shield housing by bolts and key ways. Torques produced by EM forces shall be taken up by the positioning pads at top and bottom of the side walls.
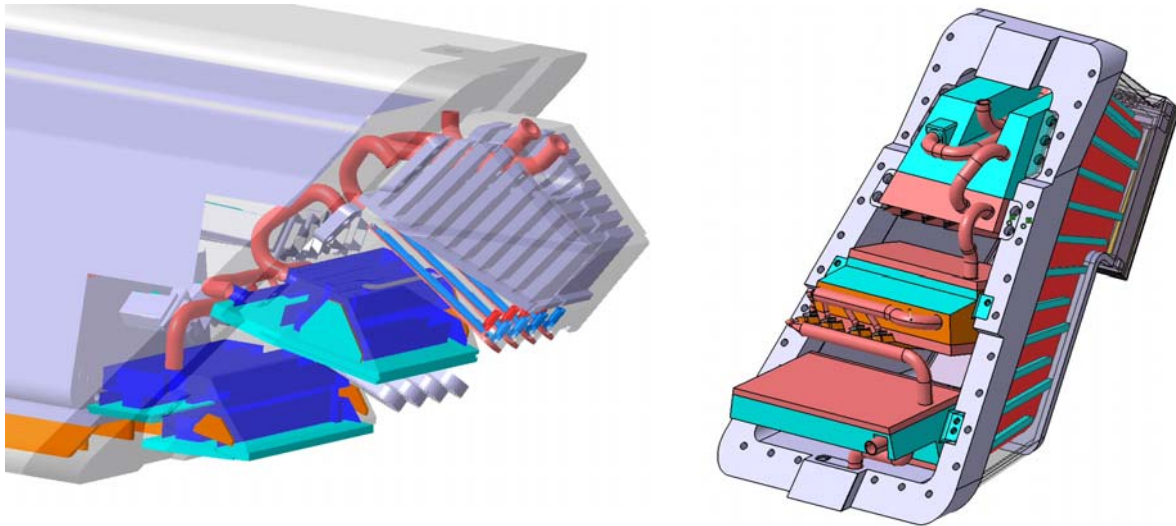
Shield blocks and piping – Housing removed   Front shield/shield block assembly

Fig. 7:   Front shield blocks designed for maximum shielding performance.

Two types of internal shields (cf. Fig. 8) have been proposed in the first run, the block design made from a solid block with drilled holes as wave guide passages, and the tank design made from a strong casing with rectangular pressure tubes and additional steel fillers. Many of the drawbacks can be alleviated by combining the two types, having the block design in the front and the tank design in the back. A third option has evolved with the modular design, consisting of cast elements, each one welded to the neighbour at the outer perimeter and the protruding sockets. This version is currently the favoured one but the choice will be made depending on the final number and location of wave guides.
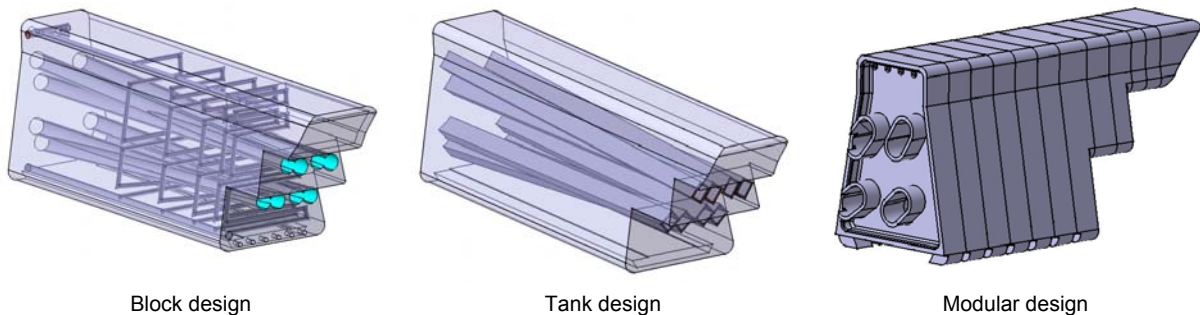
Block design   Tank design   Modular design

Fig. 8:   Internal shield options – Choice depends on final wave guide arrangement

The conceptual design of shielding components is sensitive to the beam line arrangement and to the front mirror layout, which are still in the optimisation process among participating groups. Hence, adaptations and modifications will be needed in the next year.

Deliverable b.4
Specification of cooling requirements for Upper Launcher

The design guide lines for the launcher cooling system are (1) to use regular ITER blanket water of 100°C/148°C inlet/outlet temperature at 3 MPa, (2) to consider baking conditions with 240°C/<240°C inlet/outlet temperature at 4.4 MPa, (3) to provide single in/out pipe connections with ≤76.1 mm outer diameter outside closure plate, (4) to keep launcher thermal bending and local thermal stresses small, (5) to enable remote handling compatible with disassembly/reassembly scheme, and (6) to minimise heating of launcher back end outside closure plate with regard to valves etc. Based on nuclear analysis (Deliverable b.2) the heat production in the launcher main structure and its shield components has been determined for use in cooling system layout. The results are summarised in the table below. The total heat

to be removed from the launcher amounts to about 1 MW with major contributors being the front panel, the front shield blocks, the mirrors, and above all, the wave guides. The launcher main structure and the internal shield contribute with only 0.5 %.

Table 1: Summary of Launcher cooling assessment.

Component	Heat to be removed (kW)	Coolant mass flow rate (kg/s)	Coolant temperature rise (K)	Pressure loss (MPa)
Launcher structure incl. flanges plus inlet pipe	13,7	6,1	0,54	0,018
Front panel (front tubes and return channels)	289	3,1	22,3	0,020
Front shield double wall	64,8	3,1	5	0,040
Front shield block top (without mirrors)	30	3,1	2,3	0,108
Mirror holder top	22,8	3,1	1,7	0,046
Mirrors top row (4 in parallel)	40	3,1	3,1	0,102
Front shield block middle (without mirrors)	33,6	3,1	2,6	0,050
Mirrors bottom row (4 in parallel)	40	3,1	3,1	0,102
Front shield block bottom	27,6	3,1	2,1	0,025
Internal shield (modular design)	0,8	6,1	0,02	0,1
Wave guides	480	6,1	-	-
Total	1042,3		42,76	0,611

Thermal-hydraulics studies have been performed for individual launcher components. One of the critical components in terms of thermal loads and stresses is the front panel that faces the plasma. The analysis focused on the reference design with 6 long cooling tubes and 12 short ones caused by the cut-out for the beams. The average coolant temperature rise in the panel results as 22 K, far below saturation. The total pressure drop assumes 0.02 MPa. Flow velocities are moderate with 2.4 m/s in the front channels and 0.8 m/s in the return channels. Heat transfer coefficients are adequate. Overall, the proposed cooling concept of the front panel proved to be feasible with respect to temperature limits, flow distribution and pressure drop.

Likewise, the thermal-hydraulics analysis of the shield blocks and the mirror holders yield favourable results. As example, the pressure loss in the front shield block at the top including the mirror holder and provisional mirrors results as 0.256 MPa. The temperature rise amounts to about 7 K. Flow velocities are generally small except in mirrors, where they need to be high. For the shield blocks middle and bottom equivalent analyses have been conducted. All together cause a pressure loss in the front shield of about 0.5 MPa.

The pertaining cooling flow diagram (cf. Fig.9) for the whole launcher internals consists of five blocks: ex-vessel equipment, UPP main structure, front shield, wave guides, and internal shield. Temperature and pressure limits at the main inlet and outlet pipes are set by the blanket cooling specification. The main stream is routed through the main structure to the front shield and from there via the internal shield back to the outlet. A bypass is envisaged for wave guides cooling, running parallel to the front shield. It branches off from the main structure and merges back to the main stream inside the internal shield. The flow rate in both branches is about 3 kg/s. The pressure loss in the whole launcher amounts to about 0.6 MPa.

In conclusion, an integrated cooling scheme has been developed for the launcher compatible with the ITER blanket cooling requirements. It is based on the remote steering concept with 8 beam lines per launcher and can be adapted to other launcher variants under discussion. Details of wave guide and front mirror cooling are currently worked out by external groups and may enforce modifications.
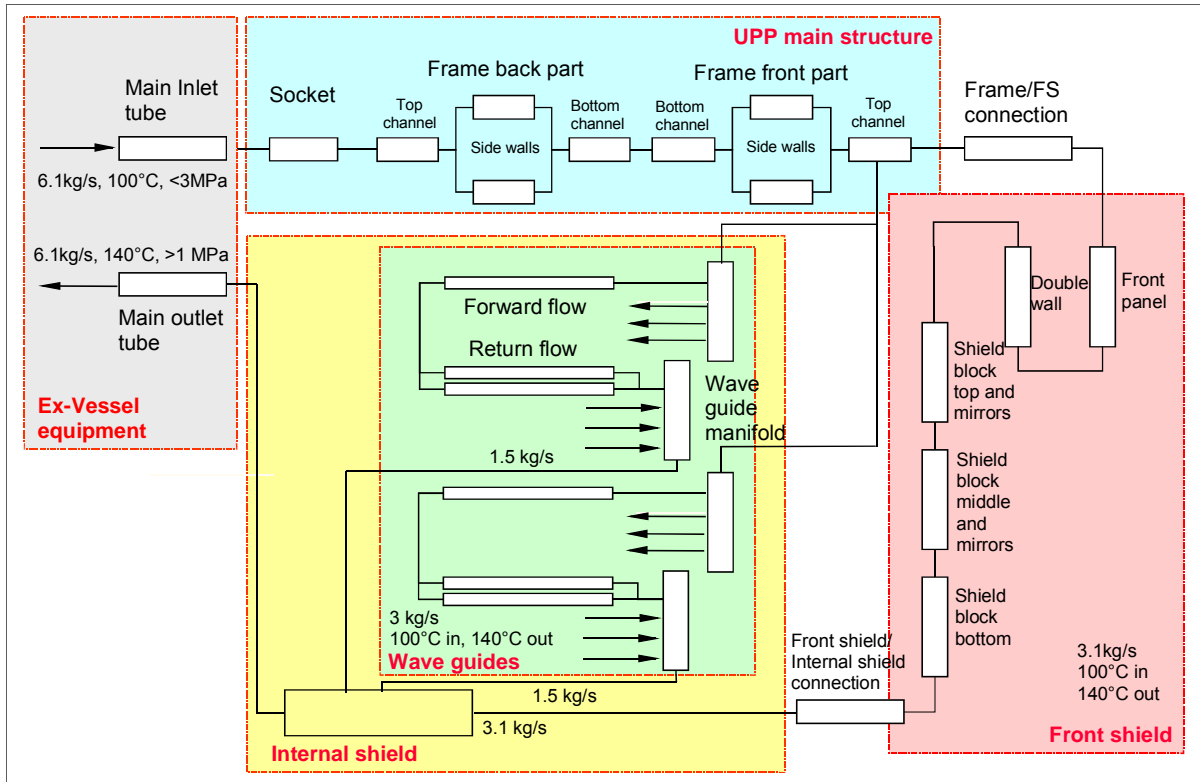
Fig. 9: Cooling flow diagram for the whole launcher internals.

Deliverable b.5
Definition of boundary conditions and interfaces

The ECRH launcher design was adapted to the location and inclination of the upper port which are far from ideal for providing efficient localized current drive. This is because of the resulting steep injection angles that are unfavourable for achieving narrow absorption layers at the plasma (compared to the expected island widths). This problem was minimised in the design by injecting at the minimum z-position compatible with the regular blanket position 10. Limited interference with the neighbouring lower regular blanket module (position 11) was identified to be tolerable if at most two of the first wall panel sections are affected.

The original assignment of ports 12, 13 and 15 for plasma stabilisation has been extended to include port 16, to open the potential for substantial increase of current drive efficiency. The extension in the numbers of ports/launchers (as well as the potential of launching more than 1 MW/line) has opened the possibility of alternative RS launcher configurations. In particular, multipurpose (targeting both q=2 and q=3/2 flux surfaces) or dedicated (targeting only one flux surface) beam lines were considered and their performance analysed by parametric studies of different front mirror configurations. Actually, a major potential of a 4 port arrangement is that the critical space requests for the mm-wave can be relieved by reducing the number of beamlines per port from 8 to 6.

Staff:

J. Burbach
Y. Chen
I. Danilov
U. Fischer
G. Hailfinger
R. Heidinger
V. Heinzel
K. Kleefeldt
K. Lang
M. Lux
A. Meier
A. Serikov
P. Späh
E. Stratmanns
H. Tsige-Tamirat

Literature:

[1] A. Serikov, U. Fischer, Y. Chen, K. Lang, R. Heidinger, Y. Luo, E. Stratmanns, H. Tsige-Tamirat, Neutronics Analysis of the ECW Launching System in the ITER Upper Port, 23rd Symposium on Fusion Technology (SOFT), 20-24 September 2004, Venice, Italy

[2] R. Heidinger, I. Danilov, G. Hailfinger, K. Kleefeldt, A. Meier, P. Späh, A.G.A. Verhoeven: Cooling concepts of the ECRH launcher structure and the torus window for the upper port plug, 23rd Symp. on Fusion Technology (SOFT), Venezia, I, September 20-24, 2004

[3] A.G.A. Verhoeven, W.A. Bongers, A. Bruschi, S. Cirant, I. Danilov, B.S.Q. Elzendoorn, J.W. Genuit, M.F. Graswinckel, R. Heidinger, W. Kasparek, K. Kleefeldt, O.G. Kruijt, S. Nowak, B. Piosczyk, B. Plaum, T.C. Plomp, D.M.S. Ronden, H. Zohm: Design of the mm-wave system of the ECRH upper launcher for ITER,23rd Symp.on Fusion Technology (SOFT), Venezia, I, September 20-24, 2004

[4] B.S.Q. Elzendoorn, M.P.A. Van Asselen, W.A. Bongers, J.W. Genuit, M.F. Graswinckel, R. Heidinger, B. Piosczyk, T.C. Plomp, D.M.S. Ronden, A.G.A. Verhoeven: Testing a full scale ECRH mm-wave launching system mock-up, 23rd Symp.on Fusion Technology (SOFT), Venezia, I, September 20-24, 2004

[5] R. Heidinger, I. Danilov, U. Fischer, G. Hailfinger, K. Kleefeldt, A. Meier, E. Stratmanns, M. Thumm, A.G.A. Verhoeven: Design and analysis of windows and structural components for the ITER ECRH upper port plug, 13th Joint Workshop on Electron Cyclotron Emission and Electron Cyclotron Resonance Heating (EC 13), Nizhny Novgorod, Russia, May 17-20, 2004.

[6] H. Zohm, D. Farina, R. Heidinger, B. Lloyd, S. Nowak, E. Poli, G. Ramponi, G. Saibene, O. Sauter, A.G.A. Verhoeven, F. Volpe, E. Westerhof: The ITER ECRH Upper Launcher – Physics Goals and design requirements, Proc. 13th Joint Workshop on Electron Cyclotron Emission and Electron Cyclotron Resonance Heating, Nizhny Novgorod, Russia, May 17-20, 2004

Subtask C: Torus and Gyrotron Window Design and Development

Objectives

The ITER electron cyclotron heating and current drive (ECH&CD) system is composed of high power millimeter - wave (mm-wave) generators (gyrotrons), transmission lines and mm-wave launching systems ("launchers"). "Upper" launchers are projected to launch a total of 20 MW power from 3 or 4 ports, present launcher configurations consider 6 – 8 beam lines per port. The beam lines are being developed taking into account upgrading potentials from 1 MW up to 2 MW consistent with the concurrent 170 GHz gyrotron development programme. The required steering capability in the launching angle can be achieved by two basically different concepts: the "front steering" (FS) with movable mirrors close to the plasma and the "remote steering" (RS) with movable mirrors outside the torus vacuum barrier formed by a high power CVD diamond window. The objective of the subtask was to perform design studies and research and development studies to establish the torus and gyrotron window design capable of handling 2 MW in continuous wave operation. The task is structured to define the high power mm-wave window components for ITER and to ensure the availability of CVD diamond windows for launcher mock-up testing.

Deliverable c.1
Material characterisation for CVD diamond growth qualification

The design development of high power mm-wave windows relies on the availability of large area CVD diamond disks produced by 'Microwave Plasma Assisted (MPA)' chemical vapour deposition with extremely low dielectric absorption. The lateral homogeneity of the discs are measured by an recognised and internationally outstanding measurement technique based on a hemispherical open resonator set-up. The homogeneity of the dielectric loss is quantified in terms of the D50 and D90 values which indicate the values of the dielectric loss tangent ($\tan\delta$) which forms the upper limit for 50% and 90% respectively of the disk area. Two CVD diamond disks with diameters of 106 mm and thickness of 1.855 mm were ordered from Element Six (Ascot, UK) to establish the window material basis for mock-up tests. Critical issues were demonstrated in the dielectric loss qualification as the first disks were far off the characteristic parameters for the diamond window material obtained for the W7-X project (see also TW2-TPHE-ECRWIN), i.e. D50= $2\cdot10^{-5}$; D90= $3\cdot10^{-5}$. Original specifications which were requiring to ensure $\tan\delta < 1\cdot10^{-5}$ at any spot of the measurable inner area of 80 mm diameter were accordingly reviewed and the definition of the loss properties in terms of the homogeneity parameters were agreed with the producer. This means that given the present development status, only specifications for D50 = $3\cdot10^{-5}$ and D90= $5\cdot10^{-5}$ can be obtained. These 'guaranteed loss' level according to specifications are at stake to provide disks with the previously characteristic values for W7-X in the search of an 'best effort'. This approach was almost accomplished in the growth of the final mock-up windows (60DB1 and 61DB1) (cf. Fig. 1).

Deliverable c.2
Finalisation of gyrotron window design

The windows for the 2 MW coaxial gyrotron development will be based on CVD diamond disks with 'guaranteed loss' (see above). The following geometrical parameters were defined for the windows being part of the coaxial gyrotron development together with Thales Electron Devices (Velizy, F):

- outer diameter of the disk	(106 ± 0.5) mm
- disk thickness:	(1.852 ± 0.006) mm
- diameter of the window aperture ϕ:	96 mm
- width of the RF - beam (E-field $\rightarrow$ 1/e)	25.44 mm
- tilt angle:	~ 1.5°

Thermo-mechanical analyses of window performance were performed by Finite Element (FE) modeling to demonstrate the established design specifications. The calculations modeled the case of the CVD diamond disk brazed to a copper cuff (typical brazing method: Ag(-Cu)). For the chosen water edge cooling, the cooling conditions at the surfaces were modeled with a heat transfer coefficient h = 8500 W/(m^2·K) (corresponding to a water flow velocity of about 1 m/s) and with the temperature of the cooling water of T_{cool} = 293 K. The temperature at the center of the diamond disk reaches a value of T_{cent} = 367 K, the edge temperature is T_{edge} = 313 K, which confirms very well the estimated design value for the temperature gradient between centre and edge of 50 K.
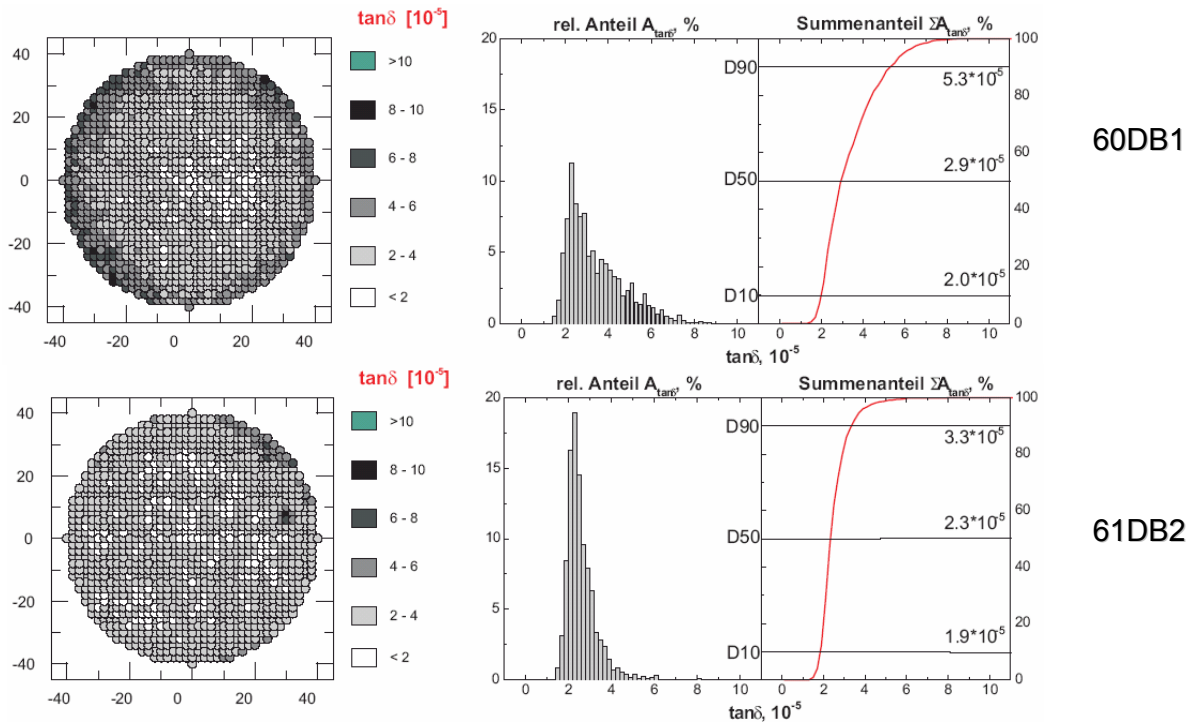
Fig. 1: Qualification of the homogeneity in dielectric loss (at 140 GHz) of the two CVD diamond disks grown at Element Six (Ascot, UK) forming the window material for the mock-up tests of the mm-wave beamline of the RS launcher.

FEM analysis of the mechanical stress formed in the window structure under 2 MW operation with the thermal field being the dominant origin of the mechanical load showed that inside the diamond disk, the tensile stress reaches a maximum value of 55 – 65 MPa, depending on the options in Yield stress chosen for copper (50 or 150 MPa) which is still far off the proposed S_m values of 120-140 MPa (median strength: 350-400 MPa).

Deliverable c.4
Manufacture of a single-disk window for the transmission line mock-up at 170 GHz

For the separation between the primary (plasma) and secondary vacuum in the RS Upper launcher, the torus window unit has to be designed as a compact structure which allows off-axis transmission of 2 MW beams at 170 GHz. Off-axis transmission is a new aspect as compared to the design of related high power windows for the mm-wave sources (gyrotrons) and for front steered systems at the equatorial launcher. In the course of the conceptual design development for the upper launcher, first designs were developed for a launcher system with no focusing in the steering plane (RSU with steering range: ± 5°). In the course of the extended physics requirements on reaching wider plasma areas and on enhanced current drive efficiencies, the injection mirror was given full focusing capabilities including the steer-

ing plane. As a consequence, the maximum available input steering range to the square mm-wave waveguide system ($\pm$ 12°) had to be implemented at the window.

The location of the window calls for an asymmetric cooling structure at the diamond disks also (cf. Fig 2) allowing the window aperture to be maximised. Given a diameter for the CVD diamond disk of 106 mm, an aperture of 95 mm could be realised when a single copper cuff is brazed to the each face of the disk. Among the alternative cooling concepts (see next chapter), preference was given to edge cooling, because of the pronounced temperature rise inherent to indirect face cooling. The copper cuff facing the steering mirrors was essentially reduced to the size of the spring-like connection of the cuff the window housing. The main problem arises from non-axial transmission of the mm-wave beams. For steering angles up to $\pm$12°, the asymmetric power deposition profile leads to Von-Mises stresses in the copper cuff which are at the onset of plastic deformation in soft OFHC copper (yield strength: $\approx$ 50 MPa). For the same reason, the torus window cannot be integrated into the available cooling loop ("blanket water") as it will not withstand the membrane stresses formed the operation water pressure of 3 MPa. Therefore its connection to the component cooling water loop is foreseen. By a reduction of the water pressure below 0.8 MPa, tolerable membrane stresses in the body of the copper cuffs are obtained.
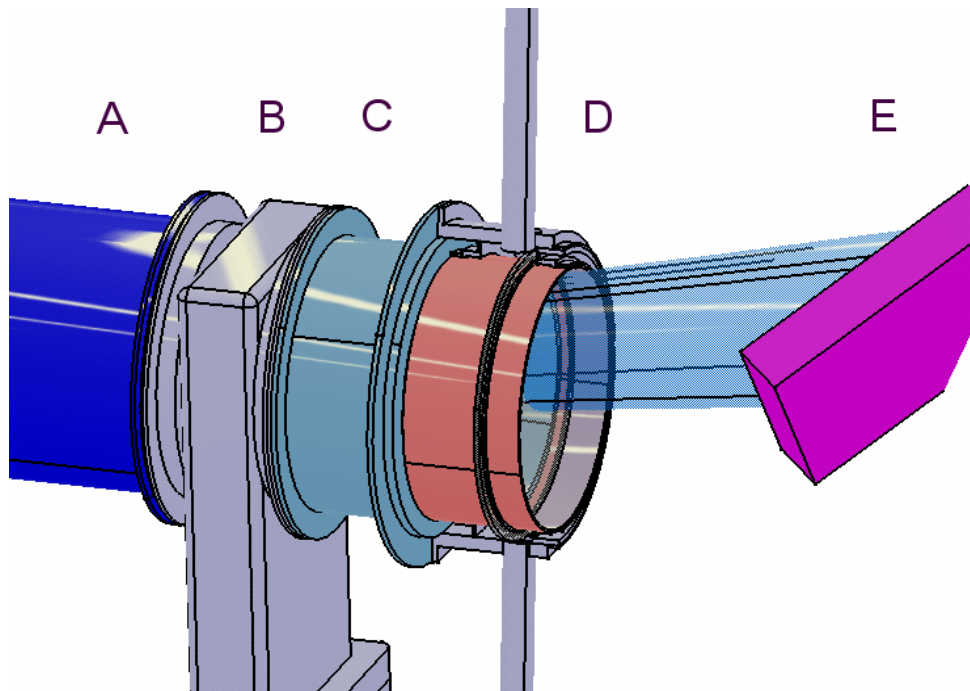
Fig. 2:   Sketch of the torus window environment for the remotely steerable launcher at the ITER upper ports: A waveguide (socket); B isolation valve; C window socket; D window unit; E end mirror of the remote steering unit.

The window unit has been manufactured using the CVD diamond disk 60DB1. In a first step, two U-shaped steel springs were electron beam-welded to the corresponding two copper cuffs (length: 16 mm and 25.4 mm), these cuff structures were joint to the diamond disk at Thales (Velizy) by the Ag(Cu)-brazing technology and the window unit assembled by electron welding of the window insert to the outer housing and then to the window socket and flange (cf. Fig. 3). The window unit was vacuum tested and proved that level of 10^{-7} mbar can be obtained.

Deliverable c.5
Design review of a double-disk window

The present reference design of the upper launcher foresees a single disk arrangement at the closure plate to form the primary tritium confinement. The typical failure mode of CVD

diamond windows is the formation of one or two cracks in the CVD diamond disk which will not destroy the geometrical integrity of the window structure. Yet, the primary tritium confinement is broken in one beam line. Still a valve neighbouring the window, which then isolates the in-vessel section of the beam line, can avoid immediate removal of the plug from port, even though it is not fully compatible with requirements of a primary safety-related component.

60DB1 - original   Cu-cuffs with welded springs   window insert

window unit with welded outer housing

window with the socket and flange
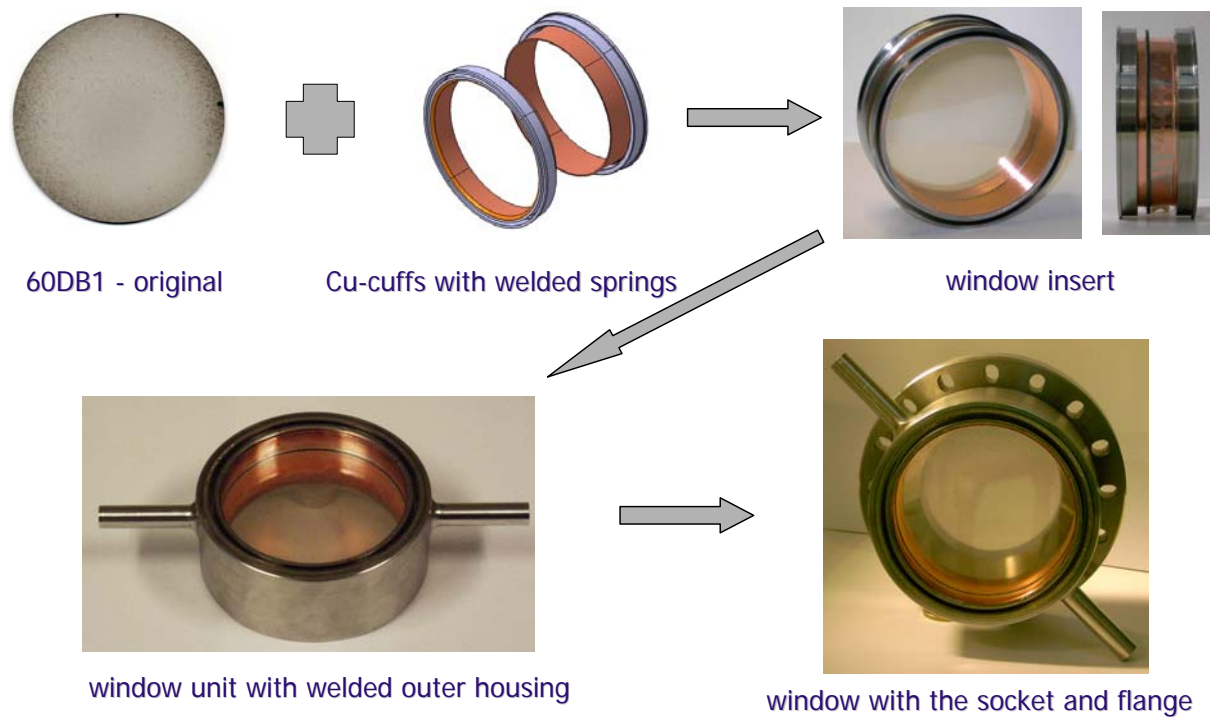
Fig. 3: Sequence of the manufacturing stages of the torus window developed for the mock-up testing of the mm-wave beam line for the RS launcher

An enhanced barrier function of the window unit may be achieved by a double disk window. However, space in the port plug section between the closure plate and the vacuum vessel flange is restricted both in lateral and axial window dimensions. The double disk design is based on the limits of the well-proven technologies for CVD diamond growth and brazing technologies to metallic structures. This implies that a maximum diameter for the CVD diamond disk is fixed to 106 mm, according the experience gained with the procurement of the CVD diamond disks for the ECRH system for W7-X. Larger diameters are principally available at least up to 120 mm, but they lack so far in established dielectric loss specifications and in experience in brazing. Three basically different approaches are available for cooling of high power CVD diamond windows: edge cooling, remote face cooling, direct face cooling (cf. Fig. 4).
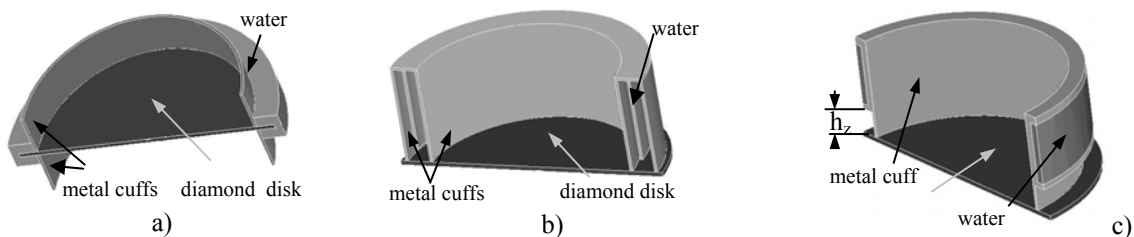
Fig. 4: Major variants of cooling structures for window units
a) edge cooling , b) direct face cooling , c) indirect face cooling (h_z distance of water jacket)

Face - cooling concepts were studied for setting up the double-disk window for ITER. For the direct cooling concept, the Ag(Cu-)brazing technology has been exemplified, it is found that

the required double ring brazing is more critical than the standard (single ring) concept presently used for gyrotrons. The main problem is to provide vacuum tight bonds. The concept is limited to the reference concept for limited beaming steering because of a maximum available aperture of 80 mm. The parameters of the cooling circuits were determined and found to be adequate for 2 MW operation. The extension to larger apertures can be based on an indirect facing cooling arrangement provided that the substantial increase in window temperature can be avoided by using a cooling system with lower input temperatures such as the system for the transmission line.

Staff:

J. Burbach
I. Danilov
R. Heidinger
A. Meier

Literature:

[1] I: Danilov, R. Heidinger, A. Meier: Method for separating surface loss terms on CVD-diamond disks, Conf. Dig. of Joint 29th Int.Conf. on Infrared and Millimeter Waves and 12th Int.Conf.on Terahertz Electronics, Karlsruhe, September 27 - October 1, 2004, Piscataway, N.J. : IEEE, 2004 pp.213-4

[2] R. Heidinger, I. Danilov, A. Meier, M. Rohde: Material and engineering issues of CVD diamond windows for high power mm-waves, Conf. Dig. of Joint 29th Int.Conf. on Infrared and Millimeter Waves and 12th Int.Conf.on Terahertz Electronics, Karlsruhe, September 27 - October 1, 2004, Piscataway, N.J. : IEEE, 2004 pp.59-62

[3] R. Heidinger, I. Danilov, U. Fischer, G. Hailfinger, K. Kleefeldt, A. Meier, E. Stratmanns, M. Thumm, A.G.A. Verhoeven: Design and analysis of windows and structural components for the ITER ECRH upper port plug, 13th Joint Workshop on Electron Cyclotron Emission and Electron Cyclotron Resonance Heating (EC 13), Nizhny Novgorod, Russia, May 17-20, 2004.

[4] R. Heidinger, I. Danilov, A. Meier: Window development for remotely steerable mm-wave launchers, Proc. of the 10th Triennial ITG-Conf.,Displays and Vacuum Electronics, Garmisch-Partenkirchen, May 3-4, 2004; Berlin [u.a.] : VDE Verl.GmbH, 2004 S.395-99; (ITG-Fachbericht 183)

[5] R. Heidinger, I. Danilov, A. Meier: Development of a tunable torus window, 16th Joint Russian-German STC Workshop on ECRH and Gyrotrons, Nizhny Novgorod, Russia, May 21-22, 2004

[6] R. Heidinger, I. Danilov, G. Hailfinger, K. Kleefeldt, A. Meier, P. Späh, A.G.A. Verhoeven: Cooling concepts of the ECRH launcher structure and the torus window for the upper port plug, 23rd Symp. on Fusion Technology (SOFT), Venezia, I, September 20-24, 2004

[7] A.G.A. Verhoeven, W.A. Bongers, A. Bruschi, S. Cirant, I. Danilov, B.S.Q. Elzendoorn, J.W. Genuit, M.F. Graswinckel, R. Heidinger, W. Kasparek, K. Kleefeldt, O.G. Kruijt, S. Nowak, B. Piosczyk, B. Plaum, T.C. Plomp, D.M.S. Ronden, H. Zohm: Design of the mm-wave system of the ECRH upper launcher for ITER,23rd Symp.on Fusion Technology (SOFT), Venezia, I, September 20-24, 2004

[8] K. Takahashi, S. Illy, R. Heidinger, A. Kasugai, R. Minami, K. Sakamoto, M. Thumm, T. Imai: Development of reliable diamond window for EC launcher on fusion reactors, 23rd Symp.on Fusion Technology (SOFT), Venezia, I, September 20-24, 2004

[9] B.S.Q. Elzendoorn, M.P.A. Van Asselen, W.A. Bongers, J.W. Genuit, M.F. Graswinckel, R. Heidinger, B. Piosczyk, T.C. Plomp, D.M.S. Ronden, A.G.A. Verhoeven: Testing a full scale ECRH mm-wave launching system mock-up, 23rd Symp.on Fusion Technology (SOFT), Venezia, I, September 20-24, 2004

Subtask D

Deliverables e.6.2 and e.7.2

In the time since the last annual report from 27 November 2003 the 170 GHz coaxial cavity gyrotron has been brought into operation. Gyrotron operation started with some delay due to late delivery of components. In the meantime stable gyrotron operation has been obtained and the operation of the gyrotron has been investigated in detail. Based on the results the following gyrotron performance can be expected for the tests of the remote launcher:

- RF output power	~ 1 MW
- pulse length:	5 – 10 ms
- frequency:	169.9 – 170.0 GHz
- Duty factor:	~ 0.001

The distribution of the RF output beam has been measured at different positions using an infrared camera. Unfortunately, the RF output pattern is not Gaussian. Fig. 1 shows the measured power distribution in a plane 850 mm outside the gyrotron window. Further measurements will be performed in order to provide data to IPF Stuttgart needed for designing mirrors of the matching optics.
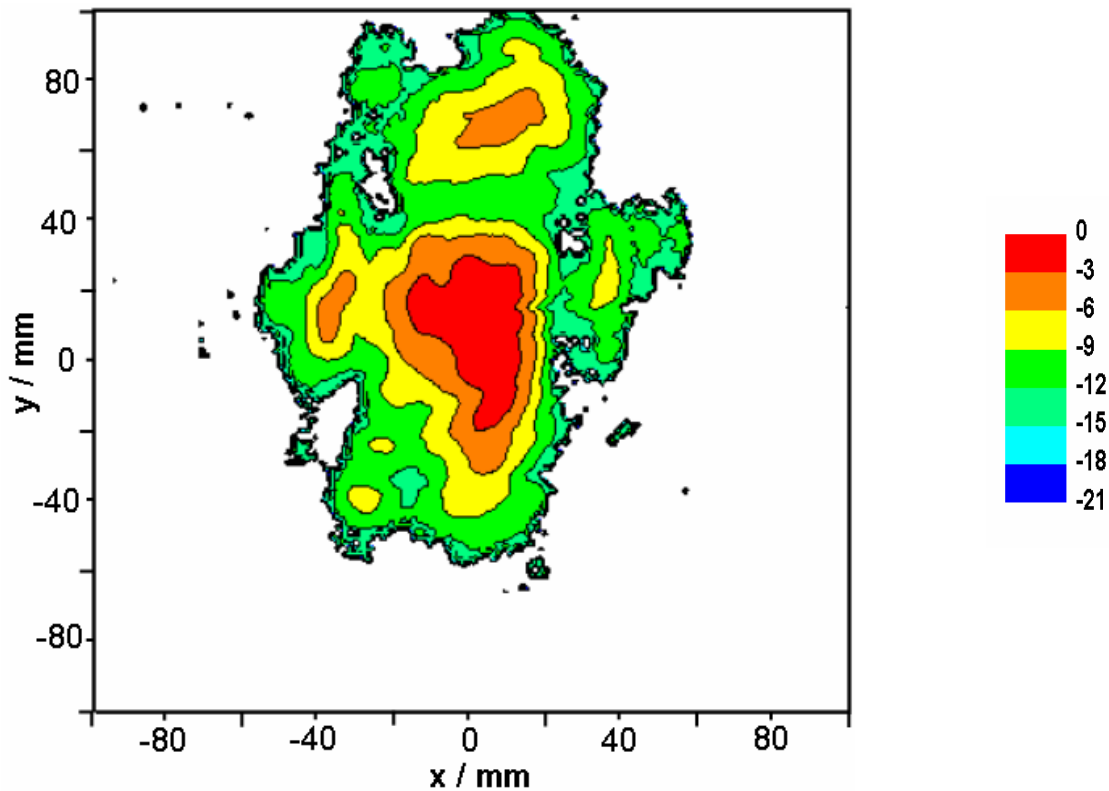
Fig. 1: The distribution of the RF output beam in a plane at 850 mm outside the window. The colours in the contour plot correspond to 3 dB steps.

The arrangement of the launcher and including all auxiliary components inside the microwave and diagnostic box the has been agreed with FOM (details have been discussed in different meetings and exchanged via e-mail). For the tests a microwave window out of fused silica is in preparation. The diagnostic box and the modifications on the microwave box will be performed in the first part of 2005.

Staff:

H. Budig
G. Dammertz
S. Illy
W. Leonhardt
D. Mellein
B. Piosczyk
T. Rzesnicki
M. Schmid
W. Spiess
J. Szczesny
M. Thumm
R. Vincon

Literature:

[1] VERHOEVEN, A.G.A.; VAN ASSELEN, M.P.A.; BONGERS, W.A.; BRUSCHI, A.; CIRANT, S.; ELZEN-DOORN, B.S.Q.; GANTENBEIN, G.; GRASWINCKEL, M.F.; HEIDINGER, R.; KASPAREK, W.; PIOSCZYK, B.; PLAUM, B.; RONDEN, D.M.S. "*Design of the mm-wave system of the ITER ECRH upper launcher.*", 13th Joint Workshop on Electron Cyclotron Emission and Electron Cyclotron Resonance Heating, Nizhny Novgorod, Russia, May 17-20, 2004.

[2] PIOSCZYK, B.; ARNOLD, A.; BUDIG, H.; DAMMERTZ, G.; DUMBRAJS, O.; HEIDINGER, R.; ILLY, S.; JIN, J.; MICHEL, G.; RZESNICKI, T.; THUMM, M.; YANG, X. "*Experiments on a 170 GHz coaxial cavity gyrotron*", 23rd Symp. on Fusion Technology (SOFT), Venezia, I, September 20-24, 2004.

TW2-TPHE/ECRWIN
ITER ECRF Window Development

Introduction

The ITER electron cyclotron heating and current drive system (ECRH&CD) will launch 20 MW of power at 170 GHz into the plasma for heating and current drive applications. Each line of the microwave system must be capable of delivering 1-2 MW under essentially steady-state conditions and therefore requires a high power CW vacuum transmission window both for the gyrotron sources and for the vacuum vessel. Previous developments involving the EU Fusion Associations and European industry have demonstrated that CVD diamond is capable of satisfying the demanding requirements for efficient high power transmission with a high thermal conductivity which allows effective cooling of the window.

The objective of this task has been:

- to manufacture and test a gyrotron and torus window demonstrator for 170 GHz,

- to develop design and technology variants to consolidate the safety criteria at the windows,

- to study the material properties of a CVD diamond window at medium radiation damage

- to provide methods and data which qualify CVD diamond disks for ECRH windows.

Subtask 1   Report on the final design, fabrication and test of a 1-2 MW, 170 GHz, CW, CVD-diamond gyrotron window in collaboration with the RF ITER partner

1.1 Final design and fabrication of the 170 GHz CVD-diamond gyrotron window

The general design of the gyrotron window has been described in the Final Report on ITER Task No.: G55 TT 19 EU (TWO-ECRF/WIN) published as FZKA-Report 6705 in June 2002 (see Fig. 1 and 2).

1   CVD diamond disk

2   Inconel cuffs

3   Stainless steel cuffs

4   Cooling channel forming unit

5   Housing

6   Flange for reusable joint of Conflat type
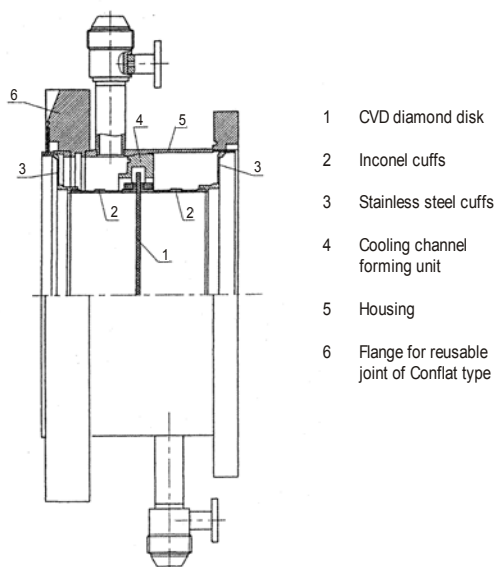
Fig. 1: Design of the 170 GHz RF-ITER gyrotron output window with CVD diamond disk ("Star of FZK").
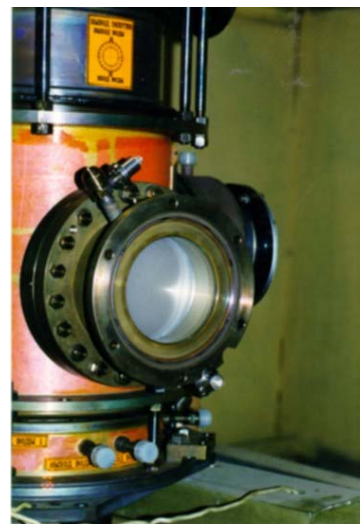
Fig. 2: Photograph of the 170 GHz RF-ITER gyrotron output window with CVD-diamond disk ("Star of FZK").

Two improvements have been added to achieve the final design:

(1) The water cooling rim of the CVD-diamond disk has been covered with a transparent lacquer in order to avoid corrosion of the Al-braze.

(2) Copper sleeves have been inserted from both sides of the window aperture in order to avoid microwave heating of the Inconel cuffs.

In total, four gyrotron window units were fabricated and tested in collaboration with the Russian Partner. The parameters of the CVD-diamond disks are summarized in Table 1.

1.2 Test of the 170 GHz CVD-diamond gyrotron window

Unfortunately, the first 3 window disks, all provided by the EU partner (FZK, DeBeers), cracked after operation at mm-wave power and pulse lengths of up to 1 MW and 20 s, respectively. The reasons are listed in Table 1. In the cases of the disks ITER 1 (FZK) (Fig. 3) and ITER 4 (FZK) (Fig. 4) it was due to RF arcing since the protection system was not save. Disk ITER 3 (FZK) had after brazing a sag of 0.12-0.14 mm which corresponds to a static stress of approximately 0.7-0.8 MPa. Nevertheless, in order to fulfil this ITER task in time, high power tests have been performed. The gyrotron was operated at 1 MW output power and 1.5 s pulse length with 50% efficiency. On 24.05.2001 the window disk was broken after a pulse length of 0.2 s. The crack pattern is characteristic for failure induced by homogeneous and biaxial stress and thus reveals that the static stress due to the bow of the window was too large. A basic mechanical stress estimation which parameterises also the effective rigidity of the braze indicates that the tensile stress in the diamond disk at the brazed rim amounts to some 300 MPa. The fact, that the sag after the crack was even larger (0.2 mm), proves that it was introduced during the brazing to the Inconel waveguide cuffs.

Finally, the Russian Partner provided the disk ITER RUS (IAP) which was also purchased from DeBeers and has been successfully tested in collaboration of both teams at 0.54 MW, 170 GHz mm-wave power and 80 s pulse duration [1].

The 140 GHz prototype gyrotron for W7-X which is also equipped with a CVD-diamond window (disk thickness = 1.8 mm) has been successfully operated at 1 MW, 0.9 MW,

0.54 MW and 0.26 MW with a pulse duration of 12 s, 180 s, 940 s and 1500 s, respectively [2-4]. At 1 MW the window losses are only 400 Watt. The experiments show the unique features of such CVD-diamond windows which can be even used at 2 MW unit power.

Table 1: Parameter of the various CVD-diamond disks used for 1 MW, 170 GHz gyrotron windows.

	Disk Diameter (mm)	Window Aperture (mm)	Thickness (mm)	Bulk Losses ($\tan\delta$) at 145 GHz			Remarks
				D10 (10^{-5})	D50 (10^{-5})	D90 (10^{-5})	
ITER 1 (FZK) "Star of FZK"	119	100	2.230	2.7	3.5	5.5	Two radial cracks (17-23 mm long) from the brazing rim on 09 Nov 1999 due to RF arcing.
ITER 3 (FZK)	106	88	1.865	2.0			Several cracks on 24 May 2001. Disk had a 0.12-0.14 mm sag introduced by the brazing.
ITER 4 (FZK)	106	88	1.849	2.4	3.3	5.1	Two radial cracks (15-20 mm long) from the brazing rim on 25 Jan 2002 due to RF arcing.
ITER RUS (IAP)	106	88	1.489	0.6			Gyrotron is still operating.
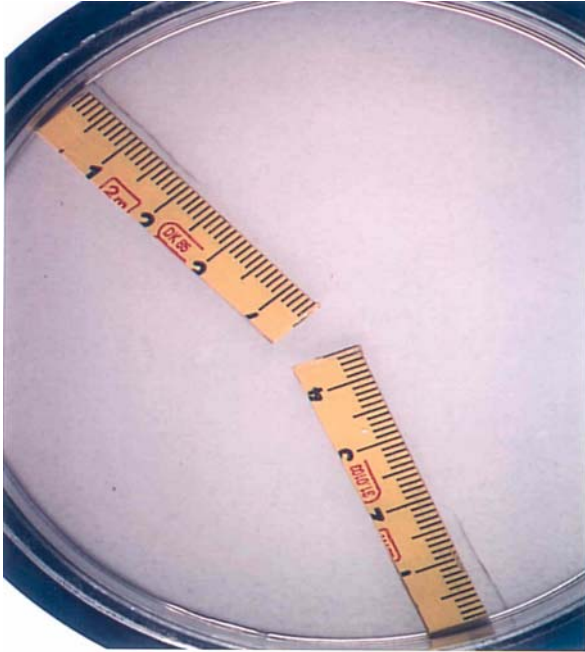
Fig. 3: Two radial cracks, 17 and 23 mm long, starting from the brazing rim (aperture diameter 100 mm) of CVD-diamond window disk ITER 1 (FZK) ("Star of FZK").
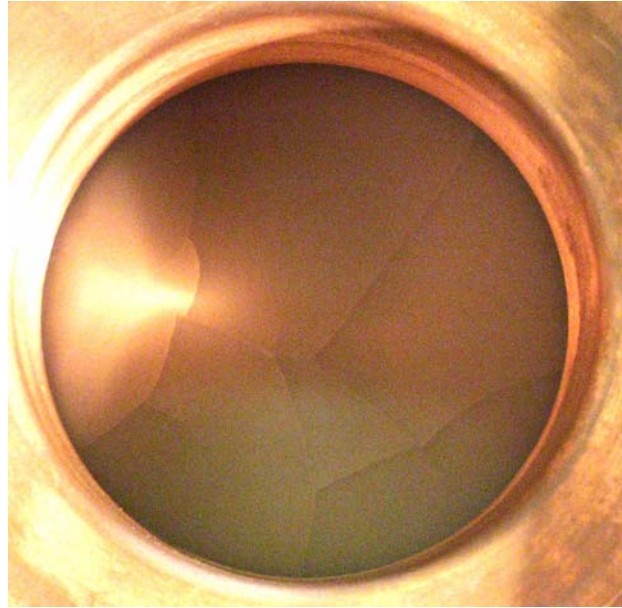
Fig. 4: Several cracks in the broken CVD-diamond window disk ITER 3 (FZK) (aperture diameter 88 mm). The disk had a sag of 0.12-0.14 mm after brazing.

Subtask 2:   Report on pressure tests (3 bar) of a neutron-irradiated 1 MW, 170 GHz, CW CVD-diamond torus window in collaboration with JA ITER partner

2.1   Basics of the pressure tests

The primary vacuum boundary for the beam lines in the ECRH systems at the upper and equatorial port plug is formed by the CVD-diamond window [5]. The attachment of the window housing has to be formed by a fully welded construction which is designed to withstand an internal pressure of 0.2 MPa at the operating temperature.

In the case of differential pressure (p) applied to the two faces of a single-disk diamond window, the window failure will result from spontaneous crack formation. This will occur when the maximum of the main principal (tensile) stress (σ_{max}) is exceeding the critical stress (σ_c). There is a direct proportionality between the pressure and the maximum of main principle stress:

$$\sigma_{max} = g^* \cdot A^{-2} \cdot p \tag{1}$$

The proportionality factors are composed of a boundary factor g*, which describes the rigidity of the window fixation at the 'supporting' rim, and a geometrical factor related to the aperture radius R and the disk thickness t (A=t/R).

The difference imposed by the rigidity of the window fixation is confined by the two limiting cases of a rigidly clamped rim and of a simply supported rim. In general the boundary factors depend on the Poisson number ν. For CVD diamond (ν = 0.1), the g* values are between 0.75 ('rigid clamp') and 1.163 ('free support'). Consequently there is a 50% uncertainty in the calculation of safety margins with respect to pressure tolerance.

A test facility for studying the CVD windows under overpressure is operated at JAERI Naka [6,7]. By applying pressurised nitrogen gas to one of the faces of the integrated window structure, a bow is induced in the diamond disk which is measured at the centre (Fig. 5). Originally the test stand was set up for qualifying the first high power gyrotron window demonstrator which was based on a 'medium' loss diamond disk, which was typical for the initial stage of large area diamond window development.
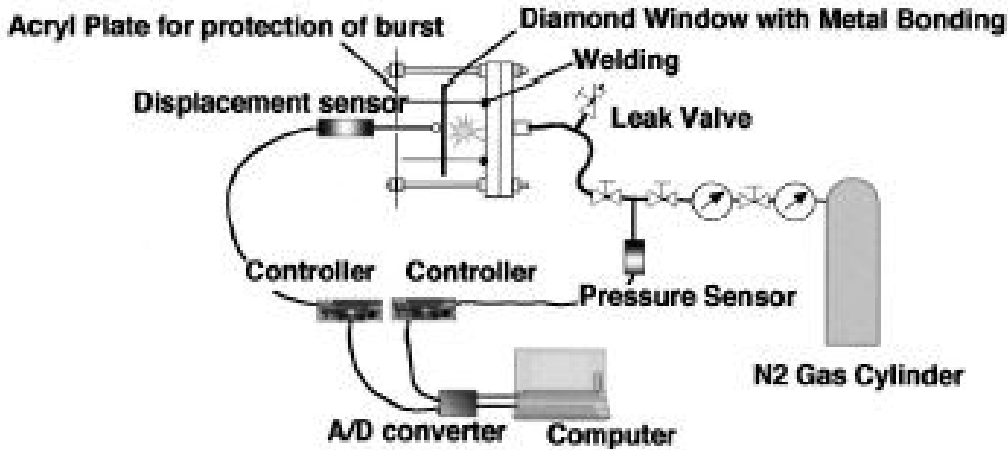
Fig. 5: Experimental scheme of the JAERI pressure test facility for brazed CVD-diamond window structures.

The basic motivation of this experimental approach is to provide a direct proof that the ITER relevant safety specifications can be maintained. Further more it is an outstanding characterisation tool as it provides a quantitative measure for the state of 'rigidity' of the clamping for the CVD-diamond disk as defined by the brazing technology.

The quantification of the 'clamping state' is based on the linear relationship between the bow b measured at the disk centre and the applied (homogeneous) pressure loading p

$$b^* = \frac{b}{t} = g \cdot A^{-4} \cdot \frac{p}{E} \qquad (2)$$

where g is again a boundary factor and E the Young's modulus.

The bow produced is especially sensitive to the clamping state, as g varies between 0.186 (rigid clamp) and 0.861 (simply supported).

2.2 Results

The so-called 'torus window demonstrator unit' was formed by brazing a neutron irradiated large CVD diamond disk by the Al-brazing technology to copper cuffs and integrating it at JAERI into an edge-cooled window housing. The neutron irradiation (fluence: $0.9 \cdot 10^{21}$ n/m^2 – E>0.1 MeV) and the high power mm-wave transmission studies were part of the previous window development task (EFDA Contract TW0-ECRF/WIN). The pressure tests are a continuation of the cooperation with JAERI Naka.

In the JAERI pressure test facility, a differential pressure was applied to the torus window demonstrator up to value of 0.4 MPa. The bow measured in the centre was found to be linear to the applied pressure difference with a slope of 120 – 130 µm/MPa, this compares to a slope of 40 µm/MPa for the early gyrotron window demonstrator tests (Fig. 6).
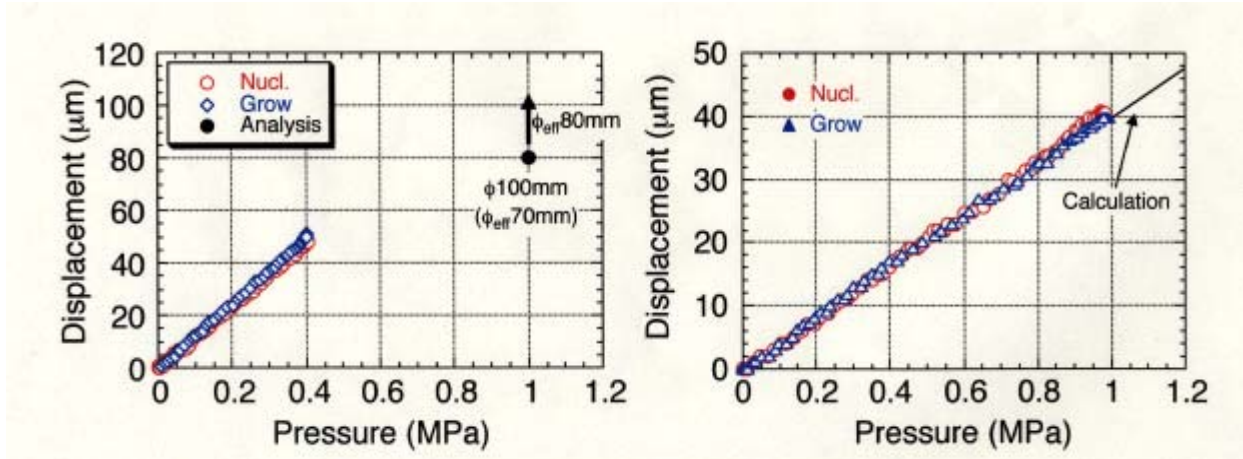
Fig. 6: Bow measured at the centre of the torus window demonstrator disk (left) as compared to the first (unirradiated) gyrotron window demonstrator disk (right).

There is an essential difference in the geometrical parameters which determine the window response to the applied pressure, as documented in Tab. 2. By separation of the geometry effects according to (see Eq.2):

$$\frac{b}{p} = \gamma \cdot g \qquad ; \qquad \gamma = A^{-4} \cdot \frac{t}{E} \tag{3}$$

it is found that both boundary factors are practically identical.

Table 2: Separation of the geometrical parameters from the observed linear relationship between bow and pressure difference: Comparison of the present observation for the torus window demonstrator to earlier bow data obtained by JAERI for a gyrotron window demonstrator.

Window Demonstrator	D [mm]	R_{app} [mm]	t [mm]	A^{-4}	t/E [mm/GPa]	γ [mm/GPa]	b/p [mm/GPa]	g
Torus	106	40	1.825	2.31E+05	1.66E-03	383	125	0.33
Gyrotron	100	35	2.25	5.86E+04	2.05E-03	120	40	0.33

NB: Rapp: Effective rim radius defined by the window aperture.
The Young's modulus was taken as E = 1100 GPa.

Discussion

The results clearly prove that the studied geometry for manufacturing an edge-cooled torus window is safe for pressure excursions up to least 0.4 MPa (in the absence of additonal stress induced by mm-wave power absorption). The boundary factor, which is quantified from the linear relationship of the bow in the centre of the disk to the applied pressure, is higher than expected for a fully rigid attachment of the disk to the metallic cuff. Thus standard analytical considerations may be misleading when they assume a rigid attachment.

The numerical coincidence to the boundary factor g extracted from the comparison with earlier studies of the gyrotron window demonstrator give a strong evidence that the 'clamping condition' is a well-defined parameter for the Al-brazing technology which was used in both cases.

From these findings, it is of particular interest to attempt a quantitative estimate for the maximum stress that were present in the experiments. For this purpose, it is important to

notice that the effective g (0.33) is close to the geometrical mean of g for the limiting cases (0.40). As for the g* factor, that determines the stress levels for a given pressure value, an effective value is assessed for the g* factors applicable for the centre in both cases (0.69 resulting from 0.41 and 1.16). This value is still lower than the g* value at the rim (0.75) which means that the maximum stress is to be expected at the rim, even though the stress maximum tends to move into the centre of the disk when reducing the rigidity of the attachment. Therefore the standard approach of a rigid attachment for estimating the maximum stress values appears to be still justified for an estimate (see Tab. 3).

Tab. 3: Analytical estimate of the maximum stress level in the CVD diamond disk under the maximum pressure levels chosen for the pressure tests.

Window Demonstrator	D [mm]	R_{app} [mm]	t [mm]	A^{-2}	p [MPa]	$g*_{eff}$		σ_{max} [MPa]
Torus	106	40	1.825	480	0.4	0.75		144
Gyrotron	100	35	2.25	242	1.0	0.75		181

This estimate shows that the maximum stress reached about 1/3 to 1/2 of the ultimate bending stress determined for unirradiated and irradiated specimens of CVD diamond of approximately similar material quality. An earlier FEM modelling of the stress distribution of the gyrotron window demonstrator under a pressure of 0.7 MPa indicates that the maximum of equivalent (Von Mises) stress is to be found at the rim, its value is in the same order (130 – 147 MPa) as the results of the estimate according to Tab.2 using 0.7 MPa instead of 1.0 MPa (127 MPa). However, this coincidence should not be over-stressed as different stress states (main principal stress, equivalent stress) need to be differentiated for a proper performance assignment. Yet, it is remarkable to note that the typical upper safety limits for tensile stress in diamond (120-150 MPa, i.e. 1/3 of σ_0) were apparently reached (torus window demonstrator) or even possibly (gyrotron window demonstrator) exceeded in the pressure tests.

Subtask 3: Report on studies of the recovery in thermal conductivity of neutron irradiated CVD-diamond induced by high temperature processing

Background to the recovery studies

The effect of structural (displacement) damage produced by fast neutrons on thermal conductivity, mm-wave absorption and mechanical strength was established on test disks of limited size (diameter 13 mm – 50 mm) in the previous stages of the CVD-diamond window development. All irradiations were performed with flooded capsules, meaning that the specimen temperature was close to pool conditions ($T_{irr} \approx 320$ K). With these irradiation conditions, the first distinct reduction in thermal conductivity was found for a neutron fluence of 10^{21} n/m^2. This observation justified to set the limit of tolerable neutron fluence at the torus window to 10^{20} n/m^2. The dielectric loss measurements on the as-irradiated specimens indicated that mm-wave absorption did not experience any similar degradation for 10^{21} n/m^2, and no effect on mechanical strength was observed up to the maximum fluence studied (10^{22} n/m^2).

The disk prepared for the torus window demonstrator was irradiated to 10^{21} n/m^2 to provide a high power transmission test at a moderate degradation level of the disk. Indeed in the as-irradiated state (T_{irr} =310 K), thermal conductivity was measured to amount to 840 W•(m•K)$^{-1}$, which has to be compared to the thermal conductivity of 1800 – 2000 W•(m•K)$^{-1}$ for the window grade materials (unirradiated).

A striking difference was found during the transmission experiments performed in cooperation with JAERI Naka. The temperature rise observed in the window center under moderate pulse lengths (500 kW / 600 ms) and in absence of external water cooling could be best modelled assuming a thermal conductivity of 1200 W•(m•K)$^{-1}$ and an effective loss tangent tanδ of 4.8•10^{-5}. The dielectric loss was expected to be lower, as the dielectric loss mapping had shown that in the centre of disks loss varied between 2 – 4•10^{-5} in the pre-irradiation and the as-irradiation state of the disk. It was inferred that a change in the nature of defects was introduced during the brazing process, during which the as-irradiated disk was exposed to temperatures of 600°C when joining it to the Inconel cuffs using the Al-brazing technology. As the laser flash technique could not be implied to the mounted CVD-diamond disk, this conjecture was to be verified by measuring the thermal conductivity after the dismounting of the window structure.

3.2 Results of the material parameter measurements on the CVD-diamond disk dismounted from torus window demonstrator

The torus window was shipped from JAERI to FZK after completion of the pressure tests reported in previous section (Subtask 2). Here it was disassembled by cutting out the window insert from the window housing (cf. Fig. 7 - 10). Finally the CVD-diamond disk (22DB1, cf. Fig. 11) was removed from the inconel cuffs by dissolving the Al braze by sodium hydroxide.

A characteristic feature of the CVD-diamond of the torus window demonstrator was its green colour when it was illuminated to view it under intensive light transmission. Therefore it was often briefly called the green window. Under normal viewing (scattered/reflected light) it looked essential grey (compare Fig. 7-8 to Fig. 9-10). This distinct green colour was only observed after the brazing, in the as-irradiated condition it looked brownish.
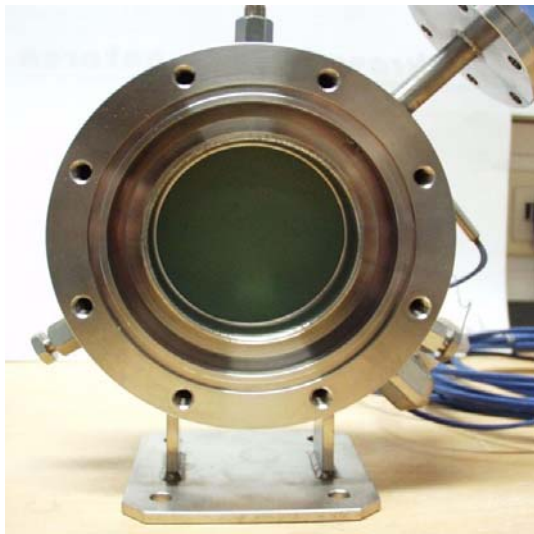
Fig. 7: Torus window demonstrator as used in the 170 GHz high power transmission test at JAERI.

Fig. 8: Window insert consisting of CVD-diamond disk, Inconel cuff and Steel side walls of cooling chamber as removed from torus window demonstrator.

The distinct optical appearance called for a measurement of the spectral transmission. A spectrometer was set up using with optical fibers guiding the light to the disk studied over its thickness. As the need for the optical qualification became only evident after the manufacturing of the brazed window, the changes induced in optical transmission could only be assigned by comparison with unirradiated and irradiated model disks.

Fig. 9: Torus window demonstrator unit with special illumination to show the green transparency effect of the irradiated CVD-diamond disk (22DB2).

Fig. 10: Torus window demonstrator disassembled into outer housing and window insert.
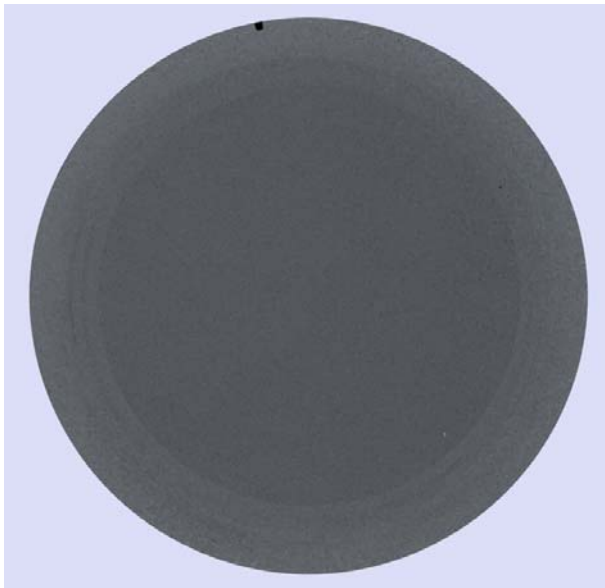
Fig. 11: Diamond disk 22DB2 after removal of window unit (brazing chemically removed).

The optical spectra give clear evidence that the absorption regime of CVD diamond is strongly modified in the visible range by the structural damage introduced at the fast neutron irradiations at the 10^{-5} and 10^{-4} dpa (displacement per atom) levels, which correspond to the fast neutron fluences of 10^{20} n/m^2 and 10^{21} n/m^2 (cf. Fig. 12a). The characteristic green colour is caused by a local transmission maximum around 520 nm (cf. Fig. 12b). This feature is not present in the as-irradiated test specimen ER4_56_1 which had received similar neutron fluence, but was not exposed to high temperatures. The comparison between the various spectra cannot be made on quantitative grounds, as the test specimens were thinner (typically 1 mm instead of 1.82 mm). Also scattering losses due to limited surface polish were not separated and contribute significantly at the short wavelength section. Yet it is apparent that the spectrum of the CVD diamond in the torus window demonstrator gives evidence for structural damage which is intermediate to the as-irradiated test specimens with 10^{-5} and 10^{-4} dpa.

The thermal conductivity was measured on the disassembled test disk by the laser flash technique. The measurements confirmed the implications from the calorimetry performed at high power transmission experiments (cf. Fig. 13). The apparent partial recovery of the thermal conductivity induced by the brazing process goes along with increase in dielectric absorption by about 2/3 in the median loss value D50 (cf. Fig. 14).
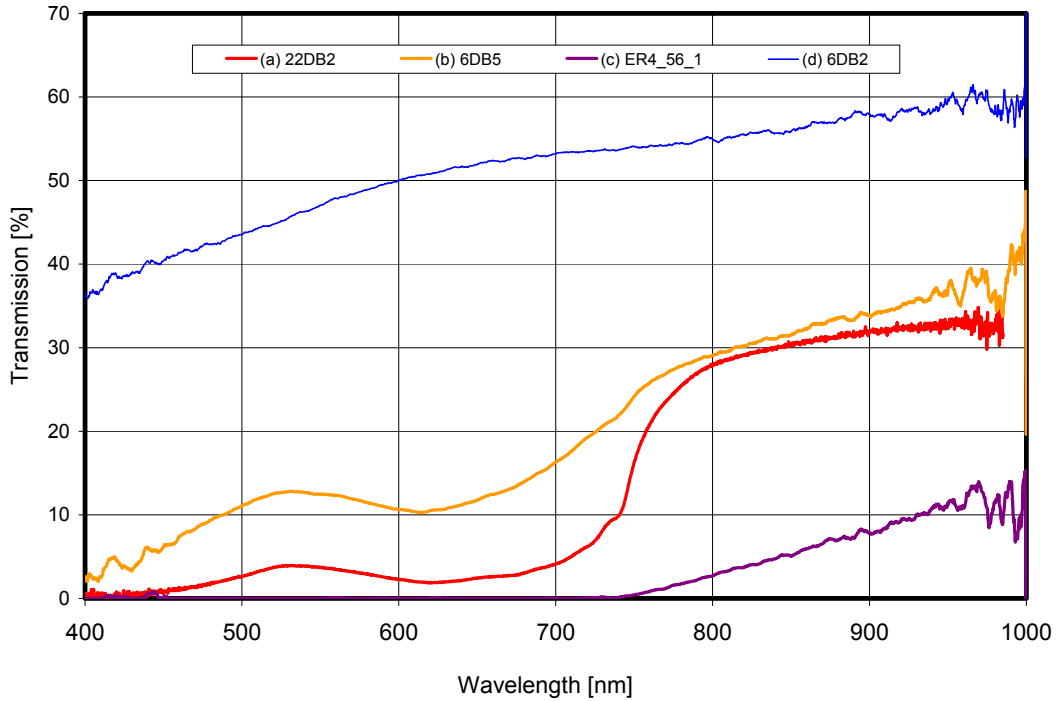
Fig. 12a: Spectrum of power transmission at the VIS/NIR range for the CVD-diamond disk of the torus window demonstrator (a), compared to those obtained with smaller and thinner test disks irradiated to 10^{20} n/m^2 (b) and 10^{21} n/m^2(c) and an unirradiated control (d).
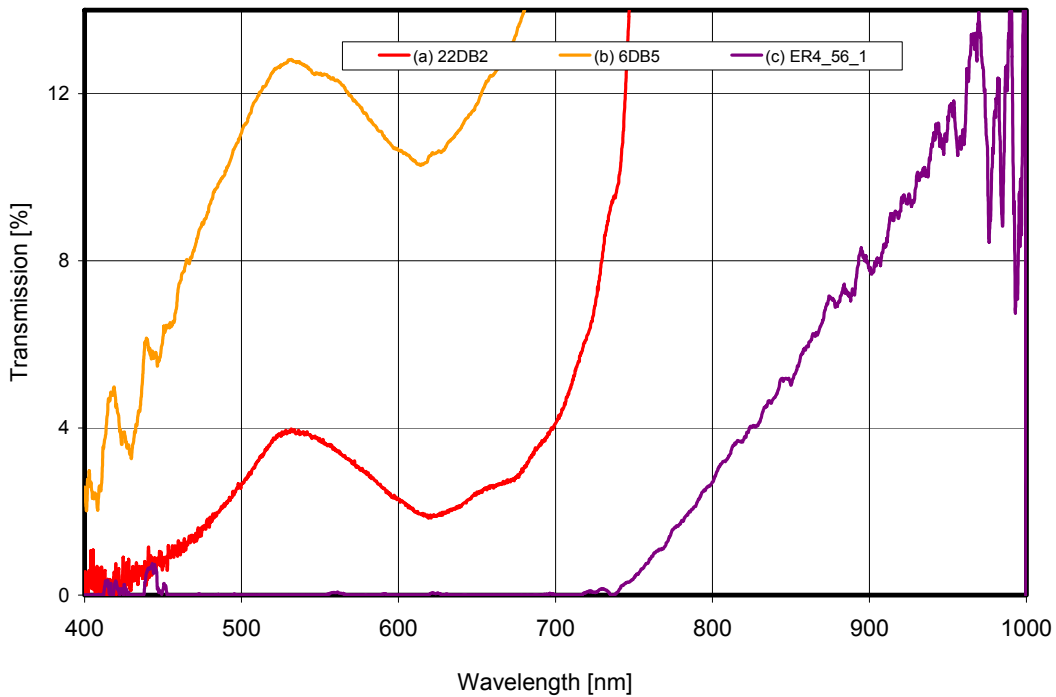
Fig. 12b: Enlarged plot of the spectrum of power transmission at the VIS/NIR range for the CVD-diamond disk of the torus window demonstrator (a) as compared to those for as-irradiated test specimens: 10^{20} n/m^2 (b) and 10^{21} n/m^2(c).

All results are consistent with conjecture that thermal conductivity is essentially governed by the concentration of point defects (with are also the predominant factor for optical absorption) and that dielectric loss is affected by more complex damage structures formed at higher flu-

ences and also to certain fraction at intermediate annealing stages of point defects. This model was originally set up to explain the higher fluences required to induce degradation in dielectric loss for the 'room temperature' neutron irradiations.
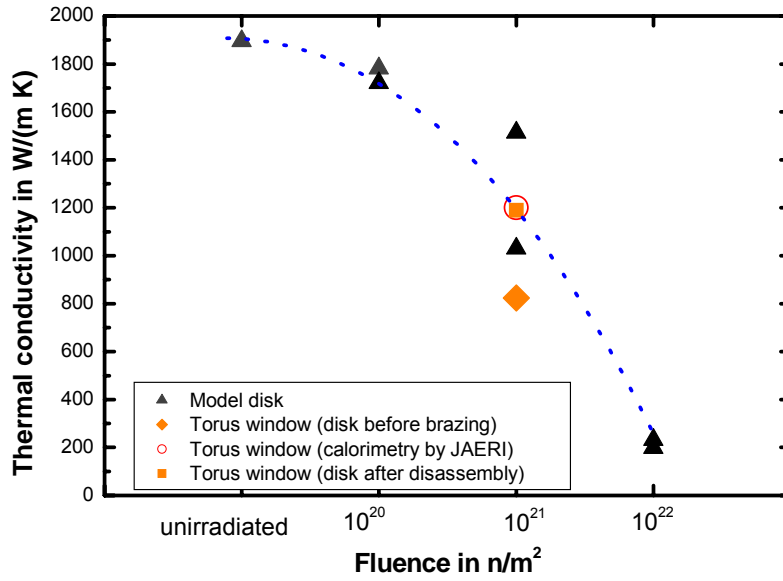
Fig. 13: The thermal conductivity measured on the CVD-diamond disk 22DB2 at different stages of torus window integration as compared to results obtained with model disks.
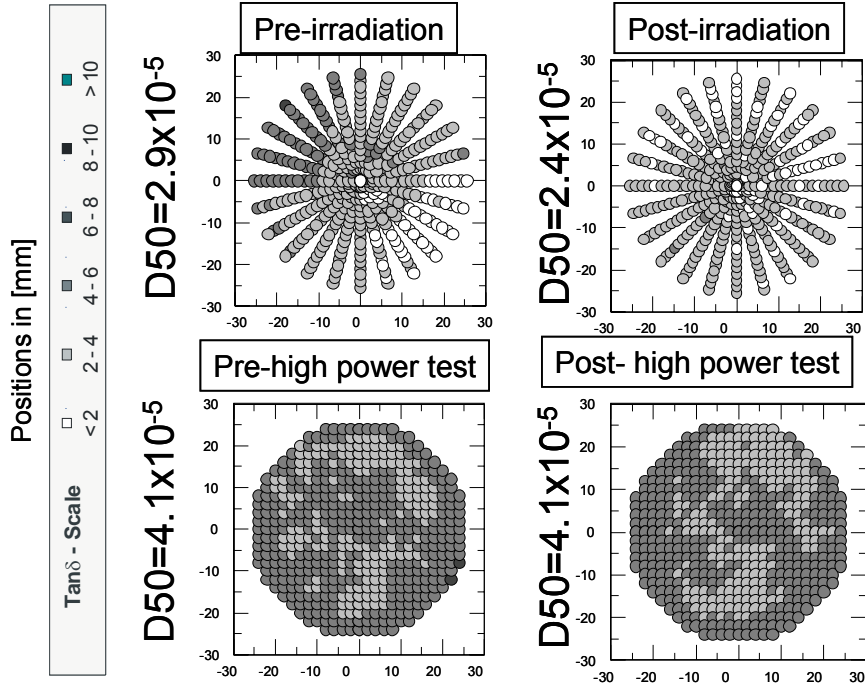
Fig. 14: Dielectric loss measured at 145 GHz at the different investigation stages of the disk 22DB2.

Subtask 4: Report on tests on the enclosure of the torus window disk cooling rim by electroplated copper in collaboration with JA ITER partner.

Principle of the copper-coated disk rim

In terms of safety, the synthetic diamond window of the ITER EC launcher is a primary tritium barrier, like the vacuum vessel (primary boundary) [5]. Therefore, the window structure must satisfy the same safety design requirements as the primary boundary. The window may have the possibility of failure (crack) due to arcing resulting from RF break-down or unexpected stress on it. In case of the unanticipated failure of the window disk, the cooling water could leak into the evacuated transmission line that is connected to the vessel since edge water cooling is applied to the window. In order to prevent the leakage and to avoid the penetration of tritium into the window cooling water circuit, a new window with a copper (Cu) coated edge has been proposed. A mock-up of the Cu-coated window was fabricated in collaboration of the JA and EU PT for high power RF transmission experiments to investigate the water cooling capability of the window [6, 7] Thermal and stress analysis should also be carried out to estimate the experimental results and the applicability of the new diamond structure to a fusion reactor.
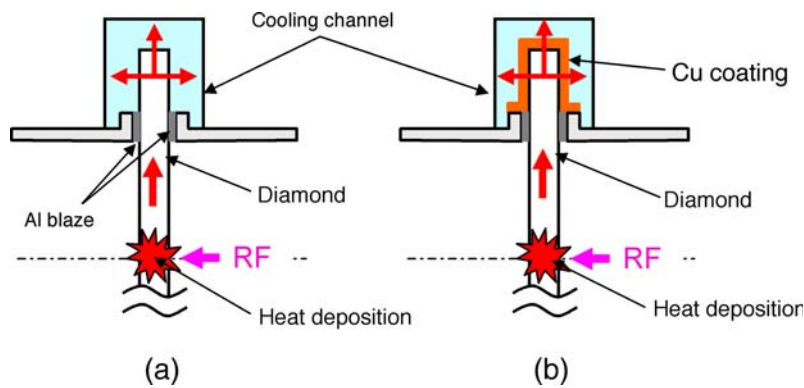
Fig. 15: Conceptual drawing of (a) conventional and (b) Cu-coated torus-window disk.
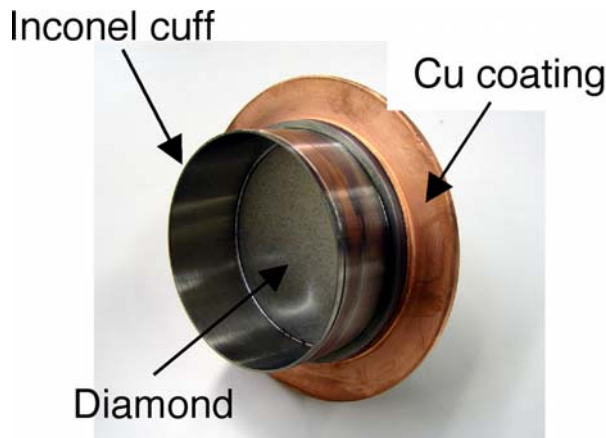
Fig. 16: Photography of the Cu-coated window including Inconel cuffs.

The conceptual drawings of the conventional and Cu-coated window are shown in Fig. 15(a) and (b), respectively. At first, a thin Ti layer is metalized on the window disk cooling rim, then the Cu-coating is electroformed (see Fig. 16). The 0.5 mm thick Cu-coating covers the entire edge of the window disk. The radius, aperture and thickness of the window are 100 mm, 70 mm and 2.15 mm. The radial length of the cooling region (Cu-coating) is 11 mm. The aluminum braze region between the diamond disk edge and the Inconel cuffs is also covered completely by the Cu-coating layer. Therefore, the Cu-coating is effective to avoid aluminum corrosion by cooling water as well. The Cu-coated window assembly for the high power mm-wave transmission experiment was fabricated with a stainless steel housing that contains the water cooling channel (see Fig. 17).
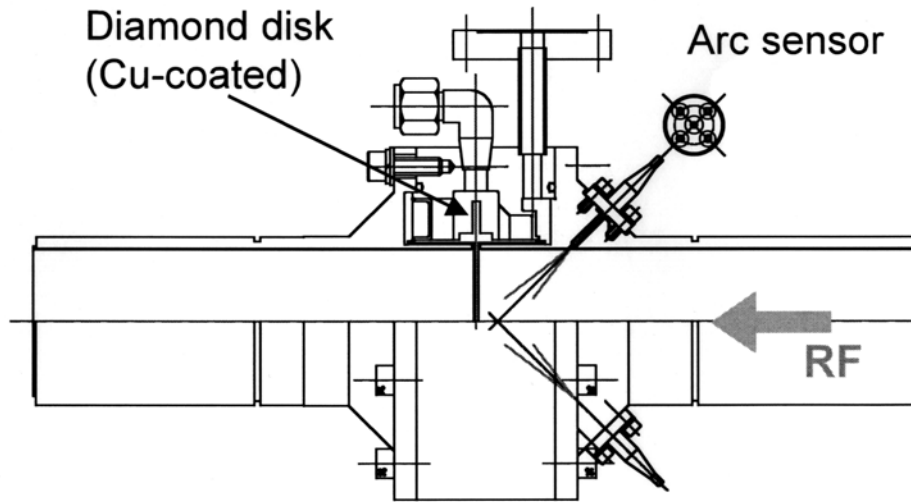
Fig. 17: Design of the torus-window assembly.

High power mm-wave transmission experiment

The schematic drawing of the experimental set-up of the high power RF transmission is shown in Fig. 18. A 170 GHz mm-wave beam generated by the gyrotron is guided to the inlet of the transmission line by a mirror optical unit (MOU). The Cu-coated window is connected to the evacuated transmission line. Since the thickness of the diamond window used in the experiment is unmatched to 170 GHz, the window is obliquely installed by 1° to prevent the reflected RF power to go back to the gyrotron. In addition, a teflon load is installed in front of the window to attenuate the reflected wave power. The transmitted RF power is also absorbed and measured by a metal dummy load installed behind the window. The load is evacuated although the transmission between the window and the load is in air. The window temperature is measured by an infrared (IR) camera. A VTR video camera is also used to monitor visible lights during RF beam transmission. The Cu-coated edge of the window is cooled by water.
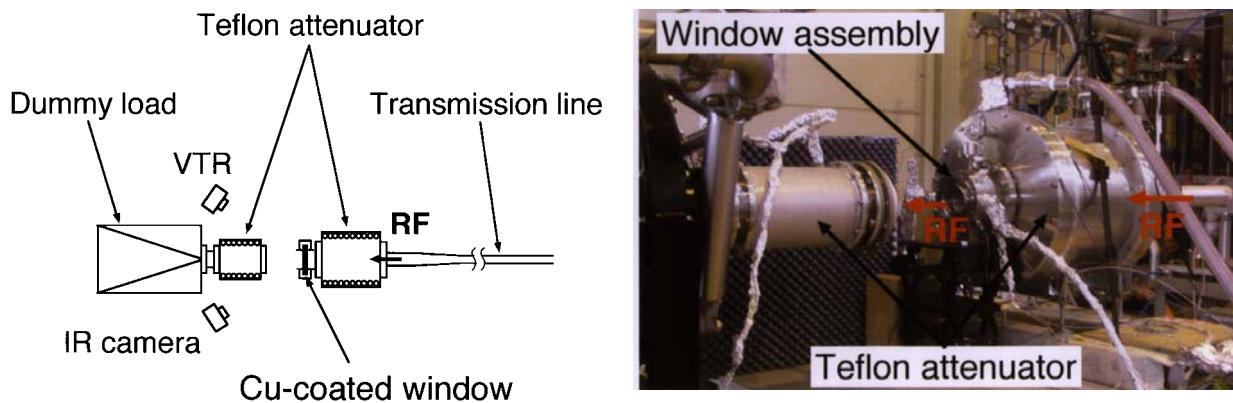
Fig. 18: Set-up of the high power 170 GHz transmission experiment.

In Fig. 19, the time evolution of the temperature increase at the window center is shown. The mm-wave power and pulse length are 55 kW and 3.5 sec, respectively. The circles and the solid curve are the experimental data and the calculation results, respectively. It is obvious that the experiment agrees well with the calculation using ABAQUS version 6.2. In the calculation, a loss tangent of 8.5×10^{-4} was applied. This value has been obtained by a low power measurement using a Fabry-Perot resonator prior to the high power experiment. In addition, the thermal conductivity of CVD-diamond of 1.9 kW/m/K was applied in the calculation. The

heat removal coefficient at the cooling region is estimated to be 5 kW/m²/K based on the size of the cooling channel and the flow rate of cooling water is 18 l/min. The thickness of the window disk is unmatched to 170 GHz and the absorption factor is about 0.7-0.75 compared to the matched case. Considering this condition, the high loss tangent and the transmitted RF power, it is recognized that this 55 kW experiment is comparable to 1.75 MW RF transmission with a standard CVD-diamond window whose loss tangent is 2×10^{-5}.

A mm-wave transmission of 120 kW/3sec, which is equivalent to 3.7 MW, was also demonstrated. It could be shown that the experimental result also agreed with thermal calculation using the same calculation parameters as those of 55 kW. The window was visually inspected after the experiments and no obvious damage was observed.

4.3 Thermal and stress analysis.

In order to estimate the reliability of the Cu-coated diamond window, thermal and stress analysis were carried out using ABAQUS ver. 6.2 [8]. The calculation model is based on a two-dimensional rotationally by symmetric solid model around the window center axis. Since the cooling region is placed at the Cu-

Fig. 19: Time evolution of temperature increase at the window center. The solid circles and the curve are the experimental data and the calculation, respectively. Loss tangent, thermal conductivity of diamond and heat transfer coefficient at the cooling region are 8.5×10^{-4}, 1.9 kW/m/K and 5 kW/m²/K, respectively.

coated edge and some parts of the Inconel cuffs, the heat removal regions are set there in the calculation. A heat deposition of a 1.75 MW, CW wave beam in the window, is assumed. The Gaussian distribution with 26 mm in width is considered. These boundary conditions are the same as those of the high power experiment described in the previous section. In the stress analysis, elastic and plastic conditions are considered since aluminum and copper are ductile and malleable. The material data used for the analysis are summarized in Table 4.

Tab. 4: Material data for the thermal and stress analysis.

Property	Unit	Diamond	Copper	Inconel	Aluminum
Density	kg/m³	3520	8900	8300	2700
Thermal expan. coeff	10⁻⁶/K	1	16	13	23
Thermal cond.	W/m/K	1900	400	14	237
Specific heat	J/kg/K	520	385	420	920
Poisson ratio		0.1	0.37	0.28	0.35
Young module	GPa	1050	130	210	70
Yield strength	MPa	300	80	350	50
Loss tangent	x10⁻⁴	8.5	-	-	-
Permittivity		5.7	-	-	-

A maximum temperature increase of 57°C was obtained at the window center, while the temperature of the cooling water is 25°C. It was also found that this result was nearly equivalent to that of the conventional window structure with the same calculation conditions. Loss tangent, thermal conductivity of the CVD-diamond and RF power are 8.5×10^{-4}, 1.9 kW/m/K, 55 kW, respectively. The heat transfer coefficient of the heat removal regions is 5 kW/m²/K as estimated from the flow rate of cooling water and the size of the cooling channel in use. Using this temperature distribution, the stress analysis was carried out. The

maximum stress established in the diamond disk is 65 MPa (obtained at the boundary between diamond and copper), which is less than fracture stress of diamond 350 MPa. While the peak stress of 97 MPa is obtained at the Inconel cuff where it is covered by the Cu-coating. This value is, however, less than the yield stress of Inconel (350 MPa). It has been confirmed that the Cu-coated window has the same capability of edge cooling as the conventional window and that the reliability of its structure at MW-level wave transmission is also comparable.

Subtask 5: Report on the manufacture and test of a double-disk CVD-diamond torus window unit with evacuated interspace between the two disks

5.1 Principles

The limited space available for the CVD diamond window in the ITER upper port ECH&CD plug calls for a very compact design of a double-disk window with an evacuated interspace which should be designed to allow a direct replacement for the present ITER reference concept of a single-disk window. For this target, a new design has been developed that is based on a double-ring structure which provides face cooling only to one side of both diamond disks (cf. Fig. 20a, b). The thermal properties of the brazing contact were measured using a small model disk and a copper tube. No increase in thermal resistance inside the brazing area was found.

a   b
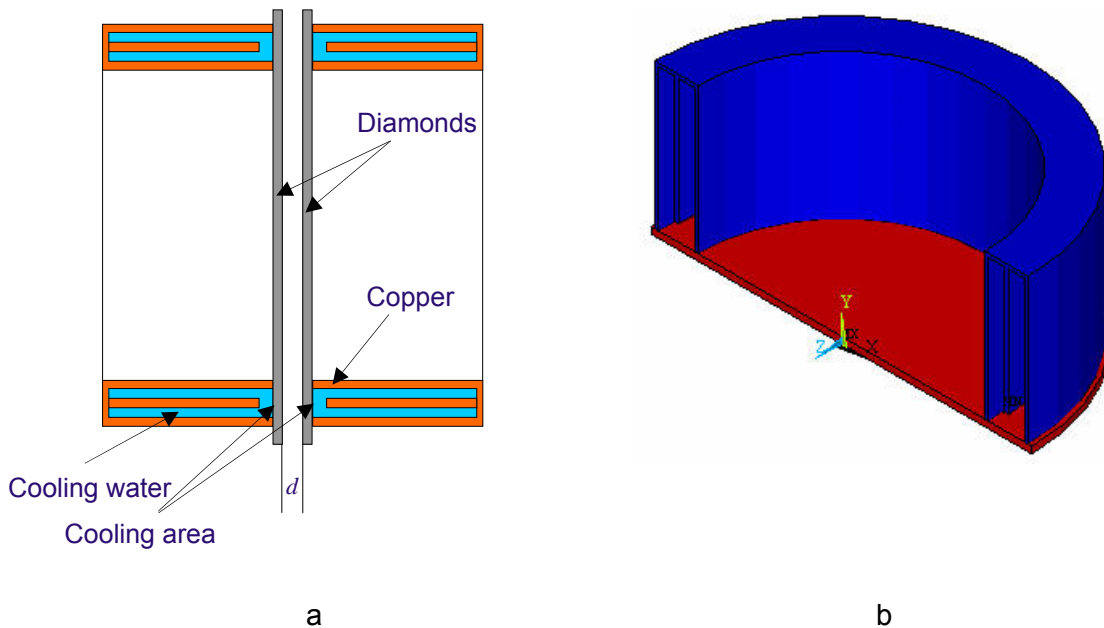
Fig. 20: Two (a) and tree (b) dimensional sketch view of the double-ring structure.

For the manufacturing and testing testing of the double-disk window, two CVD-diamond disks (55DB1, 56DB1) were procured by Element 6 having a thickness identical within 1 µm. The actual thickness was chosen to be resonant at 140 GHz (t=1.803 mm) to allow high power testing with available 140 GHz gyrotrons.

The window housing is arranged to allow remote adjustment of the window separation over the range of 4 – 6 mm with a setting accuracy of ± 5 µm. This is achieved by 3 motor driven shafts and 3 additional guiding shafts (cf. Fig. 21).

A		Torus vacuum
B		Interspace vacuum
C		Secondary pressure side
D		2 (of 3) shafts for gap adjustments
E		2 (of 3) guiding shafts
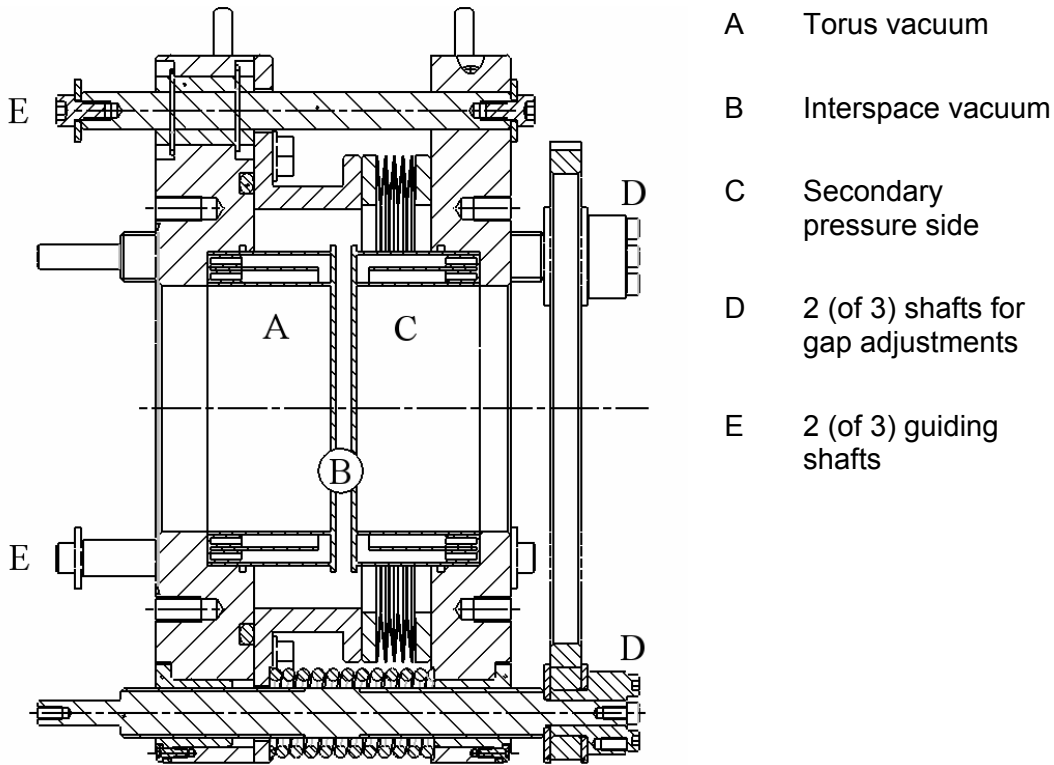
Fig. 21: Schematic arrangement of the double-disk window housing with the integrated basic window disk unit.

5.2 Thermo-hydraulic and thermo-mechanical analysis

A heating power of 350 W per disk was taken as typical high power test conditions for which an efficient cooling concept was to be developed. The required water flow rates were assessed by thermo-hydraulic analysis (using ANSYS Flotran CFD) The following beam parameters were chosen:

Window aperture	d_{eff}	80 mm
Radius of the RF-beam	w	25.7 mm
Absorbed power (P_0 =1MW, $\tan\delta$=2·0-5, f = 140GHz)	P_{abs}	350 Watt

The 3D finite element thermo-hydraulic analysis assigns the temperature field (absolute value of the temperature in each node of the meshed structure) for different water flow rates. Although the temperature field has a complex 3D distribution, it is possible to summarize the key results in terms of the temperature of the center and edge of the disk (T_{centre}, T_{edge}, see Table 5). From thermo-hydraulic analysis, it follows that a rate of 10 l/min provides an effective cooling of the disk. Increasing of the rate above 10 l/min has no major effect on T_{centre}. The only effect achieved is to improve the temperature homogeneity in the copper (cooling) cuffs. In this case, the temperature along the circumference of the cooling structure becomes constant. It means that it is possible to obtain an effective heat transfer coefficient which corresponds to an axi-symmetrical (i.e. 2D) temperature distribution. This step couples 3D thermo-hydraulic and 2D axi-symmetrical thermostatic models allowing later to provide 2D axi-symmetrical thermo-mechanical analysis of the structure. Heat transfer coefficient α_T was calculated in FEMLAB. The adjustment criteria was T_{centre}.

Table 5: Results of the thermo-hydraulic analysis of the face cooling.

Parameters	Water consumption, l/min					Limit
	0.6	3	10	18	30	-
T_{centre} / K	380	338	322	320	318	312
T_{edge} / K	361-362	317-321	301-303	298-303	296-300	293
ΔT / K	18-19	17-21	19-21	17-22	18-22	19
α_T / $Wm^{-2}K^{-1}$ (FEMLAB)	-	-	5000	7500	12500	∞

As an adequate value for the heat transfer coefficient α_T = 6 kWm^{-2}K^{-1} was chosen which corresponds to flow rate between 10 and 18 l/min . It was introduced into the thermo-mechanical analysis of the structure. Thus T_{centre} can be assigned to about 320 K (47°C) and the temperature gradient between centre and edge of the disk to about 20 K.

There are three main factors that introduce stresses in the structure: brazing process, pressure and absorption of microwave power in the diamond. In order to avoid inelastic deformation of the cooling cuffs as well as to avoid breaking of the diamond during window operation maximum stresses must be kept below the critical limits. The combined effects are summarized in the Table 6.

I. Brazing

The double-ring structure required for the double-disk window is formed by copper cuffs joined to the diamond by Ag/Cu brazing technology at Thales. The idea of using thin copper structures is that the cuffs can deform close to braze and thus do not leave any residual stresses in the CVD diamond disk. The reason is the softening of copper by recrystallisation when slowly cooling down from the typical brazing temperatures (800- 840°C); the typical yield strength is taken as 50 MPa.

II. Pressure

In off normal ITER events 0.2MPa overpressure will have to be tolerated. Maximum pressure introduces stresses of about 50 MPa in the centre of the disk and 60 MPa in brazing area. The additional displacement of the centre of the disk to its edge can reach 27 μm.

III. Microwave absorption

A maximum stress of 18 MPa due to microwave absorption arises near the brazing area of the outer cuff. The same order of magnitude stress arises in the diamond disk in brazing areas. Displacements due to this effect are 2 μm.

Table 6:   Stress analysis for the different parts of the double-disk window.

Place		Principal stress S_1, MPa			
		pressure	absorption	total	Limits
Diamond	inner brazing	60	15	67	100-150
	outer brazing	4	18	22	(1/3 of ultimate
	center	53	-	46	bending strength)
	displacements, μm	27	2	29	
Copper cuffs	Inner	16	7	24	50
	Outer	4	16	21	(Yield stress)

Manufacturing

The two CVD-diamond disks were produced by Element6 (Ascot, UK). The loss mapping performed at our laboratories showed a pronounced increase towards the edge, while the centre values, namely for disk 56DB1, proved to be typical for a low loss CVD-diamond grade (cf. Fig. 22).

55DB1:
D10: $2.0 \cdot 10^{-5}$; D50: $2.7 \cdot 10^{-5}$; D90: $4.0 \cdot 10^{-5}$

56DB1:
D10: $1.2 \cdot 10^{-5}$; D50: $1.8 \cdot 10^{-5}$; D90: $3.7 \cdot 10^{-5}$
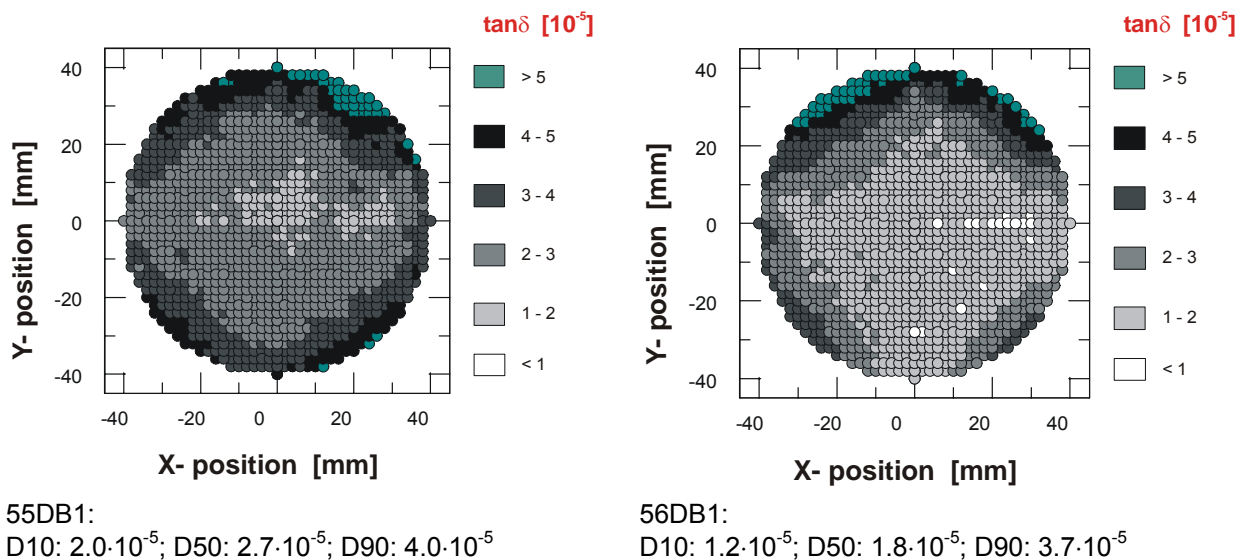
Fig. 22:   Dielectric loss mapping of the CVD-diamond disks procured for the manufacturing of the double-disk window.

To manufacture the CVD-diamond window units, copper cuffs (OFHC) with inner diameters of 80 mm and 100 mm (thickness: 1 mm) were brazed at Thales by the reactive Ag(Cu) brazing technology at 840°C on both faces of each disk (Fig. 23). The symmetrical arrangement of the cuffs during the brazing process was chosen to avoid any axial anisotropy in the stresses in the disk. The brazing process proved to be very critical with respect to vacuum tightness.

For the disk 55DB1, five brazing runs had to be made, and still leakage could not be avoided in the brazing zones of all four cuffs. However a manageable arrangement was achieved for one face where both the inner and the outer cuffs were vacuum tight at the end. Then the leaky set of cuffs was cut off to provide the direct cooling arrangement. The second structure

(called 56DB1) was treated alike. A small 'microleak' remained (leakage rate below 10-8 mbar•l/s) at the outer cuff.
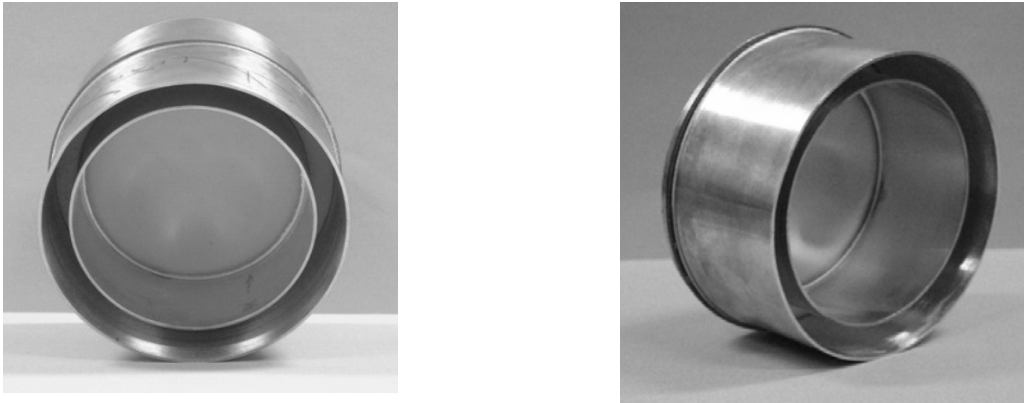
Fig. 23: Basic window disk unit (55DB1) after brazing (left) and after removal of the double ring structure at the counter-face (right).

The window was then to be joined by Reuter (Alzenau, Germany) with the flange structure in which a socket guided the cuffs. The brazing temperature was at 735°C which is by 50°-100°C below the temperatures used for joining the diamond to the copper cuffs. The insertion of the cuffs into the socket required high precision on their circularity and concentricity. The produced double-ring cuffs were markedly distorted, varying by ±130 µm around the average distance. Therefore mechanical reworking had to be applied to achieve tolerance of 50 µm.

The structure 56DB1 could be joint successfully, however a bow appeared which amounted to about 20 µm within the inner radius of 25 mm relevant for the beam. FEM modelling showed that it resulted from radial deflections which differ for two cuffs. This can be avoided in future by reshaping the height of the sockets in the flange. The structure 55DB1 was prepared for joining accordingly but the brazing could not be performed as the diamond disk failed during mechanical reworking as cracks formed between the double rings.

At first instance, given the low yield stress of recrystallised copper, no analytical scenario could be identified to explain the excessive stress levels occuring in this process, neither a subsequent FEM modelling succeeded to find among likely loading cases the one with critical stress levels. Finally by experimental tests, stress could be quantified close to the brazing of the outer ring by attachment of a resistive stress sensor. It turned out that there is indeed a critical case when the circular tool that was used to widen the distance between the two rings gets stuck and a bending

Fig. 24: Status of window structures at the end of the double disk manufacturing study:
Top: Disk 56DB1 brazed into flange and waiting for integration into window housing
Bottom: Disk 55DB1 broken under mechanical adjustment of the deviations from circularity at the ends of the copper rings.

force is applied to release it.

The consequence of this failure now is that the disk 55DB1 is removed from the cuff structure and will be laser cut to diameter of 84 mm. In this form, it assigned for further use in special window configurations (cf. Fig. 25). A replacement disk is procured and the final integration will made after reordering a double ring brazing with stringent specifications on the circularity of the disks. This part will be performed by a follow-up of this project for which it is proposed to use resources outside the present EFDA task.
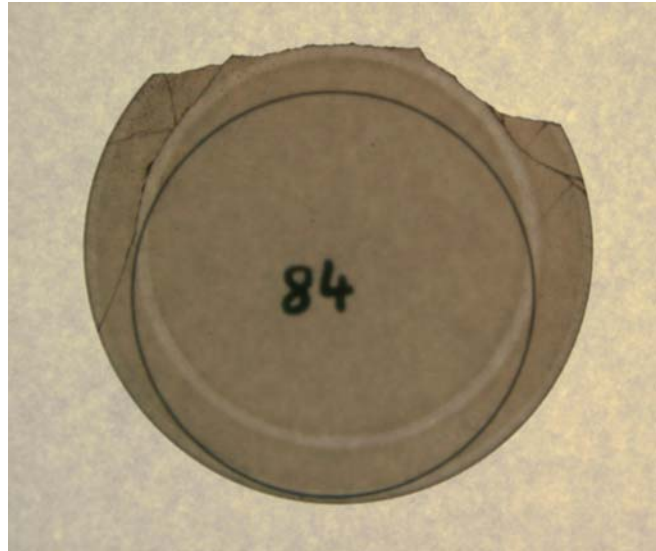
Fig. 25: Identification of the remaining useable diameter (84 mm) of disk 55DB1 after removal of the double-ring copper cuffs.

Subtask 6: Report on the dielectric characterisation of CVD-diamond window disks for gyrotron and torus windows and identification of bulk and surface loss

6.1 Principles

In diamond, the intrinsic level of mm-wave absorption is given by multiphonon absorption which is principally very low because of its homopolar lattice structure. Theoretical estimations indicate levels of the corresponding dielectric loss tangent (tanδ) below 10^{-8}. Experimentally observed values reached levels as low as $6 \cdot 10^{-6}$ at 145 GHz and $8 \cdot 10^{-6}$ at 170 GHz. The extrinsic sources for absorption can be quantitatively related to the contribution of non-diamond like phases which can vary extremely sensitively under modifications of the CVD process parameters. All suitable technologically available grades are formed by the Microwave Plasma Assisted (MPA-) variant of the CVD process. The prominent source is a specialised product line (Diafilm "RF-grade") established by Element6 (Charters, UK), demonstrator disks are also available for MPACVD diamond produced by the "Ellipsoidal reactor (ER)" approach developed by the Fraunhofer Institut für Angewandte Festkörperphysik (FhG-IAF) (Freiburg, Germany).

6.2 Results on bare CVD diamond disks

As a result of a 24 months production effort, 22 large area disks were procured from De-Beers all in the dimension of 106 mm dia. x 1.81 mm for high power windows to be installed at the W7-X experiment (IPP Greifswald, Germany): 10 gyrotron windows, 10 torus windows and 2 spare windows. The dielectric characterisation (cf. Tab. 7) documents a high degree in the parallelism of the disks (consistency of thickness values determined mechanically and electrically). Further it can be concluded that typically over the mapped inner 80 mm dia. section, mean tanδ values are kept at $2 \cdot 10^{-5}$ and upper tanδ values hardly exceed $4 \cdot 10^{-5}$. In the best disks (such as W7-X #14, #15 and ASDEX-Upgrade A1), the loss map shows only very small scatter with no systematic lateral inhomogeneity. Still untypical disks, such the replaced disk W7-X #4, show higher base lines and significantly increased losses towards the outer zones which is related to the concentration of 'non-diamond like' phase inclusions (cf . Fig. 26). In the bare disks, surface losses are generally not observed, therefore the mapped effective loss distribution was governed by the bulk loss. Two demonstrator disks for the alternative window grade (ER4_69 and ER4_70) available at FhG-IAF prove that the dielectric properties ensure a competitive level.
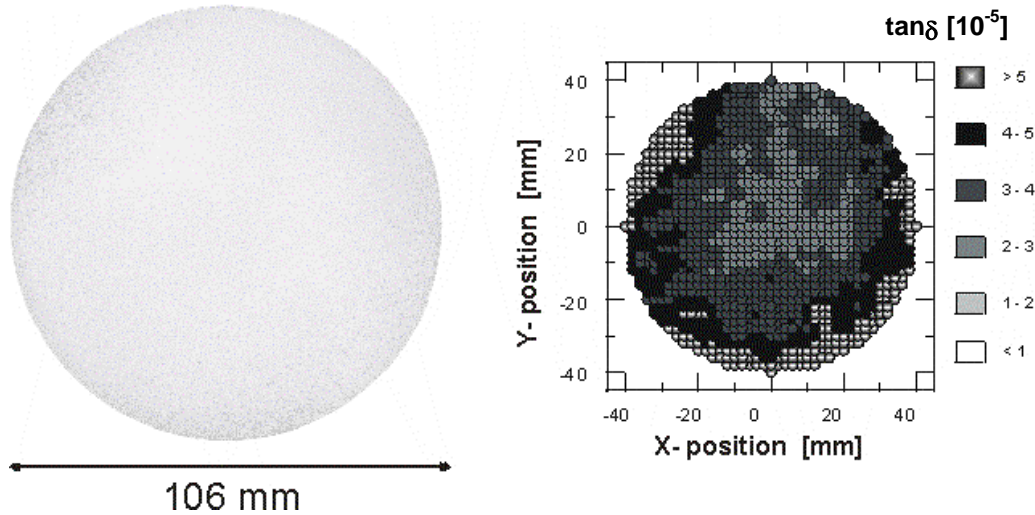
Fig. 26: Optical image of lapped W7-X disk #4 showing non-diamond like phase inclusions as black spots compared to dielectric loss mapping performed at 145 GHz.

Dielectric characterisation was also performed on 3 sets of disks which were developed for Brewster windows, double disk/multifrequency windows and ITER upper launcher windows, respectively. The most recent and outstanding achievement is the growth of a 140 mm disk (with two isolated cracks at the edge) suitable for use as a broadband Brewster window for studies of frequency tunable gyrotrons for the ASDEX-Upgrade experiment (IPP Garching, Germany)

Table 7: The mm-wave property profile measured for potential high power windows produced by Element 6 for ECW systems at the Wendelstein W7-X stellarator, the ASDEX-Upgrade tokamak and the ITER Upper Port Plug.

DB-Code	Disc #	Thickness (mechanical) [mm]	Thickness (electr.) [mm]	90 - 100 GHz		145 GHz			Use
				ε_r	$\tan\delta$ $[10^{-5}]$	$\tan\delta$			
						D10 $[10^{-5}]$	D50 $[10^{-5}]$	D90 $[10^{-5}]$	
	W7-X								
28DB1	1	1.806 - 1.810	1.811	5.672	2.5	0.9	1.7	3.7	Gyrotron
28DB2	2	1.788 - 1.818	1.816	5.675	3.0	1.1	1.9	3.9	CPI
29DB1	3	1.792 - 1.797	1.817	5.672	2.4	<1	1.3	3.5	CPI
31DB1	4	1.795 - 1.797	1.806	5.672	3.0	2.7	3.7	6.1	replaced
31DB2	4A	1.786 - 1.806	1.793	5.669	1.6	1.0	1.4	2.7	Torus
32DB1	5	1.808 - 1.811	1.810	5.674	2.6	0.9	1.5	2.3	Gyrotron
33DB1	6	1.796 - 1.810	1.799	5.670	2.5	0.9	1.3	3.3	Gyrotron
34DB1	7	1.799 - 1.801	1.805	5.675	2.3	1.5	2.0	2.7	broken
35DB1	8	1.798 - 1.806	1.806	5.673	2.8	1.6	2.3	3.6	Torus
36DB1	9	1.809 - 1.813	1.805	5.673	3.4	1.5	2.1	2.9	Gyrotron-spare
37DB1	10	1.805 - 1.808	1.813	5.669	4.0	2.3	2.9	4.0	replaced
37DB2	10A	1.789 - 1.802	1.790	5.670	1.6	1.3	2.3	4.1	Torus
38DB1	11	1.807 - 1.809	1.818	5.669	2.3	1.2	1.7	2.7	Gyrotron
39DB1	12	1.798 - 1.804	1.806	5.667	2.2	2.2	2.8	4.3	Torus
39DB2	12A	1.796 - 1.806	1.803	5.670	1.2	1.2	1.6	2.7	Gyrotron
40DB1	13	1.813 - 1.817	1.802	5.671	2.8	2.4	3.0	4.0	Torus
41DB1	14	1.805 - 1.811	1.806	5.672	1.5	1.2	1.4	1.7	Gyrotron

Table 7 cont.

42DB1	15	1.809 - 1.818	1.813	5.670	1.7	1.0	1.4	1.7	Gyrotron-spare
43DB1	16	1.806 - 1.817	1.805	5.669	2.5	2.1	2.6	3.7	Torus
44DB1	17	1.790 - 1.800	1.782	5.670	1.4	1.2	1.7	2.5	Torus-spare
45DB1	18	1.794 - 1.805	1.798	5.671	1.1	1.0	1.5	3.7	Gyrotron
46DB1	19	1.790 - 1.806	1.801	5.670	1.3	1.5	2.5	5.1	Torus
47DB1	20	1.786 - 1.800	1.796	5.672	2.2	2.3	2.8	4.1	Torus
48DB1	21	1.803 - 1.808	1.806	5.669	1.9	1.8	2.7	4.4	Torus
49DB1	22	1.788 - 1.800	1.799	5.670	1.8	1.8	2.5	3.9	Torus
	Brewster								
50DB1	BR1	1.918 - 1.920	1.923	5.669	4.4	2.5	3.6	6.4	120mm
51DB1	BR2	1.913 - 1.919	1.916	5.671	3.4	3.1	4.3	6.9	120mm
57DB1	BR3	0.404 - 0.426	Bulk losses : 4x10^{-5}						140mm
57DB2	BR4	0.505 - 0.510	Total losses : 6x10^{-5}						140mm
57DB3	BR5	1.690 – 1.703	1.700	5.670	1.4	<1,0	<1,0	2.2	140mm
	DoubleDisk / Multifrequency								
52DB1	HGF1	1.797 - 1.801	1.797	5.672	1.4	1.0	1.3	2.1	broken
53DB1	HGF2	1.795 - 1.802	1.799	5.670	2.9	2.8	3.9	6.9	Gyrotron
54DB1	HGF3	1.786 - 1.795	1.787	5.670	1.8	1.4	2.2	3.7	Gyrotron
55DB1	HGF4	1.807 - 1.809	1.803	5.671	2.0	1.8	2.7	4.0	broken
56DB1	HGF5	1.805 - 1.809	1.803	5.671	1.2	1.2	1.8	3.7	Torus
	ITER Upper Launcher								
59DB1	ITER		1.859	5.669	10.0	5.1	7.1	11.6	returned
60DB1	ITER	1.856 - 1.860	1.862	5.670	2.1	2.1	2.7	4.7	Torus
61DB1	ITER	2.585 - 2.635	2.594	5.668	4.5	3.1	3.6	4.3	returned
61DB2	ITER	1.851 - 1.860	1.856	5.669	2.1	1.9	2.3	3.3	Torus

6.3 Separation of bulk and surface loss in CVD diamond disks

The separation of the contribution of surface loss and bulk loss terms to the effective dielectric loss tangent was performed by using two special arrangements of open resonator technique: hemispherical and spherical configuration (cf. Fig. 27).
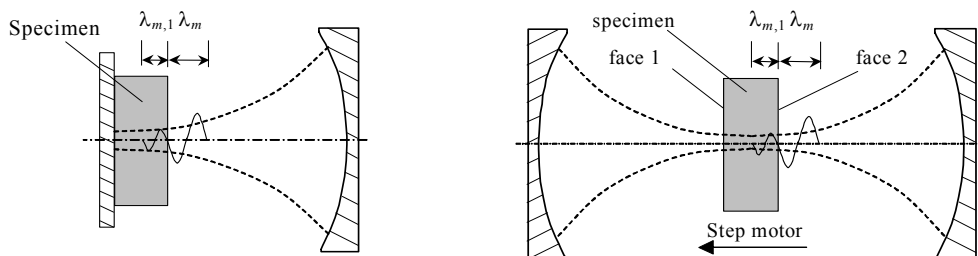
Fig. 27: Sketch view of the open resonator set-ups: hemispherical (left) and spherical/ symmetrical (right).

The effective dielectric losses ($\tan\delta_{(eff)}$) are separated as follows into the bulk ($\tan\delta_b$) and surface ($\tan\delta_S$) terms:

$$\tan\delta_{(eff)} = \tan\delta_b + \tan\delta_{S,1} + \tan\delta_{S,2} \tag{1}$$

where $\tan\delta_{S,1}$ and $\tan\delta_{S,2}$ relate to the growth (GF) and nucleation (NF) faces. These terms arise from lossy surface layers (films).

$$\tan\delta_{S,i} = a\frac{t_{f,i} \cdot \tan\delta_{f,i}}{t_B} \; . \tag{2}$$

Here a = 1.7…2 is a weight factor, t_f is the film thickness, $\tan\delta_f$ is film loss, t_B is the bulk thickness.

Obviously the exact value of t_f depends on many conditions, but in most cases it can be considered as very thin compared with the wave length in the specimen ($t_f << \lambda_{m,1}$). Therefore one can determine only the product term of $t_f\tan\delta_f$.

These tasks can be solved by introducing the IT- theory which allows the direct analysis of resonators with specimens of arbitrary thickness [9]. The procedures used for hemispherical and spherical resonator methods are exemplified [10] by a test window provided by CPI (Palo Alto, USA). This brazed structure was under study due to pronounced surface loss.
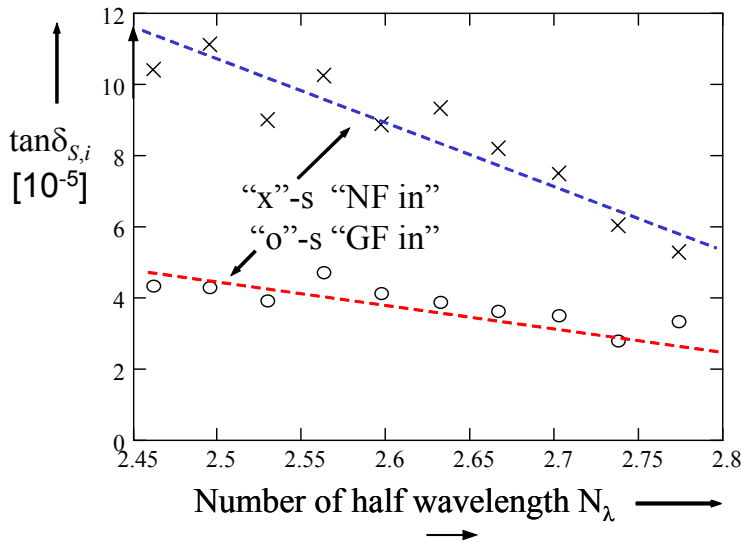
Fig. 28: Dielectric measurements by hemispherical resonator.

In the hemispherical resonator arrangement, the presence of surface loss can be put to evidence by a systematic frequency trend in the apparent $\tan\delta$ data obtained over a frequency range. Two extreme cases are given for 'resonant' and for 'anti-resonant' specimen thickness identified by integer and half-integer numbers of half-wavelengths contained in the dielectric disk (N_λ). Whereas the surface loss term is always minimum for the face placed at the metallic mirror, the contribution of the face opposite to the mirror ('in-resonator orientation') increases as the field changes from the node to anti-node condition. A steady increase of the apparent $\tan\delta$ value when the N_λ parameter is steadily approaching the anti-resonant case identifies the presence of surface loss. In order to characterize both surfaces (GF, NF) two measurements with "GF in" and "NF in" are performed. For the CPI window results of IT-modelling are given in Table 8.

Table 8: IT-modelling for hemispherical setup

Meas. technique		Loss tangent, $\tan\delta$ [10^{-5}]		
		$\tan\delta_b$	$\tan\delta_S$, NF	$\tan\delta_S$, GF
Hemispherical, f_m = 88-102 GHz	NF	2.0	6.9	-
	GF	2.0	-	1.9

Normally measurements in the spherical resonators are performed at frequencies which fulfil the resonant thickness conditions. In this case the centre frequency of the measurement mode does not change during sample displacement along the resonator axis. Because of the E-field symmetry in the resonator it is possible only to separate bulk and total surface terms from both surfaces.

If the specimen thickness is off-resonant both frequency and Q factor vary with the specimen position. Moreover because of the E-field asymmetry the Q-factor depends not only on the absolute value of the total dielectric losses, but on the ratio between the surface loss terms. This feature of the off-resonant behaviour is used for evaluation of the dielectric properties of the diamond disks with the help of the IT-theory.

Practically one starts with a model of the frequency shift as a function of the specimen position along the resonator axis to track resonant peaks. During measurements the specimen is moved by steps at which a program traces resonant peaks and determines their centre frequency and Q factor (Fig. 29). Then the IT-model can be applied to evaluate dielectric properties of the specimen: total and surface terms of each side of the disks. The results of the IT-modelling for both resonant arrangements are summarized in Table 9.
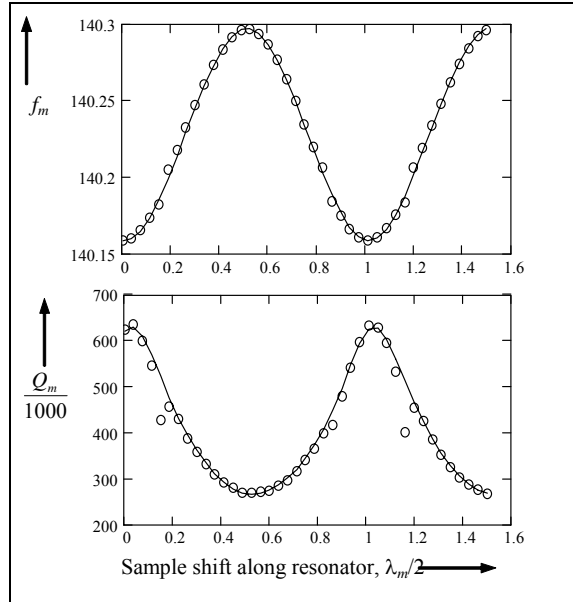
Fig. 29: Dielectric loss measurement with symmetrical open resonator set up on the CPI-window: Frequency (f_m) and Q-factor diagrams: "o"-s are experimental points, solid lines correspond to IT-modelling.

Table 9: Total losses and surface terms of CPI-window.

Measurement technique	Loss tangent, $\tan\delta$ [10^{-5}]			
	$\tan\delta_{eff}$	$\tan\delta_b$	$\tan\delta_{S,\ NF}$	$\tan\delta_{S,\ GF}$
Symmetrical, $f_m \approx 140.2$ GHz	10.3	1.5	6.9	1.8
for comparison: hemispherical, f_m = 88-102 GHz	10.8	2.0	6.9	1.9

Subtask 7: Report on the investigations of procedures to reduce surface losses on CVD-diamond disks introduced by brazing

7.1 Principles

Three major technologies exist to braze large area CVD-diamond disks into vacuum tight window structures: the aluminium brazing of Culham Technologies/Element6, the Au(/Cu) brazing of CPI (Palo Alto, USA) and the Ag/Cu brazing of Thales (Velizy, F) . The aluminium braze requires much lower brazing temperatures (up to 680°C) than the gold braze (up to 1000°C) with the draw-back of lower maximum bake-out temperatures for the gyrotron tube (limited to about 450°C) and of potential corrosion by the cooling water. An intermediate temperature level is available by the Ag/Cu brazing (780°-840° C). For typical brazing runs of

the latter technology, no critical loss increase was observed. Also in existing high power windows produced by this technology low power loads have been observed. Namely for the window of the W7-X prototype tube, which still holds the world records in total energy output for long pulse operation of Megawatt gyrotrons, the power load on the window could be fully assigned by the bulk loss.

7.2 Experiments
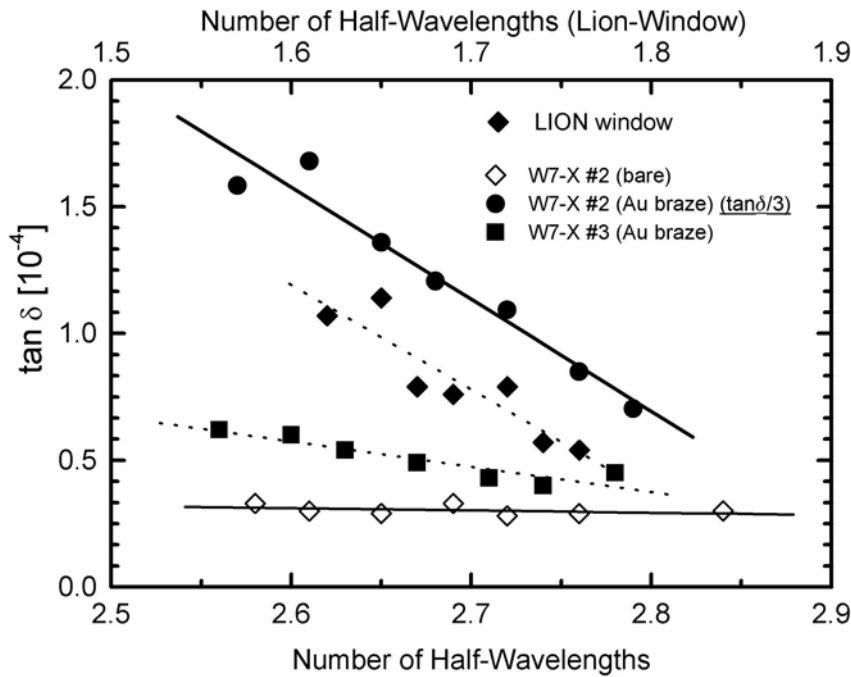
Fig. 30a: Surface losses in Au-brazed CVD-diamond windows (growth face 'in-resonator') put to evidence by systematic variation of the effective tanδ for the 'resonant' and 'anti-resonant' thickness conditions at 90 – 100 GHz.
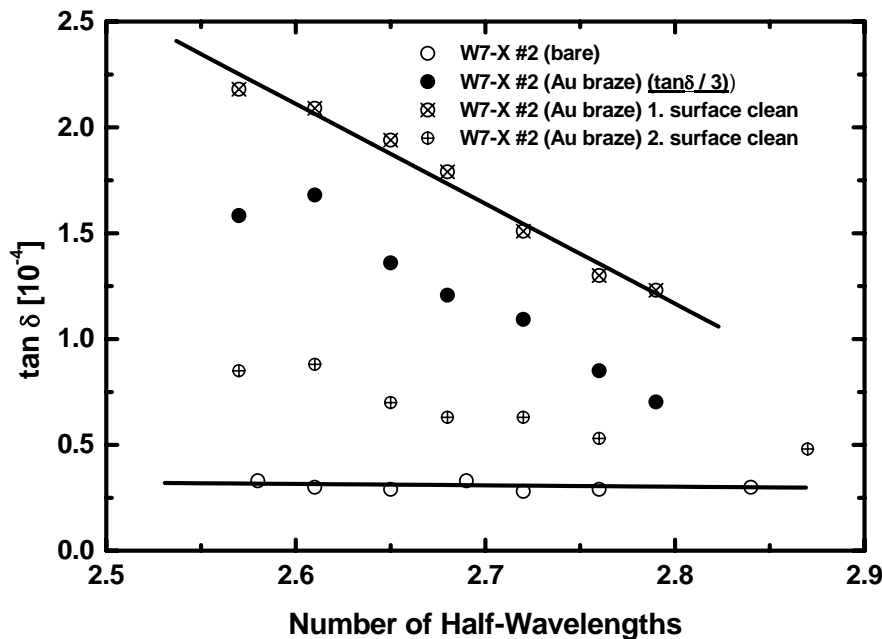
Fig. 30b: Surface losses in the Au-brazed CVD-diamond window W7-X #2 (growth face 'in-resonator') at different stages of the surface treatment.

Window failure is an issue under concurrent inspection. For example the Au-brazed window in the "LION" gyrotron tested at the DIII-D experiment by General Atomics (San Diego, USA) failed by crack formation just like the Al-brazed 'Star-of-FZK' window tested in the 170 GHz ITER tube at GY-COM (Moscow and Nizhny Novgorod, RF), both under relaxed power load conditions. The brazed CVD - diamond disk (69 mm dia. x 1.15mm) in the LION window was investigated after failure in high-power tests for apparent surface losses at 90 – 100 GHz. Specially with the growth face 'in-resonator' substantial contributions were observed; with the nucleation face 'in-resonator' the effect was much smaller, in this case it remained within the experimental scatter. The generation of surface losses as a consequence of the brazing conditions were further substantiated for disks W7-X #2 and #3 (cf. Fig. 30a). Again the effect was

substantially larger for the growth face 'in-resonator'. Raman scattering gave clear evidence of graphite at the surface of the disks with the highest losses; by blasting with alumina grit of various sizes this absorptive layer could be very efficiently reduced (cf. Fig. 30b).

A close inspection of the effects produced by the Al-brazing process was performed for the demonstrator window of a 170 GHz ITER torus system using the large area disk (22DB2) described in detail in Section 3. After brazing, no significant surface loss terms were observed. However, by acid cleaning (HNO_3, H_2SO_4), substantial contributions could be induced which were removed by caustic treatment (15% NaOH). The disk was then subjected by DeBeers to Ti/Au sputtering at the disk edge to produce a starting layer for electrochemically deposited copper at the cooling edges to inhibit corrosion of the braze and tritium diffusion. Clearly this treatment resulted for the masked inner diamond section in a similar surface contamination as shown for the HNO_3 cleaning. Again the caustic cleaning was efficient to eliminate the surface losses (cf.Fig. 31). This is in clear contrast to the Au brazed windows where the same chemical treatments were tested for the brazed disk W7-X #2 and found to be ineffective.

Staff:

IHM

H. Budig
G. Dammertz
S. Illy
B. Piosczyk
R. Schneider
J. Szczesny
M. Thumm

IMF I

J. Burbach
I. Danilov
R. Heidinger
A. Meier
M. Rohde
P. Severloh
P. Willing
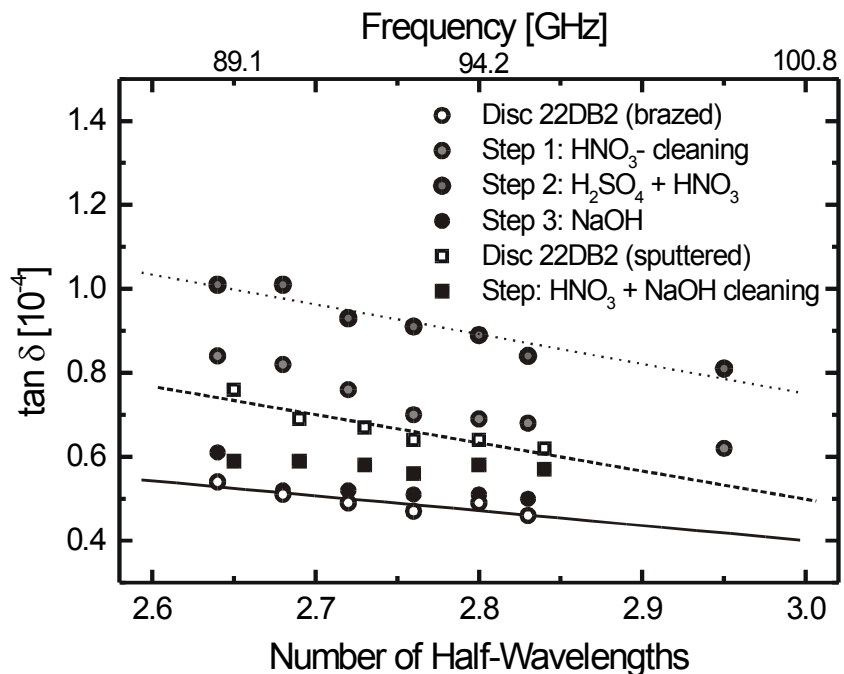
Fig. 31: Characterisation of Al brazed ITER torus demonstrator window with respect to surface losses (90 – 100 GHz) affected by chemical surface treatment (growth face 'in-resonator').

Literature:

[1] Thumm, M.: MW gyrotron development for fusion plasma applications, Plasma Phys. Control. Fusion 45, A143-A161 (2003).

[2] Dammertz, G., K. Koppenburg, B. Piosczyk, M. Thumm, R. Heidinger: Gyrotronröhren und Millimeterwellentechnik für die Kernfusion, Nachrichten – Forschungszentrum Karlsruhe, 36, 30-35 (2004).

[3] Tran, M.Q., S. Alberti, A. Arnold, D. Bariou, E. Borie, G. Dammertz, C. Darbos, O. Dumbrajs, G. Gantenbein, E. Giguet, R. Heidinger, J.-P. Hogge, S. Illy, W. Kasparek, C. Liévin, R. Magne, G. Michel, B. Piosczyk, M. Thumm, I. Yovchev: Development of high power gyrotrons for fusion plasma applications in the EU, Conf. Digest Joint 29th Int. Conf. on Infrared and Millimeter Waves and 12th Int. Conf. on Terahertz Electronics, 2004, Karlsruhe, Germany, Plenary Paper, pp. 59-62.

[4] Dammertz, G., H. Braune, V. Erckmann, G. Gantenbein, W. Kasparek, H.P. Laqua, W. Leonhardt, G. Michel, G. Müller, G. Neffe, B. Piosczyk, M. Schmid, M.K. Thumm: Progress in the 10-MW ECRH system for the stellarator W7-X, IEEE Trans. on Plasma Science, 32, 144-151 (2004).

[5] Heidinger, R., I. Danilov, U. Fischer, G. Hailfinger, K. Kleefeldt, A. Meier, E. Stratmanns, M. Thumm, A.G.A. Verhoeven: Design and analysis of windows and structural components for the ITER ECRH upper port plug, 13th Joint Workshop on Electron Cyclotron Emission and Electron Cyclotron Resonance Heating (EC 13), Nizhny Novgorod, Russia, May 17-20, 2004.

[6] Takahashi, K., S. Illy, R. Heidinger, A. Kasugai, R. Minami, K. Sakamoto, T. Imai, M. Thumm: Recent results of ECH diamond window development, Conf. Digest Joint 29th Int. Conf. on Infrared and Millimeter Waves and 12th Int. Conf. on Terahertz Electronics, 2004, Karlsruhe, Germany, pp. 721-722.

[7] Takahashi, K., S. Illy, A. Kasugai, K. Sakamoto, R. Heidinger, M. Thumm, R. Minami, T. Imai: Development of reliable diamond window for EC launcher on fusion reactors, 23rd Symp. on Fusion Technology (SOFT), Venice, Italy, September 20-24, 2004.

[8] Danilov, I., R. Heidinger, A. Meier, M. Thumm: Design and thermo-mechanical analysis of a double disk window for step-tuneable gyrotrons, Proc. 10th Int. Conf. Displays and Vacuum Electronics, Garmisch-Partenkirchen, ITG-Fachbericht 183, 2004, pp. 301-304, Invited Paper.

[9] Danilov, I., R. Heidinger: New approach for open resonator analysis for dielectric measurements at mm-wavelengths, J. of European Ceramic Society, 23, 2003, pp. 2623-2626.

[10] Danilov, I., R. Heidinger, A. Meier: Method for separating surface loss terms on CVD-diamond disks, Conf. Digest Joint 29th Int. Conf. on Infrared and Millimeter Waves and 12th Int. Conf. on Terahertz Electronics, 2004, Karlsruhe, Germany, pp. 723-24.

TW3-TPDE-IRRCER
Irradiation Effects in Ceramics for Heating and Current Drive, and Diagnostics Systems

Objectives

The overall objective of this task is to provide the required irradiation testing and screening of small prototype diagnostic components, and the necessary insulator research and database for heating and current drive, and diagnostic systems for ITER. Especially for EC components work was carried out to assess the effect of tritium on the optical and dielectric (loss) properties of CVD diamond for ECRH applications. To reduce cost it was decided that deuterium rather than tritium will be employed. Thermal conductivity of diamond was to be determined as a function of annealing temperature for the assessment of the role of radiation damage.

TW3-TPDE-IRRCER D3
Effect of Tritium on ECRH Dielectric Loss of Diamond

Two large area CVD diamond windows of actual window size for high power Electron Cyclotron (EC) wave transmission lines were exposed to deuterium in a permeation test facility where D_2 pressure up to 0.5 MPa were applied at the upstream side, the gas composition is analysed by a quadrupole mass spectrometer and the downstream side.

The two window units formed with different brazing methods:
a) 34DB1: Al-braze to Inconel; b) 36DB1: Ag-braze to copper

For both CVD window units, no evidence for D_2 permeation at room temperature was found. Several experiments performed at elevated temperatures (typically 200°C and 240° C) indicate the built-up/presence of increased D_2 signals at the downstream side for the window using the Inconel structure. Measurements of dummy units which reproduce the window geometry without the presence of the CVD diamond disk support the strong evidence that the built-up process goes along with solution of deuterium in the inconel cuff. This window structure was out-gassed at temperatures up to 300°C. Dielectric measurements in the disk show a built-up of surface loss which is in the order of 5 times the bulk loss. Similar values were observed in the disk during the brazing process and are typical for surface loss induced by carbon contaminants which are conductive by protonic 'activation'. These conditions which were believed to be fully removed by oxidising chemical treatment were apparently reactivated by the exposure to deuterium.

TW3-TPDE-IRRCER D4
Studies of Thermal Conductivity at Room Temperature of Neutron-irradiated CVD Diamond before and after High Temperature Exposure

In a large area CVD diamond disk irradiated with fast neutrons to a fluence of 10^{21} n/m^2 (E>0.1 MeV) thermal conductivity was decreased to 800 W/(m·K), but this degradation recovered to about 1200 W/(m·K) after its brazing at 600-650°C into a window structure. The bare disk removed from the window housing after high power testing was subjected to annealing in vacuum (< 10^{-6} mbar) at increasing temperature steps. For the studies, the specimen was kept at the annealing temperature for 4 h and then cooled to down to room temperature. The thermal conductivity showed an fast increase which became saturated at 700°C, this goes along with fast recovery of transparency in optical spectrum at wavelengths of 550 - 750 nm. In contrast, the dielectric loss measured at 140 GHz, showed an initial increase peaking at 650°C and only a gradual recovery not reaching the level of the as-irradiated disk (cf. Fig 1). This confirms the conjecture that point defect formation governs thermal conductivity while increase dielectric loss is caused by smaller defect clusters.
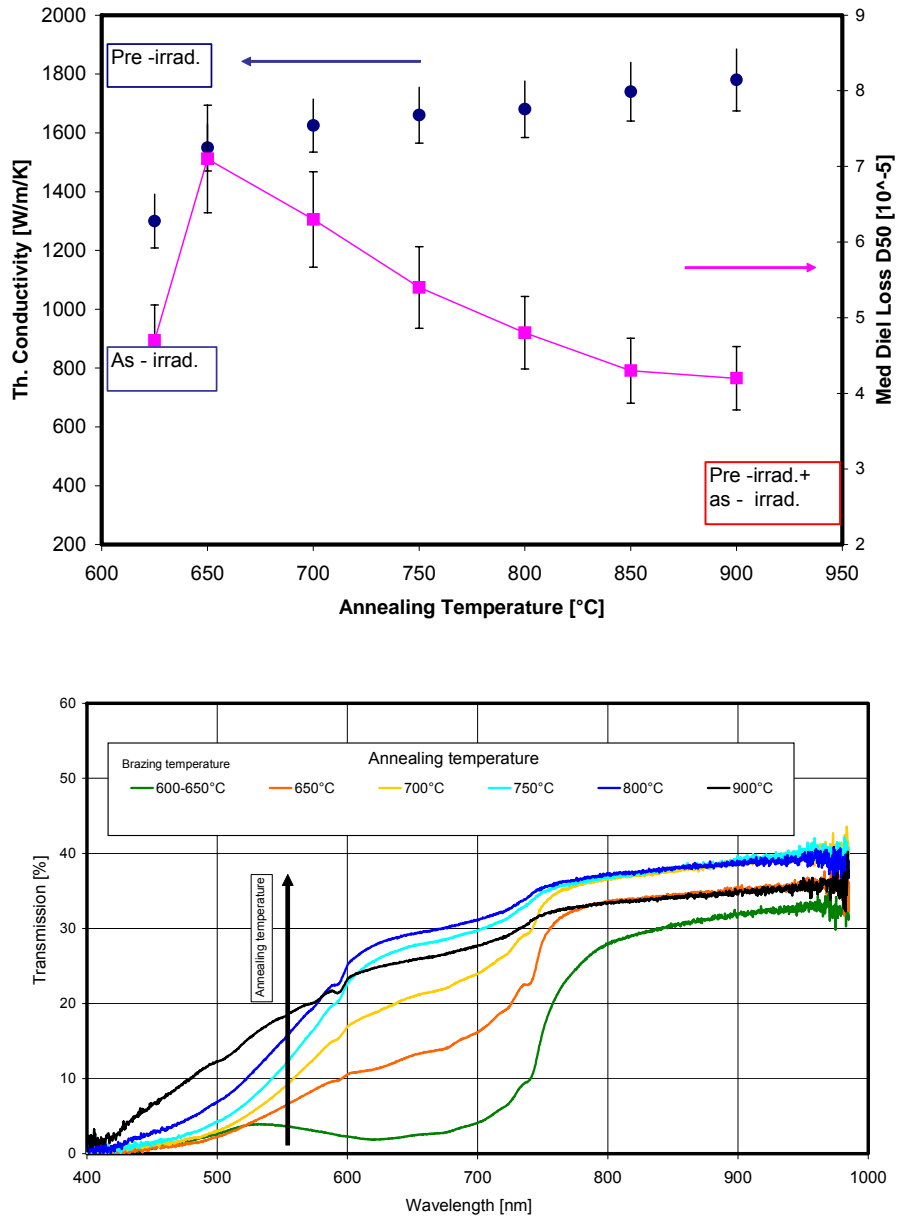
Fig. 1: Annealing behaviour of neutron irradiated CVD diamond (10^{21} n/m^2) as evidenced by thermal conductivity, dielectric loss (145 GHz) and optical transmission.

Staff:

J. Burbach
I. Danilov
R. Heidinger
K. Litfin
A. Meier
M. Rohde
P. Willing

Literature:

[1] Heidinger, R., I. Danilov, A. Meier, M. Rohde, Material and engineering issues of CVD diamond windows for high power mm-waves, Conf. Dig. of Joint 29th Int. Conf. on Infrared and Millimeter Waves and 12th Int. Conf. on Terahertz Electronics, Karlsruhe, September 27 - October 1, 2004, Piscataway, N.J. : IEEE, 2004 S.59-62

EFDA/01-653 (JW2-EP-ECRH.FZK-TPH-Amend)
Design and Development Studies on CVD-Diamond Window Assemblies for the ITER ECRH System (Permeation and Radioactivation Assessment)

Objectives

The ITER electron cyclotron heating and current drive system (ECH&CD) requires mm-wave beam lines capable of delivering 1 – 2 MW. The high power window unit, which forms the first tritium confinement, is composed of a CVD diamond disk brazed to metallic sleeves. The objective of this task was to study potential tritium permeation through the window structures as a key aspect for operation at ITER. Another challenge for the adequate choice of the material composition at the window structure is to permit hands-on maintenance at the window, which limits the γ- dose rate locally to 10^{-4} Sv/h after 10 days of shutdown time. For this purpose potential contributions from the radioactivation of the braze materials are assessed.

Experimental permeation studies through window structures by time lag experiments

A test stand for measuring hydrogen isotope permeation through CVD window units was set up for studying deuterium as a model gas to simulate tritium permeation. The window unit was exposed on its upstream side to D_2. To specify potential risks of tritium permeation, experiments were typically performed at 0.3 MPa, which is slightly above the limit of 0.2 MPa, which is considered as the worst-case scenario for an off-normal pressure increase in the primary vacuum. Room temperature and elevated temperature ($\approx 200°C$) conditions were studied as limiting cases. In the downstream side, the vacuum was kept under UHV conditions (typically at $3 \cdot 10^{-8}$ mbar). The permeation of deuterium through the window unit is determined by a quadrupole mass spectrometer placed in the downstream side.

The mass spectrometer signal yielded the D_2 signal in terms of ion currents in pA registered for the atomic mass A=4. The limit of minimum resolved gas flow and the calibration of the mass spectrometer signal to absolute leakage (permeation) rates was determined by a diaphragm formed with a UHV flange which was thinned in the centre and had central bore hole of 100 µm. The slope in the linear regression of the D_2 signals measured as a function of upstream pressure could be related to D_2 permeation rate by a constant of $0.55 \cdot 10^{-11}$ (mbar m^3/s)/pA. Given a resolution in the D_2 signal of typically 1 pA, deuterium permeation can be resolved at a rate of $< 10^{-8}$ mbar l/s (as 2pA $\approx 1 \cdot 10^{-8}$ mbar l/s).

Window units with either copper or Inconel sleeves were investigated which are joined to the CVD diamond disk using Ag- and Al-brazing technologies, respectively, as two major process alternatives. At room temperature, D_2 permeation rates are below the typical detection limit of the set-up, i.e. $< 10^{-8}$ mbar l/s. Experiments performed at elevated temperatures (T=200°C-240°C) prove that there is a risk of significant hydrogen isotope permeation through the window structures which is essentially due to the metal used in the sleeves. Note that the criterion for leakage intervention at the window structure forming the first tritium confinement at ITER is defined as a permeation rate of $> 10^{-8}$ mbar l/s, as this is the level which can be reasonably measured by a mass spectrometer-based vacuum equipment.

On the basis of this safety limit, it is shown that the Ag(Cu-) brazed window with the Cu sleeves allows safe operation up to the maximum temperatures tested (220°C at the disk and >170°C at the sleeve). Performance concerns were identified for the window with CVD diamond disk joint to Inconel sleeves by the Al-brazing technology. Operation at room temperature does not pose a hydrogen-isotope permeation problem. However, critical behaviour was observed when the window unit was operated under D_2 pressure at temperatures of 200°C. After a time lag which amounted to about $2 \cdot 10^4$ s, the observed deuterium permeation reached an order of 10^{-6} – 10^{-5} mbar l/s. Following an intermediate state, an additional increase to the 10^{-3} mbar l/s level set in.
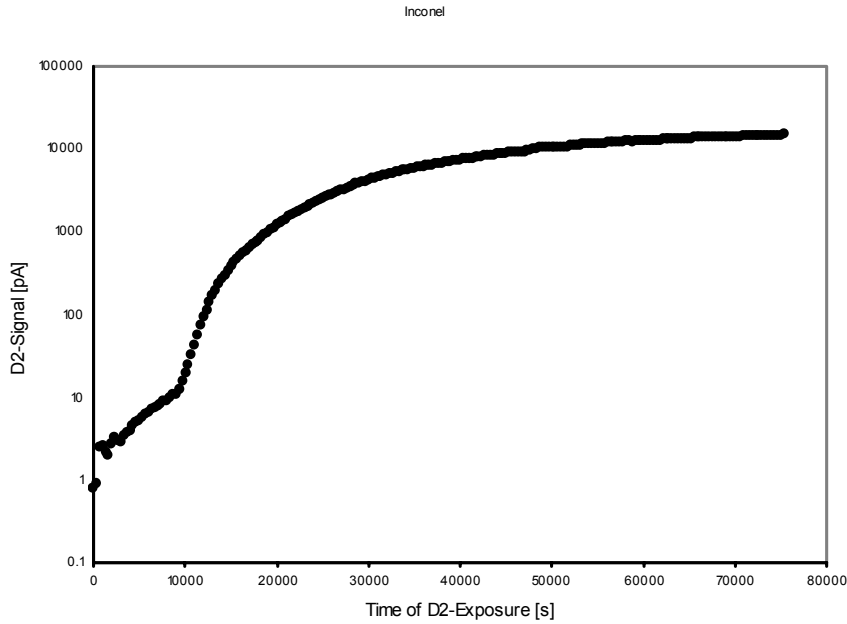
Fig. 1: Time evolution of deuterium signals observed which a dummy window structure made of Inconel 600 showing a strong onset of deuterium permeation after a time lag of $2.5 \cdot 10^4$ s (maximum Inconel temperature of 210°C)

Dummy units for the 'Inconel window' were prepared where the diamond part of the window model was replaced by an Inconel part. Here, the D_2 signal stayed at background level for temperatures of 175°C. At 200°C, the first stage of the D_2 permeation effect could be reproduced. The dummy unit was then modified by machining the outer structures of the Inconel parts to high surface quality and reducing further surface oxidation by storing in inert atmosphere before the permeation tests. With this pre-conditioning, the second stage could be reproduced which sets in a after a time lag of $2.5 \cdot 10^4$ s (cf. Fig. 1). This proves that the permeation is affected by two different phenomena involving diffusion in the bulk as well as surface layers acting as "permeation barriers" (most likely oxide layers) which govern the different time scales and the strength of the effect according to component history.

Analysis of γ-dose rates due to radioactivation of the braze materials

For the assessment of the γ- dose rate levels originating from the radioactivation of the brazing materials, the relevant neutron flux was evaluated together with the chemical composition of the brazing materials using the data base established at FZK to study the radioactivation on low activation materials for the DEMO First Wall. The window case at ITER is then described by a fixed scaling factor of $0.8 \cdot 10^{-7}$ which is obtained as the ratio of the fast neutron fluences at the ITER ECRH torus window (10^{20} m^{-2}) and to the level of the DEMO first wall case ($1.25 \cdot 10^{27}$ m^{-2}).

As the dose rates calculated for the DEMO First Wall case are only valid for the pure ('not-diluted') element forming an infinite material plate with a plane surface, the extrapolations to the ITER Window case cannot be discussed for the absolute figures. Indeed both metal cuffs and brazing materials form small limited areas in the plane of the CVD diamond disk. Accordingly there will be a major reduction in the actual dose rate at the ITER window (cf. Tab. 1).

Nonetheless these results are valid for establishing the ranking of radioactivation concerns by comparing the determined dose rate levels between the different parts of the window structure. Above all, any contribution from CVD diamond can be fully discarded. The background from the structural material (AISI 316-L) in the neighbourhood of the window is found to be comparable to the term arising from the metallic parts in the window structure (braze and sleeves). The main advantage of Al-brazing technology over reactive Ag- brazing technology with respect to the radioactivation of the main element, is lost with the use of Inconel for the metallic cuffs as it contains Ni a major alloying element. Therefore it can be concluded that both types of brazed windows are approximately equivalent from a radioactivation point of view.

Table 1: Scaling of γ-dose rates from the data base established for the DEMO First Wall case to the ITER window case (lower cut-off energy for γ-radiation: 100 keV) Data taken selected for $3 \cdot 10^{-3}$ years after irradiation

Element	Origin	DEMO First Wall Case [Sv/h]	ITER Window case [Sv/h]	Relative to AISI 316 L
Ref: AISI 316L	Structural material	$8 \cdot 10^4$	$6.4 \cdot 10^{-3}$	1
CVD Diamond window formed by Al-brazing technology to Inconel cuff				
Al	Al-braze	$8 \cdot 10^1$	$6.4 \cdot 10^{-6}$	$1 \cdot 10^{-3}$
Ti	Adhesion promoter for Al	$8 \cdot 10^4$	$6.4 \cdot 10^{-3}$	1
Ni	Inconel cuff	$3 \cdot 10^5$	$2.4 \cdot 10^{-2}$	3.75
Cr	Inconel cuff	$6 \cdot 10^3$	$4.8 \cdot 10^{-4}$	$7.5 \cdot 10^{-2}$
Fe	Inconel cuff	$2 \cdot 10^4$	$1.6 \cdot 10^{-3}$	0.25
CVD Diamond window formed by Ag-brazing technology to copper cuff				
Cu	Ag-braze + Cu cuff	$2 \cdot 10^4$	$1.6 \cdot 10^{-3}$	0.25
Ag	Ag-braze	$2 \cdot 10^5$	$1.6 \cdot 10^{-2}$	2.5
Sn	Ag-braze	$3 \cdot 10^4$	$2.4 \cdot 10^{-3}$	0.375
Ti	Ag-braze	$8 \cdot 10^4$	$6.4 \cdot 10^{-3}$	1

Staff:

J. Burbach
I. Danilov
R. Heidinger
A. Meier

Literature:

[1] Heidinger, R., I. Danilov, A. Meier, M. Rohde, Material and engineering issues of CVD diamond windows for high power mm-waves, Conf. Dig. of Joint 29th Int.Conf. on Infrared and Millimeter Waves and 12th Int.Conf.on Terahertz Electronics, Karlsruhe, September 27 - October 1, 2004, Piscataway, N.J. : IEEE, 2004 S.59-62

Magnet Structure and Integration

EFDA/03-1055

**Study of the Transient Voltage Behaviour of the Present ITER TF Coil Design
for Determination of the Maximum Voltages and Procedures**

For transient voltages, superconducting coils have to be considered like an electrical net-
work, which can be excited to internal oscillations. Large coils have relative low resonance
frequencies as shown by the transient voltage calculations for the full size ITER EDA mag-
nets. During a fast discharge or fault excitation high dielectric stress can occur within the
ITER coil system (Fig. 1). The goal of the task was the determination of the voltage stress of
the ITER TF coils under rated and fault conditions to give a reliable basis for the high voltage
test specifications and for the verification of the insulation coordination of the TF coils. The
work was performed in collaboration with the "Institut für Elektroenergiesysteme und
Hochspannungstechnik" (IEH) of the University of Karlsruhe.

A network model of the TF coil system with 18 simplified coils and 9 Fast Discharge Units
had been established for the simulation of the fast discharge without a fault. Two detailed
network models (for 50 kHz and for 1 kHz) of a single TF coil had been established and ex-
cited with the calculated terminal voltage from the TF system.

In the present time frame the TF system was examined for two fault cases specified in
agreement with EFDA. For the first fault case, a failure of 2 neighboured Fast Discharge
Units was assumed. The second fault case (Fig. 2) is based on fault case 1 but with an addi-
tional breakdown to earth at location and time when the highest voltage to ground appears
caused by the local potential lifting to ground by fault case 1.
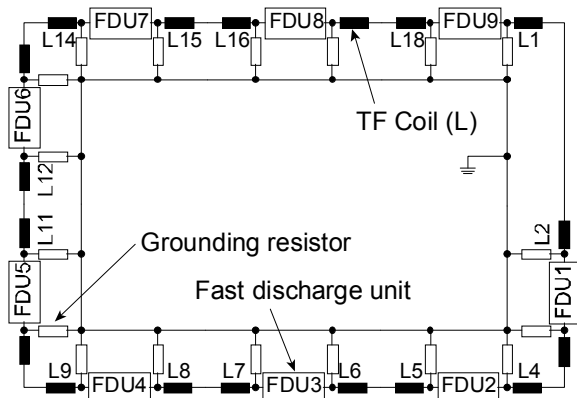
Fig. 1: Simplified analogue circuit of the ITER torus (TF) coil
system during a fast discharge (power supply already dis-
connected). The network model itself is more comprehen-
sive e. g. it includes instrumentation cables and internal
elements of the Fast Discharge Units.
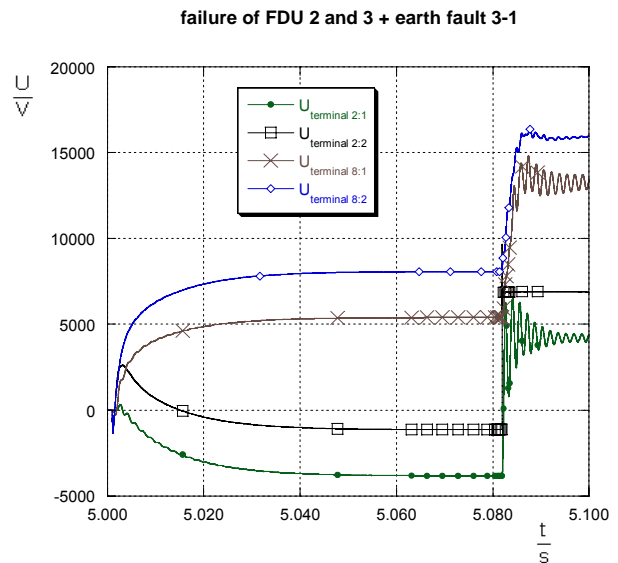
Fig. 2: Terminal voltages to ground during a fast discharge with
failure of Fast Discharge Unit 2 and 3 and additional earth
fault at a terminal 3:1 (i. e. end 1 of coil 3). Highest volt-
age over a coil within the ITER system was found for coil
2. Highest voltage to ground was found for terminal 8:2.

The maximum voltages appearing for ground, radial plate and conductor insulation are de-
termined for both fault cases with both network models of the single TF coil and compared in
Tab. 1 with the values of the fast discharge without a fault.

Two different sets of test voltages for DC, AC and impulse testing were proposed depending
on the selection of the fault case (Tab. 2). Test arrangements for the coils, test circuits and
criteria were planned based of the described calculations and the experiences gained with
the testing of ITER TF model coil. The test sequence and safety aspects were added.

Tab. 1: Overview of the calculated maximum voltage at ground, radial plate and conductor insulation for the 1 kHz and 50 kHz model.

Insulation type	f	Maximum calculated voltage		
	kHz	kV		
		fast discharge	fault case 1	fault case 2
Ground	1	3.5	8.1	16.4
	50	3.5	8.1	16.4
Radial plate	1	0.7	0.7	4.8
	50	0.6	0.7	4.3
Conductor	1	0.6	0.8	4.3
	50	0.5	0.8	3.7

Tab. 2: DC and AC (peak value) test voltages for ground, radial plate and conductor insulation based on the calculated voltages for the two different fault cases.

Insulation type	Test voltage	
	kV	
	Based on fault case 1	Based on fault case 2
Ground	18	34
Radial plate	5	11
Conductor	5	11

For the future a decision is necessary which worst case scenario is the basis for the test voltages. It is recommended to calculate a scenario with a single earth fault if fault case 2 is not considered because the dielectric stress of the conductor insulation after the appearance of the ground fault may be critical. In this case tests on conductor insulation mock-ups are necessary to be performed as soon as possible.

A change of the actual ITER design is recommended concerning the location of the current limiting resistors. Otherwise measurements of fast signals and AC testing of conductor and radial plate insulation cannot be performed. High voltage tests under Paschen Minimum condition or in conductive liquid are necessary to ensure sufficient dielectric strength for undefined dielectric strength of the surrounding. A cold test for all coils is also strongly recommended to verify that no relevant degradation of the insulation properties occurs caused by cool down or warm up.

Calculations of the transient behaviour of the PF coils are not reported so far from other associations and therefore proposed to be performed in the frame of a future task.

Staff:

W.H. Fietz
S. Fink
A. Ulbricht (till 31.03.2004)

Literature:

[1] S. Fink, W. H. Fietz, A. M. Miri, X. Quan, A. Ulbricht; Study of the transient voltage behaviour of the present ITER TF coil design for determination of the test voltages and procedures, FZKA-Bericht 7053, Karlsruhe, October 2004

[2] S. Fink, T. Bonicelli, W. H. Fietz, A. M. Miri, X. Quan, A. Ulbircht; Transient electrical behaviour of the ITER TF coils during fast discharge and two fault cases, 23rd SOFT Conference, Venice, Italy, Sept. 20-24, 2004 (to be published in Fusion, Engineering and Design)

[3] S. Fink, T. Bonicelli, W. H. Fietz, A. M. Miri, X. Quan, A. Ulbircht; Transient electrical behaviour of the ITER TF coils during fast discharge and two fault cases, 23rd SOFT Conference, Venice, Italy, Sept. 20-24, 2004 (Posterpresentation)

EFDA/03-1085
Cryogenic Testing of Materials and Welds for Magnet Structures

The cryogenic material testing and qualification program within the framework of the European fusion technology task in the reporting period consists of investigations on poloidal field conductor insert qualification tests and various material characterizations at cryogenics according to the EFDA requirements.

Investigations on PF Insert Coil Transition

A transition piece of PF conductor insert coil has been provided by EFDA to Forschungszentrum Karlsruhe for the reason of mechanical measurements in cryogenic regime. The measurements comprised the determination of the cryogenic tensile and fracture properties using the ready manufactured full size sample. The assembly of the transition sample using a variety of materials and joining techniques addressed beside standard tests also non standard measurement techniques developed in recent years at Forschungszentrum Karlsruhe. Figure 1 shows the overall view of the test pieces along with the different zones, which should be qualified by means of cryogenic mechanical measurements. The measurements to be performed are collected in the Table 1. This table gives also the detailed information about the type of specimens used and the file numbers of each specimen. All these measurements are carried out using the 25 kN variable temperature helium flow cryogenic test facility except for the Cu/SS joint tensile tests, which are performed in liquid helium environment using the 630 kN tensile test machine.
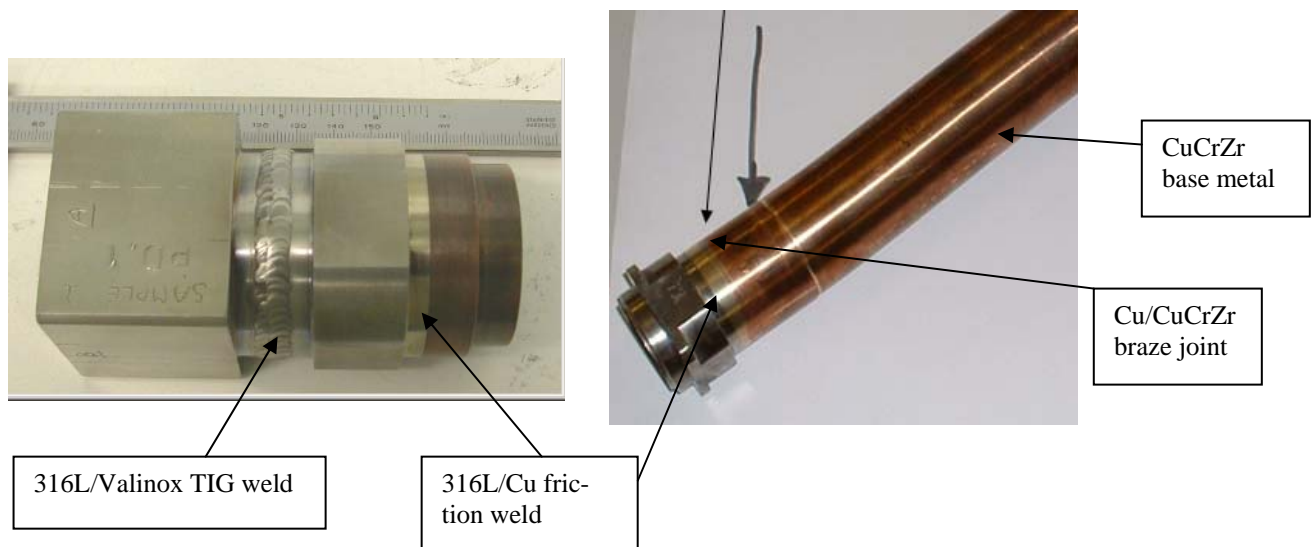
Fig. 1: Image shows the assembled transition pieces and the position of the different joints.

Fracture Toughness of Weld Joint 316L/Valinox at 7 K

These measurements have been performed with the provided test weld sample having a 100 mm long weld seam with the material combination of 316L and Valinox (316LN). The plate with its 3.5 mm nominal thickness decreased after the specimen machining to 2.8 mm due to the strong distortion of the plate. This test sample with the TIG weld in the centre has been machined to provide two ASTM proportional compact tension specimens of 45 x 43 x 2.8 mm. To minimize the danger of large crack tunnelling during the specimen loading these compact tension specimens have been side grooved using electro discharge machining (EDM). The used method for these measurements was ASTM standard E 813 J-integral single specimen test method, however, further improved according to the reference [1]. The

crack orientation of one of the specimens has been positioned in the weld centre line, whereas the second specimen's crack orientation has been positioned near the weld zone at heat affected zone (HAZ). Table 2 gives the obtained results of these measurements.

The manufactured original PF transition section could not be used for compact tension specimen preparation. In reality no information about the actual fracture toughness performance can be determined from the existing real sample unless one uses sophisticated test methods such as the recently developed JETT (J Evaluation on Tensile Test) tests method. The method is applicable with small round bar tensile specimens having a circumferential EDM cut along the girth. This method has been widely used in recent years and showed reliable results due to several international round robin tests. For the current task we used flat double edge EDM notched specimens to measure the critical J. Table 3 shows the evaluated JETT results with the weld joint 316L/Valinox of the tube sample, which are well in line with the obtained findings of compact tension specimens evaluated according to E 813 standard.

Table 1: Details of the measurements.

Task No & Material combination	Specimen machined	Type of specimen	Measurements method	Specimen designation
Task 1: Valinox/316L TIG weld joint	100 mm long weld of a blank sheet of 3.5 mm thickness	Compact tension type 45 x 43 x 2.8 mm	J-Integral test of weld zone and heat affected zone according to E-813	WeldJ-1 & weldJ-2 HAZJ-1 & HAZJ-2 All tests at 7 K
Task 2: Valinox/ 316L TIG weld joint	Machined from the original sample with the weld in the centre of the specimens	JETT, double edged notched plate specimen of 53 mm length with circumferential EDM cuts	JETT test Load versus displacement and estimation of critical J according to Rice equation	Weld-1, Weld-2, and Weld 3 HAZ-1, HAZ-2, and HAZ-3 All tests at 7 K
Task 3: 316L/Cu friction joint	Machined from the original sample	Flat type tensile specimen of 55 mm length with ~ 2.8 x 2 mm cross section	Standard tensile test according to ISO/TC 164/SC 1 N 489	FR-1, FR-2, and FR-3 at 295 K FR-4, FR-5, and FR-6 at 7 K
Task 4: Cu/CuCrZr brazed joint	Machined from the original sample with the overlapped brazed joint in centre of specimen	Flat type tensile specimen of 55 mm length with ~ 2.8 mm x 2 mm cross section	Standard tensile test according to ISO/TC 164/SC 1 N 489	Braze-1, Braze-2, and Braze-3 at 7 K
Task 5: CuCrZr base alloy	Machined from original sample in swaged and un-swaged condition	Flat type tensile specimen of 55 mm length with ~ 2.8 mm x 2 mm cross section	Standard tensile test according to ISO/TC 164/SC 1 N 489	Swag-1, -2, -3 at 295 K; Swag-4, -5, -6 at 7 K Unswag-1, -2, -3 at 295 K; Unswag-4, -5, -6 at 7 K
Task 6: CuCrZr base alloy	Machined from original sample in swaged and un-swaged condition	JETT, double edged notched plate specimen of 53 mm length and with EDM cuts	JETT test Load versus displacement and estimation of critical J according to Rice equation	SwagJ-1 and -2 at 7 K UnswagJ-1 and -2 at 7 K

Table 2: Fracture mechanics results determined at 7 K with welded 316L/Valinox compact tension specimens according to ASTM test method.

File & specimen characteristics	Critical J value N/mm	Fracture toughness MPa√m
WeldJ-1, crack inside the weld zone	~ 200	195
HAZJ-1, crack inside the HAZ zone	~ 250	224

Table 3: Fracture mechanics results determined at 7 K using the JETT test procedure with welded 316L/Valinox double edge notched specimens of samples machined from the original PF insert weld.

File & specimen characteristics	Critical J value N/mm	Fracture toughness MPa√m
Weld-2, crack inside the weld zone	209	199
Weld-3, crack inside the weld zone	225	206
HAZ-2, crack inside the HAZ zone	244	223
HAZ-3, crack inside the HAZ zone	311	249

Performance of the Friction Joint 316L/Copper at 295 K and at 4.2 K

The following paragraph gives the obtained results of tensile properties with friction welded joints between 316L stainless steel and copper material at different temperatures. All specimens are machined from the manufactured original PF insert section and are flat type. Table 4 shows the determined engineering data of these tests.

Table 4: Collected tensile property results of SS/Cu friction joint at 295 and 4.2 K.

File	T K	Young's Modulus GPa	Yield Strength MPa	Ultimate Tensile strength MPa	Uniform elongation %	Total elongation %
Fr-1	295	120	99	215	18	~23
Fr-2	295	119	98	215	18	~22
Fr-3	295	121	99	214	19	~28
Fr-4*	4.2	130	93	403	40	41
Fr-5	4.2	130	105	404	44	62
Fr-6	4.2	132	113	413	48	71

* Fracture occurred at the friction joint interface

Performance of the Brazed Joint between Copper and CuCrZr Alloy at 295 K and at 4.2 K

Within this task the overlapped Cu/CuCrZr had been tensile tested at 7 K for the reason of joint assessment. Altogether three tensile measurements have been carried out at 7 K with flat specimens machined carefully from the brazed joint section. All these specimens failed in the copper region and the brazed joint remained intact until final fracture. The copper mate-

rial shows within this context large constraints, whereas the CuCrZr material is less strained. Table 5 gives the collected tensile properties of the brazed joint measured at 7 K.

Table 5: Determined tensile properties of the CuCrZr to OFE Copper Brazed Joint at 7 K.

File	Young's Modulus GPa	Yield Strength MPa	Ultimate Tensile strength MPa	Uniform elongation %	Total elongation %
Braze-1	119	130	427	25	25
Braze-2	110	110	398	29	29
Braze-3	116	110	397	24	24

Tensile Results of CuCrZr Alloy in two Different Conditions at 7 K and at 295 K

The alloy CuCrZr, which is the tube material for the PF insert section, has been characterized with flat tensile specimens machined from the original tube. These investigations were carried out with two conditions of this alloy. These were a swaged condition and as received un-swaged condition. These tensile tests were performed at 295 K as well as at 7 K. Table 6 and Table 7 give the determined engineering values for the alloy CuCrZr in swaged and un-swaged conditions at two different temperatures.

Table 6: Determined tensile properties of the CuCrZr alloy in swaged and un-swaged condition at 295 K and at 7 K.

File	T K	Young's Modulus GPa	Yield Strength MPa	Ultimate Tensile strength MPa	Uniform elongation %	Total elongation %
Unswag-1	295	125	133	238	30	35
Unswag-2	295	111	140	245	32	38
Unswag-3	295	117	133	245	32	34
Swag-1	295	116	281	293	0.7	8
Swag-2	295	120	282	294	0.7	16
Swag-3	295	122	277	293	0.7	9
Unswag-4	7	123	129	467	47	47
Unswag-5	7	119	140	465	42	42
Unswag-6	7	120	147	474	55	61
Swag-4	7	127	347	516	40	41
Swag-5	7	122	337	511	35	35
Swag-6	7	123	335	511	38	41

Table 7: Determined fracture mechanical properties of CuCrZr material at 295 K and at 7 K.

File	T K	Critical J N/mm	Fracture toughness MPa√m
UswagJ-1	295	830	315
SwagJ-1	7	590	266
SwagJ-2	7	595	267

Fatigue Life of CS-Jacket Materials

Figure 2 gives the calculations with respect to full size jacket cyclic loading at 4 K. The performed FE analyses after the cyclic failure confirm the achieved stress versus displacement data. The failure stress of ~1100 MPa matches well with the experimental observations already described in reference [2] and in the last annual fusion report [3].
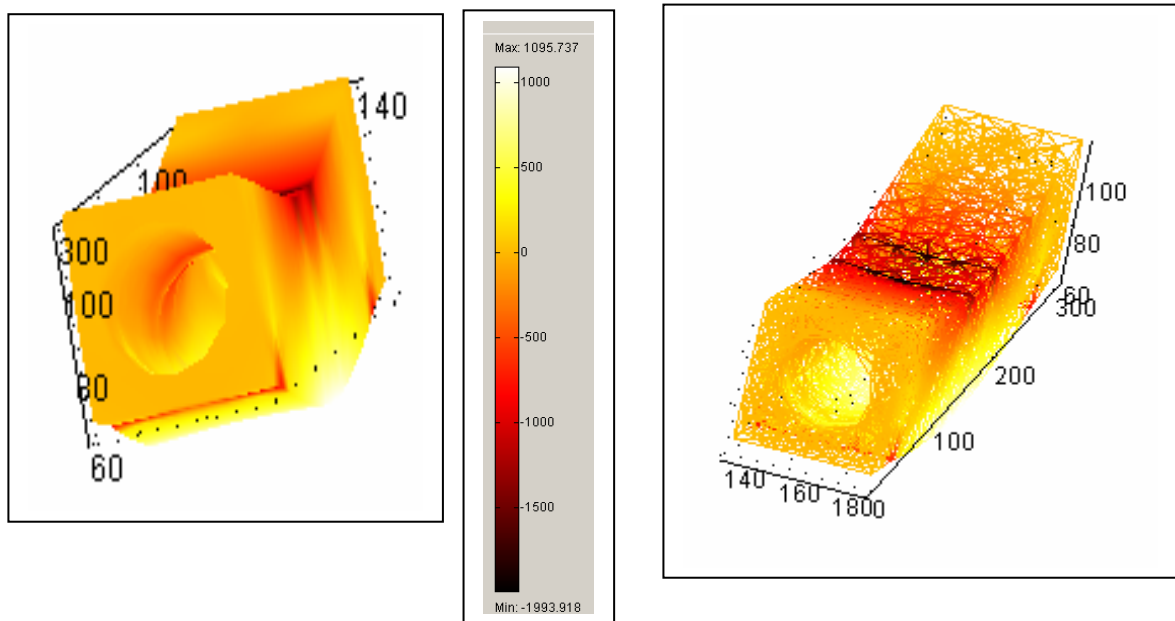
Fig. 2: Three dimensional FE analysis of the full size jacket shows the structural stresses during the four point bending fatigue load measurement. The computed maximum stress is the reason of the fatigue failure at 4 K and this value matches well with the experimental result as given in reference [2].

Staff:

A. Nyilas
K. Weiss
H. Kiesel

Literature:

[1] Weiss K. and Nyilas, A., "Specific aspects on crack advance during J-test method for structural materials at cryogenic temperatures", to be published in Fatigue & Fracture of Engineering Materials & Structures

[2] Nyilas, A., Nikbin, K., Portone, A., and Sborchia, C., "Tensile, fracture, fatigue life, and fatigue crack growth rate behavior of structural materials for the ITER magnets: The European contribution", in *Advances in Cryogenic Engineering (Materials)* 50, edited by U. B. Balachandran et al., Plenum, New York, 2004, pp. 176-183.

[3] Nyilas A., Annual Report of Association Forschungszentrum Karlsruhe/Euratom, EFDA 02-692 Report on Cryogenic Testing of Materials and Welds for Magnet Structures, FZKA 6966 Eur21019 EN October 2002-September 2003, pp. 63-67

EFDA/02-1013
Testing of the HTS 70 kA Current Lead

In the frame of the European Fusion Technology Programme, the Forschungszentrum Karlsruhe and the CRPP Villigen have designed and built a 70 kA current lead for the ITER TF Coils using High Temperature Superconductors (HTS). At the beginning of 2004 the HTS current lead was installed in the TOSKA facility of the Forschungszentrum Karlsruhe. The preparation of the HTS current lead experiment was done in strong co-operation between the Forschungszentrum Karlsruhe and CRPP leading to a test procedure for the experiment.

As add-on to the experimental campaign, the NbTi bus bar (BB-III) was also used for current distribution measurements (CDM), both in steady state as well as in current sharing and during quench. The corresponding EFDA task was running under "Validation of the THELMA-Code". For this purpose, the BB-III was equipped with voltage taps, temperature sensors and Hall probes. The experiment was carried out in collaboration of ENEA, ENEA/CREATE, IEE Bratislava, UT Twente and the THELMA Group.

Both experiments were prepared and organized under the supervision of the HTS-CL/CDM Test and Analysis group.

The experiment was done in two test campaigns from April until June 2004: Phase I started on April 14 and ended on May 9, phase II started on June 1 and ended on June 21, followed by one week test campaign (June 21 – June 25) dedicated to CDM.

Preparation of the TOSKA facility and installation of the HTS current lead
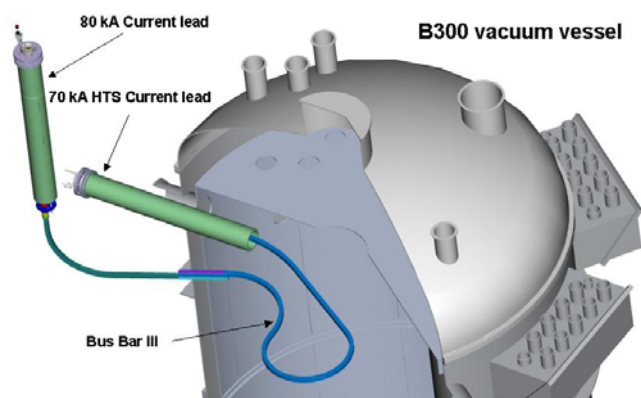
Fig. 1: Schematic view of the arrangement of the HTS current lead experiment in TOSKA.

After completion of the TFMC experiment, the TOSKA facility was modified for the test of the 70 kA HTS-CL and the current distribution measurement (CDM) on the superconducting bus bar III (BB-III). Major changes were done for the cryogenic system, i.e., providing a helium gas of 20 – 80 K temperature to the heat exchanger of the current lead, and for the current supply, i.e., extension of the aluminium bus bar from the 80 kA end connector downwards to the position of the (horizontally) current lead. After modification of the facility and completion of the HTS-CL, the conventional 80 kA current lead including the superconducting bus bar II (BB-II), the BB-III and the HTS-CL were installed in the designated ports of the vacuum vessel. Fig. 1 shows a schematic view of the test arrangement and Fig. 2 shows a picture of the HTS current lead installed in the TOSKA vacuum vessel port.

Experimental Results

The experiment covered the electrical and thermal behaviour of the HTS-CL under steady state conditions and in case of a quench. To characterize the performance of the current lead, the temperature profile, the contact resistances, the heat load at 4.5 K, the minimum required mass flow rate of 50 K helium, and the critical current were evaluated. In addition, the safety margin in case of a loss of mass flow was studied.
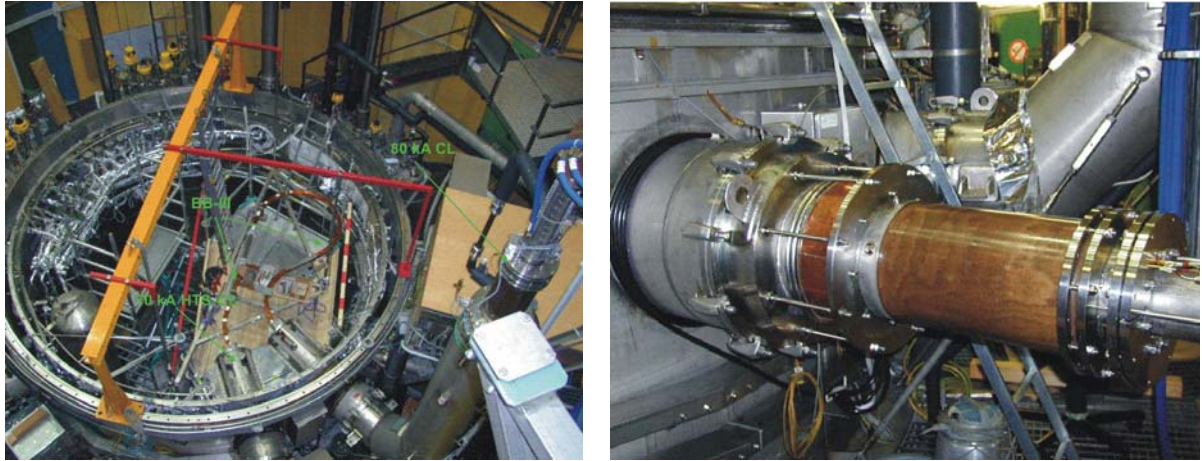
Fig. 2: The HTS current lead in the TOSKA facility: Left: HTS-CL & CDM test configuration installed inside the vacuum vessel B300. Right: HTS-CL outside the vacuum vessel.

The results can be summarized as follows:

- The 70 kA HTS current lead is very robust and can be operated stable near to its limit. It was operated stable up to 70 kA at a temperature of the warm copper end cap of the HTS module of approx. 65 K using 50 K helium for cooling of the copper heat exchanger (Fig. 3 left shows the temperature profiles at 0 and 68 kA). It was even possible to stabilize the lead at 80 K which was higher than the current sharing temperature guaranteed by the manufacturer. The current lead could even be operated stable for more than 30 minutes at 80 kA with a slightly reduced Helium inlet temperature. This demonstrates the high current capacity of the HTS module and denotes a world record for HTS current leads.
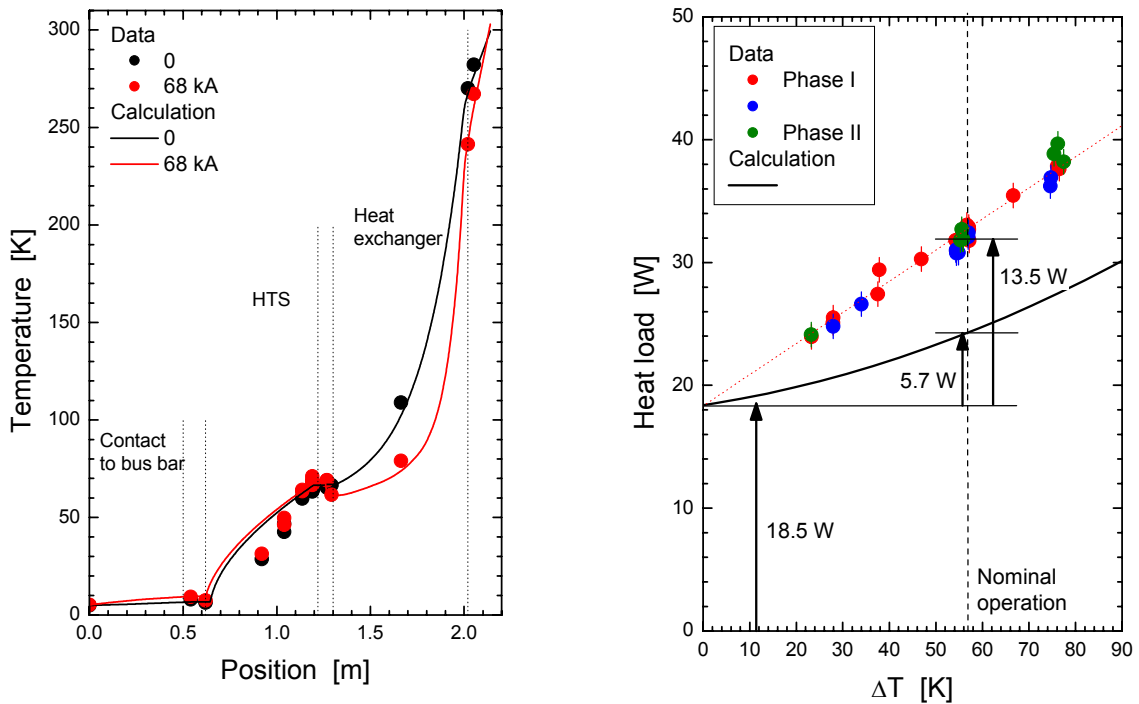
Fig. 3: Performance of the HTS current lead – left: Measured and calculated temperature profiles. Right: heat load at 4.5 K vs. temperature gradient along the HTS module.

- The HTS current lead module showed good performance both in DC and pulse operation. All contact resistances in the HTS module are in the specified range. The clamp contact resistances to the sc bus bars and between BB-II and BB-III are 0.7 – 1.6 nOhm and approx. 1 nOhm, respectively. Especially the BB-II/III contact showed the same performance as the others which demonstrates that the joining technique using indium foil results in good DC resistance values.

- The conical screw contact resistance between the HTS module and the heat exchanger was much larger than expected and results in larger He mass flow rates than estimated during the design phase. It also affects the current distribution among the HTS panels which could be clearly seen in transient operation when temperatures change in the contact region. An alternative solution using a low temperature melting solder is under investigation.

- It was possible to extract the He mass flow rate needed to remove the resistive losses of the screw contact. The resultant corrected He mass flow rate is as expected for a zero con-tact resistance which means that the heat exchanger was operating as designed.

- The conduction heat load at the 4.5 K level at nominal operation was measured to be about 14 W which is much higher than the design value of 5.7 W (Fig. 3 right). This can not be explained from the material data base provided by the manufacturer and may be due to background losses of the facility. Nevertheless, the heat load is more than a factor 6 lower than the corresponding value for a conventional gas-cooled current lead.

- The total refrigerator load of the HTS current lead has been compared to the conventional current lead as given in the ITER DDD. The calculations were done for zero current as well as for 68 kA. The result is a reduction of the refrigerator power by a factor of 5.4 (zero current) and 3.7 (68 kA) or about 5 for a current operation duty cycle of 25%.

- The quench performance of the HTS module was excellent. Extended tests were performed by changing the parameters of the quench detector resulting in maximum temperatures near to the upper end of the panels of 155 K and resistive voltages of 90 mV (including the copper end caps). Both parameters scale linear with the delay time of the quench detector.

- The quench temperature of the HTS module was measured at 50, 68, and 80 kA and was as expected. All quenches showed the same pattern, e.g., the panel #12 was the first one which showed a resistive signal and all other panels became resistive very close to the quench, i.e., current redistribution took place.
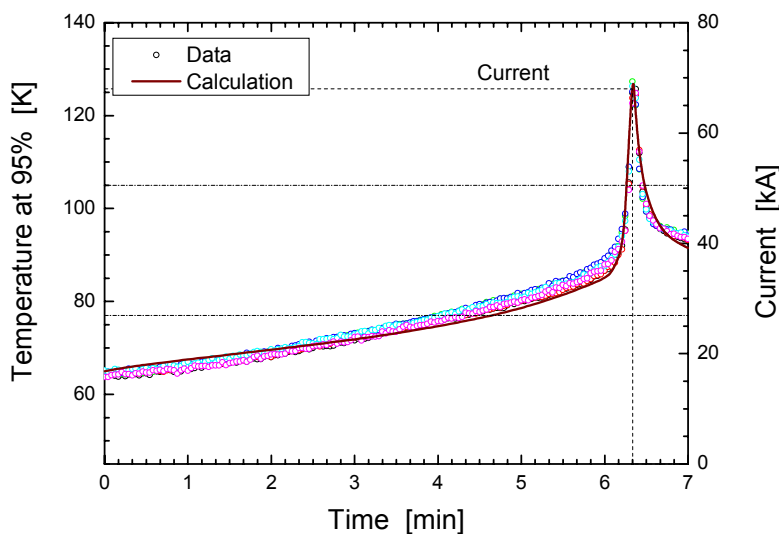
Fig: 4:   Safety margin of the HTS current lead –Measured and calculated maximum temperature vs. time during loss of helium mass flow simulation at 68 kA.

- The safety margin in case of a loss of flow accident, i.e., interruption of the He mass flow through the cop-

per heat exchanger, is a factor of two larger than specified. It took more than 6 minutes from the mass flow stoppage until a quench occurred (Fig. 4).

As a final conclusion it can be said that the HTS current lead design is ready to be used in ITER.

Staff:

M. Darweschsad
G. Dittrich
W.H. Fietz
S. Fink
U. Fuhrmann
R. Heller
W. Herz
A. Kienzler
V. Leibrand
A. Lingor
V. Marchese
I. Meyer
G. Nöther
E. Specht
M. Süsser
V.L. Tanna
D. Weigert
F. Wüchner
G. Zahn

Literature:

[1] R. Heller, A. Kienzler and A. Lingor, "Design, Development and Construction of High Temperature Superconductor Current Leads for 70 kA -Final Report on 70 kA HTS Current Leads, EFDA Contract EFDA 01-598, Deliverable 3.", Forschungszentrum Karlsruhe Internal Report FE.5130.0031.0012/K, Dec 2003, unpublished

[2] R. Heller, S.M. Darweschsad, G. Dittrich, W.H. Fietz, S. Fink, W. Herz, A. Lingor, A. Kienzler, I. Meyer, G. Nöther, M. Süsser, V.L. Tanna, R. Wesche, F. Wüchner and G. Zahn, "Test of the 70 kA HTS Current Lead in the TOSKA Facility - Final Report EFDA Contract EFDA 02-1013 Deliverable 4.2", Forschungszentrum Karlsruhe Internal Report FE.5130.0061.0012/A, Oct 2004, unpublished

[3] R. Heller, S.M. Darweschsad, G. Dittrich, W.H. Fietz, S. Fink, W. Herz, F. Hurd, A. Kienzler, A. Lingor, I. Meyer, G. Nöther, M. Süsser, V.L. Tanna, A. Vostner, R. Wesche, F. Wüchner, G. Zahn, "Experimental Results of a 70 kA High Temperature Superconductor Current Lead Demonstrator for the ITER Magnet System", presented at 2004 Appl. Supercond. Conf., Jacksonville, FL, Oct 3-8, 2004

TW4-TMSF-HTSCOM
Conceptual Design of External HTS Busbars

High temperature superconductors have successfully demonstrated their considerable advantages over conventional materials and entered the market. Therefore, a R&D program was launched in Japan and EU to design and construct high temperature superconductor (HTS) components for ITER. As a result of this program a 60 kA HTS current lead was successfully manufactured and tested in Japan in 2002. The EU 70 kA ITER prototype current lead using HTS was assembled in 2003 and tested in 2004 (see EFDA-Contract No. EFDA/02-1013).

The introduction of HTS current leads between conventional superconductors and the resistive heat exchanger significantly reduces the heat load at the 4.5 K level, thereby considerable saving costs of the cryogenic system.

The primary objective of this task is to compare the actual ITER design with and without using HTS current leads. This study will not only elaborate the differences in initial and operating costs but also point out implications with other ITER components and the required ITER design changes. The performance assessment of the HTS current leads should be based on the test results of the EU 70 kA prototype current lead.

Furthermore, the study should assess the possible benefits of a third ITER design option which not only replaces the conventional current leads but also the water-cooled bus bars by HTS materials. The substitution of these aluminium bus bars would not only reduce the electrical power losses but would also require significantly less space for their installation. This option includes a conceptual design of a HTS bus bar suitable for ITER.

Status

Presently, a detailed comparison between a conventional current lead and a HTS current lead option for ITER is under investigation. This includes both the investment and operation costs. A first rough estimation taking into account the TF- CS- and PF-coil systems results in an amortisation of the higher investment costs of the HTS modules after 2 to 3 years of ITER operation.

In parallel, different layouts of an HTS bus bar for 68 kA are under consideration. For this, the boundary conditions of ITER, like the spatial requirements of the coil terminal boxes, the aluminium DC bus bars, have to be evaluated.

Staff:

R. Heller
V.L. Tanna

EFDA/03-1059
Validation of the THELMA Code and its Application to Experimental Results:
BB3 Current Distribution Measurement (CDM) Experiment

A non-uniform current distribution in cables affects both the steady state and the transient performance of superconducting magnets. A good understanding of the phenomena leading to non-uniform current distributions in sub-cables and the validation of computer codes able to interpret experimental results and to predict the behaviour of complete superconducting systems is therefore essential for a reliable design of those magnets and for an optimisation of their design parameters.

The aim of the task was the validation of a Thermo – Hydraulic Electro – Magnetic (THELMA) code developed for the analysis of superconducting magnets in transient conditions [1]. The code includes a detailed electromagnetic description of both the joints and the superconducting cable with thermohydraulic models, as well as current reconstruction algorithms. The validation of the code is performed using voltage, current, magnetic field, temperature and mass flow measurements suitably located as near as possible to the conductor. The experimental work was performed in the TOSKA facility of the Forschungszentrum Karlsruhe in collaboration with ENEA, ENEA-Create, IEE Bratislava, University of Bologna, University of Udine and Polytechnic of Turin under the coordination of EFDA and in parallel with the High Temperature Superconducting (HTS) Current Lead (CL) tests [2].

The aim of the subtask was the participation in the design and assembly of the measurement and data acquisition systems and the assistance during the tests. Some of the tests were parasitic (i.e., performed during the HTS current lead test runs up to 80 kA), followed by one week of dedicated tests to investigate the effect of a re-distribution of the current at the current sharing temperature T_{cs}.
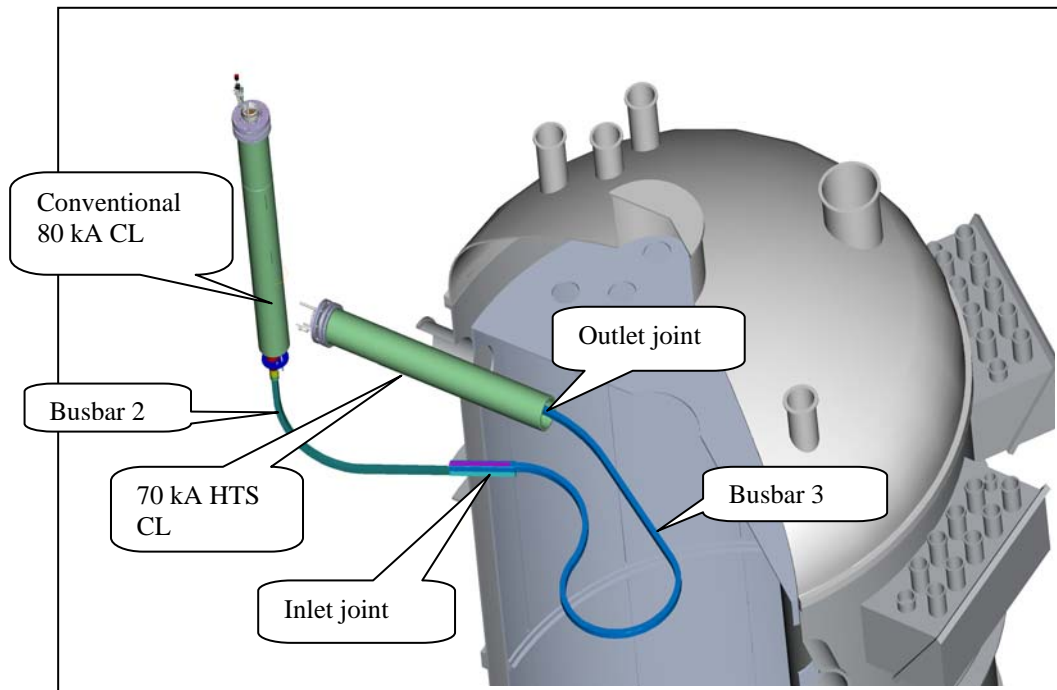
Fig. 1: 70 kA HTS current lead test arrangement in TOSKA.

The test specimen was a NbTi conductor, called busbar 3 (BB3), which connected busbar 2 (see Fig 1) and the cold end of the HTS current lead. The conductor is a Cable in Conduit

Conductor (CICC) made of 1152 strands grouped in six sub-cables ("petals") and embedded in a 51 mm x 51 mm steel jacket. Two resistive heaters were used: the first one with an input power up to 1 kW, was located at the Helium inlet and the second one, with an input power up to 500 W, was positioned directly around the busbar steel jacket. The control of the heaters was performed by using an existing application of DIADEM, distributed by National Instruments (NI), developed in the Forschungszentrum Karlsruhe for the tests of the ITER TFMC and located in the TOSKA control room.

The measurement system included 48 Hall probes, 10 temperature sensors, 4 pressure measurements (3 absolute and 1 differential), 2 heating power signals, 1 transport current, 1 sensing current, 6 voltage rings and 6 voltage taps positioned on BB3 and 2 voltage taps across the inlet and outlet joints for a total of 80 channels (Fig. 2). The Hall probes included two circular measuring heads each fitted with 12 Hall probes, installed one twist pitch apart, and a 2D linear array fitted in between. Two additional Hall probe carriers were fitted at the inlet joint and three carriers at the outlet joint BB3 to measure the longitudinal and transverse field. Further details on the installation can be found in [3]. The whole test set up was able to withstand the insulation test voltage of 1 kV DC for one minute which was applied daily to the system before the start of the tests.
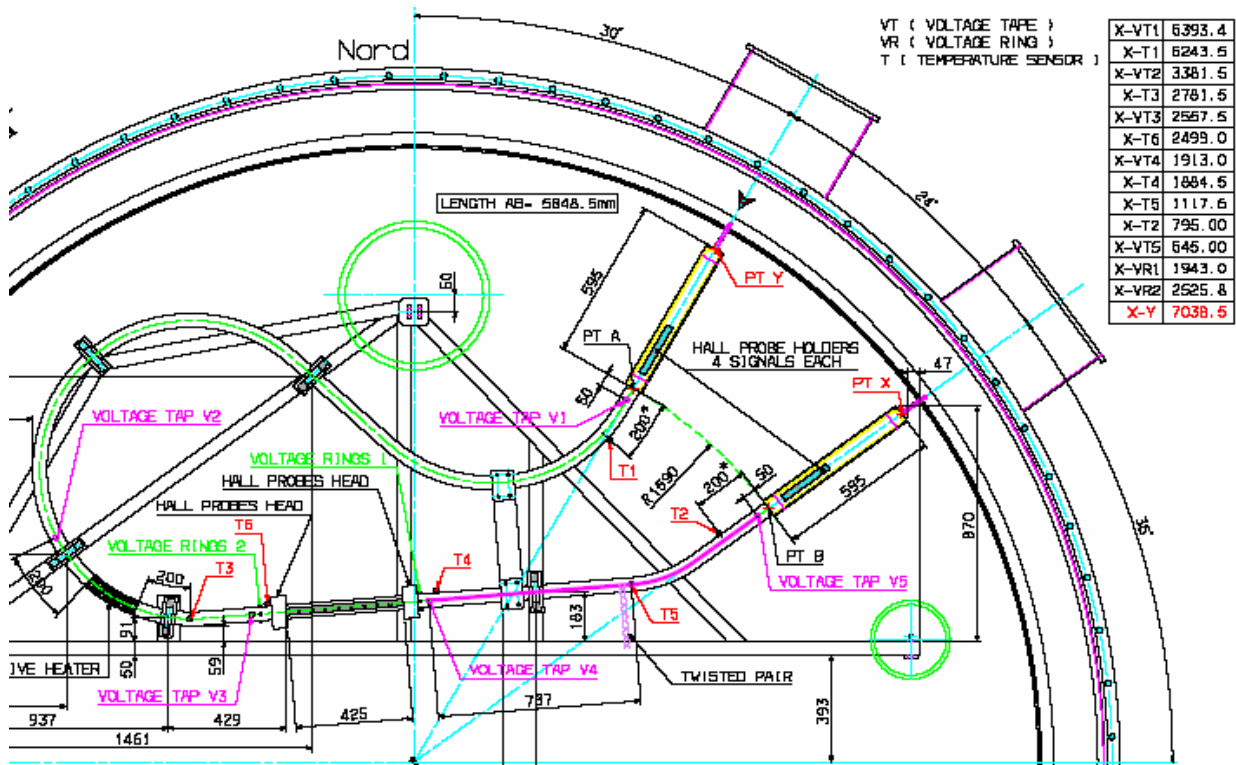
Fig. 2: CDM busbar 3 instrumentation overview.

The transport current of 70 kA was delivered from two 12 pulse ac-dc thyristor converters, at 30 and 50 kA, respectively, connected in parallel (Fig. 3). A preliminary analysis on the behaviour of the circuit during current ramp up and ramp down transients (e.g., inverter mode discharge, IMD) and in steady state (current ripple) is reported in [4]. Due to the very low circuit inductance the power supply voltage ripple components superimposed to the dc output, mainly at 300, 600 and 1200 Hz (see Fig. 4), would have introduced unwanted aliasing on the measured signals if suitable low pass filters had not been used before the analogue to digital converter.

The data acquisition system hardware includes two NI-1102B signal conditioning modules (i.e., 32 differential inputs and 200 Hz anti-aliasing filter), two NI-1120 isolation amplifiers

(i.e., 8 differential inputs and 4 Hz anti-aliasing filters), the SCXI multiplexer and a 16 bit ADC board (i.e., PCI 6032E) with a maximum sampling speed of 200 kSample/s. The data acquisition system software was developed by ENEA using LabVIEW from NI. The application included the data sampling at 2 kHz, the conversion in engineering units, a graphical user interface, an additional smoothing to reduce even further the effect of the voltage ripple and a data decimation to reduce data storage.
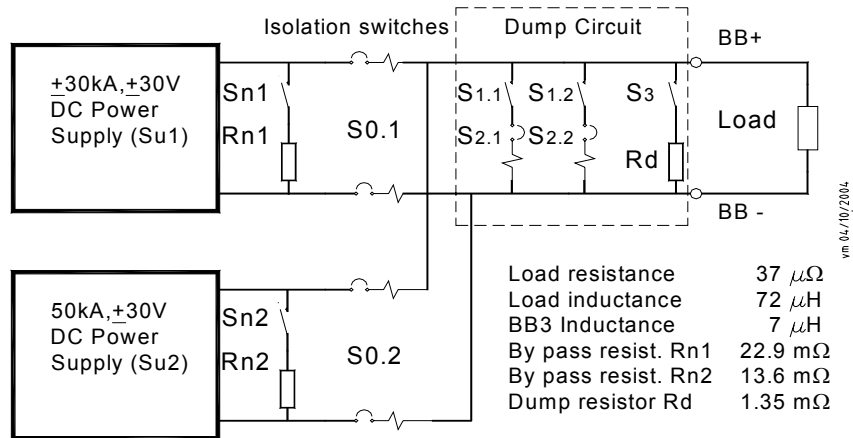
Fig. 3:   Power supply circuit diagram for HTS CL – CDM experiment.
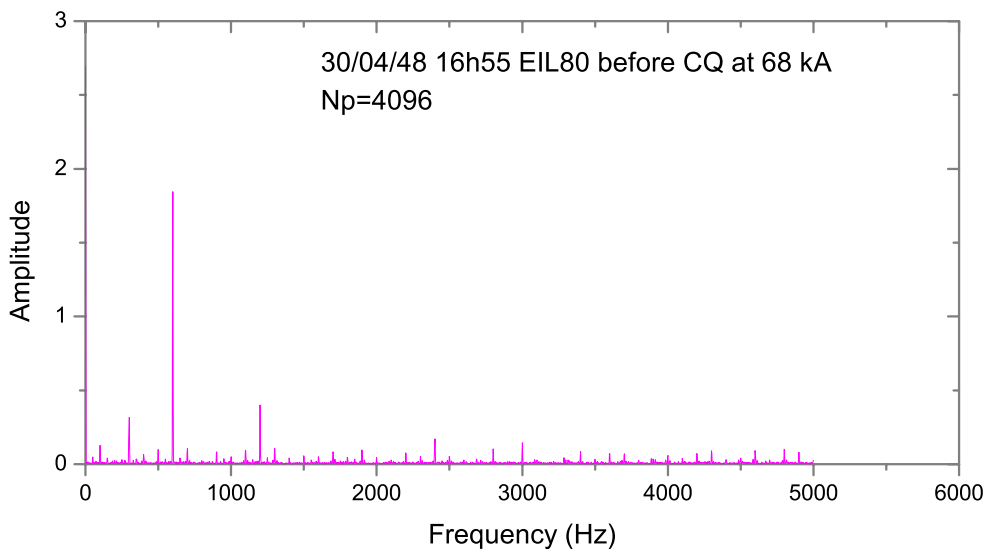
Fig. 4:   Fast Fourier Transform (FFT) of the voltage signals across the load during a flat-top at 68 kA (CQ=current quench, Np=number of data points).

The experimental data (i.e., 747 MB covering 119 separate shots) are made available on a FTP Server of the Forschungszentrum Karlsruhe to all potential users. 56% of the data were collected parasitically during the HTS CL experiment, while the remaining 44% were collected during the tests especially dedicated to the CDM-BB3 experiment. Some results, mainly concentrated on T_{CS} experiments, have been presented this year at the ASC conference held the 3-8 October 2004 in Jacksonville, Florida [5].

Staff:

W.H. Fietz
S. Fink
R. Heller
V. Marchese
M. Süßer
F. Wüchner
G. Zahn

Literature:

[1] T. Bonicelli, A. Vostner, Instrumentation of Busbar 3 for the Current Distribution Measurements, EFDA Call for Tender, 18.03.2003.

[2] R. Heller, S.M. Darweschsad, G. Dittrich, W.H. Fietz, S. Fink, W. Herz, A. Lingor, A. Kienzler, I. Meyer, G. Nöther, M. Süsser, V.L. Tanna, R. Wesche, F. Wüchner and G. Zahn, "Test of the 70 kA HTS Current Lead in the TOSKA Facility - Final Report EFDA Contract EFDA 02-1013 Deliverable 4.2", Forschungszentrum Karlsruhe Internal Report FE.5130.0061.0012/A, Oct 2004, unpublished

[3] V. Marchese, W. Fietz, R. Heller, M. Süßer, F. Wüchner, G. Zahn, Final Report for EFDA Subtask 03 -1059, Contract FU06-CT-2003-00154, 15.10.2004.

[4] V. Marchese, Circuit analysis in CDM BB3, Presented at the 3rd joint HTS-CDM Test Group Meeting, 6th October 2003.

[5] R. Zanino, M. Bagnasco, F. Bellina, T. Bonicelli, A. Della Corte, A. Di Zenobio, W.H. Fietz, A. Formisano, R. Heller, V. Marchese, R. Martone, L. Muzzi, M. Polak, P.L. Ribani, E. Salpietro, L. Savoldi Richard, S. Turtù, L. Verdini and G.R. Zahn, Current Distribution Measurements on the ITER-type NbTi Bus Bar III, presented at 2004 Appl. Supercond. Conf., Jacksonville, FL, Oct 3-8, 2004.

EFDA/03-1105
Cryogenic Laboratory Tests for V-I Characterisation of Subcable Samples

The main objective of this work is to perform measurements of the V-I characteristics of Nb_3Sn sub-size (>30 strands) CICCs under applied longitudinal strain in liquid He (T=4.2K) and high magnetic fields (up to B=13 T).

Emphasis shall be put on the measurement of the thermal pre-strain of the strands. To this end the experimental set-up shall be capable of performing accurate measurements of specimens having – in particular - different conduit materials, thickness, cables sizes and void fractions. The strain applied to the strand shall be – typically – up to ≈ 1.5 %. The instrumentation sensitivity is planned to allow measurements of critical electric fields as low as E=10 µV/m with a sensitivity better than 1 µV/m.

After the experimental set-up has been completed, instrumented and accurately calibrated, specimen testing shall be started. All specimens (not heat treated) will be made available by EFDA. In total, during the contract period, about 25 specimens shall be tested.

One of the most important characteristics of Nb_3Sn strands is the strain dependence of the critical current density which has to be taken into account for every conductor design, especially for cable-in-conduit conductors (CICC) due to the additional influence of the jacket material. Therefore, this task has been launched in the framework of the European Fusion Technology Program to determine the residual thermal strain of single strands and different multi-stage conductors on absolute scale which is essential for the final optimization of the ITER TF conductor. For this purpose, an existing test rig for critical current measurements on single strands and multi-stage CICCs as a function of strain $\varepsilon_{applied}$ and magnetic field, the FBI facility (**F**orce **B** magnetic field **I** current) at the Forschungszentrum Karlsruhe, has been recently modified and modernized to improve the overall accuracy and resolution of the system samples. To cover these experiments two facilities exist, the 1 kN FBI (Fig. 1a) for single strand measurement and the 100 kN FBI (Fig. 1b) for the CICC sub size samples.

(a)   (b)
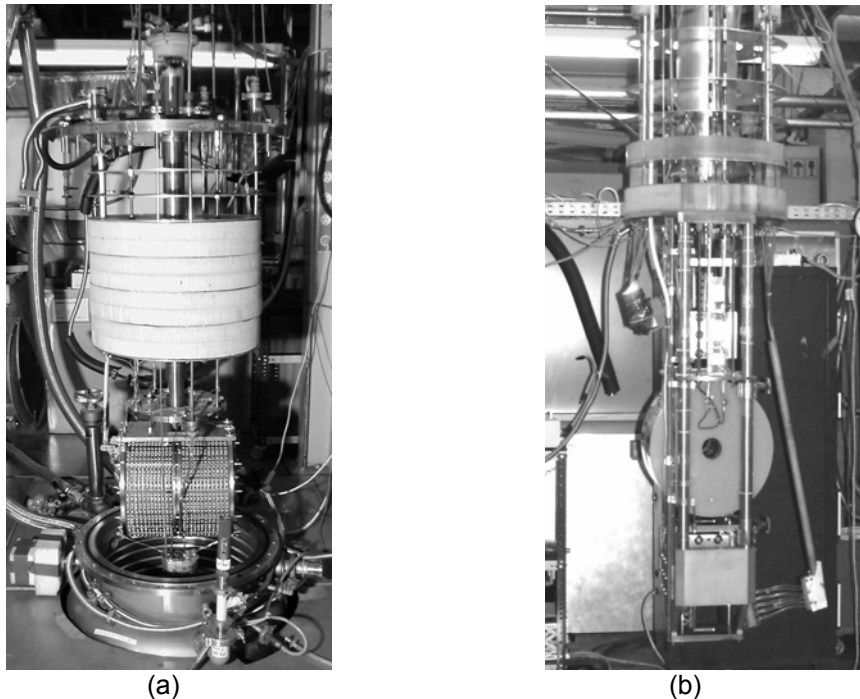
Fig. 1:   Test rig with the split coil magnet of the (a) 1 kN and (b) 100 kN FBI facility.

The task is divided into two major parts. First is the upgrade of the two FBI facilities, that were used until 2000. This work has become necessary to cover the specifications given

from the new industrial superconducting strands with enhanced electrical properties. In the second part the characterization of strands and sub size samples will be carried out.

The 1 kN FBI facility

The strands (SC-wires < 2.1 mm Ø) will be tested under magnetic field of <13.5 T using the 1 kN/<250 A cryogenic rig at 4.2 K (IGC split coil). Voltage versus current will be determined (voltage taps = 20 mm) at different strains using a 50 mm gauge length double extensometer system with the same data acquisition as already described.

Until 2000 the overall electronic equipment limited the sensitivity of the FBI facility. In fact, only a 100 µV/m criterion had been used to determine I_c. Additionally the current leads of the small FBI allowed only a maximum current of 250 A, which is to date too small for the new single strands.

To improve the sensitivity of the facility for commonly used 10 µV/m criterion and furthermore to increase the maximum current, three steps were necessary:

− replacement of the old cables for voltage measurement and the current leads
− implementation of a computer controlled power sweep and data acquisition with appropriate electronics (e.g. high sensitive nanovolt-meter from Agilent technology)
− an improved measurement procedure of V-I measurement.

Step one:
The cross section of the current leads was increased. Presently a maximum current of approximately 350 A is possible. The old separate single wires for voltage measurement are replaced with two shielded twisted pairs. Now two distances, 20 mm and 40 mm, for voltage measurement can be used.
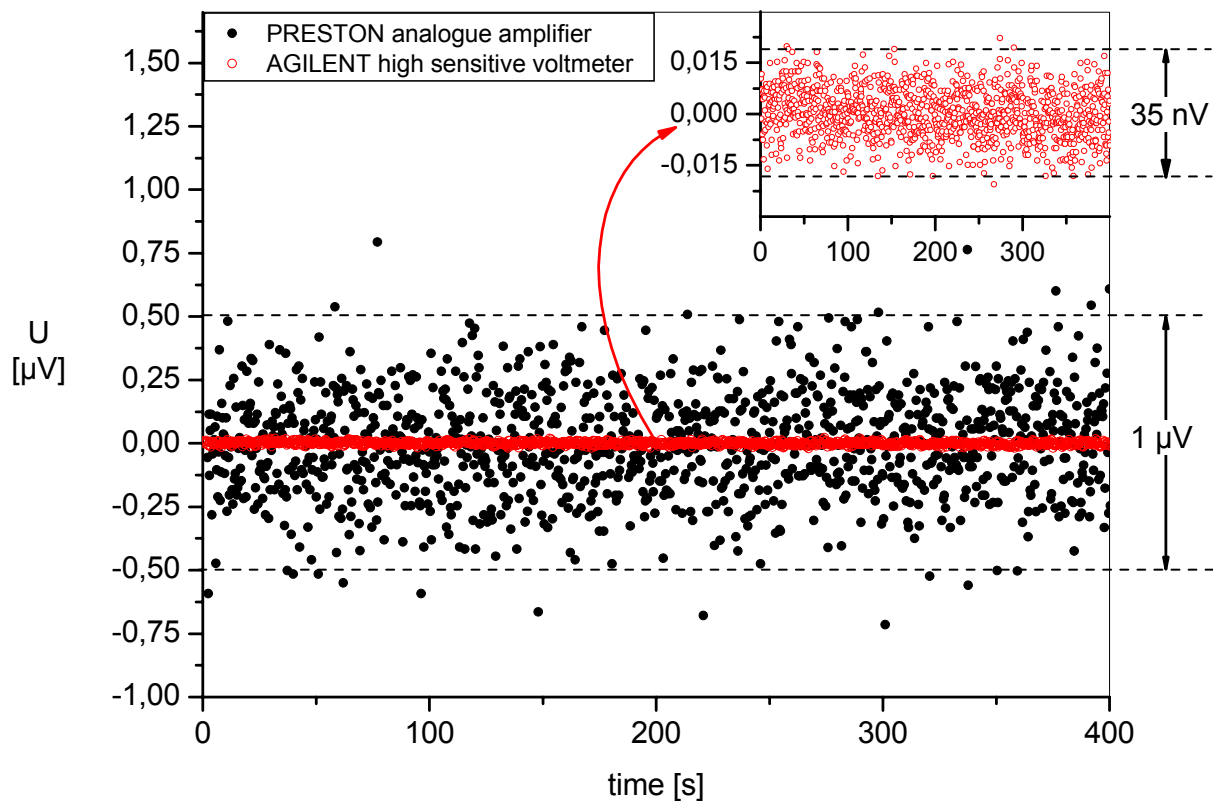
Fig. 2: Noise comparison during voltage measurement using old PRESTON analogue amplifier (black dots) or using AGILENT high sensitive voltmeter (red circles).

Step two:
The old analogue amplifiers are replaced with a sensitive voltmeter for current determination and temperature control. The voltage measurement of the superconducting strand is done with a high sensitive nanovolt-meter. The whole measurement is done computer controlled (TestPoint, DasyLab) and all data can be accessed immediately. Only the magnet control is still done manually, because no computer interface exists.

Step three:
During V-I measurement the current was normally increased continuously. This increased the noise of the voltage measurement tremendously due to dynamical processes (approx. between 1 and 3 µV). To reduce this noise a stable situation must be reached to get a useful voltage measurement. Therefore the current is still increased continuously, but at each high sensitive voltage measurement the current control is triggered to stay constant for this time. The noise is now reduced to <40 nV (Fig. 2) and the 10 µV/m criterion can be used to determine I_c. In figure 3 a typical measurement of a Nb3Sn wire is shown using all the above mentioned improvements.
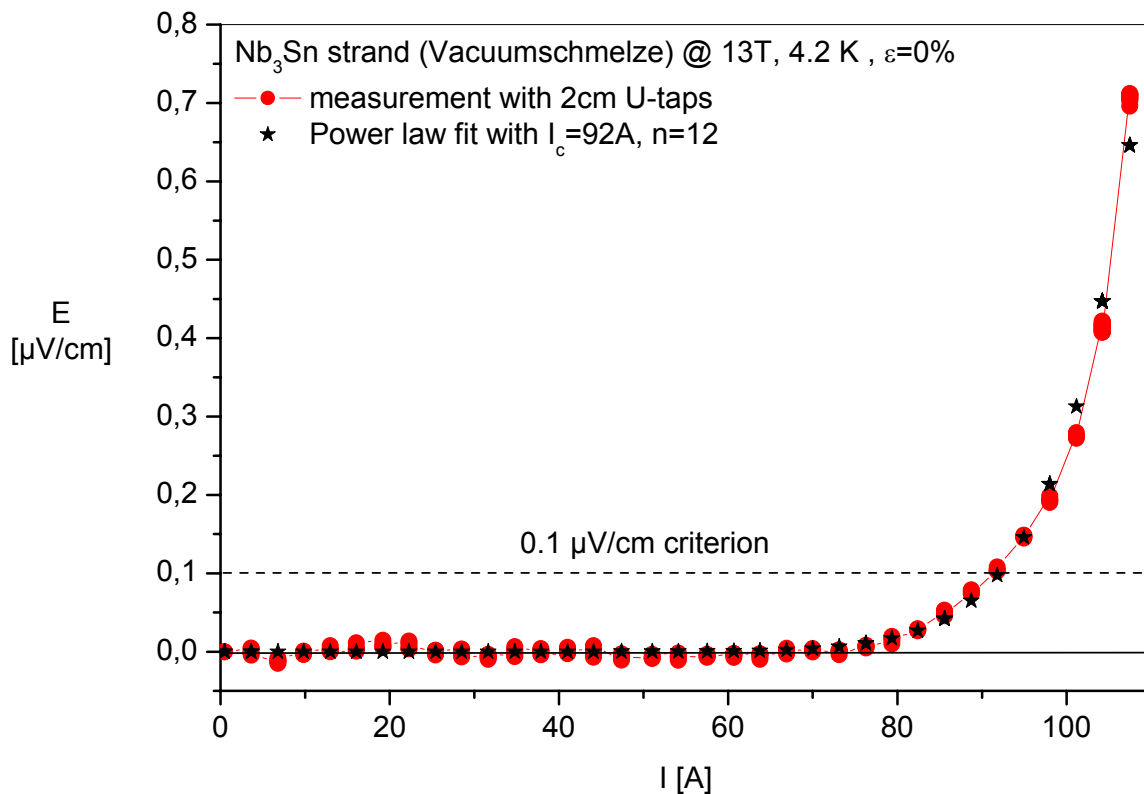
Fig. 3:   Typical measurement of a VAC strand with upgraded 1kN FBI facility.

Several measurements were carried out on different strands to test the performance of the 1 kN FBI facility. First a strand from EAS (former Vacuumschmelze, VAC) was characterised and compared with the obtained values from the Report of Specking [EFDA GB5-M27 1997]. Figure 4 shows the improvement of using the 10 µV/m instead of the 100 µV/m criterion to determine the critical current I_c under applied strain. Figure 5 demonstrates that the stress strain curve of this strand can be reproduced. More measurements will be done on the single enhanced strands, as soon as they are available.

Another experiment is to examine the different behaviour of a bare strand and a jacketed single strand. Therefore a Nb_3Sn strand from LMI was jacketed in a stainless steel tube (ID = 0.81 mm, OD = 1.2 mm). The dependence of I_c on magnetic field B is shown in Figure 6 for

both samples. Overall, the I_c is shifted to lower values, but more experiments will be done to check the steel jacket contribution on the $I_c(\varepsilon_{applied})$ dependence.
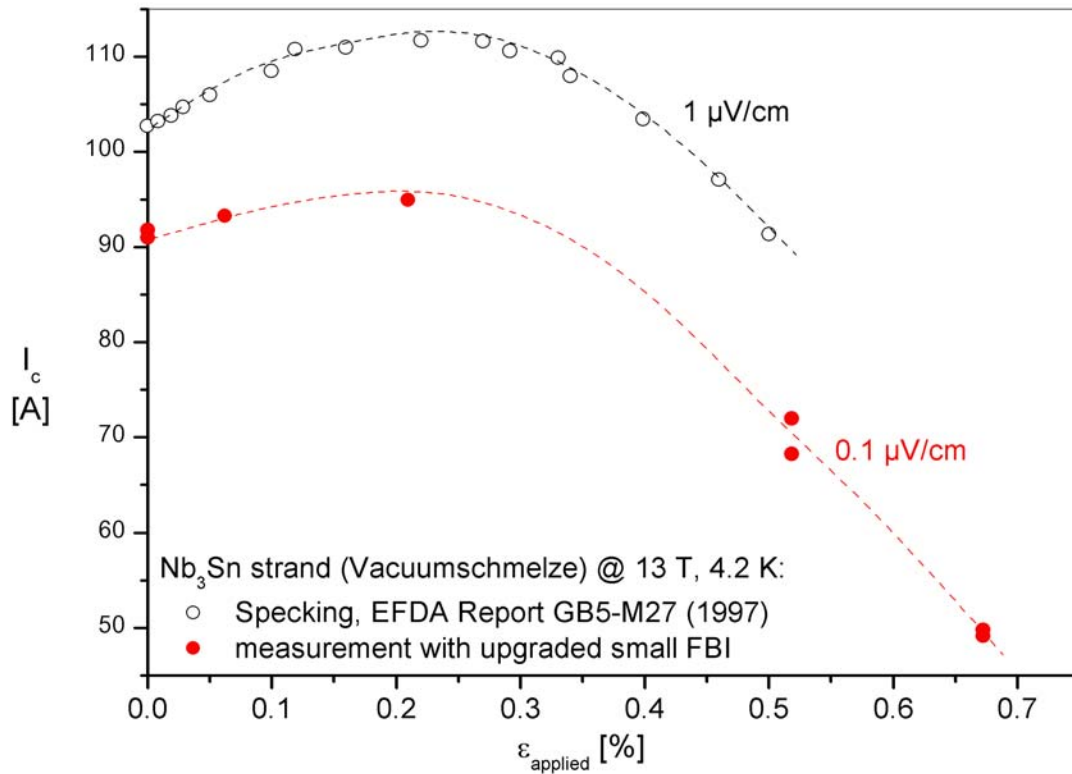
Fig. 4: Comparing the obtained critical current of a Nb3Sn strand using the 1 µV/cm (open circles) or the 0.1 µV/cm criterion (red circles).
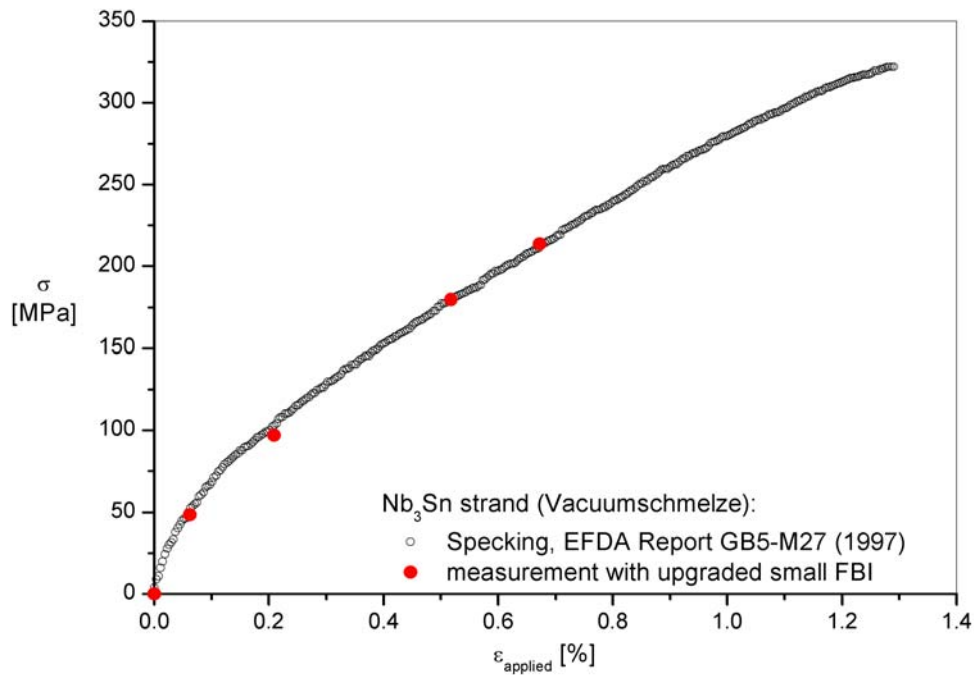
Fig. 5: Obtained stress-strain curve of a former measurement (open circles) compared with new measurement (red circles).
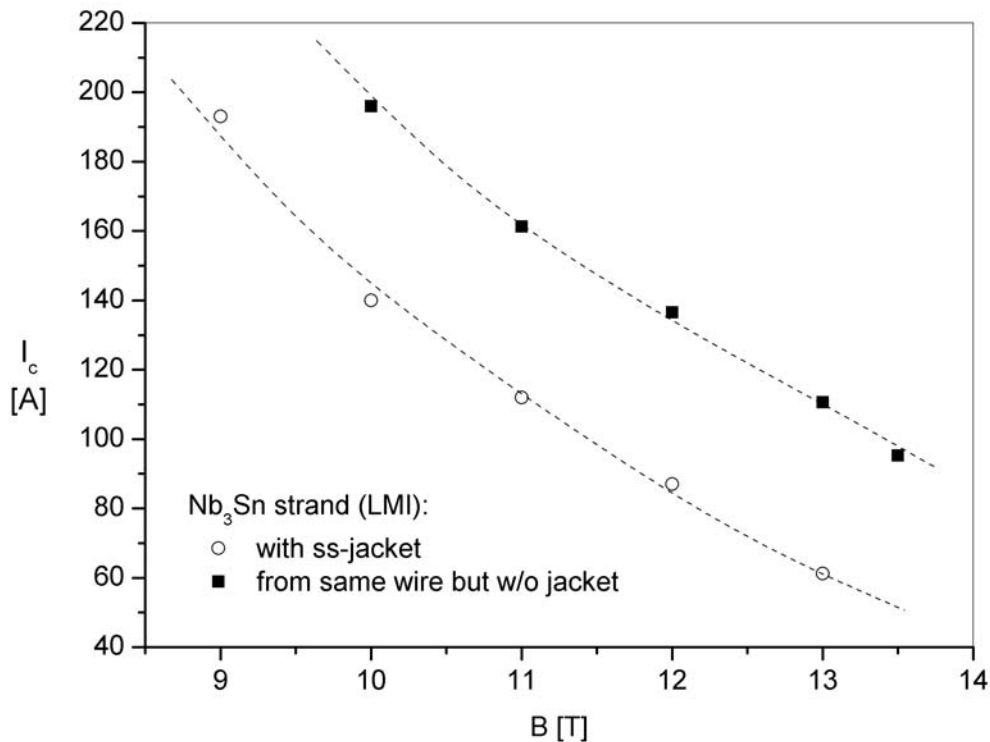
Fig. 6: Measurement of a single Nb3Sn strand (black squares) and a strand in a stainless steel jacket (open circles).

The 100 kN FBI facility

The sub-size CICC cable with a length of 1135 mm will be inserted into the existing large test facility of 100 kN load capacity. The upper and lower current grips will be electrically connected to the power supply of < 10 kA. The field is generated by a 14 T split coil (Oxford magnet) at 4.2 K and the electrical signal is monitored using voltage taps soldered onto the conduit with a distance of 50 mm. The measurement of strain using two FRP rods with a gauge length distance of 450 mm is accomplished with two high resolution extensometers. The voltage versus current curve is determined using a high precision 22 bit data acquisition system with a nanovolt-meter. These tests will be conducted at different levels of strains to obtain the sample's I_c versus strain at pre set magnetic fields.

Still some work is necessary to prepare this facility for future measurements. To check the experimental setup for remaining problems, a dummy CICC sub size sample was mounted into the cryostat. Adjustments on the mechanical part were performed to connect the 100 kN tensile machine to the pulling rod of the cryostat. Now it is possible to apply a defined axial load to the sub size sample. At present the 10 kA current source and the current leads to the cryostat are under inspection. The data control to determine the critical current I_c will be mainly similar as for the 1 kN FBI since the same electronics will be used, here only little adjustments will be necessary.

As soon as all above mentioned work is finished, it is possible to cool down the cryostat and test all functions, like temperature control and the split coil magnet with an old sub size cable inserted.

Staff:

Dr. K.-P. Weiss

Breeding Blanket
HCPB Blanket Concept

TTBB-001
Helium Cooled: TBM Design, Integration and Analysis

TW2-TTBB-001b D1
Upgrading of the TBM Design and Performance Analyses

In 2003 a new modular Helium blanket for the DEMO reactor has been developed and documented in fall 2003. Consequently the test blanket module for ITER developed so far had to be adapted to the new DEMO blanket concept. The requirements were to cope with a maximum heat load on the first wall surface of 500 kW/m² an outlet temperature from the TBM of 500 °C and the ability to withstand an internal pressure of 8 MPa, and to achieve temperatures in the pebble beds around 920 °C for the Lithium ceramic and 650 °C for the Beryllium. For the design steel structures should be foreseen with imbedded cooling channels fabricated by hipping. The material to be used was EUROFER. The module should be horizontal oriented in an equatorial port of ITER. The size should be 1270 mm in width, 740 mm in height and about 700 mm deep.

The TBM is composed of the subcomponents

1) First wall   (FW)
2) Caps
3) Stiffening grid (SG)
4) Breeding unit (BU)
5) Manifolds
6) Attachment

The coolant flow through the TBM is different to DEMO. Because of the reduced neutron flux the volumetric heat source in the TBM is only about 1/3 compared to DEMO. The radiation heat flux to the FW from the plasma is similar. To be able to safely cool the first wall and to reach in the same module the desired outlet temperatures, the introduction of a bypass was necessary, which is different from the DEMO blanket concept. The coolant flows first through the first wall to manifold two. There the flow is split 30% to 50% of the flow leave the TBM through the bypass. The residual flow goes from manifold 2 in parallel through the stiffening grid and the caps, with mass flows of about 0.4 kg/s and 0.2 kg/s. From caps and grid the flow is collected in manifold 3 which supplies the breeding units. The mass flow through the bypass is controlled such, that the outlet temperature is 500 °C.
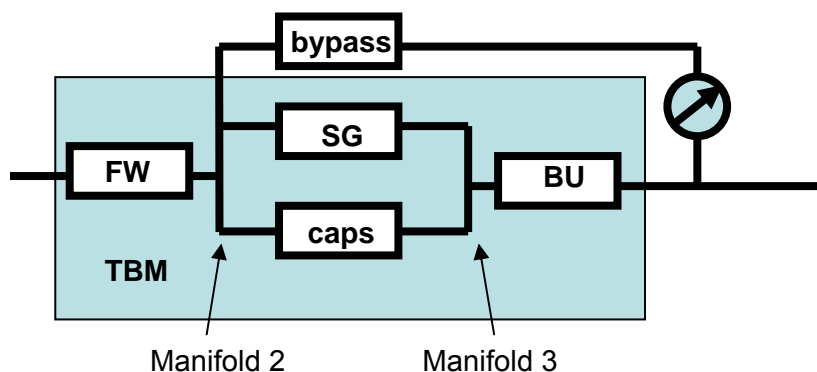
Fig. 1: Schematic of coolant flow in TBM

The first wall, after several iterations, has the following design: Like in DEMO the FW is 'U' shaped with channels in the radial toroidal plane. There are 14 cooling channels with 3 sweeps each. The cooling channel cross section is 12.5 mm in poloidal direction and 16 mm in radial or toroidal direction respectively. Towards the plasma the steel wall thickness is 3.5 mm and towards the breeding zone 10.5 mm.

Detailed thermal and stress analyses, done with 2d and 3d models, have been performed. The coolant mass flow is 1.3 kg/s; typical heat transfer coefficients are 6000 $W/m^2/K$ to 7000 $W/m^2/K$. From the breeder zone the FW is heated with about 35 kW/m^2 on the sides and 60 kW/m^2 on the plasma oriented portion of the FW: Three cases were analysed: a) normal operation with a heat load of 250 kW/m^2 b) upset conditions according top a MARFE with 500 kW/m^2 and c) like b) but superimposed a LOCA in the Helium cooling system pressurizing the TBM box to 8 MPa. Temperatures and stresses are in an acceptable range, for the stresses, however, comparison with the interim criteria is still to be done.

The thermal analysis used a thermo-hydraulic model where mass flow rate and heat transfer coefficients were given. Because of concerns whether the standard formulas do well for the conditions here a detailed k-ε model has been applied to check these data. This detailed analysis indicated for the FW, with Re numbers beyond 2.0 E+5, that classical formulas underestimate the pressure loss for bends by about 20 % and they also underestimate the heat transfer coefficients for developed flow by about 15 %. For the FW this means that the pressure loss is higher than initially expected, about 0.22 MPa instead of 0.17 MPa, but due to the increased heat transfer the mass flow rate could be throttled in the next iteration cycle.

For case b) the temperatures and for case c) the stresses are shown in Fig. 2.
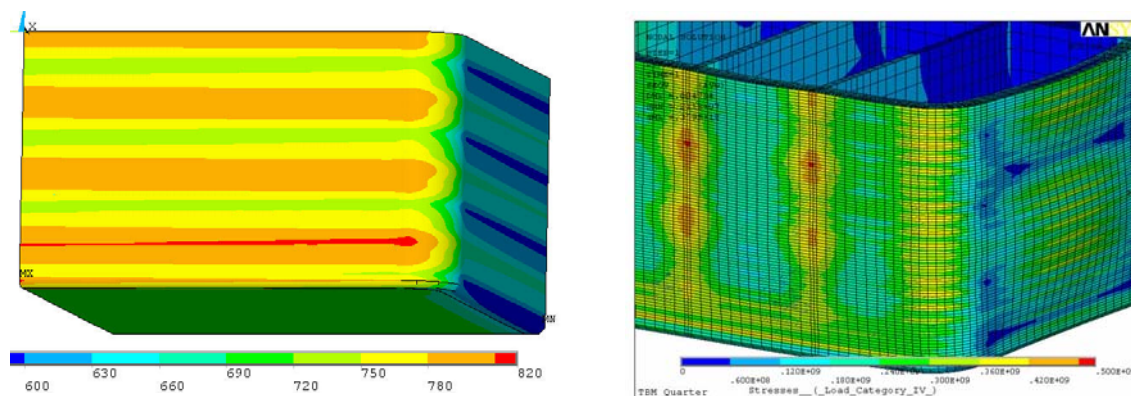
Fig. 2: Left: Temperatures for a plasma heat load of 500 kW/m^2;
right: v. Mieses stresses for box under 8 MPa and heat load on plasma side of 500 kW/m^2.

The caps close the 'U' formed by the first wall on bottom and top. The poloidal thickness is 40 mm. There are 9 imbedded channels having different number of sweeps. The helium flow through one cap is in the order of 0.1 kg/s. As the heat load on the cap is reduced as compared to the FW, a separate stress analysis has not been done. A thermal analysis, however, has been performed for the upper cap. The volumetric heat source is about 28 kW and the heat absorbed from the breeding units is about 16.5 kW. The losses are 35 kW via coolant flow and 7 kW radiation heat transfer to the port plug frame. The residual heat is conducted from the cap to the Helium manifolds. Temperatures are rather homogeneous and of no concern regarding thermal stresses.

Analysis of the breeding unit is done with a detailed model considering ¼ of a breeding unit and the adjacent stiffening grid. In order to achieve the required peak temperature of 920 °C in the ceramic it was necessary to redesign the canisters housing the ceramic bed. Now, instead of the two double canisters only one double canister is used. The ceramic bed height is increased from 11 mm to 26 mm. For this design the required temperature in the Beryllium is not achieved, therefore another breeding unit, similar to the DEMO design is used in order to match also the required temperature for Beryllium. An important outcome of the breeding unit analysis is the heat and mass flow distribution for the different load cases to be considered for the TBM. Four different heat loads for the first wall have been considered, 100 kW/m^2, 250 kW/m^2, 250 kW/m^2 +20% 500 kW/m^2 and 500 kW/m^2. The temperatures at the end of the different flow paths and the necessary mass flows are given in table 1.

Table 1: Temperature and mass flow distribution for the TBM for different plasma heat load.

FW	Surf load kW	94	234	281	469
	Vol. gen. kW	122	122	122	122
	Exchange BU<>FW kW	64	63	65	64
	Temp. after FW °C	341	362	369	397
Grid / Cap	Vol. gen. kW grid	26	26	26	26
	Cap	56	56	56	56
	Exchange BU <> grid	127	127	127	126
	kW Cap <> grid	29	29	28	28
BU	Vol. gen. kW	450	450	450	450
	Exchange (loss) kW	220	219	220	218
Required temperature rise to reach 500 °C at TBM outlet °C		159	138	131	103
Power to be removed from the TBM without FW kW		468	469	467	468
Mass flow in BU kg/s		0.5664	0.6535	0.6883	0.8743
Mass flow in grid kg/s		0.3398	0.3926	0.4142	0.5243
Mass flow in the caps		0.2266	0.2609	0.2741	0.35
Mass flow in bypass kg/s		0.7336	0.6465	0.6117	0.4257
Temperature after grid / cap		422	432	435	449
TBM outlet temperature		505	505	505	505
Max.Li.Temp.		937	938	938	940
Max.Be.Temp.		569	573	574	580

Another important area to be analysed is the flow field in manifold 2. This manifold is modelled with STAR CD for the upper half of the TBM. The model includes also some representative grid plates, one cap and half of the bypass. Because the design of the TBM is still under progress final results are not yet available, however, valuable hints were found for the coolant supply of the cap and the flow splitter in the grid.

The analysis for the breeding units was steady state. As at least at the beginning of ITER operation the plasma will be pulsed the temperature history in the TBM was investigated during a typical pulse cycle of 400 s plasma burn and 1400 s dwell time. It turned out that the desired temperatures in the bed cannot be achieved with such short pulses. They have to be at least 1000 s, preferred 2000 s. This means that the investigation of the pebble bed mechanics for the TM module in ITER will possibly not be done at representative conditions, more likely for the PI module for which longer pluses are planned should be used for these investigations.

In terms of integration of the TBM into ITER four different areas have to be considered: a) port plug design to integrate the TBM into the vacuum vessel, b) hot cell operations and tests on the TBM before and after port plug irradiation, c) pipe routing and component arrangement in the port cell and d) design of the Helium cooling system for the TBM. For a) the previous design has been revised taking into account the new requirements of a bypass line and four additional coolant lines for individual breeding unit cooling. A cut through the port plug is given in Fig. 2, where for clarity the surrounding port plug frame is not shown. For b) no important activities were done. For c) the complete piping has been designed under the main aspect of quick dismantling of the piping. For this purpose a pipe integration cask (PIC) has been introduced. With this cask only two separation planes are needed to remove all the piping in front of the vacuum vessel port as indicated in Figure 2 left. This was possible by installation of a portion of the bio shield on the cask. Another important boundary condition is the accommodation of the thermal expansion from cold state to operation. The radial dis-

placement is about 100 mm, 40 mm from the vacuum vessel and 60 mm from the piping. The poloidal displacement is 20 mm due to thermal expansion of the vacuum vessel. For d) possible circuit options have been designed. One with a so called 'O' shaped loop using a Helium circulator allowing operational temperatures up to 300 °C and a so called '8' shape loop with a circulator operating between 50 °C and 100 °C. Both circuit types are modelled with RELAP5. These models will support the decision which of the circuit types should be used for ITER.
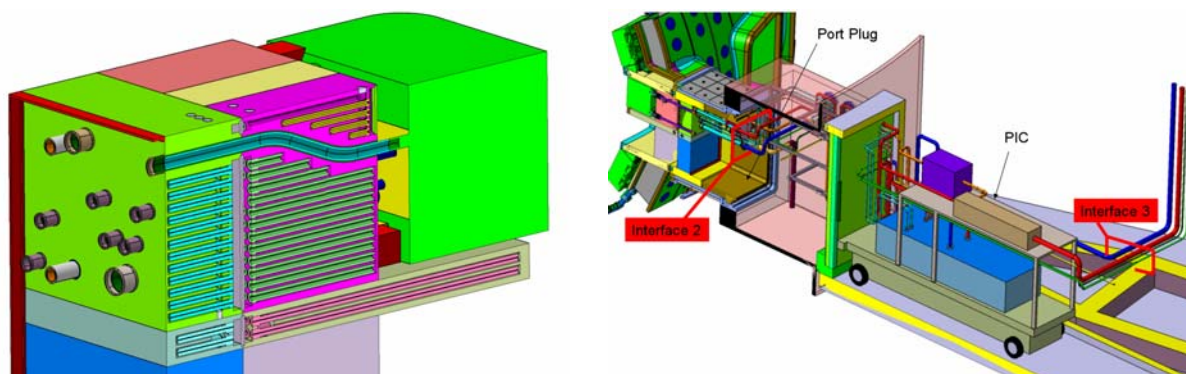
Fig. 2: Left cut through the port plug. Right: Piping integration cask and piping in the port cell.

The work done so far has lead to an acceptable design solution for the TBM under the conditions defined a year ago. Depending on whether or not the ITER IT decides that the protecting frame between the TBM and the ITER blanket should be reduced in thickness from 200 mm to 100 mm the described design will require to be adapted accordingly. Besides this design and performance of experiments are the next steps. Here key questions of the hydraulics in the TBM, e.g. manifold and first wall channel are to be investigated and the design of test mock ups will start.

Staff :

L. Boccaccini
B. Dolensky
M. Ilic
X. Jin
H. Neuberger
R. Meyder
V. Pereslavtsev
S. Polixa
S. Raff
P. Schanz
Z. Xu

Literature:

[1] R. Meyder, et al. : New modular concept for the Helium cooled pebble bed Test Blanket Module for ITER. Contribution to SOFT 23 in Venedig 2004.

[2] L.V. Boccaccini, et al : Test strategy for the european HCPB Test Blanket Module in ITER. Contribution to TOFE 16 Madison 2004.

[3] X, Jin, R. Meyder: Thermal-Hydraulic System Study of the Helium Cooled Pebble Bed Test Blanket Module for ITER Using System Code RELAP5. Contribution to: 3rd Workshop of Chinese Academy of Sciences on Plasma Physics and Fusion Research. Hefei China, July 4, 2004

TW4-TTBB-001 D2
Review of the Material Data Base and Material Assessment Reports for the Breeder and Multiplier Materials of the HCLL and HCPB Concepts

1) Objectives

The irradiated and nonirradiated material properties including the physical and chemical properties of Beryllium multiplier and ceramic breeders (lithium orthosilicate and metatitanate) pebbles and pebble beds, and PbLi will be compiled and assessed in order to provide a data base for the design of the HCPB and HCLL concept.

2) Work performed

The data collection has started including the following materials:

– Be multiplier (HCPB):

- Be NGK pebbles in the initial state as well as under the influence of in-service conditions, including irradiation data and data resulting from compatibility and interaction experiments with various materials and the current properties of pebble beds.

- All available preliminary data on other Be grades and alloys (e.g. small grain Be and Be12Ti)

– Ceramic Breeders (HCPB): Li_4SiO_4 and Li_2TiO_3 pebbles in the initial state as well as under the influence of in-service conditions, including irradiation data and data resulting from compatibility and interaction experiments with various materials and the current properties of pebble beds.

– Liquid metal breeder/multiplier (HCLL): Pb17Li in the reference eutectic composition and in the initial state as well as under the influence of in-service conditions, including irradiation data and data resulting from compatibility and interaction experiments with various materials and all MHD relevant properties.

The final compilation of data will be provided in the same format as for the ITER MDB and MAR reports and in a user friendly electronic version.

3) Next Steps

Due to personnel bottle-neck a delay was caused, the termination of the subtask is expected to be 6/2005.

Staff:

J. Reimann

TTBB-002b
Helium Cooled: Blanket Manufacturing Technologies

TW2-TTBB-002b D5
FW Manufacturing by HIPing

Introduction

This task is dedicated to investigate manufacturing technologies of <u>B</u>lanket <u>B</u>ox (BB) components and of the <u>B</u>reeder <u>U</u>nit (BU). A BB represents a large box that contains the BUs like a crate of beverages. Typical dimensions and numbers are under discussion. At the moment, a BB will contain from 18 to 100 BUs. The BU dimensions are about 50 x 20 x 20 cm. A high energy load has to be absorbed by all components of the BB. Consequently the main tasks to be fulfilled by the BB are: Mechanical cover of the vacuum chamber, heat transfer, and containment of the breeder material and the beryllium neutron multiplier. The incident energy from the fusion plasma requires a very efficient high-pressure helium cooling system. All components are made of plates with cooling channels. These plates will be manufactured by a variant of HIPing, called U-DW (<u>U</u>niaxial <u>D</u>iffusion <u>W</u>elding). The development of a fitting U-DW procedure is the main objective of the current task. The U-DW process has the significant advantage that it produces ideal welds. This means that tensile and charpy impact properties are the same as of the base material EUROFER. The necessary highly efficient cooling system needs curved plates with cooling channels. The plates are manufactured first by milling half plates and then they are connected by a U-DW process. The channels are filled with a filler metal to prevent destruction of the cooling channels by the bending process. Consequently, a cold bending process is unfortunately required for many components of the blanket box. This bending process will be the subject of the first experiment this year.

Bending experiment

It has to be investigated whether the structural material EUROFER is damaged by a bending process. Such an investigation has not yet been performed. The experiments are carried out to study the mechanical damage of a bent workpiece part. Furthermore it has to be investigated whether a heat treatment can reduce this damage. Three 4.5 mm thick EUROFER tin stripes are bent with an inner radius of about 6 mm (tolerance 0.5 mm, high-strength material) according to U-plate dimensions.

Fig. 1: Photo of a bent EUROFER tin stripe.

Every rectangular arc (angle tolerance 1°, three per tin stripe, see Fig. 1) was subdivided into four specimens (KLST). The specimens were numbered to express the individual position as shown in Fig. 2. The specimens of the second tin were tempered 3 hours at 730°C. Specimens of the third tin were additionally subjected to a normalization (0.5 hours, 980°C).
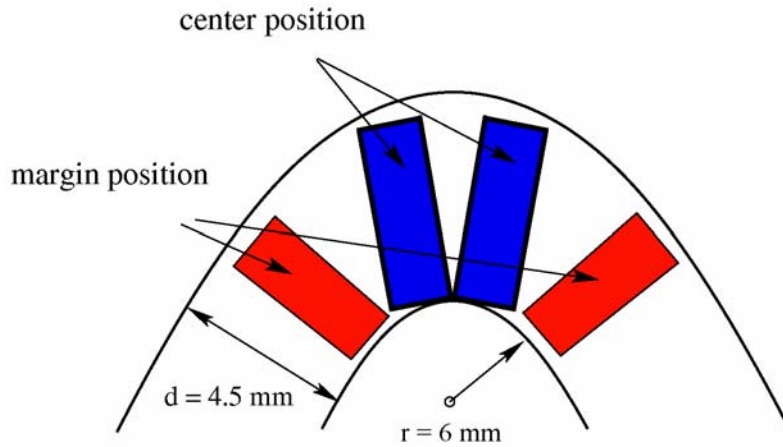
Fig. 2: Sketch of individual specimen positions.

The experimental results are shown in Fig. 3. It is rather surprising that the material damage caused by bending obviously depends on the position of the specimens taken from the first tin without any heat treatment, see red and blue symbols in Figs. 2 and 3. The damage can be quantified easily by a huge increase of the ductile to brittle transition temperature. The DBTT of specimens taken from the margin position, see Fig. 3, is increased by 20°C compared to the base material. In contrast to the latter result, the DBTT of neighboring specimens from the *center position* increased by **60°C** which is a critical value for the lifetime of the BU or e.g. an FW plate.

The specimens (green symbols) of the second tin (heat treatment at 730°C for 3 h) do not display any difference between the specimen from the center position and those from the margin position. This can be interpreted in the following way: Such a heat treatment does not completely lower the bending-caused damage, but nearly to a fixed amount. The best results are reached with a complete heat treatment, which is reflected by a third tin (violet upper triangular symbols in Fig. 3). However, a small base material damage can be noticed even in specimens with such a full heat treatment (see the black lines in Fig. 3). But this can be neglected.
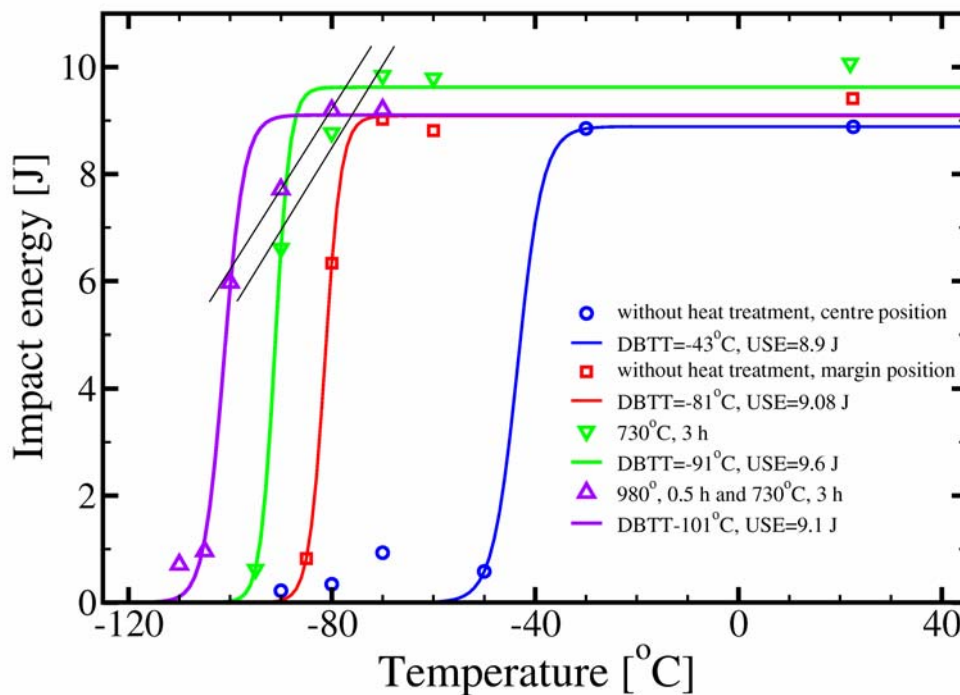
Fig. 3: Charpy impact test results of the bent tins. The violet line represents the properties of the base material.

Creep experiments

A new series of creep experiments has been performed. The experimental setup has been improved by a better algorithm for adjusting the force. A better planning of experiments and most important improvements of the creep model allow for a better prediction of the creep behavior of EUROFER.

Uniaxial diffusion welding improvements

Former theoretical simulations of a diffusion welding process predicted a partially reversible character of a hot (≈1000°C) diffusion weld. The effect consists in an opening of very small voids in the weld under changing process conditions. Experiments using a two-step method confirm the simulation results. However, a direct experimental proof has been missing so far. The simplest experiment would be to weld diffusion-welded specimens under the same conditions. One specimen is cooled down under the condition of applied welding pressure, the other one is cooled down with a negligible pressure after the welding time. For experimental proof, the bonding pressure producing non-ideal welding conditions has to be lowered. It is expected that the specimen cooled down with pressure shows better charpy impact test results. Fig. 4 displays the experimental results: The blue line represents the base material properties. The difference is clearly obvious from comparing the results of specimen D 24 cooled down with pressure and specimen D 23 cooled down *without* pressure. A second pair of specimens was investigated at a lower bonding pressure of 10 MPa. The fracture areas of some charpy impact specimens, however, show the milling structure of non-welded specimens. This light microscope observation can be interpreted as an influence of the "long-range" (1000 μm) lateral roughness of the specimen. The welding pressure of 10 MPa was not sufficient to level off this roughness. This is confirmed by the results of the diffusion welding model. The results agree with the specimen at high bonding pressure, while the results of D 21 and D 22 that were subjected to a lower bonding pressure disagree with the model results.
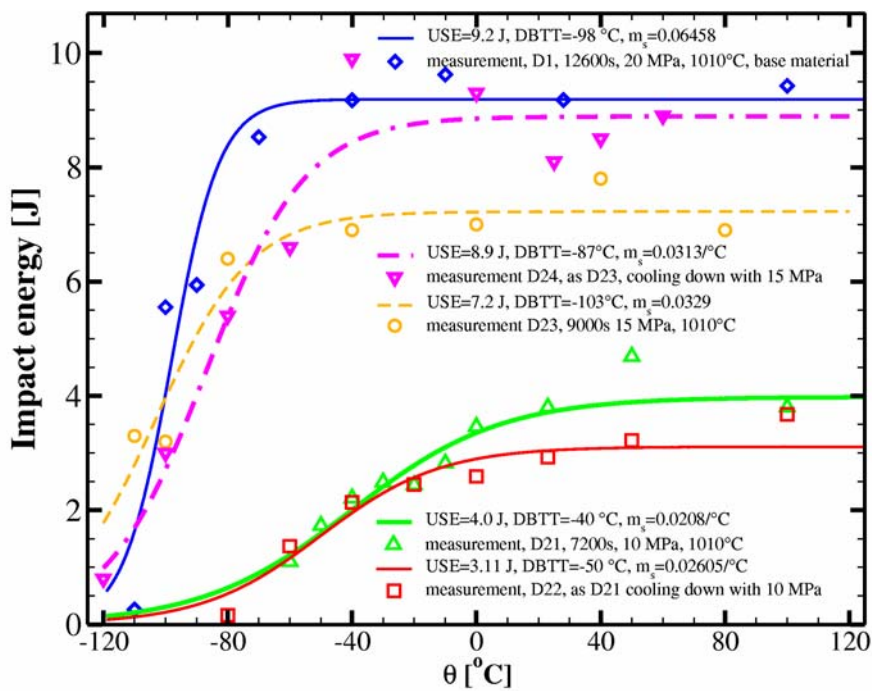
Fig. 4:   Charpy impact test results of diffusion-welded specimens under different welding conditions.

Conclusions

The bending experiments of the year 2004 show that a cold bending process will cause a huge material damage. A normalization will heal this damage. A heat treatment will be *frequently* applied to the BB and its components for other reasons. It is therefore required to investigate the mechanical material properties of EUROFER under such a frequently repeated heat treatment.

The results of the U-DW experiments confirm the effect of a partially reversible diffusion welding. It will be an interesting challenge to investigate whether such a process is associated with an advantage like less deformation or not. The empirical creep model to be improved this year will be an absolutely necessary tool. The other results show that a bonding pressure of 15 MPa will not be sufficient for ideal welds at 1010°C. However, industrial set-ups reach a maximum bonding pressure of 16.6 MPa only in current drafts of BB and BU components. Transfer to industry of the EUROFER U-DW process will result in a new series of welding experiments at a higher temperature in the next year.

Staff:

J. Aktaa
B. Dafferner
H. Kempe
H. C. Schneider
A. von der Weth

TTBB-005
Helium Cooled: Breeder and Neutron Multiplier Materials

TW4-TTBB-005 D2
Procurements of Li$_4$SiO$_4$ Pebbles and Quality Control of the Produced Material

In collaboration with Schott, Mainz, FZK develops and investigates slightly overstoichiometric lithium orthosilicate pebbles (Li$_4$SiO$_4$ + 2.5 wt% SiO$_2$) to be used in the HCPB blanket. The pebbles are fabricated in a semi-industrial scale facility, which allows a production between 200 and 300 kg/year. Since 2003 only LiOH and SiO$_2$ have been used as raw materials [1]. The characteristics of the final product are strongly influenced by the fabrication parameters, which are rather difficult to monitor in the small facility and difficult to maintain for different batches. Consequently, the reproducibility from one production run to the other is not very high, and it is therefore required to control the quality of every batch of pebbles received from the industrial producer, in order to use a well-defined standard material in all experimental activities with pebbles or pebble beds. The objective of the task is to maintain the know-how in the production of the pebbles and to perform the quality control of the delivered material.

Long-term annealing of ceramic pebbles

Two different lithium orthosilicate pebble batches (OSi 01/3-3 fabricated from Li$_2$CO$_3$ + SiO$_2$ and OSi 01/3-4 fabricated from LiOH + SiO$_2$) and lithium metatitanate pebbles (produced by CEA) were annealed for up to 96 days at 970°C under helium + 0.1 vol% hydrogen [2]. As observed in earlier annealing experiments all samples showed a more or less distinct discolouring with increasing annealing times due to oxygen deficits.
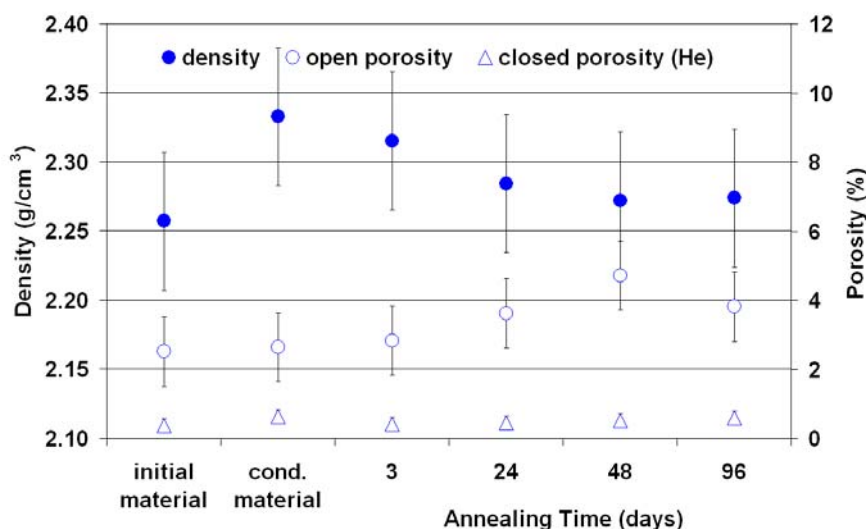
Fig. 1: Density and open porosity of orthosilicate pebbles OSi 01/3-3 measured by Hg-porosimetry, and closed porosity measured by He-pycnometry.

After thermal conditioning and during annealing, no significant differences could be observed within the accuracy of measurement for the properties of the two different orthosilicate batches. The closed porosity of all samples is lower than 1 % and can be neglected. The initial density of about 94-95 %TD was slightly increased by the thermal conditioning to 96-97 %TD and was lowered again nearly to the initial value during annealing (figs. 1+2). The initial crush load of about 7 N was reduced to about 5 N during annealing, which is consistent with former annealing experiments. Within the accuracy of measurement no change in the composition, neither by chemical analysis nor by x-ray diffraction, could be deduced during conditioning or annealing.

During annealing of the metatitanate pebbles a significant grain growth took place. The initially grain size of 2 µm was increased to about 20 µm after 96 days of annealing. At the same time an agglomeration of the small inter- and intracrystalline pores took place. The initial density of about 83 %TD was increased during annealing to about 87 %TD by an increase of the closed porosity and a decrease of the
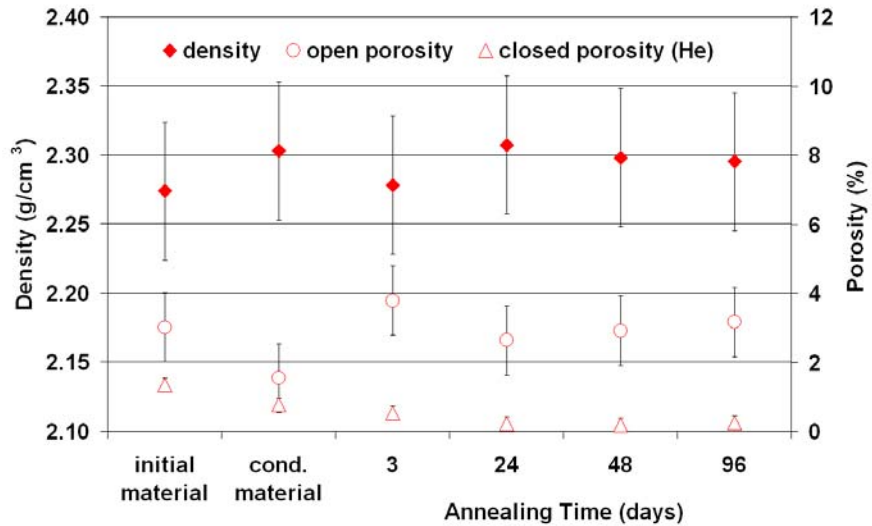
Fig. 2: Density and open porosity of orthosilicate pebbles OSi 01/3-4 measured by Hg-porosimetry, and closed porosity measured by He-pycnometry.

open porosity. This is consistent with the microscopic observations and may be caused by a post-sintering effect. The crush load of the initial material of 49 N was slightly decreased by the conditioning but remained constant within accuracy of measurement during annealing at a value of about 43 N. As in case of the lithium orthosilicate pebbles, no change in the composition of the lithium metatitanate pebbles, neither by chemical analysis nor by x-ray diffraction, could be deduced during conditioning or annealing.

Investigation of the yield of the melt-spraying process
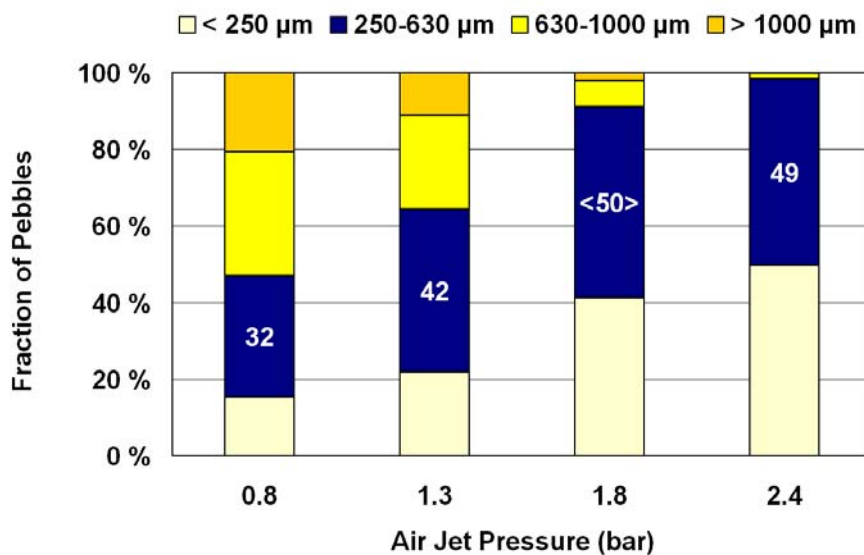
Fig. 3: Variation of pebble size fraction at different pressures of the air jet. At a pressure of 1.8 bar three different batches were fabricated, as it corresponds to the pressure used for the fabrication of reference material.

To determine the parameters that influence the pebble characteristics and the yield, fundamental experiments were carried out at Schott, Mainz, in November 2003. In these experiments 10 different batches (OSi 03/2-1 … 10) were produced, where parameters such as pressure and temperature of the air jet and the melt temperature were varied [3]. Three batches were fabricated with the standard parameters usually used for the fabrication of the reference material. The results showed that the pressure at the nozzle has the major influence on the rate of yield of the desired pebble size fraction between 250 and 630 µm. In the investigated pressure range from 0.8 to 2.3 bar, the rate of yield varied from 32 % up to a maximum of 50 % at a pressure of 1.8 bar (fig. 3). Whereas the influence of the air temperature as well as of the melt temperature were

found to be negligible. The experiments confirmed that the parameter chosen in the past for the fabrication of the reference material are the optimum parameters, but also revealed that the yield can not be increased beyond 50 %.

A sampling of pebbles carried out at different times during the production of one batch revealed that the average pebble size increased with increasing time (fig. 4). At the end of the fabrication process, which took about 10 minutes, not only larger pebbles but also more irregularly shaped particles were observed. This is caused by the continuous decrease of the amount of melt in the crucible during the fabrication of one batch. With a decreasing hydrostatic pressure also the flow of the melt decreases and leads to unstable spray condition. The rate of yield and the reproducibility should hence be increased in a continuous process in an upgraded facility, which provides a better control of the process parameters.
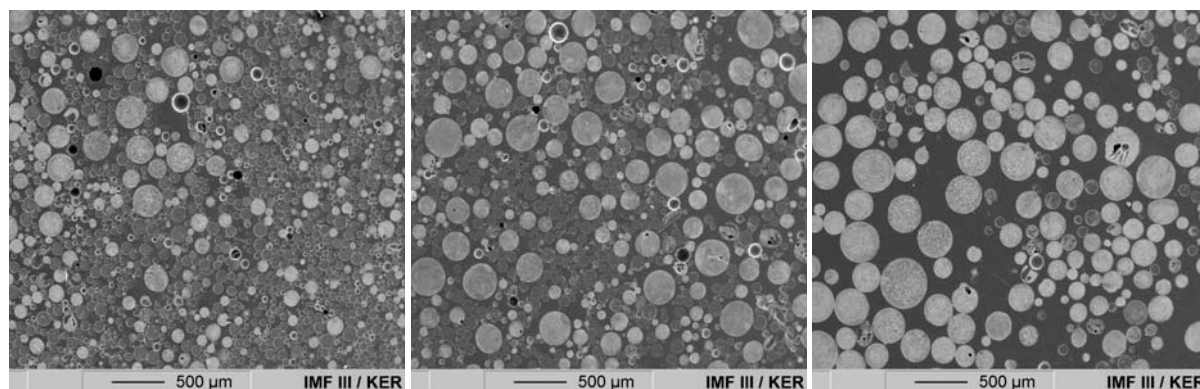
Fig. 4: Cross-sections of pebble samples collected during the fabrication of batch OSi 03/2-9 after
(left) 1 minute, (middle) 4 minutes, and (right) 8 minutes.

Quality control of reference material

The three reference batches of lithium orthosilicate pebbles (OSi 03/2-1, 2-8 and 2-9) were fully characterized as usual [3]. Although these batches were produced under the same conditions using identical parameters, the microscopic investigation already showed a relatively high amount of pores in batch 2-1 (fig. 5). This was also confirmed by Hg-porosimetry, where a density of only 92 %TD was measured for batch 2-1, while densities of 94 %TD were determined for the batches 2-8 and 2-9 (table 1). As a consequence, the crush load of single pebbles of the first batch of only 4 N is also much lower than the values of 8 - 9 N measured for the other two batches. The dissimilarity in the material properties can not be explained by a variation in the production process, and the results of the characterization of these batches demonstrate that the reproducibility in the small-scale facility at Schott in Mainz is not very high. A quality control of every delivered batch is therefore necessary to ensure well-defined properties of the reference material used in experimental activities.
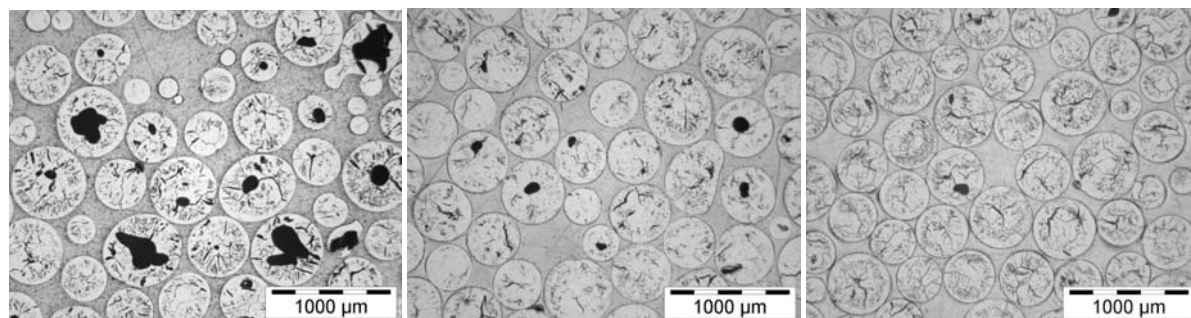
Fig. 5: Cross-sections of orthosilicate batches fabricated using the standard parameters for reference material.
(left) OSi 03/2-1, (middle) OSi 03/2-8, and (right) OSi 03/2-9.

Table 1: Properties of lithium orthosilicate pebbles.

Batch	OSi 03/2-1	OSi 03/2-8	OSi 03/2-9
Size Distribution			
d_{50} / µm	360	310	320
He-Pycnometry			
inner density / % TD	99.7 ± 0.3	99.7 ± 0.2	99.5 ± 0.1
closed porosity (calc.) / %	0.3 ± 0.3	0.3 ± 0.2	0.5 ± 0.1
Hg-Porosimetry			
density / g cm^{-3}	2.20 ± 0.04	2.25 ± 0.06	2.26 ± 0.02
density / % TD	91.6 ± 1.5	93.7 ± 2.5	94.0 ± 0.8
open porosity / %	6.7 ± 0.4	4.2 ± 0.7	5.2 ± 0.3
closed porosity (calc.) / %	1.8 ± 1.3	2.2 ± 2.0	0.9 ± 0.8
Pebble Bed Density			
tap density / g cm^{-3}	1.41	1.44	1.46
Crush Load Tests (IMF II)			
mean crush load / N	4.3 ± 1.1	8.9 ± 1.8	8.5 ± 1.9
Specific Surface Area			
specific surface area / m^2 g^{-1}	0.11	0.13	0.09
Chemical Analysis of Principal Constituents (Schott)			
Li_2O / wt%	48.57 ± 0.06	48.08 ± 0.05	48.27 ± 0.02
SiO_2 / wt%	50.99 ± 0.14	51.59 ± 0.04	51.38 ± 0.11

Deliveries for irradiation experiments

Additional samples of orthosilicate pebbles conditioned at 970°C for 1 week were delivered to Petten for the high fluence irradiation (HICU) in the HFR Petten [4].

For the HEXCALIBER experiment in Brasimone, 7 kg of lithium orthosilicate pebbles were ordered with a pebble size fraction of 0.2-0.4 mm (OSi 04/1). 6 kg the produced material were sent to Brasimone, 1 kg will be used for quality control and characterisation.

Staff:

C. Adelhelm
B. Alm
A. Erbe
R. Knitter
C. Odemer
P. Risthaus
R. Rolli
O. Romer

Literature:

[1] Knitter, R.; Piazza, G.; Reimann, J.; Risthaus, P.; Boccaccini, L. V., Fabrication and characterization of lithium orthosilicate pebbles using LiOH as a new raw material. CBBI-11, 11th Int. Workshop on Ceramic Breeder Blanket Interactions, 15-17 Dec. 2003, Tokyo, Japan. In: Proceeding of the 11th International Workshop on Ceramic Breeder Blanket Interactions, Ed. M. Enoeda, Japan Atomic Energy Research Institute, 2004, 108-119.

[2] Knitter, R., Quality control of lithium orthosilicate pebbles and long-term annealing behaviour of ceramic breeder materials. Interner Bericht, März 2004 (final report on the EFDA Task TW2-TTBB-002b-D2)

[3] Knitter, R.; Risthaus, P., Fabrication of Lithium Orthosilicate Pebbles by Melt-Spraying – Reproducibility and Yield. CBBI-12, 12th Int. Workshop on Ceramic Breeder Blanket Interactions, Sept. 16-17, 2004, Karlsruhe, to be published in: Wissenschaftliche Berichte Forschungszentrum Karlsruhe.

[4] Hegeman, J. B. J.; van der Laan, J. G.; Knitter, R.; Reimann, J.; Lulewicz, J. D., A high fluence irradiation of ceramic breeder materials in HFR Petten, materials characterisation and test matrix. SOFT23, 23rd Symposium on Fusion Technology, September 20-24, 2004, Fondazione Cini, Venice, Italy.

[5] Piazza, G.; Erbe, A.; Rolli, R.; Romer, O., Post-irradiation examinations of Li_4SiO_4 pebbles irradiated in the EXOTIC-8 experiment. 11th Internat. Conf. on Fusion Reactor Materials (ICFRM-11), Kyoto, J, December 7-12, 2003, Journal of Nuclear Materials 329-333 (2004) 1260-1265.

TW4-TTBB-005 D3
Fabrication and Characterisation of Beryllium and Be Alloys

1. Introduction

In order to improve the tritium release capability of beryllium in HCPB type blankets, beryllium tablets with small grain sizes ranging from 0.4 – 10 μm and 15 mm diameter and a few millimetres height have been produced by a wet ball milling process with subsequent hot pressing. X-ray investigations, SEM and EDX confirmed among others that the impurity concentrations could be kept very close to the raw material. As grain coarsening of Be is at a given temperature besides pressure and possible grain surface layers a sensitive function of the initial grain size, Be tablets have been subjected to isochronal annealing between 500 and 900 °C in high vacuum. As a main result, grains in the 5 μm range and above remain practically stable during annealing at 900 °C for 2 h. On the basis of the initial datasets, substantial grain coarsening has been found below about 1μm. A major milestone during the reporting period was the very successful fabrication of intermetallic Be-30.8%Ti alloys without porosity, that is, with the highest possible density. Even more, X-ray analyses revealed nearly pure $Be_{12}Ti$ which is presently considered most attractive for blanket applications among all intermetallic Be alloys.

2. Production and characterization of Be and Be-Ti alloys

2.1 Experimental setup

The main aim of this work was to obtain Be and Be-Ti samples for further characterization by means of available analyzing tools and devices (EDX-analysis by SEM, X-Ray analysis, optical microscopy and porosity measurements). Different technological methods have been, at first, tested on Ti, and then used on Be in order to fabricate these probes. Ti was selected as a material for simulation of the process of production due to its similar physical properties to beryllium (crystal lattice, melting point, mechanical properties and some technological characteristics). Also some investigation of titanium was necessary in the view of further studying of Be-Ti alloys. The main technological equipment includes:

- a ball milling device, NETZSCH MINIZETA 03b made by company NETZSCH-Feinmahltechnik GmbH for powder production or mechanical alloying has been installed capable of producing microcrystalline powder of Be and Be-alloys.

- an arc furnace for ingot production of Be-alloys under controlled atmospheres;

- a 20-ton hydraulic press, PW 20 made by company Paul-Otto Weber GmbH, to produce tablets e.g. from Be and Be-Ti powders at temperatures of several hundred degrees.

2.2 Mechanical alloying

Mechanical alloying (milling) is the most attractive process to produce fine metallic powders with the suitable properties (shape of particles, a narrow range of particle distribution by their sizes, etc.). Furthermore this process could be very promising for the production of intermetallic powders ($Be_{12}Ti$, in our case) already during milling of initial Be and Ti powders in appropriate stoichiometric proportions. Obtaining a powder mixture having 1-2 μm particle size is the preferred technology. The following materials have been chosen as grinding bodies for milling:

- Be pebbles with 2 mm diameter produced by NGK;
- Be powder having 200-300 μm particle size produced by BrushWellman.

And in the case of alloying with Ti:

- Ti powder which has less than 44 μm size of particles (Alfa Aesar).

Above mentioned materials were milled in the grinding vessel of the milling-machine (NETZSCH MINIZETA 03b). Be pebbles played a role of grinding bodies, so that, practically, only the particle size of powder mixture has been decreased down to 1-2 μm in size. In addition, already milled powder could be used repeatedly in this process.

Tetradecane $C_{14}H_{30}$ was selected as a liquid media for the milling process. The choice in favour of tetradecane has been determined by its relatively high vapour pressure in the temperature range 100-250 ^{0}C, melting point at 6 ^{0}C (so, this liquid can easily be removed out of fine powder mixture during heating or to be frozen in the case of emergency) and absence of oxygen to be sure that any oxygen-containing compounds could be formed during this process. Also, the presence of liquid keeps Be small particles in a solution what prevents from any kind of possible contamination.

2.3. Uniaxial pressing

After fabrication, the wet microcrystalline Be powders have been filled into the chamber of the pressing device to evaporate tetradecane in high vacuum at about 200 °C. The matrix and pistol of the hot press have been fixed insight a chamber made of high-quality steel with flanges for the vacuum pump and for thermocouples. The design of matrix consists of two cylindrical parts screwed together. Ohmic heating systems can be adjusted independently, allowing a controlled tablet temperature of about 600 °C. Depending on processing conditions, Be and Be-Ti tablets with 15.5 mm diameter, heights of 1.0 – 3.0 mm and theoretical densities up to 93 % have been produced. Fig. 1 shows one of tablets pressed out from a powder mixture of Be and Ti (Be – 30.8 wt.%Ti).

Fig. 1: Be-30.8 wt.% Ti pressed tablet.

2.4 Arc-melting process

Arc-melting provides melting of a tablet pressed out of powder mixture of Be and Ti in stoichiometric proportions (in our case, Be-30.8 wt.% Ti which corresponds to $Be_{12}Ti$ chemical composition) in the chamber filled with inert-gas atmosphere of an arc-melting facility. This process is characterised by relatively high speed of material alloying. The operation of arc-melting unit is based on a melting with the electrode of materials placed on a copper water-cooled plate.

3. Characterisation of fabricated Be and Be-Ti probes incl. $Be_{12}Ti$

It is well known for a variety of alloys that at a given high temperature grain coarsening enhances with decreasing of grain size. While in Be pebbles produced with the rotating electrode process the average grain size is typically in the range of its radius and therefore hardly can grow further, the question arises whether the grains of the Be tablets with their typical diameter of a few μm undergo grain coarsening at typical HCPB blanket temperatures of 500 – 760 °C. In order to examine the thermal stability of fabricated microcrystalline Be tablets, five annealing tests in vacuum oven have been performed. Tablets were annealed at 500, 600, 700, 800 and 900 C for 2 hours at $4*10^{-5}$ mbar.
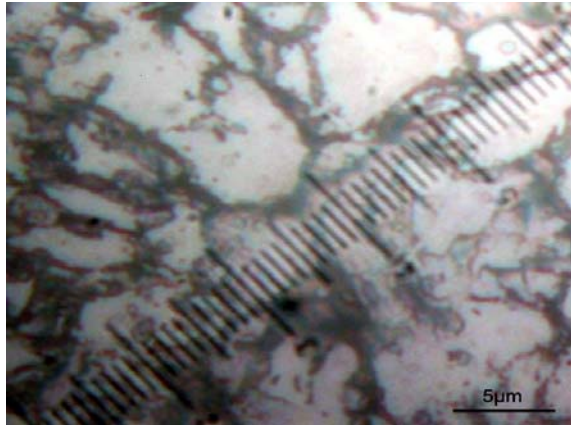
Fig. 2: Microstructure of Be tablet annealed for 2 hours at 900 ^{0}C.

Fig. 2 shows micrograph of the Be tablet after annealing at 900 °C / 2h.

While the larger grains above about 5 μm remain almost stable within the statistical uncertainties, the population of the small grains around 1 μm obviously decreases after 900 °C annealing. This process starts on the edges of "old" particles where they have a contact surface between each other.

Fig. 3a and 3b show histograms reflecting the changes in grain size distributions of not-annealed and annealed tablets at 900 ^{0}C. The population of fine grains (1-2 μm) grows in annealed samples what means the initiation of the process of recrystallisation.
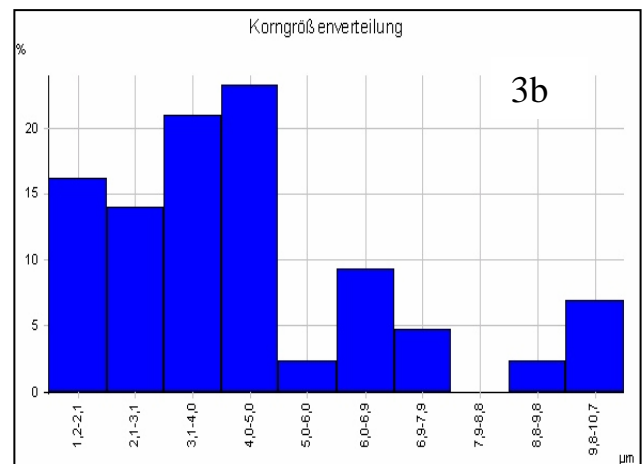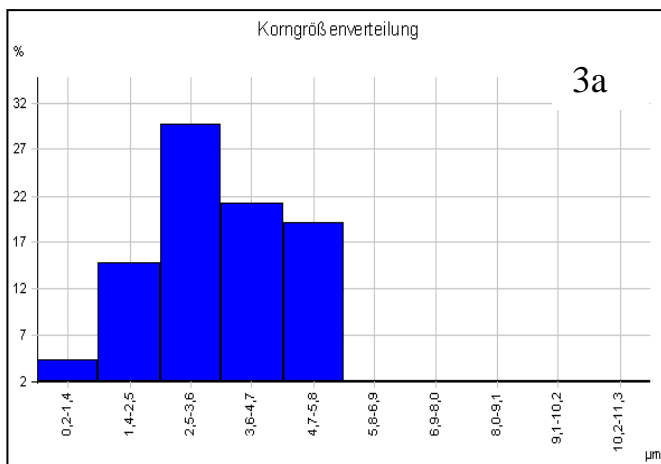
Fig. 3a and 3b: Grain size distribution in not-annealed Be sample (a), and annealed at 900 ^{0}C for 2 hours (b)

Impurity analyses of the beryllium tablets have been made mostly by EDX investigations during SEM observations. All analysed impurities were within the statistical uncertainties in the range of the raw Be products, as shown in Table 1.

Table 1: Results of EDX-analysis

Element	O_2	Fe	Al	Si	Mg	Be
wt. %	0.62	0.042	0.062	0.025	0.03	$\geq$ 99,0

X-Ray diffraction technique allows to make qualitative identification of elements and compounds found in a sample. X-Ray diffraction analysis was performed by means of D500 X-Ray Diffractometer. Tablets pressed out of Be-Ti powder mixtures have been investigated as well: Figure 4a shows X-Ray data of one of the Be-Ti probes in as-pressed condition and Figure 4b reflects structural changes in this sample caused by arc-melting process. In this case, tablet was pressed out of powder mixture of Be and Ti in stoichiometric proportions (Be-30.8 wt.% Ti what corresponds to $Be_{12}Ti$ chemical composition).
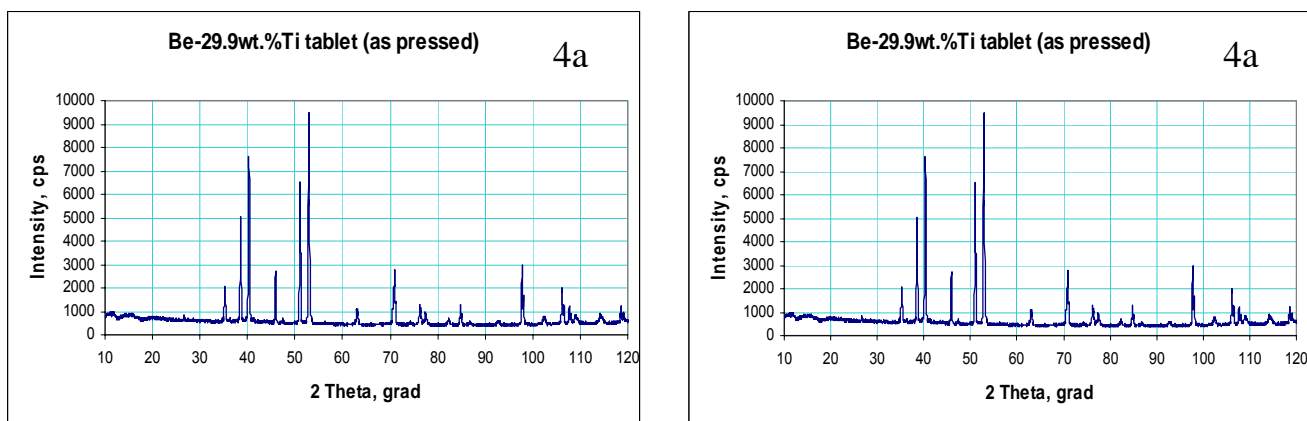
Fig. 4a and 4b: X-Ray analysis of Be-30.8 wt.% Ti tablet after pressing (a) and the same tablet after arc-melting process (b)

Conclusions and future prospective

Microcristalline Be and Be-Ti samples have been produced using two technological methods:

- by using powder metallurgical process
- by arc-melting (obtaining of $Be_{12}Ti$)

Fabricated samples have been characterised by means of available analyzing techniques like SEM including EDX-analysis, optical microscopy, X-Ray analysis, and porosity measurements.

Alternative and promising methods of material fabrication (microwave sintering using 2 kW gyrotron and mechanical activation during wet-ball milling process) will be investigated in the year 2005. Further fabrication and characterization of Be and Be-Ti samples is planned, and the technological scalability of the different fabrication routes will be assessed. Finally, long term stability of the microcrystalline Be and BeTi products at Blanket relevant temperatures will be validated, and the tritium release performance will be analysed.

Staff:

G. Bürkle
M. Klimiankou
P. Kurinskiy
A. Möslang

Literature:

[1] P. Kurinskiy, A. Cardella, M. Klimiankou, A. Möslang, A. A. Goraieb, Production and Thermal Stability of Beryllium with Fine Grain Structure to Improve Tritium Release During Neutron Irradiation, presented at 23rd Symp.on Fusion Technology (SOFT-23), Venice, September 20-24, 2004

TTBB-005b
Helium Cooled: Modelling of Swelling and Tritium Release in Beryllium under Irradiation

TW2-TTBB-005b D3
Tritium Release Enhancement from Beryllium

1. Objectives

The tritium accumulation in currently used beryllium pebble materials of ceramic breeder blankets could reach unacceptably high values at the end of blanket life and, therefore, is a critical issue. There are several attempts to develop beryllium-based materials with properties which result in an enhanced tritium release during blanket operation. In the frame of the present subtask, methods were also considered to enhance the tritium release either by i) using a purge gas with a higher protium partial pressure than presently anticipated (helium at 0.1MPa with 0.1% protium)], or b) Intermittently swamping the blanket with protium.

The idea behind these concepts was to load the beryllium pebbles with sufficient protium in order to saturate any hydrogen traps with protium instead of tritium and, therefore, to increase the probability that tritium diffuses to the outer surface of the pebbles.

The problem of the proposed method is that the hydrogen solubility in beryllium at blanket relevant conditions is very low, in the order of some appm, compare [1]. Accurate measurements of the dissolved hydrogen are extremely difficult because hydrogen is readily trapped at BeO surface layers.

This subtask was therefore modified in 2002 and it was decided to concentrate on issues connected with the pick-up and release kinetics of hydrogen isotopes of/from beryllium pebbles, with the special attention on the influence of pebble surface conditions.

In 2003, experiments with nonirradiated 1mm diameter NGK pebbles started in FZK in a test facility used for similar experiments in the past [4]. Protium at 0.2MPa with an addition of 50ppm tritium was used and the tritium activity in the gas was measured by an

an ionisation chamber. It proved that in order to increase the measurement both the protium pressure should be increased and the ionisation chamber should be exchanged with a proportional counter.

2. Work performed in 2004

2.1 Experiments with 1mm NGK pebbles

After the installation of a proportional counter and the manufacture of a new sample holder for a maximum hydrogen pressure of 2MPa, detailed experiments, see Table 1, were performed where i) pebbles were first loaded with hydrogen (parameter: hydrogen pressure), and ii) in another test set-up, the hydrogen release kinetics were studied (parameter: temperature). In a part of the experiments, surface layers were removed by grinding in a diamond-propanol suspension. However, there was no quantitative control of the effectiveness of this method. Different surface conditions were investigated:

a) before loading: surface as received (no treatment, n.t.); before release: n.t.,
b) before loading: n.t.; before release: surface layer mechanically removed by grinding in a diamond suspension (treatment, t.),
c) before loading: t.; before release: n.t.,
d) before loading: t.; before release: t..

Figure 1 shows characteristic results for release experiments: the first release peak at about 100°C is connected with the release of desorbed HTO from the surface; a peak between 400 and 500°C is attributed to the dissociation of BeOT; the tritium dissolution from the bulk of beryllium should become visible by the development of a peak above 600°C. The latter peak

Table 1:   Experiments with nonirradiated 1mm NGK beryllium pebbles.

Nr	pebble diameter d(mm)	treatment before loading	loading parameter T(°C)/p(MPa)/t(hr)	treatment before release	release	
					ramp (K/min)	T$_{max}$ (°C)
B1	0.8-1.2	t. ,1)	850/2/6	n.t.	7.5 until 500°C, then15	1100
B2	0.8-1.2	t., 1)	850/2/6	n.t.		750
B3	zero level measurement					1100
B4	0.8-1.2.	n.t.	850/2/6	n.t.		750
B5	0.8-1.2	n.t	850/2/6	t. (3)		750
B6	> 1.12	n.t	850/2/6	n.t.	7.5	750
B7	0.56-1.12	n.t	850/2/6	n.t.		
B8	> 0.9	(1)	850/2/6	n.t.		
B9	0.56-0.9	(2)	850/2/6	n.t.		
B10	1,00-1.12	(1)	850/2/6	t. (3)		
B11	> 1.12	n.t	850/2/6	n.t.		
B12	> 1.12	n.t	850/**6**/6	n.t.		
B13	> 1.12	n.t	850/**13**/6	n.t.		
B14	> 1.12	t.	850/**13**/6	n.t.		
B15	> 1.12	t.(3)	850/**10,5**/6	t.		
B16	> 1.12	t. (1)	850/**14,8**/6	t.		
B17	zero level measurement					
B18	zero level measurement					
B19	> 1.12	t.(4)	850/**14,8**/6	n.t.		

(1): grinding in diamond suspension: 60min; (2): 120min; (3): 30min; (4): 120min.

could never be clearly detected which means that the tritium solubility cannot be determined accurately. For case c) the hydrogen pick-up was significantly larger than for case a) which was attributed to the fact that for a) an oxide layer existed, whereas for b) the absence of the oxide layer at the surface enhanced hydrogen pick-up.
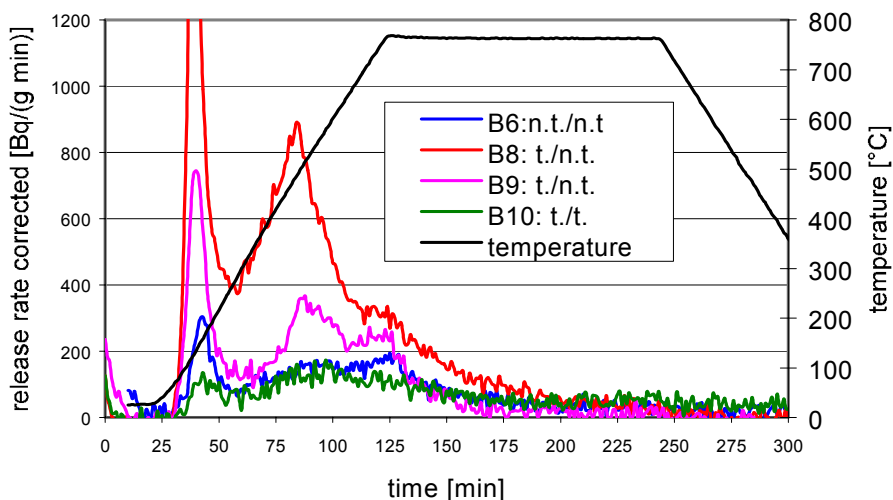
Fig. 1:   Tritium release experiments with nonirradiated 1mm NGK beryllium pebbles.

If the surface layer is removed between hydrogen loading and release experiments (case and d)), the peak at about 100°C does no longer occur but the dissolution of bulk tritium can still not be clearly separated from tritium desorption originating from residual surface layers. In conclusion this means that even with the increased hydrogen (and tritium) pressure and the more sensitive proportional counter no accurate solubility data could be obtained.

2.2 Tritium release experiments with irradiated 2mm Brush Wellman beryllium pebbles.

The tritium release kinetics from these pebbles irradiated in the HFR Petten at temperatures between 450 and 550°C was already investigated in the past [2], applying temperature ramps of 5K/min up to 850°C and using the pebbles "as received". In the present experiments; the surface conditions were varied, and different heating-up rates were applied in order to generate data useful for the validation of the ANFIBE code [3]. For these experiments with higher tritium activities, the ionisation chamber was used.
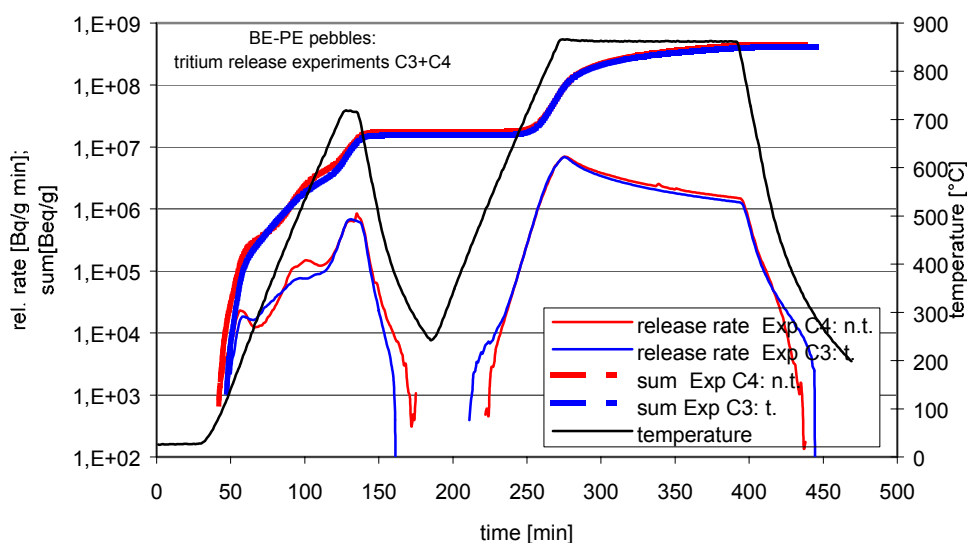
Fig. 2:   Tritium release experiments with irradiated 2mm beryllium pebbles: effect of surface layer.

Figure 2 shows for two experiments where first a release experiment was performed with a maximum temperature of 600°C, followed by a release experiment with T_{max}=850°C. The heat-up ramps were 7K/min. Again a pronounced release peak is observed during the first release experiment at ≈ 500°C for "as received" pebbles (Exp C4) in contrast to the experiment where the surface layer was removed by grinding (Exp C3). During the subsequent release experiment, the tritium release is dominated by bulk effects and the curves of Exps C3 and C4 do not differ.

Figure 3 shows the effect of heat-up ramps for two samples where the surface layer was removed; maximum temperatures of the two release experiments were 850 and 1150°C. Whereas for 7K/min a peak at ≈ 500°C is again not detected, it is clearly seen for the ramp with 3.5K/min. Further experiments will be performed to check this tendency.
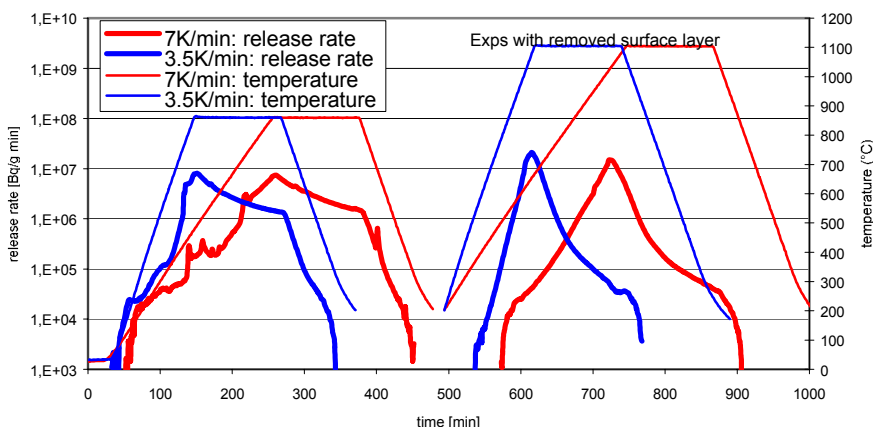
Fig. 3: Tritium release experiments with irradiated 2mm beryllium pebbles: effect of surface layer.

3. Conclusions

Experiments with nonirradiated beryllium pebbles were performed in order to investigate hydrogen solubility and the capture of hydrogen at surface layers. It proved that accurate measurements of the tritium solubility of beryllium would require much larger tritium pressures than can be realised within the present experimental facility, the important role of surface layers for tritium trapping in has been demonstrated.

Experiments with irradiated beryllium pebbles were performed varying again the surface conditions and using different heat-up ramps. These experiments should be well suited for the validation of the ANFIBE code.

Staff:

A. Erbe
E. Damm
E. Rabaglino
D. Reichmann
J. Reimann
R. Rolli

Literature:

[1] V. I. Shapovalov, Y- M-Dukel'ski, The beryllium-hydrogen phase diagram, Russian Metallurgy, 5 (1988), 201-203.

[2] F. Scaffidi-Argentina, H.Werle, 2nd IEA Int. Workshop on Beryllium Techn. for Fusion, Jackson Lake Lodge, Wyoming, USA, Sept. 1995.

[3] E. Rabaglino, Helium and Tritium in Neutron-irradiated Beryllium, FZKA 6939, Dec. 2004.

TTBB-006b
Helium Cooled: Thermo-mechanical Modelling of Pebble Bed Assembly

TW2-TTBB-006b D1
Thermomechanical Tests of Ceramic Breeder Pebble Beds

1. Objectives

The development and qualification of computer codes for the modelling of the thermo-mechanical behaviour of HCPB pebble bed assemblies requires the generation of characteristic pebble bed data and the validation of the codes in simple experiments.

Concerning the generation of pebble bed data, experiments were performed with orthosilicate pebble beds consisting of pebbles using a new production route. In respect to code validation, mechanical cycling tests at different temperatures were carried out, for details, see [1].

2. Pebble bed data for OSi ex hydroxide

In the past, the orthosilicate pebbles were produced from a mixture of Li_4SiO_4 and SiO_2 powders (designated as OSi ex silicate). However, enriched Li_4SiO_4 is not commercially available, therefore, in respect to the future nedd of enriched OSi, a new production route was pursued using LiOH powder (OSi ex hydroxide), for details, see [2].

The thermal-mechanical characterisation consisted of uniaxial compression tests (UCTs) performed in the test facility decribed previously [3] in order to determine stress-strain relationships during pressure (uniaxial stress) increase and decrease and thermal creep correlations for elevated temperatures.
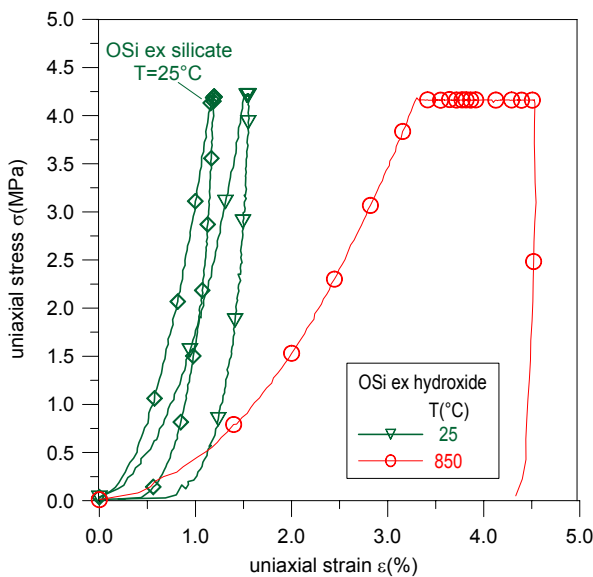
Fig. 1.   Characteristic UCT results.

Figure 1 shows that at ambient temperature the presently developed OSi ex hydroxide (batch 03/1-3) behaves softer (larger strains for a given stress value) than the OSi ex silicate. In agreement with previous measurements, the pebble beds become softer with increasing temperature; at T=850°C, this effect is significantly influenced by thermal creep occurring during the stress increase period (stress ramp ≈ 0.6MPa/min). After reaching σ_{max} ≈ 4MPa, the stress was kept constant for about 10mins in all experiments; at 850°C strain increases remarkably due to thermal creep whereas at ambient temperature strain increases marginally due to relocations of pebbles. This type of experiments is used to determine the modulus of deformation $E=\sigma(MPa)/\varepsilon(1)$; results are summarised in Table1.

Table 1: Correlations for modulus of deformation, E, and thermal creep strain, ε_{cr}.

Granular material	$E(MPa)=Cs(MPa)^m$		$\varepsilon_{cr}(1) = A \exp(-B/T(K)) \sigma(MPa)^p t(s)^n$			
	C	m	A	B	p	n
OSi ex silicate [12-14]	180*	0.47	12.1	10220	0.65	0.20
OSi ex hydroxide (OSi 03/1-3)	125*	0.50	20.1	11005	0.65	0.23

*T=25°C

Figure 2 shows a comparison for both granular materials: thermal creep strain is slightly larger for the new OSi ex hydroxide and the temperature dependence is somewhat more expressed (for $t=10^5$s: $\varepsilon_{cr}/\varepsilon_{cr\ OSi\ ex\ silicate}$ = 1.05, 1.16 for T= 700°C and 850°C, respectively).

3. Mechanical cycling of pebble beds

In ITER, the test blanket mock-ups (TBMs) will be subjected to many thermal cycles. Stresses are expected to relax quite fast because of thermal creep [7], and during subsequent cycles, the stress build-up will be significantly reduced.

In mechanical cycling experiments, described in the following, in each cycle the stresses are varied between a value

Fig. 2: Comparison of creep stains for OSi ex silica and OSi ex hydroxide.

close to zero and the maximum value. Therefore, these conditions are not blanket relevant. The objectives for performing these tests were twofold:

a) to improve the general understanding of pebble beds,

b) to provide data to validate codes which describe thermal creep behaviour.

Table 2 shows experimental details: the experiments were performed using the same material both at ambient temperature and at 750°C (OSi1 and 2, MTi 1 and 2). The pressure ramps during the pressure increase and decrease period were about 0.86 MPa/min and the dwell time at p_{max} was about 0.3 mins. With OSi ex hydroxide pebbles, an experiment was performed at 850°C a smaller pressure ramp and a significantly larger dwell time (10 mins) compared to the other experiments.

Table 2: Cycling experiments

Pebble bed dimensions: height H ≈ 10.7mm; diameter D =61mm

Exp.	material	PF g(%)	T (°C)	s_{max} (MPa)	number of cycles	cycles (min) Dt_1/ Dt_2/ Dt_3 [4]
OSi 1	OSi ex silica[1]	63	25	4.3	117	5/0.3/5
OSi 2	OSi ex silica[1]	63	750	6.5	337	7.5/0.3/7.5
MTi 1	MTi [2]	62	25	6.5	77	7.5/0.3/7.5
MTi 2	MTi [2]	62	750	6.5	166	7.5/0.3/7.5
OSi 3	OSi ex hydroxide[3]	66	840	4,1	112	7.5/10/10

[1] Orthosilicate, batches from 2001, thermally unconditioned,
[2] Metatitanate, batch D
[3] Orthosilicate ex hydroxide, batch from 2003

[4] Dt_1: s increase time
Dt_2: dwell time at s_{max}
Dt_3: s decrease time

Figure 3 shows characteristic results for T=25 and 750°C in a $\sigma-\varepsilon$ plot: For 25°C, the irreversible compaction is still continuing at the end of the experiments. It is not clear if this progressing compaction is only caused by pebble relocation, or also by pebble cracking. For 750°C, the compaction is considerably increased due to thermal creep. The process of pro-

gressing compaction is illustrated in Fig. 4 where the strain values at σ_{max} are plotted as a function of time. The differences between OSi and MTi pebble beds are not significant.
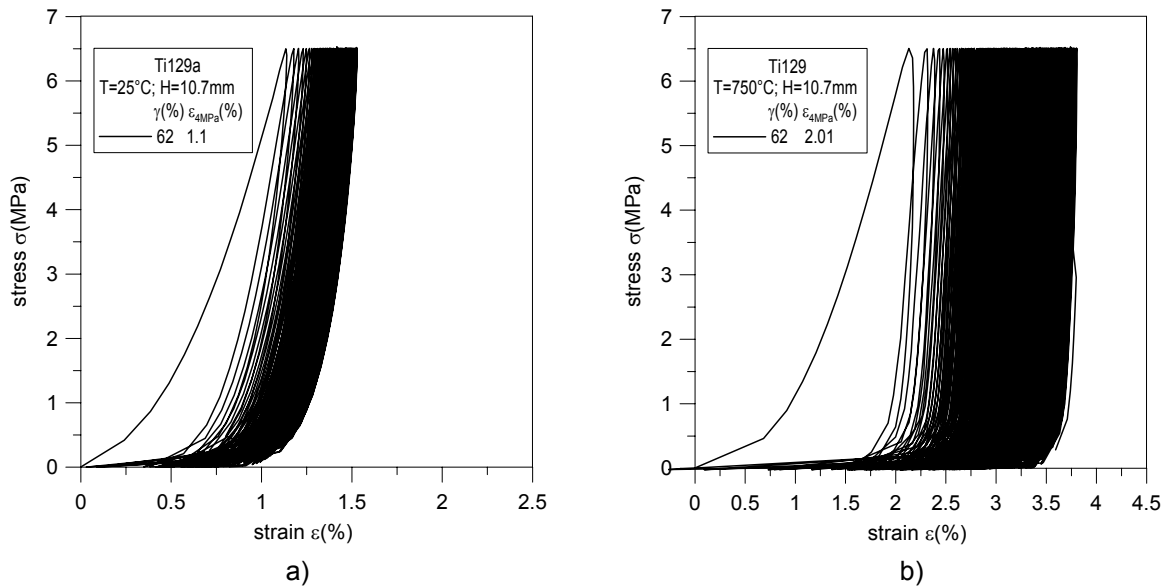
Fig. 3: Mechanical cycling of MTi pebble beds at a) ambient, and b) elevated temperature.

Fig. 4: Strain at σ_{max} as a function of time.

Figure 5 shows for MTi pebble beds the strain for the first two cycles and the last cycle: for ambient temperature, the second cycle and the last cycle are very similar. For 750°C, the strain occurring during the first pressure increase phase is much larger due to thermal creep, the strain during the second stress increase is also larger than the strain occurring during the last cycle where the bed behaves very stiffly. These data are believed to be very suitable for the validation of pebble bed codes because in these experiments creep occurs when stress is changing with time.

4. Conclusions

The new pebble batches OSi 03/1-3 and 03/1-4 produced from lithium hydroxide and silica (OSi ex hydroxide) were subjected to uniaxial compression tests. Compared to the old material (OSi ex silicate), the OSi ex hydroxide pebble beds are characterised by a softer behaviour during the first pressure increase period and, to a smaller extent, in respect to thermal. A softer behaviour results in smaller stresses during the heat-up phase and faster stress relaxation processes at high temperatures; effects which are presumed to be favourable for blanket operation. In the future, more experiments are required in order to enlarge the pebble bed data base for this new material.

Fig. 5: First and last cycles for MTi pebble bed experiments.

Furthermore , cycling tests were performed where metatitanate and orthosilicate pebble beds were mechanically cycled between zero pressure and a maximum pressure either 4.3 or 6.5MPa. Temperatures were between ambient and 840°C. For ambient temperature, progressing compaction was still observable after more than hundred cycles. At elevated temperatures, the compaction was significantly increased because of thermal creep. These experiments are expected to be suited to validate pebble bed codes and should be used in the future for corresponding calculations.

Staff:

J. Reimann
Fa Goraieb

Literature:

[1] J. Reimann, H. Harsch, Characterisation of Orthosilicate ex Hydroxide Pebble Beds and Mechanical Cycling of Different Types of Ceramic Breeder Materials, CBBI-12, Sep. 16-17, 2004, Karlsruhe, Japan, in Proceeding of the 12th International Workshop on Ceramic Breeder Blanket Interactions, Ed. R. Knitter, FZKA 7078, 2004.

[2] R. Knitter, G. Piazza, J. Reimann, P. Risthaus, L.V. Boccaccini, "Fabrication and characterisation of lithium orthosilicate pebbles using LiOH as a new raw material", CBBI-11, Dec. 15-17, 2003, Tokyo, Japan, in Proceeding of the 11th International Workshop on Ceramic Breeder Blanket Interactions, Ed. M. Enoeda, Japan Atomic Energy Research Institute, 2004, 108-119.

[3] J. Reimann, E. Arbogast, M. Behnke, S. Müller, K. Thomauske. Thermomechanical behaviour of ceramic breeder and beryllium pebble beds. Fusion Eng. and Design, 49-50, (2000), 643-649.

[4] L. Bühler, J. Reimann, Thermal creep of granular breeder materials in fusion blankets, Journal of Nuclear Materials 307-311 (2002), 807-810.

TW2-TTBB-006b D2
Thermo-mechanical Modelling of Pebble Bed Assembly:
Development of Pebble Bed Models

Modelling of thermal and mechanical behaviour of pebble beds for fusion blankets is an important issue to understand the interaction of solid breeder and beryllium pebble beds with the surrounding structural material. Especially the differing coefficients of thermal expansion of these materials cause high stresses and strains during irradiation induced volumetric heating. To describe this process, the coupled thermomechanical behaviour of both pebble bed materials has to be modelled. Additionally, creep has to be considered contributing to bed deformations and stress relaxation.

Motivated by experiments, we use a continuum mechanical approach called Drucker-Prager/Cap theory to model the macroscopic pebble bed behaviour. The model accounts for pressure dependent shear failure, inelastic hardening, and volumetric creep. The elastic part is described by a nonlinear elasticity law. The model has been implemented by user-defined routines in the commercial finite-element code ABAQUS. This work has been finished in the first half of 2004, thus closing the delayed tasks TW2-TTBB-005a-D8 and TW2-TTBB-007a-D5 [1, 2].

Simulations of the modified creep law have been done to study the behaviour under 2-step creep. A bug found in the ABAQUS creep formulation has been fixed. The corrected ABAQUS creep model was verified.

For validation purposes, the full thermo-mechanical pebble bed model was applied to some preliminary simulations of precompaction in the pebble bed assembly (PBA, NRG Petten), see figure 1.
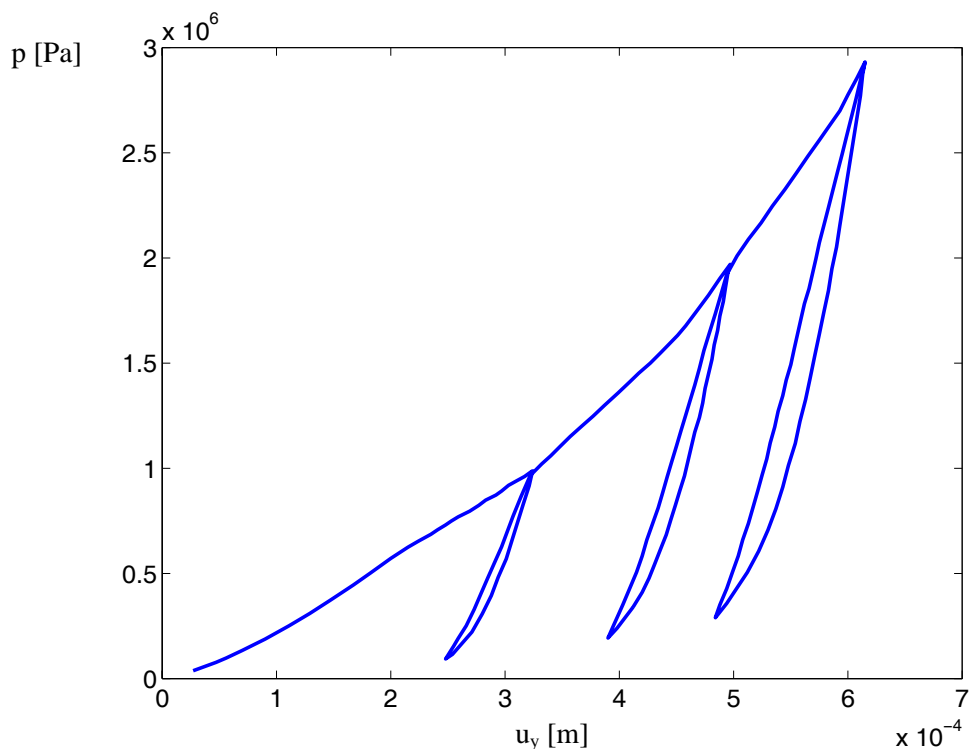
Fig. 1: Displacement of pressure lid of PBA during the first part of the precompaction proceedure.

In the second half of 2004, the professional working on this delayed task succesfully so far, left FZK and progress came to a halt, since the position could not be filled immediately. In the meantime a candidate could be found who has some knowledge in the modelling field. It is anticipated that he will join FZK in the first half of 2005.

Within this task it remains to compare our approach to various HCPB-results with a NRG-approach developed by Fokkens [3], which is estimated to take 4-6 months after filling the position.

Staff:

D. Hofer
M. Kamlah

Literature:

[1] D. Hofer, M. Kamlah, Report on the development of pebble bed models for fusion blankets, Final report on the EFDA tasks TW2-TTBB-005aD8 and TW2-TTBB-007aD5. FZK, Fusion, Interner Bericht, June 2004.

[2] D. Hofer, M. Kamlah, Modelling of ceramic breeder and beryllium pebble beds at FZK, CBBI-12, Karlsruhe, September 16-17, 2004

[3] J. H. Fokkens, Thermo-Mechanical Finite Element Analyses for the HCPB In-Pile Test Element, EFDA-Deliverable TW0-TTBB-004-D1.

TTBB-007a
Helium Cooled: Development of Beryllium Pebble Beds

TW2-TTBB-007a D2
Improvement, Verification and Application of the ANFIBE Code

TW2-TTBB-005b
Helium Cooled: Modelling of Swelling and Tritium Release in Beryllium under Irradiation

TW2-TTBB-005b D1
Modelling of the Behaviour of Irradiated Beryllium (Swelling and Tritium Release)

1. Aim and general overview of the activities

In the beryllium pebbles of the Helium Cooled Pebble Bed (HCPB) blanket, large quantities of helium and a non-negligible amount of tritium are produced under fast neutron irradiation. The code ANFIBE (ANalysis of Fusion Irradiated BEryllium) is being developed in order to predict swelling due to helium bubbles and tritium inventory in the range of operating and accidental conditions of a fusion power reactor. Due to the absence of data in this range, ANFIBE has to be extrapolated. Consequently, in comparison to codes which predict gas retention in UO2, the development of a more sophisticated solid state physics model for the description of gas kinetics and a more careful and detailed validation procedure are required. The programme for the improvement of ANFIBE runs under the European Fusion Development Agreement on a period of six years (2000 – 2005) and is carried out in collaboration with the JRC - ITU (Karlsruhe, Germany), the NRG (Petten, the Netherlands), the SCK-CEN (Mol, Belgium) and the ESRF (Grenoble, France), as far as a part of the experimental studies are concerned. The theoretical evaluation of experimental data and related development of ANFIBE, as well as the definition of open key issues to be solved with further experimental studies, is under the responsibility of FZK. The contribution of FZK to the experimental activities is focused on the following points: (1) study of gas diffusion and release during out-of-pile temperature transients up to the melting point; (2) study of the microstructure of irradiated beryllium in connection with different gas release stages. The final aim of these studies is to improve the gas kinetics model in ANFIBE and to validate it also from the microscopic point of view, i.e. to verify if the different gas diffusion phases (atomic diffusion, precipitation into bubbles, bubble diffusion and growth, gas release pathways) are correctly described.

The R&D activities aimed at improving the ANFIBE code run under EFDA contract TW2-TTBB-007a-2 in 2002, 2003 and 2004 (deliverable 2 of task TW2-TTBB-007a, "Development of beryllium pebble beds") and continue in 2005 and 2006 under EFDA contract TW2-TTBB-005b-1 (deliverable 1 of task TW2-TTBB-005b, "Modelling of swelling and tritium release in beryllium under irradiation").

2. Progress in the period October 2003 – December 2004

In 2003, on the basis of previous extensive experimental and theoretical studies of out-of-pile helium and tritium release and microstructure evolution [1, 2] in weakly irradiated beryllium pebbles from the BERYLLIUM irradiation experiment (480 appm ^{4}He [3]), it was possible to define and apply a new procedure of validation of the models for helium and tritium diffusion, precipitation and release in the ANFIBE code, where for the first time the relationship between microscopic diffusion phenomena and macroscopic swelling and release was considered [4]. The application of the *in-*

tegrated macroscopic/microscopic procedure enabled in particular to re-calibrate the model for the gas precipitation rate into bubbles inside the grain, by introducing a delay factor which limits precipitation, therefore enhances release. In-pile bubble destruction due to atom recoils under neutron irradiation was also introduced as a limiting factor of gas precipitation. The resulting new version of the ANFIBE code was found to provide a much more realistic description of helium and tritium release for the pebbles from the BERYLLIUM irradiation than the version of 1995, which was not validated from the microscopic point of view. Since pebbles from the BERYLLIUM irradiation share with the reference material to be used in the HCPB blanket (1 mm pebbles, produced by Rotating Electrode Process [5]) a coarse grain microstructure and the grain size is a fundamental material property in regard to gas release, the improved version of ANFIBE can be extrapolated with confidence to the HCPB blanket. At the end of 2003 a further validation of ANFIBE was performed on the basis of partial studies of helium and tritium release and microstructure of other beryllium samples with much higher gas content and different irradiation temperature:

In particular, the pebbles from the COBRA-1A irradiation [6] [7] (652 K, 2700 appm ^{4}He) and highly irradiated fragments from the disposed moderator of Belgian Reactor 2 [8] [7] (19500 appm ^{4}He, 420 K). A first extrapolation of the code to predict the End-Of-Life conditions of beryllium pebbles in a Fusion Power Reactor was performed. On the other side, the study of out-of-pile helium and tritium release diffusion and precipitation in the highly irradiated samples from BR2 moderator, started in 2002, was continued: in particular, Transmission Electron Microscopy analyses were performed, after the development of the necessary sample preparation technique. The aim of these studies is to extend the database available for the application of the macroscopic/microscopic validation procedure as far as material type and irradiation conditions are concerned. Finally, the development of a synchrotron light microtomography, started in 2001 with the aim of studying gas percolation through interconnected networks of porosities in the pebbles from the BERYLLIUM irradiation, reached a mature stage: it was possible for the first time to analyse quantitatively the porosity networks in a 3D geometry across a whole pebble.

In the field of the modelling and experimental characterisation of the behaviour of gas-in-solid in view to the prediction of release of irradiation-induced gases from a solid matrix, the results obtained in the frame of the studies indicate that the ANFIBE code is presently the most advanced code in predicting tritium release behaviour of neutron irradiated Be pebbles.

3. Integrated macroscopic/microscopic validation of the ANFIBE code

The integrated microscopic/macroscopic validation procedure for the ANFIBE code consists, essentially, in comparing with experimental data not only the prediction of gas release and swelling but also of a number of other quantities (bubble radius and concentration, percentage of gas in solution, in bubbles), which describe the macroscopic gas diffusion phenomena.

BERYLLIUM irradiation, out-of-pile ^{4}He /^{3}H release experiment 159bei

a. ^{4}He in solution

b. ^{3}H in solution

c. ^{4}He in intragranular bubbles

d. ^{3}H in intragranular bubbles

e. ^{4}He release

f. ^{3}H release

g. Intragranular bubble radius

h. Intragranular bubble concentration
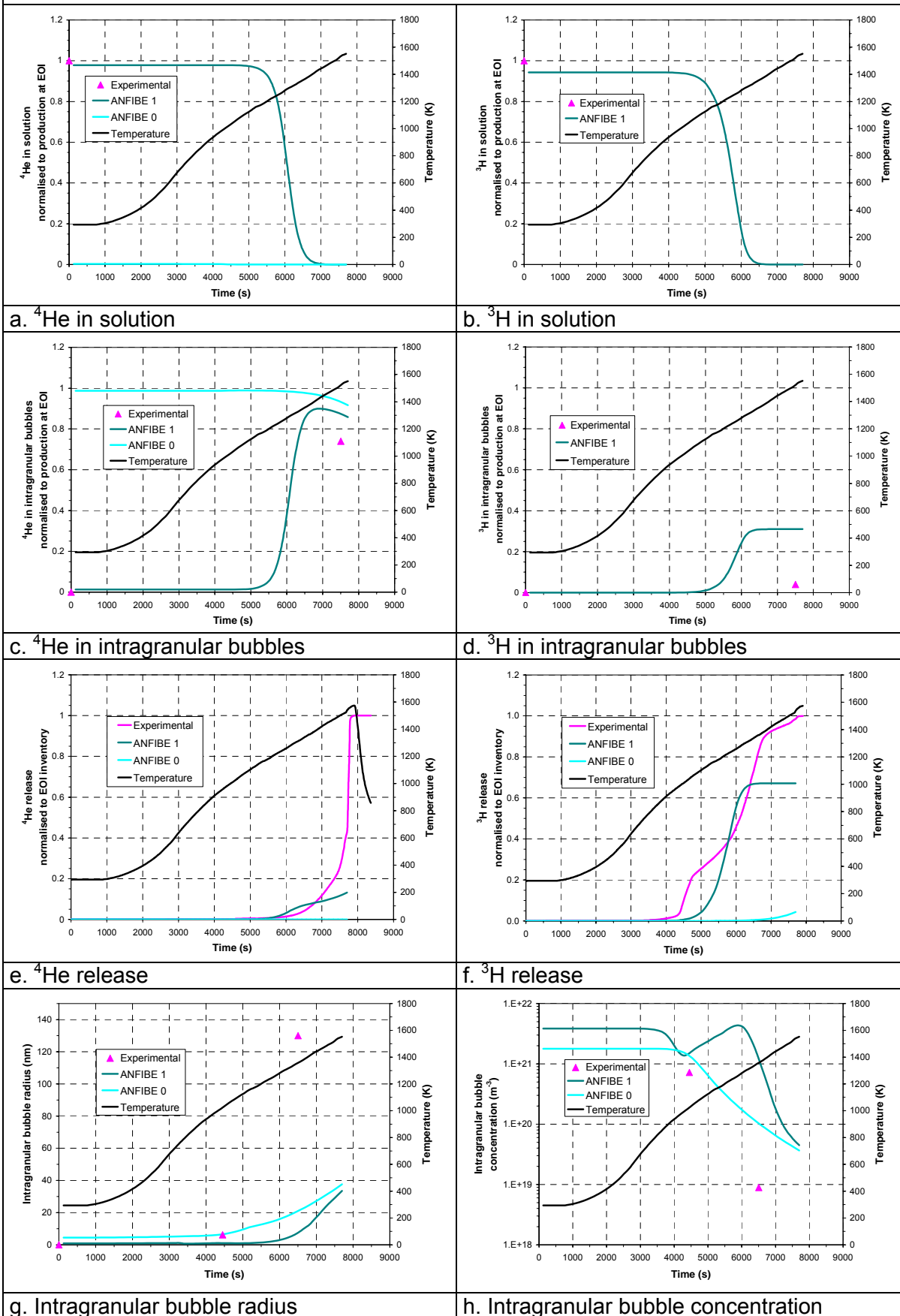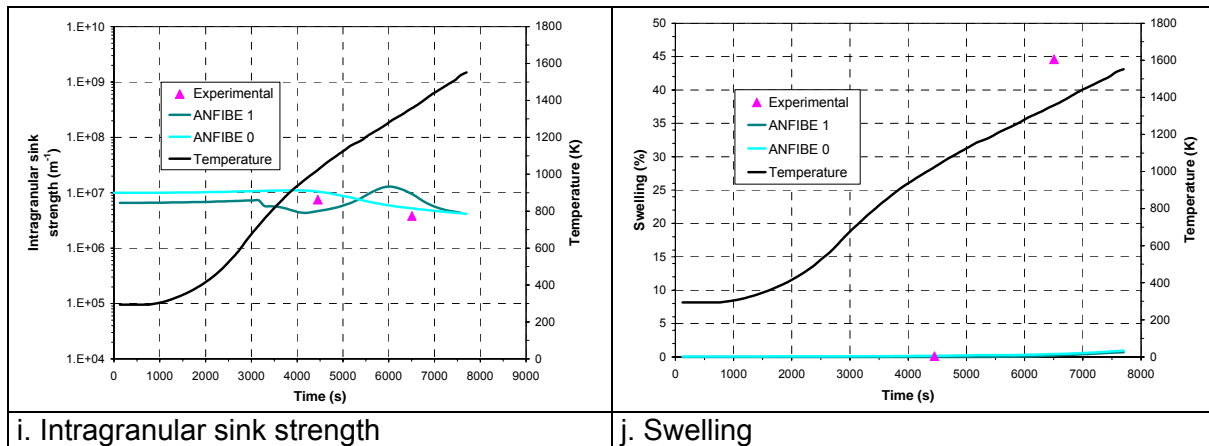
Fig. 1: The integrated macroscopic/microscopic validation for the ANFIBE code, pebbles from the BERYLLIUM irradiation, out-of-pile thermal ramp annealing at 10 K/min. The predictions of ANFIBE 0 and 1 of gas balance, gas release and microstructure are compared to the available experimental data [7].

An example of the application of the procedure for the pebbles from the BERYLLIUM irradiation, during a thermal ramp annealing at 10 K/min up to the melting point, is shown in Fig. 1 [7]: the early version of the code (ANFIBE 0 [9] [10]) is also compared to the new one (ANFIBE 1 [7]). Whilst ANFIBE 0 gives an incorrect description of gas precipitation, thus an underestimation of gas release, ANFIBE 1 predicts correctly that at EOL the whole gas is still in solution, and that during the thermal ramp most of the gas precipitates into bubbles: the inventory trapped in bubbles is then released in a peak at about 1500 K, corresponding to the formation of open porosity networks. If the bubble parameters are considered, ANFIBE 1 underestimates bubble radius and bubble growth and coalescence during the thermal ramp, therefore swelling: the improvement of the related analytical models in the code is necessary.

4. Assessment of tritium retention in beryllium at the End-Of-Life of the HCPB blanket in a reference fusion power reactor

An important safety issue of the HCPB blanket in a future fusion power reactor is the possible tritium retention in beryllium: in the reference reactor Model B of the European Power Plant Conceptual Study, 24 kg of tritium are produced under irradiation in the whole of the blanket, in 390 tons of beryllium pebbles, up to the End-Of-Life [11]. On the basis of a calculation of the helium and tritium production and of the temperature profile in the Central Outboard Module of the blanket, the tritium release at EOL was assessed by the ANFIBE code [7]: Fig. 2 shows the radial profile of the fraction of tritium released/produced in the pebble bed, corresponding to the maximum temperature between the helium cooled plates. According to the early version of the code, 80% of tritium produced is retained. After the re-calibration of the gas precipitation model following the studies in the latest years, the new version of ANFIBE predicts that practically the whole tritium is at grain boundaries and can be easily released if an interconnected porosity network is present. Therefore the issue of tritium retention in beryllium in the HCPB blanket seems to be much less critical than in the past.
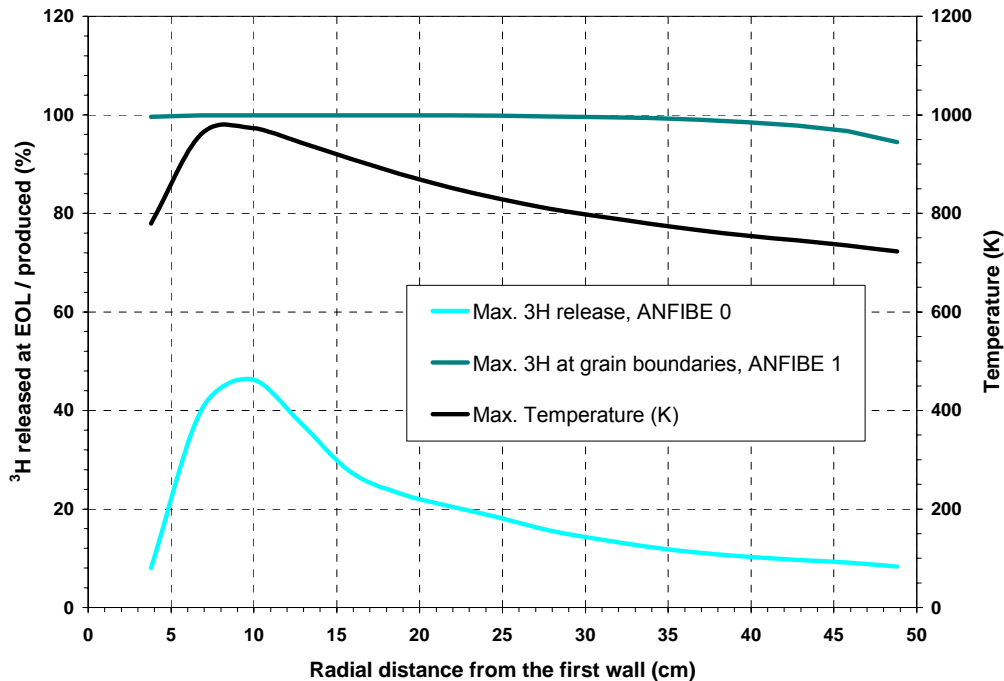
Fig. 2:   Radial profiles of tritium release according to ANFIBE 0 and of tritium at grain boundaries according to ANFIBE 1 in beryllium pebbles at the End-Of-Life of the Helium Cooled Pebble Bed blanket central outboard module, in the reference fusion power plant of the Power Plant Conceptual Study. The maximum of the parabolic temperature profile between the helium cooled plates is considered. In the assumption that the whole tritium at grain boundaries is released, because of the presence of external grain boundaries or of interconnected porosity networks, ANFIBE 1 predicts a negligible residual tritium inventory in the module, to be compared with the 171 g predicted by ANFIBE 0.

5. Study of the microstructure of highly irradiated beryllium from BR2 disposed moderator: Transmission Electron Microscopy analyses

Transmission Electron Microscopy studies of the microstructure of pebbles from the BERYLLIUM irradiation during a thermal ramp annealing were performed in order to quantify the gas precipitation rate into bubbles inside the grain. A similar study was performed on highly irradiated samples from BR2 disposed moderator, after the development of a dedicated preparation procedure. As a first step, the fragment, embedded in a resin, is polished with manipulators on both sides down to a thickness of about 0.3 mm. As a second step, a disk of 3 mm diameter is cut from the layer and the centre of the disk is polished by an electrolytic process down to about 300 nm. Such procedure was initially developed for the material in a non-irradiated state; after irradiation the brittleness of the material did not allow cutting the disk for the electrolytic polishing, therefore a sample crashing in liquid N_2 was applied as an alternative method. Fig. 3 shows the microstructure of the material before and after irradiation, as it appears under an optical microscope and under a TEM. Only at very high resolution a change in the microstructure after irradiation is detected and despite very high gas content (about 2% helium) only dislocations appear. The same absence of bubbles after irradiation was observed in the pebbles from the BERYLLIUM irradiation [7] [2] and it confirms that in-pile precipitation is very limited. Fig. 4 shows the microstructure of the samples after thermal ramp annealing at about 750 K: the formation of microbubbles (about 6 nm diameter) is observed.
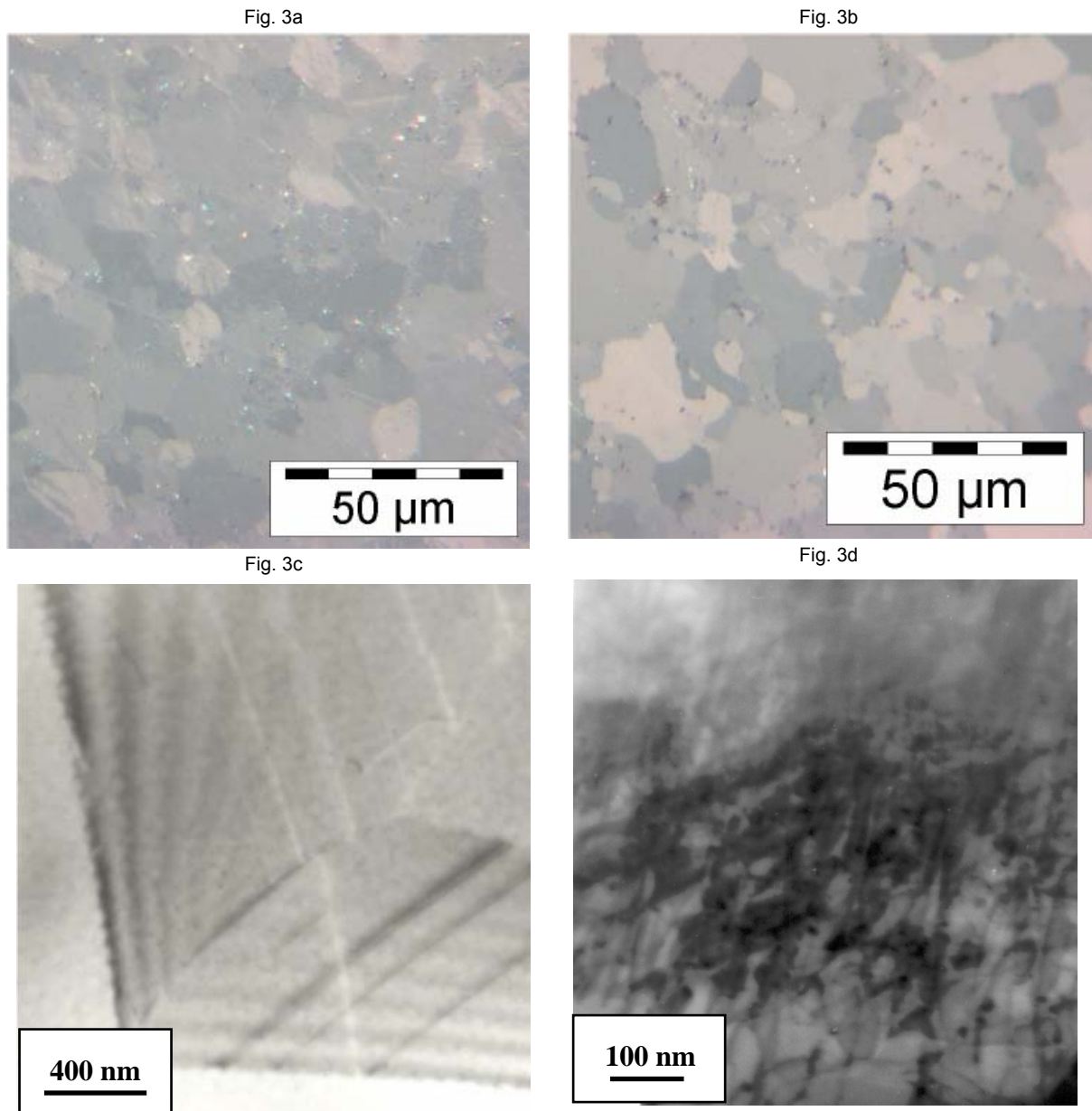
Fig. 3a

Fig. 3b

Fig. 3c

Fig. 3d

Fig. 3: Microstructure of highly irradiated beryllium from the disposed moderator of Belgian Reactor 2. (a) Optical microscopy, before irradiation; (b) Optical microscopy, after irradiation; (c) Transmission Electron Microscopy, before irradiation; (d) Transmission Electron Microscopy, after irradiation. Despite the presence of about 2% helium, no bubbles are observed, but a high dislocation density.

6. Quantitative characterisation by microtomography of the gas percolation stage in pebbles from the BERYLLIUM irradiation.

The helium and tritium trapped in bubbles are released only when, at high irradiation dose and/or high temperature, large lenticular bubbles at grain boundaries form open porosity networks [1] [7]. A correct understanding and modelling of the gas percolation stage is extremely important since this phenomenon is responsible of the release of most part of the gas inventory. In order to perform a 3D analysis of interconnected porosity networks in the pebbles from the BERYLLIUM irradiation, the
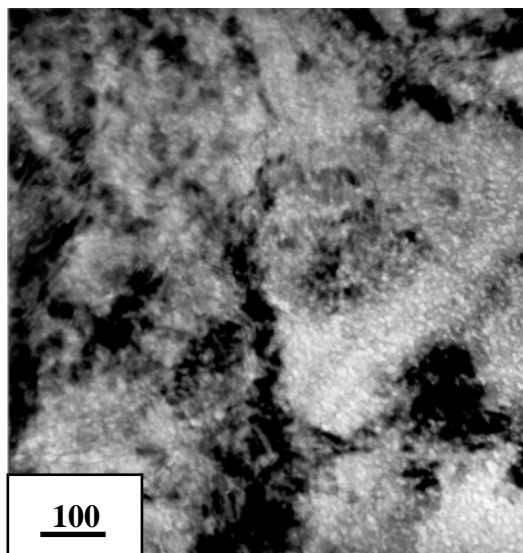
Fig. 4: Microstructure of highly irradiated beryllium from the disposed moderator of Belgian Reactor 2, after irradiation and thermal ramp annealing at 10 K/min to 750 K (Transmission Electron Microscopy). A dense population of microbubbles is formed (about 6 nm diameter) due to the precipitation of gas atoms previously in solution.

development of synchrotron light micro-tomography was started in 2001 in collaboration with the European Synchrotron Radiation Facility. After two experimental sessions, where a certain number of samples were scanned by synchrotron light at typically 4.9 μm resolution, and the development of dedicated software, the reconstruction and 3D rendering of porosities was performed, as well as their quantitative analysis [12] [13] [14]. Fig. 5 shows the distribution of porosity sizes in a pebble before irradiation and of a similar sample, after irradiation and a 10 K/min out-of-pile thermal ramp annealing to 1500 K, when a burst release starts. Whilst in the non-irradiated sample a distribution of closed porosities between 10 and 30 microns are detected, in the irradiated sample only one open and completely interconnected network of all porosities is present, consisting of channels with a maximum size of 50 and a minimum size of 10 microns. Such analysis proves that burst release of gas retained in irradiated beryllium is due to formation of open porosity networks. This study is the first of its kind and represents a milestone in opening analysis capabilities of the behaviour of gas-in-solid.

a)

b)
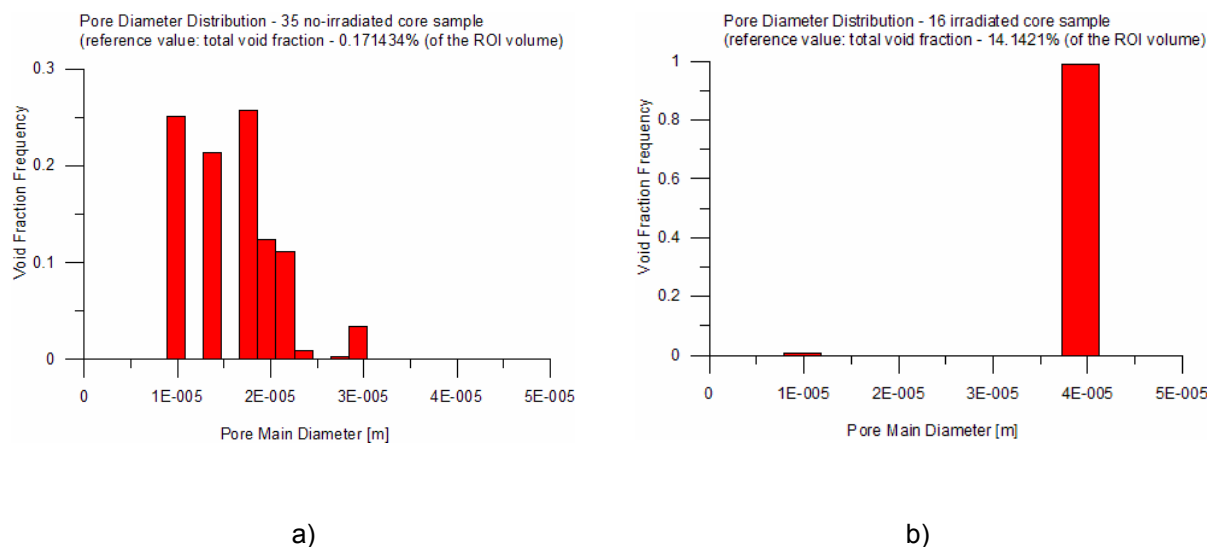
Fig. 5: 3D distribution of porosity sizes in pebbles from the BERYLLIUM irradiation, on the basis of a synchrotron light micro-tomography. (a) Before irradiation: closed porosities. (b) After irradiation: only one open interconnected network of porosities is present.

7. Conclusions and future work

The studies performed in the latest year have allowed remarkable progress in the understanding and modelling of helium and tritium diffusion, precipitation and release stages in irradiated beryllium and a first assessment of tritium retention in beryllium in a fusion power reactor. Open issues of the ANFIBE code at this stage is still an un-

satisfactory description of bubble growth and coalescence and of the resulting swelling. In 2005 the ANFIBE code will be further validated, on the basis of the data from the characterisation of highly irradiated beryllium samples from BR2 moderator. Under this aspect the studies in FZK will complete parallel studies of swelling and creep of the same material during long-term annealing under low compression load, which are being performed since 2002 at the Belgian research centre SCK-CEN under EFDA contract TW2-TTBB-005b-2. The final aim of these joint studies is to enable the improvement of the model of beryllium swelling under irradiation, since creep is the main phenomenon responsible for volume change.

<u>Staff:</u>

G. Janeschitz
M. Holzer
<u>E. Rabaglino</u>
R. Rolli
T. Schulenberg

C. Ferrero (ESRF)
R. A. Pieritz (ARS Company)
C. Ronchi (JRC-ITU)
H. Thiele (JRC-ITU)

<u>Literature:</u>

[1] E. Rabaglino, J.-P. Hiernaut, C. Ronchi, F. Scaffidi-Argentina, Helium and tritium kinetics in irradiated beryllium pebbles, J. Nucl. Mater. 307(2002) 1424-1429

[2] E. Rabaglino, C. Ferrero, J. Reimann, C. Ronchi, T. Schulenberg, Study of the microstructure of neutron irradiated beryllium for the validation of the ANFIBE code, Fus. Eng. Des. 61-62 (2002) 769-773

[3] R. Conrad, R. May, BERYLLIUM Final irradiation report, EC-JRC-IAM Report P/F1/96/15 (1996), Petten

[4] E. Rabaglino, C. Ronchi, A. Cardella, Recent progress in the modelling of the behaviour of helium and tritium in irradiated beryllium pebbles, Fus. Eng. Des. 69 (2003) 455-461

[5] G. Piazza, in W. Bahm (ed.), Nuclear Fusion Programme Annual Report of the Association Forschungszentrum Karlsruhe / EURATOM, October 2000- September 2001, Report FZKA 6650/EUR 20162 EN, Forschungszentrum Karlsruhe, 2002

[6] D. S. Gelles, L. R. Grenwood, B. M. Oliver, D. L. Baldwin, R. M. Ermi, H. Tsai, Post-irradiation examination of beryllium, Report Battelle, December 1997

[7] E. Rabaglino, Helium and tritium in neutron-irradiated beryllium, Report FZKA 6939, Forschungszentrum Karlsruhe, December 2004

[8] V. Van Alsenoy, F. Druyts, M. Gysemans, L. Sannen, C. De Raedt, J. Fays, Beryllium waste conditioning strategies 1. Physical, chemical and radiological properties of the beryllium waste from the BR2 reactor of SCK-CEN, Report R-3598, SCK-CEN, Mol, Belgium, 2002

[9] F. Scaffidi-Argentina, M. Dalle Donne, C. Ronchi, C. Ferrero, ANFIBE: a comprehensive model for swelling and tritium release from neutron irradiated beryllium - I: theory and model capabilities, Fus. Tech. 32 (1997) 179-195

[10] F. Scaffidi-Argentina, M. Dalle Donne, C. Ronchi, C. Ferrero, ANFIBE: a comprehensive model for swelling and tritium release from neutron irradiated beryllium - II: comparison of model predictions with experimental results, Fus. Tech. 33 (1998) 146-163

[11] Y. Chen, U. Fischer, P. Pereslavtsev and F. Wasastjerna, The EU Power Plant Conceptual Study - Neutronic Design Analyses for Near Term and Advanced Reactor Models, Report FZKA 6763, Forschungszentrum Karlsruhe, 2002

[12] E. Rabaglino, J. Baruchel, E. Boller, E. Elmoutaouakkil, C. Ferrero, C. Ronchi, T. Wiss, Study by microtomography of 3D porosity networks in irradiated beryllium, Nucl. Instrum. Meth. B 200 (2003) 352-357

[13] E. Rabaglino, C. Ronchi, C. Ferrero, G. Janeschitz, R. A. Pieritz, Gas percolation in irradiated beryllium pebbles, 6th IEA International Workshop on Beryllium Technology for Fusion, Miyazaki, Japan, 3 – 5 December 2003

[14] E. Rabaglino, C. Ronchi, C. Ferrero, G. Janeschitz, R. A. Pieritz, Quantitative characterisation by microtomography of 3D percolation patterns in weakly irradiated beryllium, Technical Meeting on X-Ray Tomography of Nuclear Materials, Karlsruhe, January 22-23, 2004

TW2-TTBB-007a D4
Measurements of Thermal and Mechanical Parameters of Beryllium Pebble Beds

1. Objectives and characteristic features of HECOP II

In the helium cooled pebble bed (HCPB) blanket the neutron multiplier and the breeder material are arranged in pebble beds between flat cooling plates [1]. Maximum temperatures in the breeder and beryllium pebble beds are about 900 °C and 650 °C respectively. Temperature differences and different thermal expansion coefficients between pebble beds and structural materials and irradiation effects will result in elastic and plastic pebble deformations which influence the effective thermal conductivity of the beds.

The description of the thermal mechanical behaviour the HCPB blanket requires as important input data relationships on the thermal conductivity of beryllium pebble bed as a function of pebble bed deformation and temperature, and relationships on thermal creep strain as a function of stress and temperature. Firstly, thermal conductivity measurements for strongly deformed beryllium pebble beds with an independent variation of temperature and deformation were performed with the Hot Wire method [2, 3] at maximum temperatures of 480°C. The Hot Wire method is a standard technique for low conductivity materials but the accuracy for materials like beryllium was expected to be lower.

In order to obtain more accurate measurements for temperatures up to 650°C, the test facility HECOP (**HE**at **CO**nductivity in **P**ebble beds) was built which combines uniaxial compression tests (UCTs) with the measurement of heat transfer characteristics. The second important objective of this facility was to gain thermal creep correlations which did not exist before.

Thermal conductivity experiments were carried out up to temperatures of 350°C [4], then, an important heating component failed. It was decided to redesign completely the set-up and to build HECOP II, retaining the characteristic thermal control features of the old version (HECOP I).

Figure 1 shows schematically HECOP II. The test section is positioned between the pistons of a hydraulic press (maximum load: 50 kN). For thermal control, a system of 7 heaters (H1...H7) is used. H1 and H2 generate the temperature gradient in the bed. H3, H4 are used to minimise the radial heat losses by controlling the power such that the temperature difference between two neighbouring thermocouples become zero. The axial heat flow from H2 to the press bottom plate is controlled to zero by means of heater H5. HECOP II is thermally insulated from the helium environment in the glove box by ceramic fibre (Kerlane) (not shown in Fig. 1).

Fig.1: HECOP II test section.

The heat flux q_2 [W/m^2] produced by H2 is used to calculate the thermal bed conductivity k given by

$$k(W/(mK)) = Q_2 \, \Delta x / \Delta T \qquad\qquad [1],$$

where Δx is the axial distance of thermocouples in the bed and ΔT is the corresponding temperature difference.

A detailed modelling was performed using the FLUENT code in order to understand the thermal behaviour of HECOP II, described previously [2003 report].

In 2003, measurements started in respect to thermal creep and measurement data have been analysed in 2004. In 2004, the experimental activities concentrated on measurements of thermal creep strain.

2. Thermal creep strain ε_{cr} of beryllium pebble beds

The pebble beds (packing factors about 62%) consisting of 1mm NGK beryllium pebbles were heated up to the desired temperature level; then, the piston pressure (identical with uniaxial stress σ) was increased up to the desired stress level and kept constant for time periods up to 6000 min.

Experiments were performed in a temperature range 450 < T(°) < 650 °C and stresses σ up to 3.6 MPa, for details, see [5]. Stress ramps during load increase/decrease were ≈ 1 MPa/min.

Characteristic results are presented in Fig. 2, considering the creep strain which occurred during the stress increase period. The slopes of the curves are fairly constant ($\varepsilon_{cr} \sim t^n$) and equal for all parameters. All experiments are well fitted by n = 0.35.

The temperature and stress dependence is determined from fits in a plot with axes as shown in Fig. 3. The temperature dependence is fitted assuming a straight curve, as expected for a thermally activated creep mechanism and the stress exponent p is varied such that the scatter from the straight curve becomes minimum.

The final correlation is presented in Table 1 which contains also the corresponding values for new orthosilicate pebble beds with pebbles manufactured via the hydroxide line [6].
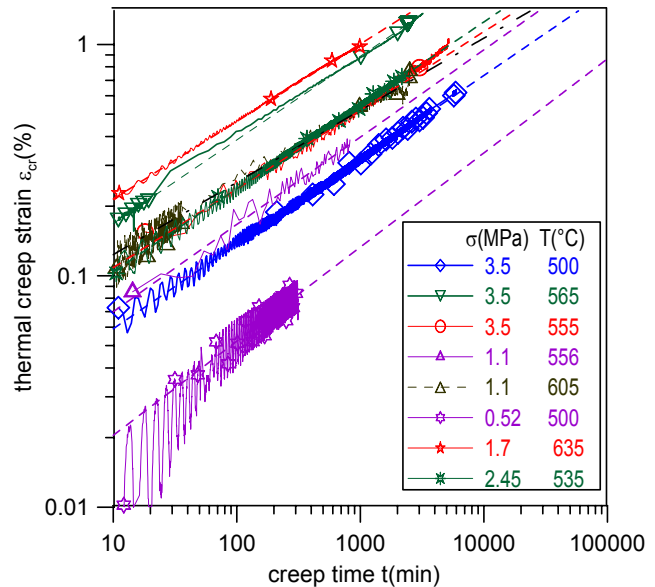
Fig. 2: Creep strains corrected for initial creep strains.

Table 1: Proposed thermal creep correlations.

Granular material	$\varepsilon_{cr}(\%) = A \exp(-B/T(K)) \, \sigma(MPa)^p \, t(min)^n$			
	A	B	p	n
1mm NGK pebbles	1614	9124	0.62	0.35
OSi ex hydroxide	5143	11005	0.65	0.23

For the same parameter values, creep strains for beryllium pebble beds are larger up to a factor of 10. However this difference becomes significantly smaller if creep strains for blanket

relevant temperatures are compared. Assuming high temperature zones of 650°C for beryllium and 900°C for orthosilicate, this factor reduces to 2-3.
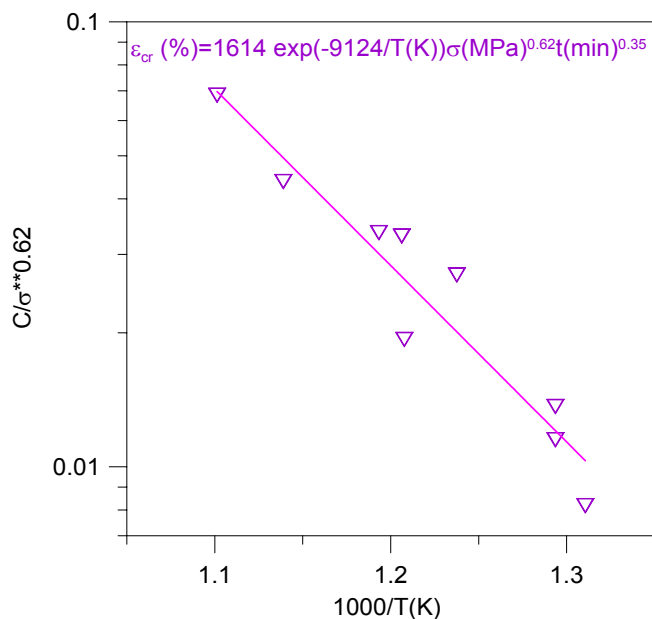
Fig. 3: Temperature and stress dependence of thermal creep strain.

3. Thermal conductivity k of beryllium pebble beds

Again, the beds were heated-up to desired mean temperature, then, thermal conductivity measurements started at small piston pressures and were continued at increased pressure levels. At elevated temperatures, creep strain occurred; the measurements were performed when creep rates became negligible. At each strain value, experiments at two different temperature differences were performed, and, additionally, an isothermal experiment which was used i) to determine residual heat losses (in the order of some Watt), and ii) to calibrate the thermocouples within the bed in order to increase the measurement accuracy. different series of experiments were performed, each series could last up to 2 weeks.

Figure 4 summarises the results: in agreement with previous measurements, again a linear relation between conductivity and strain was observed. The temperature influence is quite small; the HECOP I results obtained up to strains of about 1% agree quite well with the present experiments; the proposed correlation, however, deviates significantly above $\varepsilon \approx 2\%$.
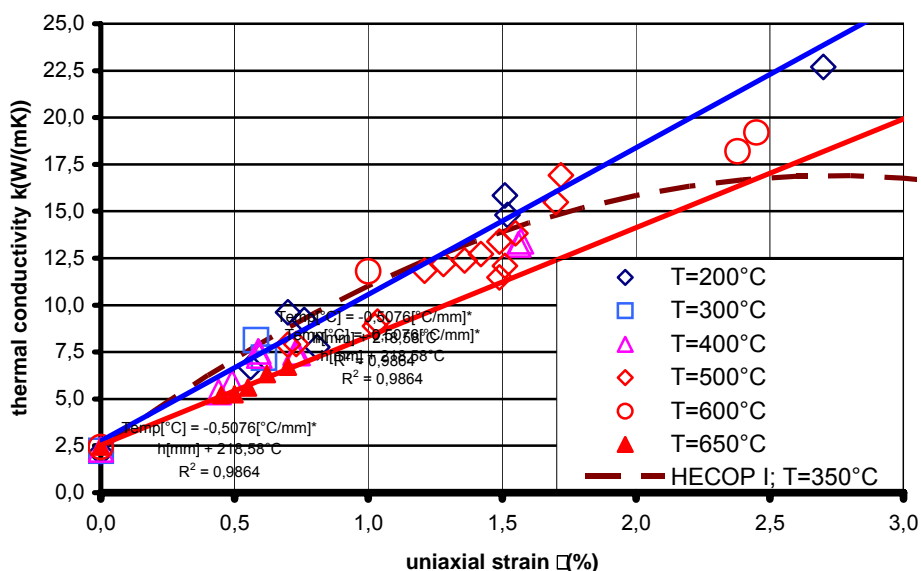
Fig. 4: Thermal conductivity k for compressed 1mm beryllium pebble beds.

At present, the new results are being analysed in more detail; results will be presented in the near future [7].

4. Conclusions

The modelling of the bed-structure thermal-mechanical interaction (BSMI) in blankets requires as input for both granular materials characteristic experimental data such as stress-strain relationships for stress increase and decrease, friction angles, dependence of thermal conductivity on strain, and thermal creep, compare [2]. At present, all data are only relevant the begin of the blanket operation (BOL) that is without taking into account the influence of irradiation on the pebble bed properties. However, there are arguments that this period might be crucial for pebble beds. For BOL, with the present correlation for thermal creep of beryllium pebble beds, and the new results for thermal conductivity, a first complete set of data exists.

Staff:

J. Reimann
Z. Xu
Fa Goraieb

Literature:

[1] S. Hermsmeyer, J.Fiek, U. Fischer, C.Köhly, S.Malang, J.Rey, Z.Xu, Revison of the EU helium cooled pebble bed blanket for DEMO, SOFE, San Diego, USA, Oct.03.

[2] J. Reimann, S. Hermsmeyer, G. Piazza, G. Wörner, Thermal conductivity measurements of deformed beryllium pebble beds by hot wire method, proceedings of the CBBI-9, Sept 27-29, Toki, Japan.

[3] J. Reimann, L. Boccaccini, M. Enoeda, A. Ying, Thermomechanics of solid breeder and Be pebble bed materials, proceedings of the 6th Int. Symp. Fusion Nucl. Techn., San Diego, USA, April 7-12, 2002.

[4] G. Piazza, J. Reimann, G. Hofmann, S. Malang, A.A. Goraieb, H. Harsch, Heat Transfer in Compressed Beryllium Pebble Beds, 22nd Symposium on Fusion Technology, Sept. 9-13, 2002 Helsinki, Finland: Paper J 2.

[5] J. Reimann; H. Harsch, Thermal Creep Of Beryllium Pebble Beds, Paper ID109, 23rd Symp. Fusion Techn., 20-24 Sept., Venice, Italy, 2004.

[6] R. Knitter, G. Piazza, J. Reimann, P. Risthaus, L.V. Boccaccini, Fabrication and characterization of lithium orthosilicate pebbles using LiOH as a new raw material, CBBI 11, Kyoto, Japan, Dec.03.

[7] J. Reimann, G. Piazza, H. Harsch, Thermal Conductivity Of Compressed Beryllium Pebble Beds, Paper submitted to ISFNT 7, May 22-27, Tokyo, Japan, 2005.

Breeding Blanket
HCLL Blanket Concept

TTBA-006b
Water-Cooled: Magneto-Hydrodynamics

TW2-TTBA-006b D1
Test and Modeling of Forced Convection MHD

The objective of the subtask was the investigation of liquid metal magnetohydrodynamic (MHD) flows in expansions or contractions which are major components of the previous WCLL blanket and of the currently considered HCLL concept. Theories and models concerning MHD flows in the blanket manifolds are important, since most of the pressure drop occurs in this part of the blanket. Abrupt changes of flow direction in feeding and draining lines as well as expansions and contractions cause flow redistributions and additional pressure drops.

Design and construction of an expansion test section and first experiments.

In order to improve the knowledge about such types of flows a detailed numerical and experimental investigation has been prepared. For that reason a forced convective MHD experiment in a sudden expansion/contraction of rectangular shape has been designed, manufactured.

The test section was nearly completed in 2003. However, since both the academic and technical personnel left the institute, it was not earlier than April 2004 when the work could be continued. This gives the total program a delay of nearly 1 year.

In 2004 it was possible to finish construction of the test section. The test section was inserted into the liquid metal NaK-loop MEKKA of the Forschungszentrum Karlsruhe. In order to achieve good wetting of the liquid metal with the walls the loop was operated at 300°C for more than one week.
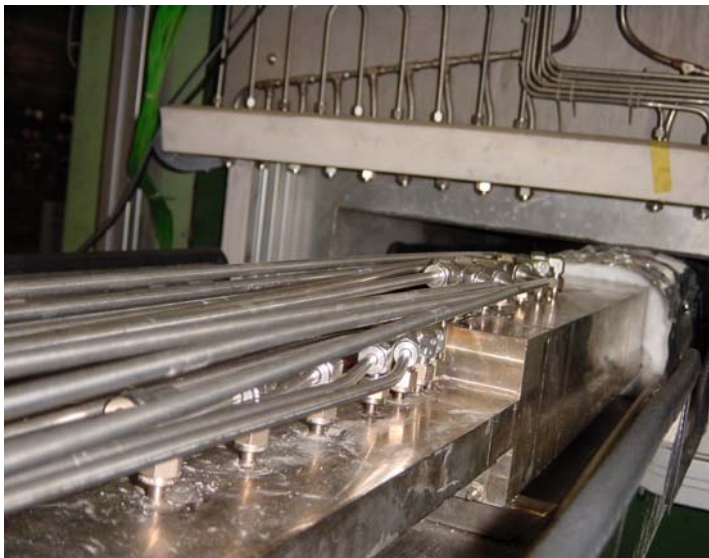
Fig. 1: Connections between pressure taps and measuring system.

Later pressure measuring tubes have been installed (see Fig. 1) and a first experimental campaign was run in which pressure distributions along the duct surface have been measured. The first experiments showed reliable operation of the test section and of the liquid metal loop. Detailed experiments are foreseen in future. Especially measurements of electric potential on the surface of the duct are planned for the next campaign. It is further foreseen to investigate internal flow properties by traversable probes.

A theoretical description of the flow had been already completed by means of asymptotic numeric computations and was published in a technical report FZK 6904 and at an international conference (Bühler 2003a). The results for pressure drop can now be compared with those theoretical predictions. An example of such a comparison is shown in Fig. 2. One can clearly identify the linear pressure gradients at the entrance and at the exit which shows that the test section is long enough for the flow to establish fully developed conditions. Near the expansion at $x = 0$, three-dimensional effects are responsible for additional pressure drop. Part of that pressure drop is

recovered in the large cross section but the major fraction remains lost due to Joule and viscous dissipation. The experimental results agree quite well with numerical predictions.
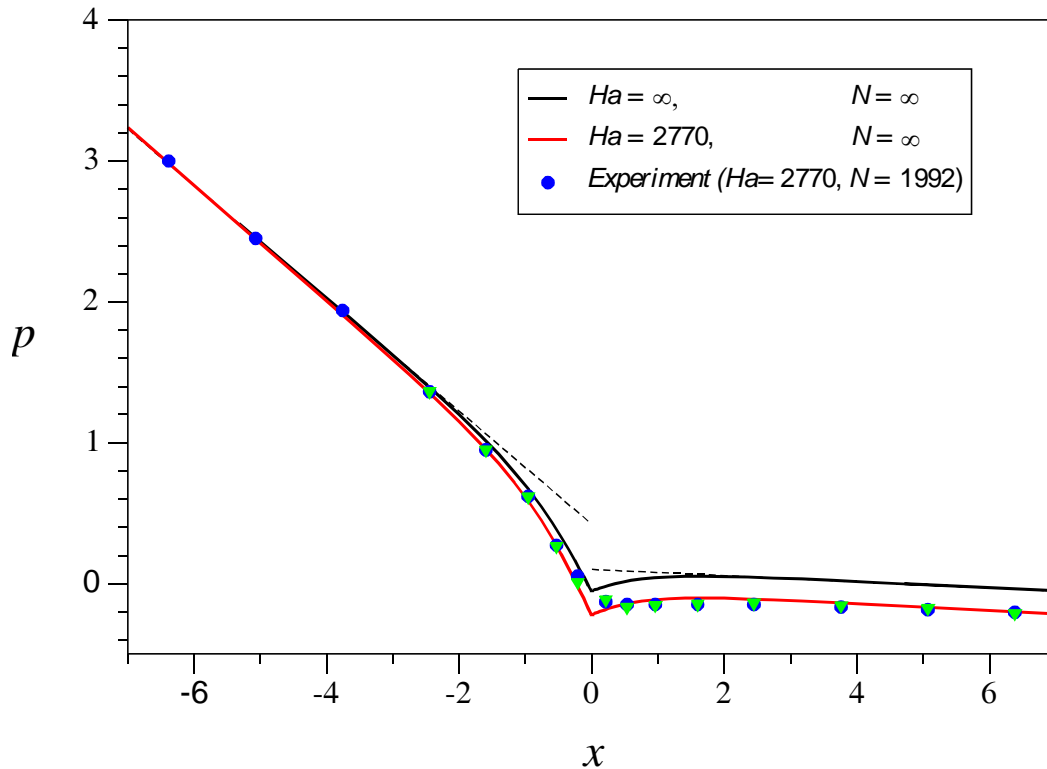
Fig. 2: Comparison of experiment and inertialess theory.

With these first experiments the subtask task TW2-TTBA-006a-D1 could be completed with a internal report. A detailed comparison and evaluation will be given in the continuing sub task TW2-TTBA-006b-D1 in 2005.

Staff:

E. Arbogast
L. Bühler
S. Horanyi
C. Mistrangelo

Literature:

[1] Bühler, L.: 2003a, Magnetohydrodynamic flows in sudden expansions in strong magnetic fields, 4th International Conference on Electromagnetic Processing of Materials, Proceedings on CD-Rom, Lyon, 14-17 October 2003.

[2] Bühler, L.: 2003b, Inertialess magnetohydrodynamic flows in expansions and contractions, *Forschungszentrum Karlsruhe,* Technical report, FZKA 6904

[3] Bühler, L., Arbogast, E. Gnieser, S., Horanyi, S., Stieglitz, R.: 2004, Design and construction of an expansion test section and first experiments, *Forschungszentrum Karlsruhe,* Internal report **,** 2004.

TW2-TTBA-006b D4
MHD Experiments and Modelling of the Reference TBM Design

The objective of the subtask was the design of a TBM-relevant test section for experimental investigations of liquid metal flows in strong magnetic fields. The work was focused on a possible Test Blanket Module (TBM) for a Helium Cooled Lead Lithium (HCLL) blanket. In such a modular blanket a number of so-called breeder units is arranged in columns and fed with liquid metal through poloidal manifolds. Most breeder units have common, electrically conducting walls, through which an electrical coupling of neighboring flow regions is possible. A full theoretical description of such electrical coupling is difficult so that major conclusions about MHD flows in a TBM should be drawn from an experiment.

Design and construction of a TMB mock-up

In 2004 a test section for experimental investigations of fusion relevant MHD flows in HCLL breeder units and their poloidal manifolds has been designed and fabrication has begun. The new test section is being manufactured as a 1:2 model of the HCLL blanket currently proposed for a DEMO or an ITER test module. It consists of a column of 4 breeder units, connected by poloidal manifolds. The model contains all major 3D elements. It is foreseen to measure pressure drop between different positions in the blanket. In the MEKKA laboratory we are able to measure a number of 5x14 individual pressure differences. The flow distribution will be investigated by potential measurements on the surface. The scale used for the mock-up has been chosen such that the new test section fits into our large dipole magnet. The magnetic gap has dimensions of about 2000x160x430 mm. In an inner region of 800x160x430 mm the magnetic field is uniform and reaches values of about 2T. Since internal heating is impossible in non-nuclear experiments and cooling of the internal walls would be difficult on the present scale, it is planned to perform isothermal experiments in which the purge flow is driven by an applied pressure difference (by the pump).

Form-closed barriers

In each of the 4 modelled breeder units the cooling plates are simulated by solid walls. The helium cooling channels, which are present in the real application, are taken into account by using a reduced thickness of the walls in order to achieve comparable electric conductivity of the walls as in the TBM.

The test section is manufactured by electro erosion from a solid piece of material. The remaining parts after machining simulate the stiffening plates and cooling plates of the TBM. One end is covered by a construction that simulates the poloidal manifold, the other end is closed by the "first wall". Some details may be seen from Fig. 1.

Fig. 1: Assembly of the TBM mock-up

A first theoretical analysis considered the modeling of MHD flows through a circular access tube into the poloidal manifold and through distributing gaps into the breeder units. The derived geometry was used also for the prediction of MHD flows in a DEMO HCLL blanket (Bühler 2004) or in a power reactor blanket (Bühler & Giancarli).

The main parts of test section are currently being manufactured at FZK. All parts will be assembled and joined by electron beam welding. It is expected that the entire mock-up will be ready for installation in the MEKKA loop in March 2005. On the surface a number of 20 pressure taps will be mounted for detection of pressure drop. It is further planned to cover the surface with an array of electrodes for detecting flow-induced electric potentials as an indication for flow pattern in the liquid metal layers.

Staff:

L. Bühler
S. Horanyi
C. Polixa
J. Rey

Literature:

[1] Bühler, L.: Magnetohydrodynamic pressure-driven flows in the HCLL blanket, 23rd Symposium on Fusion Technology (23rd SOFT), Venice, 20-24 September 2004.

[2] Bühler, L., Giancarli, L.: Magnetohydrodynamic flows in the European HCLL blanket, Forschungszentrum Karlsruhe, Technical report, FZKA 7069

TTBC-004
Helium Cooled Lithium Lead: Processes and Components

TW2-TTBC-004 D2
Assess Recovery Method of T from He Coolant

A thermonuclear D-T power plant, such as the fusion demonstration reactor DEMO, will typically consume kg amounts of tritium per full power year. As tritium does not occur naturally such a reactor will have to breed tritium to replace that burnt in the fusion process. Tritium breeding requirements are quite demanding as the process is based on the nuclear reaction between the neutron generated by the fusion reaction and the lithium filling the blanket surrounding the torus. To increase as much as possible the efficiency of the above mentioned nuclear reaction the blanket must contain not only lithium based ceramic material but also a neutron multiplier. To accomplish this goal two blanket concepts have been selected for investigation by the European Breeding Blanket Programme. A Helium Cooled Lithium Lead (HCLL) and a Helium Cooled Pebble Bed (HCPB). Both concepts are contemplating to use lithium as breeder material but while HCLL Blanket uses liquid lead as neutron multiplier the HCPB considers the use of beryllium. Both concepts are Helium cooled and are also considering using martensitic steel as structural material.

The tritium bred by neutron capture in a lithium-containing blanket has to be continuously extracted by a closed loop operation and then removed from the loop for re-introduction into the machine.

The Tritium Extraction System (TES) aims to extract tritium from the lithium ceramic beds and beryllium multiplier by using a low pressure helium stream containing 0.1% pure hydrogen. Under such conditions TES accomplishes the tritium extraction from the helium purging gas in the two main chemical forms, HT and HTO. The subsequent separation, from the purging gas, of all diluted tritiated gaseous components, independently on their chemical form (HT, HTO, CH_3T, etc) constitutes the *Tritium removal* operation. After chemical processing the tritium will eventually be recovered in the Isotope Separation System (ISS).

In view of the large differences in the feed streams of the DEMO and ITER blankets there will be considerably divergence in the layout of the respective tritium processing systems. However, the tested technologies will be basically the same and therefore the experience gained during the ITER operation will be, to a large extent, directly applicable to DEMO.

Many processes have been proposed in the past as potentially able to remove tritium from the He purge gas stream, both in HT and HTO form. Four of them have been considered under this task, because from a preliminary screening evaluation they appear to be the most suitable, especially from the point of view of the present technological maturity. They are:

a) Temperature Swing Adsorption (TSA) coupled to the Vacuum Pressure Swing Adsorption (VPSA)
b) Cold Traps associated to TSA
c) Q_2 Oxidiser associated to TSA
d) TSA associated to Q_2 permeator

Among these, only the process developed at the Tritium Laboratory Karlsruhe (TLK), i.e. process 2, is considered as the most promising, and therefore it will be analysed in some detail below. Most important advantage of this concept is that throughout the process molecular tritiated hydrogen is not converted into tritiated water, a species which comparatively to molecular hydrogen is difficult to handle. A further advantage is that after its development for ITER it could be scaled up without much conceptual modification to meet

the DEMO requirements. Assuming this granted, it appears possible to profit from the technical experience gained during the operation of ITER.

The specified feed flow rate of the TES for ITER, i.e. 12.1 Nm^3/h, is orders of magnitude lower than that of DEMO, but the stipulated efficiency of 0.95 for the removal of tritium is nearly the same. The helium purge gas effluent from the blanket, with its helium to hydrogen swamping ratio of 1000, is first pre-cooled and then passed through filters for the removal of particulate matter prior to flowing through a cryotrap maintained at 173 K (- 100 °C). In this trap water, i.e. H_2O and HTO, as well as impurities such as carbon dioxide are condensed and frozen out down to concentrations in the effluent stream of less than 1 ppm(v). Hydrogen isotopes and other impurities are adsorbed on a liquid nitrogen cooled molecular sieve bed placed further downstream.

A low concentration of Q_2O at the outlet of the cold trap is important from the point of view of the overall efficiency of the TES, i.e. protection of the cryoadsorber bed from a loss of adsorption capacity. However, an exceedingly low concentration of water partial pressure at the outlet of the cold trap is of no real advantage, because of the extremely high retention capacity for these species by the downstream installed cryoadsorber bed.

During de-icing of the cold trap for the purpose of reconditioning, the blanket effluent gas is sent through another identical and previously de-iced cold trap in standby position. It is expected that such a change will be necessary only after several days of uninterrupted operation of the TES. After liquefaction of the water collected in the cold trap, it will be drained into a water collector and then sent into a loop in which detritiation takes place by catalytic conversion of Q_2O into Q_2 via the water gas shift reaction using CO as an additional reagent. The resulting CO_2 can be adsorbed on a molecular sieve bed and the tritiated hydrogen be extracted from the loop using an integrated palladium/silver permeator. Pure hydrogen isotopes permeated into the secondary side of this diffusor are directly transferred into the ISS, where tritium is separated from the other hydrogen isotopes for its reuse in the fusion machine.

The cryo-trap tested at TLK at Forschungszentrum Karlsruhe (FZK) has approximately 1/6th of the ITER required size and operated at temperatures below 173 K. Important features of this particular trap are two separate pre-coolers, the option of variable gas throughput at comparatively small gas velocities (approx. 19 cm/sec) in the freezing zone, The presence of such pre-coolers is very important as it avoid fast cooling of the purging gas and therefore, its critical super-saturation responsible for the formation of aerosols.

The cryo-trap is also equipped with electric heating coils in five separate sections of the freezing zone allowing a segmental adjustment of the temperature. A total of 22 copper cooling plates chilled with liquid nitrogen flowing through a central coil in counter current to the gas flow direction serve to condense the water present in the process gas as ice. 13 Pt-100 resistance thermometers are available to determine the temperature profile across the cryo-trap.

Downstream to the cryo-trap the purge gas, short of water, is passing through molecular sieve beds where it is relieved of all hydrogenated molecular species that it contains. During a ultimate process the tritiated gases are recovered by the Tritium Removal System and processing system which eventually feeds ISS.

A flow diagram for the combined Tritium Extraction/Removal System concept for the Blanket Test Module of ITER is illustrated in Fig.1. The number of components, and interfaces as well as their respective flow rates and tritium levels are specified. In the diagram it is also included the Coolant Purification system (CPS) which is foreseen to remove the tritium permeated into the He coolant gas.
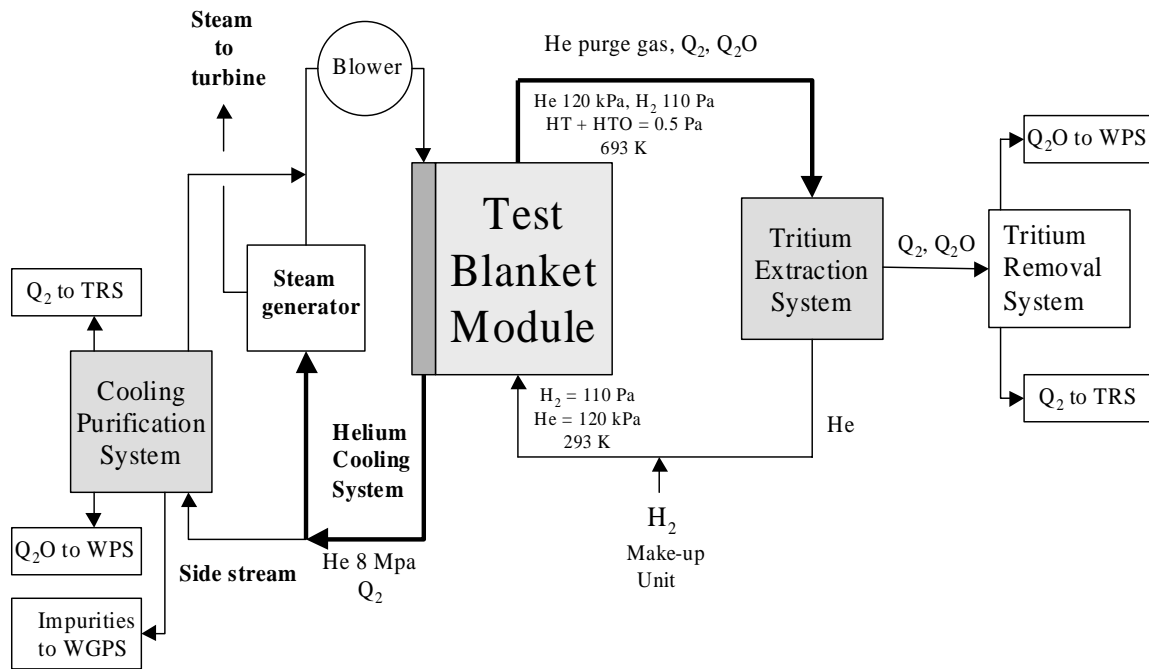
Fig. 1: Flow diagram of the TES and CPS of the Test Blanket Module for ITER

A cold trap operated at 173 K was proposed for the retention of water from the blanket helium purge gas containing tritiated hydrogen isotopes. Such a cold trap was successfully tested with hydrogen at the TLK. However, the consequences of up-scaling of the current TES design for ITER to meet the DEMO requirements needs still to be examined not only experimentally but also from the design point of view.

A semi-technical scale cryogenic molecular sieve bed was designed, and manufactured at TLK and is at present under test with protium. The bed contains 20 kg of molecular sieve 5A. It is installed in a liquid nitrogen cooled vacuum insulated vessel that chills the molecular sieve uniformly to 77 K. For regeneration the bed can be heated up to 600 K using three electrical heaters. The scalability of the bed and the technical consequences of this for the TES process have not yet been examined.

The possible replacement of the cold trap by a 3A molecular sieve bed, which appears to be capable of adsorbing water selectively at ambient (or lower temperature) temperature, should be examined from the design point of view. In this context, the minimum temperature at which hydrogen is excluded from adsorption on zeolite 3A should be determined experimentally in the temperature range 77 - 273 K.

In this respect the consequences of a certain partial pressure of hydrogen in the helium purge gas of the solid breeder blanket on the release rate of tritium from breeder material should be investigated parametrically with the goal of optimising the hydrogen partial pressure.

Staff:

N. Bekris
D. Adami
S. Beloglazov
M. Glugla
R. Wagner

Materials Development
Structural Materials

TTMS-001
Irradiation Performance

TW2-TTMS-001b D5
HFR Irradiation Programme

The HFR Phase IIB programme is abbreviated SPICE (**Sa**mp**le** Holder for **I**rradiation of Miniaturized Steel Spe**ci**m**e**ns Simultaneously at Different Temperatures). It complements the former HFR irradiation programmes MANITU, SIENA, HFR Phase IA, and IB. The phase of irradiation actually is completed, post-irradiation experiments are starting in beginning of 2005.

Table 1: Heat treatments of the irradiated alloys.

Alloy	Heat treatment
EUROFER 97, as delivered	980 °C + 760 °C
EUROFER 97	1040 °C + 760 °C
EUROFER ODS HIP powder steel	-
EUROFER 97, variations in B and ^{10}B contents	1040 °C + 760 °C
F82H mod., reference steel	950 °C + 750 °C
GA3X, reference steel	1000 °C + 700 °C

The objectives of the programme are to evaluate the mechanical properties of material samples after irradiation at doses of 15 dpa and different irradiation temperatures. The material used is the reduced activation alloy EUROFER 97 in different variations: different heat treatments, a HIP powder steel, and various boron contents to investigate the effect of He embrittlement. Heat treatments of the irradiated alloys are given in Tab. 1.

The "quasi-saturation" of irradiation-induced embrittlement between 10 and 15 dpa, found for conventional steels in former programmes (SIENA), will be investigated for the EUROFER alloys. The low irradiation temperature ranges of the High Flux Reactor will give a look at embrittlement effects increasing pro-gressively with decreasing temperature in all bcc-alloys irradiated up to now.

The TRIO irradiation capsule (cf. Fig. 1) was fixed in a central core position (C3) of the Petten High Flux Reactor. Surrounded by fuel elements, the neutron flux is approximately homogeneous and an exactly defined dose rate was reached in a comparatively short time.

The TRIO capsule offers three parallel separate channels for the different sample holders. Temperature control was effectuated by a controlled sodium flow which facilitates the formation of separate temperature areas of 250, 300, 350, 400, and 450°C in a horizontal arrangement. The neutron flux is relatively

Fig. 1: TRIO Irradiation capsule with sample holders. D330: 91 tensile specimens; D329: 130 charpy specimens; D331: 160 fatigue specimens.

homogeneous and varies over the irradiation space between 92 and 107% of the nominal value. A vertical displacement unit allows to follow the centre line of the fluence rate, which is shifted vertically with the burn-up of the fuel elements. Thermocouples were installed along

the irradiation capsule and recorded the temperature behaviour during the experiment. Activation detectors were installed to ensure the high quality level of HFR irradiations even at higher doses.

This is the first irradiation experiment, in the course of which a damage of 15 dpa was reached at five different temperature levels simultaneously. Newly applied techniques for these sample holders are the temperature control by sodium and the dosimetry inside the capsule. The liquid sodium cooling provides a highly improved temperature stability in comparison other experiments and to the gas cooling used in former HFR-experiments (cf. Fig. 2).
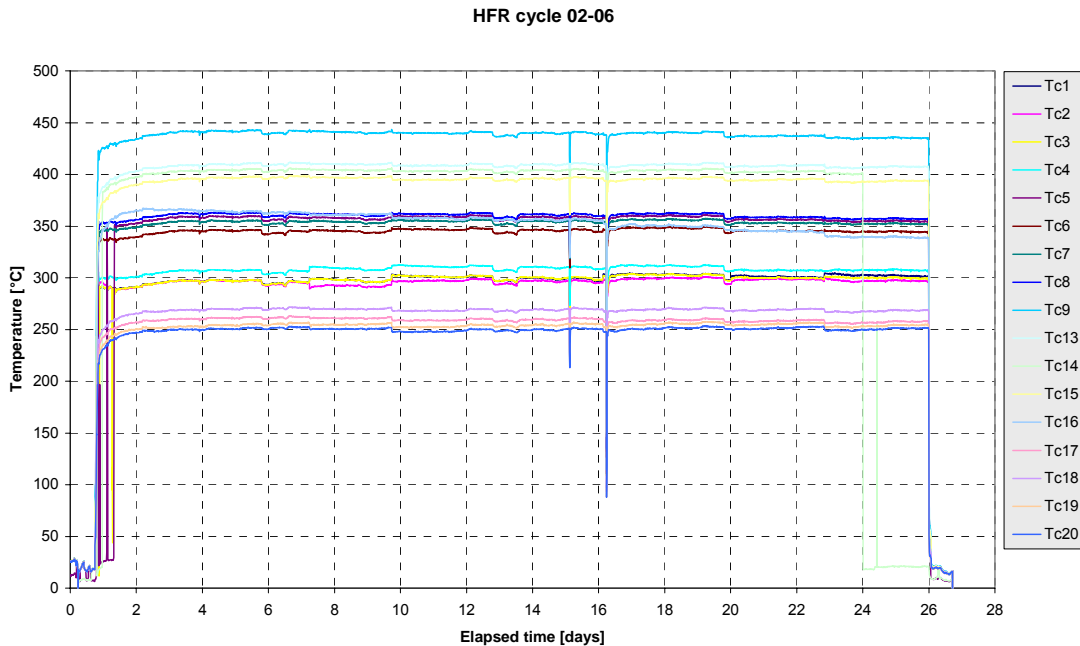
HFR cycle 02-06

Fig. 2:   Active temperature control – recorded signals of the thermocouples in the 329-capsule (KLST-specimens). Cycle 02-06, 25 full power days in July/August 2002.

Post-irradiation examinations (PIE) will be carried out in the Fusion Materials Laboratory of FZK. The design of the capsule provides space for 130 charpy, 91 tensile, and (for the first time simultaneously) 160 fatigue specimens. As result, a full data set of the irradiation effects on Charpy impact, tensile, and fatigue behaviour will be obtained. During the irradiation phase, unirradiated reference samples were investigated. Regarding the EUROFER steel, an embrittlement behaviour comparable to the best alloys investigated in former irradiation programmes is expected, accompanied by good mechanical properties. The higher irradiation dose of 15 dpa will represent a step towards fusion-relevant doses.

Charpy tests of the irradiated specimens: 130 Charpy specimens will be tested by using a fully automatic instrumented pendulum in the Fusion Materials Laboratory (hot cells facilities) of FZK. The impact properties as ductile to brittle transition temperature, upper shelf energy, and dynamic yield stress will be determined and compared with the unirradiated properties.

Tensile tests of the irradiated specimens: The 91 tensile specimens will be tested in an universal testing machine in the Hot cells facilities of FZK. These tests will be performed at the irradiation temperatures and at room temperature and will be compared with the unirradiated data, too.

Creep-fatigue tests of the irradiated specimens: The EUROFER97 specimens will be tested in strain controlled creep-fatigue in the facilities of the Hot cells of FZK. 160 tests will be performed at the temperatures of RT, 250, 300, ..., 450 °C and with a total strain rate between 0.4 and 1.5 %.

Fractographic and microstructural investigations (FMI): An important part of this program is the FMI of the irradiated and tested materials. The irradiation induced changes in the materials and the reasons of the embrittlement must be detected. These results must be correlated with the mechanical properties and the fracture behaviour of the materials. These investigations will be performed at the Charpy, tensile and fatigue specimens.

Assembly of the sample holders in Petten had started in January 2001. The start of irradiation was delayed by three months because of the intricate fabrication of the sample holders which are more complex than the ones formerly used (increased precision requirements because of the sodium cooling). The start of the irradiation was in cycle 07-01, i.e. August 2001. To reach a damage of 15 dpa, 30 cycles were needed in a central position. The first cycle was irradiated in position A7, all following cycles are irradiated in position C3. In December 2001, 3.0 dpa were reached, 5.4 dpa by end of June 2002. In December 2002, the accumulated irradiation dose was 9.3 dpa, so the subtask TW2-TTMS-001a Deliverable 5 (7-8dpa) was completed in October 2002.

SPICE Irradiation Programme - Time Schedule for Irradiations and Post Irradiations Examinations

Rev.: Nov 2004
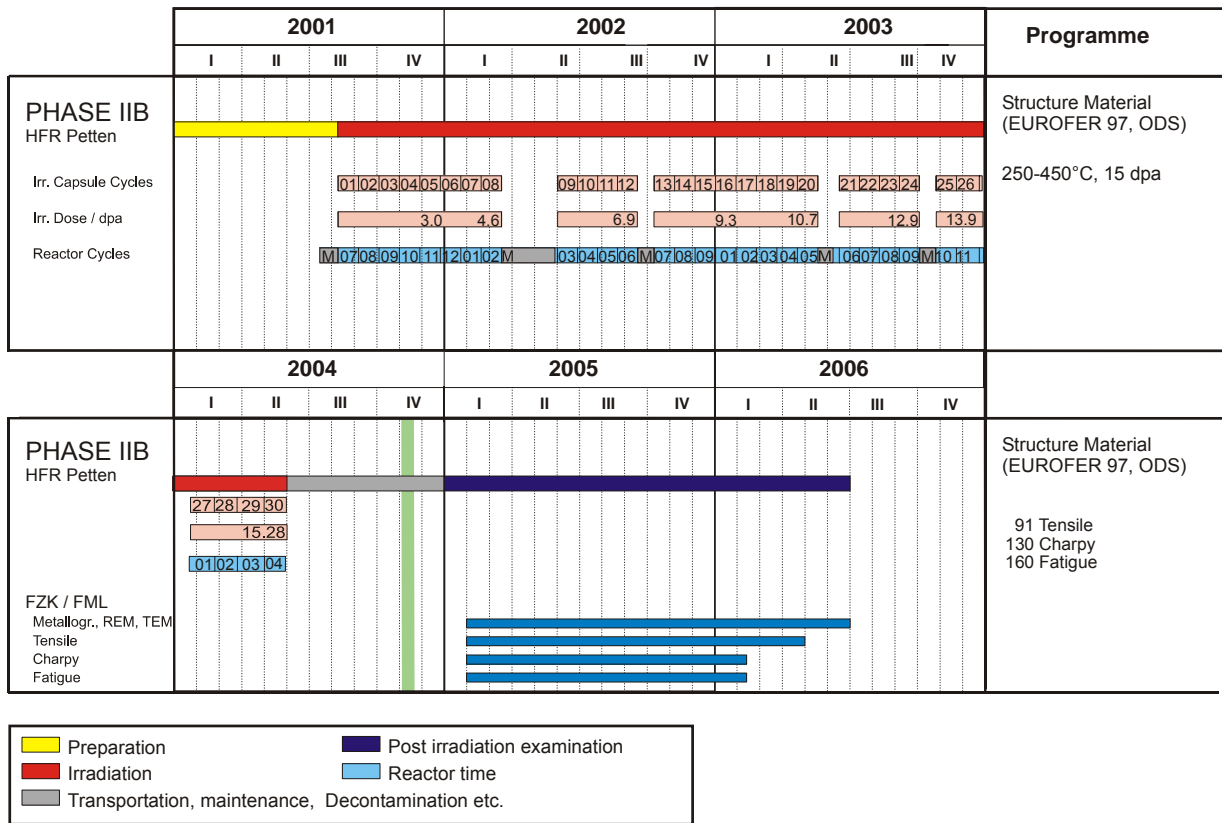
Fig. 3: Time Schedule.

In December 2003, an accumulated dose of 13.9 dpa was reached in irradiation capsule cycle 26, and the final Dose of 15.28 dpa could be reached in May 2004, cf. Fig. 3. The irradiation programme was running according to schedule, active temperature control by sodium is providing very constant temperature ranges in the different levels of the sample holders as documented in the safety report, cf. Fig. 2.

The temperature profile in the different drums of the sample holders showed a symmetrical behaviour. The average irradiation temperature ranges of the different specimens were as follows:

250°: 244 - 260°C
300°: 285 - 301°C

350°: 339 - 354°C
400°: 382 - 400°C
450°: 386 - 431°C

The dose detectors are to be analysed to provide exact information on each sample-holders real dose rate.

Specimens actually are being dismantled and prepared for transportation to the Karlsruhe Fusion Materials Laboratory. This contains dissolving of the sodium (coolant), breaking up the sample holders, assorting and first cleaning and decontamination of the samples. The specimens are assorted in a newly developed transport box which protects the cylindrical parts of the tensile- and LCF-specimens and saves a re-identification in Karlsruhe, cf. Fig. 4. The transport is foreseen to be done in the 50th or 51st week of 2004.

Fig. 4: Transport Box for assorted specimens.

Post-irradiation experiments can start in beginning of 2005 after repeated decontamination of the specimens. Difficulties similar to the transportation problems with the specimens from the HFR Phase IB programme are excluded, as a new cask with a long-lasting transport permission is under construction. PIE and FMI are foreseen to be finished by mid of 2006.

Staff:

J. Aktaa
B. Dafferner
E. Materna-Morris
H.-C. Schneider

Literature:

[1] H.-C. Schneider, B. Dafferner, H. Ries, S. Lautensack, O. Romer: Bestrahlungsprogramm HFR Phase Ib. Ergebnisse der Kerbschlagbiegeversuche mit den bis 2,4 dpa bestrahlten Werkstoffen, FZKA-6976.

[2] E. Materna-Morris, R. Rolli, O. Romer, A. Möslang: Tensile properties and structural analysis of martensitic low-activation alloys after neutron irradiation. Jahrestagung Kerntechnik 2004, Düsseldorf, 25.-27. Mai 2004, INFORUM GmbH, 2004 S.401-04 CD-ROM

[3] H.-C. Schneider, J. Aktaa, B. Dafferner: Post-irradiation examinations of ferritic-martensitic steels for structural applications in fusion reactors. Technological studies and fracture toughness evaluation. Jahrestagung Kerntechnik 2004, Düsseldorf, 25.-27. Mai 2004, INFORUM GmbH, 2004 S.405-08 CD-ROM

TW2-TTMS-001b D9
Fast Reactor Irradiations

1. Objectives

In an energy generating fusion reactor structural materials will be exposed to very high levels of irradiation damage of about 100 dpa. Due to the fact, that fast reactor irradiation facilities in Europe are not available anymore, a cooperation with the Russian institution: State Scientific Centre of Russian Federation Research Institute of Atomic Reactors (SSC RF RIAR) has been implemented.

2. The irradiation project ARBOR 1

The modernized Low Cycle Fatigue (LCF) -testing facility and the instrumented Charpy testing facility for KLST specimens under remote handling conditions are installed in the hot cell of SSC RF RIAR.

During several campaigns on the Zwick 5113-HKE Charpy tester, together with RIAR experts, the work has been mainly concentrated on reference temperature measurements with the calibrator DIGISTANT 4422 on this facility. The agreement between the demand temperature, the calculated temperature and the temperature measured with the calibrator was very good. In addition to this reference temperature measurement, a series of EUROFER 97 KLST specimens had been examined.
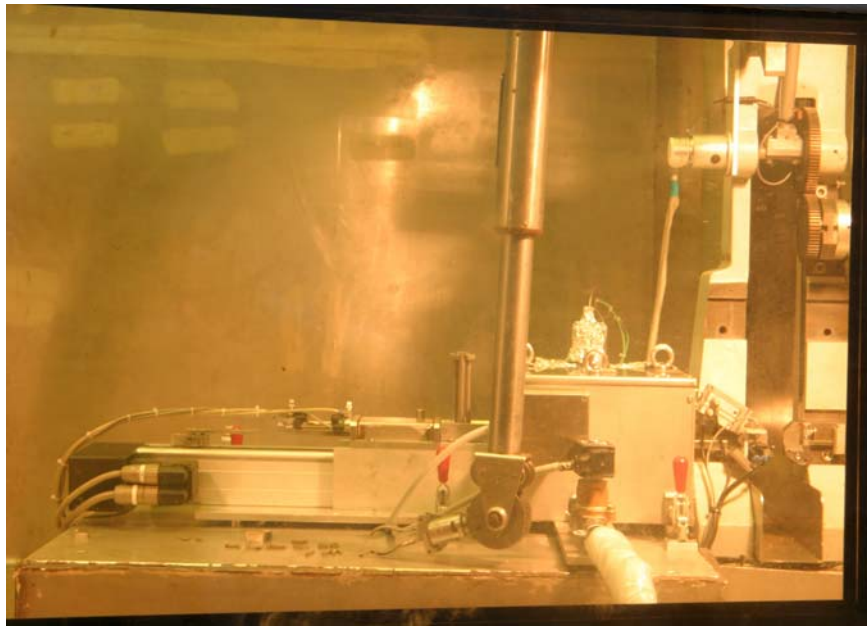
Fig. 1: Charpy testing facility in built in the Hot cell VK-39 of RIAR.

These test results had been analysed at FZK. The Zwick 5113-HKE Charpy tester is ready for testing irradiated specimens now. The priority program for the test sequence of the ARBOR 1 specimens has been discussed and accepted. The procedure is the following: FZK specifies the material, specimen number and the temperature of the test. RIAR experts perform the experiment on the basis of this infomation and send the data file by e-mail attachment to FZK. The experts of FZK analyze the data and give the next material, specimen number and testing temperature to RIAR where the next experiment is performed, and so on.

Table 1:   Results of EUROFER 2 specimens testing in Zwick 5113-HKE impact machine.

in RIAR hot cell VK-39.		in FZK's reference Laboratory.	
Temperature, °C	Absorbed energy, J	Temperature, °C	Absorbed energy, J
-96.4	6.90	-96.4	0.50
-94.4	7.88	-94.4	6.64
-89.5	8.96	-89.5	8.31
-84.6	9.14	-84.6	8.53
-79.2	9.18	-79.2	9.40
-49.6	9.30	-49.6	9.84
-99.6	1.22	-19.6	9.62
-101.5	4.72	22.6	9.62
-104.4	0.63	100.0	9.18
-109.2	0.59		
-114.0	0.77		

The INSTRON 1362-DOLI tensile and LCF testing facility is installed in cell K12, and the extensometer can be used already. The electrical connections for the furnace must still be installed. Minor uncertainties and software problems could be solved. After a principle discussion of the sequence of experiments on this facility, it was agreed to begin with tensile testing of irradiated specimens. Therefore, for some small unsolved problems in the control software of the LCF testing remains enough time to find a solution.

EUROFER 2
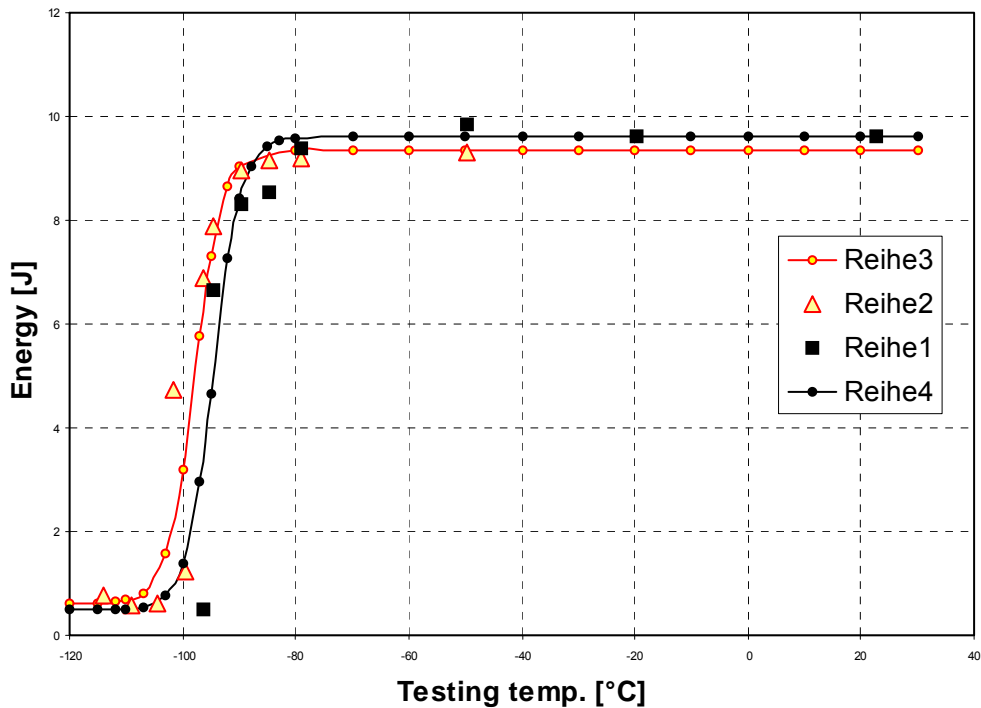
Fig. 2:   Results of the comparative testing: Row 1 – experimental points at FZK; Row 2 - experimental points at RIAR; Row 3 – processing by the hyperbolic tangent at RIAR; Row 4 - processing by the hyperbolic tangent at FZK.
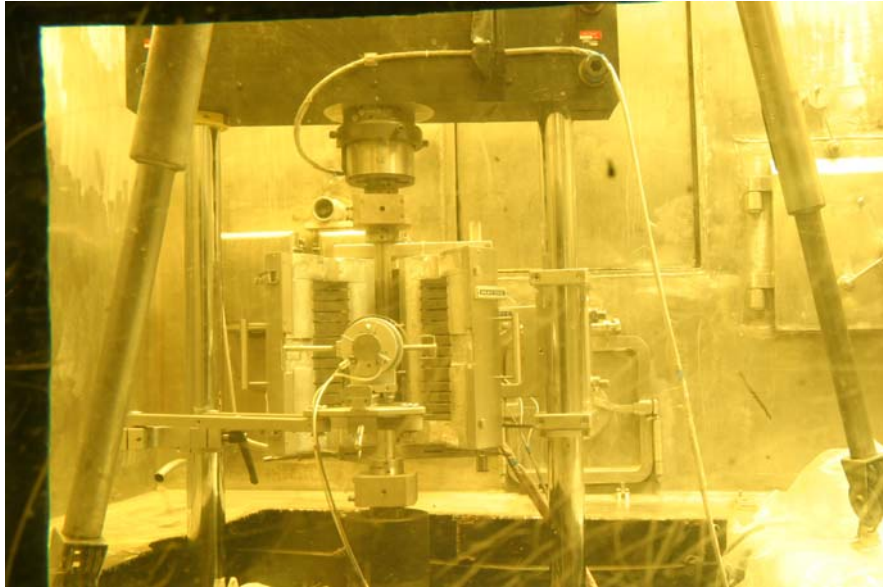
Fig. 3: Modernized LCF-testing facility with furnace, strain measurement system and control devices built in the Hot cell K12 of RIAR.

3. The irradiation project ARBOR 2

The ARBOR 2 irradiation in BOR 60 of SSC RIAR, Dimitrovgrad, with pre irradiated specimens of FZK from the ARBOR 1 irradiation (30 dpa), of CEA from the ALTAIR irradiation (40 dpa) and new specimens of FZK and CEA, running up to a damage of 40 to 80 dpa, had been started on 11 February 2003 and accumulated up to now another 30 dpa of damage, i.e. 30.1 und 48.8 dpa for the new specimens and 60.1 dpa for the specimens pre-irradiated in ARBOR 1. The specimens exchanged in June 2004 reached 5.6 dpa. The maximum damage dose will be reached in May 2005, already half a year earlier as initially planned.

Staff:

C. Petersen
B. Dafferner
M. Klotz
D. Rodrian
R. Schmitt

TW4-TTMS-001 D1
Fabrication of Samples for Fe-54 Irradiation

Overview

The structure components of future fusion reactors will suffer from specific irradiation damage, i.e. the ratio of helium production (in appm) to displacement rate (in dpa) varies around 10 appm He/dpa. Due to the lack of appropriate high energy neutron sources there seems to be only one promising way to generate such irradiation damages in a RAFM steel with common in-pile fission reactor irradiation experiments: if the content of natural iron would be replaced by the stable isotope Fe-54, helium production would be stimulated by the according (n, alpha) reactions [1] (see Figs. 1 and 2).

A significant advantage over the alternative boron-10 helium production technique would be a uniform helium distribution through the whole matrix as outlined in Fig. 2.

The goal of the task is to produce a heat similar to EUROFER using Fe-54 instead of natural iron. Then miniaturized Charpy and tensile specimens with cores of Fe-54 substituted EUROFER steel have to be fabricated. Finally some of the specimens will be used to perform instrumented Charpy and tensile tests, the remaining specimens will be provided for an according irradiation program. The whole production, processing and testing procedures have to be accompanied by chemical and micro-structural examinations.
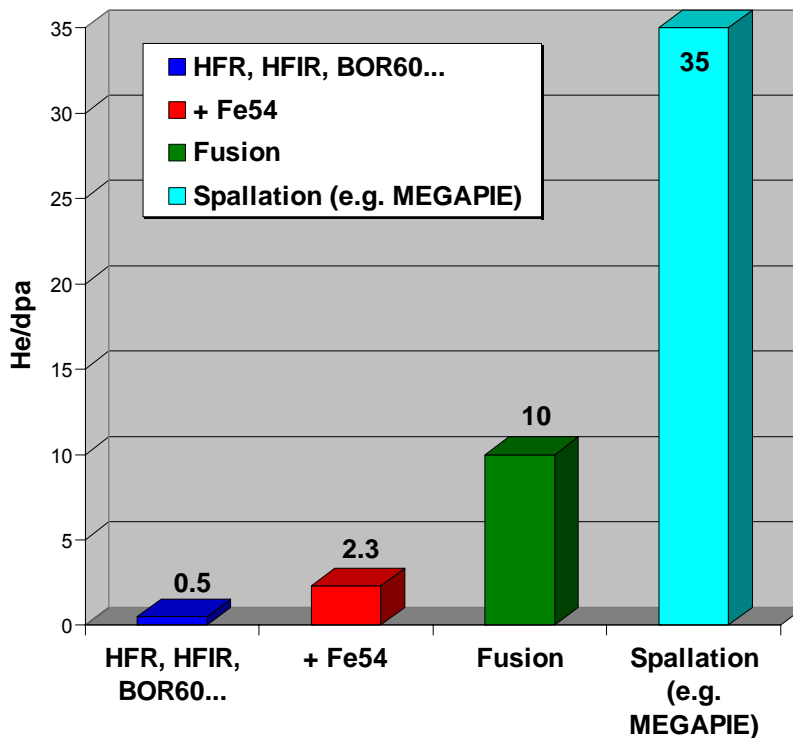
Fig. 1: Comparison of He [appm] / damage [dpa] ratios as reached in the usual fission reactors with unmodified steels, with steels where natural iron has been replaced by Fe-54 isotope, in a fusion device, and as reached by irradiation in existing spallation sources.

He distribution after irradiation

$$Fe^{54} + n \rightarrow Cr^{51} + \alpha$$

$$B^{10} + n \rightarrow ... \rightarrow 2\,\alpha$$
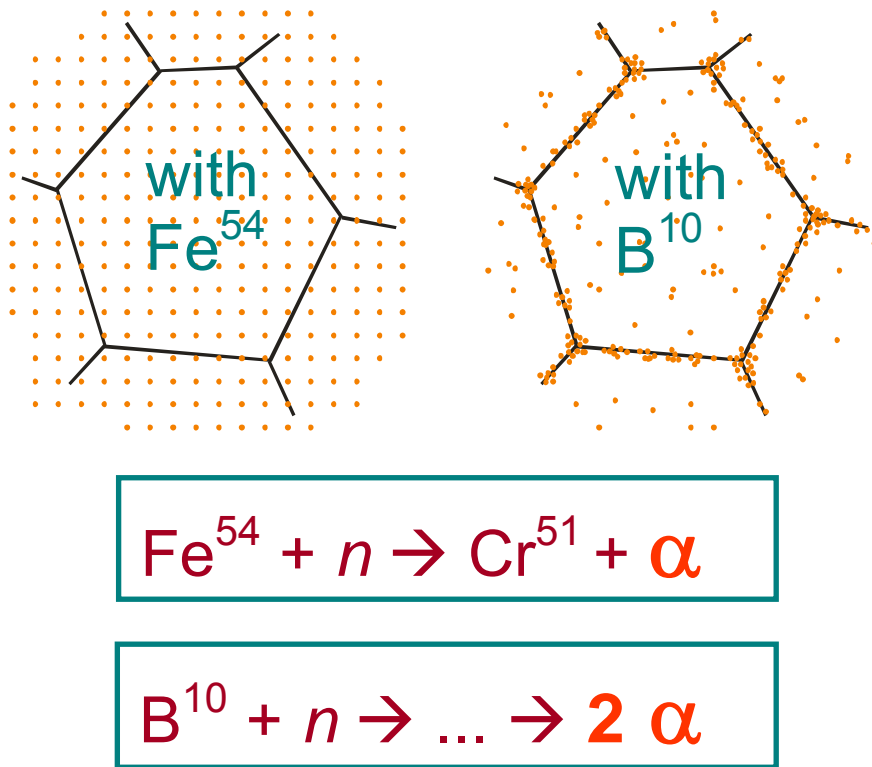
Fig. 2: Boron precipitates mainly at grain boundaries. Therefore, irradiation induced helium production is concentrated on the grain boundaries, too. Compared to the boron-10 helium production technique Fe-54 leads to a uniform helium distribution.

Results and Progress

Fig. 3: In a first step the alloy components were arc molten to pellets.

A number of different pre-tests have finally led to a more simplified production of the desired EUROFER plate as has been planned initially. Casting the heat into a suitable mould spares further forging or rolling. In a first step all alloy components have been molten to pellets in an arc melting furnace (Fig. 3). Natural iron has been included as powder (similar to the final Fe-54 isotope). The other components were available in form of foliages, small pieces, or powder. Applying this first melting step separates oxide layers and other impurities from the initial alloying components. After that the pellets were molten in a conduction furnace within a ceramic crucible in argon environment (Fig. 4). The resulting heat was then cast into a copper mould (Fig. 5). Thickness and width have been adapted to the desired plate dimensions. As can be seen from Fig. 6, the casting procedure leads to a plate with even surfaces free of oxides. In this way only a small amount of the valuable heat gets lost.

The only concern now has to be focused on the microstructure of the plate. Figure 7 shows the microstructure before and after standard heat treatment. Before heat treatment it looks inhomogeneous as expected. Further there are relatively large areas of δ-ferrite recognizable

(white fields in the lower left picture). But austenitization at 1040 °C recovers a fine grained homogeneous structure. And after annealing at 750 °C the hardness values are at about the same level as with the EUROFER steel [2]. A direct comparison with the EUROFER alloy after austenitization for 1 h at 1100 °C is given in Fig. 8. Both heats show fully martensitic microstructure with about equal grain size. Therefore, it can be expected that the plate production is possible without further forging and/or rolling.

Fig. 4: The arc molten pellets were alloyed in a ceramic crucible by induction heating.

Fig. 5: The heat was finally cast into a copper mould.

To reduce the amount of the valuable Fe-54 isotope, needed for the production of a small batch of EUROFER-Fe54, the specimen fabrication is planned as shown in Fig. 9. The final plate (6 mm thick) consists of a core of EUROFER-Fe54. Two additional stripes of standard EUROFER will be welded on both sides. Then specimens may be fabricated as indicated in Fig. 9 for the case of a Charpy specimen, i.e. the critical parts (for Charpy specimens this is the notch and for tensile specimens it is the gauge length) consist of EUROFER-Fe54 while the ends are made of standard EUROFER.

In order to find the most suitable joining of the stripes three different welding procedures (TIG with EUROFER filler wire, Electron Beam, and Laser) have been applied to EUROFER plates (further details are given in the report TW4-TTMS-004-D1 in this volume). Charpy and tensile specimens have been produced from the weld and heat affecting zones. The first mechanical tests have already shown that Electron Beam welding seems to be the best joining technique for the final EUROFER and EUROFER-FE54 stripes.

Based on the assumption that a EUROFER-Fe54 core with a width of 15 mm is sufficient for specimen fabrication and testing, an amount of 200 g of the Fe-54 isotope would suffice for 48 Charpy KLST specimens (3 mm x 4 mm x 27 mm) and 16 tensile specimens (D4 mm x 27 mm).

Fig. 6: The opened copper mould with the solidified heat.
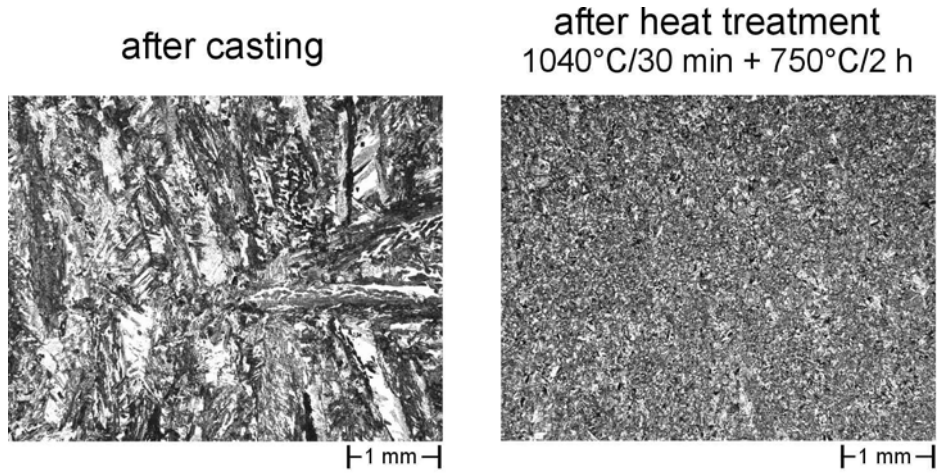
Fig. 7: Microstructure of the cast plate with and without heat treatment.
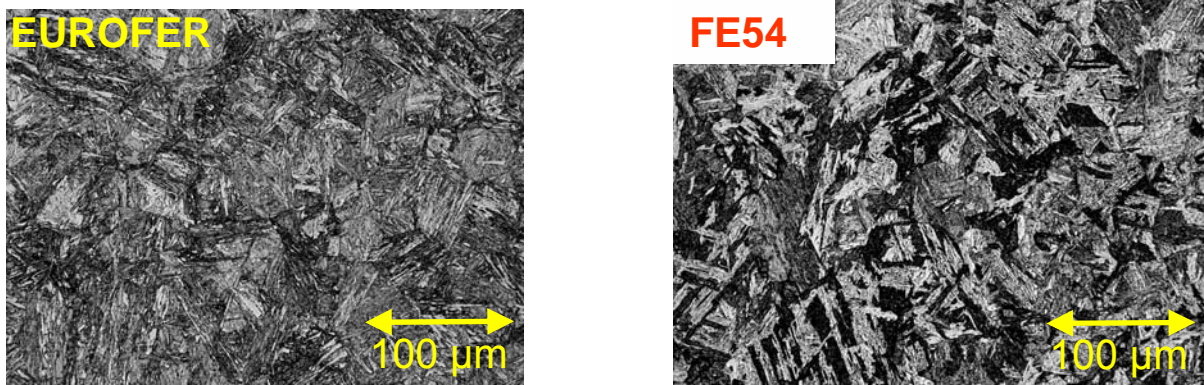
Fig. 8: After annealing at 1100 °C for 1h both EUROFER and the test heat of EUROFER FE54 show similar fully martensitic microstructures with about the same grain sizes.
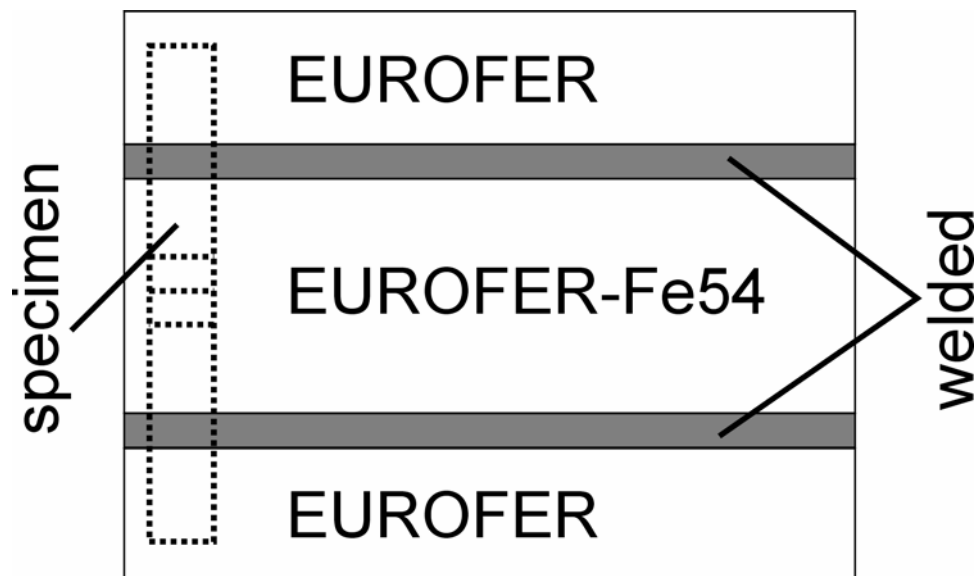
Fig. 9: Specimen fabrication. To reduce the amount of the Fe54 isotope, only critical parts of the specimens consist of EUROFER-Fe54.

Conclusions and Outlook

Up to now the feasibility for producing a small EUROFER batch with only 200 g Fe-54 isotope powder has been successfully demonstrated. By premelting, remelting, and casting it is possible to fabricate a plate in the proper dimensions which reduces the amount of waste significantly.

The ongoing and further tests focus on the optimization of the chemical composition as well as on the reproducibility of the fabrication process. The isotope will be available in April 2005. Till then the production line has to be evaluated, tested, and confirmed.

Staff:

C. Adelhelm
P. Graf
A. Falkenstein
S. Heger
U. Jäntsch
A. Möslang
M. Rieth
P. Vladimirov
H. Zimmermann

Literature:

[1] L.R. Greenwood, B.M. Oliver, S. Ohnuki, K. Shiba, Y. Kohno, A. Kohyama, J.P. Robertson, J.W. Meadows, D.S. Gelles, J. Nucl. Mat. 283-287 (2000) 1438-1442.

[2] M. Rieth, M. Schirra, A. Falkenstein, P. Graf, S. Heger, H. Kempe, R. Lindau, H. Zimmermann, EUROFER 97: Tensile, Charpy, Creep and Structural Test, Forschungszentrum Karlsruhe, Scientific Report FZKA 6911, October 2003.

TTMS-002
Metallurgical and Mechanical Characterisation

TW1-TTMS-002 D19
TW2-TTMS-002a D19
Creep Fatigue Testing on EUROFER

1. Objectives

A structural component like a Test Blanket Module (TBM) is subjected during service to alternating thermal and mechanical stresses as a consequence of the pulsed reactor operation. Since the operating temperatures of a future DEMO reactor increase due to economic considerations, the knowledge of the reasons of the creep fatigue endurance of Reduced Activation Ferrite/Martensite (RAF/M) steels like F82H mod. and EUROFER 97 becomes more important.

The Thermal-mechanical Fatigue (TMF)-experiments with hold times of 1000 s on EUROFER 97 with a heat treatment of 1040°C, 31 min/air + 760°C, 90 min/air and with temperature changes between 100°C and 450 to 600°C are finished and will be reported.

We are implementing proofed results of the Low Cycle Fatigue (LCF) tests on EUROFER 97 into the HTM-ALLOY data bank system

2. TMF-experiments on preirradiated specimens

The modified TMF-test facility for post-irradiation TMF experiments had been installed in the hot cell area of CRISM, St. Petersburg. (Under binational WTZ –contact between FZK and CRISM "Prometey") The reference experiment under hot cell conditions had been interrupted due to facility failure. The repair in the hot cells is very difficult. Furthermore the bi national WTZ-contract between CRISM, St. Petersburg, Russia, and FZK, Germany cannot be extended due to new German national regulations and was replaced by a small contract between both institutions, starting in November 2004.

2. Microstructural evaluation

The detailed microstructural examination of fatigued EUROFER-ODS will be continued to understand the damage contributions resulting from fatigue and creep-fatigue damage.

But also the binational WTZ-contract between UNR, Argentina and FZK, Germany could not be extended due to new German national regulations and was replaced by a small contract between both institutions, starting in November 2004.

Staff:

J. Aktaa
M. Klotz
C. Petersen
M. Pfeifenroth
R. Schmitt

Literature:

A. F. Armas, M. Avalos, C. Petersen, R. Schmitt and I. Alvarez-Armas: „ Cyclic Instability of Martensite Laths in Reduced Activation Ferritic/Martensitic Steels", J. of Nucl. Mat, 329–333 (2004) p. 252-256.

TW1-TTMS-002 D22
TW2-TTMS-002a D22
Fatigue Crack Growth of EUROFER 97

The objectives of these two tasks are the investigation of fatigue crack growth in EUROFER 97 at room temperature (RT), 300 and 500°C, respectively, and determining relevant data required for the assessment of cracks detected in first wall components build from EUROFER 97.

At the beginning of the reporting time period the preparation of fatigue crack growth experiments was finished so that the tests required could be started. For the tests CT specimens are used which have a geometry according to ASTM E 647 – 95a. The fatigue crack growth is measured during the test using the potential drop method which was calibrated and qualified in preliminary tests. For the high temperature tests a furnace with 3 resistive heated, separately controlled zones is used.
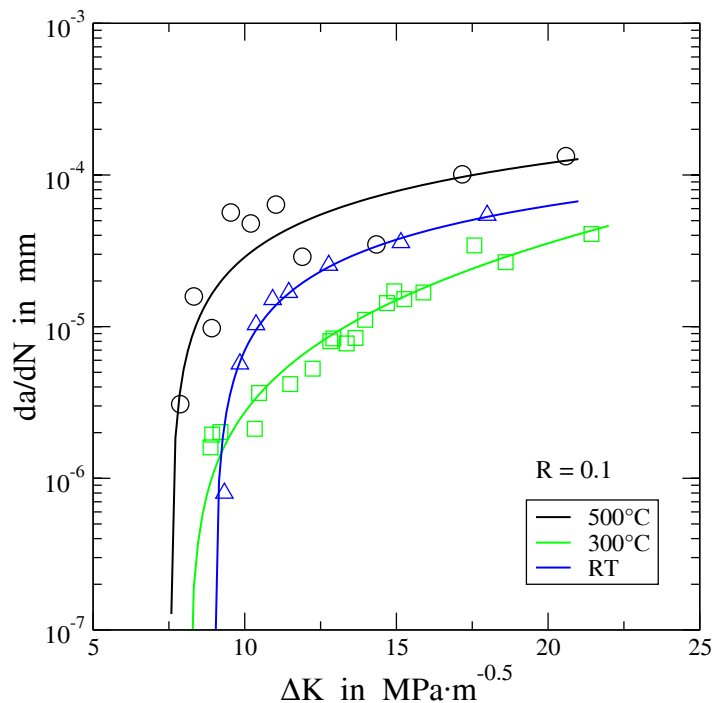
Fig 1:   Fatigue crack growth rate versus stress intensity range for R=0.1 at RT, 300 and 500°C.

Within the reporting time period fatigue crack growth tests have been performed at RT, 300 and 500°C with two different R-ratio, R=0.1 and R=0.5, respectively. In order to determine the crack growth rates particularly in the range close to fatigue crack threshold the loading level in each test is dropped in small steps - keeping the R-ratio constant - until crack growth stop is observed. Figure 1 shows representatively the courses of fatigue crack growth rate da/dN over stress intensity range DK determined for R=0.1 at the three temperatures in comparison. It can be recognized that the fatigue crack threshold as expected decreases when increasing the temperature whereas the fatigue crack rate at higher DK values shows a non-monotonic dependence on the temperature with the lowest value at 300°C and the highest value at 500°C. The low value at 300°C can be explained by stronger crack tip blunting due to decreased yield stress in comparison to that at RT. At 500°C creep and oxidation become significant yielding to higher crack growth rate.

For R=0.5, s. Figure 2, a non-monotonic dependence on the temperature of the fatigue crack rate at DK values higher than the fatigue crack threshold has not been observed. In addition the dependence on the temperature is not as high as it is for R=0.1. Also the fatigue crack threshold depends insignificantly on the temperature.
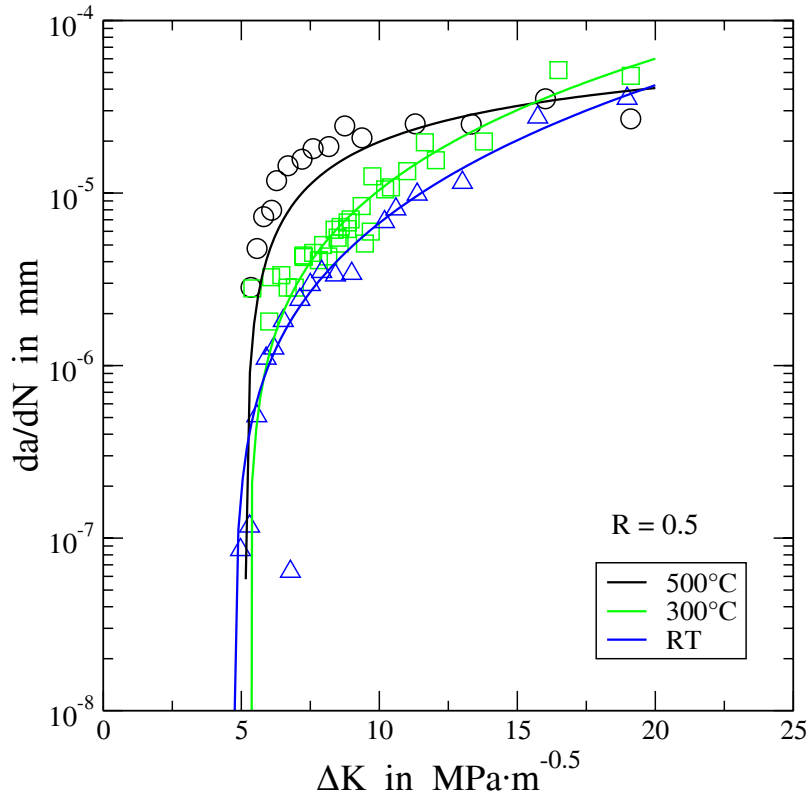
Fig. 2: Fatigue crack growth rate versus stress intensity range for R=0.5 at RT, 300 and 500°C.

Meanwhile the fatigue crack growth experiments have been finished and a final report is in preparation.

Staff:

J. Aktaa
M. Lerch

TTMS-004
Qualification Fabrication Processes

TW4-TTMS-004 D1
**Improve Design Limits of Welded Components through Improved Post Weld
Heat Treatments**

Overview

In contrast to austenitic steels untreated welded joints of ferritic-martensitic steels like
EUROFER suffer from hardening and embrittlement due to uncontrolled martensite formation
in the vicinity of the heat affecting zones. To improve the joint performance usually two-step
post welding heat treatments are applied where the temperature of the first step varies
around 1050 °C and the second between 700 °C and 780 °C. With respect to specific Test
Blanket Module (TBM) design and assembly requirements there is a significant discrepancy
between the optimum post heat treatment and its applicability. Therefore, the main objective
is the qualification of sub-components consisting of EUROFER welded joints. The
investigation of suitable and applicable post heat treatments for different available (and also
applicable) welding technologies takes place in close co-operation with the TBM design
teams.

The limiting factors for the post welding heat treatment result from the following
considerations: If future blanket modules will be assembled including beryllium pebble beds,
annealing temperatures for these structures have to be (significantly) below 750 °C.
Otherwise the beryllium pebbles would interact with their surrounding. That is, two-step post
welding heat treatments can not be applied to welded joints in the near vicinity of Be pebble-
beds. For the other parts, however, annealing temperatures above 1050 °C could be applied
in principle. But – of course – the larger the joint structures, the more extensive and
inapplicable the annealing efforts. Therefore, in these cases annealing temperatures as low
as possible would be desirable, too.

Due to the fact that up to now there are no sufficient documented investigation results on
EUROFER weldments available, during the present task all steps have been recorded in
detail following the according standards. This allows for reproduction of all preparation,
fabrication, and testing procedures.

Tungsten-Inert-Gas (TIG) with EUROFER filler wire, Electron Beam (EB), and Laser welding
have been applied to EUROFER plates in the condition as received. For the beam welds
beam stoppers (0.5 mm x 0.5 mm) were milled at the joining parts. The TIG weld geometry
was ½ V joint with a root height of 1 mm and a distance of 2 mm. All welds were fabricated
parallel to the last rolling step direction (applied during the EUROFER plate production).

Progress

The work was started with the investigation of pre-welding treatments. Spark eroded
EUROFER surfaces show severe oxidation. Welding such surfaces would neither allow for
reproducible nor for optimum joints. Therefore, a standard industrial applicable pickling
treatment was applied to the EUROFER filler wire and to the plates. Even though the result
was recognizable, it was not possible to avoid a remaining thin surface film. Therefore,
immediately before welding the joining plate surfaces have been dry milled by 0.1 mm and
the filler wire has been emerized blank.

Prior to final welding, pre-tests were performed to adjust the EB and Laser beam intensity to
the 5 mm plates. TIG welds on 5 mm and 10 mm plates were manually fabricated in a
vacuum box flooded with inert-gas. All relevant parameters like current, voltage, feed rate,
etc. were recorded. After that, the microstructure in the vicinity of the joints was examined

and specimens (charpy and tensile) were fabricated perpendicular to the weld line (and therefore also to rolling direction). In the case of charpy specimens, the notch was positioned at the weld center as well as at the heat affecting zone (HAZ).

Results

Prior to specimen fabrication the microstructure of the different welds have been investigated (see Fig. 1). Both TIG welds show coarse grain formation which is typical for solidification micro structures that form during the welding cycles. Both beam welds don't show this severe grain coarsening. But as can be seen for the case of the EB weld, the beam intensity was too low for a complete fusion of the beam stopper area. Therefore, the notches of the charpy specimens were fabricated on this side.
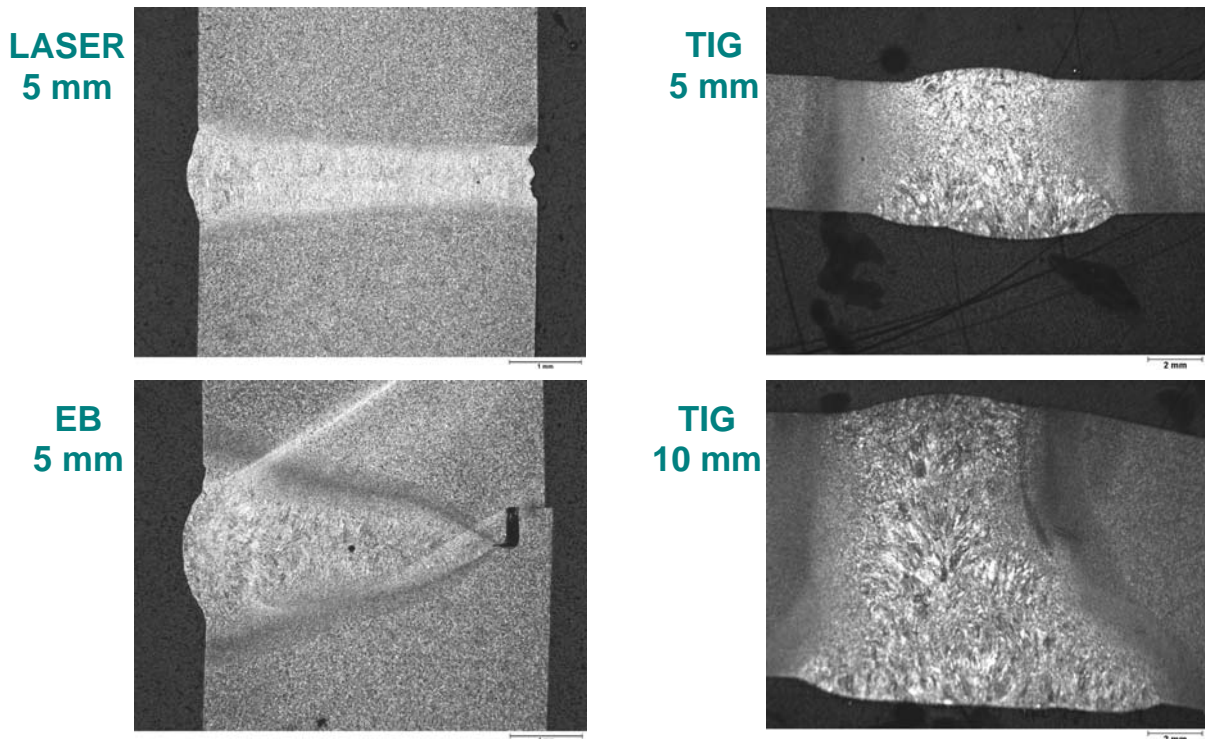
Fig. 1: Microstructure of the different welds. It can be seen that the intensity of the EB was to low to for a complete fusion of the beam stopper. Therefore, the V-notch has been placed on this side for fabrication of charpy specimens.

Also typical for TIG welds are the softened regions in the HAZ as can be seen from the hardness profiles given in Fig. 2. While the lateral extensions of the beam welds are significantly smaller, softening in the HAZ cannot be observed here.

From these microstructural examinations it is already clear that TIG welds need a full two-step heat treatment (austenitization plus annealing) in order to recover a uniform distributed fine grain. Without that, the weld will suffer from severe embrittlement which has been confirmed by charpy tests. But charpy tests on beam welded specimens have shown surprisingly good results, even without post-weld heat treatment. Therefore, the first post-weld heat treatment applied to the welds was pure annealing at 700 °C for 2 hours. The charpy test results are shown in Figs. 3 (welding zone) and 4 (HAZ).

Compared to the EUROFER base material, the Ductile-to-Brittle-Transition-Temperature (DBTT) of Laser and EB welds is almost comparable: There is only a shift by about 10-20 K. The observed higher Upper-Shelf-Energy (USE) for EB welded specimens is artificial and reflects from the fact that the crack propagation proceeds not perpendicular to the applied

stress but along the HAZ of the EB weld. Furthermore, the unacceptable poor results from TIG welds demonstrate their need for a two-step heat treatment.
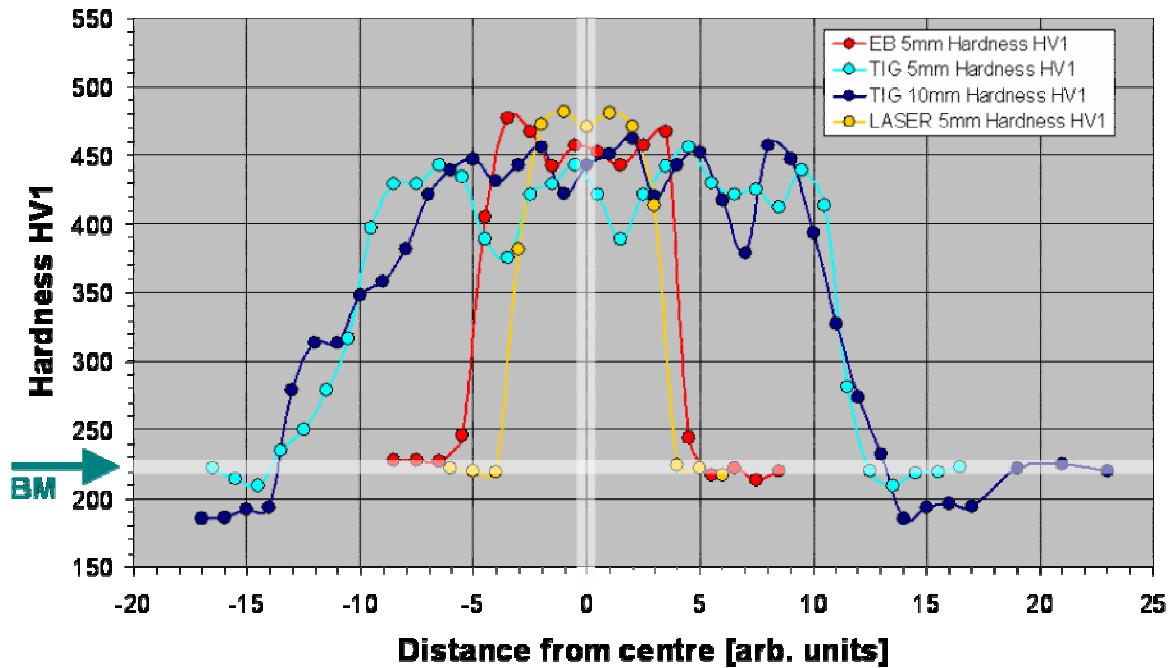
Fig. 2: Hardness profiles of the welds. The arrow labelled BM, indicates the hardness level of the base material. As can be seen, especially the 10 mm TIG weld shows an extended soft region in the HAZ.

Fig. 3: Charpy test results of the different welds after annealing at 700 °C for 2 hours. The notch of the charpy specimens was fabricated in the center of the welds.

Charpy testing the HAZs (Fig. 4) shows about the same results for the embrittlement behaviour of the beam welds. It is obvious that the results for TIG welds are better in the HAZ compared to the welding zone, since here – as previously mentioned – the microstructure consists of a fine grained softened area.

Charpy Tests with Notch in Heat Affecting Zone
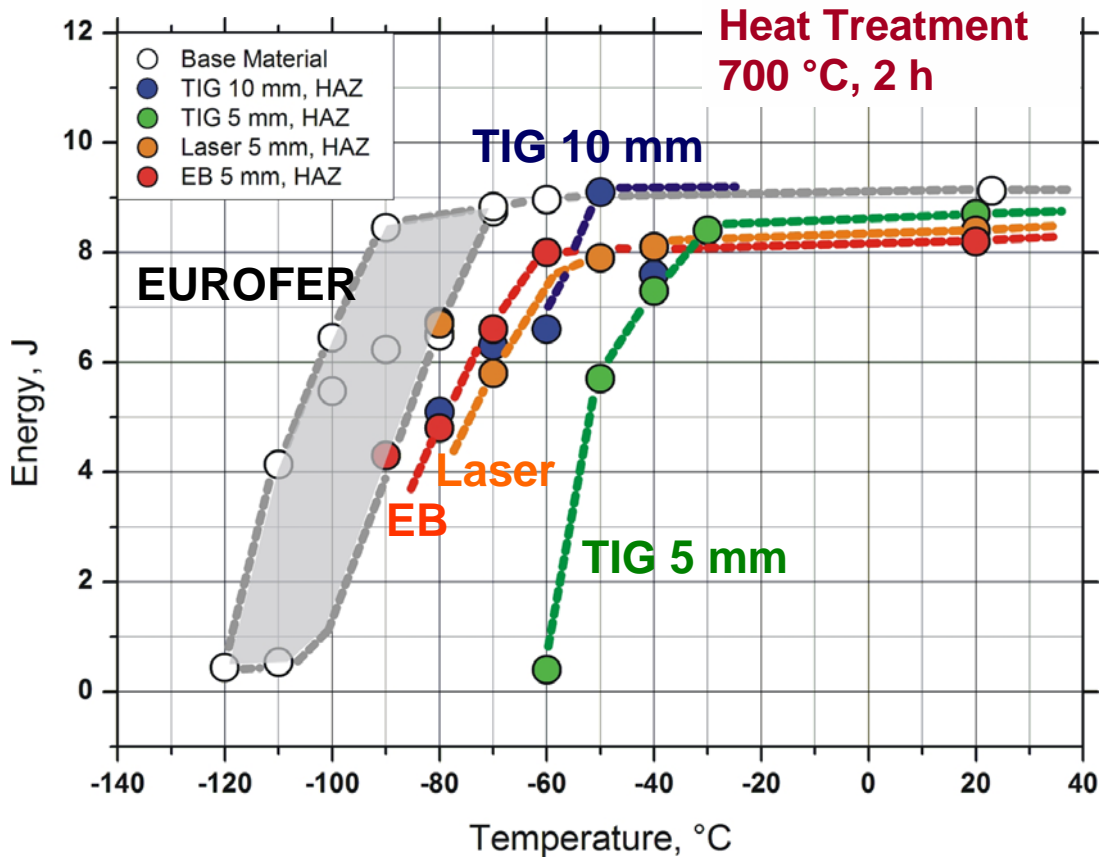
Fig. 4: Charpy test results of the different welds after annealing at 700 °C for 2 hours. The notch of the charpy specimens was fabricated in the HAZ of the welds.

Conclusions

The most important and to some extent surprising result of these investigations is that EUROFER may be welded by EB or Laser techniques without the need for a complete two-step post-welding heat treatment. Though detailed microstructural examinations have shown sporadic bubble formation, the embrittlement behaviour of these beam welds is just slightly worse compared to the base material. Therefore, the result can be considered as rather encouraging for the current TBM designs including Be pebble beds.

Furthermore, it has been confirmed and demonstrated that EUROFER TIG welds are far too brittle without a subsequent two-step heat treatment, that is, fully austenitization to recover finer grain and annealing to reduce hardness.

The ongoing investigations focus on the optimization of such two-step heat treatments within the TBM design constraints. In addition, the most promising welds will be characterized more in detail.

Staff:

C. Adelhelm
A. Baumgärtner
B. Dafferner
P. Graf
A. Falkenstein
S. Heger
U. Jäntsch
R. Lindau
A. Möslang
J. Rey
M. Rieth
H. Zimmermann

TTMS-005
Rules for Design, Fabrication and Inspection

TW2-TTMS-005b D1
TBM's Design Rules

The objective of this task is the development of design rules for ITER test blanket modules (TBM) built from RAFM steels. The TBM has to be dimensioned against different kinds of failure: ductile, creep and fatigue failure taking into account the influence of irradiation. The design rules will be build up on existing codes for nuclear applications considering the life time prediction approaches developed within TTMS-005 for RAFM steels and their specific mechanical behaviour. The assessment of the design rules formulated is also a part of this task. Therefore the performance and evaluation of suitable verification experiments, among others isothermal multi-axial fatigue tests at room temperature as well as at elevated temperature, close to the operating temperature, on the reduced activation alloy EUROFER 97 are foreseen.

The isothermal multi-axial fatigue tests will be performed using tubular specimens which can be subjected to proportional and non-proportional bi-axial cyclic loadings by varying both the load path and the phase shift. In the reporting period the multi-axial test facility needed for these tests was refurbished. With this test facility, it is possible to generate independent loadings for two different directions. For the measuring of the applied strains an extensometer was developed which is able to detect axial and shear strain simultaneously. This sensor was fabricated by modifying two norm sensors of the company WAZAU, Berlin, type WAE. Thus we are able to perform fully strain-controlled experiments.

After the successful performance of preliminary experiments with the alloy 1.4914 which has similar mechanical properties as EUROFER, we fabricated EUROFER specimens with the same geometry (s. Figure 1).
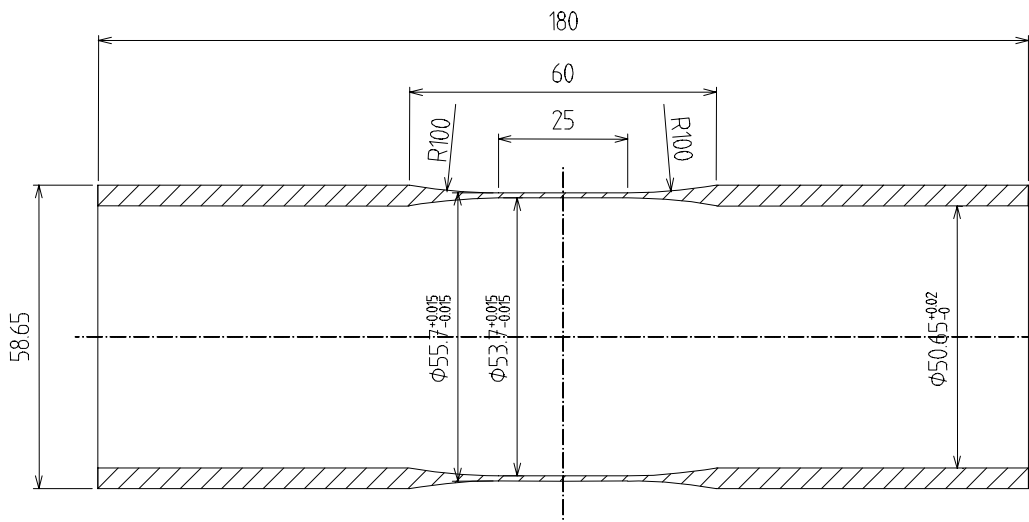
Fig. 1: Shape and dimensions (in mm) of the developed specimens for the preliminary and the finally multi-axial tests.

Proportional and non-proportional multiaxial fatigue tests were performed under purely alternating strain controlled loading. Different loading paths with different phase shifts were applied. All experiments were performed at room temperature. To compare the results of experiments at different phase shifts, the equivalent plastic strain range $\Delta\varepsilon_{pl}^{eq}$ was used.

In table 1 an overview of the until now performed experiments is given.

Table 1: Overview of the performed experiments.

No.	Phase shift [°]	Nominal amplitude [%]	$\Delta\varepsilon_{pl}^{eq}$ [%]	N_f
3	0	0.17	0.329	4007
5	0	0.17	0.345	4718
6	0	0.15	0.277	5829
7	0	0.13	0.241	19459
8	0	0.14	0.246	29233
9	180	0.18	0.1	51982
10	180	0.20	0.13	47140
11	180	0.22	0.16	14782
12	135	0.20	0.2	3052
13	135	0.18	0.175	6849
14	135	0.16	0.16	19553
15	90	0.16	0.24	6940
17	45	0.14	0.245	8503

The nominal amplitude was thereby the same for both directions (axial and circumferential). In Figure 2 the equivalent plastic strain range $\Delta\varepsilon_{pl}^{eq}$ is plotted over the nominal amplitude.
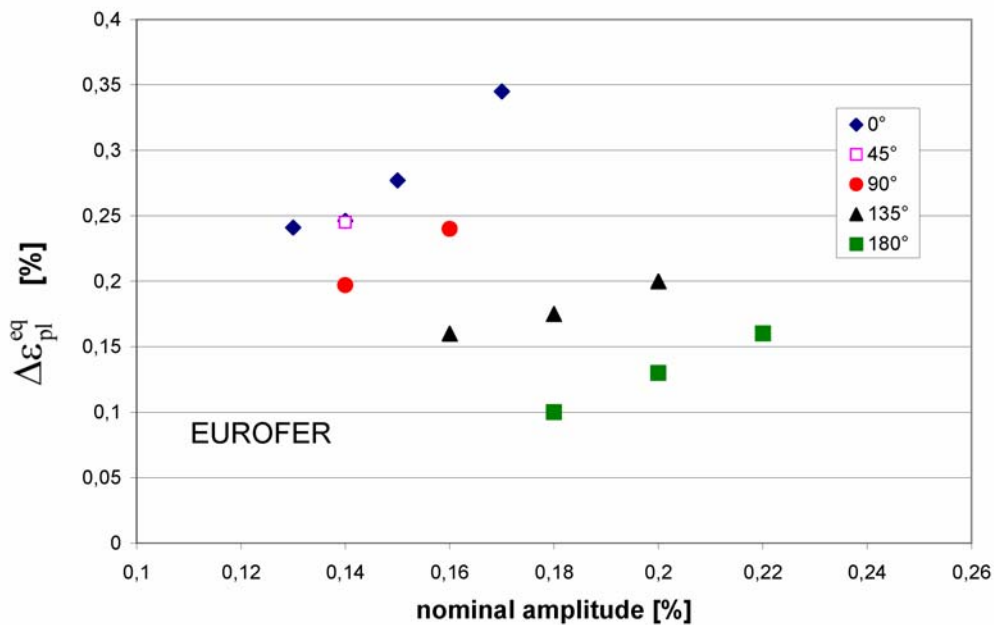
Fig. 2: $\Delta\varepsilon_{pl}^{eq}$ as a function of the nominal amplitude.

At the same nominal amplitude the resulting equivalent plastic strain range varies for the different phase shifts very clearly. This indicates the strong effect of the phase shift on the loading. For a lifetime prediction the correlation between $\Delta\varepsilon_{pl}^{eq}$ and the number of cycles is of interest. In Figure 3 the experimental determined $\Delta\varepsilon_{pl}^{eq}$ are plotted over the experimental observed lifetimes. A clearly dependence of the lifetime on the load, represented by $\Delta\varepsilon_{pl}^{eq}$, as well as on the phase shift can be noticed.
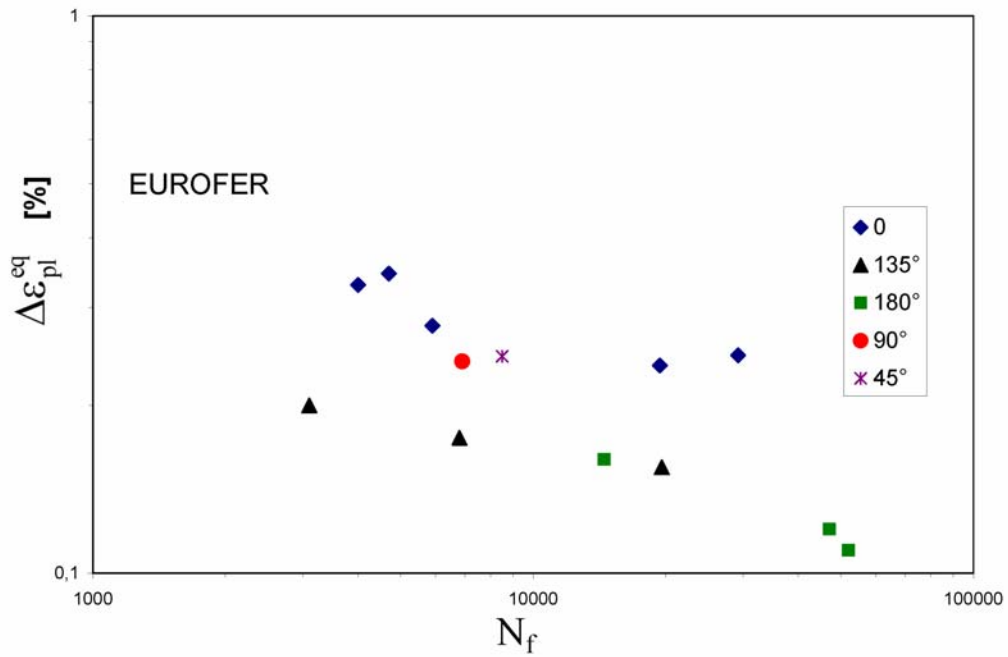
Fig. 3: $\Delta\varepsilon_{pl}^{eq}$ as a function of fatigue lifetime.

The outstanding experiments (especially for the 45° and 90° phase shift) will show the present tendencies of Figure 3 more clearly.

The experimental results will be used to verify the lifetime prediction models developed so far as well as their implementation in the design code.

Staff:

J. Aktaa
M. Weick
S. Knaak

TW2-TTMS-005b D2
Material Design Limits for TBM's Application

1. Objectives

The range of working temperature and loads on the basis of the mechanical properties including irradiation, the hydrogen effect and corrosion effect by the coolant will be defined.

The life time assessment of TBM sub-components and modules is based on finite element calculations of temperature fields and stress fields under ITER conditions and includes:

➢ The assessment and evaluation of stress and strain fields in so-called "stress-reports",

➢ The application of the SDC design rules,

➢ The comparison to material (property) limits as a function of temperature and environmental conditions.

2. Results achieved

To get started, experimental, design and simulation data already obtained in IRS/IKET of FZK related to the TBM activity have been revised. Thereby, special attention has been directed to the current TBM design, normal and accidental ITER operating conditions as well as to typical problems connected with the TBM development.

2.1 Adjustment of material parameters

To simulate a realistic behaviour of the TBM under a cyclic thermal and mechanical loading, experimental data of corresponding cyclic tests are needed. Such data stemming from a life time study of EUROFER at 450°C, 550° and 650°C [1] have been used to adjust material parameters required for a definition of an ABAQUS-own nonlinear isotropic-kinematic hardening model (see. ABAQUS/Standard User's Manual, Vol. II, Ch. 11.2.2). This model is able to account e.g. for the Bauschinger effect, a cyclic hardening with plastic shakedown as well as for a ratchetting.

To specify kinematic hardening, a ¼ of the 1st cycle is needed. Thereby, either data pairs $\sigma_i, \varepsilon_i^{pl}$ should be defined within the following ABAQUS card

*PLASTIC, HARDENING=COMBINED, DATA TYPE=HALF CYCLE

$\qquad \sigma_i, \varepsilon_i^{pl}, T$

or adjusted parameters $\sigma|_0, C$ and γ should be obtained from experimental data and used directly with the card

*PLASTIC, HARDENING=COMBINED, DATA TYPE=PARAMETERS

$\qquad \sigma|_0, C, \gamma, T$

together with the corresponding test temperature T. Here, $\sigma_i, \varepsilon_i^{pl}$ are an equivalent stress and the corresponding equivalent plastic strain, $\sigma|_0$ is the initial yield stress at zero plastic deformation and $C \& \gamma$ are parameters intended to describe the backstress α:

$$\alpha = \frac{C}{\gamma} \left[1 - \exp\left(-\gamma \varepsilon^{pl} \right) \right]$$

Thereby, γ may not depend on the temperature. Note that $\alpha_i = \sigma_i - \sigma|_0$ and therewith the backstress should vanish at zero plastic deformation.

(a)

(b)

(c)

(d)
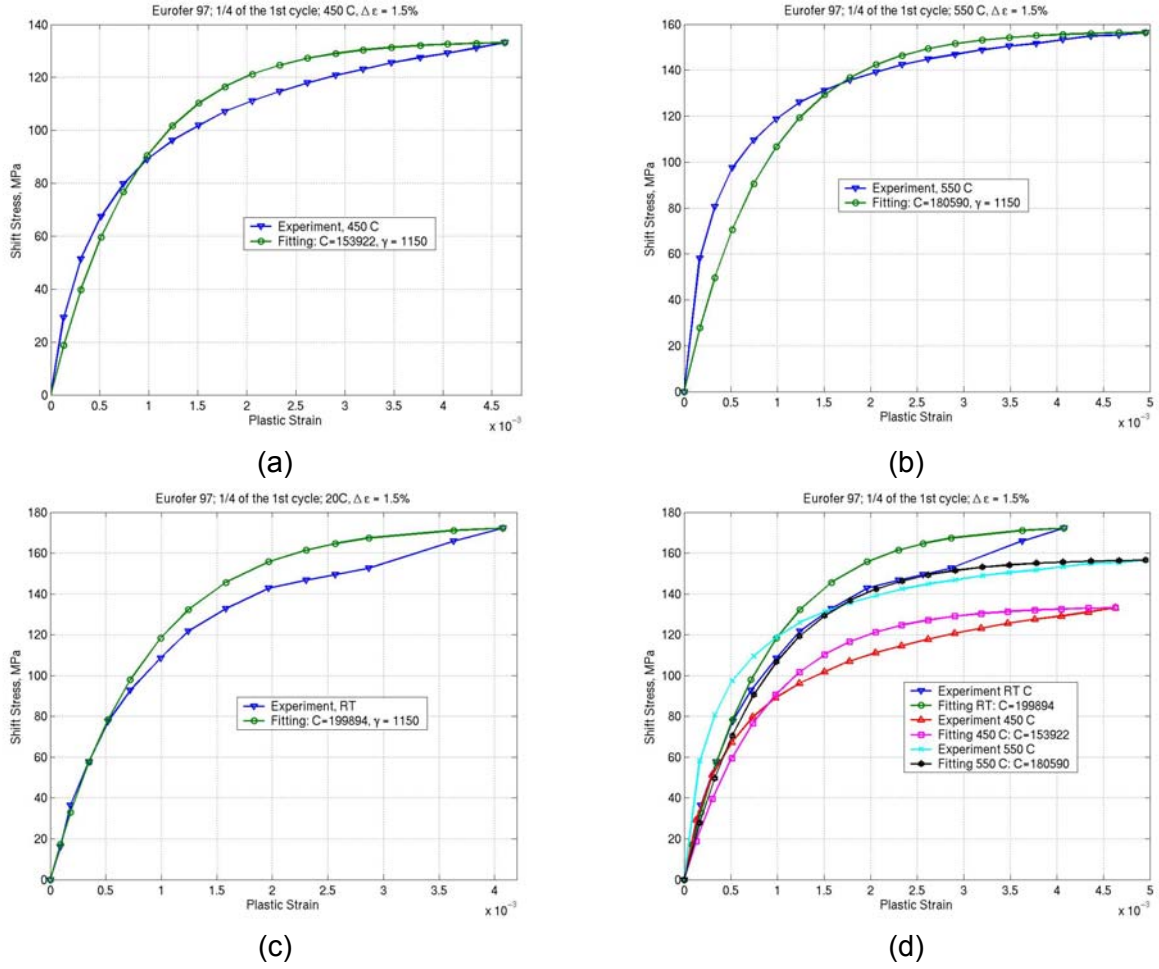
Fig. 1: Adjustment of the kinematic hardening parameters $C \& \gamma$ to the data of cycling tests with a fixed deformation range of 3% performed at different temperatures from RT up to 550°C.

Fig. 1 (a) and (b) depicts curves with the fitted parameters and corresponding experimental data for 450°C and 550°C respectively. Because of the missing data of a cycling experiment at RT, the available data of a tensile test have been used to determine the unknown parameters, see fig. 1 (c). It is probably the reason why the curve at the RT does not exhibit an expected trend: the shift stress should decrease if the temperature decreases, see fig. 1 (d). Parameter pairs obtained by fitting are listed in tab.1.

Table 1: The fitted parameter C for different temperatures. The 2nd parameter γ remains thereby constant and is equal to 1150.

T, °C	20	450	550
C, MPa	199894	153922	180590

If the backstress is known, the isotropic part of the hardening can be determined under the following assumption: The backstress remains constant for all cycles so that the yield stress σ_i^0 at the beginning of the ith cycle can be defined as follows:

$$\sigma_i^0 = \sigma_i^t - \alpha_i^s$$

with the maximum tensile stress σ_i^t and the saturated value $\alpha_i^s = \alpha_i^{max}$. The isotropic hardening can be defined again either by tabular data as

*CYCLIC HARDENING

$$\sigma_i^0, \varepsilon_i^{pl}, T$$

or by a direct specification of adjusted parameters $\sigma|_0, Q$ and b in the following card:

*CYCLIC HARDENING, PARAMETERS

$$\sigma|_0, Q, b, T$$

Within the proposed model, these parameters are used to describe the isotropic hardening by

$$\alpha = \sigma|_0 + Q\left[1 - \exp\left(-b\,\varepsilon^{pl}\right)\right]$$

with the accumulated equivalent plastic deformation ε_i^{pl}. Fig 2 shows fitting curves compared to experimental results. Note that EUROFER exhibits a softening instead of the usual hardening.
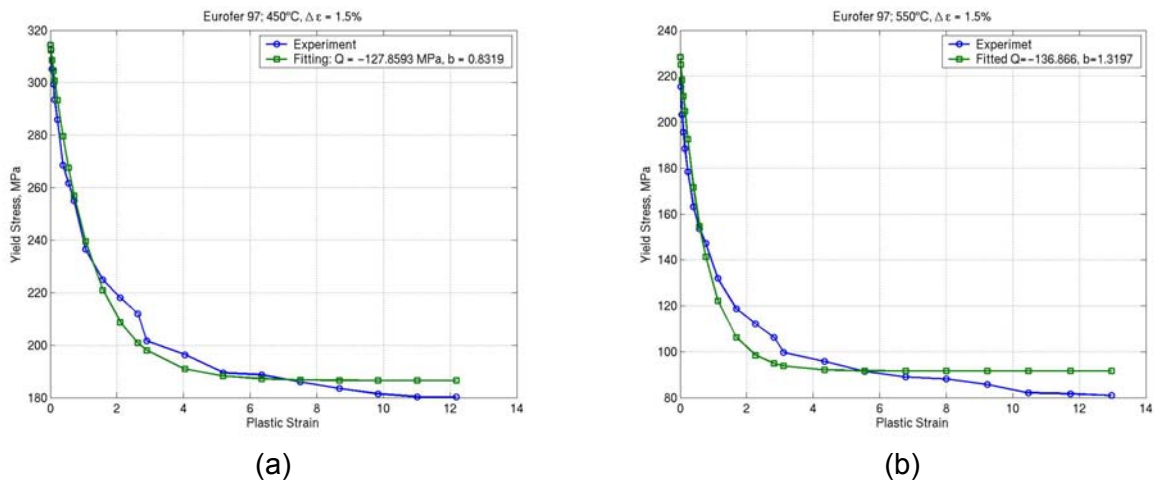
Fig. 2: Adjustment of the isotropic hardening parameters $Q \& b$ to the data of cycling tests with a fixed deformation range of 3% performed at 450°C (a) and 550°C (b).

Adjusted parameters are listed in tab.2.

Unfortunately, there is no possibility to determine these parameters for RT since only one point corresponding to the zero plastic deformation is available. This point results however in a data line for the tabular definition mentioned above. For this reason, the isotropic hardening has been defined by tabular data, whereas the kinematic hardening has been defined directly.

Table 2: The fitted parameters $Q \& b$ for 450°C and 550°C.

T, °C	450.00	550.00
Q, MPa	-127.86	-136.87
b	0.83	1.32

2.2 Verification of the material model

To verify the material model described above, a 2D model of a quarter of the TBM has been created according to the current design and meshed using PATRAN. The model is shown in fig. 3 together with mechanical constraints. The only mechanical load in the non-accidental operating mode is the hydrostatic coolant pressure of 80 bar = 8 MPa in the cooling channels.
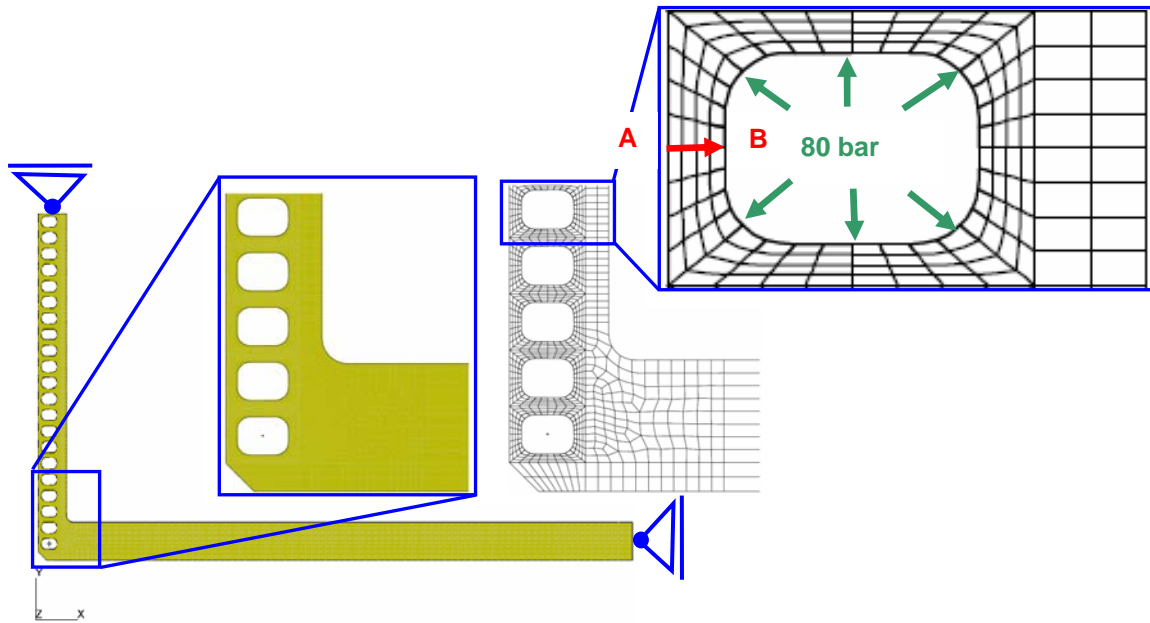
Fig. 3: A 2D TBM model with mechanical constraints and loads.

Thermal loads consist of a heat flux of 250 or 500 kW/m^2 ("MARFE") on the plasma-facing side as well as a heat flux of 60 kW/m^2 and of 35 kW/m^2 on the vertical and horizontal interior respectively due to breeder units, see fig. 4. Recall that the aim of this simulation was not to determine a realistic temperature distribution, but rather to test the material model. For this reason, boundary conditions depicted in fig. 4 have been considered. Results of a thermal computation are shown also in fig. 4.
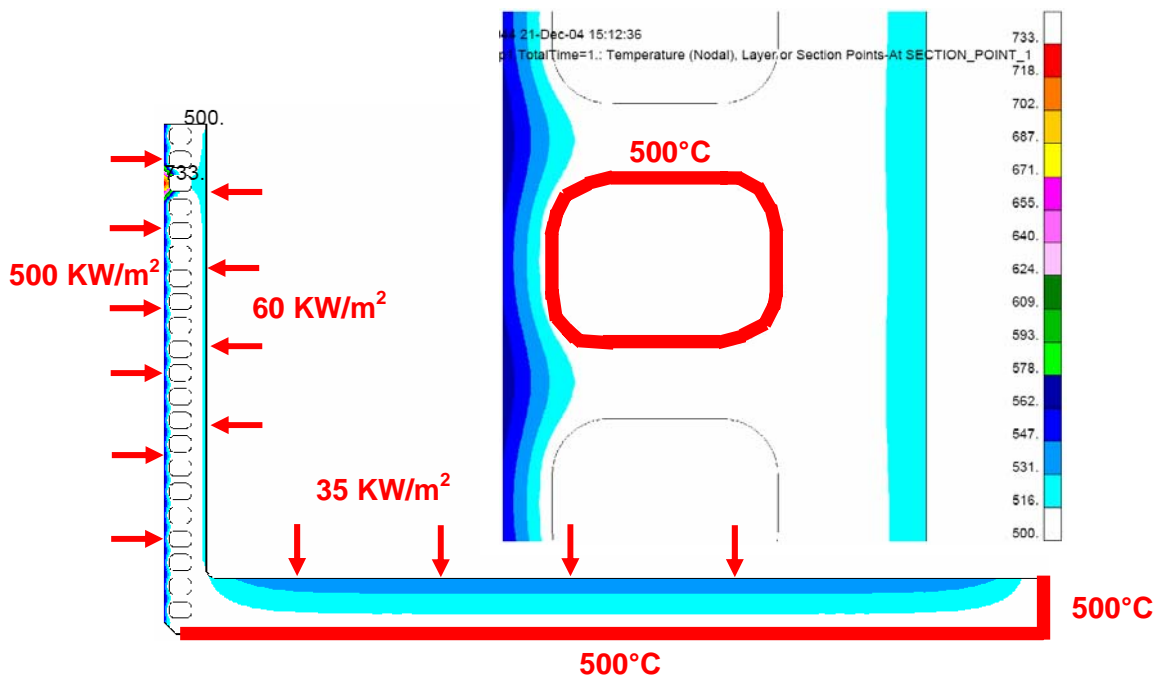
Fig. 4: Temperature distribution due to the depicted thermal constraints and loads.

The obtained temperature distribution has been used in a mechanical computation with constraints and loads shown in fig. 3. Thereby, the component has been 5 times subjected to the operating conditions and cooled again to RT. A special attention has been thereby directed to the change in the stress and plastic strain from cycle to cycle along the path AB depicted in fig. 3. The time evolution of the maximum equivalent plastic strain, accumulated equivalent plastic strain and equivalent stress are shown in fig. 5. The main result is that the

plastic deformation increases with each cycle and the material softens with time. The step time in the simulation corresponds to the real process time: 30 sec to bring the coolant pressure and the full thermal power and 100 sec to cool the component to RT.
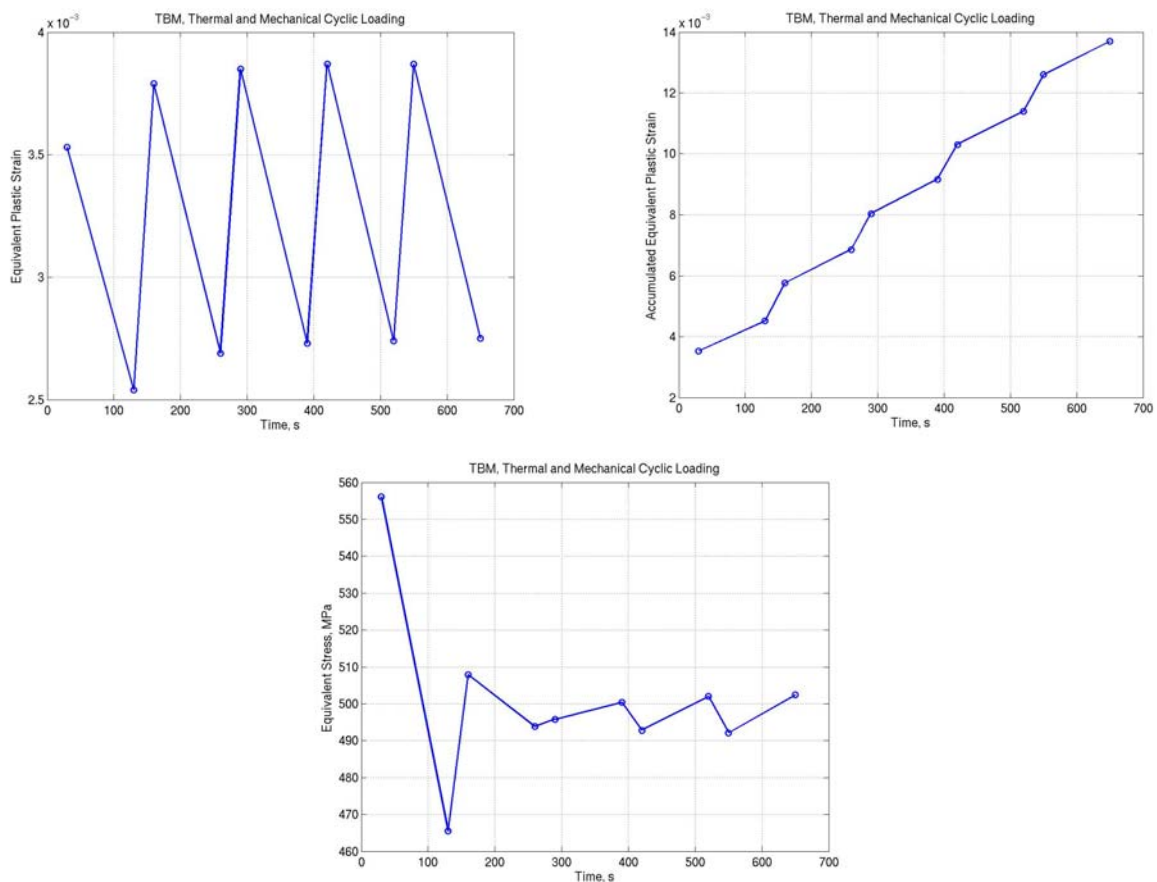
Fig. 5: Time evolutions of the maximum equivalent plastic strain (top left), accumulated equivalent plastic strain (top right) and the equivalent stress along the path AB depicted in Fig. 3.

4 Conclusions and outlook

The test simulation has proven that conditions similar to the ITER operating conditions lead to an accumulation of plastic deformation in a critical region of the FW under cyclic thermal and mechanical loads described above. It means that further simulations considering extreme heat fluxes and pressures should be carried out to check the range of admissible loads and to verify existing design rules.

On the other hand, further data of cyclic tests are needed to enhance the available material parameters e.g. at RT.

Furthermore, a consideration of creep would provide a more realistic process description and should be kept in mind as one of the next modelling steps.

Staff:

R. Sunyk

Literature:

[1] J. Aktaa, R. Schmitt, Creep-fatigue Lifetime Prediction Rules for Ferritic Martensitic Steels, FZKA 6931, May 2004

TW2-TTMS-005b D4
Creep-fatigue Lifetime Prediction Rules for Irradiated EUROFER

The objectives of this task are the modification of the lifetime prediction model developed in TTMS-005a D4 [1] for RAFM steels under creep fatigue conditions taking into account the irradiation influence and the verification of the modified model by applying it to EUROFER 97 in the post-irradiated state.

Since the post irradiation investigations of EUROFER 97 are still in preparation the modification of the lifetime prediction model will be preliminary carried out on the base of data and knowledge published in the literature about the monotonic and cyclic deformation and damage behaviour of irradiated materials similar to EUROFER 97. The proper literature study was started already last year and has been finished within the reporting time period. According to the outcome of this study irradiation dose driven terms in the evolution equations of hardening have been proposed taking into account the irradiation induced hardening and its influence on damage. This modification has been found to describe qualitatively the observed behaviour of F82H in irradiated states.

In addition, within the reporting time period the lifetime prediction model developed, which consists of a coupled deformation damage model, has been implemented in the finite element code ABAQUS providing a tool for the lifetime assessment of components made by EUROFER 97. The implementation has been conducted developing a user subroutine UMAT which will be tested at the moment simulating thermal fatigue tests performed on EUROFER 97 in the reference (unirradiated) state. It has been found that the cyclic softening of EUROFER 97 might be a serious problem as far as thermo-mechanical loading is considered because it yields to deformation localization and failure could occur due to deformation instability rather than to creep and/or fatigue.

Staff:

J. Aktaa

Literature:

[1] Aktaa, J., R. Schmitt, "Creep-fatigue lifetime prediction rules for ferritic martensitic steel. (Final report, task: TW2-TTMS-005a, D4)," Wissenschaftliche Berichte, FZKA-6931, 2004.

TW2-TTMS-005b D7
Small-scale Fracture Mechanics Specimens

1. Objectives

An integrated approach for transferability of FM rules in the ductile region for RAFM steels will be developed. The aim of the work is to find a convenient model for a fracture mechanical experiment, in particular for the Three-Point-Bending (3PB) experiment performed for variously sized samples. Such a model should yield correct results (e.g. crack tip fields and J-integrals) independent of the sample size i.e. should be based on micromechanics.

This approach includes

− FE analysis of specimen for determination of global fracture mechanics parameters,

− Micromechanical based material modelling (Gurson and Lemaitre-type coupled plasticity-damage models),

− Adjustment of fracture mechanics model parameters,

− Adjustment of model parameters. (underlying deformation and damage model),

− Design and optimization of sub-sized CT and bend-bar specimens,

− Mechanical experiments (tensile-hold-unloading) for determination of parameter of the deformation and damage model.

2. Activity status at the beginning of 2004

First test simulations have been performed up to the end of 2003. The constitutive model used in these simulations was either the linear elasticity or the simple plasticity with conventional material parameters of constructional steels. A usual focused mesh with singular elements has been used in the crack-tip vicinity for both elastic and plastic computations. The J-integral has been thereby evaluated automatically. Some attempts to perform a 3D-simulation have been also carried out.

3. Results achieved

The aim of the activity was to model FM (3PB) experiments performed in IMFII of FZK. During these experiments, standard (90 mm x18 mm x9 mm = LxHxB) as well as subsized (30 mm x6 mm x3 mm) specimens manufactured from Eurofer 97 and Manet II have been broken quasistatically and recorded force-displacement diagrams have been used to obtain an initial critical value J_C of the J-Integral. The experiments show that all samples manufactured from Manet II exhibit a brittle behaviour, whereas the Eurofer samples are ductile.

3.1 Determination of material parameters

Material parameters for Eurofer 97 such as the Young's modulus, Poisson's ratio, initial yield stress $R_{0.2}$ as well as the isotropic hardening behaviour have been obtained from 2 tensile tests performed at IMF II of FZK. An averaged experimental true stress-vs.-logarithmic strain curve has been used for the purpose of determination of the Young's modulus. Thereby, the obtained value $E = 187800 MPa$ is smaller than a usual value for steels ($210000 MPa$). The same curve allowed also a determination of the elastic limits $Rp_{0.1} = 510 MPa$ and $Rp_{0.2} = 545 MPa$ as well as data pairs σ_i, ε_i^{pl} beginning with the line $\sigma_0 = 402\ MPa$, $\varepsilon^{pl} = 0$

approximating the curve piecewise linearly and being used within the following ABAQUS card

*PLASTICITY

$$\sigma_i \, , \, \varepsilon_i^{pl} \, , T$$

to define an isotropic hardening behaviour of the material. The Ramberg-Osgood parameters $\alpha \, \& \, n$ intended to describe the well-known constitutive law of the deformation plasticity

$$\frac{\varepsilon}{\varepsilon_0} = \frac{\sigma}{\sigma_0} + \alpha \left(\frac{\sigma}{\sigma_0} \right)^n \text{ with } \varepsilon_0 = \sigma_0 / E$$

have been also obtained ($\alpha = 0.52$, $n = 13$). An application of this constitutive law using

*DEFORMATION PLASTICITY

$$E \, , \, \nu \, , \, \sigma_0 \, , \, n \, , \, \alpha \, , \, T$$

instead of the *PLASTICITY card leads however to a stable solution only within the linear material response region and fails as soon as the material behaviour becomes non-linear.

3.2 FE modelling

Fig. 1 shows the discretized model of the ½ of the subsized specimen with mechanical constraints and mesh details in the crack-tip vicinity. The model includes a fin transferring the applied displacement and a bearing fixed vertically. The simulations have been performed displacement controlled (red arrows). Thereby, the applied displacement is 2.43 mm and 5.25 mm for the subsized and standard samples respectively as follows from an analysis of recorded applied displacement-vs.-time and force response-vs.-time curves.
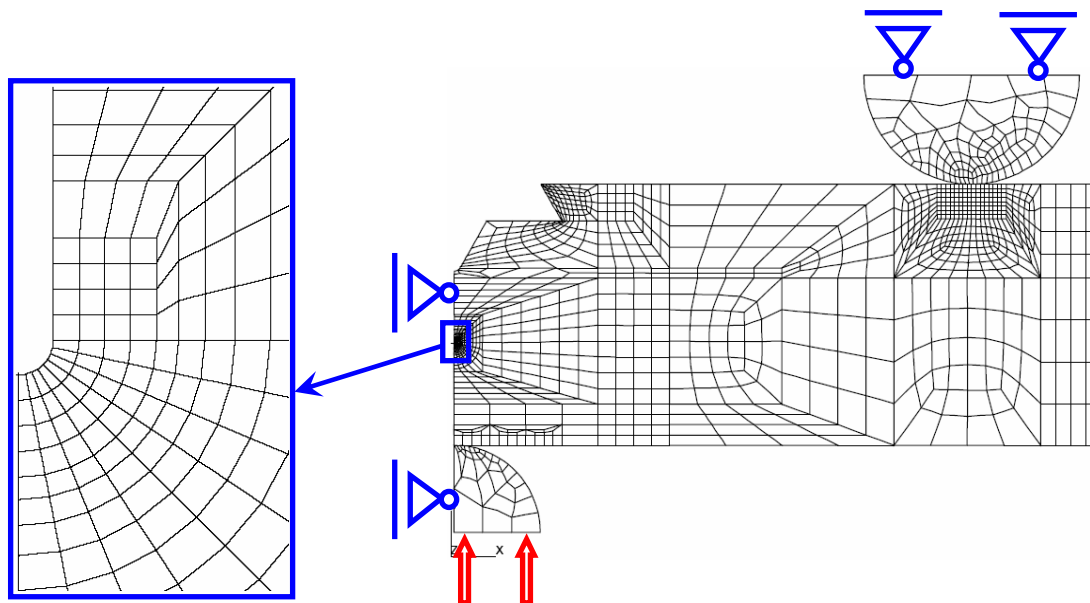
Fig. 1: Discretized subsized sample; the red arrows depict the area where nodal displacements are prescribed.

The first problem was to determine an optimum mesh in the crack-tip vicinity. For this purpose, the simulation has been performed using three blunted mesh families similar to the mesh fragment in fig. 1 near the crack tip, whereby 8-noded isoparametrical plain strain elements with reduced as well as full integration scheme have been used in the model.

The comparison of the different meshes is based on a comparison of different field values in the crack tip vicinity. Firstly, the deformation, which occurs near the crack tip should be checked in respect of its physical admissibility. It is evident that the reduced integration leads to the so called "hourglassing" effect when elements are twisted.

Additionally, a tangent to the blunted crack at the symmetry plane should be directed horizontally to provide a smooth connection of both model parts. Neither full nor reduced integration fulfil this requirement. The hourglassing occurs at approximately 20 % (t = 1000 to 1300) of the total step time. Up to this time, also the tangent criterion is fulfilled for both reduced and full integration so that it is not possible to choose a mesh on the basis of the geometrical criterions alone.
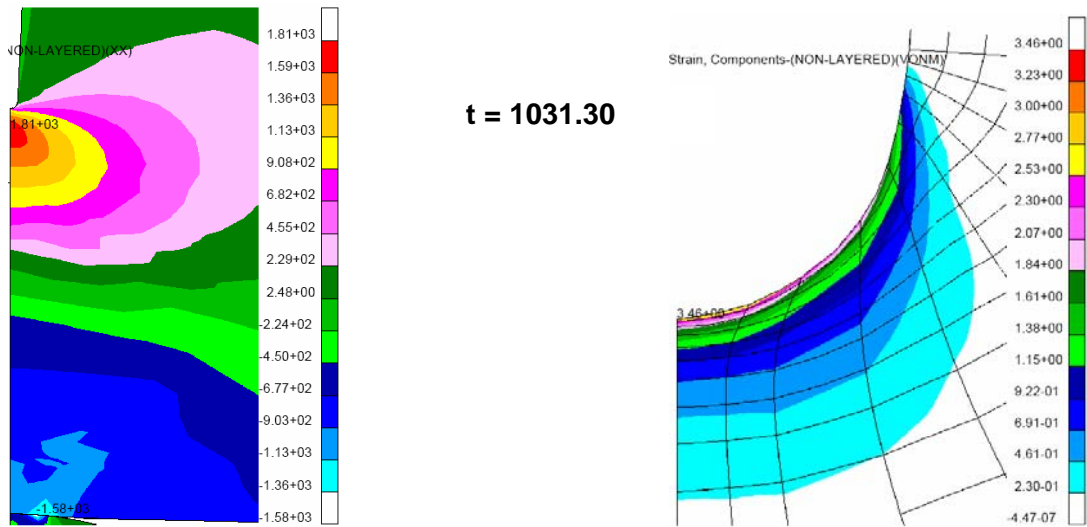
Fig. 2: Distribution of the stress component σ_{xx} (on the left, MPa) and the plastic strain component ε_{xx}^{pl} in the crack tip vicinity obtained using the model 1a.

However, besides the physical admissibility of the deformation other additional criterions of the mesh choice can be considered. For instance, the plastic strain ε_{xx}^{pl} should be positive as well as no compressive stress σ_{xx} may occur in the crack tip vicinity. The failure of both criterions occurs using the full integration earlier than using the reduced integration. Under these considerations as well as based on a comparison of the computed J-integral with the values obtained from the experiment (see below), 2 mesh families labelled as 1a & 2a have been chosen. Thereby, the size of the smallest element is 1.917 μm x 7.433 μm for 1a and 1.221 μm x 2.954 μm for 2a. Furthermore, 1a and 2a contain 9 and 13 elements along the blunted crack respectively. Fig. 2 represents a distribution of the stress component σ_{xx} and plastic strain component ε_{xx}^{pl} along the ligament for the mesh 1a at such a step time when the deformation is still physical plausible.

As the next step, the standard-sized specimen has been meshed with mesh parameters in the crack tip vicinity corresponding to the mesh parameters of the model 1a. To overcome the localisation of the plastic deformation occurring near the crack tip, another stronger hardening, see fig. 3, has been used in this simulation besides the hardening behaviour given by the experimental curve shown in fig. 3 (blue curve).
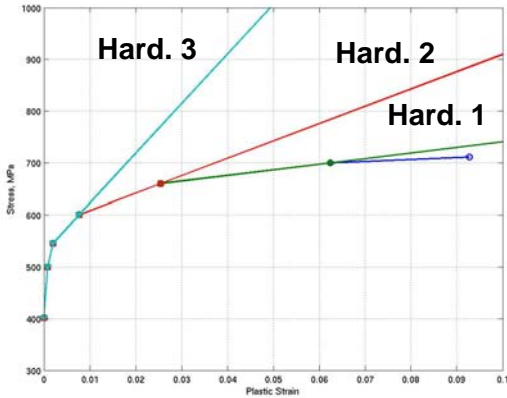
Fig. 3: Constitutive curves used in the simulation: experimental curve (blue) together with three other curves providing a stronger hardening than it follows from the tensile experiment.

The use of such non-experimental hardening evidently leads to non-physically high stresses. For the same reason, zones of the plastic deformation around the crack tip are smaller than plastic zones obtained using the experimental constitutive curve. On the other hand, a higher hardening provides a physically plausible deformation near the crack tip vicinity even for large deformations and reduced integration. Furthermore, the constitutive curves with the high hardening provide neither a negative plastic deformation nor a compressive stress in the crack-tip vicinity at any step time. Note also that an application of the full integration method with e.g. the hardening behaviour 3 does not lead to a plastic strain localisation as in the case of the experimental constitutive curve. In spite of absolutely different stresses and plastic strains around the crack tip, all hardening models lead to quite identical J-integral values. However, J-integral values obtained using the experimental constitutive curve as well as the curve with the hardening 2 are slightly smaller than values obtained under application of the hardening 3 combined with both reduced and full integration methods.

The upper diagram in fig. 4 compares the J-Integral as a function of time for the small and standard specimens. Independent of the hardening behaviour used, the J(t)-curves are different for the small and large samples. As follows from experiments, the initial critical value of the J-integral for the large probe is comparable with the initial value for the miniaturised sample. The lower diagram in fig. 4 allows to suggest that the crack growth initiation takes place either at approximately t = 3000 ms (at the maximum load) or at t = 5700 ms. It means that the simulation with the large sample using the described plasticity model yields wrong values for the J-integral, whereas the results obtained for the small sample are in a good agreement with experiments.

3.3 Verification of damage parameters

Among a variety of different ABAQUS-own material models, there is also the local Gurson, Tvergaard and Needleman (GTN) damage model, which can be inserted using

*POROUS METAL PLASTICITY, RELATIVE DENSITY=d

$$q_1, q_2, q_1^2$$

in the material definition.

IF this card is applied additionally to the material model described above, the damage localises along the ligament so that the stiffness of affected elements becomes zero. This phenomenon is probably mesh-dependent and requires further study.
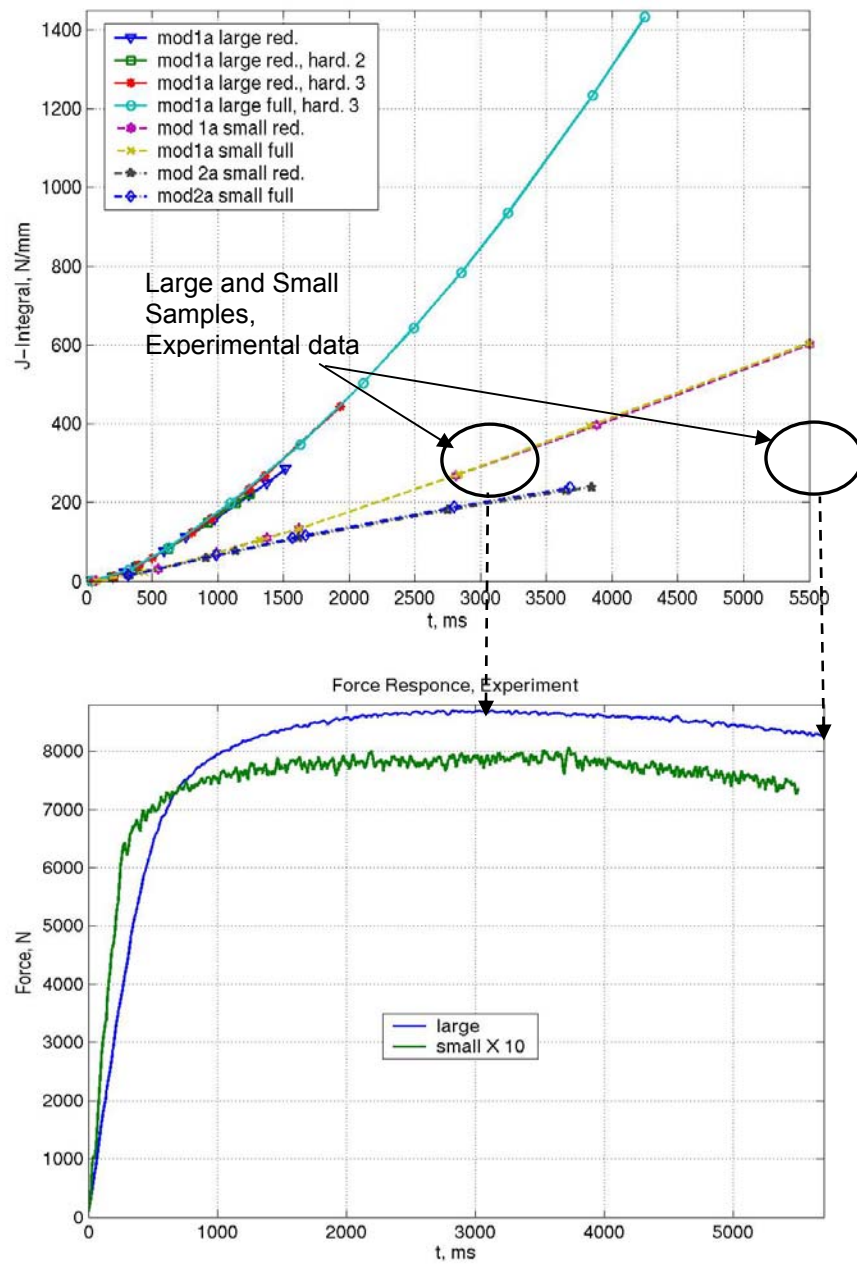
Fig. 4: Comparison of the J-Integral as a function of time for the small and standard specimens (upper diagram); experimentally recorded material response from the small and large specimens (lower diagram). Gray-filled areas in the upper figure represent a range of possible experimental values for a critical J-integral value J_{1C} for both small and large probes.

To verify estimated parameters used in the simulation, the tensile experiment described above has been modelled. Results of this modelling are represented in fig. 5. Thereby, labels 1, 2 and 3 denote different constraints and areas where the displacement was applied during the simulation. It is easy to recognize that the results are independent of these details.
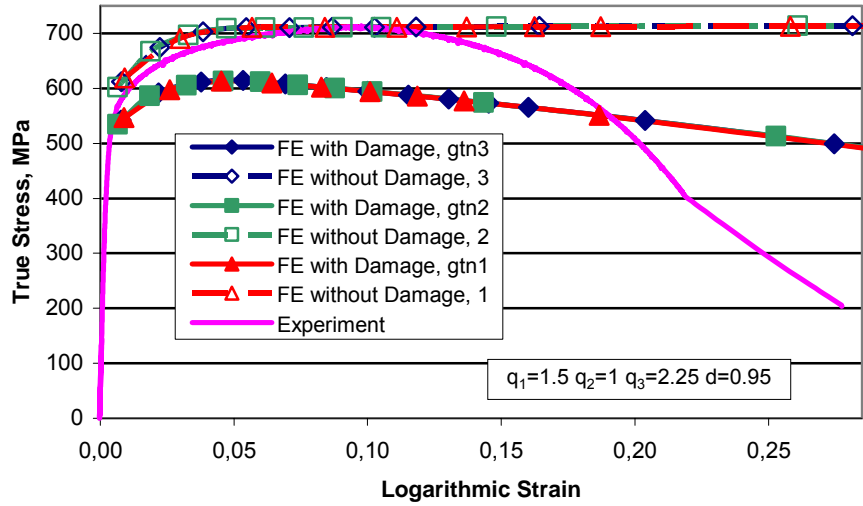
Fig. 5: Tensile experiment: FE simulation with and without the consideration of damage compared to the experimental curve.

4. Outlook

A co-operation with University of Dortmund (Prof. B. Svendsen) related to the non-local GTN damage model will be established. The unknown local as well as non-local damage parameters for Eurofer will be adjusted based on corresponding verification tensile tests. of The 3PB FM experiments will be modelled using the non-local GTN model and the results obtained for standard as well as subsized specimens will be compared.

Staff:

R. Sunyk

TW4-TTMS-005 D2
Mechanical and Structural Characterization of EUROFER 97-2

On the basis of the reduced activation ferritic/martensitic (RAFM) steel EUROFER 97 a new batch of about 8 tons was ordered. First round forgings of two heats were delivered at the end of 2003. The new material was called EUROFER 97-2. The technical specifications based on the experience of various RAFM 9CrWTaV-alloys. The use of carefully selected raw materials was essential to achieve high cleanness and low contents of undesired elements or impurities such as Nb, Mo, Ni, Cu, Al, Co, and others, which produce long-live radio-active isotopes under neutron irradiation.

One important goal of the procurement was to achieve a good reproducibility of the satisfying properties of the former EUROFER 97 alloy. This additional EUROFER97-2 material was needed for technological tests and further fabrication trials particular to build the Test Blanket Modules (TMB) mock-ups.

The material was melted in a 16-ton vacuum induction furnace, re-melted in a vacuum arc device and forged to billets, necessary for the production of round bars, plates, and tubes. The last heat treatment was normalizing 960 °C 1.5 h/oil and tempering 750 °C 4 h/air. At the beginning of 2004, material structural investigations began with the first round forgings with a diameter of 100 mm. Metallographic cuts were prepared in three different orientations and near the material surface of the as received state of heat 993378 and 993394. The material was δ-ferrite free. A very fine grain could be observed up to 1 mm from the surface, due to the last mechanical surface treatment. In the centers of the bars, there were some areas of coarse grains, but there was no anomaly in hardness to other basic material. The hardness in both heats was between 216 and 229 HV 30. No difference was found in grain shape, grain size (ASTM 10-11), and hardness due to the orientation of the samples (Fig. 1). One`s attention was turned to the inclusions. There was no orientation dependence, too (Fig. 2). By Energy Dispersive X-Ray analysis (EDX-analysis), the desoxidation detergents could be analyzed mainly as Ce and some Al.

EUROFER 97-2 as received state, heat 993 378

Fig. 1: Grain structure of the etched cut.
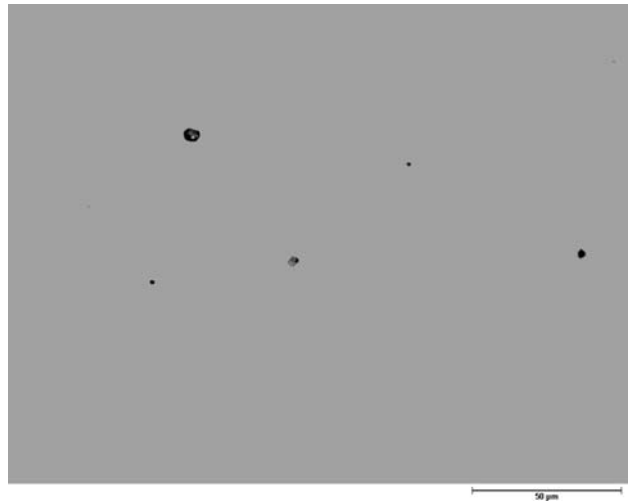
Fig. 2: Inclusions in the polished cut.

The 9CrWTaV-type of steel as EUROFER 97-7 is hardenable by austenitizing, quenching and annealing. It is always the aim to achieve a high strength with a adequate toughness. These properties are controlled by grain size and hardness. To determine the hardening and annealing behavior specimens have been fabricated of a 20 mm disc from $\varnothing$ 100 mm rods, of both heats. The hardening temperatures were chosen between 900 and 1150 °C 30 min V/V. The data of hardness HV30 and grain size are shown in Fig.3. A fine grain is necessary

EUROFER 97-2 hardening behavior
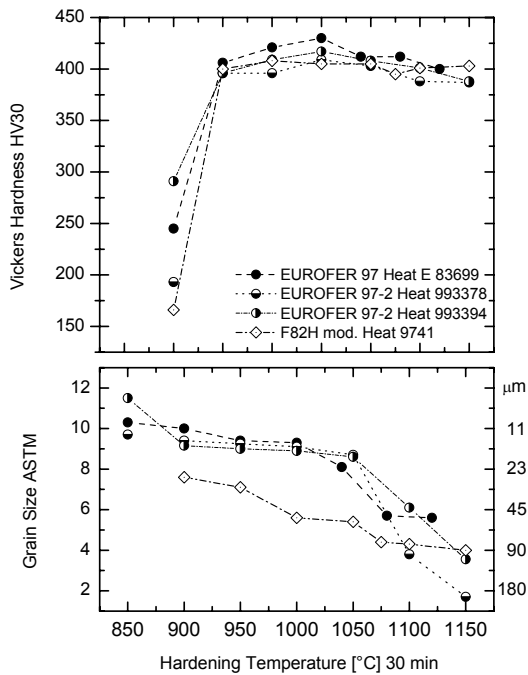
Fig. 3: Hardness and grain size vs hardening temperatures.

to get a good strength. Up to an austenitization temperature of 1050 °C 30 min, the grain size of both heats were in the range of ASTM 8 – 10. After quenching and during the annealing there was no change in the grain size but in the hardness. The specimens of the two heats were tempered at two austenitization or hardening temperatures, 980 and 1040 °C 30 min. The annealing behavior between 300 and 900°C 2 h V/V is presented in Fig.4. The hardness was stable up to 500 °C. The secondary hardness at 525 °C 2 h was not so accentuated as in former alloys. With 550 °C, a softening occurred up to 800 °C. At higher temperatures (>800 °C) the hardness increased again due to the α-γ-transformation. All results are shown together with the first EUROFER 97 alloy and the data could render a satisfied accordance of the technical alloys.

This material qualification will be continued by mechanical tests in the as received state 960 °C 1.5 h/oil + 750 °C 4 h/air and the two heat treatments 980 °C 30 min + 750 °C 2h and 1040 °C 30 min + 750 °C 2h. The anticipated results will give the range of the technological machining and application.

Staff:

B. Dafferner
M. Klimiankou
P. Graf
A. Falkenstein
U. Jäntsch
R. Lindau
E. Materna-Morris
C. Petersen
D. Preininger
H. Zimmermann

EUROFER 97-2 annealing behavior
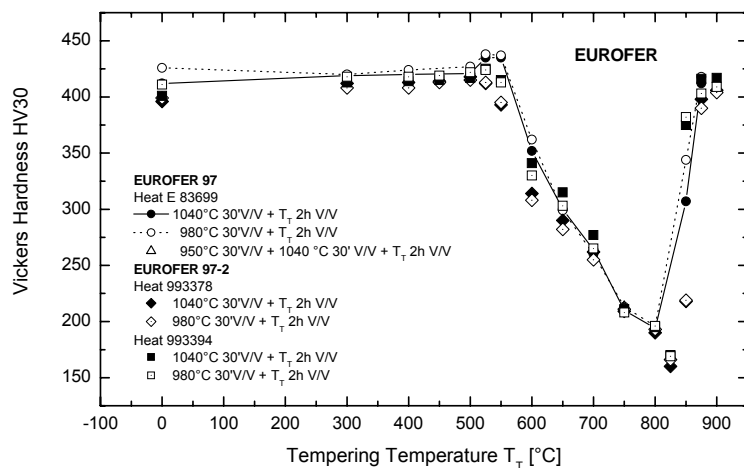
Fig. 4: Hardness and grain size vs annealing temperatures.

TTMS-006
High Performance Steels

TW3-TTMS-006 D1
EU ODS Steel Specification and Production

D1a)   EU ODS production (about 50kg) according to the selected manufacturing route

In the frame of the 2002 activities on high performance steels, CEA and CRPP had to produce independently 5 kg batches of "improved" ODS in two different production routes (TW2-TTMS-006 D1 and D10). The chemical, physical and metallurgical properties of these 2 improved ODS batches was investigated by FZK (TW2-TTMS-006 D2), mechanical tests were performed at different laboratories (TW3-TTMS-006 D3, D5, D6). The results of all these investigations should help to define a European RAFM ODS steel, which then should be produced as a 50 kg batch according to the selected manufacturing route (TW3-TTMS-006 D1). In the course of these investigations it turned out that the drawback of the ODS-EUROFER steels of the first generation, designed and produced by FZK and Plansee, respectively, the poor impact behaviour, could not be overcome. Independently FZK developed together with Plansee a production route for ODS-EUROFER, which included a thermo-mechanical treatment. This thermo-mechanical treatment led finally, after some optimisation work (TW4-TTMS-006 D1), to a material with much higher ductility and improved impact properties without considerable losses in tensile and creep strength.

Table 1: Amount of different ordered product forms.

Productform	Percentage	Amount	Mass
6 mm plate	55%	0.6 m^2	27.5 kg
17 mm plate	30%	0.1 m^2	15 kg
12.5 mm rod	5%	2.6 m	2.5 kg
20 mm rod	10%	2.0 m	5 kg
		Total	50 kg

On a review meeting in April 2004, this production route was chosen for the production of a 50 kg ODS-EUROFER batch in different product forms (6 and 17mm rolled plates, and 12.5 and 20 mm extruded bars, see Table 1). The production of this batch is in progress; the delivery of the material is scheduled for end of February 2005. After some optimisation work with respect to the heat treatment, the material can be delivered to the different associations for further testing and characterisation.

D1b)   Assessment of the influence of Carbon and Oxygen content during the production on the mechanical and microstructural properties

During the above-mentioned review meeting it also turned out, that the content of carbon and oxygen could have an effect on the mechanical and microstructural properties. It was decided to investigate the development of the C-, and O-content during the different production steps including the initial steel powder production, the mechanical alloying process and the consolidation process by hot isostatic pressing.

In former productions (Starck) it was observed, that the carbon content decreased during the inert gas atomisation of the EUROFER steel while it remained nearly constant during the following mechanical alloying and hipping process. It can be assumed that this decrease is due to irregularly high oxygen content of the argon, which has been used as protective gas for the atomisation process. This decrease of the C-content was not observed in other productions (Studsvik, Nanoval). A certain minimum carbon content is necessary to achieve an air-hardening material. The oxygen content, which is suspected to have a negative effect on the mechanical properties, especially on the ductility, was measured after the different production steps. The oxygen content of the atomised powder is increased compared to the solid ingot, which is melted and sprayed into the inert gas that contains also a small amount of oxygen. The O-content of the steel powder depends on the powder particle size. This can

be attributed to the surface to volume ratio, which is reverse proportional to the particle radius. During mechanical alloying process the O-content is further increased. Fig. 1 gives the carbon and oxygen contents measured after different production steps. For the mechanical alloyed materials, the excessive oxygen, which is the difference between the total oxygen content and the oxygen chemically bound in the Yttrium oxide, is the most important value.
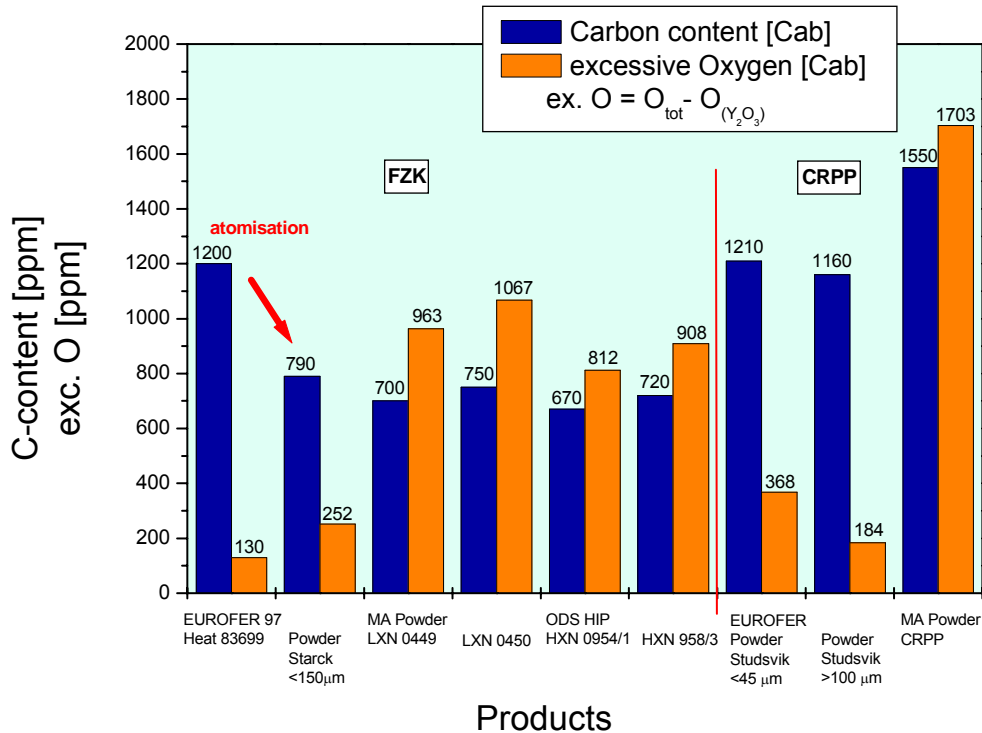
Fig. 1: Carbon and oxygen content of materials after different production steps. (MA = mechanically alloyed).

Staff:

Ch. Adelhelm
S. Baumgärtner
A. Falkenstein
P. Graf
M. Klimiankou
T. Kaiser
R. Lindau
U. Jäntsch
H. Zimmermann

Literature:

[1] Cayron C., Chu I., Rath E., Heenequin J.M., Launois S., Bucci P., Leibold J.M, "ODS processing and qualification, screening of various parameters, basic characterisation, production of 5 kg improved batch", Note Technique DTEN No. 129/2002, Final report task TW2-TTMS006-D1, CEA Grenoble, December 2002.

[2] Schäublin R., Leguy T., Bonjour C., Baluc N., "ODS processing and qualification (2nd route), screening of various parameters (powder alloying, consolidation, PHT) basic characterisation, production of 5 kg batch improved batch." Final report on task TW2-TTMS006-D10, CRPP Switzerland, December 2002.

[3] Klimiankou M., Lindau R., Falkenstein A., Jäntsch U., Zimmermann H., "Chemical, physical and metallurgical properties of the 2 improved ODS batches". (Final report TW2-TTMS-006-D2) FZK internal report.

[4] Klimiankou M., Lindau R.; Möslang A., "TEM characterization of structure and composition of nanosized ODS particles in reduced activation ferritic-marthensitic steels." 11th Internat. Conf.on Fusion Reactor Materials (ICFRM-11), Kyoto, J, December 7- 12, 2003, Book of Abstracts S.209, Journal of Nuclear Materials, 329-33 (2004) S.347-51

[5] Klimiankou M., Lindau R., Möslang A., "TEM Characterization Of Nanosized Ar Bubbles In Reduced Activation Ferritic-Martensitic Steels". European Microscopy Congress, Antwerpen August 23-27, 2004

[6] Lindau R., Möslang A.; Rieth M., Klimiankou M., Materna-Morris E.; Alamo A., Tavassoli F.,. Cayron, C., Lancha A., Fernandez P., Baluc N., Schäublin R., Diegele E., Filacchioni, G., Rensman J.-W., v.d. Schaaf B., Lucon E., Dietz, W., "Present Development Status of EUROFER and ODS for Application in Blanket Concepts". 23rd Symposium on Fusion Technology, 20.–24. September 2004, Venice, Italy

[7] Möslang A., Diegele E., Klimiankou M., Lässer R., Lindau R., Lucon E., Materna-Morris E., Petersen C., Pippan R., Rensman J.W., Rieth M., van der Schaaf B., Schneider H.-C., Tavassoli F., "Toward a Reduced Activation Structural Materials Database for Fusion DEMO Reactors" IAEA conference in Vilamoura, 1.-6. November 2004, eingereicht bei Fusion Technology

[8] Preininger D., "Effect of particle morphology and microstructure on strength, work-hardening and ductility behaviour of ODS-(7-13)Cr steels." 11th Internat.Conf.on Fusion Reactor Materials, Kyoto, J, December 7-12, 2003, Journal of Nuclear Materials, 329-33(2004) S.362-68

[9] Preininger D., "Grain refinement and strain rate effects on ductility and impact behaviour of dispersion-strengthened Ta-W alloys", Werkstoffwoche 2004, München, 21.-23.September 2004

[10] Preininger D., "Plasticity behaviour of nanocrystalline, dispersion-hardened metals". Werkstoffwoche 2004, München, 21.-23.September 2004

[11] Antonio P., Montes O.M., Alves E., Alves L.C., Lindau R., Odriozola J.A., "Microstructural characterisation of Eurofer-ODS RAFM steel in the normalized and tempered condition and after thermal aging in simulated fusion conditions". 23rd Symposium on Fusion Technology, 20.–24. September 2004, Venice, Italy

TW4-TTMS-006 D1
Optimisation of Fabrication Parameters of Current EUROFER ODS Plate Material

This deliverable should be based on the ongoing activities already launched in TW2 and TW3. The aim of the study is to improve ductility at low temperature, in particular the very low fracture toughness in the upper shelf and the relatively high DBTT. At the same time the good high temperature properties should be maintained. The aim is here to reach comparable tensile and creep strength at 600-700°C as EUROFER at 100 K lower.

In particular any development of ODS material should not contravene the goal to produce a low activation steel.
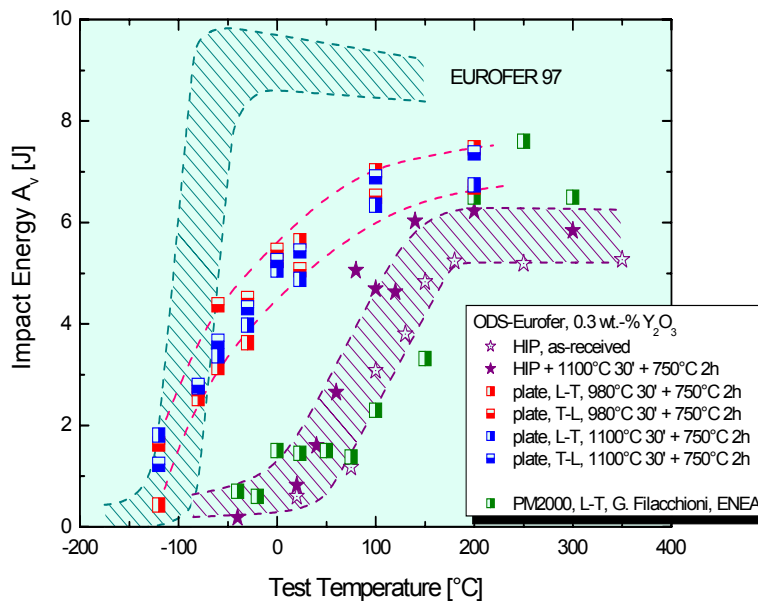
Fig 1: Test temperature dependence of total absorbed energy of different ODS-EUROFER steels in comparison with EUROFER 97 (KLST specimens).

In the frame of the 2002 activities on high performance steels, CEA and CRPP had to produce independently 5 kg batches of "improved" ODS in two different production routes (TW2-TTMS-006 D1 and D10). The chemical, physical and metallurgical proper-ties of these 2 im-proved ODS batches was investigated by FZK (TW2-TTMS-006 D2), mechanical tests were performed at different laboratories (TW3-TTMS-006 D3, D5, D6). The results of all these investigations should help to define a European RAFM ODS steel, which then should be produced as a 50 kg batch according to the selected manufacturing route (TW3-TTMS-006 D1). In the course of these investigations it turned out that the drawback of the ODS-EUROFER steels of the first generation, designed and produced by FZK and Plansee, respectively, the poor impact behaviour, could not be overcome. Independently FZK developed together with Plansee a production route for ODS-EUROFER, which included a thermo-mechanical treatment. This thermo-mechanical treatment led finally, after some optimisation work, to a material with much higher ductility and improved impact properties without considerable losses in tensile and creep strength. Fig. 1 shows the results of tests on sub-size KLST specimens of rolled and heat-treated ODS-EUROFER (plate) compared to only hipped ODS-EUROFER of the first generation and to a commercial ferritic ODS alloy (PM2000). DBTT could be shifted from values between +60 and +100°C for hipped ODS-Eurofer of the first generation to values between –40 and –80°C. The upper shelf energy (USE) was increased by about 40%.

Staff:

S. Baumgärtner	M. Klimiankou
B. Dafferner	R. Lindau
A. Falkenstein	U. Jäntsch
P. Graf	M. Rieth
S. Heger	H. Zimmerman

Literature:

[1] Klimiankou M., Lindau R.; Möslang A., "TEM characterization of structure and composition of nanosized ODS particles in reduced activation ferritic-marthensitic steels." 11th Internat. Conf.on Fusion Reactor Materials (ICFRM-11), Kyoto, J, December 7- 12, 2003, Book of Abstracts S.209, Journal of Nuclear Materials, 329-33 (2004) S.347-51

[2] Klimiankou M., Lindau R., Möslang A., "TEM Characterization Of Nanosized Ar Bubbles In Reduced Activation Ferritic-Martensitic Steels". European Microscopy Congress, Antwerpen August 23-27, 2004

[3] Lindau R., Möslang A.; Rieth M., Klimiankou M., Materna-Morris E.; Alamo A., Tavassoli F.,. Cayron, C., Lancha A., Fernandez P., Baluc N., Schäublin R., Diegele E., Filacchioni, G., Rensman J.-W., v.d. Schaaf B., Lucon E., Dietz, W., "Present Development Status of EUROFER and ODS for Application in Blanket Concepts". 23rd Symposium on Fusion Technology, 20.–24. September 2004, Venice, Italy

[4] Möslang A., Diegele E., Klimiankou M., Lässer R., Lindau R., Lucon E., Materna-Morris E., Petersen C., Pippan R., Rensman J.W., Rieth M., van der Schaaf B., Schneider H.-C., Tavassoli F., "Toward a Reduced Activation Structural Materials Database for Fusion DEMO Reactors" IAEA conference in Vilamoura, 1.-6. November 2004, eingereicht bei Fusion Technology

[5] Preininger D., "Effect of particle morphology and microstructure on strength, work-hardening and ductility behaviour of ODS-(7-13)Cr steels." 11th Internat.Conf.on Fusion Reactor Materials, Kyoto, J, December 7-12, 2003, Journal of Nuclear Materials, 329-33(2004) S.362-68

[6] Preininger D., "Grain refinement and strain rate effects on ductility and impact behaviour of dispersion-strengthened Ta-W alloys", Werkstoffwoche 2004, München, 21.-23.September 2004

[7] Preininger D., "Plasticity behaviour of nanocrystalline, dispersion-hardened metals". Werkstoffwoche 2004, München, 21.-23.September 2004

[8] Antonio P., Montes O.M., Alves E., Alves L.C., Lindau R., Odriozola J.A., "Microstructural characterisation of Eurofer-ODS RAFM steel in the normalized and tempered condition and after thermal aging in simulated fusion conditions". 23rd Symposium on Fusion Technology, 20.–24. September 2004, Venice, Italy

TW2-TTMS-006a D2
Chemical, Physical and Metallurgical Properties of the 2 Improved ODS Batches

Within the 2002 structural materials development program, CEA Grenoble (TW2-TTMS-006-D1) and CRPP Villigen (TW2-TTMS-006-D10) were obliged to improve the production process for ODS-Eurofer by screening different production parameters (powder alloying, consolidation, PHT) in two different independent production routes. Finally an amount of 5kg each should be provided to the community for testing and characterisation. The best production route should then be applied for the production of a larger EU-reference batch of about 50 kg. In order to limit the variables, the Yttria content was agreed to 0.3 wt.-% Y_2O_3.

The work to be performed within this task was mainly to screen these two batches, to perform heat treatment experiments and finally to give a recommendation for an appropriate heat treatment. Microstructural examinations and optimisation of heat treatments were performed at FZK. Due to the different production routes both materials behave different with respect to heat treatment and microstructure and are discussed separately.

CEA-ODS

CEA Grenoble followed the well-developed traditional production route consisting of mechanical alloying in attritor or ball mills and consolidating the material after canning and degassing by a HIPping procedure at 1100°C/100 MPa/2 h. The material delivered were plates of 6 and 10 mm thickness that were cut from the hipped cylinders. CEA performed a preliminary heat treatment with a normalisation treatment at 950°C 30 min and water quenching and a subsequent tempering at 750°C 2 h [1]. The microstructural examinations by optical microscopy and TEM were performed on samples taken from different orientations according to ASTM E3 and E399.

Four different samples were taken to check hardenability and tempering behaviour. The normalisation temperature 1100°C was chosen according to our experience with ODS-EUROFER developed at FZK, high enough to get enough carbon into solution to promote a martensitic transformation, and not to high to avoid grain growth. The time for austenitisation was varied between 30 and 60 minutes. The tempering treatment, 750°C for 2 h was also chosen according to own experience with similar material.

The hardness measurements (Table 1), as well as the metallographic examinations of sample 1 and 2 clearly show, that the material undergoes a martensitic transformation. Due to the low carbon content of the initial Eurofer powder, this martensitic transformation can only be achieved by water quenching. This is well in line with experience made with FZK-ODS-EUROFER. From the hardness values of the normalised samples no advantage for longer annealing times can be found.

Table 1: Vickers Hardness HV30 of CEA-ODS after different heat treatments.

Specimen-No.	Aust. Treatment	Ann. Treatment	HV30	HV30	HV30	HV30 (Mean)
1	1100°C 30' Ar/W	0	492	487	487	489
2	1100°C 60' Ar/W	0	484	490	482	485
3	1100°C 30' Ar/W	750°C 2h V/V	319	326	322	322
4	1100°C 60' Ar/W	750°C 2h V/V	310	306	313	310
CEA-Treatment	950°C 30' Air/W	750°C 2h	320	321	322	321

0304A00064   ├──200 µm──┤

0304A00073   ├──50 µm──┤
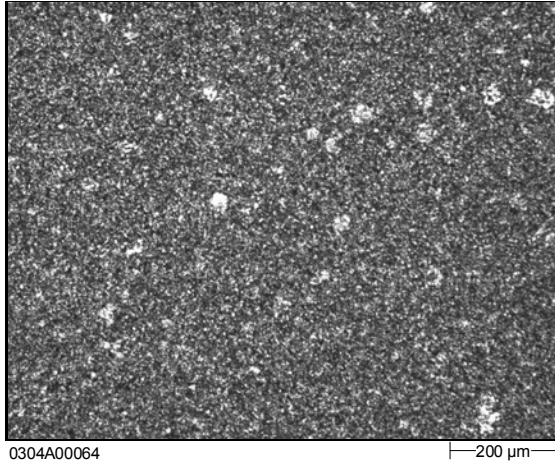
Fig. 1: Etched cross section: mainly tempered martensite (HV30 ~ 320), more ferritic (?) islands (white spots) Specimen orientation: L-S, sample taken from plate 155 x 62 x 10 mm³ Heat treatment: 1100°C 30 min Ar/water + 750°C 2 h V/V.

The heat-treated samples were investigated by optical microscopy, Vickers hardness measurements, and TEM.

Samples 3 and 4 are normalised and tempered. A comparison of the hardness values of these samples gives no preference for a certain heat treatment. The HV30 values of sample 4 are slightly lower than those of sample 3, but if there were any advantages for the mechanical properties, particularly the ductility, they must be checked in mechanical tests.

The CEA heat treatment of **950°C 60 min air/water + 750°C 2 h** air nearly gives the same hardness values as heat treatment number 3 (**1100°C 30 min Argon/water + 750°C Argon**).

The heat treatments at FZK were performed in a muffle furnace under flowing argon in order to avoid oxidation and decarburisation. From the different heat treatment trials that were performed no clear recommendation for a certain heat treatment can be given. The optimum heat treatment must be found out in mechanical tests but it can be assumed that only slight differences will be found.

In the micrographs in Fig. 1 a growth of ferritic islands, which can be also suspected to appear in the hardened material, can be observed. The hardness values support the assumption of ferrite formation.

Fig. 2 shows a TEM micrograph taken with a High Angle Annular Dark Field (HAADF) detector in an analytical transmission electron microscope FEI Tecnai F20. The grain size is between 100 and 1200 nm. From the TEM investigations also no preference for a certain heat treatment can be given.

It can finally be concluded, that the optimum heat treatment for the CEA ODS-EUROFER must be found in mechanical tests, i.e. tensile and impact tests

CRPP-ODS

CRPP chose an alternative route which included mechanical alloying in a high energy attritor (ZOZ), a hot pre-pressing at 1270°C/35 MPa/7 min and a final canning-less HIPping at 1000°C/180 MPa/1 h. The resulting products were discs of 53 mm diameter and 7 mm
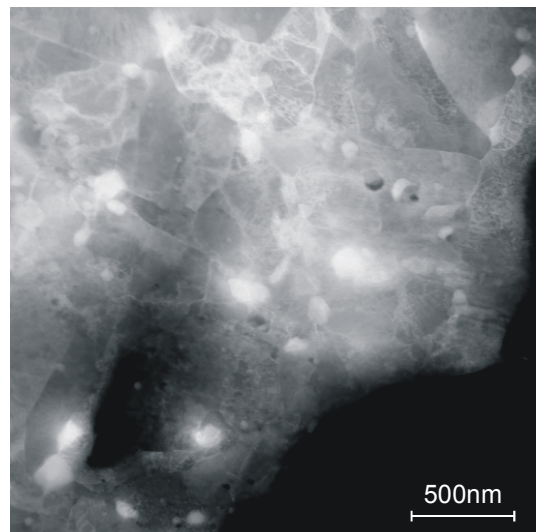
Fig. 2: HAADF images of CEA-ODS with 950°C 60' Air/W + 750°C 2 h heat treatment.

thickness. The microstructural examinations by optical microscopy and TEM were performed on samples taken from different orientations according to ASTM E3 and E399.

For the CRPP-ODS material 1100°C for 30 minutes was chosen as normalisation treatment followed by a tempering treatment at 750°C for 2 hours.

Table 2: Vickers Hardness HV30 after different heat treatments on CRPP-ODS discs.

Specimen-No.	Aust. Treatment	Ann. Treatment	HV30	HV30	HV30	HV30 (Mean)
11-1	1100°C 30' V/V	0	496	492	487	492
11-2	1100°C 30' V/V	750°C 2 h V/V	362	362	367	364
11-3	as-receved		473	486	486	482

During the first examinations, some samples turned out to be porous although the nominal density determined by measuring and weighing was quite high. The heat treatment was performed by annealing of the samples under vacuum (1.7×10^{-7} mbar) in a quartz recipient inside a tubular 3-zone furnace. Quenching was performed by withdrawal of this tubular furnace. The achievable cooling rate for the small specimens is equivalent to air-cooling. The hardness measurements (Table 2) of disc 11 show, that the material undergoes a martensitic transformation. After normalisation at 1100°C for 30 minutes and "air"-quenching hardness values HV 30 of about 540, i.e. ~10% higher than the hardness of CEA-ODS, were achieved. The etched cross section shows a fine-grained structure with few white spots, which are presumably ferrite islands. In contrast to the CEA-ODS, air quenching is sufficient to achieve a martensitic transformation. This is due to an increase of the carbon content during the mechanical alloying. After tempering at 750°C for two hours the hardness deceases to HV30 ~370, which is also higher than the hardness of CEA-ODS after tempering.
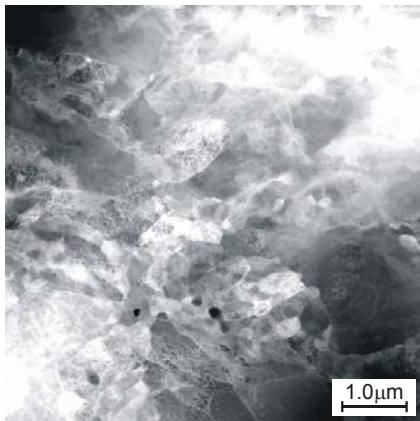
Fig. 3: Overview HAADF
1100°C 30 min V/V, sample (11-1).

Fig. 3 shows TEM micrograph taken with a High Angle Annular Dark Field (HAADF) detector in an analytical transmission electron microscope FEI Tecnai F20. The grain size is between 200 and 1500 nm. Some particles with (VCrMnFe) composition can be observed as dark spots. The EDX-spectrum taken from one precipitation clearly shows the VCrMnFe composition as presented in Fig. 4. The spatial distribution of such precipitations is non homogenous as is clearly visible in Fig. 5a. The line form of precipitations may indicate the particle boundary after the mechanical alloying procedure. Analytical investigations using EDX mapping show an elemental distribution in the precipitations, which appear to be conform with the composition indicated in Fig. 4.

It can be assumed that this treatment will give good mechanical properties. If the ductility is not satisfying, an increase of the tempering temperature to 760°C and longer tempering times can be recommended. The tempering temperature should not be too high to avoid re-austenitisation and thus the formation of martensite in the cooling phase.

Fig. 4: EDX spectrum of a precipitation, sample (11-1).

TEM investigations show that some white spots can be seen adhering to the Y_2O_3 particles or being freely distributed in the matrix, looking like (He-) bubbles, well known from irradiated samples [4]. The EDX analyses of

these spots and bubbles clearly reveal their character.

These bubbles contain Argon, which is used as protective gas in the milling device to avoid oxidation during mechanical alloying. Although a degassing is usually made before hipping, some Argon remains in the material. It can be assumed that a certain quantity of Argon is getting solved in the material during the mechanical alloying process and forms bubbles during the hipping process or the subsequent heat treatments at high temperatures.
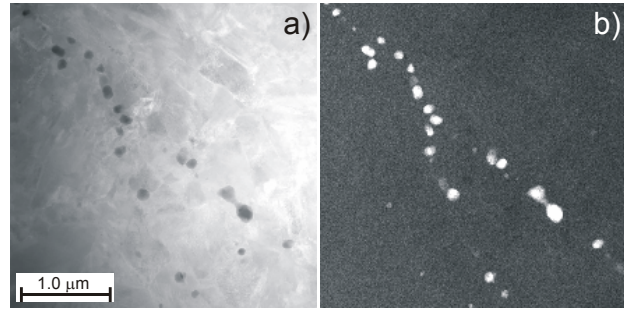
Fig. 5: HAADF image of VCrMnFe precipitations **a)**, and its image using EDX mapping **b).**

Staff:

S. Baumgärtner
A. Falkenstein
P. Graf
M. Klimiankou
R. Lindau
U. Jäntsch
H. Zimmermann

Literature:

[1] C. Cayron, I. Chu, E. Rath, J.M. Heenequin, S. Launois, P. Bucci, J.M. Leibold, "ODS processing and qualification, screening of various parameters, basic characterisation, production of 5 kg improved batch", Note Technique DTEN No. 129/2002, Final report task TW2-TTMS006-D1, CEA Grenoble, December 2002.

[2] R. Schäublin, T. Leguy, C. Bonjour, N. Baluc, "ODS processing and qualification (2nd route), screening of various parameters (powder alloying, consolidation, PHT) basic characterisation, production of 5 kg batch improved batch." Final report on task TW2-TTMS006-D10, CRPP Switzerland, December 2002.

[3] M. Klimiankou, R. Lindau, A. Falkenstein, U. Jäntsch, H. Zimmermann, "Chemical, physical and metallurgical properties of the 2 improved ODS batches". (Final report TW2-TTMS-006-D2) FZK internal report, November 2004.

[4] M. Klimiankou, R. Lindau, A. Möslang „Energy-filtered TEM Imaging and EELS Study of ODS Particles and Argon-filled Cavities in Ferritic-martensitic Steels" Micron, Micron 36(2005) 1-8

EFDA/01-622
Order of EUROFER Heats

The European programme related to fusion reactor relevant structural materials aims at developing a low activation material, which can withstand high neutron loads under temperature and coolant conditions required in a fusion reactor based on magnetic confinement plasma.

For that purpose the 8-12 Cr reduced activation ferritic/martensitic (RAFM) steel was selected as reference structural material and the present R&D aims at:

- develop, characterise and implement a RAFM steel to be used for the fabrication of the Test Blanket Modules (TBM) to be installed in ITER,

- optimise such a RAFM steel for the utilisation in a Fusion reactor (DEMO and Power Plant).

Based on the substantial experience gained from various RAFM alloys developed in JA and EU and in order to reduce the long-term activation and improve the mechanical properties of such a steel prior and after irradiation, an industrial 3.5 tons batch of 9 CrWVTa RAFM steel, named EUROFER 97 was specified, ordered, and produced.

Additional EUROFER 97 material is needed for further fabrication trials, particularly to build TBM mock-ups. This new procurement has also as major objective to check the reproducibility of properties compared to batches available from the previous fabrication, to assess the achievable limits of reduction of detrimental impurities like Nb, Mo, Ni, Cu, Al, Co and others and to improve the quality of the tubing production.

Under operation the material will be exposed to temperatures up to 550°C, cyclic loading and neutron irradiation. The limitation of the undesired elements like Nb, Mo, Ni, Cu, Al, Co and others, that produce long-lived radio-active isotopes under neutron irradiation, makes this steel a so-called reduced activation steel. Components made of such a steel can be handled and stored within a manageable period of time after reactor shut down. This steel will be used for components with high reliability requirements.

The scope of this task was to provide a normalised and tempered martensitic steel type 9 CrWTaV designated EUROFER 97-2, under different product forms.

Therefore a technical specification had been elaborated considering all the experiences with the procurement of the first heats of EUROFER 97.

Since reproducibility of the good properties of EUROFER 97 is one important goal of the procurement, the technical specification leans close to that of the first heats produced by Böhler in Austria.

After evaluation of the offers, SaarSchmiede, an experienced German manufacturer of special and super clean steels and producer of the OPTIFER RAFM steels, was selected for the production of about 8 tons of different product forms (forgings, plates and tubes). The use of carefully selected raw materials is essential to achieve high cleanliness and low contents of undesired elements. Table 1 gives the required chemical analysis as specified in the technical specification, and the achieved results according to the manufacturer's analyses given in the inspection certificates.

Table 1: Chemical composition of Eurofer 97.

		Radiologically desired (ppm)	Eurofer 97-2 specified (mass-%)	Eurofer 97-2 achieved [*] (mass-%)
A)	C		0.09 - 0.12 [0.11]	0.10 - 0.12
	Cr		8.5 - 9.5 [9.0]	8.95 – 9.06
	W		1.0 - 1.2 [1.1]	1.04 - 1.14 (1.33)
	Mn		0.20 - 0.60 [0.40]	0.50 - 0.56
	V		0. 15 - 0.25	0.20 - 0.24
	Ta		0.10 - 0.14 [0.12]	0.12 - 0.14
	N_2		0.015 - 0.045 [0.030]	(0.011) 0.22 - 0.040
	P		< 0.005	0.001 - 0.003
	S		< 0.005	0.001
	B		< 0.002	0.0007 - 0.0009
	O_2		< 0.01	0.0007 - 0.0011
B)	Nb	< 0.01 ppm	[< 0.005 (50 ppm)]	0.0001 - 0.005
	Mo	< 1 ppm	[< 0.005 (50 ppm)]	0.005 (0.01)
	Ni	< 10 ppm	[< 0.01 (100 ppm)]	0.01 (0.013)
	Cu	< 10 ppm	[< 0.01 (100 ppm)]	0.005
	Al	< 1 ppm	[< 0.01 (100 ppm)]	0.009 - 0.002 (0.013)
	Ti	< 200 ppm	< 0.01 (100 ppm)	0.001 - 0.002
	Si	< 400 ppm	<0.05 (500 ppm)	0.016 - 0.031
	Co	< 10 ppm	[< 0.01 (100 ppm)] target values [ ]	0.006 - 0.010

A) main alloying elements in mass%
B) radiologically undesired elements in mass% and (μg/g = ppm)

[*] all analyses by manufacturer
Eurofer 97-2: range of 5 heats, 8 tons of 8 different product forms (forged bar, plates, tubes)

The production of EUROFER 97-2, except for the production of some additional plates, is finished. Most of the products have been delivered to the different associations; the rest is stockpiled for future use.

Staff:

R. Lindau

Materials Development
Advanced Materials

TTMA-002
Advanced Materials: Divertor and Plasma Facing Materials

TW4-TTMA-002 D2
Developing of Improved W-alloys for Application in a Power Plant with He Cooled Divertor

Fusion power plants will be equipped with a He-cooled divertor which has to withstand thermal surface loads of up to about 15 MW/m² and exhibit low activation. Thermal loads and sputtering behaviour of the plasma facing components imply that tungsten is the preferred material due to its physical properties. However the thermally introduced stresses require a modular structured surface in shape of cooling fingers which are connected at lower cooler levels to structural components e.g. made of LAFM-steel (e.g. EUROFER). The actual design (Fig.1) [1] is based on state of the art parameters for standard unirradiated materials (Tab.1). The foreseen W-components have to fulfil functional aspects (the component tile) and structural functions (the 100 MPa He pressure loaded thimble). Up to yet W-alloys are used in technology only as functional components but they were never applied for structural purposes. Analyses of W-alloy properties (e.g. listed by Plansee Corp. [2]) show that materials improvement (e.g. recrystallization behaviour, DBTT, strength or ductility) is absolutely required for application as construction material. In refractory metal PM metallurgy it is well known, that alloy properties depend on the raw material (precursor) and on processing technology (sintering, deformation, annealing etc.). Based on these facts the development of an improved W-alloy has to start with investigations on fabrication of homogeneous ODS-W powders with ODS particles in the nanoscale range. The process of mechanical alloying is favoured to reach this goal.
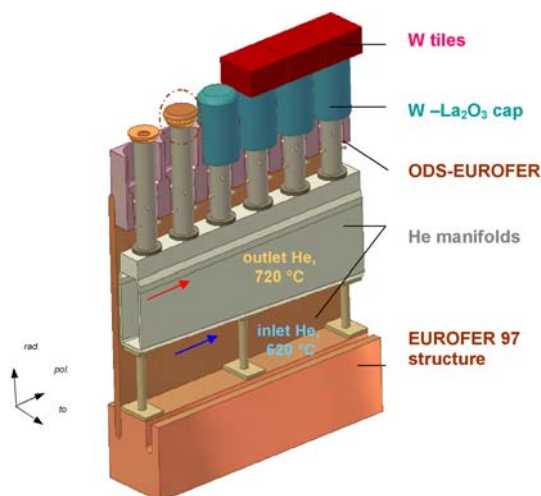
Fig. 1: Design of a He cooled divertor.

The W-tiles have to withstand functional loads e.g. evaporation and sputtering

The thimbles or caps fabricated from W-La_2O_3 are gas pressure loaded. This W alloy has structural functions.

Tungsten qualities - State of the art:

For determination of tungsten alloy properties (tensile properties, microstructure) raw materials (rods) fabricated by the state of the art were bought from Plansee company and analysed. The tested alloys were the qualities pure W and WL10 (W-1%La_2O_3) forged to rods. Fig. 2 and 3 show the metallographic microstructure of the analysed W and WL10 qualities, respectively. Both qualities exhibit a similar microstructure characterized by longitudinally elongated grains partially with a rather big diameter of approx. 20 µm for W. In the WL10 quality the ODS particles are not homogeneously dispersed. The primary ODS particles are elongated and arranged in a channel like structure with approx. 1 µm diameter of the traces.

The principle duty of the ODS particles is to reduce grain growth at elevated temperature and increase re-crystallization temperature. The detected microstructure implies that the ODS distribution is inhomogeneous and not optimized to small grain growth ability. Thus re-crystallization temperature should rise by more homogeneous and finer dispersions.

Table 1: Properties of refractory metals
W and W-ODS exhibit best heat conductivity values and activation behaviour.

Properties	Unit	W	W-ODS	Mo	Ta
Melting	[°C]	3410	3410	2620	2996
Density	[kg/m³]	19300	19300	10200	16600
DBTT Irradiated to 1 dpa	[°C]	100-400 > 800	100-400	20-150	< -200
Recryst.	Begin, 1h Total [°C] Begin 2y	1150 1350 800	1450 1750 1100	900 1200	900 1400
Expansion	at 20°C [10^{-6} 1/K]	4.36	~4.36	5.3	6.5
Activation *	1 y 1000y [Sv/h]	10^{-2} < 10^{-4}	10^{-2} < 10^{-4}	100 100	10^{-2} 10^{-4}
Heat Conductivity	RT 1500°C [W/mK]	129 105	129 105	142 88	54 74

*Activity of Fe after 1 y and 1000 y storage: approx. 10^2 and 10^{-5} Sv/h, respectively. Expansion of steels $14*10^{-6}$ 1/K
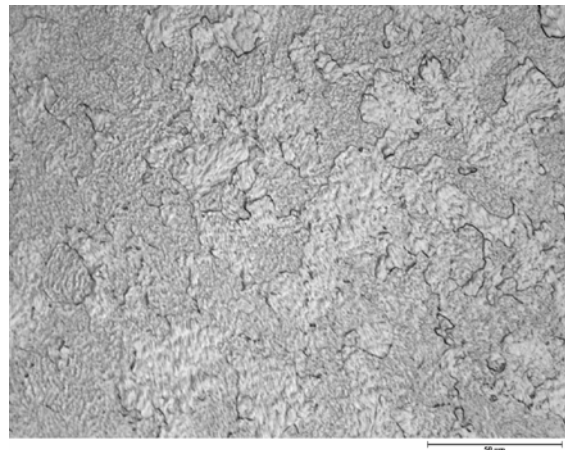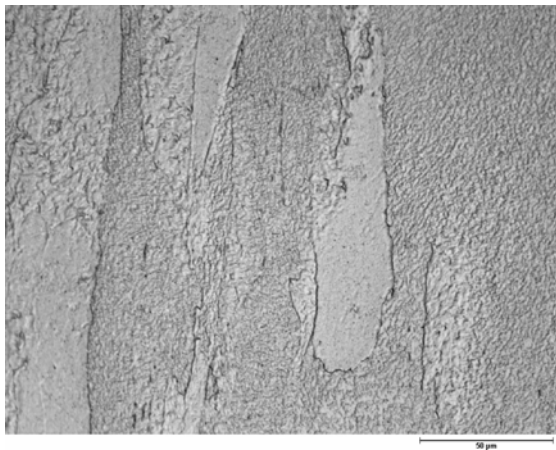
Fig. 2: Longitudinal (left) and transversal (right) cross section of a W rod with diameter 16 mm.
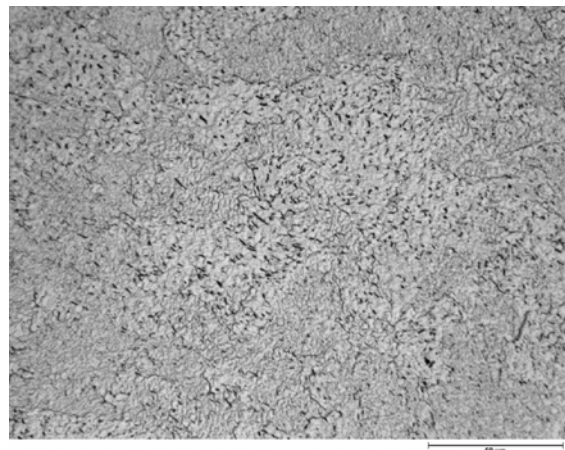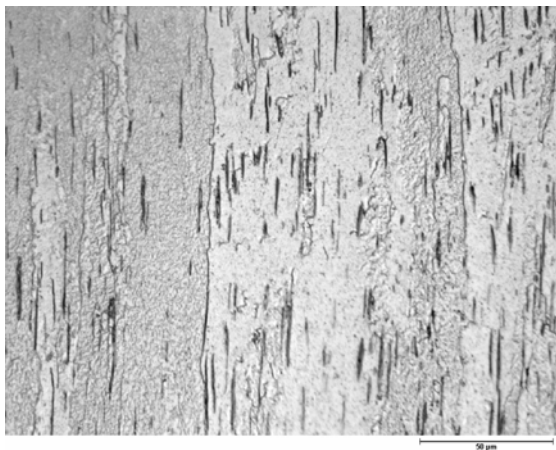
Fig. 3: Longitudinal (left) and transversal (right) cross section of a WL10 rod with diameter 19 mm.

Smaller and more interlinked W grains will reduce DBTT as known e.g. from wire fabrication. The use of finer W precursors should assist the fabrication of W with finer grain structure e.g. in shape of rods (16 mm) with low or restricted deformation ratio compared to wires below 1 mm in diameter.

The concluding result of our analyses on the state of the art W qualities can be condensed in:

- The commercially available W grades are not optimized to structural application.
- The microstructure give clear hints for alloy improvement.
- The 'large grains' indicate that there is potential present for alloy improvement

Equipment:

Different types of ball milling equipments were analysed concerning the energy input during alloying, possibility for adaptation to special needs in refractory metal handling and similarity of process type used in industrial fabrication. The selected equipment with type name Simoloyer CM01 fabricated by ZOZ Corp. (Fig. 4) is by our evaluation the best compromise for the syntheses of W precursors with relevance to technological fabrication and basic research in testing new W alloys. The Simoloyer CM01 is a milling equipment based on the attritor technology and belongs to the systems with low to medium energy input by the milling balls. The surface speed of the attritor can by varied up to a maximum velocity of 10.9 m/s. In this energy classification drum mills (a 'slowly' rotating container is filled with powder and balls) are low energy milling systems caused by the free falling balls and high energy systems are mostly realized using shaker technology.

In the first stage a steel container will be used for performing studies on the grinding down behaviour of used W powders and ODS powder additions. As ODS material La_2O_3 is used. A powder to ball ratio of 1 to 10 is expected to be optimal for W alloying by extrapolation form our EUROFER ODS tests. The containers will be loaded by an volume fraction of about 40 %. The attritor wings are plated in our first designed container configuration by hard metal and steel balls are applied.

At the moment commissioning tests are under execution for testing the vacuum system, the behaviour of feed through in contact with very fine oxide powders and studies on the impact of our designed externally mounted container heating device. Fig. 5 shows the opened milling container and the attritor rotor.

Simoloyer® CM01

Fig. 4: Milling equipment after installation

Type: Simoloyer CM01

Left side: Control unit and vacuum system

Right side: Attritor gearing box with flanged attritor milling container and gas supply system

Detail view:

Motor drive (blue color)
Milling container (grey color)

Rotational speed 200 – 1800 rpm
Max. relative velocity   10.9 m/s [3]

Fig. 5: Opened milling container [3]

Volume: 2 l
Special features:
Vacuum tight closure of top flange and feed through for rotor drive
External heater (T up to 200°C)

In the second step for working with a refractory metal milling system an upgrade of the container is under planning and evaluation. Due to technological restrictions a fabrication of the vessel from tungsten as given in our first design is withdrawn at the moment and coating technologies are under evaluation. In these improved systems tungsten milling balls will be applied to reduce contaminations by e.g. Fe and C resulting from abrasion of the steel or hard metal balls.

Fabrication and analyses of milling balls:

Due to the abrasive conditions during mechanical alloying the milling ball material has to be adopted to the processed powders to eliminate contamination by impurities. For W alloys it is well known that small traces of non-metals e.g. C influence DBTT strongly and shift the transition temperature to higher values. Elements like Fe will reduce sintering temperatures of W and reduce its re-crystallization temperature. Both type of elements (non-metals and metals) will be introduced into the synthesized precursor by applying hardened steel balls or hard metal balls.

Different paths to reduce precursor contamination are tested at the moment ranging from self coating by handling of steel or hard metal balls in W powders up to applying refractory metal balls (Mo, W or WL10). However, in contrast to steel or hard metal balls W-balls are not offered commercially. Sintered balls will have not the required strength and stability. Whereby the strength of W balls fabricated from drawn rods have to be tested. For these analyses fabrication of W balls was tested by turning. Fig. 6 shows a machined W ball with diameter 8 mm. The analyses of surface roughness is given in Fig. 7.

Fig. 6: W ball fabricated by turning
Diameter 8 mm
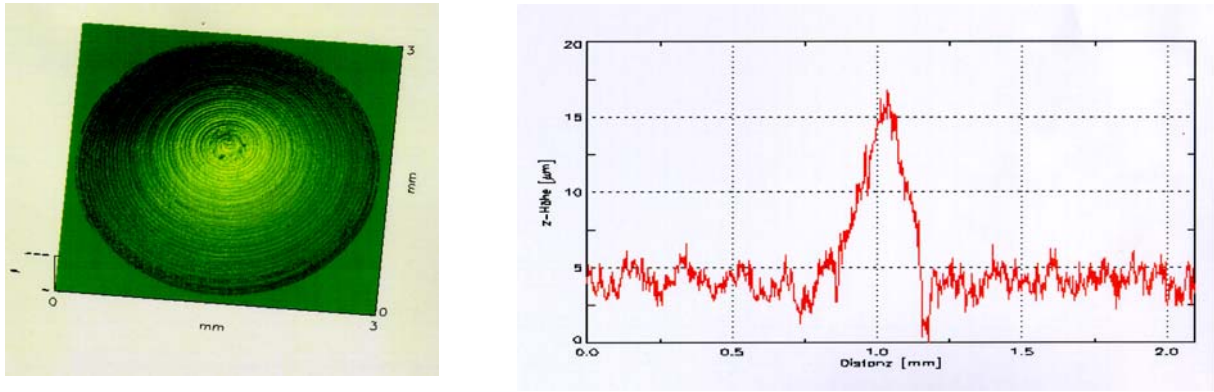
Fig. 7: Surface analyses of fabricated W milling balls
Left: 3 D view of ball segment, Right: roughness diagram
R_{max} = 10.6 µm, R_z = 5.6 µm and R_a = 0.86 µm

Analyses of W powders:

In the first test series it is planned to use fine W powders (sub-micron size) for the mechanical alloying process. Several commercially available products were analysed concerning particle shape and particle size distribution. Characteristic for the size distribution of the tested powders was a multi humped curve. The fine fraction of the analysed powders was found to be near 200 nm, however, most particles were bigger than 500 nm. Maxima of the distribution were found near 1 µm and several 10 µm. The

Fig. 8: TEM analyses of a W powder fabricated by Zhuzhou Cemented Carbide Group Co.

bigger particles can be described as agglomerates with complex geometries and voids resulting from the reduction process. These agglomerates can not be cracked by simple methods e.g. ultrasonic methods due to their strong binding.

Caused by this feature of the precursors the first milling tests will be focused on cracking these agglomerates before performing tests on mixing the powders with ODS particles.

Fig. 9: Distribution of particle size of the ZCC W powder [4]

Actual status:

The work on designing the milling equipment to the evaluated requirements in Mechanical Alloying of W-alloys was started in 2004. The basic milling equipment was installed in the second half of this year and equipped with the first delivered heat able milling container fabricated from steel. The inserted rotor system is fabricated from steel with hard metal plated rotor wings. In the 4th quarter of 2004 commissioning tests with steel were successfully performed and first loading with W powders is under execution. In the first step basic milling cycles for analysing the cracking behaviour of commercially available W powders are planned. Parameters of these tests will be the rotor frequency (rpm) and milling time. The analyses of the synthesized powders will be mainly focused on particle size and contaminations. First analytical results are expected for first quarter of 2005.

Planned work 2005:

After successfully performing the commissioning tests in 2004 with the installed Mechanical Alloying System and performing the first milling and de-agglomeration tests of W powders the work in 2005 will deal mainly in:

- Analyses of milling parameters (Frequency, time, temperature, loading ratio) on parameters of synthesized W powders (e.g. particle size, morphology, contamination)
- Analyses of ODS powder behaviour during milling (size, morphology).
- Testing of mixed W – ODS systems.
- Development and testing of tools for upgrade of milling container and rotor (e.g. W coating).
- Testing of pressing behaviour of synthesised powders.
- Performing of sintering tests.
- First tests on grain growth.
- Preparation of canning methods for HIP compaction.

The main expected result in 2005 will be the demonstration of homogeneous fine (sub-µm range) dispersion of ODS particles in the precursors. This would be the first step for improving commercially available W alloys which show as large handicap the arrangement of ODS particles in channel structures with size in the µm range.

Staff:

W. Krauss
J. Konys
R. Lindau
A. Moeslang
M. Rieth
S. Baumgärtner

Literature:

[1] P. Norajitra, et al., State of the Art: Development of a Helium-cooled Divertor for Demo, 20th Symposium on Fusion Engineering (SOFE), San Diego, CA, USA, 13. – 17.10.2003.

[2] Metallwerk Plansee, Product information, Reutte, Austria.

[3] Zoz GmbH, Technical Product Information, 57482 Wenden, Germany.

[4] B. Zeep, Analyses for powder injection moulding, private communication.

TW3-TTMA-002 D3
Characterization of Tungsten Alloys

1. Objectives

A structural component like the divertor is subjected during service to very high heat loads and also to alternating thermal and mechanical stresses as a consequence of the pulsed reactor operation. Even for helium cooled ITER divertor concepts the operating temperatures override the recrystallization of pure tungsten or tungsten alloys. The knowledge of the reasons of the creep fatigue endurance of these materials becomes more important.

2. Testing facility

To perform tensile experiments in a temperature range between 600 and 1300°C on improved divertor structural materials on tungsten basis it is necessary to qualify our high temperature tensile testing facility.

The delivery of the specimen gripping and strain measurement system was end of September 2004. Since the high temperature high vacuum furnace, necessary for testing, was occupied by diffusion welding activities of EUROFER 97 the beginning of the experiments is delayed until January 2005.

The fabrication of 10 specimen on pure tungsten and on WLa_2O_3, respectively, had been performed and the specimens are ready for testing.

Fig. 1: High temperature pull rods for tensile- and LCF-testing.

Staff:

C. Petersen
D. Rodrian
M. Klotz

TW4-TTMA-002 D3

Development of Testing Procedures for Mechanical Characterisation of Plasma Sprayed or CVD Coated W Layers on EUROFER Steel before and after Irradiation

Introduction

Tungsten coatings of several millimetres in thickness can be produced by plasma spraying or CVD. Such coatings are of interest as a protection material for plasma facing first wall components made of EUROFER steel. The mechanical behaviour of such tungsten coatings and its behaviour after irradiation is totally unknown.

Because only small volumes can be irradiated a method is required with which the mechanical properties, such as yield strength and hardening behaviour, of small volumes can be tested. In addition, tungsten is very brittle and it is practically impossible to perform standard tensile tests at temperatures below about 600 °C. One possible alternative to tensile testing is the use of depth-sensing indentation, which supplies information on the viscoplastic deformation properties of a small volume under simple experimental conditions. The capabilities for testing W-coatings on EUROFER steel will be investigated. The goal of this deliverable is to install an indentation testing device in the Fusion Materials Lab (FML) at the Forschungszentrum Karlsruhe and use it for mechanical characterisation of materials before and after irradiation.

State of the Art

This deliverable has been established spring 2004. At Forschungszentrum Karlsruhe Experience on indentation testing gained during 10 years in microsystem technology was available. Analysis methods for identification of viscoplastic mechanical properties of thin films have been under development, but are yet not fully available. Parallel to this deliverable, a cooperation with Bundesanstalt für Materialforschung und –prüfung (BAM) Berlin has been established with the common goal to investigate the practical applicability and measurement uncertainty of the analysis software under development. The neural network based software performs the determination of a stress-strain curve and viscosity parameters from spherical indentation load-depth curves. Substantial knowledge about the specific requirements for mechanical testing in the FML existed.

Results

The notification on the acceptance of the proposal for this delivery and the available budget was passed to the principle investigator end of May 2004. Until that time the work was focussed on the development of the analysis method. After notification on acceptance discussions with ZWICK were conducted and preparatory experiments have been carried out to specify the testing device.

Purchase and installation of an indentation testing device in FML (hot cells)

A list of special requirements was identified in collaboration with FML in order to ensure a proper functionality and reliability of a mechanical testing device with depth and force sensing hardness tester under a radiating environment. This includes a special varnishing, radiation sensitivity and shielding of the electronics in the hardness measurement head, radiation resistance of the included depth sensor made of glass, possibilities of distant location of electronic components from the machine, possible wire lengths, additional requirements for remote control, procedure for manual exchange of measurement head and indenter tips, and specimen handling and positioning.

The result of the discussions with specialists from ZWICK and FML was, that only a currently available standard equipment can satisfy both, the time plan and available funds. All other alternatives would lead to a complete new development for shielding the sensitive measurement head and electronics from the surrounding radiation. In order to reduce the radiation, the machine will be located instead in a separate cell that exposes the device to a significantly reduced radiation.

For a specification of an optimum load and depth resolution of the hardness measurement head, preparatory work was carried out using an available Zwick ZHU2.5 (maximum force F=2500 N) at IMF II and a Zwick with hardness head at BAM Berlin (maximum force F=200 N) for tungsten, EUROFER and MANET-II. The comparison of the experiments revealed that the 2.5 kN head shows significant deviations in the lower loading range compared to the 200 N head. However, the lower loading range is of significant importance for the further analysis of the stress-strain curve. To ensure that the 200 N head provides sufficient maximum force for all materials, experiments have been conducted, which are shown in figure 1. Table 1 gives an overview about maximum loads for the materials at indentation depth h=0.1R for a diamond indenter with R=0.25 mm. It has been found that all materials can be tested using a standard Rockwell indenter with a tip radius of 200 μm and a hardness measurement head with a maximum load range of 200 N. This will, in addition, produce much smaller indents so that more experiments can be carried out with a single specimen compared to the 2.5 kN measurement head. As a result, a basis for an improved statistical evaluation of the identified stress-strain curves is provided. Also valuable information on the variation of local mechanical properties, like e.g. influence of the radiation on the mechanical properties over the cross-section of a specimen, can be obtained in this way.
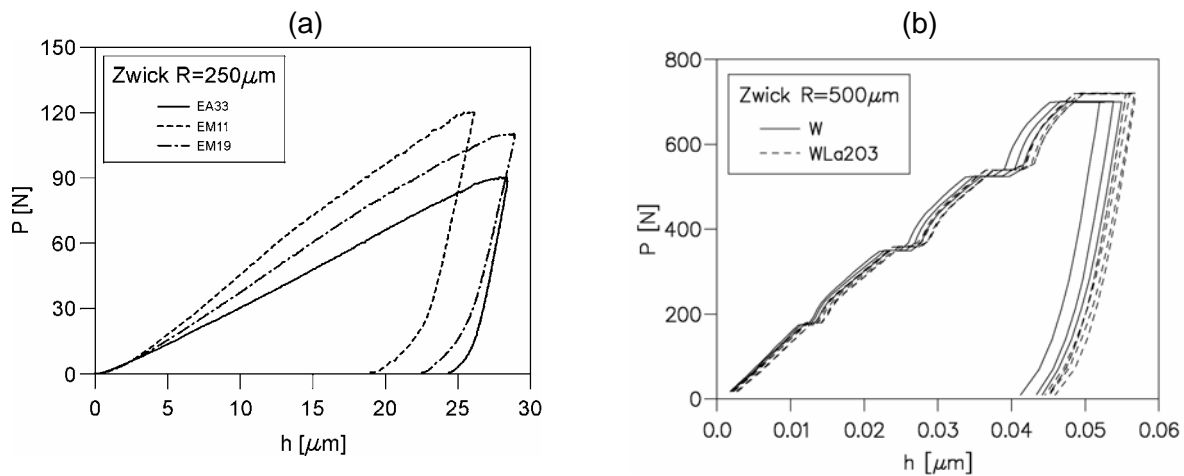
Fig. 1:   Indentation experiments with Zwick-Indenter for (a) MANET-II (EM11, EM14) and EUROFER 97 (EA33) (b) Bulk W and W-1%La$_2$O$_3$.

The purchase of the Zwick ZHU2.5 has been started November 2004. Soonest delivery of the machine is therefore May 2005. As a consequence installation and testing of the device in the FML is expected to take till end of 2005, i.e. a delay of at least 6 months is expected compared to the original time plan.

Table 1:   Maximum load necessary for spherical indentation with tip radius R=0.25 mm.

Material	EUROFER 97 EA33	MANET-II EM19	MANET-II EM11	W	W-La$_2$O$_3$
Max Load at h=0.1R	83 N	100 N	118 N	175 N	180 N

Development of indentation testing procedure and application to unirradiated W-layers at room-temperature for measurement of Young's modulus, stress-strain behaviour and creep properties

The neural network software developed for the analysis of bulk materials and coatings has been developed and then experimentally verified in cooperation with BAM Berlin. Due to the reduction of the tip radius to 200 µm, the maximum indentation depth will be 20 µm. The thickness of W-coatings currently under discussion is about 2.5 mm and the ratio of maximum indentation depth to coating thickness is less than 10 %. Under such conditions the influence of the substrate can be neglected and the analysis can be conducted in the same manner as for a bulk case. In figure 2 micrographs of plasma sprayed W-coating on top of an EUROFER substrate are shown. The specimen was provided by IPP Garching. It can be seen that the W-coating consists of two layers, a thinner one with a thickness of about 1 mm is next to the substrate. The W-coating is rich of large pores with diameters from 10 to 200 µm. To carry out indentation experiments, the specimen was carefully polished and only good places were used for indents. This underlines the requirement that the indenter must be equipped with a calibrated optical microscope and a remote controlled x-y-stage to place the indents at appropriate places.
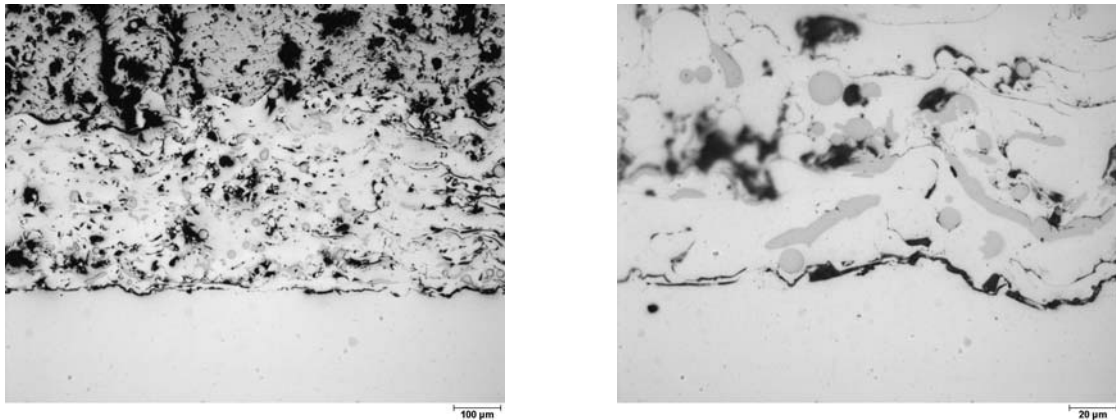
Fig. 2:   Micrographs of a plasma sprayed W-coating on EUROFER (Scale:100 µm; 20 µm).

In figure 3 the indentation curves and results of the neural network analysis are shown for the EUROFER substrate. The homogeneity of this material yields a very good agreement of the monotonic load-depth curves for two very different indenter tip radii of 250 µm and 10 µm measured with the Zwick ZHU2.5 and the Nanoindenter XP, respectively. Since Nanoindenter tips show always a deviation from the ideal spherical tip shape, an additional correction method has been developed and verified using very fine grained nanocristalline nickel.
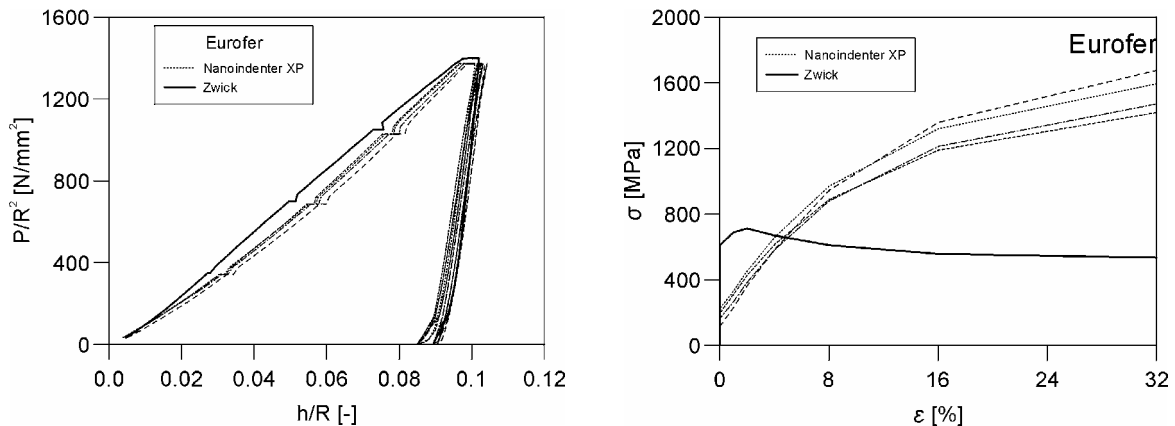
Fig. 3:   Results for EUROFER: (a) Load-depth curves measured with Zwick ZHU2.5 (R=250µm) and Nanoindenter XP (R=10µm); (b) Stress-strain curves from analysis.

The deviation in the loading curves between the two indenters arises very likely from the measurement uncertainty of the 2,5 kN hardness measurement head, which has been used below 10% of its force range. Despite this problem, the good agreement of the curves at maximum load and the low scatter of the nanoindentation data indicates clearly, that the material is very homogeneous and, consequently, the load-depth curves and the stress-strain curves show a very low scatter. Regarding the viscous properties it can be seen that also the creep phases are in very good agreement between Zwick and nanoindentation data.

Further experiments have been carried out on the W-coating and are presented in figure 4. Here a clear difference has been found for the two tip radii. The nanoindenter experiment can be considered without pores since the indentation depth is 1 μm and the indent can be located easily in a region far away from pores. On the other hand, the Zwick measurement shows much softer behaviour, which can be regarded as an effective material behaviour of the W-coating including pores. With increasing indenter radius the effect of pores increases and the material effectively softens. It can be seen that the stress-strain curve obtained from the Zwick indenter is below all curves obtained from the analysis of the nanoindentation data. For verification, the stress-strain curve obtained from macro indents in bulk W from figure 1(b) is included in figure 4(b). It can be seen, that this curve represents a good average of the stress-strain curves obtained from nanoindentation experiments.
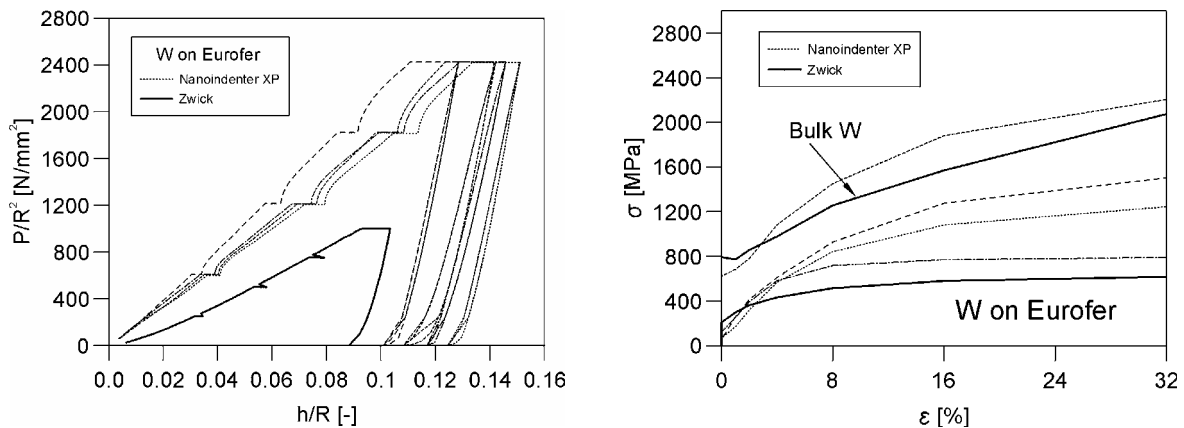
Fig. 4: Results for W-Coating: (a) Load-depth curves measured with Zwick ZHU2.5 (R=250μm) and Nanoindenter XP (R=10μm); (b) Stress-strain curves from analysis.

Conclusions and Outlook

The results obtained during the first year of this deliverable has shown the feasibility and potential of an indentation device in the Fusion Materials Lab (FML). Brittle materials like bulk W and W-Coatings can be tested easily with indentation methods. In addition rich information on the mechanical properties, like e.g. Young's modulus, true stress-strain curve, and creep properties can be obtained before and after irradiation. However, due to the measurement principle experiments will be restricted to room temperature.

Regarding the thickness of W-coatings under consideration and due to the reduction of the indenter size below 250 μm, the analysis can be restricted to consider the W-coating as a bulk material what is in advantage with respect to the robustness of the method. Nevertheless, the analysis software has been extended and experimentally verified for application on thin coatings as well.

The purchase and installation of the specified indentation test setup will exceed the original time plan of the deliverable by about 6 months so that first experimental tests are will be conducted in the second half of 2005.

Staff:

N. Huber
R. Rolli
M. Rieth
H.-Ch. Schneider

E. Tyulyukovskiy, IZBS/Universität Karlsruhe
D. Klötzer, Ch. Ullner, BAM-Berlin
J.-H. You, IPP/Garching

Literature:

[1] N. Huber, E. Tyulyukovskiy: A new loading history for identification of viscoplastic properties by spherical indentation, *Journal of Materials Research*, Vol. 19, pp. 101-113, 2004.

[2] E. Tyulyukovskiy, D. Shakhvorostov, O. Kraft, N. Huber: Ermittlung des viskoplastischen Spannungs-Dehnungsverhaltens metallischer Werkstoffe in Mikrodimension (Poster), 5. Statuskolloquium des Programms Mikrosystemtechnik, Karlsruhe, 10.-11.02.2004.

[3] E. Tyulyukovskiy, N. Huber: Identifikation viskoplastischer Materialeigenschaften dünner Metallschichten mit Nanoindentierung, Materials Week, München, Sept. 2004

[4] D. Klötzer: Bewertung eines Auswerteverfahrens zur Bestimmung der mechanischen Kenngrößen mit der instrumentierten Eindringprüfung. Diplomarbeit, Technische Fachhochschule Wildau, 2004, carried out at BAM Berlin in collaboration with FZK/IMF II.

[5] N. Huber, T. Dietz, E. Tyulyukovskiy: An investigation of non-linear stress-strain behavior of thin metal films, MRS 2004 Fall-Meeting, Boston, Dec. 2004.

[6] N. Huber, E. Tyulyukovskiy: Neural networks for tip correction of spherical indentation curves from bulk metals and thin metal films., MRS 2004 Fall-Meeting, Boston, Dec. 2004.

TW3-TTMA-002 D7
Screening of Promising Tungsten Candidate Alloys by Creep Testing and Microstructural Characterization

Overview

Since the recrystallization temperature of W and its alloys decreases significantly with aging time, even dispersion strengthened W alloys can re-crystallize during DEMO relevant exposure times in the temperature range where the structural material of advanced divertors must operate. Tungsten and selected W-alloys are considered to be the primary candidates for armour and structural materials of ITER and of even more ambitious DEMO divertor designs. For the later, present design outlines are based on an armour material with temperatures up to about 2000 °C or even more, and a structural material with temperatures up to about 1300 °C. A critical issue is the recrystallization of W-alloys and its interaction with aging time and elastic-plastic deformation during mechanical loading.

Therefore, the goal of this task is to perform instrumented creep rupture tests on selected reference refractory alloys (W and W-La$_2$O$_3$) in high vacuum up to about 5000 h at 1100 °C and 1300 °C, in order to provide the designers with data on relevant creep and creep rupture properties.

Progress

A special creep testing facility has been developed and implemented successfully for the present task (see Fig. 1). It allows for performing fully instrumented creep and creep rupture tests on selected reference W-alloys at typical temperatures of the divertor structural material.

From Plansee pure tungsten and W-La$_2$O$_3$ (WL10) rods (D8 mm x 1000 mm) were purchased. From these, standard sized creep specimens (M8 x 56 mm) have been fabricated, surface treated and tested in the creep test facility at 1100 °C and 1300 °C. Within the test program special emphasis has been laid on the effect of any interaction between recrystallization and long term creep properties. Besides aging tests and microstructural analysis of the materials as-delivered, up to now 6 creep rupture tests have been performed with rupture times between 35 h and 3000 h.

Results

First the recrystallization behaviour has been investigated and compared to the data sheet provided by the manufacturer. As can be seen from Fig. 2, the tungsten material under investigation ranges in the upper part of the scatter band, that is, at 1100 °C recrystallization starts after about 200 hours and at 1300 °C immediate recrystallization has to be expected.

Fig. 1: High temperature creep rupture facility. A ceramic vacuum tube is used as container for the whole specimen test and measuring equipment. All flanges and seals are water cooled. For easier installation a fold-away furnace is applied to the testing device.

Microstructural investigations on the materials as delivered by TEM and SEM (see Fig. 3) have shown that the grain size is inhomogeneous and varies between 2 and 6 µm. Further the grains are oriented along the rod axis which results from forging during rod production. As a consequence, the formerly spherical shaped La_2O_3 particles have been deformed to needles – also aligned parallel to rod direction – with diameters of about 0.5-1 µm and lengths between 10 and 20 µm.
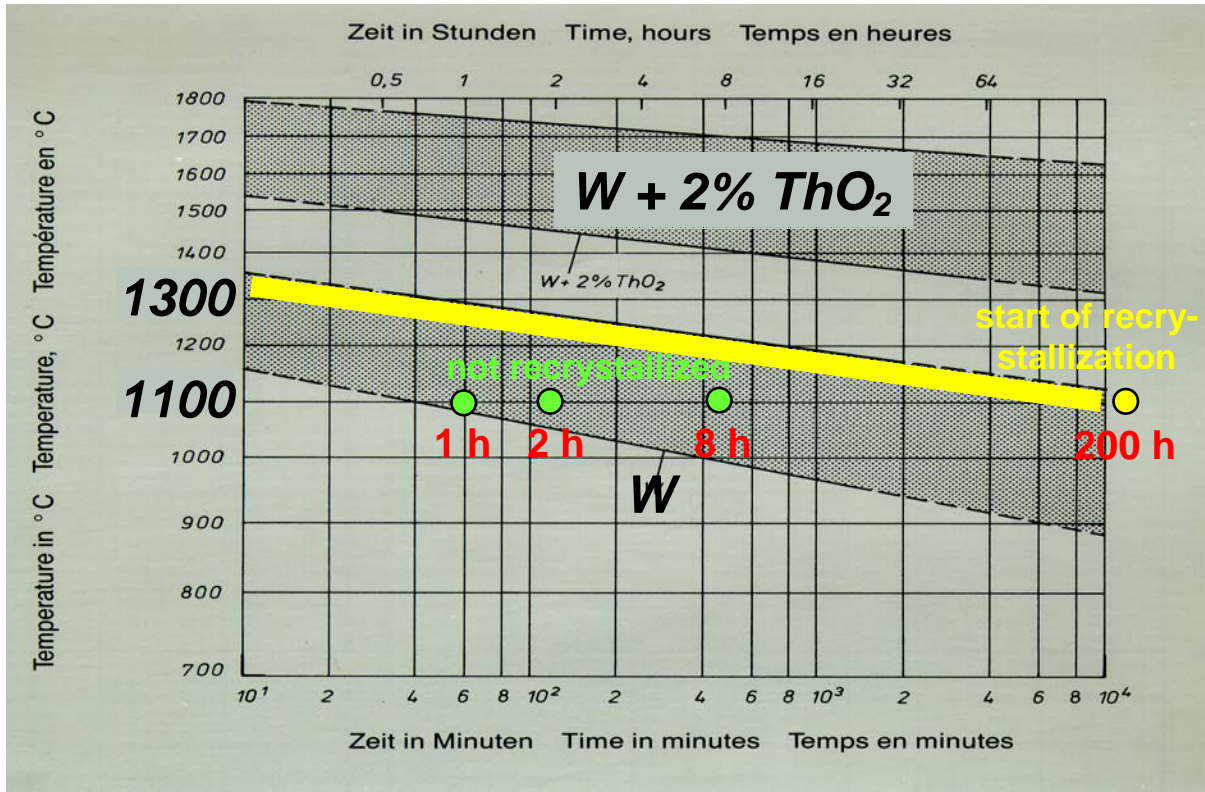
Fig. 2: The original recrystallization data sheet from the manufacturer (Plansee). According to our aging tests at 1100 °C the W rod under investigation shows no recrystallization up to about 200 hours. That is, the upper range of the scatter band (yellow stripe) applies to the tungsten material. For WL10 the manufacturer provides no recrystallization data. Instead, the effect of dispersion strengthening on recrystallization behaviour can be seen for the example of ThO_2.
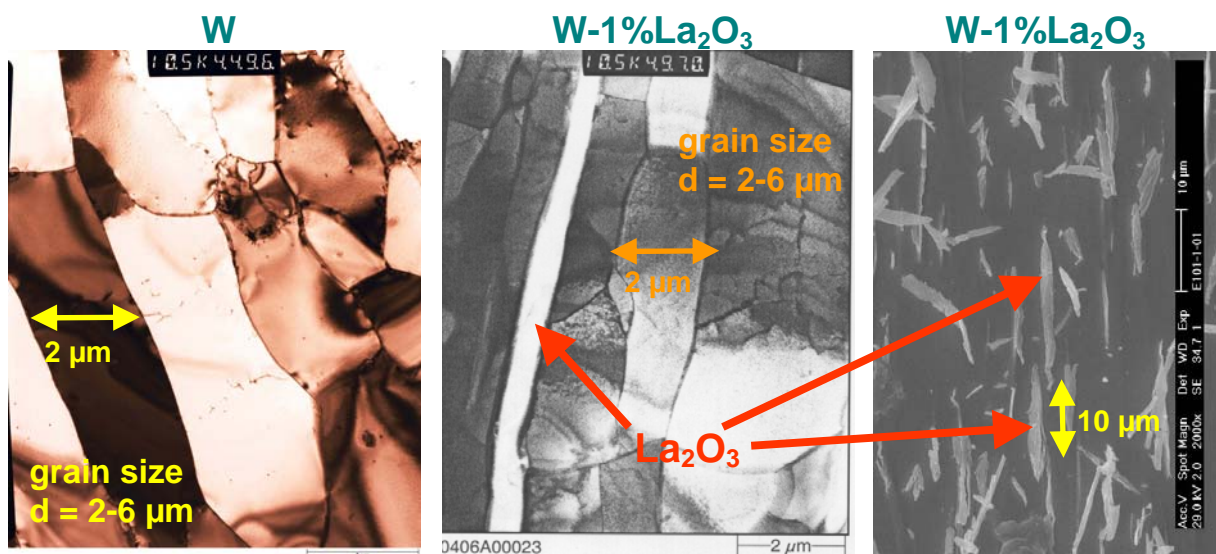
Fig. 3: Microstructure of the materials as delivered by TEM and SEM examination. Both materials show inhomogeneous grain size. The grains as well as the La_2O_3 particles are deformed along the rod axis due to forging during fabrication.

A comparison between our own creep rupture test results and those known from literature is given in Figure 4. It clearly demonstrates the lack of data in the rupture time range above 500 hours. Our first two tests at 1100 °C and 150 MPa show that the test facility is able to reproduce data (the according rupture times are 198 h and 201 h). Furthermore, the tungsten material under investigation leads to similar results as reported in the literature (the creep rupture strength is better only by approximately 5-10 MPa).
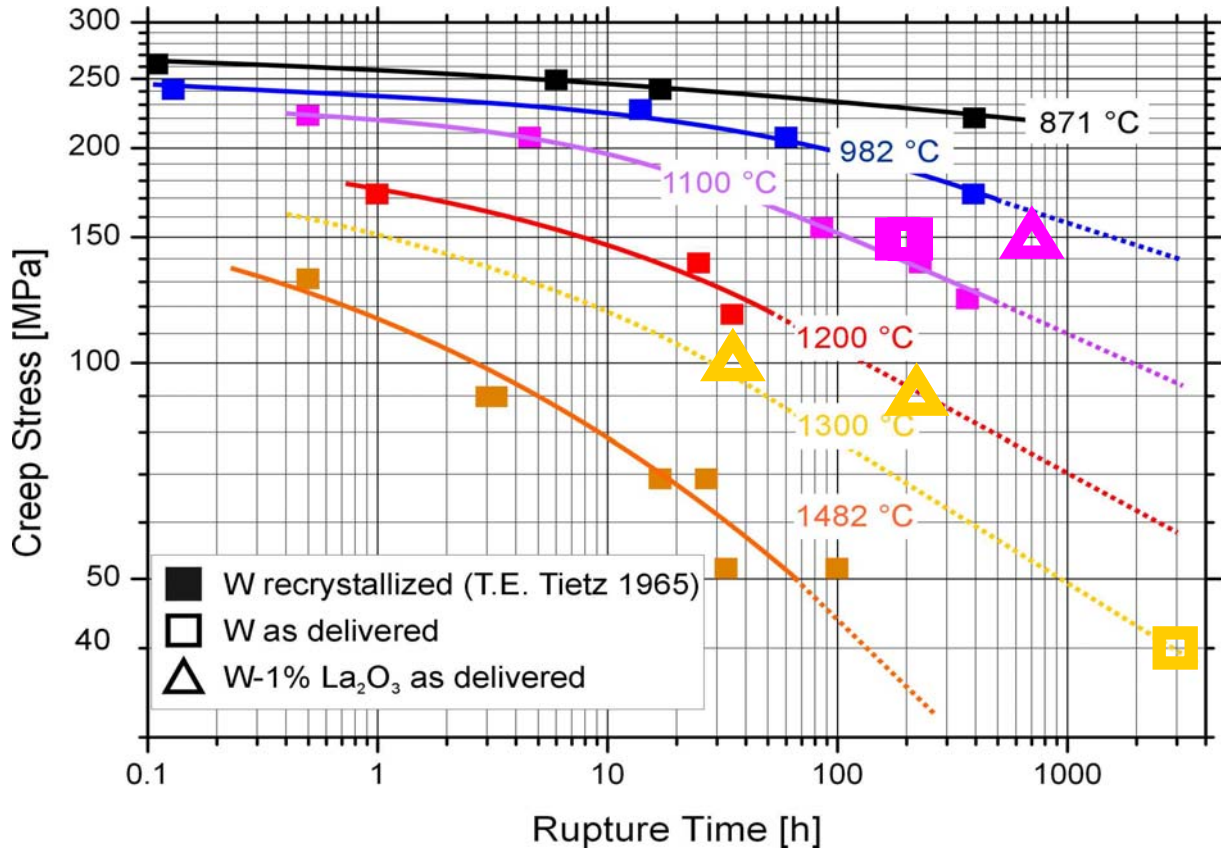
Fig. 4: Own creep rupture test results (large open symbols) compared to those available from literature (small filled symbols). The dotted lines are highly speculative and have still to be confirmed by experiments.

The third test was performed with WL10 at the same temperature and load (1100 °C, 150 MPa) which led to a rupture time of 709 hours. That is, dispersion strengthening tungsten with 1% La_2O_3 leads to longer life-times by a factor of 3 to 4 – at least in the range of the applied test parameters. This would correspond to a higher possible load of about 10-20 % for same rupture times. The other three tests were performed at 1300 °C and all ongoing investigations are focused on a full characterization at this temperature.

The results may be summarized best by looking on the specimen fractures (Fig. 5). Only pure tungsten tested at 1100 °C shows the typical ductile behaviour known, for example, from EUROFER (necking of more than 90 %). At 1300 °C after 3000 h tungsten is fully recrystallized. Therefore, the fracture looks quite different. As can be seen in Fig. 6, the grain size has increased to about 40-50 µm which is visible to the naked eye by looking on the specimen surface. It is also clearly visible that the fracture is initiated by pore formation at grain triple points and by crack propagation along grain boundaries.

All fractures of the WL10 specimens are similar (Fig. 5). Although they show no recrystallization, the fracture surface seems to be different compared to the fracture of pure tungsten at 1100 °C. But a closer look on the surface reveals also dimples. Therefore the different fracture appearance may be based on the La_2O_3 dispersoids, which reduce ductility and, therefore, lead to the different fracture surface.
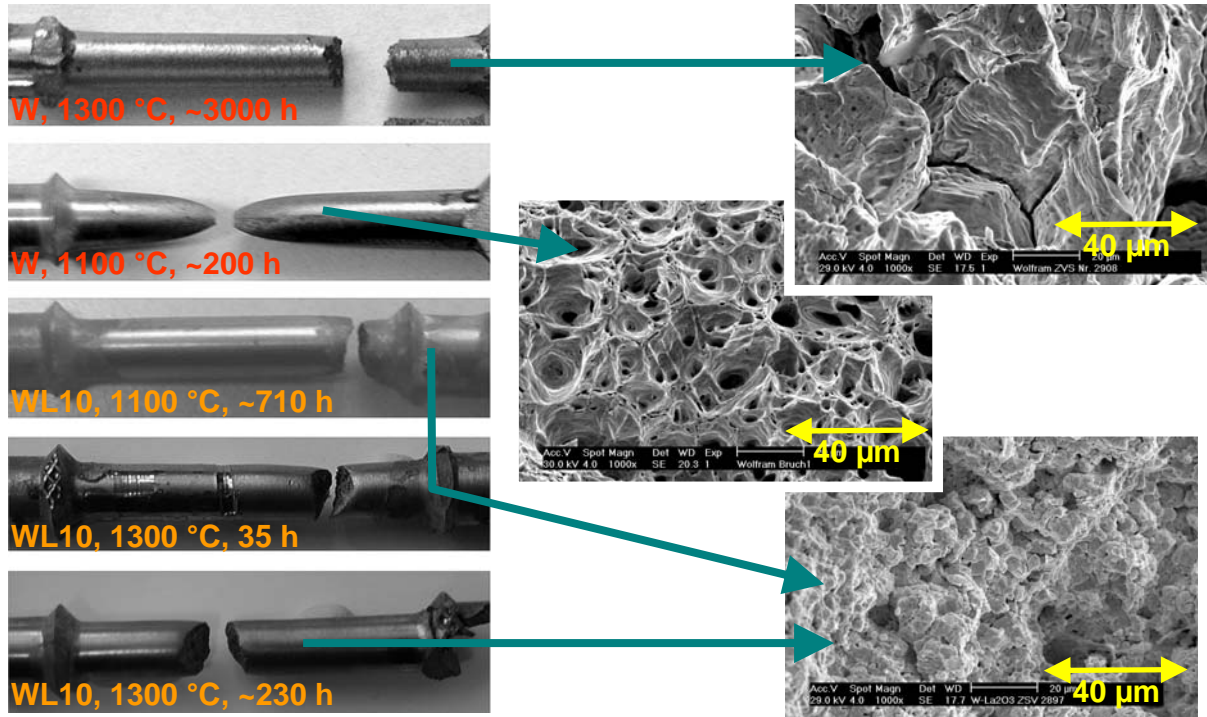
Fig. 5: Fractured specimens and the according fracture surfaces.
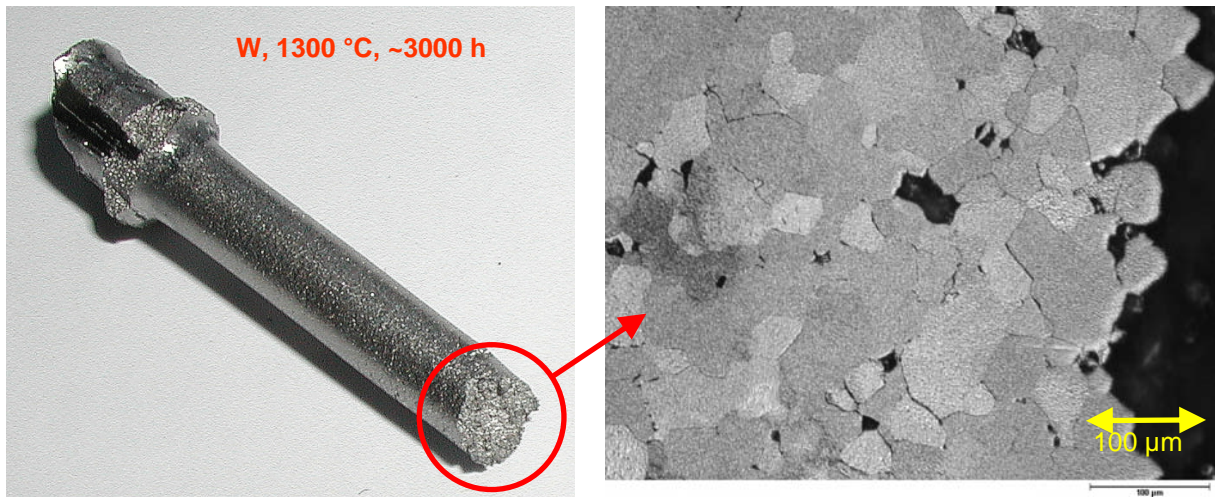
Fig. 6: After about 3000 hours at 1300 °C the tungsten specimens is fully recrystallized. This is already visible to the naked eye due to the grainy surface appearance (left image). The fracture is initiated by pore formation at triple points and crack propagation along grain boundaries (right image).

Conclusions

The pure tungsten rod material from Plansee shows starting recrystallization at 1100 °C after 200 hours whereas the La_2O_3 dispersion strengthened tungsten material (WL10) remains stable. Further, if not recrystallized, tungsten shows a very high plasticity at 1100 °C that leads to necking of more than 90 %. At the same condition WL10 shows less ductility (necking of only 20 %) but increased creep strength by about 10-20 %.

At 1300 °C, creep strength of pure tungsten drops dramatically due to severe recrystallization. First pores develop at grain triple points, and then cracks propagate along grain boundaries, which finally lead to inter-granular fractures.

The ongoing and future investigations are focused on the characterization of W and WL10 at 1300 °C in the rupture time range of 1000-5000 hours. Recrystallization of WL10 has not yet been observed, but is likely to appear during these tests.

Staff:

G. Bürkle
P. Graf
A. Falkenstein
S. Heger
U. Jäntsch
M. Klimiankou
A. Möslang
M. Rieth
H. Zimmermann

Materials Development
Nuclear Data

TTMN-001
Nuclear Data: EFF/EAF Data File Upgrade, Processing and Benchmark Analyses

The European Fusion File (EFF) and Activation File (EAF) projects aim at developing a quali-fied nuclear data base and validated computational tools for nuclear calculations of fusion reactors. The related Task TTMN-001 of the EFDA technology work programme is devoted to the evaluation, processing, application, and benchmarking of required nuclear cross sec-tion and uncertainty data as well as the development of computational tools for uncertainty calculations. The FZK contribution to Task TTMN-001 is on the evaluation of EFF-3 data, the qualification of new and updated EFF data evaluations through computational benchmark analyses including sensitivity/uncertainty analyses and the development of advanced compu-tational schemes for sensitivity calculations based on the Monte Carlo technique.

TW4-TTMN-001 D1
Evaluation of W Cross-sections up to 150 MeV

The overall objective is to develop during FP6 a general-purpose nuclear data library up to 150 MeV by adopting existing high-energy evaluations, up-grading and adapting them to the EFF/JEFF data and performing new evaluations as required. According to the priority list elaborated in 2003 to satisfy, in particular, the data needs of the IFMIF project, the objective of the 2004 work programme was to provide 150 MeV data evaluations for the W isotopes [1,2].

In the frame of the preceding sub-task TW3-TTMN-001, D2 [3], the evaluation effort was started for the most abundant W isotope 184 to complement the corresponding EFF-3 data evaluation below 20 MeV in the high-energy range relevant to IFMIF. Accordingly, a com-plete evaluation for the n + ^{184}W reaction system up to 150 MeV was performed. In the evaluation process use was made of the codes ECIS95 for optical model calculations and GNASH for reaction cross section calculations. Recent high energy experimental data were taken into account for evaluating the total and non-elastic cross sections. Both global and local optical potentials for neutrons, protons, deuterons, tritons and alphas were considered. To improve the neutron emission spectra, collective excitations were included in the GNASH calculations. Double-differential cross sections of the emitted particles were calculated on the basis of the Kalbach systematics. A complete ENDF data file was finally prepared for ^{184}W covering the full energy range data up to 150 MeV. ENDF/B-VI.8 data were adopted to some extent below 20 MeV. Extensive revisions based on GNASH-calculations were, however, applied to the ENDF/B-VI.8 data to achieve better agreement with recent experimental data. The ^{184}W data file was processed with NJOY/ACER and checked by means of MCNP calcu-lations for a tungsten benchmark experiment (see Deliverable 5 below).

The same methodological approach was applied for the evaluation of the cross-sections for the W isotopes 182, 183 and 186 performed in the frame of the current sub-task TW4-TTMN-001, D1 [4, 5]. Fig. 1 shows the flowchart of the evaluation process. Total, reaction, elastic and inelastic scattering cross sections were calculated with ECIS95 applying both spherical and deformed optical model potentials. Nuclear model calculations were performed with the GNASH code utilizing the Hauser-Feshbach theory for multiple equilibrium and the exciton model for pre-equilibrium particle emissions up to 150 MeV.
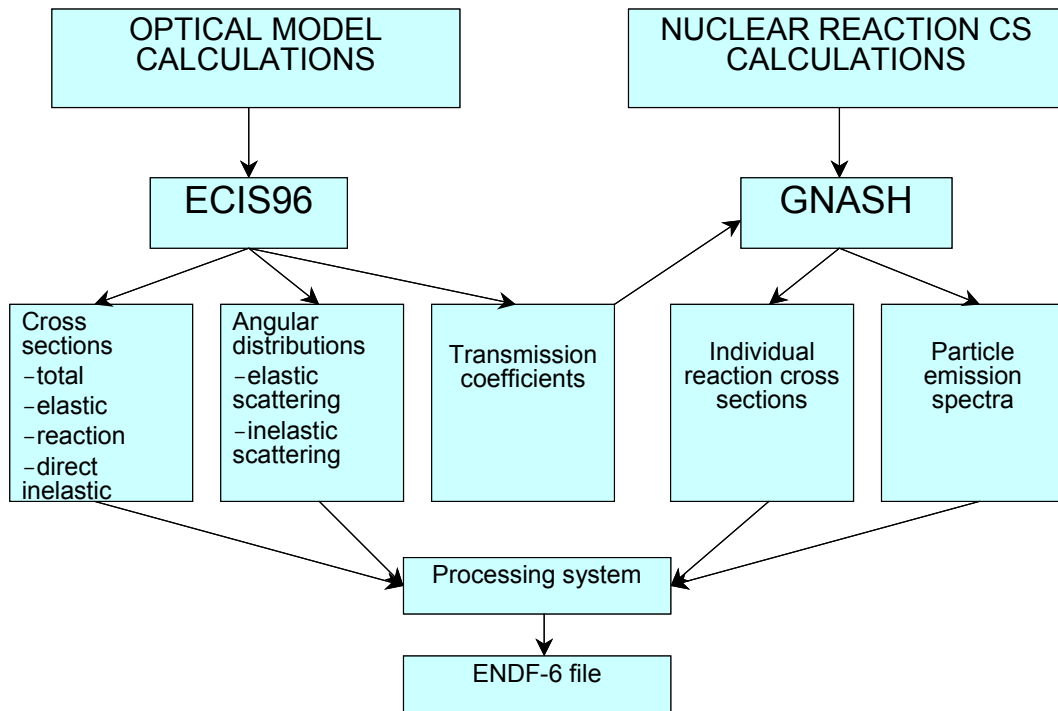
Fig. 1:   Flowchart for the evaluation of neutron cross section data of the W isotopes up to 150 MeV neutron energy.

Measurements of the total cross-sections performed recently at Los Alamos for the tungsten isotopes were used to select the high energy neutron optical model potential. The global potential of Koning & Delaroche proved to be the most suitable. It was also used for the proton exit channel. For the other outgoing charged particles, i. e. deuterons, tritons and α-particles, the potentials of Bojowald, Becchetti & Greenlees and Avrigeanu & Hodgson, respectively, were applied. Figs. 2 a-d compare evaluated and measured total cross-sections for the four W isotopes. Note the perfect agreement of the new evaluations (red curves) with the measured cross-sections over the entire energy range.
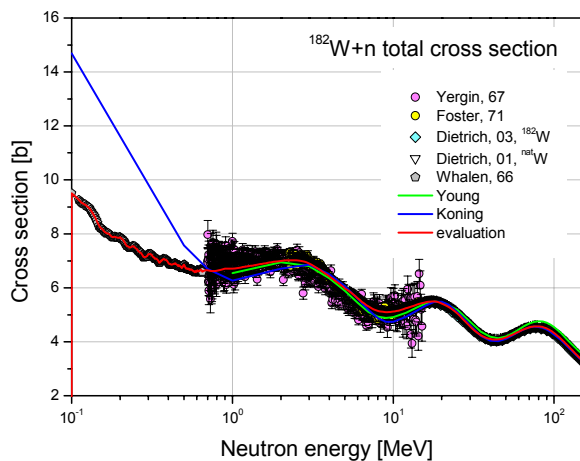
Fig. 2a: Total cross-section for n+ ^{182}W
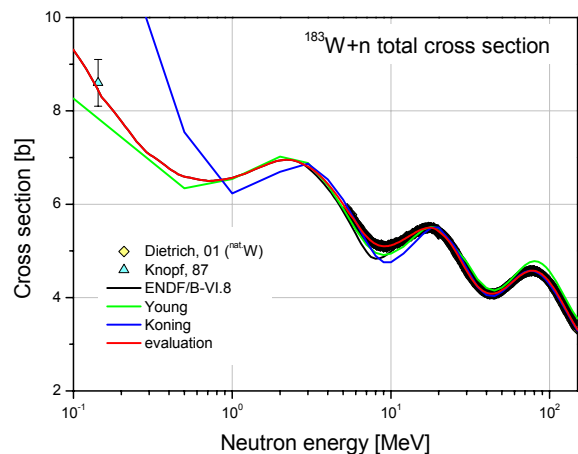
Fig. 2b: Total cross-section for n+ ^{183}W
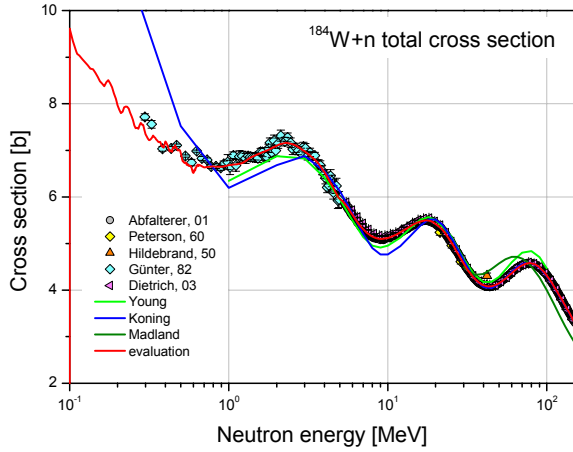
Fig. 2c: Total cross-section for n+ ^{184}W
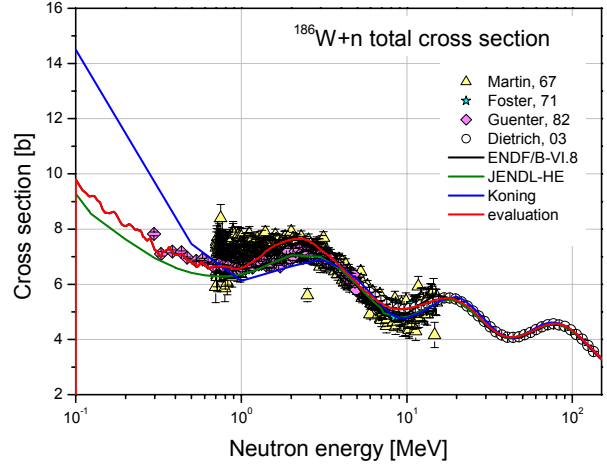
Fig. 2d: Total cross-section for n+ ^{184}W

Examples of particle emission spectra calculated with GNASH are shown in Fig. 3 for ^{182}W. The good agreement of the new evaluation with the measured emission spectra at higher secondary energies is due to the fact that collective excitations have been taken into account. These have not been included in the ENDF/B-VI.8 evaluation.
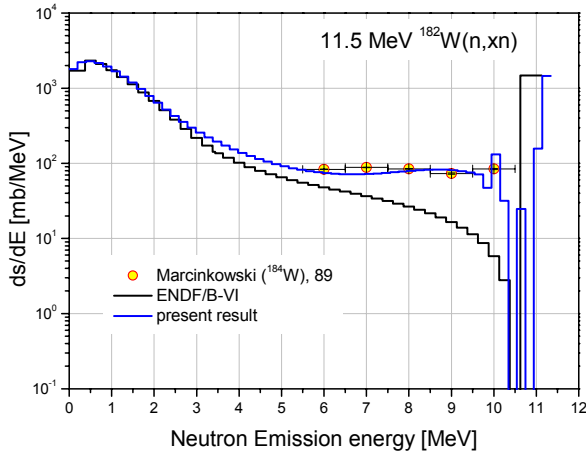
Fig. 3a: 11.5 MeV neutron incidence energy
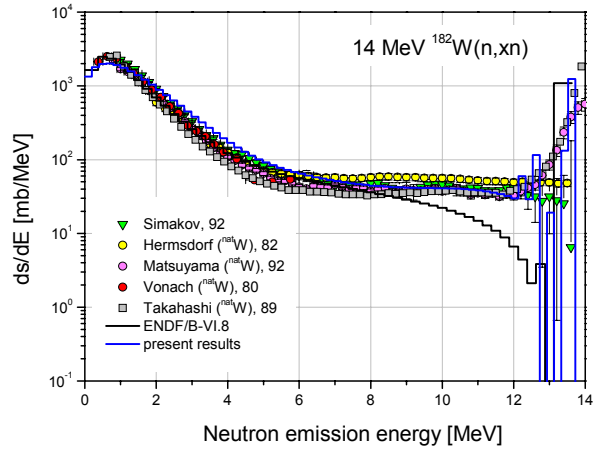
Fig. 3b: 14 MeV neutron incidence energy
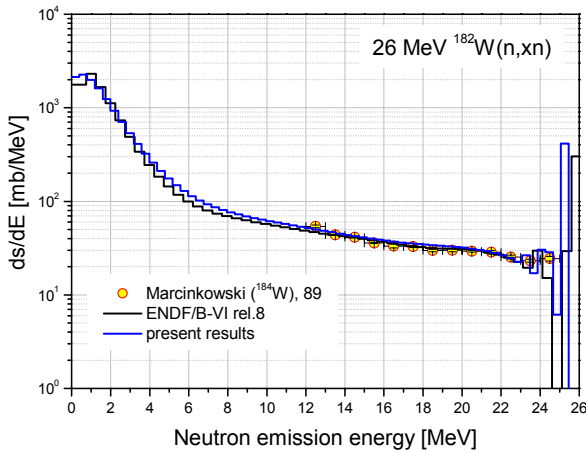
Fig. 3c: 26 MeV neutron incidence energy
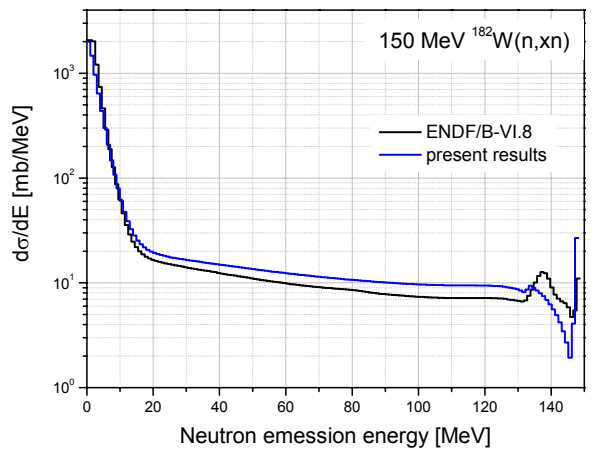
Fig. 3d: 150 MeV neutron incidence energy

Figs. 3a-d: Neutron emission spectra for n+ ^{182}W

In the final step, the evaluated data were processed into ENDF-6 formatted data files. Below 20 MeV, the ENDF/B-VI.8 data were used as starter file for the evaluation. The main modifications applied to the MF=3 file data concern the total and elastic scattering cross sections (MT=1,2), the (n,3n), (n,p), and (n,α) activation cross sections (MT=17,103,107) and the inelastic scattering cross sections (MT=51-55,91). Differential neutron emission data were modified in file sections MF=4 (angle distributions) for the reactions MT=2, 51-55 and in file sections MF=5 (energy distributions) for MT=91. Above 20 MeV, the files contain complete new evaluations. The high energy data are stored in file sections MF=3 (MT=2, MT=5), MF=4 (MT=2) and MF=6 (MT=5). The MT=5 cross-section accounts for all reactions with the emission of secondary particles. MF=6 contains particle emission spectra in the centre of mass frame and photon and recoil spectra in the laboratory system. Table 1 shows an overview of the contents of the evaluated ENDF data files for the W isotopes.

Table 1: Contents of the evaluated ENDF data files for the reaction systems n + [182, 183, 184, 186]W up to 150 MeV neutron incidence energy.

File section		Reaction type (MT)	Comments
MF			
1	Comment section	451	
2	Resonance parametrs	151	ENDF/B-VI.8
3	Reaction cross-sections	1, 2, 4, 5, 16, 17, 28, 51-91, 102, 103, 105, 107	GNASH based evaluations
4	Angular distributions	2, 51-91 16, 17, 28	new evaluations ENDF/B-VI.8
5	Energy distributions	91	new evaluation
6	Correlated energy-angle distributions	5	new evaluation for n, p, d, t, a, photons and recoils
12-15	Photon production data		below 20 MeV only; ENDF/B-VI.8 data

TW4-TTMN-001 D3
Development of Track Length Estimator Sensitivity Calculation Method with Local Version of MCNP: Implementation and Testing

The overall objective of this sub-task was to develop computational tools that allow the calculation of sensitivities and uncertainties of neutron fluxes and nuclear responses in the Test Blanket Module (TBM) on the basis of the Monte Carlo technique. To this end algorithms were developed and implemented in a local version of the MCNP4C Monte Carlo code called MCSEN that enable the calculation of sensitivities with the track length estimator (F4 tally).

Suitable algorithms for efficient track length estimator sensitivity calculations have been developed in the frame of the preceding sub-task TW3-TTMN-001, D4 [6, 7].The algorithms enable the calculation of sensitivities for fluxes and other similar responses such as reaction rates based on the track-length estimator. The method can be also applied to estimators representing surface currents and fluxes.

In the frame of the current sub-task TW4-TTMN-001, D3, the algorithms have been implemented in the MCSEN code [8]. This implementation modified the logical flow-chart of the MCSEN sensitivity calculation. With point-detectors, contributions to the response and to the sensitivity are processed at each collision and at the source, while track-length contributions are made only while crossing the sensitivity cell - with or without collisions. Track-length es-

timator sensitivities can be calculated to reaction cross sections, density, average number of fission neutrons and secondaries' angular distributions.

Testing of the code testing was performed by comparing for simple sensitivity test cases the flux sensitivities calculated with the track-length estimator in a cell and the flux sensitivities calculated by the point detector. It is noted that the calculation of point detector sensitivities with MCSEN has been tested thoroughly in the past [9]. The correct implementation of the track-length sensitivities therefore implies agreement between sensitivities (and responses) calculated with both methods.

These test cases were built so that the sensitivities can be easily calculated and convincingly presented. Most test cases were time-of-flight spectra of pulsed spheres with a 14 MeV neutron source. The sensitivity to secondaries' angular distributions was checked with a strongly anisotropically pulsed sphere. The pulsed sphere had a hole to introduce the source. The source energy was 13.182-15.090 MeV correlated with the emission angle. The leakage flux was calculated at a detector at 30 degrees at a distance of typically 7.66 m. The point detector was actually a ring detector. The cell flux was calculated in a thin spherical shell segment at that same distance.

For a 2.9 mean free path pulsed carbon sphere, Fig. 4 compares the calculated leakage time-of-flight spectra and the sensitivity to the (n, α) cross section of carbon at the source energy. The radius of this sphere was 20.96 cm. Note the very good agreement between the point detector and track length estimator calculations both for the flux spectra and the sensitivities.

Time-of-flight neutron leakage spectra

Sensitivities to (n, α) cross section of carbon
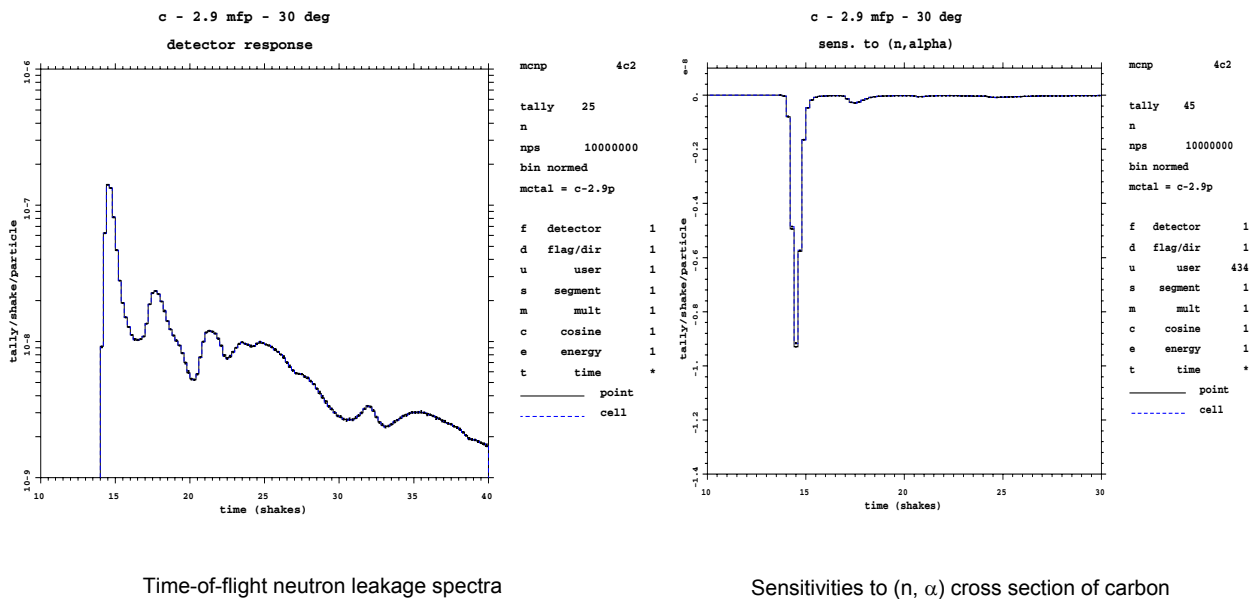
Fig. 4: Track length vs. point detector calculation of neutron time-of-flight spectra and sensitivities for 2.9 m.f.p. pulsed carbon sphere (straight lines: point detector, broken lines: track length estimator).

Similar good agreement was obtained for the other test cases including a pulsed U238 sphere with a radius of 3.63 cm and 3 different pulsed Al spheres with radii of 8.94, 16.50 and 25.50 cm, respectively. Comparisons calculations were performed for the flux spectra and the sensitivities of the leakage time-of-flight flux spectra to specific cross-sections.

The code was also tested with regard to the sensitivity to secondaries' angular distributions (SAD). In this case the test assembly was a spherical ^{56}Fe shell with inner radius of 2 cm and outer radius of 9.5 cm and a 14 MeV neutron point source in the centre. Flux sensitivities

were calculated to the Legendre moments of the elastic scattering reaction of ^{56}Fe. Again the agreement between the sensitivities calculated with the point detector and track length estimator was very good.

The track length estimator sensitivity algorithms, as implemented in the MCSEN code, were thus shown to provide reliable results. The method therefore can be applied with confidence to the sensitivity/uncertainty analyses of the TBM in ITER and the neutronics mock-up experiment.

TW4-TTMN-001 D5
Benchmark Analyses Based on Monte Carlo Calculations with MCNP for Revised/updated EFF-3 Evaluations

The objective of this sub-task is to check and validate the new EFF-3 data evaluations for a reliable use in design calculations and provide feed-back to the evaluators

Comprehensive benchmark analyses for the transmission experiment on tungsten were performed previously as part of Task TW3-TTMN-002 [10]. A detailed Monte Carlo based computational analysis of the experiment was performed using W data evaluations from EFF-2.4, FENDL-1 and –2. Neutron and photon flux spectra were calculated at the four locations of the spectrum measurements (5, 15, 25 and 35 cm) in the 49 cm thick tungsten assembly.

A re-analysis of the benchmark experiment on tungsten with measurements of the neutron and photon spectra has been performed using the recently released JENDL-3.3 tungsten data and the ^{184}W data evaluation provided with TW3-TTMN-001, Deliverable 2. As compared to FENDL-2 data, a better agreement of the high energy flux above 12.5 MeV was obtained with JENDL-3.3 data (Fig. 5a) due to a reduced (n,2n) cross-section at 14 MeV. A strong underestimation of the neutron flux in the 1–5 MeV range was found, however (Fig. 5b), resulting in a severe underestimation of the fast (E> 1 MeV) neutron flux up to 25% (Fig. 5c). This results from the underestimation of the neutron emission spectrum as revealed in Fig. 5d. Thus the use of JENDL-3.3 W data is considered not an optimal choice for fusion applications.

The first use of the new EFF-3 data evaluation for ^{184}W indicated significant improvements as compared to FENDL-2 and JENDL-3.3. As shown in Fig. 5d, there is a very good reproduction of the experimental neutron emission spectra. With the availability of the ongoing EFF-3 data evaluations for all four W isotopes (TW4-TTMN-001, Deliverable 1), a better agreement is thus expected for the neutron spectra measured in the tungsten transmission experiment.

First benchmark analyses have been performed on Titanium using data evaluations available from EFF-2.4, FENDL-1/2, JENDL-3.3 and NRG-2003. The latter two evaluations provide isotopic data while the first ones are for elements only. Both the neutron emission spectra at 14 MeV neutron incidence energy and the neutron leakage spectra calculated for the OKTA-VIAN spherical shell experiment have shown significant discrepancies as compared to the measurements [11]. This is also true for the most recent JENDL-3.3 and NRG-2003 Ti evaluations which show pronounced differences of the neutron emission spectra. Improvements are required for EFF-3 since the NRG-2003 data are used for evaluating the EFF-3 Ti data files which are currently close to completion.
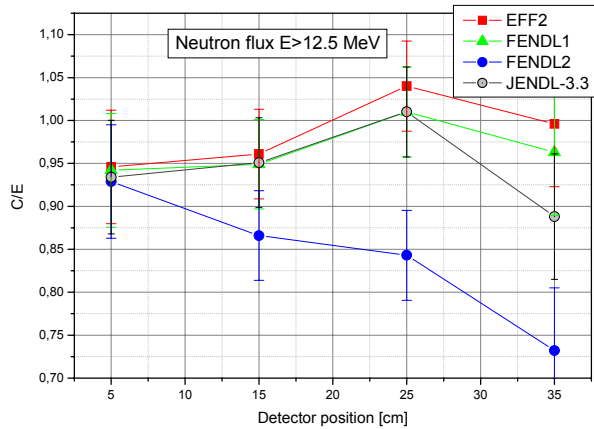
Fig. 5a: Comparison of calculated and measured neutron flux integrals (E> 12.5 MeV)
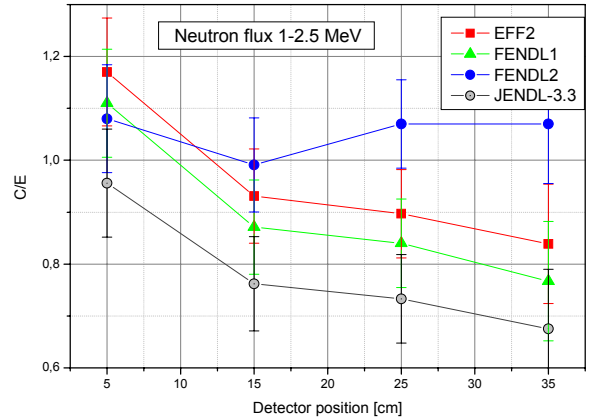
Fig. 5b: Comparison of calculated and measured neutron flux integrals (1 MeV $\leq E \leq$ 2.5 MeV).
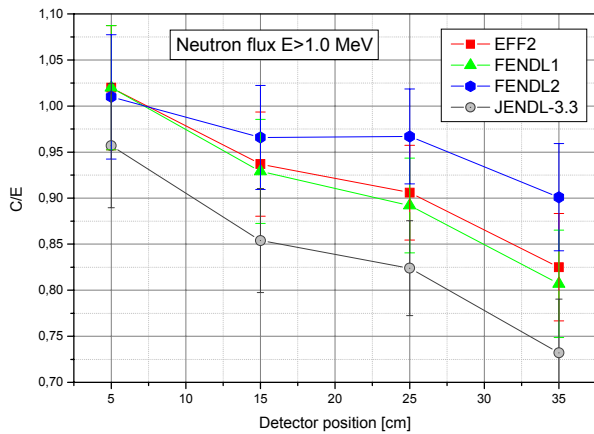
Fig. 5c: Comparison of calculated and measured neutron flux integrals (E> 1.0 MeV).
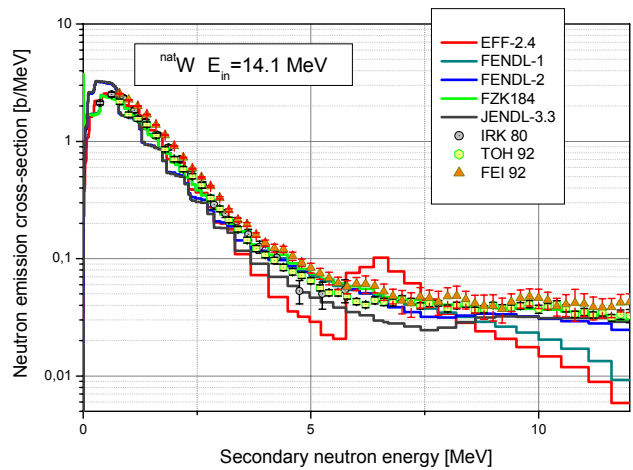
Fig. 5d: Neutron emission cross section of ^{nat}W at 14.1 MeV incident neutron energy

Staff:

Y. Chen
U. Fischer
D. Leichtle
R. Perel (Hebrew University of Jerusalem)
P. Pereslavtsev
S. P. Simakov
I. Schmuck

Literature:

[1] U. Fischer, Nuclear Data for Design Analyses of the Test Blanket Modules in ITER: Review and Recommendations for EFF/JEFF Evaluations, EFF-DOC-852, NEA Data Bank, Paris, April 2003; see also: U. Fischer, Final report on the EFDA task TW3-TTMN-001, Deliverable 1 "Review of EFF-3 data files required for TBM design", Forschungszentrum Karlsruhe, January 2004

[2] U. Fischer, P. Batistoni, E. Cheng, R. A. Forrest, T. Nishitani, Nuclear Data for Fusion Energy Technologies: Requests, Status and Development Needs, Int. Conf, on Nuclear Data for Science and Technology, Santa Fe, NM, September 26-October 1, 2004

[3] P. Pereslavtsev, U. Fischer, Evaluation of n + [184]W cross-section data for EFF up to 150 MeV, EFF-DOC-872, NEA Data Bank, Paris, November 2003; see also: U. Fischer, P. Pereslavtsev, Final report on the EFDA task TW3-TTMN-001, Deliverable 2, Forschungszentrum Karlsruhe, January 2004.

[4] P. Pereslavtsev, U. Fischer, Evaluation of n + W cross section data up to 150 MeV neutron energy, Int. Conf, on Nuclear Data for Science and Technology, Santa Fe, NM, September 26-October 1, 2004

[5] P. Pereslavtsev, U. Fischer, Evaluation of n + [182,183,184,186]W cross-sections for EFF up to 150 MeV, EFF-DOC- 912, NEA Data Bank, Paris, November 2004;

[6] U. Fischer, R. L. Perel, Final report on the EFDA task TW3-TTMN-001, Deliverable 4: "Development of algorithms for track length estimator sensitivity calculations with local version of MCNP", Forschungszentrum Karlsruhe, January 2004

[7] R. L. Perel, Sensitivity Calculation of Monte Carlo Track-Length Estimators for Cross-Section Sensitivity and Uncertainty Analyses, EFF-DOC-873, NEA Data Bank, Paris, November 2003.

[8] R. L. Perel, Implementation and testing of sensitivity calculations of Monte Carlo track length estimators in MCSEN, EFF-DOC-915, NEA Data Bank, Paris, November 2004.

[9] U. Fischer, I. Kodeli, C. Konno, R. L. Perel, Sensitivity analysis for a 14 MeV neutron bench-mark using Monte Carlo and deterministic computational methods, Fus. Eng. Des. 70 (2004), 221-232.

[10] U. Fischer, D. Leichtle, R. Perel, Monte Carlo transport and sensitivity analyses for the TUD neutron transport benchmark experiment on tungsten, EFF-DOC-860, NEA Data Bank, Paris, April 2003; see also: U. Fischer, D. Leichtle, R. Perel, S. Simakov, Final report on the EFDA task TW3-TTMN-001, Deliverable 6 "EFF-3 benchmark analyses using MCNP for new EFF files", Forschungszentrum Karlsruhe, January 2004.

[11] U. Fischer, S. Simakov, I. Schmuck, First benchmark analyses for Ti data evaluations, EFF-DOC-911, NEA Data Bank, Paris, November 2004.

TTMN-002
Nuclear Data: Benchmark Experiments to Validate EFF/EAF Data

TW3-TTMN-002 D7
TW4-TTMN-002 D2
TBM Neutronics Experiment: Design and Preparation of Measurement of Tritium Production and Neutron and Gamma Fluxes in Ceramic Breeder Material

Objectives

A neutronics experiment with a mock-up of the HCPB Test Blanket Module (TBM) shall be carried out in 2005 with the objective to validate the nuclear design calculations of the TBM. The mock-up will be irradiated with 14 MeV neutrons and the main nuclear responses will be measured and compared with the calculated values using the design tools of the TBM, i. e. nuclear data of the European Fusion File and the Monte Carlo code MCNP. In a collaboration of groups from FZ Karlsruhe, ENEA Frascati and Slovenia the Dresden Technical University will contribute with measurements of tritium production rates and of neutron and gamma-ray flux spectra in the mock-up. In 2003 and 2004 the experimental methods have to be selected and prepared.

Measurement of tritium production rates

Tritium self-sufficiency is a key issue in the development of a breeding blanket. Given the difficulty of performing reliable measurements of tritium production rates in such a mock-up experiment, a benchmark of experimental techniques was carried out in collaboration between groups of ENEA Frascati, JAERI Tokai-mura and Dresden.

In a first step, samples of tritiated water (HTO) were considered starting from certified HTO standards. Sample sets with different specific activities were prepared by each laboratory. One sample for each activity level was measured in the laboratory of sample origin, the other samples were sent as blind samples to the partners. Each laboratory measured the activities of the own samples and those of the samples received from the other two laboratories. The measured data with their uncertainties were

Fig. 1: Ratio of measured-to-expected tritium activity versus specific activity of the HTO samples.

analysed in comparison with the expected values in order to find out any systematic errors. An example of the analyses is presented in Fig. 1. All measurements were in agreement with the expected value within their total uncertainties.

Li_2CO_3 has been selected as probe material for the TBM mock-up experiment. Therefore, in a second step tritium produced by neutron irradiation in Li_2CO_3 pellets was measured. The pellets, all prepared by JAERI, were of two types: $^7Li_2CO_3$ and $^6Li_2CO_3$. The $^7Li_2CO_3$ pellets were attached to a rotating disk in order to provide identical irradiation conditions with 14 MeV neutrons. The $^6Li_2CO_3$ pellets were irradiated in a Be assembly. The pellets were also attached to the rotating disk inserted into the cavity of a bulk beryllium stack. A comparison

of tritium activities determined by the three groups is presented in Fig. 2. They agree within about 20%. The uncertainties estimated range from about 5% to 7%. Further measurements to reduce the deviations are in progress.

More detailed results of these benchmark activities were presented at SOFT-23 [1].

Measurement of neutron and gamma-ray flux spectra

The nuclear parameters of a blanket, such as tritium production rate, nuclear heating, activation and dose rate, are calculated by integral folding of an energy

Fig. 2: Ratio of tritium activities measured by the participants in the benchmark for different Li_2CO_3 pellets versus specific activity of the samples.

dependent cross section (or coefficient) with the neutron (or gamma-ray) flux energy spectrum. The uncertainty of the calculated nuclear parameter is determined by the uncertainty of both the cross section data and the flux spectrum obtained by transport calculations. Also the analysis of possible discrepancies between measured and calculated integral nuclear parameter represents a two-step procedure. First, the energy region and the amount of flux discrepancies has to be found out and second, the cross section data have to be checked. Therefore, the neutron and gamma-ray flux spectra shall be measured in the TBM mock-up and compared with the results of transport calculations.

In order to find the relevant energy ranges for the measurement of spectra, the neutron and gamma-ray flux distributions were calculated for the two positions in the mock-up that have been selected for measurements. Fig. 3 shows a typical result.

Fig. 3: Neutron group fluence in the mock-up normalized to one 14 MeV source neutron and tritium atoms produced in these energy groups on ^{6}Li, ^{7}Li and ^{9}Be.

It has been concluded [2] that the neutron flux spectra in the energy range E > 1 MeV and the gamma-ray flux spectra can be measured with an NE-213 spectrometer used already in previous fusion neutronics experiments. For the energy range E < 1 MeV which is very important for the tritium production on ^{6}Li, a new technique has to be applied. I was shown by detailed Monte Carlo calculations that time-of-arrival spectroscopy with pulsed 14 MeV neutron source represents an appropriate method [2]. In order to demonstrate this technique a LiAlPb assembly (Fig. 4) was developed which has similar

neutron flux spectra as the TBM mock-up [2]. LiAl ceramics are used as breeder material and Pb as neutron multiplier. The assembly was installed at the pulsed neutron generator of TUD. The final measurements are in progress.

Conclusions

An appropriate method for measuring tritium production rates of the TBM mock-up in 2005 has been prepared and tested.

For measurements of fast neutron and gamma-ray flux spectra in the mock-up a NE-213 spectrometer used in previous fusion neu-tronics experiments is available. For the slow neutron energy range that is important for trit-ium breeding on ^{6}Li, the time-of-arrival spectroscopy with pulsed neutron source represents an appropriate method. For the demonstration of this technique a LiAlPb assembly was in-stalled at the TUD neutron generator. Measurements are in progress.
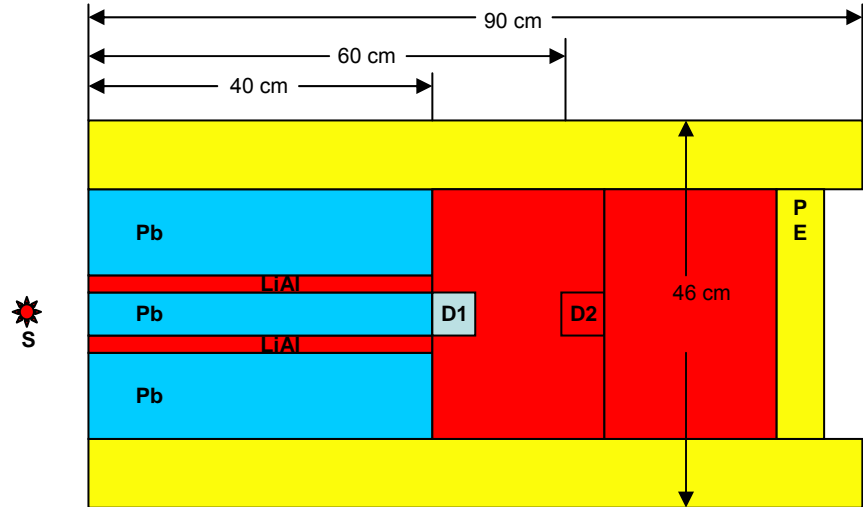
Fig. 4: Vertical section of the LiAlPb assembly installed at the pulsed neutron source (S) with the positions of time-of-arrival spectra measurements (D1 and D2).

Staff:

H. Freiesleben
E. Pönitz
I. Schäfer
K. Seidel
S. Unholzer

Literature:

[1] P. Batistoni, M. Angelone, P. Carconi, K. Ochiai, I. Schäfer, K. Seidel, Y. Verzilov, G. Zappa, SOFT-23, Veni-ce, September 20-24, 2004.

[2] K. Seidel, H. Freiesleben, Final Report of Subtask TW3-TTMN-002-D7, January 2004.

TW3-TTMN-002 D3
Validation Experiment of Gamma Activities of Yttrium Irradiated in Fusion Peak Neutron Field

Objectives

Oxide dispersion strengthened steels (ODS) are primary candidates of materials with a potential to be used at high temperatures under strong neutron flux environments, like in fusion DEMO plant first wall and blanket structural material. The characteristic feature of ODS steels is to introduce Y_2O_3 oxide particles into the matrix of ferritic/martensitic steels, which serve as a block for mobile dislocations to improve the high-temperature strength and as a sink of point defects induced by radiation displacement to maintain superior radiation resistance.[1]

For structural materials the radioactivity induced by neutrons is a central safety related topic. The short-term radioactivity with half-lives in the range of minutes to weeks is of interest for the heat production and the shut-down dose rate, whereas the long-term radioactivity in the range up to several hundreds of years is interesting for waste management. Most of the steels used in fusion design, like AISI316-IG, F82H and EUROFER, have already been investigated [2]. In the present work pure Y was irradiated, to investigate the activation performance of this new constituent in the ODS steels.

Experiment

In a calculation with the European Activation System [3], this material was assumed to be irradiated at power plant conditions; this means with a flux density of 14 MeV neutrons corresponding to a power density of 1.0 MW/m^2, for a period of one year. The results obtained for the contact dose rate as a function of the decay time after irradiation, are shown in Fig.1.
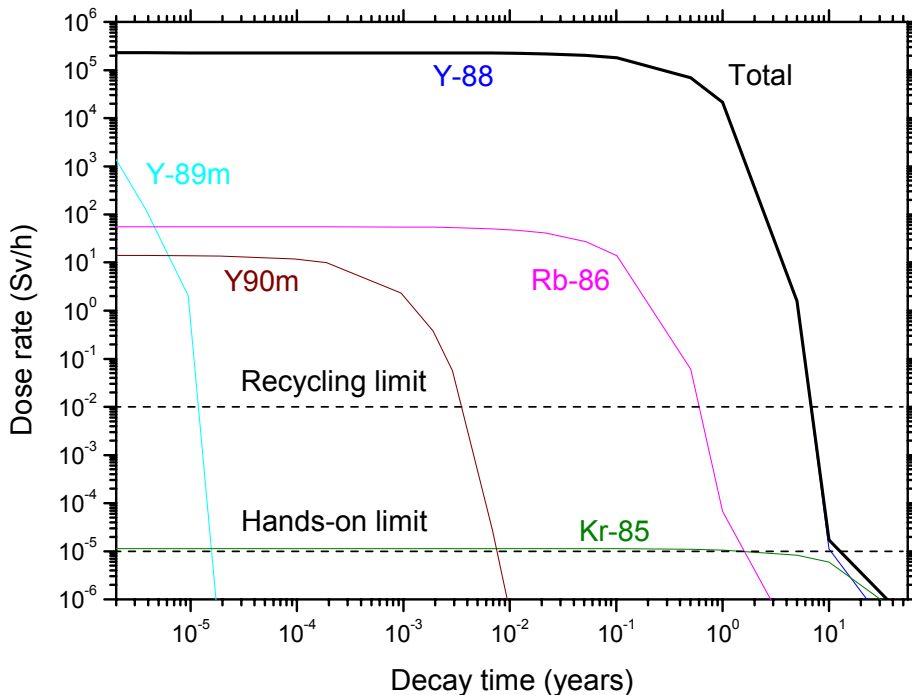
Fig. 1: Calculated total contact dose rate and contribution of the different nuclides after irradiation of Y with fusion peak neutrons of 1.0 MW/m^2 power density for one year as a function of the decay time.

The dominant radionuclide is ^{88}Y up to the hands-on limit which is reached at about 10 years. ^{89m}Y, ^{90m}Y and ^{86}Rb contribute only a very small amount. To measure the radioactivity induced by neutrons in Y, gamma-ray spectra were taken from an irradiated sample at decay times in the region between 10^{-5} and $5 \cdot 10^{-2}$ years.

The sample had a thickness of 0.64 mm, a circular front area with a diameter of 25 mm and a mass of 1.3850 g. The irradiation of the sample was performed at a neutron generator of TUD. The mean neutron energy of the fusion peak was 14.70 MeV; the full width of the peak at half maximum was 0.33 MeV. During t_{irr} = 229 min a total neutron fluence of $1.179 \cdot 10^{11}$ cm^{-2} was applied. It was determined by simultaneous activation of niobium foils and by evaluating the activity induced by the ^{93}Nb(n,2n)^{92m}Nb reaction. The cross section of this reaction was considered to be constant in the range of 14 –15 MeV with a value of 464 mb and an uncertainty of 4.2%.

Gamma-ray spectra were taken with an HPGe-spectrometer at a distance of 50 mm to the irradiated sample. The gamma-activities identified by energy and half-life were used to determine the nuclide activities using gamma-yield data from EASY. The attenuation of the neutron and gamma-ray fluxes in the sample as well as the geometry factors (source-sample and sample-detector) were determined by 3D Monte Carlo calculations.

Results

The measured activities were analysed with the version EASY-2003 [3] of the European Activation System. Results of the analysis are presented in Table 1. The uncertainty of the calculated activities ($\Delta C/C$) includes both cross section and half-life errors as estimated by EASY-2003. The uncertainty of the experimental values ($\Delta E/E$) takes into account possible errors of the gamma-activity measurements (statistical uncertainty of the gamma-ray counting, the uncertainty of the efficiency determination of the spectrometer including the geometry factor) of the sample mass, of the gamma-yield data and of the neutron flux monitoring.

The measured activities nearly agree with the calculated values within the uncertainty range. In the case of ^{90m}Y the deviation from unity is approximately covered by the experimental uncertainty. This result may be used to improve the relatively large uncertainty estimation of the EASY calculation.

It was not possible to measure the activity of the other three nuclides of Fig. 1. For ^{89m}Y, the half-life (16.6 s) was too short. For ^{86}Rb, the gamma-ray count rate was within the background, since the half-life (18.6 d) was two orders of magnitude higher than t_{irr} and the gamma-yield is only 8.78%. Also the ^{85}Kr activity (half-life of 10.8 y, gamma-yield of 0.43%) was too small to be measured.

For the two reactions producing the measured activities, ^{89}Y(n, 2n)^{88}Y and ^{89}Y(n, γ)^{90m}Y, the cross section data of EASY-2003 and EASY-2001 are compared in the Final Report of the Subtask [4] with evaluated data of other libraries and with recent experimental data. The good C/E ratios found in the present integral experiment are confirmed by these comparisons.

Table 1: Results of the irradiation;
nuclides identified, their half-life and gamma-rays with yield data used to determine the activity, the neutron reaction producing the nuclide, the ratio of calculated-to-experimental activity (C/E) and the uncertainty of both calculated and experimental activity.

Nuclide	Half-life	E_γ (keV)	Y_γ (%)	Reaction Contr. (%)		C/E	ΔC/C (%)	ΔE/E (%)
^{88}Y	106.6 d	898.02 1836.01	94 99.36	^{89}Y(n, 2n)	100	1.13	5.0	9.4
^{90m}Y	3.19 h	202.51 479.53	95.81 89.98	^{89}Y(n, γ)	100	1.14	50.0	11.7

Conclusions

The activation performance of pure Y in a fusion peak neutron field was investigated. Calculations with the European Activation System EASY-2003 predict the hands-on limit of the material after irradiation at fusion power plant conditions (power density of 1 MW/m^2, exposition of 1 year) to be reached after about 10 years. During this time the only dominant radionuclide is ^{88}Y. The activity measured for ^{88}Y in the present experiment agrees with the calculated value within 13%. Hence, the activation performance calculated with EASY-2003 is validated on this level. This is also in agreement with recent experimental cross section data. For the ^{90m}Y activity experimental and calculated values agree within 14%. The results contribute to the validation process of EASY [5].

The dose rate of pure ^{89}Y irradiated at fusion power plant condition is about ten times higher than those of steels [2].
Some of the results have been published [6].

Staff:

R. Eichin
H. Freiesleben
K. Seidel
S. Unholzer

Literature:

[1] S. Ukai, M. Fujiwara, J. Nucl. Mat. 307-311 (2002) 749; R. Lindau, A. Moeslang, M. Schirra, P. Sclossmacher and M. Klimenkov, J. Nucl. Mat. 307-311 (2002) 769.

[2] K. Seidel, R.A. Forrest, H. Freiesleben, V.D. Kovalchuk, D.V. Markovskij, D.V. Maximov, S. Unholzer, J. Nucl. Mat. 307-311 (2002) 1037.

[3] R. A. Forrest and J-Ch. Sublet, Reports Culham Science Centre, UKAEA FUS 484 and FUS 485, April 2002.

[4] R. Eichin, R.A. Forrest, H. Freiesleben, K. Seidel, S. Unholzer, Report TUD-IKTP/02-03, TU Dresden, December 2003.

[5] R.A. Forrest, M. Pillon, U. von Moellendorff, K. Seidel, J. Kopecky and J-Ch. Sublet, Report UKAEA FUS 467, 2003.

[6]   K. Seidel, R. Eichin, R.A. Forrest, H. Freiesleben, S. Unholzer, SOFT-23, Venice, September 20-24, 2004.

TW4-TTMN-002
Nuclear Data: Benchmark Experiments to Validate EFF/EAF Data

The objective of Task TTMN-002 is to provide the experimental data base required for the validation of the nuclear data libraries EFF (European Fusion File) and EAF (European Activation File) developed in the frame of Task TTMN-001 of the EU Fusion Technology Programme. According to the FP6 programme orientation on ITER (TBM) and IFMIF, the focus is on the experimental validation of TBM design calculations by means of a neutronics mock-up experiment and cross-section validation experiments relevant for IFMIF.

TW4-TTMN-002 D3
Design of TBM Neutronics Experiments: Pre-analysis of Final Mock-up Configuration

The TBM mock-up neutronics experiment aims at validating the capability of the neutronics codes and nuclear data to predict the nuclear performance of the HCPB (Helium-Cooled Pebble Bed) test blanket module (TBM) in ITER in terms of important nuclear responses such as the neutron flux spectra, the tritium production and the nuclear heating. The objective of sub-task TW4-TTMN-002, D3, was to demonstrate, by means of Monte Carlo pre-calculations, that the benchmark experiment can represent the essential nuclear features of the HCPB TBM in ITER. To this end, Monte Carlo calculations were performed for both the TBM in ITER and the TBM mock-up under preparation for the neutronics experiment at ENEA Frascati.

A suitable TBM model of the modular HCPB breeder blanket was developed with the MCNP code and integrated into the (horizontal) test blanket port of the standard ITER 20° torus sector model. Figs. 1a shows a vertical cut of the resulting MCNP model of ITER with integrated test blanket modules of the HCPB type. Fig. 1b shows an enlarged view of the TBM with the breeder units and the beryllium pebble beds.
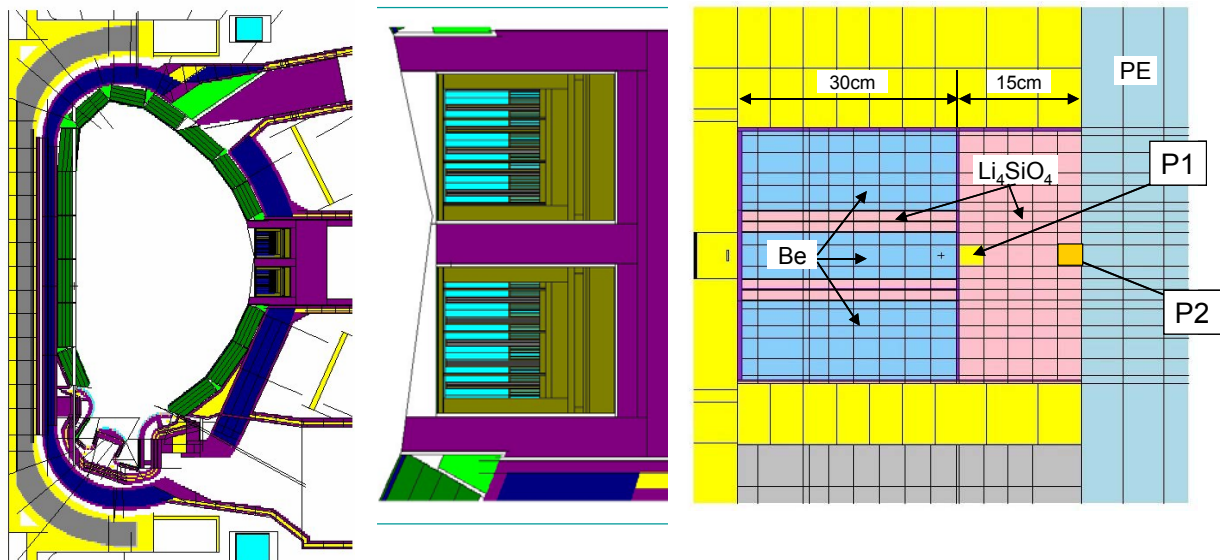
Fig. 1a: Complete torus sector model

Fig. 1b: Enlarged view of the test blanket port

Fig. 1: MCNP model of ITER with integrated HCPB TBM (vertical cross sections).

Fig. 2: MCNP model of HCPB TBM mock-up with flux measurement positions P1 and P2 indicated (vertical cross section)

A TBM mock-up assembly was designed at ENEA Frascati on the basis of the modular HCPB blanket reference design. The mock-up aims at reproducing a breeder unit embedded in a beryllium assembly. The main characteristics such as the radial thickness, the distance between ceramic layers, the thickness of the ceramic layers and the steel walls are replicated in the mock-up, see Fig. 2 for a vertical cross-section of the MCNP model.

The mock-up consists of a box of SS-316 steel box with external dimensions of 31.0 cm (x) x 29.0 cm (y) x 31.0 cm (z). The box is filled with metallic beryllium and contains two double layers of breeder materials. The breeder layers have a height of 12 mm and are assumed to be filled with Li_4SiO_4 pebbles and a natural isotope composition of lithium (7.5 at% ^6Li). At the rear end, the mock-up consists of a box with breeder ceramics with external dimensions of 31.0 cm (x) x 12.7 cm (y) x 31.0 cm (z). The blanket mock-up is backed by a thick polyethylene layer to shield the assembly from room-return neutrons. At two positions in the rear block, denoted as P1 and P2 in Fig. 2, neutron and photon flux spectra as well as tritium production rates will be measured by the team of the Technical University Dresden (TUD). The neutron flux spectra and the energy distribution of the tritium production rate at this positions, therefore, should be representative for the corresponding positions in the ITER TBM.
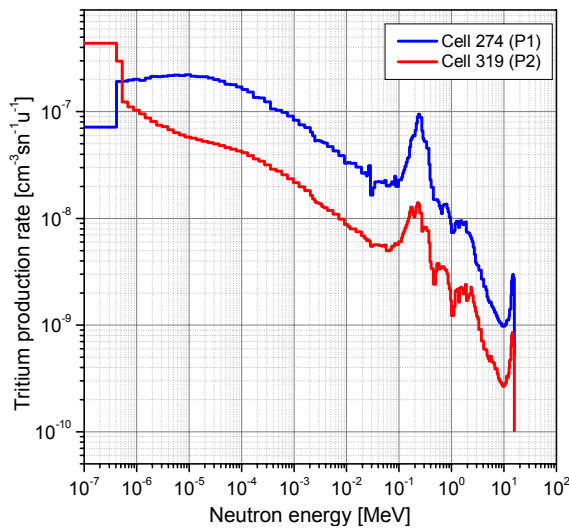
Fig. 2a: Energy distribution of the tritium production rates in detector positions P1 and P2 of the HCPB blanket mock-up.
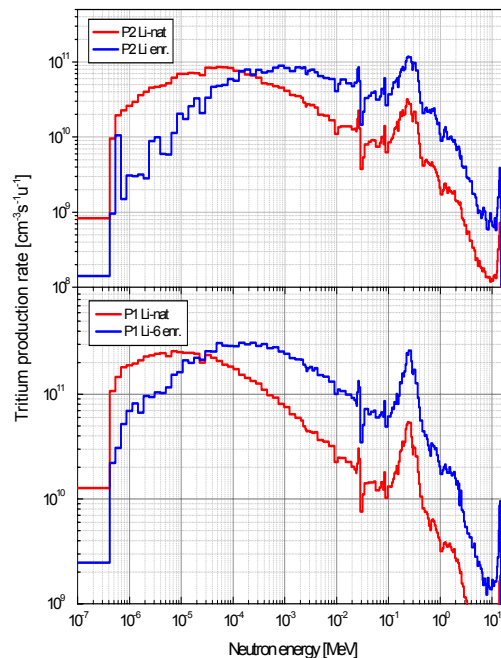
Fig. 2b: Energy distribution of the tritium production rates at the corresponding locations in the ITER TBM using natural and enriched (40at% ^6Li) Li_4SiO_4 breeder ceramics.

Neutron flux spectra distributions were calculated in the beryllium bed, the breeder ceramics and the EUROFER structure of the HCPB TBM in ITER. Energy distributions of the tritium production rates were calculated for the breeder ceramics beds. Two different lithium enrichment levels were considered in the TBM calculations: 40 at% as assumed for the HCPB Demo blanket and 7.5 at% as used in the neutronics mock-up experiment.

For the TBM mock-up experiment, the neutron flux spectra and the energy distributions of the tritium production rates were calculated at the detector positions P1 and P2 in the rear block of the mock-up. It was revealed that the neutron spectra in the mock-up are rather soft due to the large amount of beryllium and the use of non-enriched lithium ceramics.

The tritium production is mainly in the thermal/epithermal energy range as can be taken from Figs. 2 and 3. Note that there is a considerable spectral shift of the tritium production when

switching from natural to enriched lithium. The neutron spectrum at position P2 of the TBM mock-up was found to be too soft as compared to the ITER TBM conditions. As a consequence, the tritium production at P2 in the mock-up takes place in the thermal energy range which is not the case for the ITER TBM. The soft neutron spectrum at P2 in the mock-up is caused by neutrons slowed down and back scattered from the polyethylene back shield. It was thus recommended to back the mock-up assembly by a neutron reflector made of steel instead of the polyethylene back shield.
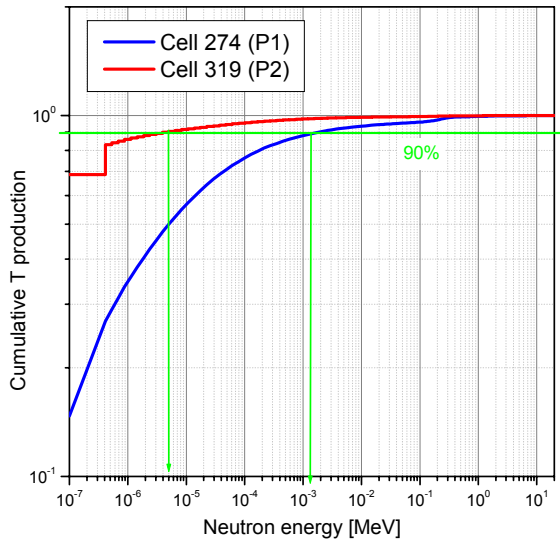
Fig. 3a: Cumulative tritium production in detector positions P1 and P2 of the HCPB blanket mock-up.
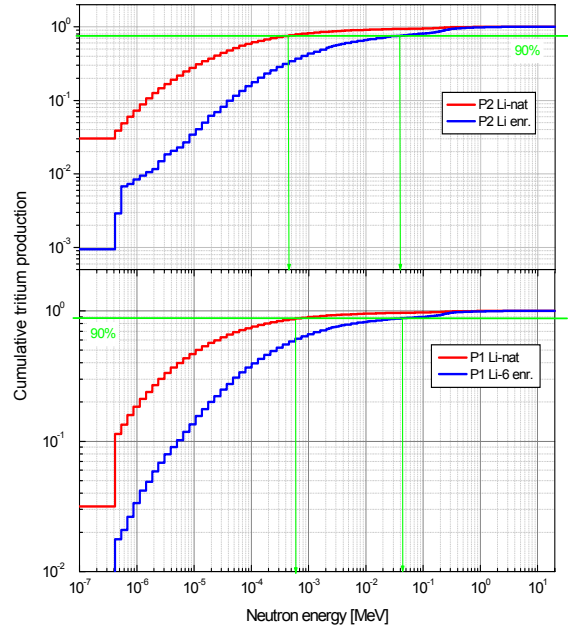
Fig. 3b: Cumulative tritium production at the corresponding locations in the ITER TBM using natural and enriched (40at% ^{6}Li) Li$_4$SiO$_4$ breeder ceramics.

Monte Carlo sensitivity calculations were performed with the MCSEN code using the point detector estimator at the two positions P1 and P2 in the TBM mock-up. The sensitivities were calculated to the cross-sections of Be, ^{6,7}Li, Si and O. The neutron fluxes and the tritium production were shown to have similar sensitivities, see e. g. Table 1 for the integrated sensitivities at detector position 1. The energy-integrated totals showed a rather moderate sensitivity to the cross-section data (less than 1% /%). The greatest sensitivity was obtained for the responses in the thermal energy range (E<1 eV). The responses are most sensitive to the beryllium elastic, the (n,2n) and the ^{6}Li(n,α) t cross-section. Uncertainties of these cross-section will therefore give the greatest contribution to the uncertainties of the calculated neutron fluxes and tritium production rates both for the TBM in ITER and the mock-up. The responses in position P2 at the far end of the mock-up were shown to be less sensitive to mock-up materials since they are dominated by back-scattered neutrons from the polyethylene shield. This result supported the above recommendation to replace the polyethylene back shield by a more suitable neutron reflector such as steel.

Table 1: Integrated sensitivities [%/%] of neutron fluxes to Be, ^{6,7}Li, Si and O total cross-sections at detector position P1.

	<1eV	1eV-1keV	1-100 keV	0.1-1 MeV	1-10 MeV	10-15 MeV	total
Be	3.17	0.53	-0.40	-0.80	-0.97	-1.77	-0.54
Li-6	-1.01	-0.40	-0.06	-0.02	-0.01	0.00	-0.10
Li-7	0.06	0.10	0.09	0.04	-0.03	-0.02	0.05
Si	0.01	0.03	0.02	0.01	-0.02	-0.04	0.01
O	0.14	0.27	0.26	0.03	-0.03	-0.07	0.12

Table 2: Integrated sensitivities [%/%] of ^{6}Li (n,α)t reaction rate to Be, ^{6,7}Li, Si and O total cross-sections at detector position P1.

	<1eV	1eV-1keV	1-100 keV	0.1-1 MeV	1-10 MeV	10-15 MeV	total
Be	3.07	0.05	0.00	0.00	0.00	0.00	0.03
Li-6	-0.84	-0.03	0.00	0.00	0.00	0.00	-0.01
Li-7	0.04	0.00	0.00	0.00	0.00	0.00	0.00
Si	0.00	0.00	0.00	0.00	0.00	0.00	0.00
O	0.10	0.01	0.00	0.00	0.00	0.00	0.00

Staff:

U. Fischer
R. Perel (Hebrew University of Jerusalem)
P. Pereslavtsev

Literature:

[1] U. Fischer, R. Perel, P. Pereslavstev, Final report on the EFDA task TW3-TTMN-002, Deliverable 6: "Design of TBM neutronics experiments: Pre-analysis for measurements of neutron and gamma flux spectra", Forschungszentrum Karlsruhe, November 2004

[2] U. Fischer, R. Perel, P. Pereslavstev, Monte Carlo Based Pre-analysis of the HCPB Breeder Blanket Mock-up Experiment: Neutron Spectra, Tritium Production and Sensitivities to Cross-Sections, EFF-DOC-898, NEA Data Bank, Paris, May 2004

TW4-TTMN-002 D5
Pre- and Post-analysis of the Validation experiments for W Cross Sections up to 55 MeV in an IFMIF – Like Neutron Spectrum

In the frame of Task TW4-TTMN-002, Deliverable 6, an activation experiment on Tungsten was performed at the cyclotron of the Nuclear Physics Institute (NPI), Řež, with the objective to provide the experimental data base for validating the activation cross-section data in the energy range relevant to the International Fusion Material Irradiation Facility (IFMIF) [1]. The objective of Task TTMN-002, Deliverable 5, conducted by FZK, was to perform the computational pre-analysis required for optimizing the experimental set-up and the measurements and to conduct the post-analysis to check and validate the high-energy cross-section data for neutron activation calculations. The computational analyses comprised transport calculations with the MCNPX Monte Carlo code for the neutron source characterization and activation calculations with the ALARA inventory code [3] and cross-section from the Intermediate Energy Activation File IEAF-2001 [4, 5]. Previous efforts to check and validate IEAF-2001 activation cross-section were performed for EUROFER-97, SS-316 and F82H steels [6-8].

Neutron source spectrum characterization

A 37 MeV proton beam impinging on a heavy water target has been used to produce a neutron spectrum up to 35 MeV similar to that of the IFMIF neutron source which employs the d-Li reaction. The objective of the present task was to reproduce the experimental neutron spectrum at the position where the W foils were irradiated. The MCNPX Monte Carlo code with the Los Alamos proton library LA-150h was used to model the experimental set-up (Fig. 1) and calculate the differential neutron yield at the points of interest. These calculations were checked against measurements of the neutron spectrum at large distance from the D_2O target using a scintillation detector. As shown in Fig. 2, MCNPX calculations with LA-150h data fail to reproduce both the absolute yield and the energy distribution of the source neutrons. By investigating the reason for the observed large discrepancy it was shown that (i) the neutron production is dominated by the proton reactions on deuterons rather than on oxygen; (ii) the LA-150h library does not properly reproduce the double differential cross sections for the D(p,n)2p reaction (Fig. 3). Therefore, the neutron flux spectrum at the positions of the W foils was constructed by combining the measured spectrum above 4 MeV neutron energy at large distance from the target with the one calculated by MCNPX

Fig. 1: MCNPX model of the experimental configuration with incident proton beam indicated.
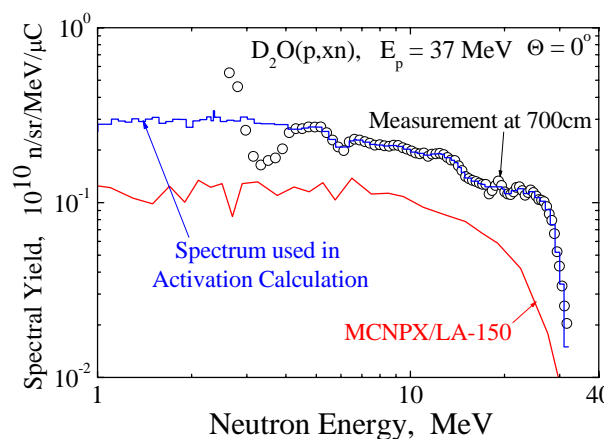
Fig. 2: p-D_2O neutron spectrum as measured and calculated by the MCNPX code with LA-150h data

below this energy. The absolute normalization has been performed relative to the yield of ^{24}Na generated in the Al monitoring foils.

In the experiment three W foils (labeled as W#4, W#7 and W#14, each containing 99.5% tungsten) have been irradiated for 2 to12 hours in different runs at distances of 2.3 – 2.7 mm from the D_2O target bottom. The irradiation history was derived from the proton beam current recorded as a function of time during the irradiations. For the short run, the time dependent proton beam current is shown in Fig. 4 together with a three pulses approximation used for representing the time-varying neutron flux in the activation calculations.
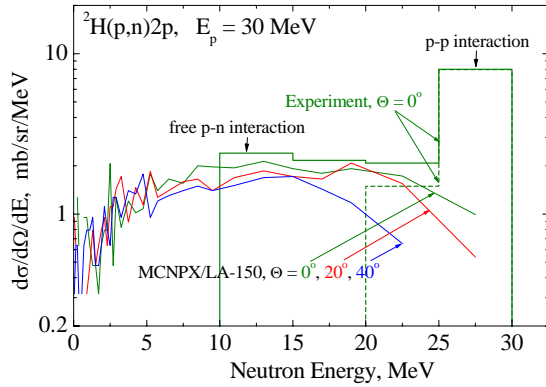
Fig. 3: D(p,xn) cross sections of the LA-150h library (curves) compared to measurements (histogrammes).
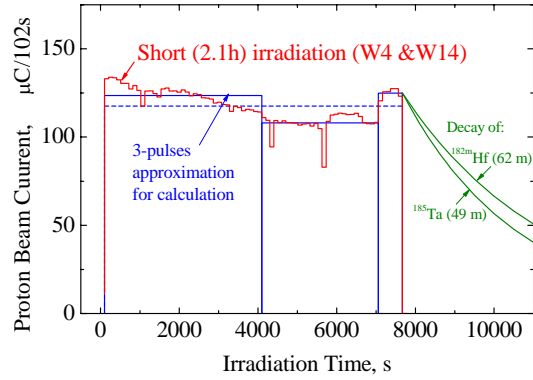
Fig. 4: Irradiation time profile as measured (red curve) and approximated for the activation calculations (blue curve).

Computational analysis of the activation experiment using IEAF-2001 cross-section data

The activation calculations have been performed with the ALARA code [3] which is capable of handling as many reaction channels as available in the Intermediate Energy Activation File IEAF-2001 [4-5]. Fig. 5 compares calculated and measured activities for the 12 radio-isotopes detected at the end of irradiation in terms of C(calculation)/E (Experiment) ratios. A reasonable agreement is found between the results of the different tungsten foil experiments (W#4, W#7 and W#14) thus confirming the consistency of the measurement and simulation procedures. For comparison, Fig. 5 also includes C/E ratios of the radioactive products generated in irradiation experiments in EUROFER-97 (p-D_2O neutron source) [6-7] and F82H (d-Li neutron source) [8] steels.

Fig. 5 shows that the ALARA calculations with IEAF-2001 data overesti-mate the activities of many of the measured radio-nuclides. Pathway analyses for the production of the specific radio-nuclides have been performed to identify possible reasons of the ob-served discrepancies. The result of such an analysis is displayed in Table 1 and Figs. 6, 7 for two hafnium isotopes. It is seen that the overestimation of the ^{182m}Hf-activity is due to a too high IEAF-2001 cross-section for the ^{186}W(n,nα) reaction ex-
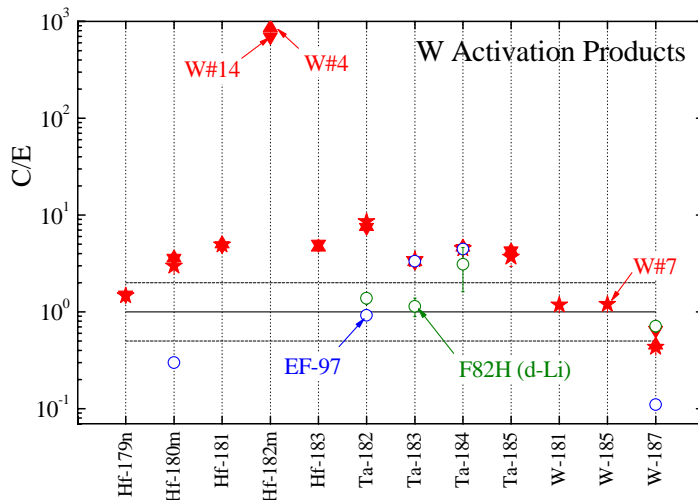
Fig. 5: C(calculation)/E (Experiment) ratios of specific activities for radioactive nu-clides produced by irradiating W and EUROFER-97 and F82H steels.

ceeding the total ^{182}Hf production cross-section of ENDF/B-VI by a factor 100.

The activation of W in a white neutron spectrum extending up to 35 MeV also indicates an overestimation of the ^{182}Hf generation with IEAF-2001 data by factor of 5. In contrast, the activation of W with 14 MeV neutrons [9] has confirmed the ^{182}Hf production cross-section of the European Activation File EAF-2003 (Table 1). The analysis of the cross section of the relevant ^{184}W(n,α) reaction (Fig. 7), which is the dominant pathway for generating ^{182}Hf, showed that both the IEAF-2001 and the EAF-2003 data agree with the available experimental data at 14 MeV. At high energies, however, IEAF-2001 overestimates this cross-section according to the present benchmark results. This is also indicated by the new evaluation of the W data performed in the frame of TW4-TTMN-001, Deliverable 1 [10].

The analysis of the tungsten activation experiment and activation cross sections up to 35 MeV thus reveals the strong need for updating the relevant cross sections in the IEAF-2001 library.

Table 1: Dominant activation reactions for the production of ^{182m}Hf an ^{181}Hf from W and C/E ratios for the activity.

Lab (Sample)	E, MeV	Library	Reaction Path	C/E
Production of ^{182m}Hf				
NPI (W)	0 - 35	IEAF-2001	^{186}W(n,nα) – 95% ^{183}W(n,2p) – 5%	693 ± 70
Production of ^{181}Hf				
NPI (W)	0 - 35	IEAF-2001	^{184}W(n,α) – 95%	4.8 ± 0.5
TUD/SNEG (W)	14 – 15	EAF-2003	^{184}W(n,α) – 100%	1.4 ± 0.2
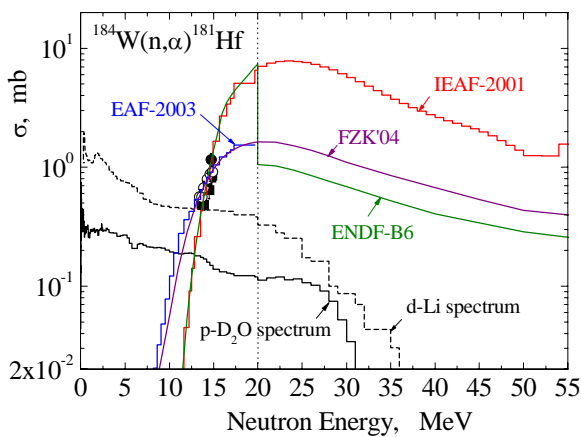
Fig. 6: ^{184}W(n,α)^{181}Hf reaction cross section: symbols – experiments, curves – evaluations IEAF-2001 (red), ENDF-B6 (green), FZK-04 (pink), EAF-2003 (blue).
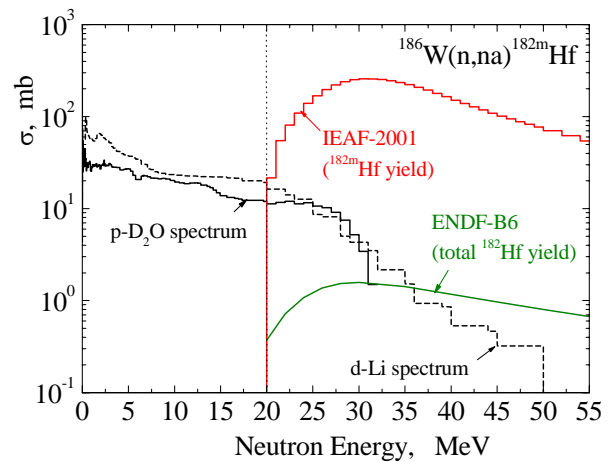
Fig. 7. ^{186}W(n,nα)^{182m}Hf reaction cross section: symbols – experiments, curves – evaluations IEAF-2001 (red), ENDF-B6 (total ^{182}Hf production, green):

Staff:

U. Fischer
S.P. Simakov

NPI Řež:
P. Bém
V. Burjan
M. Götz
M. Honusek
V. Kroha
J. Novák
E. Šimečková

Literature:

[1] P. Bém, V. Burjan, M. Götz, U. Fischer, V. Kroha, U. v. Möllendorff, J. Novák, S. Simakov and E. Šimečková,. Activation Benchmark Tests at the NPI Fast Neutron Facility, EFF-DOC-910, NEA Data Bank, Paris, November 2004.

[2] S.P. Simakov, U. Fischer, P. Bém, V. Burjan, M. Götz, M. Honusek, V. Kroha, J. Novák, E. Šimečková, Analysis of the NPI irradiation experiment for Tungsten activation cross-sections up to 35 MeV, EFF-DOC-913, NEA Data Bank, Paris, November 2004.

[3] P. P. H. Wilson, D. L. Henderson, ALARA: Analytical and Laplacian Adaptive Radioactivity Analysis, Volume I, Technical Manual", University of Wisconsin, Report UWFDM 1080, January 1998.

[4] Yu. Korovin, A. Yu. Konobeev, P.E. Pereslavtsev et al., Intermediate Energy Activation File IEAF 2001, Journ. Nucl. Sci. Techn., Suppl. 2, p. 68-71 (August 2002).

[5] U. Fischer, D. Leichtle, U. v. Möllendorff et al., Intermediate Energy Activation File IEAF-2001, NEA data bank Programme Library Package NEA-1656/01 (2001), RSICC Oak Ridge, DLC-217/IEAF-2001 (2002).

[6] P. Bém, V. Burjan, M. Götz, M. Honusek, U. Fischer, V. Kroha, U. von Möllendorff, J. Novák, S. Simakov and E. Šimečková, Activation of Eurofer in an IFMIF-like neutron field, 23rd Symp. on Fusion Technology, Venice, 20-24 September 2004.

[7] P. Bém, V. Burjan, U. Fischer, M. Götz, M. Honusek, V. Kroha, U. von Möllendorff, J. Novák, S.P. Simakov, E. Šimečková, Analysis of the NPI irradiation experiment on Eurofer up to 35 MeV using IEAF-2001 activation cross-sections, Workshop on Activation Data EAF 2005, Prague, 7-9 June 2004.

[8] S.P. Simakov, U. Fischer, U. v. Möllendorff, I. Schmuck, H. Tsige-Tamirat, P.P.H. Wilson Validation Analyses of IEAF-2001 Activation Cross-Section Data for SS-316 and F82H Steels Irradiated in a White d-Li Neutron Field, Int. Conf. on Nuclear Data for Science and Technology, Santa Fe, NM, September 26-October 1, 2004; see also: EFF-DOC-922, NEA Data Bank, Paris, November 2004.

[9] K. Seidel, R. A. Forrest, H. Freiesleben, S. A. Goncharov, V. D. Kovalchuk, D. V. Markovskij, D. V. Maximovich, S. Unholzer and R. Weigel, Activation experiment with Tungsten in fusion peak neutron field, EFF-DOC-821, NEA Data Bank, Paris, April 2002.

[10] P. Pereslavtsev, U. Fischer. Evaluation of n + W cross section data up to 150 MeV neutron energy, Int. Conf. on Nuclear Data for Science and Technology, Santa Fe, NM, September 26-October 1, 2004; see also this report on TW4-TTMN-001 and EFF-DOC-921, NEA Data Bank, Paris, November 2004.

TW4-TTMN-002 D7
Validation Experiment of Gamma Activities of Lead Irradiated in Fusion Peak Neutron Field

Objectives

Lead is a major element of some breeding blanket concepts for the DEMO reactor and for an ITER Test Blanket Module. The helium cooled lithium lead (HCLL) and the water cooled lithium lead (WCLL) blanket concepts are based on molten Pb-17Li alloys that act as coolant, breeding material and neutron multiplier [1].

For fusion relevant materials the radioactivity induced by neutrons is a central safety related topic. The short-term radioactivity with half-lives in the range of minutes to weeks is of interest for the heat production and the shut-down dose rate, whereas the long-term radioactivity in the range up to several hundreds of years is interesting for waste management. It is expected that Pb-17Li used for the operation of a power plant can be recycled and used in the next reactor after about 50 years of cooling [2].

The aim of the present work is to contribute experimentally to the validation of the activation predictions based on calculations with codes and data libraries such as the European Activation System EASY [3]. The activation of Li with fusion peak neutrons was previously investigated [4]. Therefore, pure Pb was irradiated in the present work.

Experiment

In order to determine the time region during which measurements of the neutron induced activities should be done after irradiation, a calculation with EASY was carried out. Lead was assumed to be irradiated at power plant conditions; this means with a flux of the 14 MeV neutrons corresponding to a power density of 1.0 MW/m^2, for a period of one year. The results obtained for the contact dose rate as a function of the decay time after irradiation, are shown in Fig. 1.
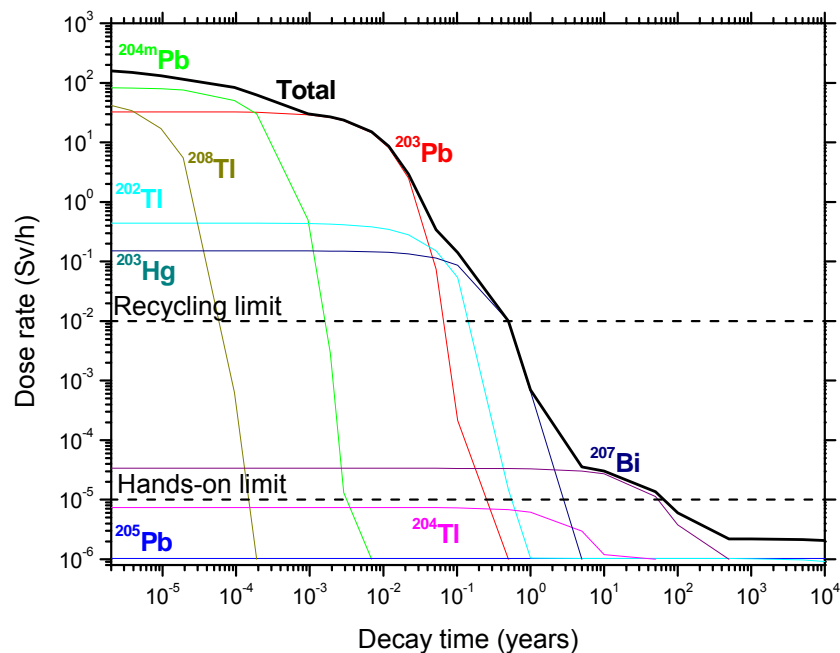
Fig. 1: Calculated total contact dose rate and contribution of the different nuclides after irradiation of Pb with fusion peak neutrons of 1.0 MW/m^2 power density for one year as a function of the decay time.

The nuclides dominant in Pb in the first month after the irradiation are ^{204m}Pb and ^{203}Pb. After that, up to the recycling-limit, reached at about 8 month, ^{202}Tl and ^{203}Hg are the dominant nuclides. The hands-on limit reached at about 40 years is determined by ^{207}Bi. Considering the different half-lives, two irradiations were carried out. A short one with only 32 min of irradiation time followed by γ-ray acquisition in the range between $2 \cdot 10^{-6}$ and 10^{-4} years and a long one of 8.8 hours irradiation and spectra measurements in the range $2 \cdot 10^{-4}$ – 0.2 years.

The samples had a thickness of 1 mm, a circular front area with a diameter of 25 mm and a mass of 5.5527 g and 5.5345 g, respectively. The irradiation of the samples was carried out at a neutron generator of TUD. The mean neutron energy of the fusion peak was 14.76 MeV; the full width of the peak at half maximum was 0.30 MeV. In the long irradiation a total neutron fluence of $1.11 \cdot 10^{12}$ cm^{-2} was applied, and in the short one a fluence of $7.93 \cdot 10^{10}$ cm^{-2}. The fluence was determined by simultaneous activation of niobium foils and evaluating the activity induced by the ^{93}Nb(n,2n)^{92m}Nb reaction. The cross section of this reaction was considered to be 405 mb with an uncertainty of 4.2%.

γ-ray spectra were taken with an HPGe-spectrometer at a distance of 50 mm to the irradiated sample. The γ-activities identified by energy and half-life were used to determine the nuclide activities using γ-yield data from EASY. The attenuation of the neutron and of the γ-ray fluxes in the sample as well as the geometry factors (neutron source – sample and sample – γ-ray detector) were determined by 3D Monte Carlo calculations.

Results

The experimental data were analysed with version EASY-2003 of the European Activation System. Results of the analyses are presented in Table 1.

The uncertainty of the calculated activities ($\Delta C/C$) includes both cross section and half-life errors as estimated by EASY-2003. The uncertainties of the experimental values ($\Delta E/E$) take into account possible errors of the γ-activity measurements (statistical uncertainty of the γ-ray counting, the uncertainty of the efficiency of the spectrometer including the geometry factor), of the sample mass, of the γ-yield data and of the neutron flux monitoring.

Table 1: Results obtained for the activity of nuclides;
nuclides identified, their half-life and γ-rays with yield data used to determine the activity, the neutron reactions producing the activity, the ratio of calculated-to-experimental activity (C/E) and the uncertainty of both calculated and experimental activity.

Nuclide	Half-life	E_γ (keV)	Y_γ (%)	Reaction Contr. (%)	C/E	$\Delta C/C$ (%)	$\Delta E/E$ (%)
^{203}Pb	2.17 d	279 401	81 3.4	^{204}Pb(n, 2n) 40 ^{204}Pb(n, 2n)IT 60	0.97	18.5	8.6
^{204m}Pb	1.12 h	375 899	89 99	^{204}Pb(n, n') 100	0.92	20.0	9.1
^{208}Tl	3.05 min	583	84.5	^{208}Pb(n, p) 100	0.84	20.0	10.6
^{203}Hg	46.6 d	279	81	^{206}Pb(n, α) 93.1 ^{207}Pb(n,n'α) 6.9	1.04	23.1	10.8

In the Final Report of the Subtask [5] the results have been discussed in detail including recent cross section measurements for the neutron reactions of Table 1 and evaluated data of other libraries

Conclusions

The activation performance of pure Pb in a fusion peak neutron field was investigated. Calculations with the European Activation System EASY-2003 predict the recycling limit of the material after irradiation under fusion power plant conditions (power density of 1 MW/m^2, exposition of 1 year) to be reached at about half of a year and the hands-on limit at about 40 years of cooling. All activities that are dominant up to the recycling limit were experimentally investigated. The measured activities agree with the corresponding calculated values for ^{203}Pb, ^{204m}Pb and ^{203}Hg within 8%. Hence the activation performance of Pb calculated with EASY is validated on this level up to the recycling limit. Only the minor important activity of ^{208}Tl showed a deviation of the calculated from the measured value of 16%. The experimental uncertainties of all the activities investigated are smaller than the uncertainties of the EASY calculations. Hence, the measurements may contribute to a further reduction of the EASY uncertainties [6].

The radionuclide that determines the hands-on limit is ^{207}Bi. It is produced by the reaction ^{207}Pb(p,n) in a second step with protons from previous (n,p) reactions. This secondary charged particle reaction should further be investigated.

If Pb-17Li is irradiated at fusion power plant fluxes, a contact dose rate of about 8·10^{-4} Sv/h is predicted to be produced by the sequential charged particle reaction ^{7}Li(p,n)^{7}Be. In a previous irradiation of Li$_4$SiO$_4$ [4] a C/E = 0.9 was found for the ^{7}Be activity. Fortunately, the half life of ^{7}Be (53 days) is sufficiently short not to significantly influence the total dose rate of Pb-17Li.
Some of the results have been published [7].

Staff:

R. Eichin
H. Freiesleben
K. Seidel
S. Unholzer

Literature:

[1] L. V. Boccaccini et al., Materials and design of the European DEMO blankets, J. Nucl. Mat. 329-333 (2004) 148-155.

[2] K. Tobita at al., Design choice and radioactive waste on fusion reactors, J. Nucl. Mat. 329-333 (2004) 1610-1614.

[3] R. A. Forrest, The European Activation File: EASY-2003 overview, Report Culham Science Centre, UKAEA FUS 484.

[4] K. Seidel, et al., Experimental investigation of radioactivity induced in the fusion power plant structural material SiC and in the breeder material Li4SiO4 by 14-MeV neutrons, Fusion Eng. Design 58-59 (2001) 585 and EFF DOC-755.

[5] R. Eichin, R.A. Forrest, H. Freiesleben, K. Seidel, S. Unholzer, Report TUD-IKTP/01-04, TU Dresden, November 2004.

[6] R. A. Forrest et al., Validation of EASY-2003 using integral measurements, Report UKAEA FUS 500, EURATOM/UKAEA Fusion Association, Culham, December 2003.

[7] K. Seidel, R. Eichin, R.A. Forrest, H. Freiesleben, S. Unholzer, SOFT-23, Venice, September 20-24, 2004-11-24

Materials Development
IFMIF

TTMI-001
IFMIF-Accelerator Facilities

TW3-TTMI-001 D2
Development of Critical Accelerator Components

D2a - Volume source for H^+ and H_2^+ - beams

At the Intsitut für Angewandte Physik a 200 mA proton source was developed and successfully tested [1]. The installation works of the exhaust system for the ion source lab were finished at March 2004. The installation of such a system was a precondition to use of the lab. Due to the limited time left the new experiments have been concentrated on the H_2^+ generation because this is very important for the commissioning of the IFMIF Linac. In contrast, further investigations with proton beams are not necessary, because the ECR source was chosen for the D^+ source. The ECR source has not a better beam performance, however the data promise a higher life lifetime. Therefore during the last month the Frankfurt proton source has been used to test their ability to produce H_2^+ beams. This would allow a commissioning of the accelerator without an activation of the Linac by means of the d-d reaction. In this context the influence of the source parameters gas pressure, filter field flux density and arc power on the beam parameter have been investigated. This has been done with a new spectrometer (D2b). It was not the goal to produce very high currents.

First of all, the influence of the filter field flux density on the H_2^+ fraction was investigated for a constant gas pressure of 25 Pa. The filter field was created by means of two CoSm magnets; the strength was varied by changing of the distance of the magnets. As shown in Fig. 1 the maximum of the H_2^+ fraction is achieved in operation without a filter field. Consequently, henceforth the source has been operated without a filter magnet.
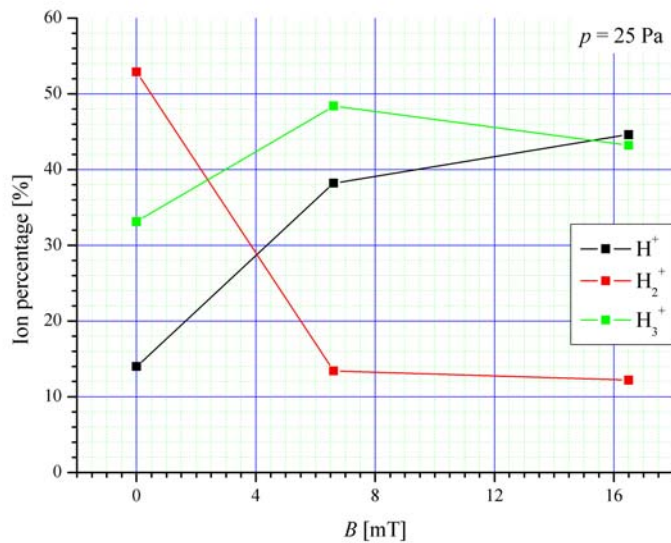
Fig. 1: Ion percentage as function of the filter field flux density.

Secondly, the influence of the arc power on the H_2^+ fraction was investigated. For this investigation the gas pressure and the arc voltage were kept constant. As demonstrated in Fig. 2 the H_2^+ fraction rises from 40 % at 165 W to 48 % at an arc power of 440 W.

In Fig. 3 is displayed the total extracted current for the measurement row shown in Fig. 2. A comparison shows that for an arc power of 440 W about 20 mA H_2^+ has been extracted. For these measurement the extraction voltage was adapted to the plasma density, leading to a variation of the voltage from 12,5 kV to 22 kV. The fact that with an arc power of 440 W only the extraction of a total current of 40 mA is possible demonstrates the high power efficiency of the ion source.
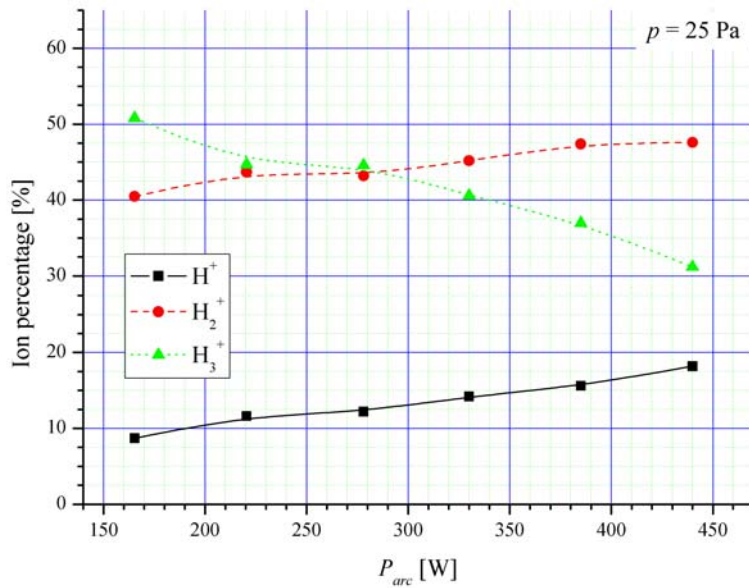
Fig. 2: Ion percentage as function of the arc power.
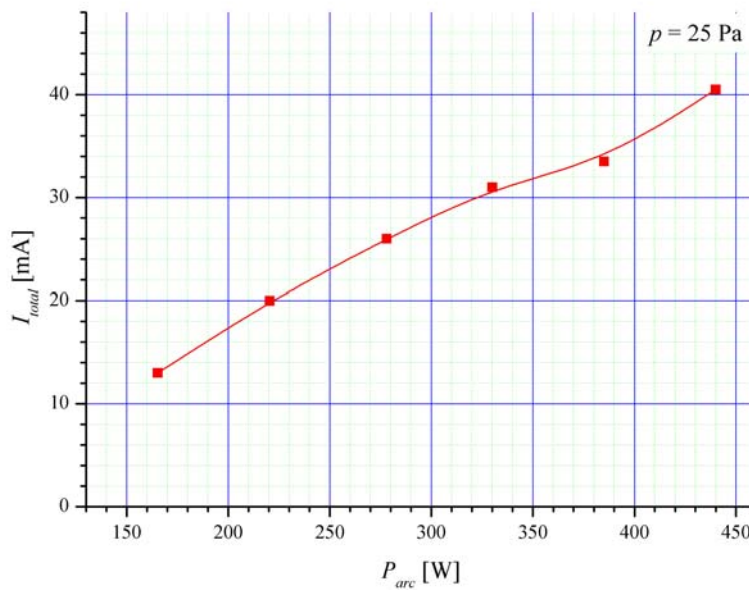
Fig. 3: Total extracted current as function of the arc power.

Furthermore, the influence of the gas pressure in the plasma chamber on the H_2^+ fraction was investigated. As shown in Fig. 4 the H_2^+ fraction decreases from 59 % at a gas pressure of 18 Pa to 27 % at a gas pressure of 55 Pa. A source operation in a pressure range between 18 Pa and 25 Pa is critical because in this operation mode, the gas pressure inside the plasma chamber is to low, leading to an uncontrolled pulsing of the arc discharge. Therefore all the other measurements were performed with a gas pressure of 25 Pa, which is a compromise between a stable operation mode and an optimal H_2^+ fraction.
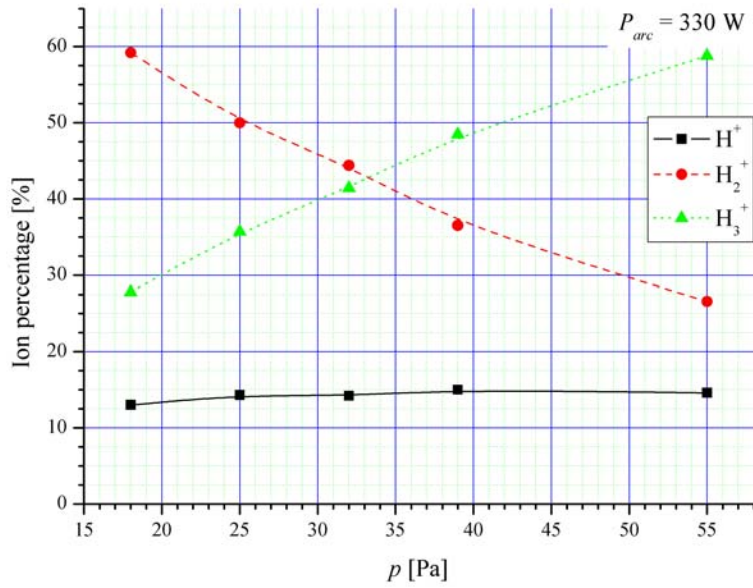
Fig. 4:   Ion percentage as function of the gas pressure.

Fig. 5 displays a mass spectrum of the hydrogen beam for an arc power of 440 W.

On balance with the 'old' proton source we produced 20 mA H_2^+ with an extraction voltage of 25 kV. As demonstrated in the measurements as well as in our earlier report, for a high H_2^+ fraction it is necessary to reduce the source pressure to values as low as possible. Furthermore as demonstrated in our theoretical studies a transverse filter is not necessary. In a next step a new source has to be designed with a shorter distance between the filament(s) and the extraction region.
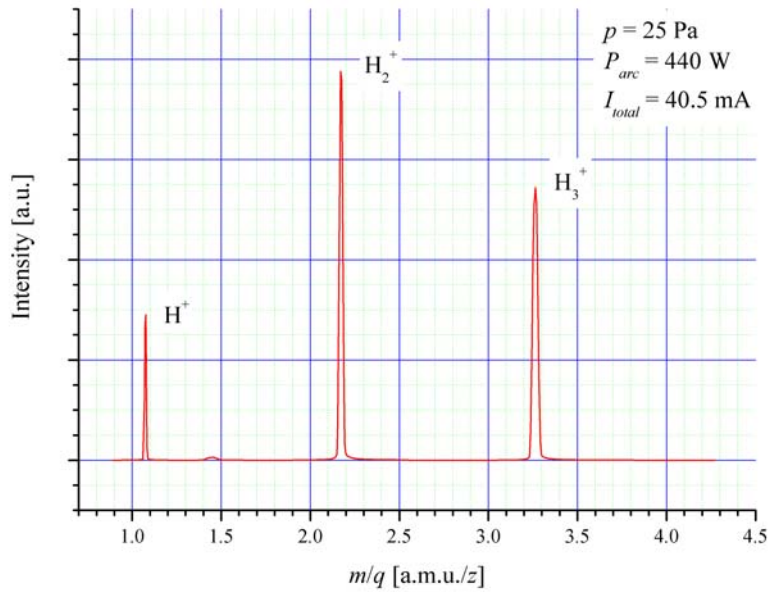
Fig. 5: Mass spectrum of the hydrogen beam.

D2b - LEBT, Development of Non Interceptive New Diagnostics, Modelling of 4rod RFQ

1. LEBT

At the University of Frankfurt, a high current H^+ source was developped. From great importance is the development of a high current H_2^+ ion source, which is inevitable for the run of the accelerator. Therefore the high current source was tested in order to extract H_2^+. Up to now a beam current of 20mA H_2^+ has beeb reached (see TW3-TTMI-001, D2a).

Further on design studies were done for a LEBT-system transporting H^+ and H_2^+ beams. Fig. 6 shows calculations of the envelopes of an 100mA, 38keV H^+ and an 50mA, 30keV H_2^+ beam. A compensation degree of 90% was assumed. The calculation were done for a normalized RMS emittance $\pi_{rms,100\%,norm.}$ of 0.062π mm mrad, a divergence angle of 50mrad and a distance between the extraction system of the ion source and the first solenoid of 200mm. An homogeneous magnetic field of 0.22T (H^+) and 0.28T (H_2^+) for the first solenoid and 0.19T (H^+) and 0.24T (H_2^+) for the second solenoid was assumed. The vacuum chamber inside of the solenoid at the Institut für Angewandte Physik has a diameter of 100mm.
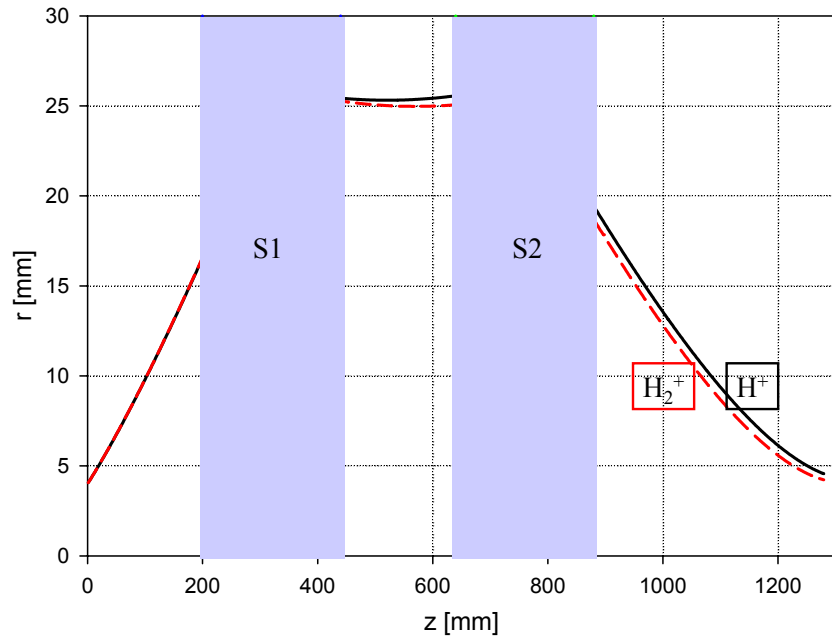
Fig. 6: Calculation of the beam envelope of a 100mA, 38keV proton beam and a 50mA, 30keV, H_2^+ beam for the Frankfurt LEBT-system.

Figure 7 shows calculations of the envelopes for the same beam parameter (fig. 6), but for a distance between the extraction system of the ion source and the first solenoid of 350mm. An homogeneous magnetic field of 0.182T (H^+) and 0.23T (H_2^+) for the first solenoid and 0.175T (H^+) and 0.22T (H_2^+) for the second solenoid was assumed.
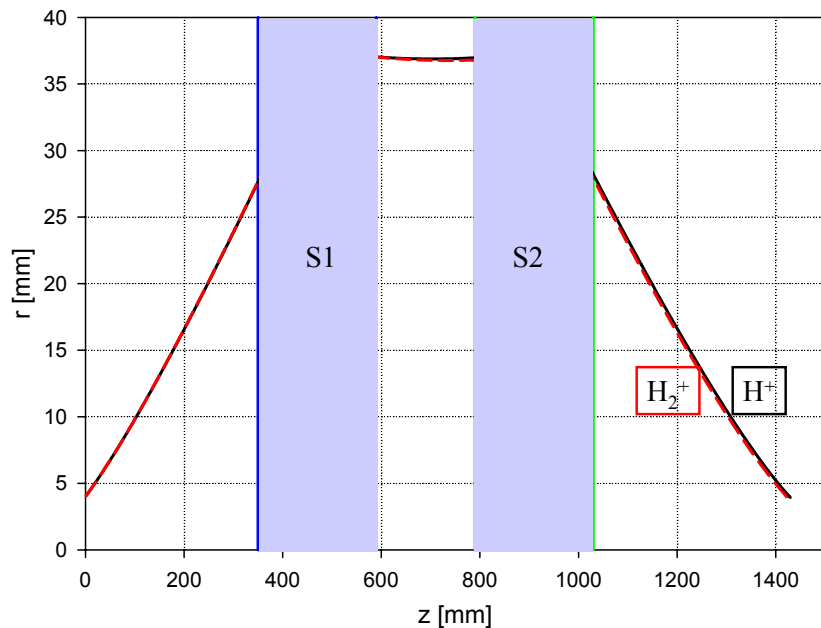
Fig. 7: Calculation of the beam envelope of a 100mA, 38keV proton beam and a 50mA, 30keV, H_2^+ beam for the Frankfurt LEBT-system.

Conclusion:

The second calculation shows, that the apperture of the solenoids is filled up to 70%. A distance between ion source and first solenoid of 350mm is cruicial. For the transport a compensation degree of minimum 90% is necessary.

2. Non interceptive diagnostics

A new intensified slow scan CCD camera was bought by the IAP. The camera was used to observe the beam profile. In comparision to an old CCD-camera the new one has several

advantages (for detail see Annual Report 2003). Beside the advantage, that the coupling between intensifier and CCD chip by glass interconnects instead of lens coupling reduces vignitation, the main advantages of the new system using Peltier cooling instead of liquid nitrogen cooling is the possibility of an operation in orthogonal orientation.
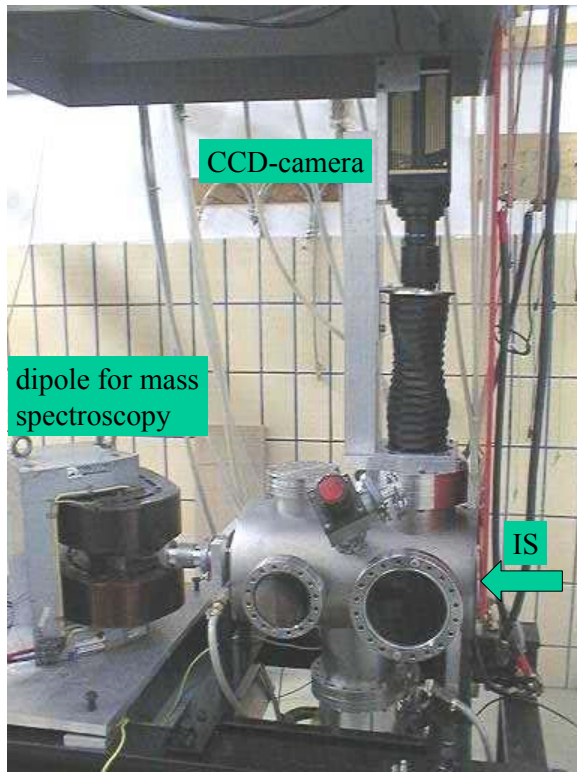
Fig. 8: Experimental Set Up with mounted Faraday cup, CCD-camera and the separation magnet for mass spectroscopy.
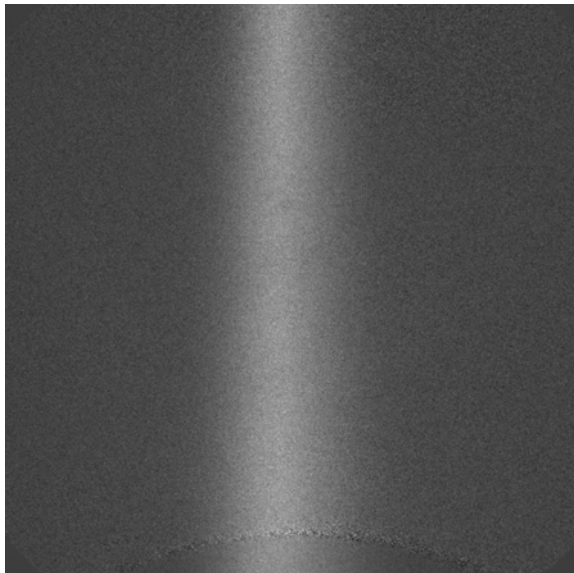
Fig. 9: Light intensity measurements at an 20mA H_2^+ beam, using the new CCD-camera.

Figure 8 shows the set-up with mounted diagnostic to investigate the beam performance. For current measurements a Faraday cup was used. The CCD-camera was mounted in orthogonal orientation in the same position downstrem the beam as the faraday cup (200mm from the ectraction system).

Figure 9 shows an image of the light intensity measurement at an 20mA H_2^+ beam using the new CCD-camera. The lense coverage was 80mm x 80mm. Therefore the spatial resolution was 0.078mm. The diameter of the beam was approximately 30mm.

Conclusion:
The diagnostic was tested at H_2^+ beams and is ready for operation. It gives a non destructive diagnostic tool to observe the beam profile and to esimate the phase space of the ion beam [2].

3. New diagnostic

To optimise the production of the H_2^+ fraction delivered by the ion source, a magnetic dipole was upgraded to full fill the requirements for the experiments. Therefore the old vacuum chamber was removed and a new one was designed, constructed and build. A technical drawing of the chamber is shown in figure 10. The deflection angle of the Dipole is 60^0, the radius 250 mm. Therefrom a mass resolution of 1 % can be reached by the use of 2 - 1 mm pinhole plates at the entrance and exit of the spectrometer. Further features of the new chamber are additional pumping ports for effective reduction of the residual gas pressure within the dipole and an improved alignment of the dipole to the ion beam axis by the use of the additional Faraday cup for the undeflected beam. Further more the faraday cups used for the detection of the beam particles have an additional electrode for the suppression of secondary electrons.
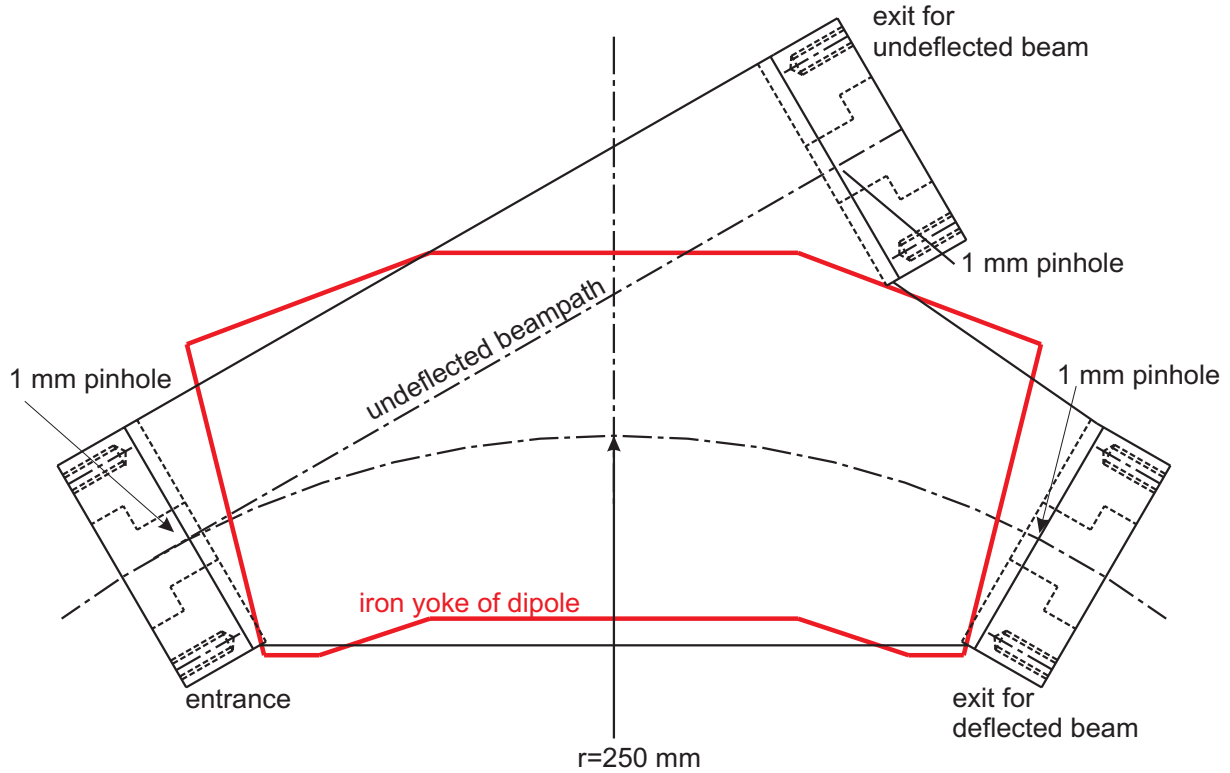
Fig. 10: Layout of the vacuum chamber for the analyses of the fractional ion currents. A second port in the direction of the undeflected beam axis, facilitates the alignment of the dipole and improves the accuracy of the measurements.

In figure 11 the dependence of the deflecting magnetic field from of the dipole current is shown. The measured values can be very well approximated by a linear dependency with an remanence of 0.0036 T. Furthermore due to the controlling of the current through the windings of the dipole is now by computer, a higher resolution and better reproducibility of the dipole current can be accieved. This function gained by measurements is loaded and used in the computer code to calculate the corresponding values of magnetic field and particle momentum for the output file.
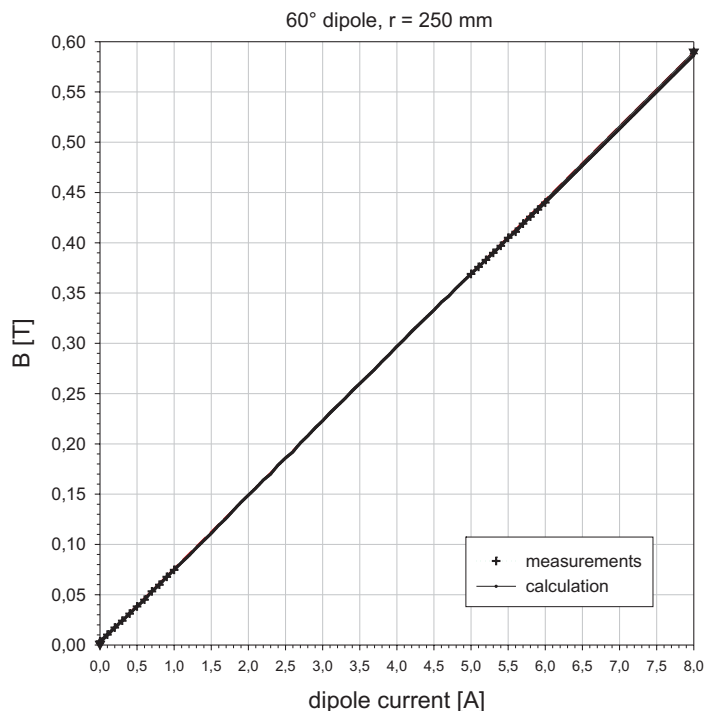
Fig. 11: Magnetic dipole field as a function of the dipole current. The function is in good approximation linear, the dipole yoke has an remanence of 0.0036 T.

Further improvements have been made by the use of a computer code to control the power supply and the measurement device. The flow diagram of the code is shown in figure 12. In the beginning default values for the measurements are loaded. Those can be change, loaded and saved by the use of set up subroutine. Two options of measurements are available in the moment. Ordinary measurement of a single spectrum or permanent sweep (with in an intervall) of a specific mass for optimisation of the production, extraction an transport of this mass.
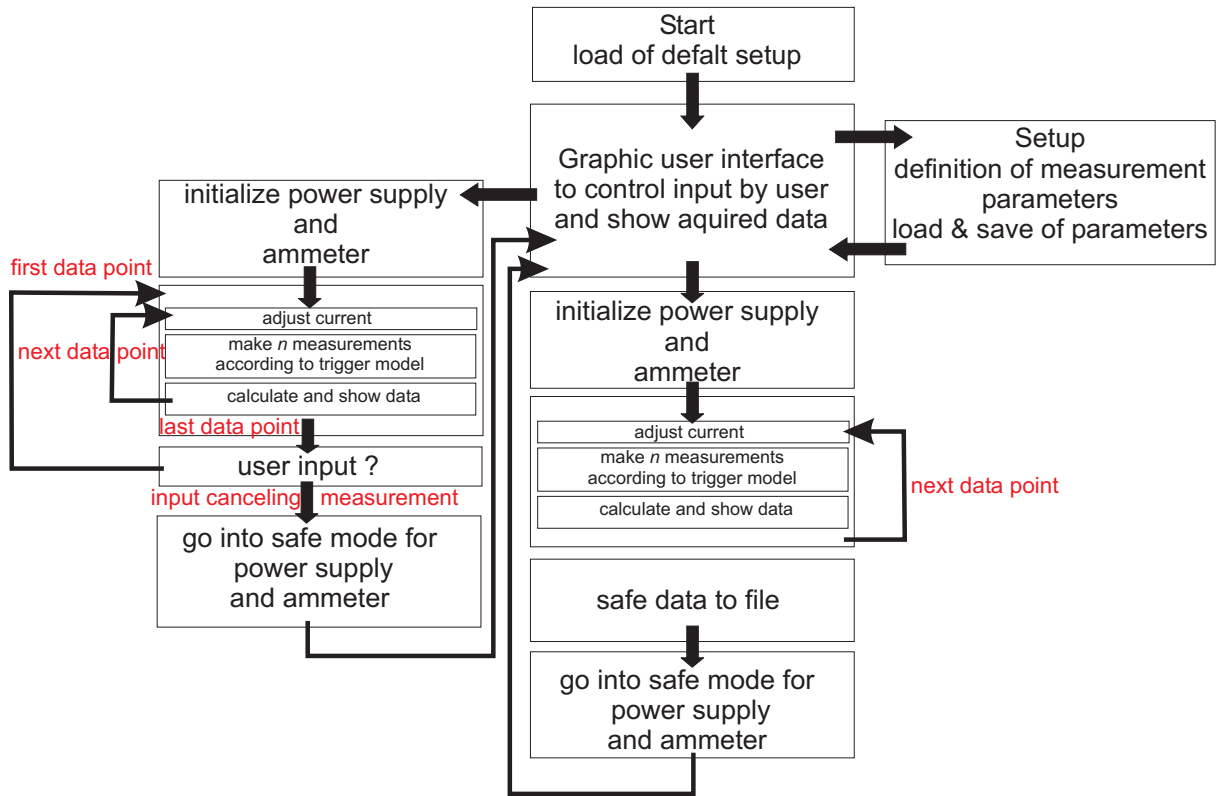
Fig. 12: Flow diagram of the computer code used to control the measurements.
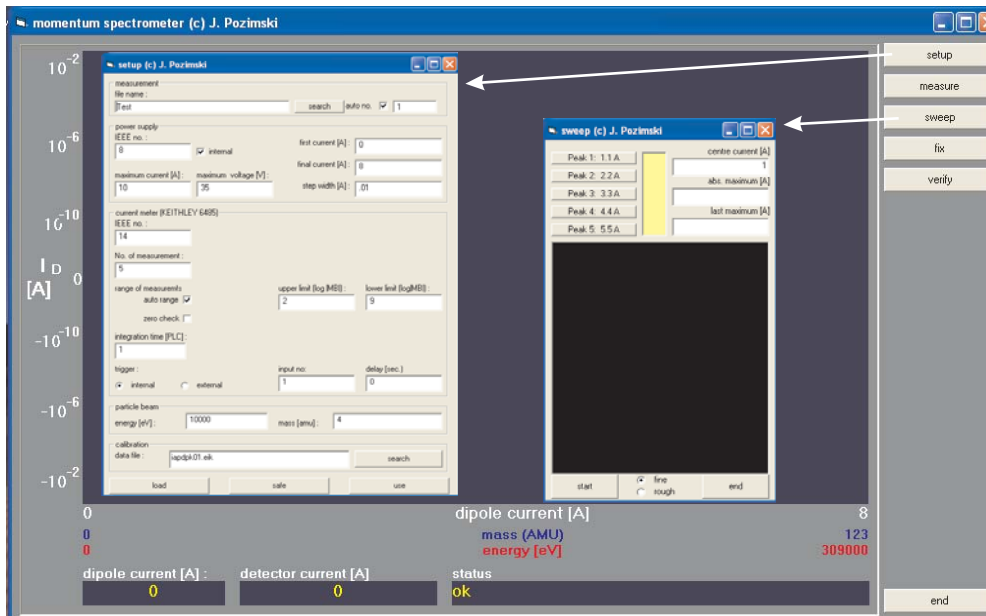
Fig. 13: Screen copy of the GUI for the momentum spectrometer code. The additional subroutines for the control of the measurement (set up) and for the sweep option are also presented.

Additionally for the measurement of the ion current in the faraday cups the mechanical x-y plotter was substituted by a programmable high resolution current meter (Keithley 6485). Due to the use of this instrument, the new vaccum chamber and the computer control the new momentum measurement system has the following advantages:

1) fully computer controlled measurements for high reproducability
2) improved resolution (10 fA) of current measurements

3) noise reduction by averaging
4) syncronized measurements for pulsed beams and time resolved measurements
5) improved measurement speed at high resolution
6) easy analyses of gained spectra by computer

For the commissioning of the new instrument test measurements using beams of hydrogen, helium and argon have been performed successfully. In figure 14 one of the gained results is shown.
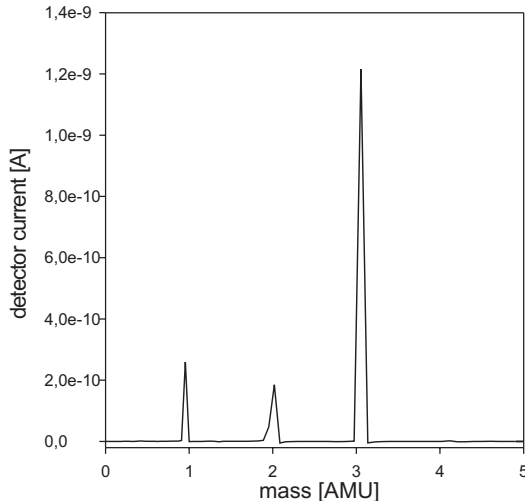
Fig. 14: Results of the test of the spectrometer using a hydrogen beam (U=3 keV, $I_{peak.}$ 200 μA, duty factor 1 %, H^+ 18 %, H_2^+ 12 %, H_3^+ 70 %).

4. Modelling of 4-rod-RFQ

The RFQ design for the IFMIF accelerator requires a RFQ at 175 MHz and cw-operation. Extrapolating from our experience from existing pulsed (with a high duty cycle of 20%) machines at 200 MHz where we successfully accelerated proton beams, we have concentrated in rf-modelling of a suitable CW 175 RFQ-resonator. MWS simulations have been done to optimize the design. Shunt impedances of up to 95kΩm have been achieved. But simulations of the thermal distribution and possible cooling schemes resulted in maximum temperature deviations of up to 90°C for IFMIF parameters, which is too high for operation.

Presently we work on a set up of a cw RFQ with an average power of 55 kW/m, much less than the 120kW/m necessary for IFMIF, as an intermediate step and we will study thermal effects in a resonator with length of 3.8m for a proton beam of up to 20mA.

Concluding, the particle dynamics in our 4-Rod design for IFMIF is excellent and the results are close to those of Saclay. The total power consumption is similar and the 4-Rod RFQ has the advantage of a more simple mechanical design and higher rf-stability. But the present results show, that it can be used at duty factor of up to about 30% only, the problems of cooling at average power levels necessary for IFMIF could not been solved so far.

This cooling problem is the reason, that finally the IFMIF accelerator group decided to take a four-vane-RFQ, which is easier to cool, as reference design.

TW3 TTMI-001 D4
Numerical and Design Evaluation of the Potentiality of Novel Superconducting CH-Drift Tube Linac, Test of a Superconducting Prototype

1. Objectives

Within the IFMIF project (**I**nternational **F**usion **M**aterials **I**rradiation **F**acility) a high current D^+-linac operated in cw mode has to be developed. For the DTL part of the IFMIF linac, a novel superconducting CH-DTL linac could be a very promising alternative within the reference design. The advantages are the easy cw operation, lower rf consumption, the shorter length of the linac and a larger aperture which reduces losses and activation of the linac. Particle dynamic simulations without errors showed that the CH-DTL is capable to accelerate the high current required for IFMIF with neglectable losses.

Electrodynamic simulations of the whole 175 MHz H-mode linac have been performed. To test the promising properties obtained by simulations a superconducting CH-prototype cavity has been developed. This CH-cavity can be tested in the new cryogenic laboratory.

2. Status of the work before the time Period

A down scaled copper model (1:2) has been built at the IAP in order to determine basic rf properties. The of 0.17 model had 18 gaps and the cell length had been kept constant with a ß The tank diameter was about 30 cm and the tank length about 1.2 m. Preliminary field measurements and an Higher Order Mode analysis had been performed.

The fabrication of the down scaled 352 MHz superconducting CH-prototype cavity had started and the cryogenic laboratory had been equipped with a 3m vertical cryostat, magnetic shielding and a laminar flow box.

3. Status of the work during the time period

The superconducting CH-prototype is completely fabricated and first low level rf measurements have been performed successfully. The cryogenic laboratory has put into operation during summer 2004 successfully by testing a superconducting half wave resonator.

The room temperature CH-copper model has been modified. It could be demonstrated that a flat field distribution can be obtained in CH-structures with a β-profile. Additionally, several coupling methods have been investigated. This showed that sufficient coupling can be provided.

3.1 Model measurements

The room temperature copper model has been improved by introducing a beta profile (β=0.08-0.12). It could be demonstrated that a flat field distribution can be obtained which is essential for the beam dynamics in multi cell structures. Different coupling methods have been investigated to couple rf power to the cavity. Capacitive coupling with a coaxial coupler and inductive coupling with a loop have been used. The goal was to determine the external Q-value which measured the coupling strength. This has been done with MicrowaveStudio simulations and measurements. For the cold tests of the superconducting CH-prototype it is planned to use a capacitive coupler which couples to the electric field of a drift tube. Figure 1 shows the location of the coupler and the external Q-value as function of the coupler position. The simulation agrees with the measurement over several orders of magnitude very well. The tests will be performed with an external Q-value of 2×10^8 which is a little below the expected intrinsic Q-value of the cavity at a temperature of 4 Kelvin.
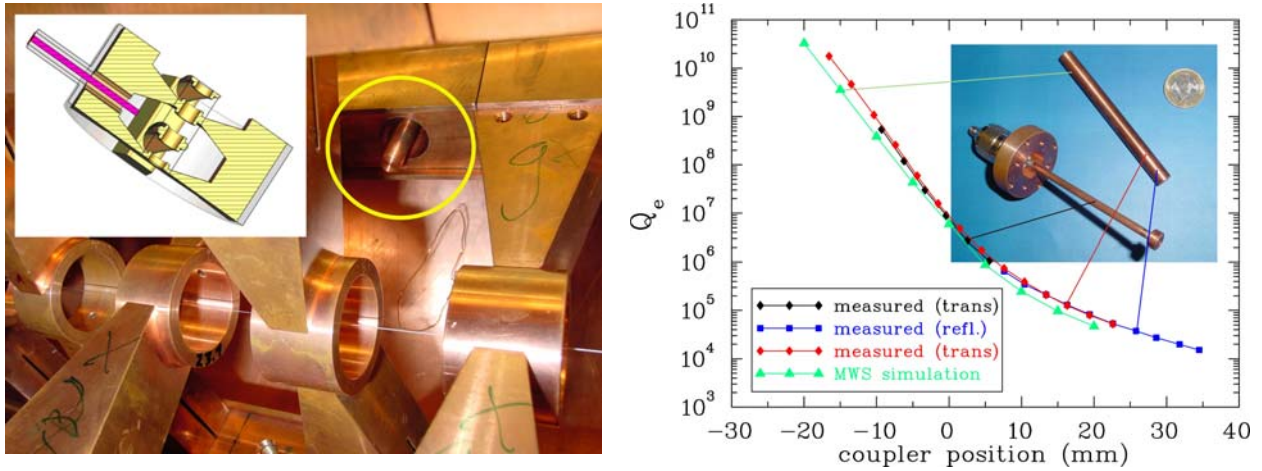
Fig. 1: Position of the capacitive coupler which will be used for the cold tests of the CH-cavity (left). Comparison of the external Q-value (coupling-strength) between measurements and simulations (right).

3.2 Development of the superconducting CH-cavity

The superconducting CH-prototype cavity which has been built at the company ACCEL, Bergisch Gladbach is completely fabricated. After the chemical treatment and high pressure rinsing the cavity is ready for the first cold test in the cryogenic laboratory in Frankfurt. Due to the complex cavity geometry it was necessary to do all fabrication steps like deep drawing, spinning and electron beam welding in copper first. After a successful trial the same step has been done with the very expensive niobium. This time consuming procedure has been chosen to develop new techniques of production and to minimize the risk of the failure of the superconducting prototype. The price which had to be paid was a time delay. Figure 2 shows a part of the inner structure in copper (left) and the completed CH-copper prototype (right).

Fig. 2: Part of the inner structure made out of copper to optimize the fabrication technology (left), the completed 1:1 CH-copper prototype cavity (right).
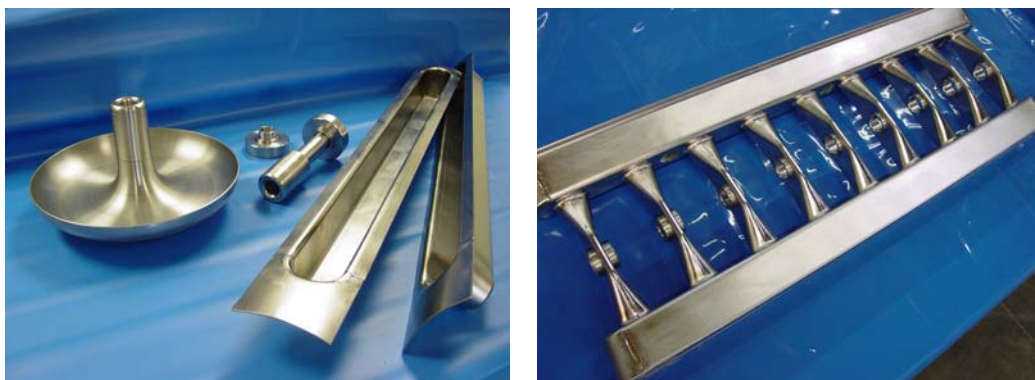
Fig. 3: Different niobium parts of the CH-prototype cavity.

Figure 3 shows some parts of the CH-cavity in niobium during different stages of the production.

Figure 4 shows the niobium CH-cavity before welding of the end cells. Measurements showed that the drift tubes and their positions are well within the tolerances.

First low level rf measurements at room temperature have been performed to measure the field distribution and the frequency. A new tuning method has been developed to tune the frequency and the field of the cavity. Ten small tuning cylinders with a diameter of 20 mm can be used in the girder to change the capacitance locally. Figure 5 shows the measured frequency

Fig. 4:   The niobium CH-prototype cavity without end cells.

as function of the tuner height. For these measurements 10 identical tuning cylinders have been used. For a height of 30 mm we obtained a tuning range of about 2.5 MHz.
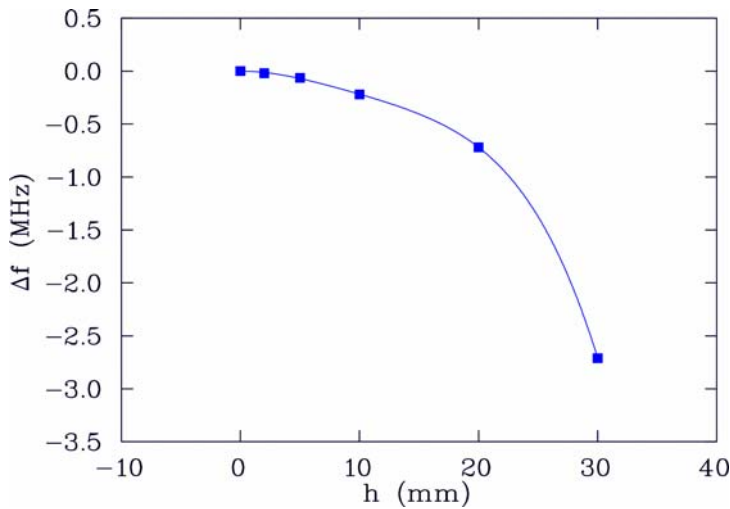
Fig. 5:   Shift of the resonance frequency as function of the tuner height. 10 identical tuners have been used.

Figure 6 shows a comparison of the field distribution obtained by bead pull measurement (blue curve) and MicrowaveStudio simulations (red curve). Left three tuners with a height of 30 mm have been used at the right side to change the field locally. The right part shows the optimized field distribution of the prototype. The agreement is excellent and it could be demonstrated to obtain a flat field distribution in a superconducting multi cell H-mode cavity.
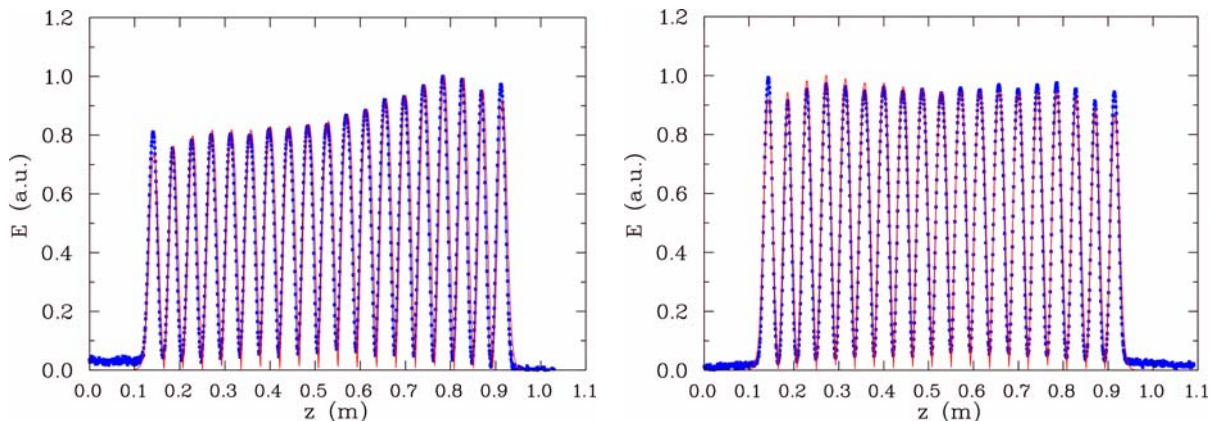
Fig. 6:   Comparison of the measured (blue) and simulated (red) field distribution of the niobium CH-prototype cavity. It shows the field with three tuners on the right side (left) and the optimized field distribution using different tuner heights (right).

The cavity will be tested in the cryogenic laboratory in Frankfurt which has been put into operation during summer 2004. A 176 MHz half wave resonator built by ACCEL has been tested several times up to an electric peak field of 25 MV/m. The infrastructure like cryostat, helium recovery system and the control system which has been developed at the IAP worked very well. Figure 7 shows the cryogenic laboratory during a cold test.

4. Conclusion and future work

The room temperature CH-model has been improved and a β-profile has been introduced. Different coupling methods for the CH-structure have been investigated by simulations and measurements with excellent agreement.

The superconducting CH-prototype cavity is completely fabricated and first low power measurements have been performed very successfully. It could be demonstrated to obtain a flat field distribution in a CH-cavity. Additionally, a new tuning method has

Fig. 7: The cryogenic laboratory during a test of a superconducting Half Wave Resonator.

been performed successfully. The cryogenic laboratory in Frankfurt has been put into operation, the infrastructure and the control system worked very well.

Acceptance test are planned in the second week of January at ACCEL. After a chemical treatment the cavity will be delivered in January 2005. It is planned to condition the cavity at room temperature first in order to reduce possible multipacting levels. Then extended cold test are foreseen to determine the performance of the CH-cavity.

TW4 TTMI-001 D4
Optional Solution Using Superconducting Crossbar-H (CH) Structure and Normal Conducting Interdigital-H (IH) Structure

1. Objectives

Within the IFMIF project (**I**nternational **F**usion **M**aterials **I**rradiation **F**acility) a high current D^+-linac operated in cw mode has to be developed. The parallel acceleration of two 125 mA D^+-beams from 0.1 MeV up to 40 MeV must be performed at an extremely low loss rate (0.1 - 0.2 µA/m) to avoid an activation the linac structures and guarantee hands-on maintenance. One optional layout of the acceleration facility, next to the normal conducting reference layout (LEBT-4-Vane-RFQ+MEBT+Alvarez), consists of a high current ion source, low energy beam transport (LEBT), room temperature Radio-Frequency-Quadrupol (RFQ) followed by one n.c. IH cavity and a chain of s.c. CH-cavities. The Institute for Applied Physics of the University Frankfurt is the only Institute, which can design and test H-mode cavities in KONUS© layout, both in room temperature and superconducting operation mode. Therefore is the development of a high current, high intensity H-mode DTL for IFMIF a key issue for us. The IAP is developing the CH-structure which is a multi cell drift tube cavity operated in the TE_{210}-mode. Due to its mechanical rigidity r.t. as well as s.c. cavities can be realized. The s.c. CH-structure in combination with a r.t IH-cavity is a promising candidate to fulfill the specifications of an IFMIF-accelerator.

2. Status of the work before the time Period

A combination of a short room temperature (r.t.) IH structure and a chain of sc CH resonators with inter tank focusing has been designed and is a promising option for an IFMIF injector. The s.c. CH DTL part provides very high rf and acceleration efficiency and due to its special cell geometry high mechanical robustness. The estimated total plug power (including all cryostat losses) per meter of this design study is $\approx$ 1.5 kW/m, which demonstrates the high rf efficiency of the s.c. CH modules. In connection with large drift tube apertures the risk of particle losses in the s.c. part is minimized. Detailed simulations showed a low sensitivity of the beam behaviour and beam quality against all combinations of statistically distributed rf, focussing and mechanical errors. In a first level design we assumed a chain of two rf couplers and transmitters per sc CH cavity which leads to 12-gap sc CH resonators with a maximal tank power of $\approx$ 1.1 MW and a cavity length range between 1.2 m @β=0.1 and up to 2.4 m @β=0.2. This design showed robust beam behaviour and no particle loss above 2 MeV.

3. Status of the work during the time period

We changed the former design to a cavity chain, fed by only one standard rf amplifier for IFMIF with an effective rf power of $P_{eff} \approx$ 0.71 MW in cw mode. This makes the production easier, increases the mechanical stability of each cavity (shorter tanks), simplifies the frequency tuning and increases the rf control possibilities. For this aim we divided the s.c. CH 2 up to CH 4 resonators of the previous design and used an intertank drift of one rf period between the subsequent cavities. This allows having some additional space for tuner devices and helium vessel between the tanks. A further external quadrupole lens is not foreseen because with the demand of one rf period between the tanks the transverse and longitudinal focussing properties are not disturbed. This strategy results in phase and amplitude independent cavities after s.c. CH 1. The Figure 1 illustrates the layout, estimated length, the number of tanks and rf input of the actual s.c. CH-DTL. The total length and the estimated rf power are unchanged to the former design. The following Figure 2 compares the total rf power supply of the old and new design.
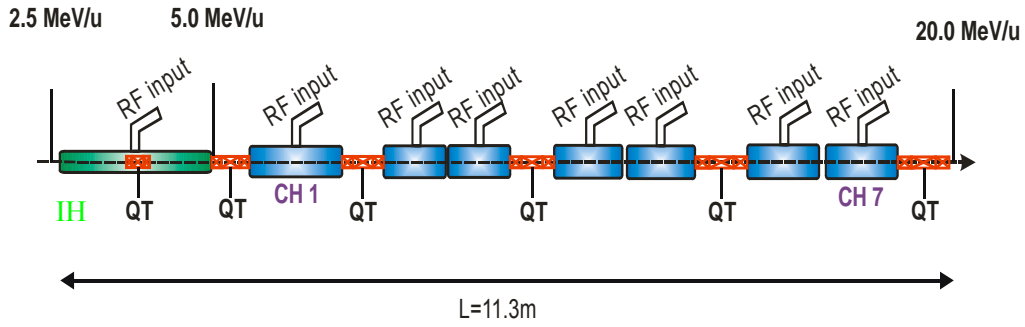
Fig. 1: Schematic layout of an optimized IH-sc CH-DTL for IFMIF. The rf input and the quadrupole triplets (QT) are also indicated.
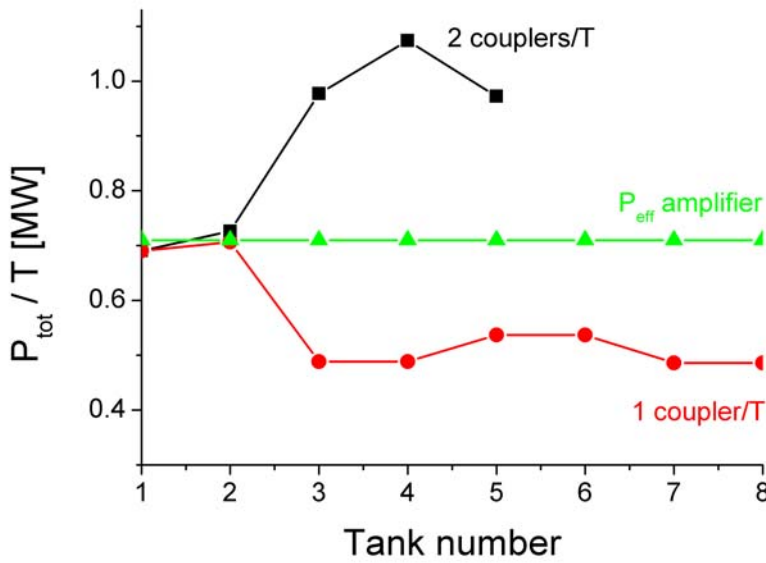
Fig. 2: Total rf power per tank of the old design (black line, 5 tanks) and the new one (red line, 8 tanks). The green line shows the effective power of one IFMIF standard rf amplifier.

The design and structure parameters are summarized in Table 1. They have been generated with the multi particle program LORASR©.

Extended beam dynamics studies showed smooth beam behaviour, no losses along the linac occurred and a good safety margin between beam size and structure wall could be reached in the s.c. linac against losses due to mismatch and standard DTL errors (quadrupole, phase and amplitude errors).

Table 1: Design parameter of a optimized 175 MHz sc IH/CH-DTL for IFMIF.

DTL parameters	SC CH-DTL	Units
A/q	2 (D$^+$)	
In-/out current	125.0 / 125.0	mA
Frequency	175.0	MHz
Number of tanks	8 (1NC+7SC)	
P_{tot}	4.44	MW
P_{max}/T / P_{min}/T	0.7 / 0.48	MW
W_{in} / W_{out}	5.0 / 40.1	MeV
Cells / Length	73 / 11.3	m
a_0 of DT rt / sc	1.5 / 2.4 - 4.0	cm
In- / Out rms ε^n_{trans}	0.035 / 0.091	cm×mrad
In- / Out rms ε^n_{long}	0.070 / 0.097	cm×mrad

3.1 MWS® simulations

3.1.1 The s.c. CH cavity

Intensive electromagnetic simulations have been performed with Microwave Studio® to optimize the geometry parameters for all tanks, from the first sc 12-gap CH tank with a β-range from 0.101 - 0.126 and the last CH-cavity up to an energy range of $0.194 < \beta < 0.204$. It was possible to further reduce the electric and magnetic peak fields to modest values, which is important for reliable routine operation. Furthermore field flatness in the first and last gap of every resonator was improved considerably. These calculations with the used cell geometry are the basis for engineering studies, which afterwards lead to detailed construction drawings. For more details about the development of the cell geometry of a s.c. CH-cavity see TW3 D4.

Table 2 gives the structure parameter of sc CH 1 and CH 7 and Fig. 3 shows 3D sketches of the actual 175 MHz sc CH tank 1 and 7 in the critical low energy part and at the high energy end of the DTL, simulated with Microwave Studio®.

Table 2: Cavity parameters of sc CH tank 1 and 7 calculated with MWS®.

Cavity parameters	CH 1	CH 7	Units
Beta	0.101 - 0.126	0.194 - 0.204	
Frequency	175.00	175.00	**MHz**
E_{acc}	4.00	3.38	MV/m
Gaps	12	5	
E_{peak}	21.21	21.92	MV/m
B_{peak}	27.33	35.11	mT
R_{eff}/Q	2.12	0.702	kΩ
G	54.92	59.12	Ω
Length	1.36	0.912	m
Aperture radius	2.2	4.0	cm
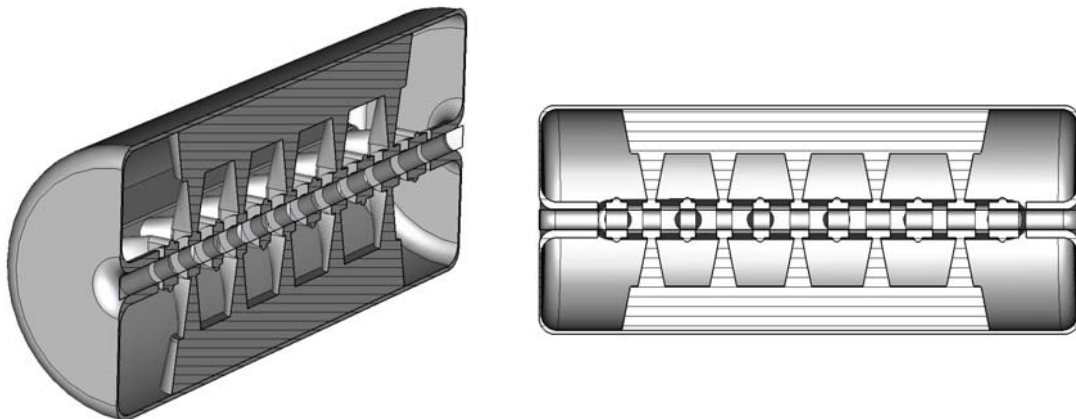
Fig. 3: 3D views of the first 175 MHz sc CH-cavities (CH 1 of figure 1) with 12 gaps and beta profile calculated with MWS®.
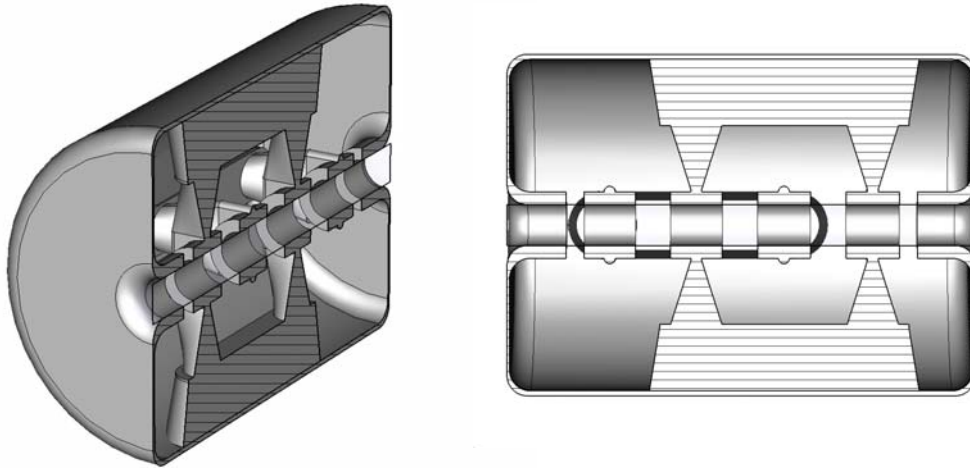
Fig. 4: 3D views of the last 175 MHz sc CH-cavities (CH 7 of figure 1) with 5 gaps and beta profile calculated with MWS®.

3.1.2 The r.t. IH cavity

Table 3: Cavity parameters of an r.t. IH-resonator for IFMIF calculated with MWS®.

Cavity parameters	r.t. IH	Units
Beta	0.073 - 0.100	
Frequency	175.00	MHz
E_{acc}	2.23	MV/m
Gaps	25	
E_{peak}	11.07	MV/m
B_{peak}	12.12	mT
Q_0	21829	
Z_{eff}	157.744	MΩ/m
R_{eff}/Q_0	15.175	kΩ
G	57.131	Ω
Length	2.10	m
Aperture radius	1.5	cm

To determine the cell parameters of the n.c. IH-cavity and get reliable data for first engineering and construction studies, we also overtake the LORASR design parameters of the IH part from table 1 to MWS®. Table 3 summarizes the tank parameters resulted from the calculations. Finally Fig. 5 gives 3D sketches of this cavity for IFMIF in an energy range of 0.073 < β < 0.100.
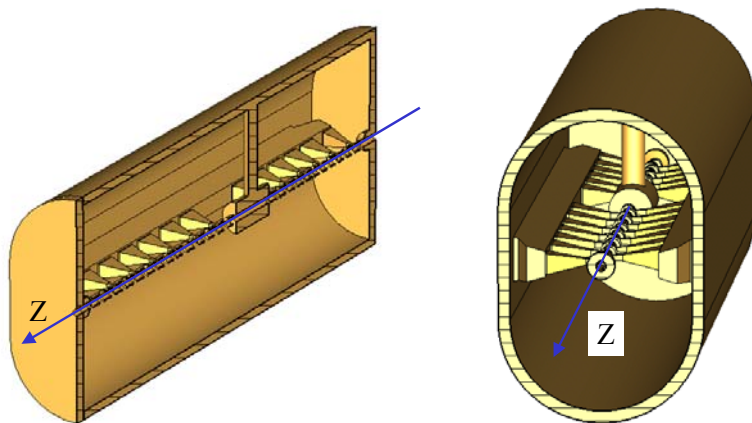
Fig. 5: 3D views of a r.t. 175 MHz IH-cavity for IFMIF (IH-tank of figure 1) with 25 gaps, one quadrupole triplet lens and beta profile calculated with MWS®.

3.2 Multi particle simulations of a complete IFMIF injector

As a very efficient method to test the global stability of the complete injector facility against particle losses, integrated overall multi particle simulation studies at full space charge of an IFMIF injector were performed. The injector consists of a LEBT (two solenoids and 85 % space charge compensation for matching into the RFQ), a 13 m long Four-Vane-RFQ with a Kilpatrick value of 1.7, a compact MEBT (one quadrupole doublet, one $\lambda/4$-4-gap buncher and a quadrupole triplet for matching into the IH/CH-DTL) and the optimized IH/CH-linac from Table 1. The multi particle simulations were performed with 10,000 macro particles, which lead to a maximum insecure loss rate of 540 nA/m for one macro particle. The programs LINTRA® for the LEBT, PARMTEQC® for the RFQ and LORASR© for the DTL were used. The output beam distribution of every section was used as an input for the following one. For the LEBT calculation an ion source input emittance of the IAP Frankfurt high current proton volume source was used. Adjusting the solenoidal fields did the matching into the RFQ. Fig. 6 shows the phase space distribution at the exit of the LEBT at 0.1 MeV, 140 mA beam current and 85% space charge compensation. There are no filamentations and the beam is well confined. Fig. 7 displays the phase space distribution at the exit of the RFQ at 5.0 MeV. The beam size in phase space is smooth, no halo but a 3% lower transmission was seen. No particle loss over 2.0 MeV inside the RFQ.

Finally in Fig. 8 we can see the phase space projections at 40.1 MeV at the exit of the IH/s.c. CH-DTL combination. For the MEBT and IH/CH-DTL we assumed statistically distributed combined standard quadrupole errors for each quad. No further losses occurred in the transport section and along the DTL. The output distribution is slightly distorted form the focussing errors of the quadrupoles but this is uncritical and the aperture factor in the s.c. part is still ≥ 2. The emittance growth was modest.

Fig. 6: Output phase space distribution of the LEBT at 0.1 MeV with 85 % space charge compensation and real solenoide fields, 10,000 macro particles used.

4. Conclusion

One r.t IH-structure followed by a chain of s.c. 12-gap and down to 5-gap CH-cavities in combination with the KONUS beam dynamics layout is well suited for the efficient acceleration of intense light ion beams. Extended electrodynamics studies of all s.c. 175 MHz CH-cavities with MWS® resulted in low peak fields and good field flatness. Also preliminary engineering studies made with MWS® of a room temperature 175 MHz IH-resonator showed low peak fields and high shunt impedance, which proved the outstanding

Fig. 7: Output distribution of the RFQ at 5.0 MeV with LEBT output as input into the IH, 9170 macro particles used.

accelerating effi-
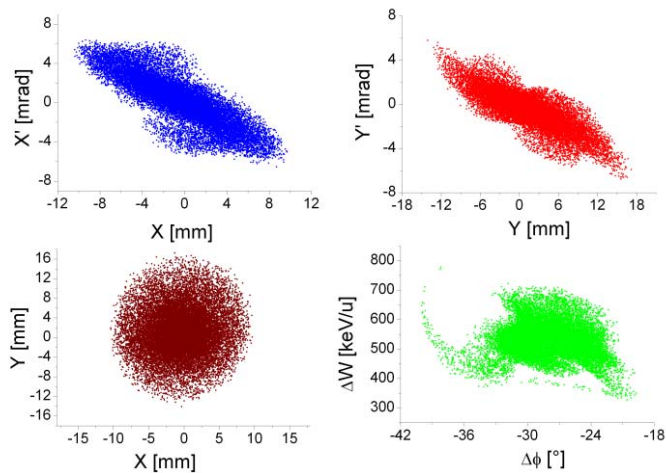
Fig. 8: Calculated output distribution of the CH-DTL at 40.1 MeV with combined quadrupole errors and RFQ output as input, 9170 macro particles used.

ciencies of an r.t. IH-type DTL in this energy region. Furthermore integrated overall simulations of a complete injector with a magnetic LEBT, a RFQ, a compact MEBT and a sc H-DTL even with standard tolerances of all linac components showed smooth beam behaviour, modest emittance growth and no particle losses after the RFQ. The matching was successfully performed with two short external transport sections. Nevertheless, the severe loss criteria of the IFMIF accelerator ($\approx$ 1 - 10 nA/m in ideal case) to guarantee hands-on maintenance require a very large number of macro particles in the beam dynamics calculations (up to 10^6 in one run for a beam current of 125 mA). In the previous end-to-end simulations of the IFMIF injector, only 10^4 macro particles were used, due to CPU time and memory limits of the codes. However, for describing high intensity bunches and halo particles in a more statistically sufficient way, 10^6 macro particles are necessary to reach the 1 W/m or 1 nA/m goal for a high intensity injectors. Therefore, the multi particle code LORASR will be improved to handle even higher number of macro particles. This is managed by implementing a new 3D space charge routine, which uses FFT-techniques to calculate the space charges of the bunch. In conclusion, the proposed work has been done successfully. But it is planned to repeat the particle dynamic calculations with the new computer code, which enables us to use up 10^6 particles. This would allow confirming the particle losses down to the nanoampere/per meter level.

Staff:

A. Bechthold
L. Brendel
H. Deitinghoff
B. Hofmann
A. Jakob
H. Klein
H. Liebermann
O. Meusel
H. Podlech
U. Ratzinger
A. Sauer
A. Schempp
J. Thibus
R. Tiede
K. Volk

Johann Wolfgang Goethe-Universität
Institut für Angewandte Physik (IAP)
Robert-Mayer-Strasse 2-4
60486 Frankfurt am Main

Literature:

[1] [R. Hollinger, P. Beller, K. Volk, M. Weber, and H. Klein, Rev. Sci. Instrum. 71, 836 (2000).

[2] "First optical beam profile measurements on an H- -source on Frankfurt", excepted for publishing in NIM A, Nuclear Instruments & Methods in Physics, Research A, Elsevier

[3] A. Sauer, H. Deitinghoff, H. Klein, H. Liebermann, O. Meusel, H. Podlech, U. Ratzinger, R. Tiede, "Status of the Superconducting D+-CH-DTL Design for IFMIF", Proceedings EPAC04, Luzern, Switzerland

[4] H. Podlech, H. Deitinghoff, H. Klein, H. Liebermann, U. Ratzinger, A. Sauer, R. Tiede, "Status of the Superconducting CH-Structure", Proceedings EPAC04, Luzern, Switzerland

[5] H. Liebermann, H. Podlech, U. Ratzinger, A. Sauer," Status of Coupler Development for the 352 MHz Superconducting CH-Cavity", Proceedings of the LINAC2004, Lübeck, Germany, August 16-20, 2004

[6] H. Podlech, "Development of Superconducting and Room Temperature CH-Structures", Proceedings of the LINAC2004, Lübeck, Germany, August 16-20, 2004

[7] O. Meusel et al., "Low Energy Beam Transport using Space Charge Lenses", Proceedings of the LINAC2004, Lübeck, Germany, August 16-20, 2004

[8] H. Podlech, H. Deitinghoff, H. Liebermann, H. Klein, U. Ratzinger, A. Sauer, "Development of Superconducting CH-Structures for Low and Medium Beta Beams and the Status of the 352 MHz Prototype Cavity", Proceedings of the ICFA-HB2004, Bensheim, Germany, September 18-22, 2004

TTMI-003
Test Facility

TW3-TTMI-003 D 1+2
Helium Cooled High-Flux-Test-Module

1. Introduction

In the last annual report on the High-Flux-Test-Module design work showed the first temperature analyses for rigs with capsules equipped with an electric triple heater system. The electric heaters have to adjust the temperature of the specimen in the capsules at beam on and beam off periods within limited tolerances. They have to cope with the helium temperature increase and heat transfer changes along the helium channels and the axial nuclear power distribution. According to the analyses with the CFD-code STAR-CD the temperature within the specimen stack at beam-on periods can be kept at about 450 °C with a tolerance of 15 °C over a stack height of 66 mm. The over all stack height of 81 mm followed investigations on several specimen arrangements with the aim to maximize the specimen number. The temperature in the stack beyond the afore mentioned 66 mm deviates more than 15 °C. The differences are well defined, so that the specimen can be used too. During beam-of periods the temperatures can be adjusted within the same range. The work of this year on the one hand was dedicated to arrange comparable temperature tolerances at different temperature levels for the same position in the container i. e. at highest nuclear power load [1]. Secondly the turbulence model used with STAR-CD was validated with an experiment from the literature. Own experiments were started too. The HTM as well the test cell were drawn with the CAD-System CATIA.

2. Description of the design with the triple heater capsules

The optimised design of the HFTM test section with chocolate plate rigs with triple heater systems is shown in Fig. 1. Based on preliminary hydraulic calculations a single rectangular duct with a cross section of 52 x 88 mm has been chosen for the helium flow to the test section. It is positioned asymmetrically at one side of the test section. The uniform feeding of helium to the rigs is improved by two baffles inserted in the 180^0 bend joining the ducts with downward and upward flow. The lateral reflectors are integral parts of the container housing the test rigs. Helium cooling of the reflectors is provided by a bypass to the main flow. The lower axial reflector is a single bloc with appropriate channels to lead the helium flow to the rigs. The upper axial reflector is split into 12 single parts according to the number of rigs. The outer shape is selected such that cooling channels of the necessary dimensions are generated. Holes in the blocs allow the insertion of thermocouples and heater wires.

Fig. 2 shows a horizontal cross section of the test section (x,z-plane) in the region of the irradiation zone. It consists of a container with an inner cross section of 203 x52 mm and the two lateral reflectors. In the y-z plane the container is divided into four compartments by stiffening plates serving to stabilise the container walls. Each compartment is filled with 3 rigs. The rigs have an outer cross section of 49x16 mm. Cooling channels are provided at all sides of the rigs with a width of 1.0 mm at the large sides and of 0.5 mm at the small sides. The dimensions of the cooling channels are assured by small vertical ribs at the corners and the side walls of the rigs. The attachment of the rigs inside the container is not yet included in the design.

Details of the rig design are shown in Fig. 3. They consist of the outer housing (rig wall) and the inner capsule containing the specimens separated by a thermal insulation with a thickness of 1.35 mm at the large side and 1 mm at the small side. The capsule has an inner cross section of 40x9.3 mm. This allows a rather dense arrangement of most of the envisaged test specimens (see Fig. 1). Electrical heaters are wrapped around the capsule in horizontal windings. This concept will lead to temperatures of the capsule close to the

irradiation temperature of the specimens, whereas the rig wall is at about the level of the helium temperature.
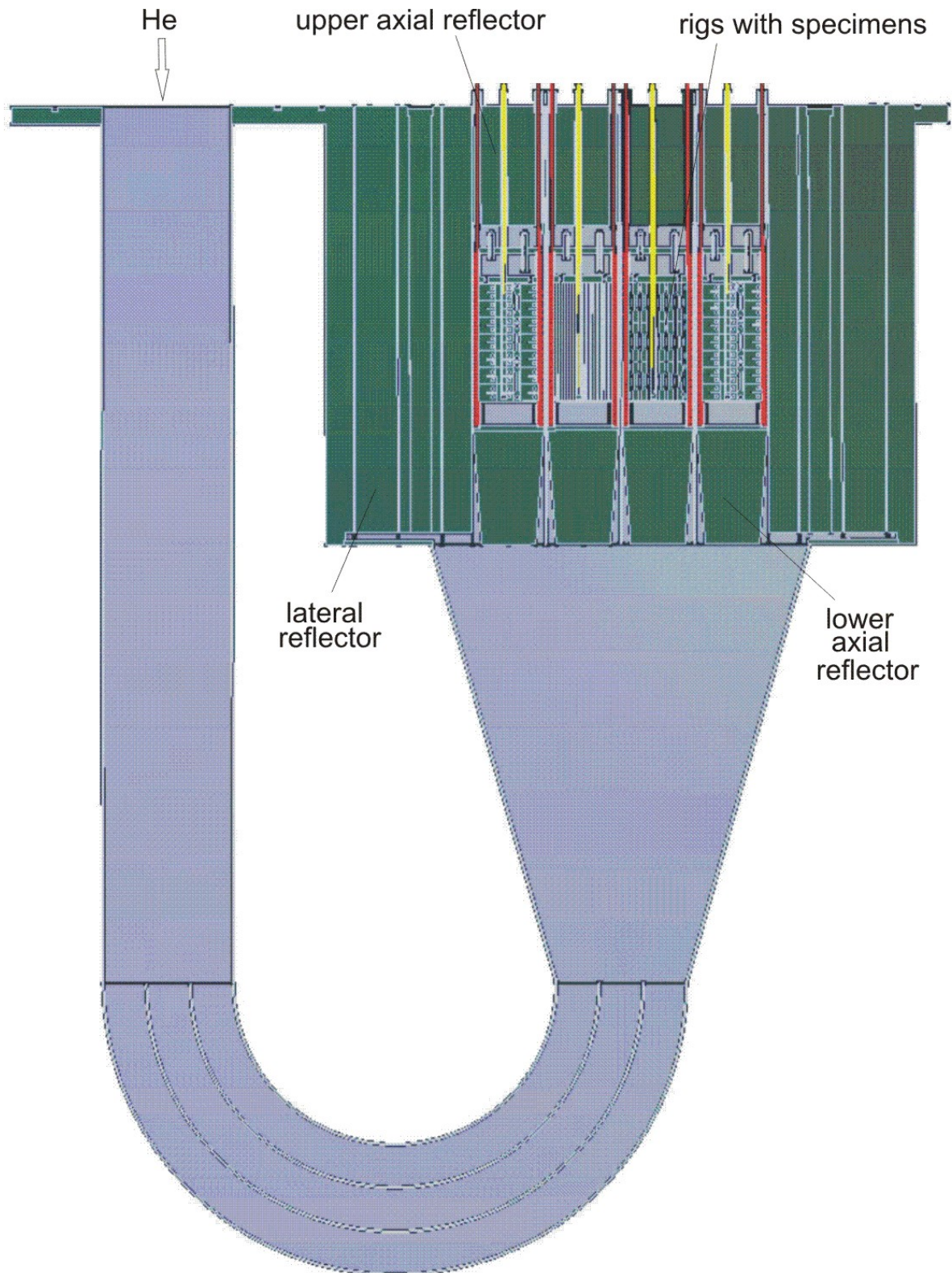
Fig. 1: IFMIF Helium cooled High Flux Test Module (HFTM).
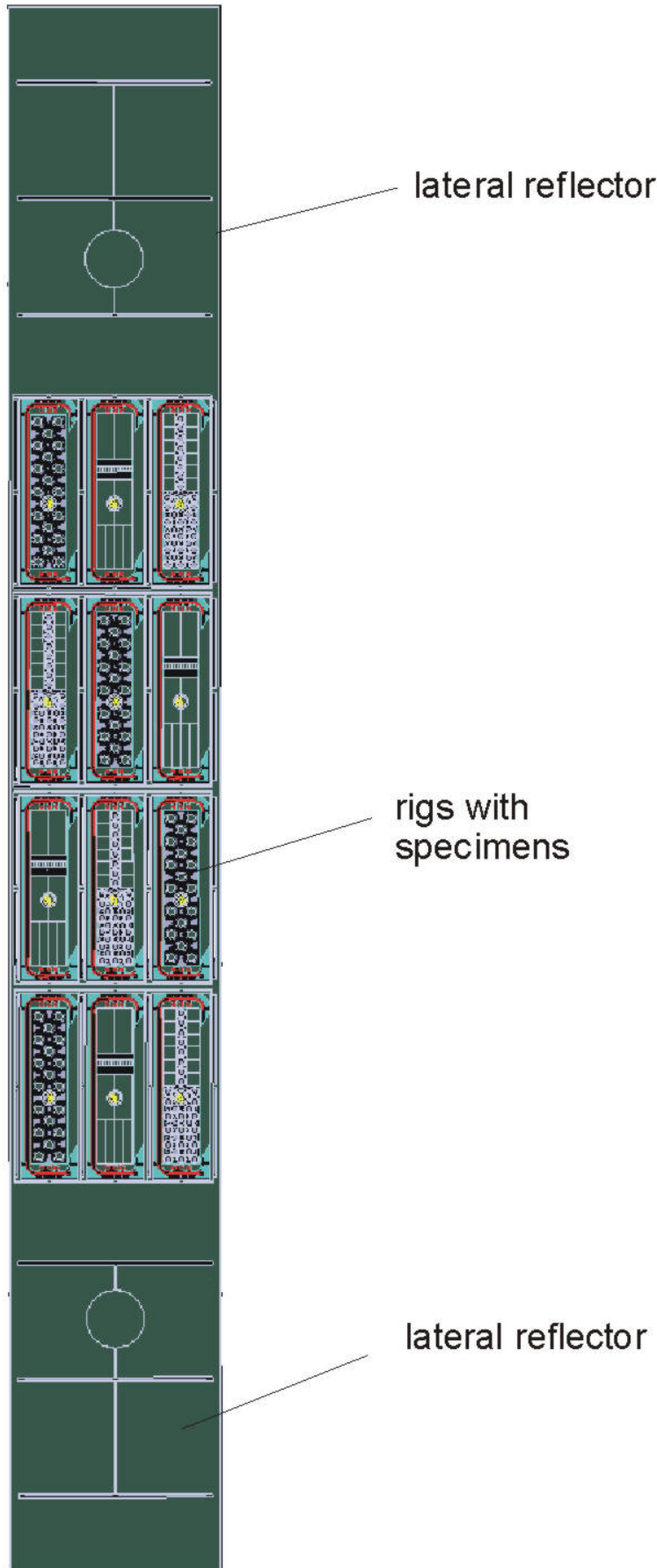
Fig. 2: High Flux Test Module cross section.

The length of the rig without the upper reflector is 144 mm. The capsules have a length of 125 mm and are closed by two cup-shaped caps giving the testing zone a length of 81.5 mm. This

includes 0.5 mm for the accommodation of thermal expansion differences. The capsules are filled with a liquid metal (Na or, if possible NaK) to increase the thermal contact between the specimens and the capsule walls. The upper cap has two holes connecting the test zone with the NaK expansion volume of about 20 mm length located at the top end of the rig. To facilitate filling of the capsule with NaK to a defined level, two tubes are provided at the top side of the expansion tank. One of these tubes dips into the tank to the envisaged filling level, the other one ends at the top plate. The filling level is established by at first filling the tank completely, and then blowing out the surplus NaK via the dip tube by applying a gas pressure to the other one. Finally, both tubes have to be cut and sealed. The volume of the expansion tank and the filling level have been determined taking into account the NaK volume, the filling temperature and the operating temperature.

The main design problem of the rigs is to realise the specified level and constancy of the irradiation temperatures. The maximum thickness of the capsule (in z-direction) is given by the power density and the thermal conductivity of the specimens/NaK mixture in connection with the allowable maximum temperature difference across the specimens. This consideration leads to a maximum thickness

of about 10 mm for the first row of rigs. At the rear side of the HFTM the capsule thickness can be larger according to the decrease in power density, but in order to minimise the design and manufacturing effort it was decided to use identical dimensions for all rigs. Taking into account the dimensions and possible arrangements of the specimens (see Fig. 2), 9.3 mm has been chosen as internal capsule widths.

3. Temperature distribution calculations at different temperature levels and design variations – calculations with STAR-CD

In total a number of 9 cases has been analysed with STAR-CD using the Low-Reynolds-Number turbulence model to calculate the heat transfer and pressure loss in the channels between the rigs. The main parameters and results are compiled in Table 1. The parameters changed against the previous case have been marked by bold printing. The cases 1a and 1b represent situations with nuclear heating only. Temperature differences of 121 °C elucidate, that electric heaters are mandatory. Cases 2 through 5b correspond to situations with nuclear and electric heating and electric heating only representing beam-on and beam-off periods respectively. The power levels of the tree heaters are given in lines 7, 8 and 9.

In case 2 the upper and lower heater were used to balance the nuclear power distribution. The temperature distribution in the central plane of the specimen stack ranges from 452 to 465 ^{0}C, i.e. the difference amounts to 13 K which is in agreement with the specification.
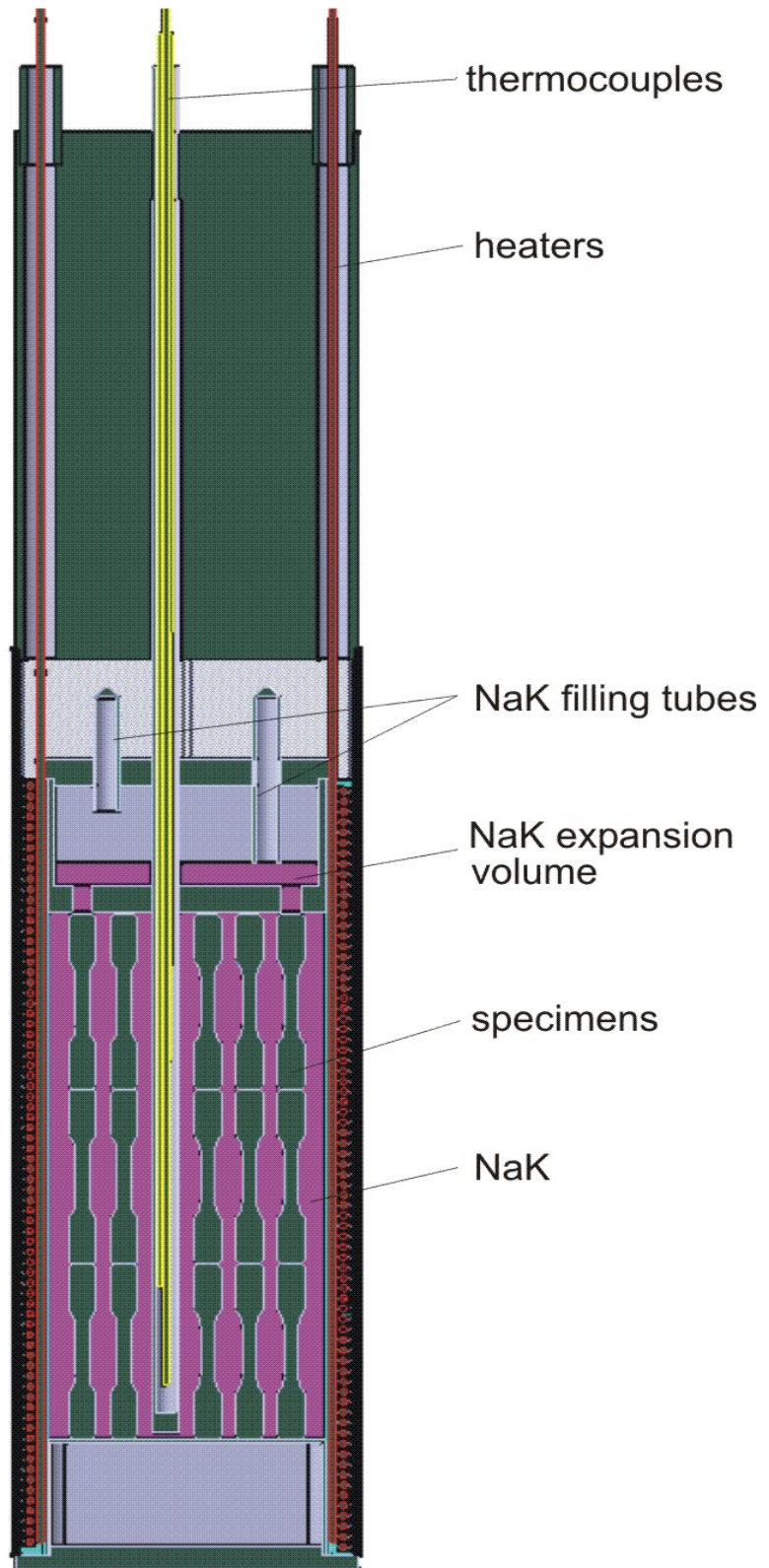
Fig. 3: Test rig with specimens.

Temperatures below 450 ^{0}C appear only at the upper and lower end of the specimen column. Limitation of the temperature difference to 15 K would reduce the usable length of the specimen column to 66 mm as described already. This is still about 30 % larger than the height of the beam footprint, i.e. the gain against the previous test volume is significant.

Table 1: STAR-CD Thermal-hydraulic Calculations and Main Results.

Case	1a	1b	2	3a	3b	4a	4b	5a	5b
Parameters									
Eff. He gap size (mm)	0.5	0.5	0.5	0.5	0.5	**0.8**	0.8	**0.25**	**0.25**
Lower cap	thin	**thick**	thick	thick	thick	thick	thick	thick	thick
Heating	nucl.	nucl.	**nucl./el**.	nucl./el.	**el.**	el.	**nucl./el.**	nucl./el.	**el.**
El. power in section									
upper (W/cm^3)	-	-	71	**149**	194	147	108	65	111
middle (W/cm^3)	-	-	-	**90**	199	148	39	-	118
lower (W/cm^3)	-	-	74	**158**	206	154	110	70	124
Results									
Fig. No.	23	24	25 to 30	31	32	33	34	35	36
Max. spec. temp.(^{0}C)	403	404	465	650	655	650	650	337	339
Max. temp. diff. in specimens (K)	121	121	30	31	35	13	22	33	33
Max. Helium velocity (m/s)	478	479	504	550	547	514	518	501	499
Stat. press. drop (MPa) -modelled section	0.086	0.086	0.089	0.095	0.095	0.091	0.092	.089	0.089
-rig only	0.053	0.053	0.056	0.06	0.06	0.057	0.058	0.055	0.055

Case 3a shows that the maximum irradiation temperature of 650 ^{0}C can be reached with the same geometry as in Case 2 by increasing the power of the electrical heaters. It is evident, that in this case heating of the middle section is necessary, too. The best temperature distribution was obtained with an electrical power of 158, 90 and 149 W/cm^3 in the lower, middle and upper section, respectively. The calculated temperature distribution in the specimens shows 650 ^{0}C at maximum which is reached along the central y-axis (x = z = 0), but a significant fraction of the test volume is below 630 ^{0}C. The maximum temperature difference amounts to about 31 K. Furthermore, rather large temperature differences (97 K) appear in the rig wall. This may cause high thermal stresses still to be analysed.

In Case 3b the power level and power distribution was determined which is necessary to hold by electrical heating only the same temperature as in Case 3a with nuclear/electric heating. An electrical power density of 209,199 and 194 W/cm^3 was obtained in the lower, middle and upper section, respectively. The calculated temperature in the specimens amounts to 655 ^{0}C at maximum and the temperature difference in the specimens to 36 K. Both values are similar to those obtained in Case 3a.

In case 4a the helium gap between the rig wall and the capsule was increased from 0.5 to 0.8 mm in order to reduce the large temperature difference in the specimens – in particular in Case 3b –. The related increase in thermal insulation should reduce the electrical power, and likewise the differences of the heat flux from the capsule to the rig wall. This expectation is confirmed. To reach a temperature of 650 ^{0}C with electrical heating only a power level between 147 and 154 W/cm^3 is necessary. The temperature difference in the specimens has dropped to 13 K, and in the rig wall to 60 K.

Case 4b corresponds to Case 4a but with nuclear and electrical heating. The temperature level of 650 ^{0}C and the optimum temperature distribution in the specimens is obtained with electrical power densities of 110, 39, and 108 W/cm^3, respectively, in the top, middle and bottom section (see Fig. 3). The temperature difference in the specimens amounts to 22 K.

Case 5a is related to the lower range of irradiation temperatures. Low temperatures can be reached by reducing the thermal resistance between the rig wall and the capsule as far as possible, e. g. by conserving all ribs between the heaters at the capsule surface, and by applying the concept with the lower pressure inside the capsule. It was estimated that in this case a thermal resistance can be achieved equivalent to a helium layer of 0.25 mm thickness. The electrical power in this case is 65 and 70 W/cm^3 in the top and bottom section, respectively. The specimen temperature is between 305 and 337 ^{0}C; this means that the average specimen temperature is about 70 K higher than the specified minimum temperature. The temperature difference in the specimens can be reduced by a further adjustment of the electrical power including the middle heating section, but this would simultaneously rise the average temperature.

Case 5b is complementary to Case 5a – i.e. the isolating gap between the rig and the capsule corresponds to a helium layer with an effective thickness of 0.25 mm – but with electrical heating only.

Table 1 demonstrates, that the temperature levels in the specimen stack can be achieved within acceptable tolerances with mainly the same design from about 320 °C up to about 650°C.

4. Code validation

STAR-CD provides several turbulence models. For the simulation calculations described above, the Linear-Low-Reynolds-Model (LLRM) was applied. The situation in the narrow channels between the rigs ($\delta \leq 1$mm) is characterized by incompletely developed hydraulic and thermal boundary layers. Furthermore the high heat fluxes at the rig walls create laminarization of the boundary layers, which impairs the heat transfer coefficient. Simulation calculations of an experiment taken from the literature [2] show, that the LLRM reproduces the experimental data in good agreement (see Fig. 4) [3]. Furthermore, the results reveal the influence of the heat flux on the heat transfer coefficient. They also uncover, that the heat transfer coefficients calculated with the Nusselt-number are too high. Though the Nusselt-numbers used, were given as valid for this application, do not regard sufficiently the gas properties in the boundary layers.

For the measurement from Shehata and McEligot were carried on with a tube with a hydraulic diameter of $d_{hr} = 27.4$ mm whereas the HFTM channels has $d_{hr} = 2$ mm. Therewith, in case of the HFTM the surface roughness is larger compared to the diameter so that addition experimental data are needed for validation. This is aimed at with the ITHEX experimental test section. It is installed in a loop which allows in a first step to reach Reynolds numbers up to 10000 with air only. Pressure loss measurements under adiabatic conditions show that experimental data, which separate clearly inlet effects and the pressure loss gradient downstream the channel, are needed for detailed comparisons with the simulation calculations.
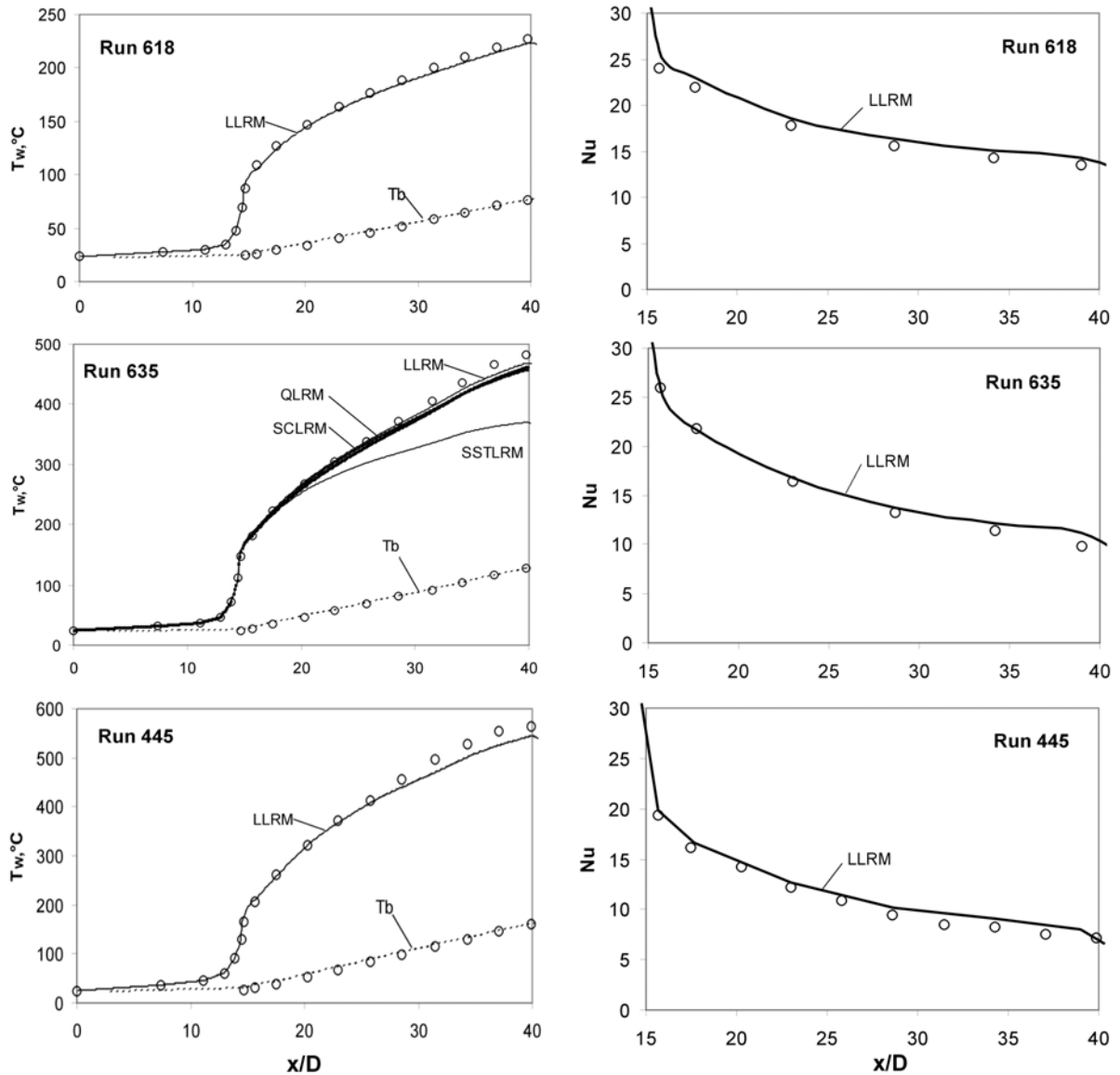
Fig. 4: Calculated local wall temperature and Nusselt number (lines) compared to measurements from Shehata and McEligot (circles) LLRM = Linear-Low-Reynolds-Model, QLRM = Quadratic-Low-Reynolds-Model, SSTLRM = Shear-Stress-Transport-Low-Reynolds-Model, SCKRM = Suga's Cubic Low-Reynolds-Model; T_b = bulk temperature.

5. CATIA drawings of the test cell

For preparing a design integration existing drawings of the IFMIF test cell and its internals were put together in a design drawn with the CAD-system CATIA (see Fig. 5).
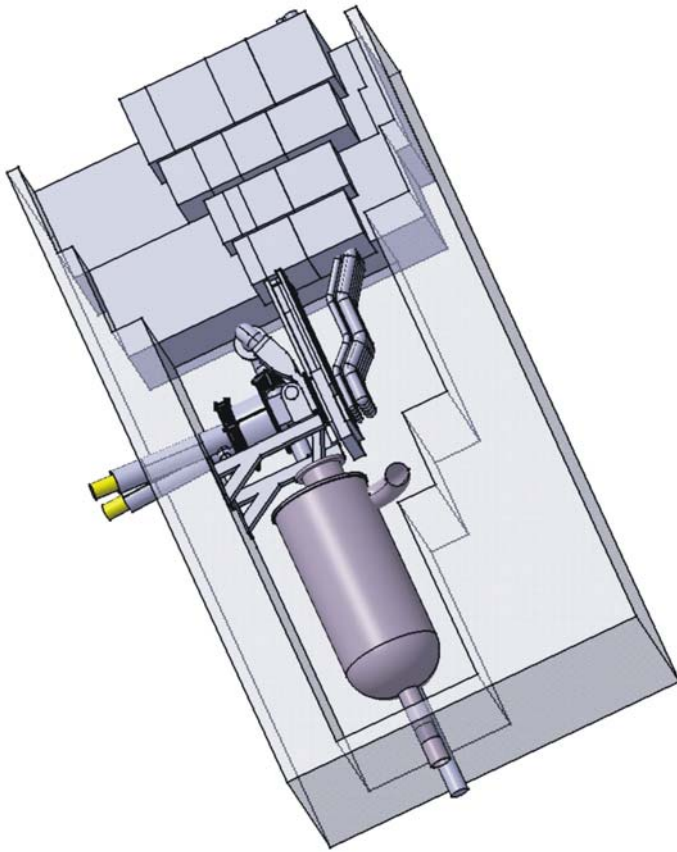
Fig. 5: CATIA drawing of the test cell.

Staff:

O. Albrecht
F. Arbeiter
A. Brecht
B. Dolensky
U. Fischer
S. Gordeev
V. Heinzel
T. Kuhn
E. Kupper
K.H. Lang
I. Schwartz
S. Simakov
V. Slobodtchouk
E. Stratmans

Literature:

[1] S. Gordeev,, V. Heinzel, K. H. Lang, A. Möslang, K. Schleisiek. V. Slobodtchouk, E. Stratmanns: Optimised Design and Thermal-Hydraulic Analyses of the IFMIF/HFTM Test Section, FZKA 6895, Oct. 2003

[2] A. Mohsen Shehata, Donald M. McEligot: Turbulence structure in the viscous layer of strongly heated gas flows, INEL-95/0223, Tech. Report, Idaho National Engineering Laboratory, November 1995

[3] S. Gordeev, V. Heinzel, V. Slobodtchouk: Features of convective heat transfer in the heated helium channel flow (to be published in an int. journal)

TW3-TTMI-003 D8
Test Facility Neutronics: 3D Calculation of the Complete Nuclear Response in HFTM, MFTM, L&VLFTM

TW4-TTMI-003 D5b
Neutronics Application and Users Tasks: 3D Calculation of the Entire Nuclear Responses in the High and Medium Flux Test Modules using up-dated Global IFMIF Geometry Model

Introduction

The International Fusion Materials Irradiation Facility (IFMIF) is a high-intense stripping neutron source intended for fusion materials testing under conditions expected for the full-scale fusion reactor. The IFMIF project is at present in the Transition Phase ending in 2004. Preparations for entering a 6-7 years EVEDA phase are already advanced both with R&D and legal entry framework. Its preliminary engineering design was already started and requires detailed study of neutronics and evaluation of the effect of irradiation conditions on material properties.

The overall objective of this task is to provide the irradiation parameters for the high and medium flux test modules to the user group and the design engineers during the design phase as well as the evaluation of damage parameter changes due to design variations.

Our previous studies have shown that IFMIF neutron spectrum can be adjusted by using tungsten spectral shifter blocks in order to reproduce primary knock-on atom spectra expected for DEMO fusion reactor in construction materials. Irradiation of lithium based breeder ceramics at tritium release module (TRM) requires increased thermal neutron tail of the spectrum, which can be obtained by using carbon moderator. On the other hand irradiation of beryllium based materials at TRM requires an increase of both fast and thermal neutrons. In this report our results on the improvement of the beryllium irradiation conditions at TRM are presented.

MFTM design variants and tritium production

The main aim of this work was to determine tritium, helium and damage production rates in beryllium irradiated at the Tritium Release Module (TRM) of the medium flux test module (MFTM).

Helium is produced by ^{9}Be(n, α) and ^{9}Be(n,2n) reactions with two resulting helium nuclei per reaction for the latter. Since both reactions have neutron energy thresholds above 1 MeV, helium production in beryllium takes place only in the high-energy range. The threshold for the direct tritium production through the ^{9}Be(n,t) ^{7}Li reaction is even higher (about 11.6 MeV). However, tritium can be also generated through the two-step reaction ^{9}Be(n,α) ^{6}He $\rightarrow$ ^{6}Li(n,α)T which, in particular, can give a significant contribution for a soft neutron spectra.

Due to the specific feature of the neutron cross sections, the two-step reaction is effective only if the neutron spectrum shows both a high population of high- (for the efficient ^{6}He production) and low-energy (for the T production on ^{6}Li) neutrons.

Five main design variants were considered for the irradiation of beryllium at TRM position (see Table 1):

- the initial model with tungsten spectral shifter and graphite reflector (fw19.6)

- a model without tungsten spectral shifter and with two additional graphite blocks (23.8 x 30.0 x 22.0 cm^3) placed behind the TRM from both sides of low flux test module (fw21.6)

- three variants without creep-fatigue testing machine (CFTM) and tungsten spectral shifter, where TRM was shifted up to the HFTM. One variant has no additional graphite blocks (md24c.5) while another (md24c.6) includes those. The third variant has extended graphite blocks (md24c.8).

Calculations of neutron energy spectra were performed using McDelicious code and for consequent calculations of tritium production ALARA radioactive inventory code was employed.

Table 2: Variants description

Name	Histories, x10^6	Library	W spectral shifter	CFTM	Additional moderator
fw19.6	100	4009.24c	Yes	Yes	No
fw21.6	10	trans .98c dam .24c	No	Yes	Yes
md24c.5	10	trans .98c dam .24c	shifted	shifted	No
md24c.6	10	trans .98c dam .24c	shifted	shifted	Yes
md24c.8	10	trans .98c dam .24c	shifted	shifted	EXTENDED

The results for the unshifted TRM have shown that in this case the total neutron flux is about one order of magnitude lower than in the fission reactors and the FPR HCPB front position and better corresponds to a position in the back of the blanket. However there is a significant tritium production due to the large fraction ($\approx$ 18%) of high-energy neutrons above the threshold of the 9Be(n,t)7Li reaction which is not present in the HFR and the BOR-60 spectra. The tungsten plate decreases neutron flux and, hence, the tritium and the helium production rates by factor of about 2.4. Thus for the beryllium irradiation at TRM the tungsten spectral shifter, which is normally used for proper simulation of fusion irradiation conditions for structural materials tested at CFTM, has a detrimental effect and should be removed.

To increase neutron flux and, hence, tritium production we have considered variants in which both tungsten spectral shifter and CFTM were removed completely and the whole TRM was shifted upstream right up to the HFTM. As a result the total flux increases more than two times, helium production rate due to Be^9(n,α) reaction increases about three times and direct tritium production rate due to Be^9(n,t) increases to a lesser degree, about 1.3 times. At the same time tritium production due to Li^6(n,t) reaction decreases by 3 times, because of the lack of low energy neutrons. After implementing additional graphite reflectors (variants md24c.2 and md24c.6) T-production rate increases again twice, but remains still lower than in the case of the unshifted TRM without tungsten spectral shifter (fw21.1). It was shown that the increase of the size of graphite reflector does not affect tritium production significantly.

The helium and tritium accumulation with time is shown in Table 3. Although the tritium production for IFMIF is less, but already comparable with fusion relevant level, the helium production is practically the same. The slope of the lines in Figure 1 reflects the important He/T ratio, which is very close to that of HCPB FPR for the case of shifted TRM.

Table 3: He and T production in Be irradiated at TRM of IFMIF.

MFTM Config.	Variant	N flux n/cm^2/s	He, appm			T, appm			He/T	
			1 y	2.28 y	4.57 y	1 y	2.3 y	4.6 y	1 y	4.6 y
With CFTM and W moderator										
no add. C	fw19.6	1.5·10^{14}	795	1821	3649	18.4	41.1	78.6	43.2	46.4
add. C	fw21.6	1.7·10^{14}	1923	4407	8833	44.6	101	199	43.1	44.4
no CFTM, no W moderator, TRM is shifted upstream										
no add. C	md24c.5	3.7·10^{14}	5566	12749	25524	116	260	497	48.0	51.4
add. C	md24c.6	3.8·10^{14}	5581	12786	25607	117	264	514	47.7	49.8
extend. C	md24c.8	3.9·10^{14}	5584	12798	25639	118	269	534	47.3	48.0
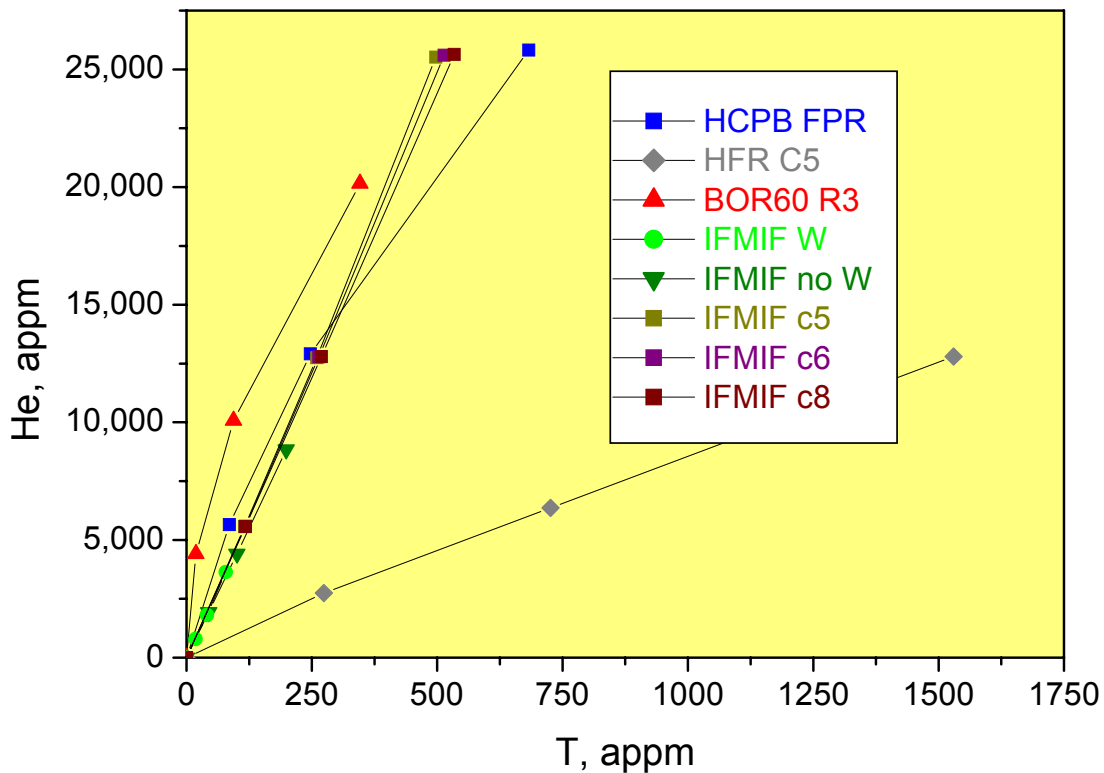
Fig. 1: Helium to tritium production ratio in beryllium irradiated in various nuclear facilities. See Table I for the description of IFMIF design variants.

Conclusions and future prospective

It was shown that in the present reference concept the in-situ creep-fatigue test module and the W-neutron spectral shifter can be temporary removed to allow tritium release experiments to be performed in TRM under conditions similar to that of DEMO reactor blanket. While tritium production at IFMIF TRM is comparable with fusion relevant level, the helium production is practically the same.

It was also concluded that graphite moderator blocks do not significantly affect tritium production at TRM and should not be implemented.

Staff:

U. Fischer
A. Möslang
S. Simakov
P. Vladimirov

Literature:

[1] A. Möslang, P. Vladimirov, Comparison of Irradiation Conditions for Fusion Materials in IFMIF and ESS, in Proceedings of the 5th International Ural Seminar on Radiation Damage Physics of Metals and Alloys , Snezhinsk, Russia, February 23 – March 1, 2003 (on CD-ROM)

[2] A. Möslang, P. Vladimirov, Fusion Material Irradiation Conditions in IFMIF and ESS, in Proceedings of AccApp'03 "Accelerator Applications in a Nuclear Renaissance", San Diego, California, USA – June 1-5, 2003

[3] A. Möslang, P. Vladimirov, *Radiation Damage Conditions for ESS Target Hull and Irradiation Rigs*, presented at IWSMT-6, Japan, Dec. 2003 (accepted for publication in J. Nucl. Mater.)

[4] U. Fischer, D. Leichtle, A. Möslang, P. Vladimirov*, Nuclear Irradiation Parameters of Beryllium under Fusion, Fission and IFMIF Irradiation Conditions*, presented at ICFRM11, Kyoto, Japan, December 6-12, 2003, Book of Abstracts, p.182.

[5] A. Möslang, P. Vladimirov, *Performance improvement of the Medium Flux Test Module by Neutronics Calculations and Revised Design*, Contribution to IFMIF-KEP Report: International Fusion Materials Irradiation Facility Key Element Technology Phase Report, Report JAERI-Tech-2003-05, March 2003, p. 307.

[6] H. Ullmaier, A. Möslang, G. S. Bauer, V. Slobodtchouk, D. Filges and P. Vladimirov, *Spallation Neutron for Radiation Damage Research on Nuclear Materials*, 16th Meeting on Int. Collaboration on Advanced Neutron Sources (ICANS-XVI), May 12-15, 2003, Düsseldorf-Neuss, Germany.

[7] P. Vladimirov, A. Möslang, Comparison of Material Irradiation Conditions for Fusion, Spallation, Stripping and Fission Neutron Sources, Journal of Nuclear Materials, **329-333**, Part 1, 1 August 2004, Pages 233-237.

[8] V. Heinzel, P. Bem, E. Esposito, S. Gordeev, U. Fischer, A. Moeslang, S. Simakov, A. Shimizu, M. Sugimoto, I. Tiseanu, P. Vladimirov et al., *Overview on the IFMIF test cell development*, Journal of Nuclear Materials, **329-333**, Part 1, 1 August 2004, Pages 223-227.

[9] S. P. Simakov, U. Fischer, A. Möslang, P. Vladimirov, F. Wasastjerna, P.P.H. Wilson, *Neutronics and Activation Characteristics of the International Fusion Material Irradiation Facility*, presented at SOFT-23 held at Venice, Italy in September 2004

[10] Heinzel, V., Arbeiter, F., Bürkle, G., Chen, J., Fischer, U., Grodeev, S., Lang, K.H., Möslang, A., Shimizu, A., Simakov, S.P., Slbodtchouk, V., Stratmanns, E., Vladimirov, P., *Prospective testing program for IFMIF,* presented at 23rd Symp.on Fusion Technology (SOFT-23), Venice, September 20-24, 2004

[11] V. Heinzel, G. Bürkle, J. Chen, U. Fischer, S. Gordeev, K.H. Lang, H. Matsui, A. Möslang, T,. Shannon, A. Shimizu, M. Sugimoto, S.P. Simakov, V. Slobodtchouk, E. Stratmanns, P. Vladimirov, *The IFMIF Test Cell – Design and Neutronics Overview*, IAEA-Conference in Vilamoura, Portugal, 1-6 November 2004.

[12] Simakov, S., Chen, Y., Fischer, U., Leichtle, D., Möslang, A., Vladimirov, P., *Fusion relevant irradiation simulation of beryllium in fission reactors and the IFMIF neutron source,* Jahrestagung Kerntechnik 2004, Düsseldorf, 25.-27 Mai 2004, Berlin : INFORUM GmbH, 2004 S.397-400 (on CD-ROM)

TW4-TTMI-003 D1
HFTM Design Optimization

1. **Experimental validation of the thermo-hydraulic code used for the design of the IFMIF - HFTM thermal heat coefficients to be used in the design of test module.**

Specific features of the HFTM resulting from the general design requirement are:

- narrow flat ducts for the rig cooling, (d = 0.5 – 1 mm), low Reynolds number (Re = 8000 – 10000) of the gas flow in the cooling channels

- The entrance conditions and channel geometry influence developing of the flow

- The heating of the flow in the test section that can lead to additional flow relaminarization.

Heat transfer and pressure losses are predicted with the CFD code STAR-CD. A dedicated validation of the turbulence models for the calculation of the flow in this transition range laminar/turbulent is based on the comparison with ITHEX experimental data on pressure loss. Concerning relaminarization experimental data from literature were used.

Comparison with ITHEX pressure loss data:
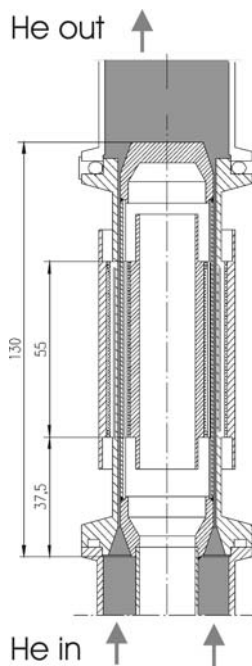
Fig. 1: ITHEX test section with an annular channel.

ITHEX is a loop designed for measuring pressure loss and heat transfer in an annular channel heated from both sides. In a first application pressure losses with air were measured without heating at 1000 < Re < 8000. Further data were: inlet pressure pin ~ 0.1 MPa, inlet temperature Tin ~ 23°C and velocity at the inlet vin ~ 0.7 – 5 m/s.

The simulation calculations with STAR-CD used the following turbulence models:

- linear k-e Low-Re number model

- cubic k-e Low-Re number model

- v2f model

In the laminar range till Re < 4000 the simulation results show good agreement with measured friction factor. In the transition range 4000 < Re < 7000 the factor is overestimated by 5-10 %. This turns to an underestimation at Re > 7000. The pressure loss measurements comprised the friction factor over the channel and the effect of the inlet. A new test section became necessary with additional accesses along the channel for separation of the different contributions to the pressure loss.
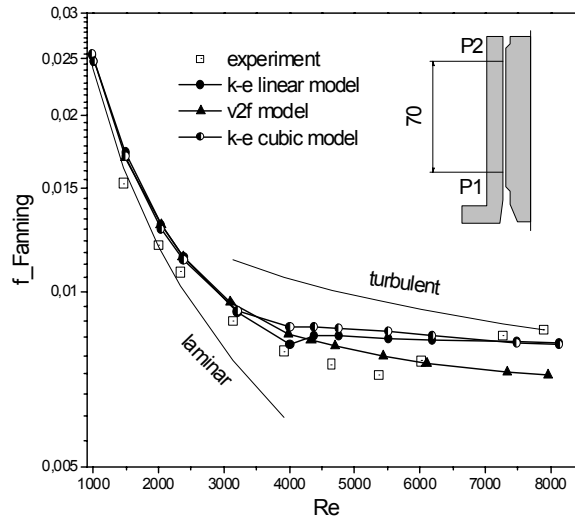
Fig. 2: Friction factor for adiabatic flow through the annular channel of the ITHEX test section.

Relaminarization – influence of the helium heating on the laminarization of the turbulent flow in the cooling channels of the IFMIF/HFTM.

A comparison of different turbulence models offered by the STAR-CD code performed on the basis of the simulation of the experimental data of Shehata and McEligot [1] shows that the linear low-Reynolds-number k-ε turbulence models predict the heat transfer characteristics close to the experimental data. This turbulence model has been used for the further investigation of the relaminarization effect and it's influence on the turbulence and temperature distribution in the IFMIF/HFTM.

Using the criterion for the relaminarization in the form of $q^+ \geq 1.05*10^{-5}*Re_b^{0.8}*Pr_b^{0.6}$ [2] one can estimate the limit of the non-dimensional heating rate q^+_{limit} for the temperature range in the specimens from 250°C up to 1000°C and also estimate the probability of the relaminarization of the flow in the HFTM cooling channels. In accordance with the boundary conditions for the HFTM $q^+_{limit} \approx 0.0017$. For the temperature range 250-650 °C where the value of q+ is less then 0.001 the flow is turbulent and the heating of the gas flow can hardly reduce the heat transfer. For the range 650-1000°C one can expect the begining of the laminarization. For three temperature levels of 650°C, 800°C and 1025°C in the volume with samples of the HFTM the heat flux on the rig wall should be equal to 0.23 MW/m^2, 0.33 MW/m^2 and 0.43 MW/m^2, respectively. This corresponds to the following values of the heating rate q^+ : q^+ = 0.0014 < q^+_{limit} for the heat flux of 0.23 MW/m^2, q^+ = 0.0018 ≈ q^+_{limit} for 0.33 MW/m^2 and q^+ = 0.00235 > q^+_{limit} for 0.43 MW/m^2 . One can see that the flow relaminarization can only occur in the case of heat flux equal to 0.33 MW/m^2 and 0.43 MW/m^2.

To investigate the influence of the heating intensity on the turbulence characteristics a two dimensional (2D) model of the HFTM cooling channel is elaborated and all the aforementioned cases are simulated with the boundary conditions in the form of the constant heat flux on the wall. The calculated turbulence characteristics of the flow show a small increase in the viscous layer thickness for 650°C and 850°C. The turbulent kinetic energy is continuously increased downstream. The process of the flow relaminarization for 1000°C is confirmed by all the turbulence characteristics. The thickness of the viscous sub-layer continuously increases and the turbulent kinetic energy continuously decreases downstream. The integral flow characteristics such as the Nusselt number along the heated section and the Stanton number also confirm the flow relaminarization for 1000°C.
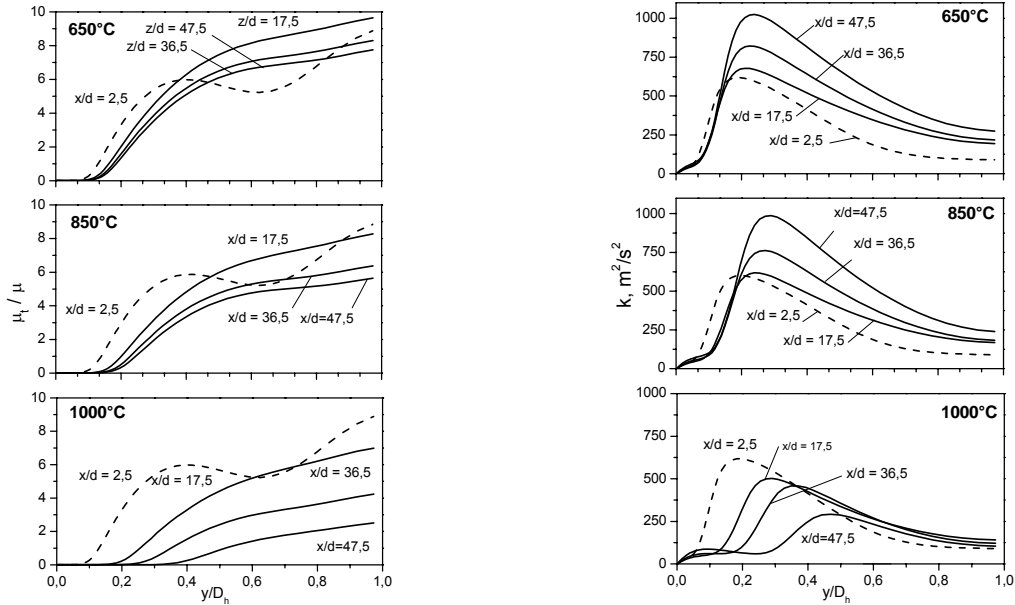
Axial development of the turbulence quantities in the channel flow of the HFTM calculated with the 2D model: a) turbulent viscosity, b) turbulent kinetic energy

To estimate the influence of the flow relaminarization on the temperature distribution in the volume with samples a 3D model of a capsule with samples was elaborated based on the reference design. Combining the nuclear and electrical heating, two cases were simulated corresponding to the samples temperature of 650°C and 1025°C. The results of calculation show that the flow relaminarization is not observed in case 650°C, though the intense heating and the gas compressibility have an adverse effect on the heat transfer. One can see the effect of the flow relaminarization in case 1025°C resulting in an increase in the viscous sub-layer and a decrease in the Reynolds stress. The diagrams of the Nusselt and Stanton numbers show that they approach the laminar values.
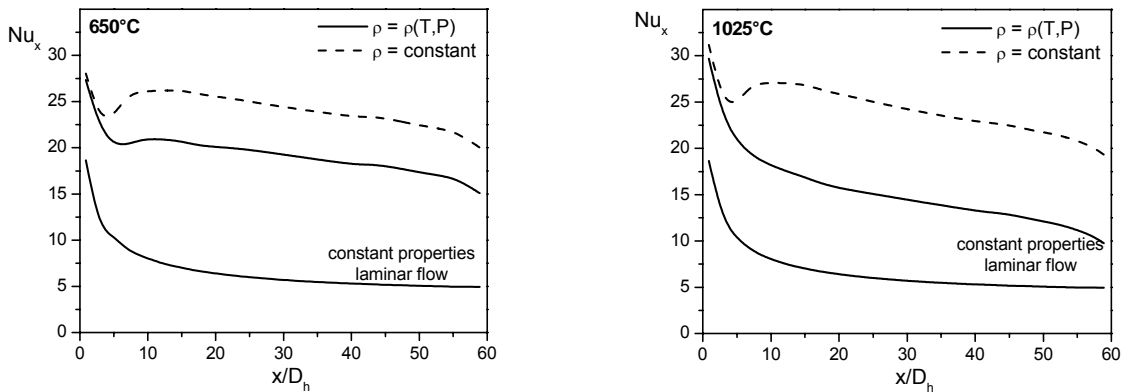
Axial distribution of the Nusselt number in the middle cross section of the channel flow calculated with 3D model of HFTM

For comparison, the calculations are repeated for cases 650°C and 1025°C under the constant properties of the gas flow, where the flow relaminarization is not taken into consideration. The difference in the temperature values is not more than 10-12°C in case 650°C, whereas it can exceed 50-70°C in case 1025°C. This value is higher than the allowable temperature variation in the volume with samples and cannot be ignored while choosing the operation loads of the IFMIF/HFTM.
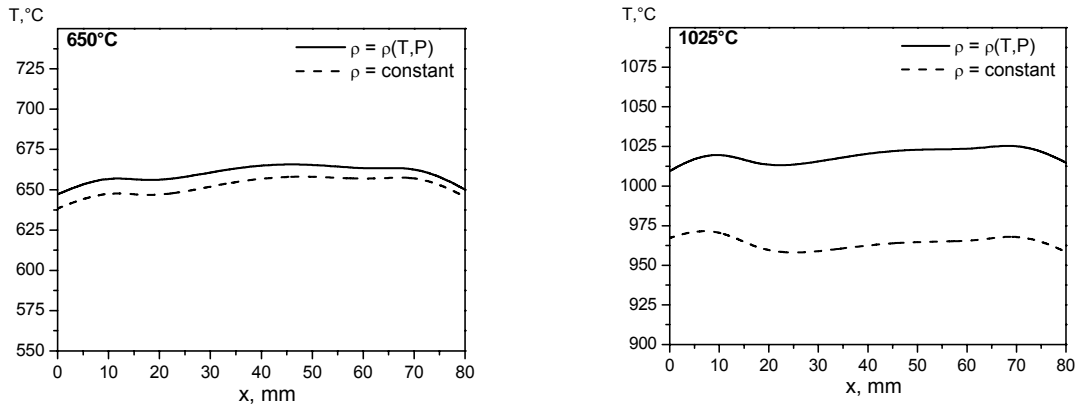
Axial temperature distribution in specimens in the middle cross section of the rig calculated with 3D model of HFTM.

2. Stress reductions in the HFTM container wall

The stress analyses of the HTFM container revealed stress peaks at the stiffening walls, which separate the container into for compartments. Also the temperature distribution in the integrated reflector caused thermal stresses.

In the first case hot gas plume downstream the 0.5 mm channels at the smaller sides of the rigs were identified for heating up the stiffening plates. An improved geometrical of the container, the inlet and outlet section, as well as the internals was built up. The new version of STAR-CD was implemented and compared to the former calculations. The results confirmed the effect of the small channels. The width was chosen with 0.5 mm, in order to save space for the rigs but more important to avoid abundant cooling at the smaller sides. Now the small channels caused a laminar flow which preserved downstream the narrow channels. The rigs were designed with lateral stiffening ribs. The stiffening plates and the ribs were heated due to the nuclear heating. Therewith, the ribs increased the heat flux to the smaller channels and enhanced the flow reduction. The possible way to reduce the temperature peaks in the stiffening walls:

- Increase in helium flow rate
- Using rig vessels without ribs on the shorter sides
- Using rig vessels with discontinuous ribs on the shorter side.

The simulations with STAR-CD using the k-ε High Reynolds turbulence model shows that the absence of the ribs on the rig vessel results in a significant decrease in the stiffening wall temperature and in insignificant decrease in the pressure loss. On the other hand, the absence of the ribs makes the rig vessel less stiff and a significant deformation of the vessel can take place. Additional stress analysis is desirable. The case with discontinuous ribs (for example case 1x20) can be considered as alternative variant to the rig design without ribs.

The maximum temperature of the stiffening wall occurs approximately at the section opposite to the middle of the short side of the rig vessel even in the case of the vessel without ribs on this side. This can be explained by the fact that this section is more intensive heated due to nuclear heating.

The cooling channels in the lateral reflector were varied. The simulation provided results for a channel system with which the highest temperature can be reduced from 155 °C to about 120 °C. Stress analyses have to show whether this reduction is acceptable.

3. Analyses of the Suitability of STAR-CD for Simulation of the Natural Convection on the Target and Test Cell

3.1 Comparison of Star-CD simulations with the experiments of Hollands et al. [3].

The natural convection in horizontal and tilted boxes filled with heated from below and cooled at the cover were simulated with STAR-CD. The results were compared with experimental data taken from the literature. The first experimental work analysed the flow regime and presented local velocities. The second publication reported on the heat transfer. In both cases the boxes had large aspect ratios. The Rayleigh-number were $7 \cdot 10^3 \leq Ra \leq 6.1 \cdot 10^4$ and in case of the heat transfer measurements they range $2.0 \cdot 10^3 \leq Ra \cdot \cos \varphi \leq 9.9 \cdot 10^4$ was covered. The ranges covered several transitions of flow regimes. The simulations were done with the Standard k-ε High Reynolds turbulence model.

In most of the situations the flow regime from the simulations were in good agreement with the experimental observations. Deviations can be explained partially with the different presentation e. g. the photos integrate over a time span due to the exposure time whereas the simulation results represent the state of an iteration step.

The simulations described the heat transfer respectively the Nusselt numbers at the "transition" laminar/turbulent in good agreement with experimental data. This is demonstrated with the plot of the Nusselt-number over the Rayleigh-Number in Fig. 3.
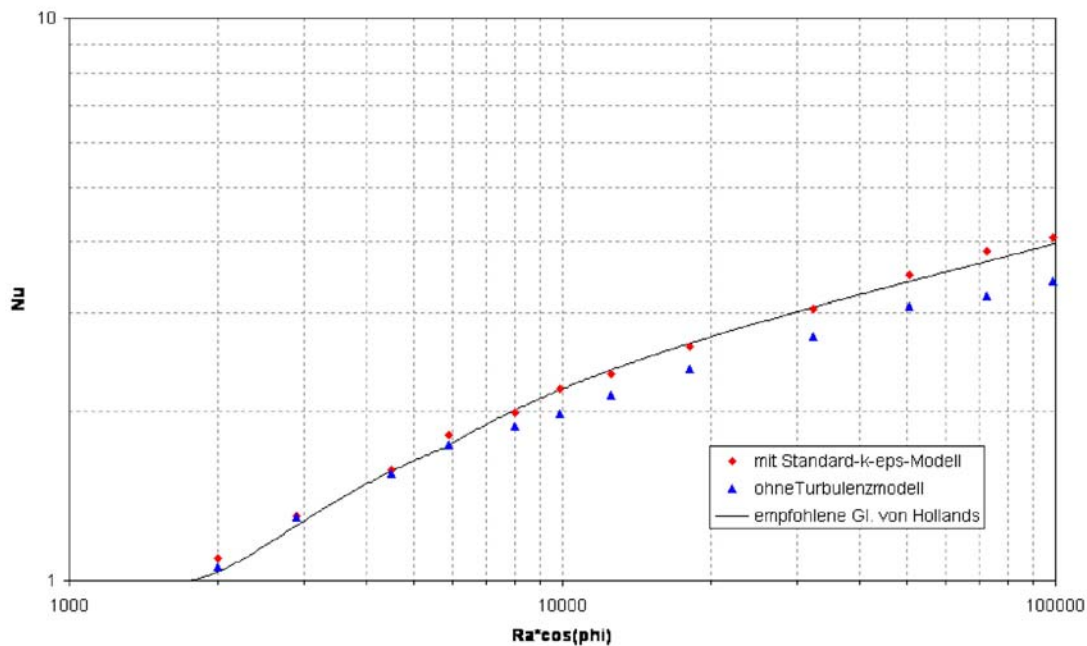
Fig. 3:   Nusselt-number over Raleigh-number for a tilted box with large aspect ratio, heated from below and cooled at the cover.

At $Ra \cdot \cos \varphi \leq 5.9 \cdot 10^3$ the simulation with and without the turbulence model are in good agreement with values of the recommended equation fitted to the experimental data. With increasing Ra-numbers the results without turbulence model deviate to lower values indicating the transition to flow regime with turbulence. At Ra-numbers $Ra \cdot \cos \varphi \geq 3.2 \cdot 10^4$ the simulations show addition transitions to further flow regime and greater deviations from the equation. The transitions in flow regimes are documented in Fig. 4, which shows the heat flux density at the bottom plate of the box. The heat flux density indicates the air flow regime over the plate. The equation does not contain a transition term to describe those transitions. As the flow regimes provided by the simulations are in good agreement with the experimental

observations of the first publication, the transitions seem to be reasonable. In principle the simulation of the natural convection in the boxes considered with STAR-CD and the Standard k-ε High Reynolds turbulence model are adequate. The code calculates 3D flow regimes.

Ra·cosφ = 2.0·10³	Ra·cosφ = 2.9·10³
Ra·cosφ = 4.5·10³	Ra·cosφ = 5.9·10³
Ra·cosφ = 8.0·10³	Ra·cosφ = 1.3·10⁴
Ra·cosφ = 5.0·10⁴	Ra·cosφ = 9.9·10⁴
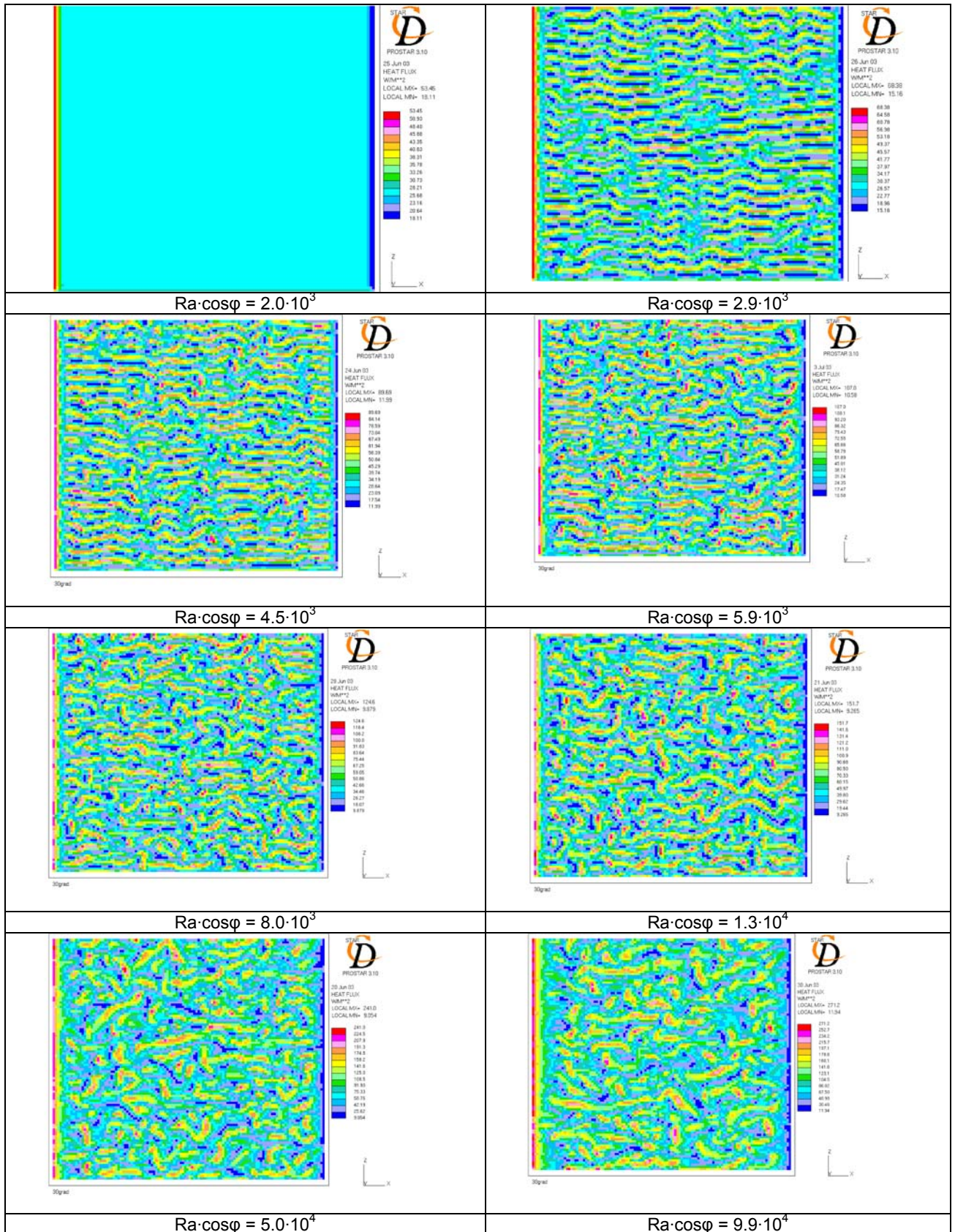
Fig. 4: Local momentary heat flux density (W/m2) distribution at the bottom plate.

The analysis was restricted to the k-ε High Reynolds turbulence model in order to get a survey at a reasonable computing time. Further work should be done.

3.2 Simulations of the natural convection in a complex cavity.

The code calculated the 3D fluctuations in the situations above. Simulations show fluctuations in larger cavity where the natural convection was super imposed by buoyancy driven through put of air.

A cubic box is considered having a heated bottom, a lateral inlet close to the bottom and a central cylindrical exit. Therewith, air can enter at the bottom and leave through the chimney like exit. The buoyancy creates a 3D complex natural convection in the box but also initiates a through put like a forced convection. Though the geometry is symmetric, those systems tend to exhibit fluctuations of flow and temperature. The simulations were done again with the Standard k-ε High Reynolds model.
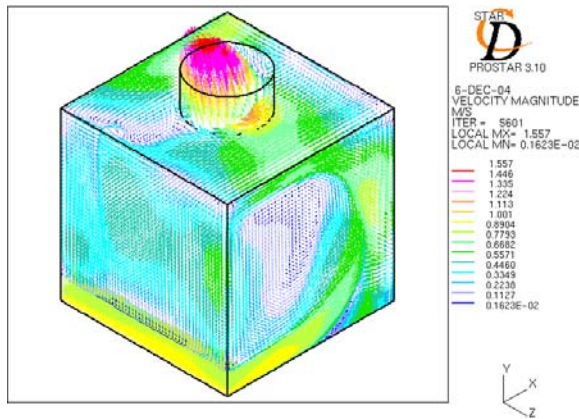
Fig. 5: 3D velocity field in a cubic enclosure heated at the bottom, with a lateral air inlet and central chimney like exit

Fig. 5 shows the velocity field in the mid-plane. There is a plume like lift on the right side and back flow zone on the left side. The air enters the exit chimney asymmetrically. Within the chimney occurs a back flow region, too. Temperature and velocity fluctuate at the chimney as expected.

3.3 Testing turbulence models for natural convection simulations

A further experimental benchmark is chosen for testing the different turbulence models offered by STAR-CD. The experimental rig is now a cavity 0.75m high x 0.75m wide x 1.5m deep filled with air and equipped by monitoring and control systems. Detailed description of the installation and experimental procedure can be found in [4]. The vertical hot and cold walls of the cavity are isothermal at 500°C and 100°C respectively giving Rayleigh number of $1.58*10^9$. Top and bottom walls are made of steel and are insulated. Such horizontal aspect ratio (deep/height = 2) results in 2D flow in the mid-plane of the cavity. So, to simulate these experimental data a 2D model is built with the square cross section of 750 x 750 mm. Top and bottom steel walls of 1.5 mm thick are simulated with adiabatic boundary conditions on the external surfaces. The mesh of the calculation domain is not uniform: it is finer near the walls and is coarser in the central zone.

The calculations are carried out using, first of all, the low Reynolds number turbulence models. These are: linear low Re number model (low-Re), quadratic low Re number model (low-ReQ), k-omega low Re number model (k-w low-Re), SST low Re number model (SST low-Re) and the v2f model is tested too (V2F). Then the high Re number models are used to simulate the experimental data: linear high Re number model (high-Re), high Re number quadratic and high Re number quadratic with non-equilibrium treatment near the wall region (high-ReQ, high-ReQ neq), k-epsilon Chen model (Chen), SST high Re number model (SST high-Re), k-omega high Re number and k-omega high Re number model with non-equilibrium near the wall treatment (k-w high-Re, k-w high-Re neq).

The velocity distribution in the boundary layer calculated with different turbulence models are compared with the experimental data and shown in Fig. 6. Low-Re, low-ReQ and V2F

turbulence models give practically identical results, so in Fig. 6 this is a single line. In general, practically all the turbulence models over-predicted the velocity value in vicinity of the wall (0 – 9 mm) and under-predicted it farer from the wall, except for some high Re number turbulence models (particularly k-w high-Re). The velocity profile predicted by the low Re number turbulence models is close to the laminar one. One can see that some of the high Re number turbulence models give better agreement with the experimental data, but this fact can not be considered as an argument that these models simulate the natural convection better. The matter is the following. It is known that the high Re number turbulence models work correctly for the mesh where the y^+ of the first cell from the wall is equal to ~30, at least y^+ should be more than 12. The velocity in the model simulated varies from 0 in stagnation zones to about 1.3 m/s near the vertical walls. So, the y^+ value varies significantly also. Additionally, to catch the behaviour of the velocity and temperature in the boundary layer correctly, the region of this layer is meshed more fine. Under these circumstances, the y^+ in the model reaches the value of 2 and even less in some places.
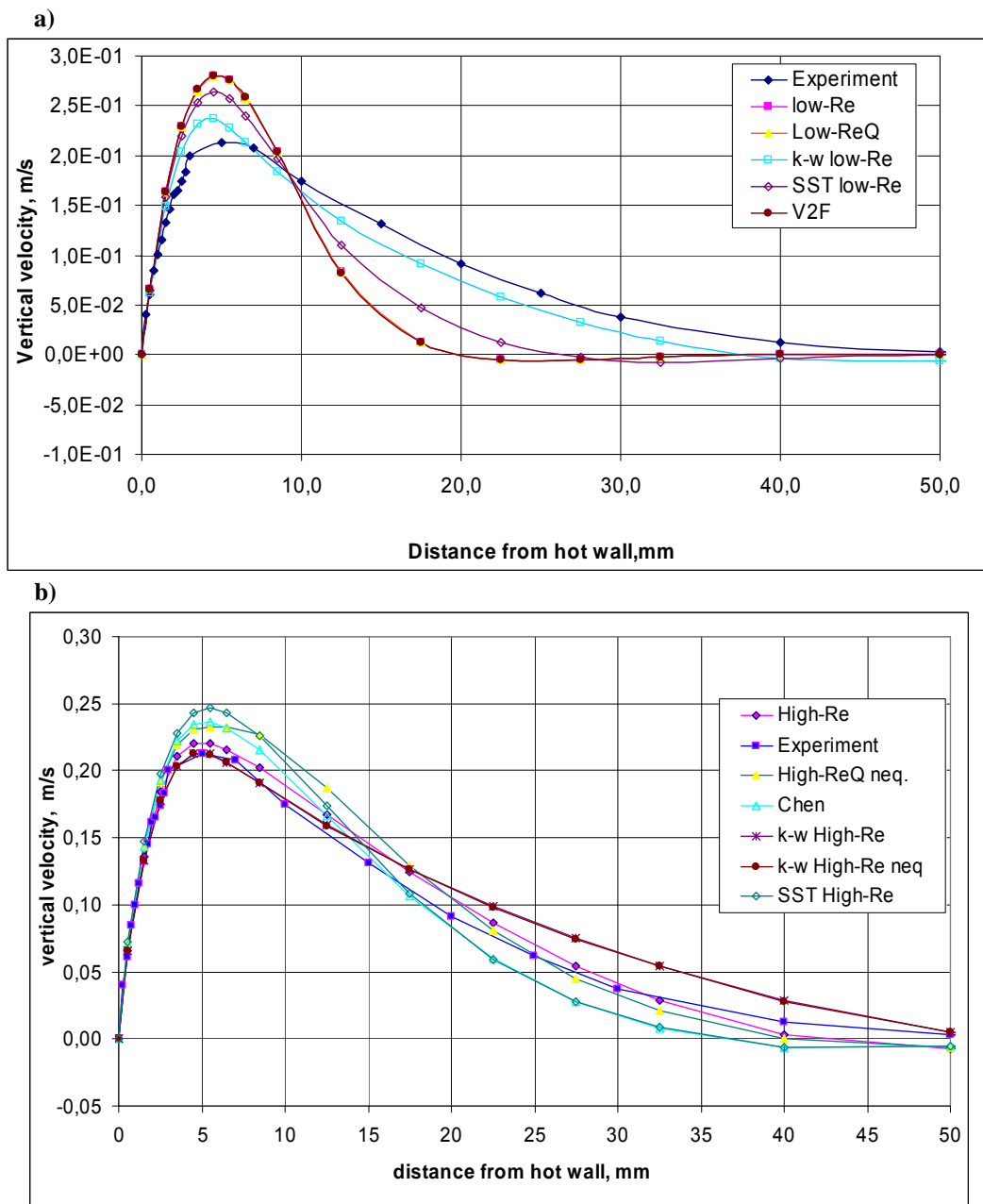
Fig. 6: Velocity distribution in the model: calculated results and experimental data; a – low Re number turbulence models, b – high Re number turbulence models.

As a conclusion, one can say that the low Re number turbulence models give velocity profile in near the wall region close to the laminar one, i.e. over-predict the experimental data. The use of the high Re number turbulence models with a strong restriction on y^+ ($y^+ \geq 30$) can result in the fact that it is difficult to describe correctly the narrow boundary layer zone (at a low velocity of the fluid flow, which it typical for the natural convection). In this connection it should be mentioned that k-omega high Re number turbulence models are more "flexible", because they are applied up to $y^+ = 5$. Moreover, at industrial applications for cases, where the natural convection plays a significant role and a cavity has several differently heated elements, the flow can be considered as combined natural-and-forced convection flow. The low Re number turbulence models require very fine mesh of the near wall region and also require much computing time and resources. In this case the use of the high Re number turbulence models (particularly, k-omega) for the flow simulation can be reasonable.

Staff:

S. Gordeev
O. Eckecukwu
V. Heinzel
T. Kurz
V. Slobodchuk

Literature:

[1] A. Mohsen Shehata, Donald M. McEligot, Turbulence structure in the viscous layer of strongly heated gas flows, INEL-95/0223, Tech. Report, Idaho National Engineering Laboratory, November 1995

[2] S. Kakac, R.K. Shah, W. Aung, Handbook of Single-Phase Convective Heat Transfer, Wiley, pp. 4.2, 22.1, 1987

[3] Hollands, K.G.T. et al. Free convective heat transfer across inclined air layers, J. of Heat Transfer, 1976

[4] F. Ampofo, T.G. Karayannis, Experimental benchmark data for turbulent natural convection in air filled square cavity, Int. J. Heat Mass Transfer, 46 (2003), 3551-3572.

TW4-TTMI-003 D2
Simulation of the IFMIF/HFTM with Deformed Cooling Channels

The operation conditions of the IFMIF/HFTM are very severe. Significant mechanical and thermal loads can result in the deformation of the rig walls and, hence, result in the deformation of the cooling channels. The cooling channels of the IFMIF/HFTM have a rectangular cross section, being 0,5 mm wide on the short side of the rig and 1 mm wide on the long side of the rig. So, even a small deformation of the cooling channels results in a significant change in the channel cross section area, which, in its turn, can change the thermo-hydraulic characteristics of the HFTM. This work is done to estimate the influence of the cooling channels deformation and the heat of the target back wall on the thermo-hydraulic characteristics of the HFTM.

Simulation of the cooling channels deformation for all channels of the model

The simulation of this part is carried out with the commercial CFD code STAR-CD, version 3.15. The following assumptions are made:

- the dimensions of the cooling channels at the inlet to the test section are not changed and are adopted as for the reference design,

- the remaining part of the section of the cooling channels is changed, but because the shape of the deformed channels is not exactly known, the width of the channel is simply reduced, except for the rib section,

- two variants are simulated: the channel width is reduced by 10% and by 20% of the reference value;

- nuclear heating only is considered as the thermal loads;

- the mass flow rate is constant.

Below the results are presented for several cases.

Case 1. Reference design.

Case 2. The width of the cooling channel on the long side of the rig is reduced by 10%, i.e. 0.9 mm instead of 1 mm. The width of the cooling channel on the short side of the rig is unchanged.

Case 3. The width of the cooling channel on the long and short sides of the rig is reduced by 10% (1mm → 0.9mm, 0.5mm → 0.45mm) compared with the reference design of the rig.

Case 4 . The same as in case 3, but without ribs on the short side of the rig.

Case 5. The width of the cooling channel on the long side of the rig is reduced by 20%, i.e. 0.8 mm instead of 1 mm. The width of the cooling channel on the short side of the rig is unchanged.

Case 6. The width of the cooling channel on the long and short sides of the rig is reduced by 20% (1mm → 0.8mm, 0.5mm → 0.4mm) compared with the reference design of the rig.

Case 7. The same as in case 6, but without ribs on the short side of the rig.

The main results of the calculation are summarised in Table 1.

Table 1: The main results of the calculation (nuclear heating only).

Parameter	Case						
	Case 1	Case 2	Case 3	Case 4	Case 5	Case 6	Case 7
W_{max}, m/s	402.5	404.6	409.8	405.6	441.1	483.8	478
W^{ref}_{max}, m/s	332.8	385.3	392	390.6	458.1	510.9	505
ΔP, bar	0.745	0.9	0.928	0.918	1.08	1.25	1.24
T_s^{max}, ^{0}C	386.2	376.9	375.5	375.2	380.3	382.3	383.6
T_w^{max}, ^{0}C	380.4	369.3	367.9	367.6	372.8	374.6	376
T_h^{max}, ^{0}C	372.4	360.9	359.6	359.3	364.5	366.2	367.5
T_r^{max}, ^{0}C	155	149.9	150.6	148.1	148.0	157.3	154.1
T_f^{max}, ^{0}C	152.5	147.5	147.4	137.1	149.3	162.9	159.2

The following nomenclature is used.

W_{max} is the maximum velocity of the helium flow in the HFTM,

W^{ref}_{max} is the maximum velocity of the helium flow in the reflector cooling channels,

ΔP is the pressure drop in the model,

T_s^{max} is the maximum temperature of the volume with samples,

T_h^{max} is the maximum temperature of the electrical heaters,

T_w^{max} is the maximum temperature of the capsule wall,

T_r^{max} is the maximum temperature of the reflector,

T_f^{max} is the maximum temperature of the helium flow.

Simulation of individual rig dimensions deviation from the reference design.

The next step of the work is the simulation of an individual rig dimensions deviation from the reference design. This deviation can be caused by the operation conditions as well as resulting from the fabrication tolerance. To estimate the influence of the local deviation of the rig from the reference design on the temperature field, the rig 2 is chosen for analysis.

Case 8. The cooling channels of rig 2 on long sides are decreased by 10% (1 mm → 0.9mm) and isolation gas gap between the rig vessel and the capsule with samples is increased accordingly by 0.1 mm. The nuclear heating only is considered.

Case 9. The cooling channel width is equal to the reference design value, but the insulation gas gap between the rig vessel and the capsule with samples is increased by 10% under nuclear heating only.

Case 10. The same as the case 9, only the isolation gas gap between the rig vessel and the capsule with samples is decreased by 10%.

Cases 11 – 13 are the same as the cases 8-10, but electric heating is added to the nuclear one (all three section of the electrical heater are into operation).

Table 2: The main results of the calculation for deviation of the dimension of rig 2 from the reference design (nuclear heating only).

Parameter	Case						
	Ref. design	Case 8		Case 9		Case 10	
		value	Rel. to ref. design, %	value	Rel. to ref. design, %	value	Rel. to ref. design, %
W_{max}, m/s	344.6	348.2	1.04	344.7	0.03	344.5	-0.03
ΔP, bar	0.696	0.707	1.58	0.696	0	0.696	0
T_s^{max}, ^{0}C	385.5	389.9	1.14	400	3.76	360.5	-6.48
T_w^{max}, ^{0}C	377	382.5	1.46	393	4.24	352.8	-6.42
T_h^{max}, ^{0}C	368.1	374.4	1.71	384.9	4.56	344.4	-6.44
T_r^{max}, ^{0}C	142.1	141.8	-0.21	142.4	0.21	142.4	0.21
T_f^{max}, ^{0}C	130.8	130.2	-0.46	130.9	0.08	130.9	0.08

Table 3: The main results of the calculation for deviation of the dimension of rig 2 from the reference design (nuclear and electrical heating).

Parameter	Case						
	Ref. design	Case 11		Case 12		Case 13	
		value	Rel. to ref. design, %	value	Rel. to ref. design, %	value	Rel. to ref. design, %
W_{max}, m/s	397	400.3	0.83	396.5	-0.12	396.1	-0.23
ΔP, bar	0.77	0.78	1.29	0.77	0	0.77	0
T_s^{max}, ^{0}C	655.2	679.5	3.71	699.8	6.81	618.7	-5.57
T_w^{max}, ^{0}C	650.2	674.9	3.8	693.6	6.67	614.8	-5.44
T_h^{max}, ^{0}C	648.4	673.4	3.86	691.9	6.7	612.8	-5.49
T_r^{max}, ^{0}C	175	174.9	-0.06	175.4	0.23	175.3	0.17
T_f^{max}, ^{0}C	217.4	219.3	0.87	218.4	0.46	217.3	-0.046

The nomenclature is the same as for Table 1, only T_s^{max}, T_w^{max}, T_h^{max} are taken for rig 2.

Influence of the heat from the target back wall on the HFTM.

The HFTM is located as close as possible (within about 2mm) to the target back wall to receive maximum neutron fluence [1]. The temperature of the target back wall is close to the one of the lithium flow. The Li flow temperature is equal to 250^{0}C at the inlet and is about 300^{0}C at the outlet of the target. On the other hand, the helium flow temperature at the inlet to the HFTM is chosen to be equal to 50^{0}C. In this connection it is important to estimate the influence of the target back wall on the thermal-hydraulic characteristics of the HFTM,

because all previous calculations are done without taking into account the heat transfer from the back wall to the HFTM.

Conclusion

The simulation carried out shows the following:

- The decrease in the cooling channels cross section by 20% may be dangerous because of increased hydrodynamics and mechanical loads to the structure.

- The decrease in the cooling channel cross section by 10% may be considered as acceptable. The deviation of the gas gap thickness inside the rig from the reference value affects the temperature distribution in the model more significant than cooling channel deformation.

- The heat of the target back wall results in a rise of the maximum temperature of the HFTM front wall by 19.2^0C and the maximum flow temperature in the first line of the cooling channels by 17.1^0C. The temperature distribution in other elements of the HFTM is practically the same as without the heat of the target back wall. There is some reserve to reduce the effect of the heat of the target back wall on the HFTM – gas gap thickness between the back wall and the HFTM can be increased to 2 mm.

Staff:

V. Heinzel
V. Slobodchuk

Literature:

[1] IFMIF Comprehensive Design Report, IFMIF International Team, January, 2004

TW4-TTMI-003 D3
Thermal-hydraulic Investigation of the Creep-fatigue Specimens in the IFMIF Medium Flux Test Module

1. Intoduction

The concept of the MFTM consists of three sub modules in series in the direction of the beam. The first sub module at the beam entrance side is housing three creep-fatigue specimens. The specimens should be tested in situ at temperatures between 250 and 650 °C. The tubular specimens with a length of about 35 mm should be kept at an almost constant temperature independently of the operational conditions of the source of radiation. The concept of the support, cooling and the loading of the specimens is based on experience obtained in related experiments in the Dual Beam Facility at the Zyklotron of Forschungszentrum Karlsruhe. The tubular specimen (inner diameter 8 mm) with its threaded ends is joint to the loading device and a screw cap. The cooling of the specimen is accomplished by helium which flows inside the tubular specimen. Direct electric heating is intended to adjust and control the temperature of the specimen. The necessary electrical isolation of the specimens from the loading drive is achieved by isolating discs against the remainder of the sub module. The discs must be installed leak tight. Appropriate clamping forces are applied by electrically isolated bolts and nuts.

2. Specimen temperature control with convective helium cooling

The nuclear heating reaches 10 W/cm^3 in the centre of the specimens and declines to about 60 % at the upper and lower ends. In the thin walled specimen the maximum heat flux is only 0.5 W/cm^2. The power in the support structure amounts to 520 W. The electric current through the specimen provides a power density of 1200 W/cm^3. In the larger cross section of the support structure the power density due to this current can be neglected. Heat will be removed with a helium velocity of 77 m/s at the inlet to the support structure (about 300 m/s inside the specimen), an inlet temperature of 50 °C and a pressure of 0.2 MPa. The temperature distribution in the specimen and the supporting structure is calculated with the CFD code STAR-CD.

Already in the initial phase of the analyses it became evident that significant temperature differences exist in the axial direction of the specimens. Therefore, it was investigated in a first step whether these difference can be reduced by varying the coolant velocity. For this purpose the inlet velocity was reduced stepwise from initially 77.7 m/s to 10 m/s. The results showed that the maximum specimen temperature of 650 °C can be kept constant by adjusting in parallel the electrical power. However, a significant reduction the temperature differences was not achieved.

In all subsequent cases the same electrical power density (1200 W/cm^3) and coolant inlet velocity (77.7 m/s) was applied, i.e. each design variation led to different maximum specimen temperature. To allow, nevertheless, the valuation of the temperature constancy of the specimens a relative unit $L_{5\%}$ was introduced which is defined as follows: $L_{5\%}$ is the relative (i.e. related to the total) length of the specimen which has a temperature variation of less than 5 % (related to the difference between the maximum specimen temperature and the coolant inlet temperature). Hence, the related absolute temperature difference depends on the maximum specimen temperature, and amounts e.g. 10 K at 250°C and 30 K at 650°C.

Table 1 gives an overview on the parameter variations and the results obtained.

Table 1: Parameter variations and results of the thermal-hydraulic simulations using the CFD code STAR-CD

Case	1	2	3	4	5	6	7	8
$q_{el,spec.}$ (W/cm^3)	1200	1200	1200	1200	1200	1200	1200	1200
q_{nucl}	+	-	+	+	-	+	+	-
Adapter-Mat.	SS	SS	Cer	SS	SS	Cer	SS	SS
$Q_{s.c.}$ (W/cm^3)	-	-	-	20	20	-	-	-
$Q_{thr.}$ (W/cm^3)	-	-	-	-	-	170	-	-
He-guide tube	-	-	-	-	-	-	with	with
$T_{max,spec.}$(°C)	549	442	540	562	483	586	499	440
$L_{5\%}$	0,46	0,38	0,43	0,48	0,37	0,83	0,52	0,42
Fig. No.	6	7				9	10	11

Fig. 1 shows the calculated temperature distribution for the reference concept with nuclear power generation (Case 1), on top of the figure for the entire model, on bottom for the specimen only. The maximum temperature in the specimen amounts to 549°C, whereas the minimum temperature at the upper end is only 424°C. $L_{5\%}$ achieves a value of 0.46, i.e. on a fraction of 46 % of the specimen length the specimen temperature is between 95 und 100% of the difference against the helium inlet temperature. In the transition region between the specimen and the specimen support the temperatures are between 350 und 450 °C.

Starting from reference case 1, several design variants were investigated subsequently with the objective to reduce the temperature differences in the specimens. In principle, the following measures seem possible: Arrangement of a thermal isolator between the specimen and the support, additional electrical heating or reduction of the cooling of the transition region between specimen and support (Fig. 7).

Finally, a design variant was investigated with modified cooling conditions in the region of the specimen support. A small guide tube is attached to the helium supply tube in such a way that a gap with stagnant helium is generated reducing the cooling in this region (see bottom of Fig. 7). The analytical results for this design variant - with and without nuclear power - have been included in Table 1 (Cases 7 and 8). The comparison with Cases 1 and 2 shows a reduction of the maximum temperature and simultaneously an improvement of the temperature constancy. E.g. the constancy criterion $L_{5\%}$ in Case 7 amounts to 52 % compared to 46 % for the reference design (Case 1).
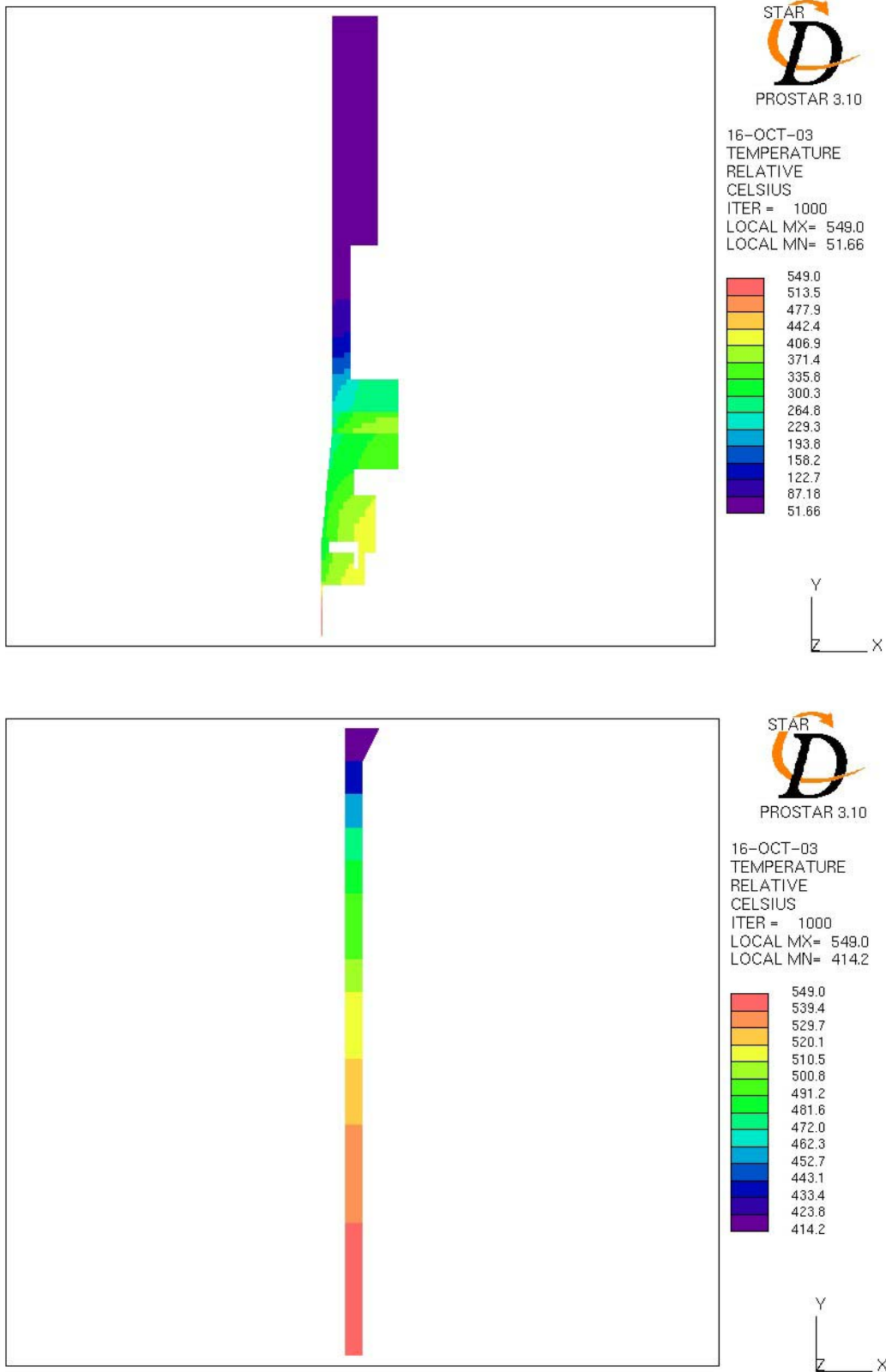
Fig. 6: Temperature distribution in the creep-fatigue test assembly calculated with STAR-CD, Case 1 (reference concept, with nuclear power); Top: entire model; bottom: specimen only.
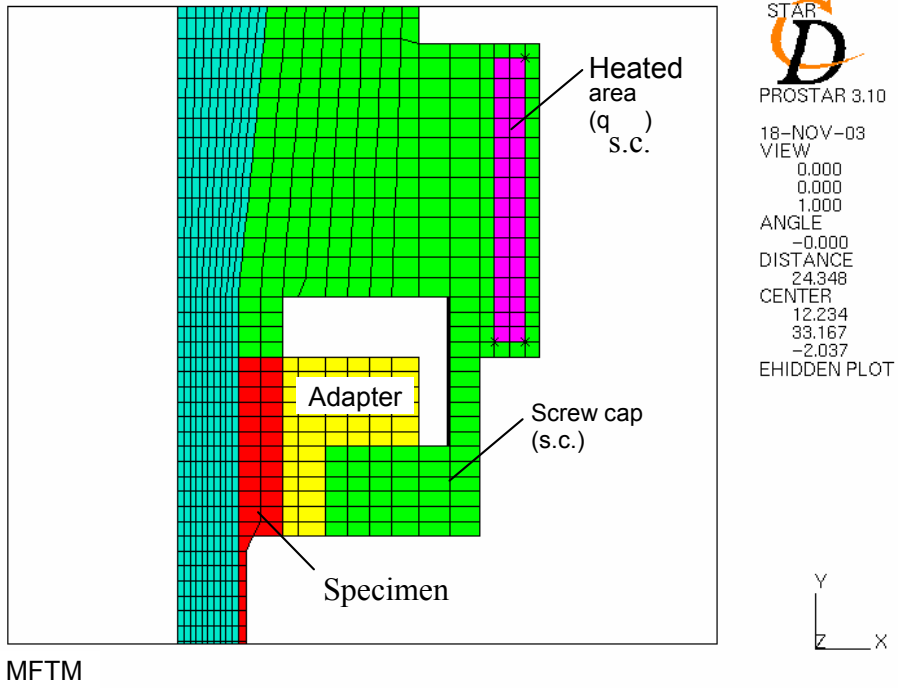
Fig. 7: Design variants with additional electrical heating in the screw cap (top) and in the specimen thread (bottom), and with helium guide tube (bottom)

The most important conclusions drawn from the investigations described above can be summarized as follows:

1. The proposed heating and cooling concept allows the adjustment and control of the envisaged irradiation temperatures of the specimens without major problems.

2. However, significant temperature differences will occur along the axis of the specimens. E.g. in the case of the reference design, the fraction of the specimen length with a temperature variation of less than 5 % (referred to the coolant inlet temperature) amounts to only 46 % (with nuclear power) and 38 % (without nuclear power), respectively.

3. The reduction of the local heat transfer by inserting a guide tube in the area of the specimen support increases in the case with nuclear power the length fraction with almost constant temperature from 46 to 52 %.

4. A further significant improvement of the temperature distribution could be reached by an additional electrical heating of the threaded ends of the specimens. However, such a concept is technically hardly feasible.

5. The other design variants investigated were found to be less suitable.

6. Whether the temperature differences occurring in the specimens can be tolerated must be clarified by the material specialists with regard of the objectives of the tests.

7. The direct electrical heating to establish and control the specimen temperature requires high electrical currents. The space needed for cables and power connections may be significant and must be determined in the further design work.

3. Specimen temperature control with helium jet cooling

The cooling concept described above limited the temperature tolerance to the $L_{5\%}$.length. Therefore, a further solution was suggested. This so called jet-cooling concept (Fig. 3) makes it possible to keep the temperature difference along the specimen length at ~ 5% of the maximum values in the range from 250 up to 650°C. For the detailed investigation of the jet-cooling a number of turbulence models offered by the commercial CFD code STAR-CD was tested on the basis of the comparison with experimental data presented in the literature. In the first case numerical predictions were compared with measured data of the single jet impingement heat transfer. In the second case turbulence models were tested on the jet array heat transfer distributions.

The following turbulence models offered by the commercial CFD code STAR-CD were employed:

*   Low Reynolds Number (LRN) linear k-ε turbulence model (Lien et. al.) with empirical damping function in the
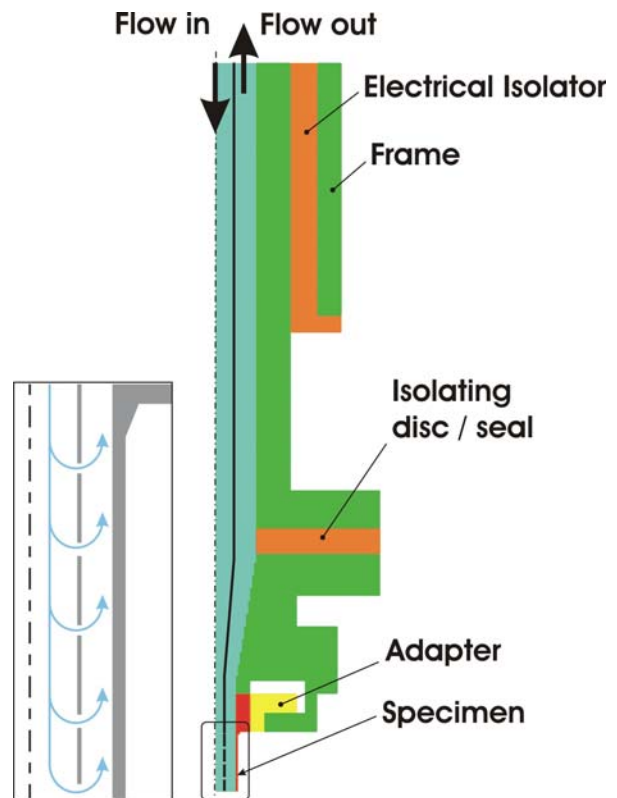
Fig. 8: Jet-array-cooling concept.

turbulent viscosity equation to account for the near wall behavior. The additional terms in the dissipation equation yield a correct level of the turbulence kinetic energy and its dissipation near the wall.

- LRN cubic k-ε turbulence model (Suga et. al.). In addition to the LRN extension this model uses a non-linear relation between the turbulent stress and the local strain rate and vorticity tensors. To reduce the departure of the turbulence length scale from the local equilibrium length scale the ε-equation of the LRN k-ε model of Suga is modified with the "Yap correction".

- High Re Number (HRN) and Two Layer (TL) RNG k-ε turbulence models. The RNG k-ε model includes in the transport equation for the dissipation rate an additional term based on the Renormalization Group Theory (RNG) which was found to increase the dissipation in high strain regions such as the stagnation zone.

- HRN and LRN k-ω turbulence models where instead of the ε-equation an equation for the turbulent frequency ω is used. This model has the Low Re formulation, which does not require additional wall damping terms and very fine grid resolution of the near wall layer.

- k-ω based Shear Stress Transport (SST) turbulence model (Menter). This model combines the k-ε and k-ω turbulence models with the help of a blending function that activates the k-ω model in the near wall region and the k-ε model for the rest of the flow.

- Elliptique relaxation V^2F (Durbin) turbulence model. The V^2F model avoids explicit Low Re number terms in the e-equation by using an elliptic relaxation equation near the wall. In addition, the V^2F model introduces a new velocity variance scale $\bar{v}^2$ (instead of k), for the evaluation of the turbulent viscosity. In general $\bar{v}^2$ should be regarded as a scale for velocity component responsible for turbulent transport. It is proportional to k far from solid walls, while in the near-wall region, it becomes the velocity fluctuation normal to the solid surface, irrespective of the orientation of the surface. Theoretically, k is unable to represent the damping of turbulent transport close to the wall whereas normal velocity fluctuations provide the right scaling. Finally, a mathematical constraint has been added to prevent non-realizability of the eddy viscosity especially in the stagnation region.

For the first test case experimental data on axisymmetric turbulent air jet impinging on a heated flat plate was used. Fig. 9 shows the impingement test plate. For the validation purpose the jet Reynolds numbers 5000, 10000 and 15000 and jet-to-plate distances of $L / D_j = 2$ and 4 were chosen. Air was treated as an ideal gas. The inflow conditions for velocity and turbulence parameters were specified using profiles for the fully turbulent flow through a pipe, which were calculated in separate simulations. The heated surface was modeled as a wall at a constant heat flux. For models with the Low Reynolds Number (LRN) treatment of the near wall region a structured axisymmetric grid consisting of 150x150 points has been used. The mean values of y^+ of the first grid point away from the impinging surface are less than 0.5. For High Reynolds Number (HRN) models the computation was performed on the 120x120 mesh with y+ on the wall not less then 10.5.
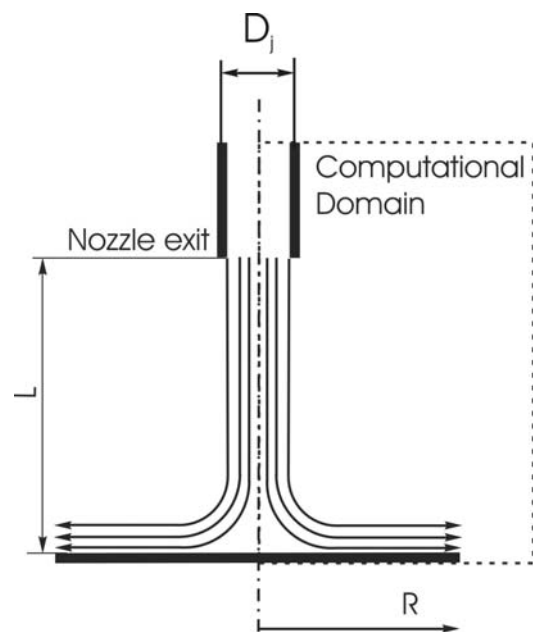
Fig. 9: Layout of the impingement plate
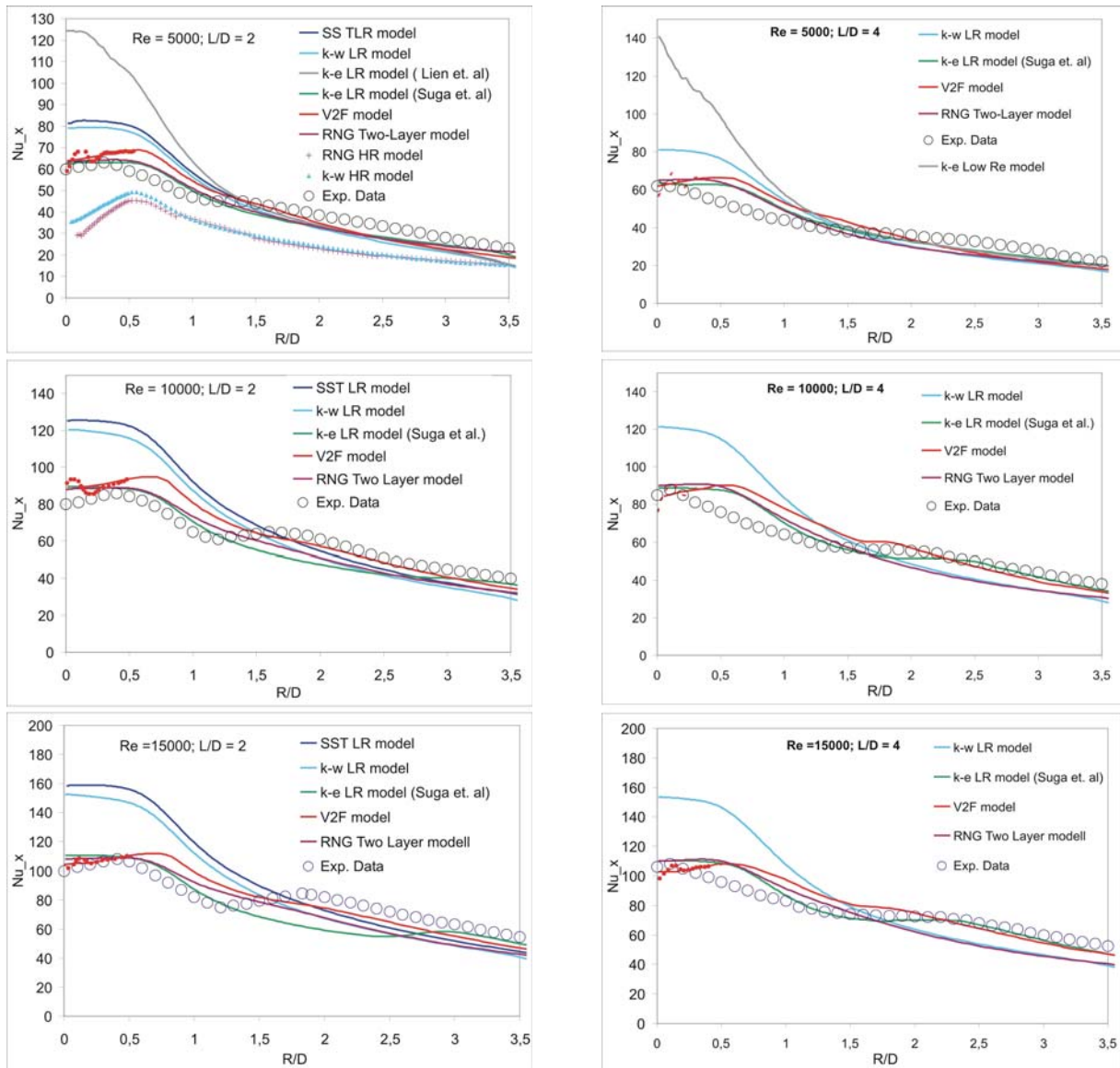
Fig. 10: Variations of the Local Nusselt numbers.

To evaluate the accuracy of the turbulence models the local Nusselt number distribution on the impingement surface Nu(x)

Nu(x) = h(x)D_j / k

was analysed, where k = k(T) is the air heat conductivity and h(x) the local heat transfer coefficient:

h(x) = q(x) / (T_{wall} − T_{jet})

Fig. 5 compares the predicted Nusselt number distribution.

For the next test case the experimental data of detailed heat transfer distribution under an array of orthogonal impinging jets were used. The test section consists of two compartments (a pressure chamber and an impingement channel) joined by an orifice plate, which has an array of jet holes. There are 4 rows of 12 holes on the orifice plate. The inlet and outlet are on the same side of the test section (X/D_j = 0). The fluid used is air. The experiments are performed for averaged jet Reynolds numbers Re = 4850, 9550 and 18300. As example for the results the local and span averaged Nusselt number distribution for Re = 9550 is shown in Fig. 6.
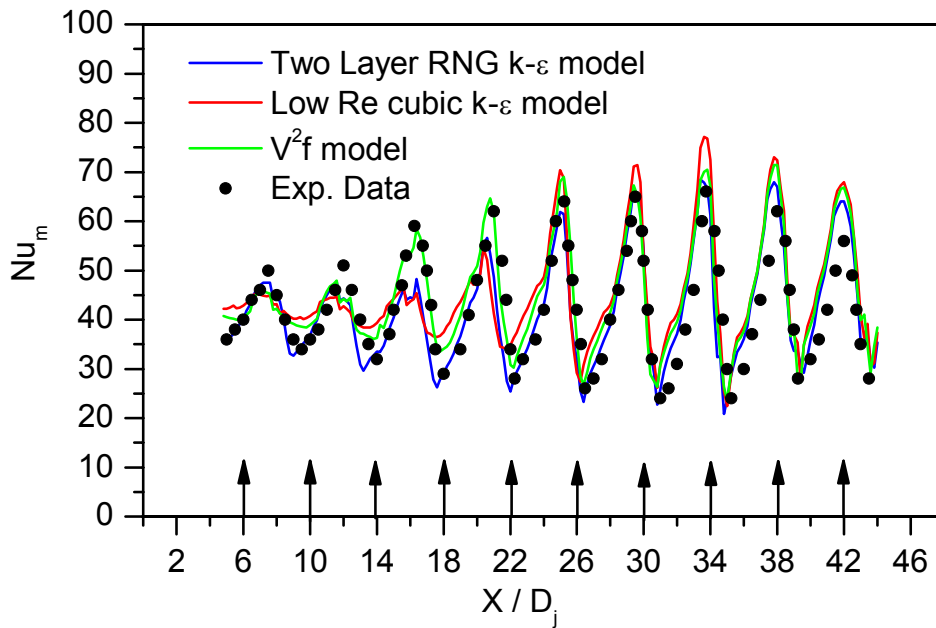
Fig. 11: Local (a) and span averaged (b) Nusselt number distribution, Re = 9550

The most important conclusions drawn from the investigations addressed above can be summarized as follows:

1. The new jet-array-cooling concept for the MFTM specimens was investigated.

2. Because of the complexity of the jet flow a number of turbulence models offered by the Star-CD code were tested on the experiments presented in the literature. The comparison of the calculation results with the experimental data shows that only turbulence models with additional limiters for turbulence production in the stagnation zone are able to predict correctly the jet impingement heat transfer.

3. Thermo-hydraulic analyses showed that the proposed jet-array-cooling concept allows the adjustment and control of the envisaged irradiation temperatures of the specimens without major problems. With the temperature variation of less than 5% over almost 80-85% of specimen length it is a significant improvement in comparison to the previous cooling concepts.

4. Further detailed thermo-hydraulic analyses will be performed for the new design work of the MFTM sub-module.

5. For the better understanding of the He-jet-array-cooling under such conditions as a strong surfaces heating, He-impinging on curved (cylindrical and spherical) surfaces and for further validation of turbulence models new experiments are required.

Staff:

S. Gordeev
V. Heinzel
K.-H. Lang
A. Möslang
P. Vladimirov
K. Schleisiek
V. Slobodtchouk

Literature:

[1] S. Gordeev, V. Heinzel, K. Schleisiek: Thermal-hydraulic investigation of the creep-fatigue specimens in the IFMIF Medium Flux Test Module, FZKA 6982, Juni 2004

[2] H. Matsui, et. al.: Present Status and Prospects for the IFMIF Project, 23rd Symp. On Fusion Technology, Sept. 20 – 24, 2004, Venedig, invited

[3] V. Heinzel, et. al.: The IFMIF Test Cell – Design and Neutronic Overview, 20th IAEA Fusion Energy Conference, 1-6 Nov. 2004, Vilamoura, Portugal

TW4-TTMI-003 D4
Development of a Reference Test Matrix

Introduction

Although the "reduced cost IFMIF" has become the international reference design around the year 2000, the test matrix developed during the CDA phase (1995-96) has never been adapted from the "original CDA-Design" towards the "revised cost IFMIF". In addition, (1) the requirements from the international fusion road maps and its considerations of a "fast track" towards fusion power are not included in the original test matrix, and (2) with the end of the IFMIF CDA phase December 2003, preliminary designs for advanced high and medium flux test modules have been suggested. With respect to the high flux test modules, the improved "vertical rig concept" has become the reference concept after in-depth discussions during a Test Cell Workshop hold from June 7-9 2004 at FZK. This improved high flux rig concept increases not only the overall IFMIF performance but has also substantial implications to the test matrix based on "small specimen test technology" (SSTT). With respect to the various in situ experiments foreseen in the medium flux test modules, additional improvements have been made mainly in the neutronics field (see separate progress report); these neutronics improvements are highly relevant to provide DEMO relevant irradiation conditions but have less impact to the test matrix.

The improvements are a substantial progress to meet the IFMIF Mission: The primary mission of IFMIF will be to generate a materials database for the design, construction, licensing and safe operation of a DEMO. This will be achieved through testing and verifying materials performance under neutron irradiation that simulates fusion reactor service up to the full lifetime of anticipated service in DEMO. Medium fluence irradiation tests of high heat flux materials for divertors, ceramic materials for a variety of uses, and functional tests of small blanket elements, (complementing the tests of blanket test modules in ITER), are also considered important uses of such a facility. In support of these missions, IFMIF will also provide calibration and validation of data from fission reactor and accelerator-based irradiation tests. Beyond DEMO, the development of high performance commercial power reactors, viable in terms of economy, safety and environmental acceptability, may require the development of advanced materials. IFMIF will provide the necessary irradiation field for testing these materials. That is, among performance criteria, any test matrix must be as flexible as possible by maximizing the available rig space and irradiation time.

Based on the improved high flux rig design, a completely revised material test matrix has been developed which will be summarized in the following. This test matrix meets specifically key requirements of the present international fusion strategy [1] with its global milestones for operation around 2014, IFMIF operation early 2017, and DEMO reactor construction in the middle of the following decade.

Specimen arrangements in the revised high flux test module design

The helium-cooled concept is basically a vessel with a number of irradiation rigs (Figure 1) containing the encapsulated specimens at the desired irradiation temperature. Although in the present reference concept the helium-cooled high flux test module is designed for the irradiation of reduced activation ferritic-martensitic (RAFM) steels with specimen temperatures between 250 and 650°C, the design allows selection of specimen irradiation temperatures in the window 250 to about 1100°C. Temperature uniformity is ±1.7% T_{irr} for almost all rigs. Each rig can be adapted in a straight forward manner for any other specimen material. Specimen temperatures above 1100°C are possible but at the expense of packing density. An advantage of the basic concept is that the rig temperature is in general much lower than the specimen temperature. The rigs inside the vessel are positioned vertically and can be individually loaded or unloaded after the test module is disconnected from the VTA1.

The actual reference availability of 70% for IFMIF leads to a damage level in RAFM steels of about 20-50 dpa/fpy in the high flux region.
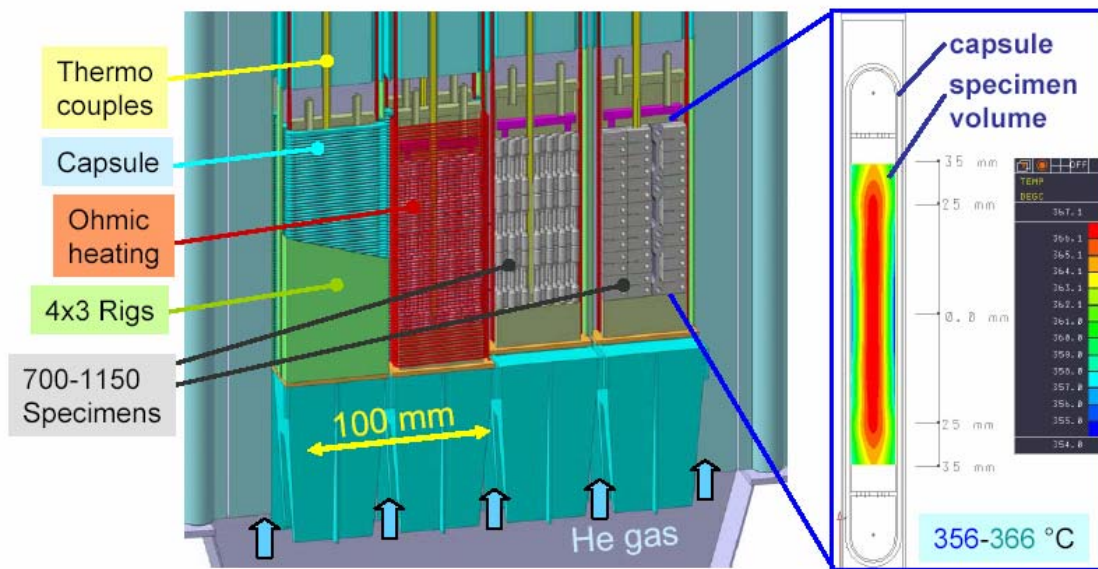
Fig. 1: Design configuration of the improved high flux test module with neutron reflector, helium inlet and 12 fully instrumented rigs with specimen capsules. The additional ohmic heating guarantees

Nuclear calculations showed that the dpa/fpy can be increased by a few percent but, more importantly, the dpa gradients are reduced when a reflector surrounds the container. The reflector effect tends to reach an asymptotic value at a thickness of 100mm. Accordingly, the container is equipped with lateral reflectors made of a reduced activation steel such as EUROFER with 90% effective density. The remaining 10% provides space for cooling. Extensions above and below the rigs (with a 60% share of the cross section) act as axial reflector elements. Corresponding to the foot print of the deuteron beams, the HFTM dimensions are (i) in the beam direction (z-axis): 50 mm, (ii) perpendicular to the beam: 200 mm in horizontal direction (x-axis) and (iii) in the vertical direction (y-axis) the nuclear calculations show a significant neutron flux or displacement rate outside of the footprint. This allows the enlargement of the irradiation volume, to achieve a volume of 0.5 litre with a displacement rate greater than 20 dpa/fpy. In order to accommodate three layers of test specimens, each of length 27 mm, the final height of the specimen stack is fixed at 81 mm.

The rigs in Fig. 1 consist of the outer housing or rig wall separated from the inner capsule containing the specimens by a thermal insulating gap with a thickness of 1.35 mm at the large sides and 1 mm at the small sides. That is, the irradiation rigs are the carriers of the capsules that in turn contain the specimens, similar to rigs used in fission irradiation technology. This allows a rather dense arrangement of most of the envisaged test specimens. Fig. 2 shows in a horizontal cross section a variety of specimen packing arrangements and demonstrates the flexibility allowed by the dimensions chosen for this design. Electrical heaters are wrapped around the capsule in horizontal windings. This concept will lead to temperatures of the capsule close to the irradiation temperature of the specimens, while the rig wall is at about the level of the helium temperature. The length of the rig without the upper reflector is 144 mm. The capsules have a length of 125 mm and are closed by two cup-shaped caps giving the test zones a length of 81.5 mm. With the cup shape the weld seams for closing the capsules are moved away from the intense neutron field. The 81.5 mm includes 0.5 mm for the accommodation of thermal expansion differences. The capsules of the first row (>40dpa/fpy) are filled with a liquid metal (Na or, if

possible, Na/K) to increase the thermal contact between the specimens and the capsule wall and to make this heat transfer predictable.
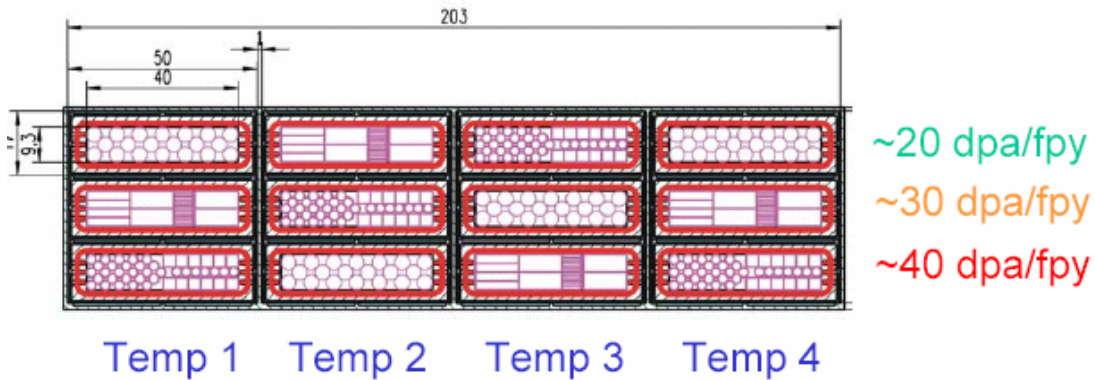
Fig. 2: Cross section of the HFTM container with segmented cross sections of the rigs; dimensions are given in mm.
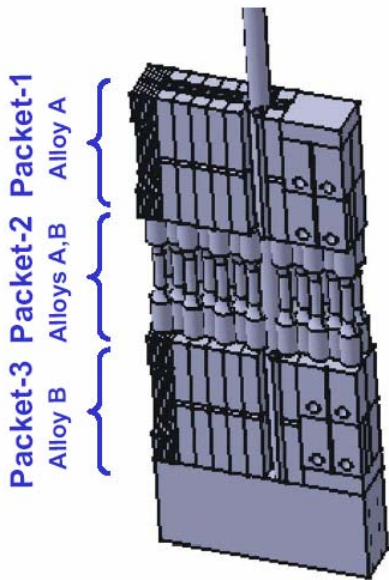
Fig. 3: Specimen package arrangement inside a capsule; for each temperature, 2 complete sets of materials or heats can be assembled

Work during the reporting period led to substantially improved irradiation performance in the high-flux test modules, based on advanced data libraries and neutron transport calculations. With respect to the design outline, the improvements include (i) irradiation volume increase ~20%, (ii) the typical number of simultaneously irradiated specimens for mechanical testing increased from ~700 to ~1150, an increase of more than one third, (iii) less sensitivity to varying heat transfer coefficients, swelling and creep, and (iv) higher flexibility and simplified loading sequences of the specimen matrices. A substantial advantage is in addition that within each individual capsule two complete alloys (alloy A and B in Fig. 3) can be assembled, allowing a high test matrix flexibility and a direct comparison of different materials or alloy compositions. That is, as each capsule represents one specific temperature, 2x12 = 24 different alloys (or heats) can be irradiated at the same time. Thereby, each rig is representing one individual temperature. The underlying multiplicities and specimen volumes for the individual specimen types are shown in Table 1. Of course, the package arrangements of individual capsules also reflect the multiplicity needed to establish a materials data base. Dimensions were determined according to standard packing arrangements used for fission neutron irradiation capsules.

Table 1: Material test specimens in a typical reference high flux test module

Specimen type	Multiplicity	Volume per specimen (cm^3)	Total No of specimens in HFTM*
Microstructure/swelling	≥ 5	0.0014	≥ 120
Tensile	6	0.075	144
Fatigue	9-10	0.249	216-240
Fracture toughness	3	0.560	72
Crack growth	2	0.280	48
Dynamic fracture toughness	12	0.291	288
Creep	8	0.133	192

Table 2: Present set of miniaturized specimens based on "Small specimen test technology"; the length of tensile, fatigue and Charpy specimens is 27 mm each.

Specimen type	Previous geometry	Proposed future geometry	Comments
Tensile			Developed
Fatigue			Developed; minor miniaturization still possible
Bend/ Charpy DFT			Developed; quasi-standard achieved
Creep			Developed
Crack growth			International R&D ongoing
Fracture toughness			International R&D ongoing

Table 2 shows the present set of the internationally achieved miniaturized specimens. It has to be emphasized that not only the specimens but also the related test technology must be developed and qualified. Up to now, the tensile, the fatigue, the Charpy and the creep tube can be considered to be practically completely qualified; these four types of specimens have been already used in the past in major fission irradiation experiments (up to about 70 dpa in mixed spectrum and fast breeder environments) and do not need further miniaturization. With respect to the tensile, fatigue and creep tube samples, the related results reflect material intrinsic properties, independent of specimen size. While for the crack growth and fracture toughness samples the R&D is ongoing, as the results depend intrinsically on specimen size and shape. Nevertheless, the bulk of the present fracture toughness samples are in the range of various millimeters and therefore typical to the thickness of many blanket structures.

The revised test matrix for the high flux test module is compatible with the international fusion strategy scenario as follows:

1 x 125 mA operation - 3 years (2017-2019)	- data base for alloys A, B, C (10,15,20 dpa) few space for screening of other materials
2 x 125 mA operation - 4 years (2020-2023) - 4 years (2024-2027) - 2028 and beyond	- data base for alloys A, B, C (40, 60, 80 dpa) - data base for alloys A, B (110, 150 dpa) space for various materials ($\leq$30dpa/fpy) - Other materials D, E, F,…….

Staff:

G. Bürkle
M. Klimiankou
A. Möslang

Literature:

[1] A. Möslang in IFMIF Comprehensive Design Report, Chapter 2 "Mission, Users' and Operational Requirements" and Chapter 3.1 "Test Facilities"; Eds.: The International Team, Printed FZK January 2004.

[2] V. Heinzel, P. Bem, E. Esposito, S. Gordeev, U. Fischer, A. Möslang, S. Simakov and P. Vladimirov, „*Overview on the IFMIF test cell development*", J. Nucl. Mater 329-333 (2004) 223-227

[3] V. Heinzel, A. Möslang, P. Vladimirov, „*Prospective testing program for IFMIF*", 23rd Symposium on Fusion technology (SOFT23), Venezia, September 20-24, 2004; submitted to Fusion Engineering and Design

TW4-TTMI-003 D 7
HFTM Component Manufacturing, Up-grading of the Helium Loop

a) –d) Manufacturing Tests for HFTM Container, Rig and Capsule

1. Introduction

The new reference design of the High-Flux-Test-Module (HFTM) for the International Fusion Material Irradiation Facility (IFMIF) is described in [1]. It has 12 flat plate rigs housed in 4 compartments of the container (Fig. 1). The container also integrates the lateral reflector. The two IFMIF deuteron beams creating the neutron source for the material irradiation have a foot print of 200 mm in horizontal, y-direction, and 50 mm in the vertical, x-direction. It produces a fast neutron beam penetrating the HFTM in z-direction. With increasing z it expands also in the other directions. A lateral reflector reduces neutron losses in y-direction. Axial reflectors are as extensions of the rigs or as lower rig support installed.

The miniaturized material specimens are inserted in capsules. Sodium or a sodium/potassium eutectic alloy fills up the space within the capsules between the specimens. The liquid metal guarantees a defined heat transfer from specimen to specimen and between specimen and capsule wall. Electric heaters are wound around the capsules. The rig walls surround the capsules whereby a gap between the rig and capsule walls filled with stagnant helium acts as thermal insulation. The rig walls wear on the outer side vertical webs. They serve as spacers forming channels between the rigs as well as between the rigs and the container wall. Through the channels flows helium upward and removes the power released from nuclear reactions and the electric heaters. The electric heaters balance the nuclear power distribution. They keep the temperature in the specimen's volume within narrow tolerances and also keep it constant during short beam off periods. The upward flowing helium is heated up and the heat transfer coefficient develops along the channels. The electric heaters have to cope with. Thermocouples in the specimens stack provide temperature signals for electric power control.

Partitioning walls strut the thin walled container and subdivide it in four compartments. Spacer webs in two corners of each compartment complete the spacers on the rig outside. The integration of the webs in the container and rig wall avoids the

Fig. 1: Cross section of the HFTM with 12 flat plate rigs within 4 compartments of the container integrating the lateral reflector.

sum up of tolerances.

The design rule derived from irradiation data for steel - no weld seam in the region of high neutron flux – is applied to the container, rig and capsule walls. It was suggested to use

stainless steel 316LN as starting material for container and rig [2]. Both will see operational temperatures < 200 °C. RAFM can be envisaged when irradiation results at low temperatures and high dpa (displacement per atom) values are available. For the capsule this decision is not compulsory.

The valuable space of the HFTM leads to the design principle – maximum space for the specimen. Consequently the helium cooling and manufacturing of the non welded and thin walled structures require sophisticated solutions. This understanding during early design stages initiated to investigate key manufacturing technologies. The CFD code and the turbulence models applied for the thermo-hydraulic lay-out are also used beyond the standard application. Appropriate validation experiments for heat transfer and pressure loss measurements are mandatory. They require test sections with the development of proper manufacturing techniques. Though the design changed during the design work in the past, the key manufacturing test and also the manufacturing of test sections for the experimental work contribute exploitable results. Costly made components are used for tests even if they do not correspond with the most recent design but allow investigating a subsequent manufacturing or qualification test.

2. Container

The rig length of 140 mm plus the two axial reflectors led to the extension of the container from 300 mm to 400 mm. The avoidance of weld seams in the region of the foot print required the fabrication from a massive forged piece. The same reason led to the integration of the lateral reflector. The processing starts with a slug having an oversize of 10 mm on each side over the outer dimension of the flange 100 x 640 mm and total length.

The length is substantiated with the rig length of 140 mm, the flange height of 10 mm and adapter pieces to 300 mm. The installation of the axial reflectors with 2x100 mm increases the dimension to 340 mm at minimum. The available electrospark machine has a maximum opening for the erosion wire of 400 mm. This is the length of the container shown in Fig. 2a. The intersection with the back plate requires an extension to 550 mm (Fig. 2b). A European market analysis indicated that no commercial electrospark machine with such a wire span length is available. Only a special model was offered. However the reliable usability for the HFTM container use would have required a dedicated development. On the other hand the design of the Medium-Flux-Test-Module (MFTM) revealed a further spatial intersection. As consequence the HFTM container with inlet and exit section are redesigned (Fig. 2c). The container has again the length of 400 mm. The upper extension is inserted with an inner stiffening flange and is welded with the container wall. Therewith, the outer dimension of the HFTM is preserved. For dismantling of the HFTM the weld seam has to be cut off.

The machining of the container is tested for one compartment for the length of 275 mm. The manufacturing was done with the following steps:

- Pre-cutting from a slug to the diameter D = 100 mm and length of L = 290 mm

- Milling the inside with a working allowance of 5 mm and the outer side of 10 mm

- Annealing stress-free 2 hours at 650 °C and cooled down in the furnace

- Milling the inner side with a working allowance of -0.5 mm and the outer side with a working allowance of +0.5mm

- Annealing 1 h at 650 °C

- Fine milling

- Rough spark erosion of the inside to a roughness of $R_{a(averaged)}$ = 2.8 μm and $R_{T,(maximum\ over\ the\ working\ distance)}$ = 22.4 μm

- Fine spark erosion to a wall thickness of 1mm with an erosion wire of 0.5 mm; The corner radius resulted in 0.25 mm; spacers are formed in two corners; roughness measured $R_{Z,\text{(averaged over 5 positions)}}$ = 16 μm;
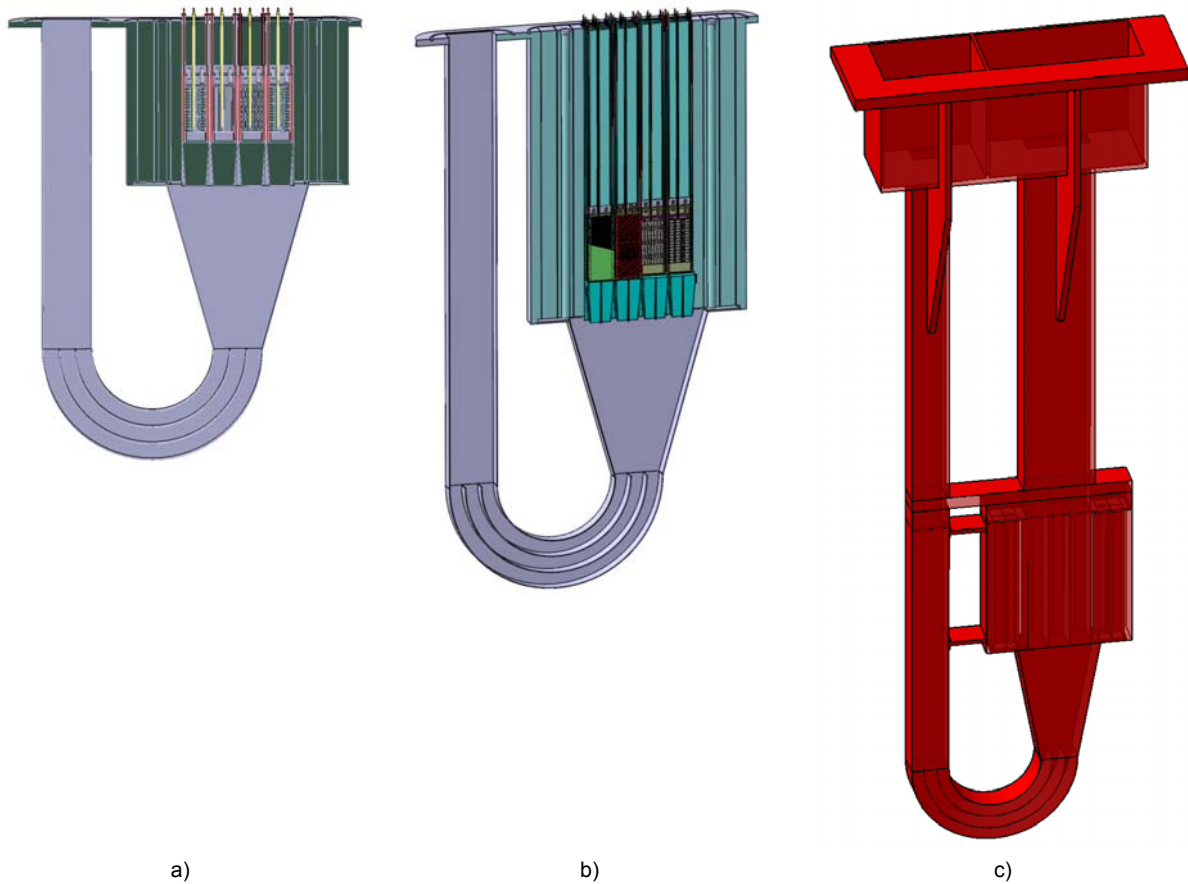
Fig. 2: Longitudinal section through the container with inlet and exit plenum; a) container with (340 mm) 400 mm, b) 550 mm height and flange, c) 400 mm and an inner flange strutting the container wall from inside

According to the machine supplier a final roughness should be achievable with R_a = 1.8 μm and R_T = 14 μm. The diameter of the erosion wire could be reduced to 0.3 mm. As the machine's opening for the erosion wire is 400 mm, this machine is suitable for the new container.

The welding procedure of the thin walled container to the inside flange still has to be tested.

3. Rig

Two rig casings were produced according to the detailed drawing in Fig. 3. They were manufactured with the same step as the container but the outer side was spark eroded. It allows the formation of the spacer webs.
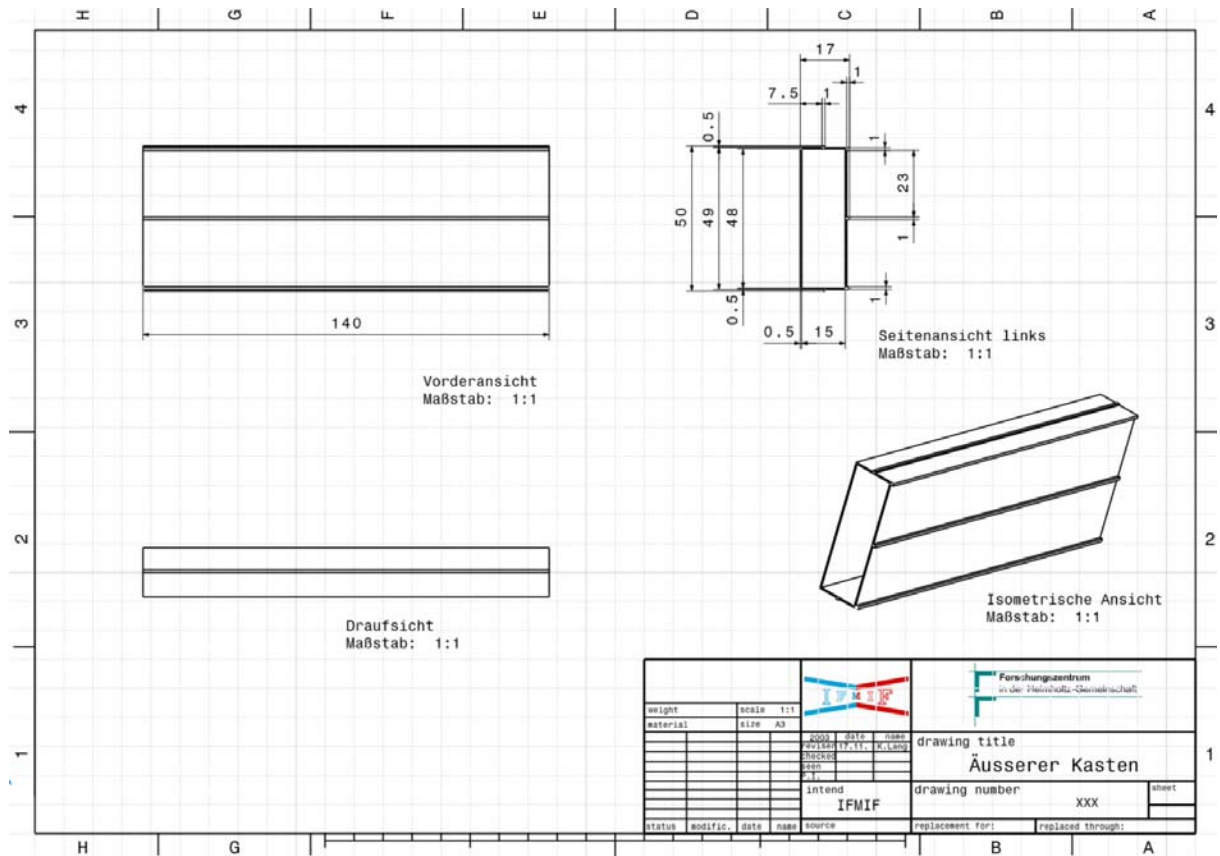
Fig. 3: Detailed drawing of the rig casing.

4. Capsule

The capsule is shown in Fig. 5 with the specimens, the electric heater system, thermocouples and plug caps. The upper plug cap wears the thermocouple sheath tube, the tubes for the sodium fill-up and the hold down disc. They are welded together and form the upper plug unit. The inner width of 9.3 mm of the capsule was chosen according heat transfer analyses and specimens arrangement studies. At the place next to the target with the highest nuclear heat release the stack width has to be below 10 mm in order to keep the temperature difference necessary for conducting the power to the capsule wall within acceptable tolerances [1]. The cross section with $9.3 \times 40 \times 82$ mm^3 is the out-come for a high number of specimen arrangements as can be seen from Fig. 1.

The specimens stack is assembled in a guide box (Fig. 4). With the upper plug unit the specimens are pushed into the capsule housing. The capsule (new design) is equipped with the heaters and the lower cap before. With the upper cap in position the capsule is closed by welding. Afterwards sodium is filled in.

The three electric heaters are sub-divided and arranged according to the thermo-hydraulic analyses [1]. The jacket heaters are of the type:

Themocoax: I-Nc-Ac with the outer diameter D_a = 1mm

R = 12.5 Ω/m

U_{max} = 100 V

Minimal bent radius $r_{B, min}$ = 2xD_a
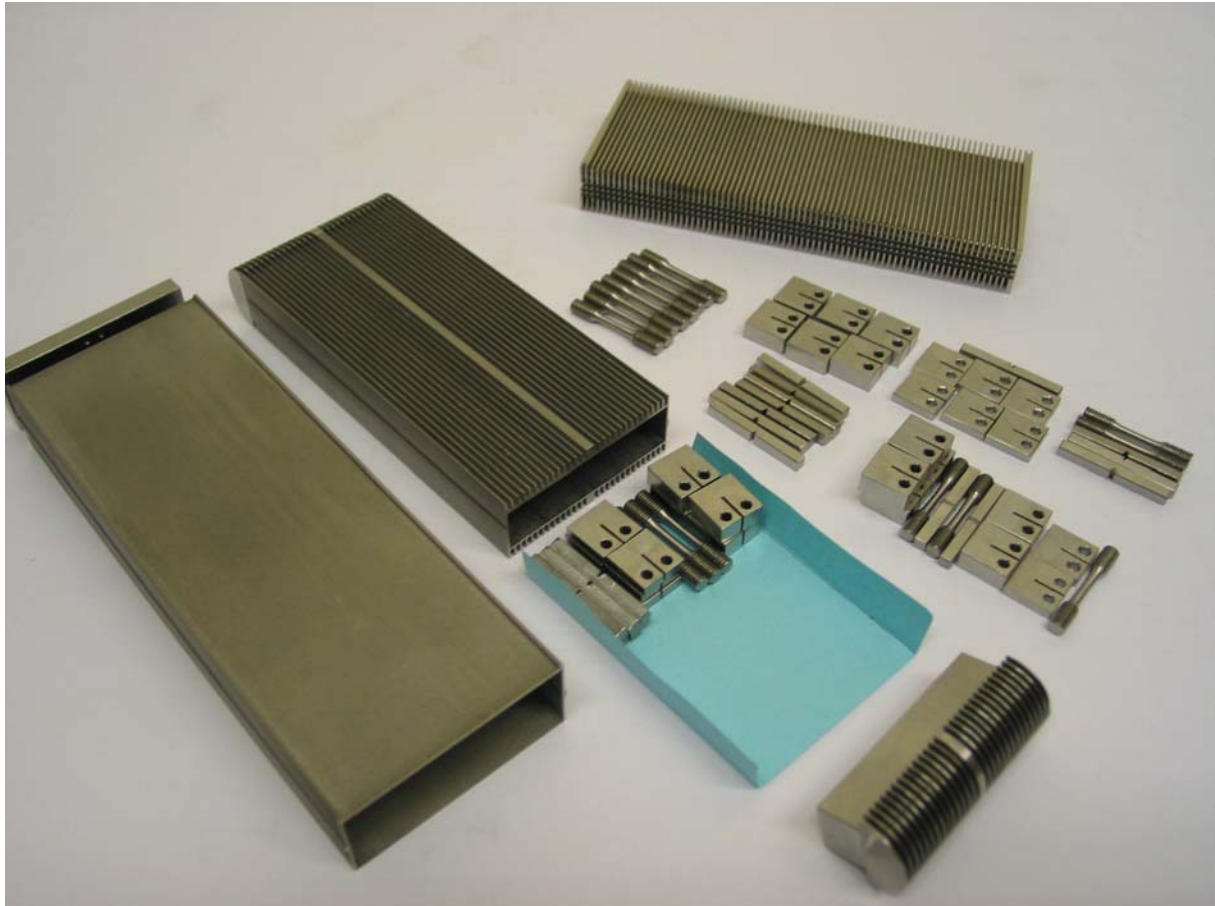
Fig. 4: Rig (left), capsule (former design), set of specimen for handling, carved work piece (right) with grooves (new design).

The heaters are led in grooves along the smaller side of the capsule Fig. 6. After a 90° bend they are pressed into grooves, which rise spirally on the capsule surface. At the upper end the heaters are bent back into a grove in the smaller side. The next heater is wound over the rising ends of the heater below. The pitch of the heater coil is 1.6 mm. The heaters are brazed into the groves for getting a reliable heat transfer. The webs between the heaters are milled afterwards so that pins are left. The pins support the rig wall. Size and numbers of pins together with the gas gap make up the heat transfer between capsule and rig walls. For high temperature rigs the pin pattern is adapted to the temperature range. With low temperature rigs it is envisaged to braze the capsule into the rig.

The capsules are inserted into the rigs. The fixed point for the capsule is the support at the bottom inside the rig casing. The upper end of the capsule can expand freely at the upper end. After the installation of the capsule the upper axial reflector is welded to the rig wall. Connections for heaters and thermocouples are guided in bore holes through the upper reflector. Sliding fits provide transportation protection. A passage through the upper reflector connects the gap between rig and capsule walls with the upper end of the helium channels outside the rig. This pressure is lower than the pressure on the outside of the rig at the level of the capsule. It creates a pressure difference with which the rig wall is pressed on the capsule webs for a reliable heat transfer. The lower reflector is welded to the container. It guides the helium to the channels between the rigs and supports the rigs. The rigs are hold down against the lift force due to the helium pressure difference by spacers below the upper inner flange. They are flexible and allow thermal expansions.
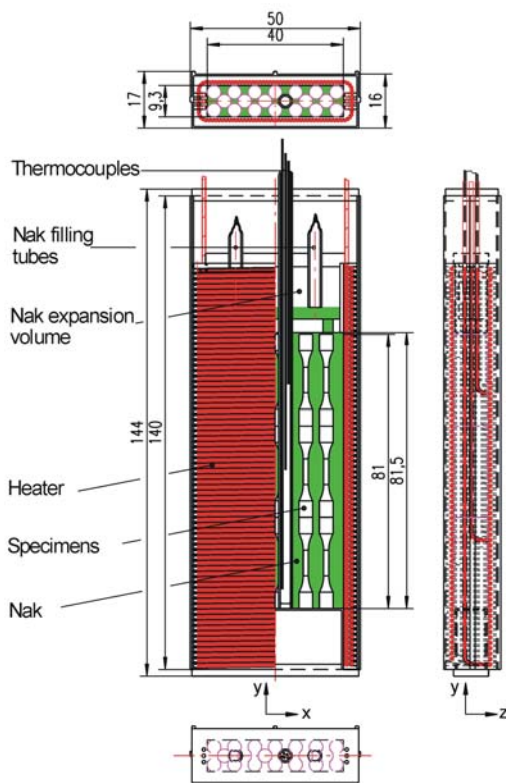
Fig. 5: Capsule with specimens, triple heater system and thermocouples.
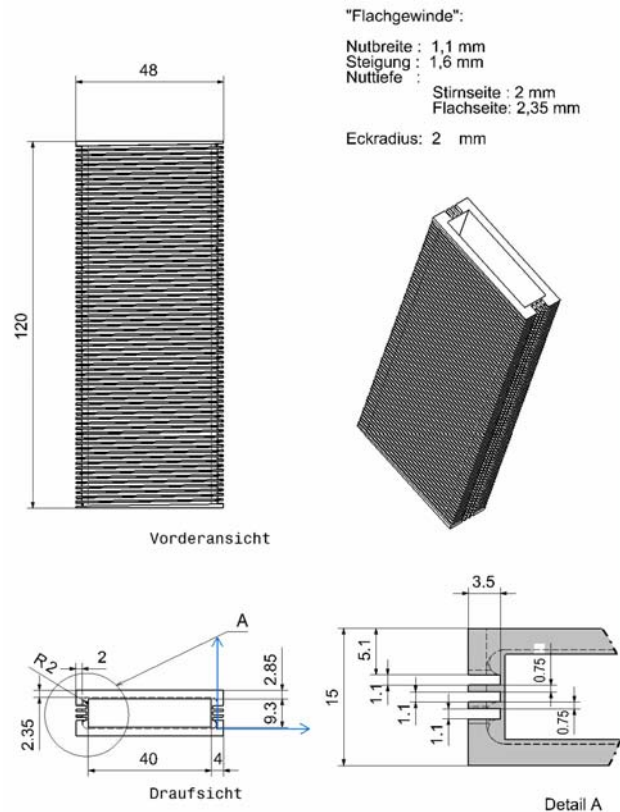
Fig. 6: Detailed drawing of the capsule.

The manufacturing of the capsule starts with the coarse and fine milling of the outside of the capsule casing from a massive slug. The technique is the same as for the container described above. It follows the milling or eroding of the grooves. The heaters get the first two bents and are wound around the capsule casing. Brazing attaches them on the capsule. Subsequently the webs are milled. Afterwards the inside is spark eroded. The lower plug is then welded at the lower end of the casing.

- Crucial manufacturing techniques for the capsule are the
- milling or eroding of the grooves for the heaters,
- bending, inserting and squeezing the heaters into the grooves
- brazing the heaters
- welding of the end cabs

4.1 Milling/spark erosion of grooves

With the former capsule design the grooves run parallel on the capsule surface). One end cap reroutes the heater to the next groove. The end caps are made from separated round rods. After the erosion of the grooves they are cut off and the structure for the connection to the capsule casing is carved off. The production showed that the erosion of the grooves is feasible. However the automatic control of the machine is 2D.

The new capsule design requires a 3D machine control. The grooves are engraved with a finger-end-mill-cutter. The results corresponds well the requirement. However the net

machine time was 100h for one piece. This is not acceptable for making test pieces for the further manufacturing steps.

4.2 Embedding the heater into the grooves

Fig. 7: Double heater helix on the inner wall fort he ITHEX annular test section.

The embedding of the two parallel heaters into the grooves of the annulus walls required a special clamping device. The transition from the cold end to the heated section had to be positioned at the designated position.

For brazing tests pieces from stainless steel 15x48x23 mm^3 are made with groove milled with the finger end cutter. A heater is pressed into the groove. It withstood the bending with radii of 2 mm. The piece is inserted in a box open at the upper side. The box serves as funnel and forms the gap for the braze seam.

4.3 Brazing

Nicrobraze 897-850-C2, a nickel base alloy, was chosen as filler material. The nickel base alloys are used as high temperature filler material as some physical properties in particular in this case the heat conduction coefficient are similar to stainless steel. The material 825 has a processing temperature of 980 °C. It is brazed under vacuum or inert gas. The material is delivered as paste with a binder. The binder evaporates before melting. The paste has to be stored at the gap, into which it flows after melting due to capillary forces.

The nickel base alloys contain boron, silicon or phosphorous for melting point reduction. For nuclear application boron free material is used. The application of nickel base filler materials has to cope with some drawbacks. They react very fast with the substrate material. The intensity depends on the substrate, brazing temperature, arrest time and the amount of filler material. The amount of filler material should be kept as small as possible. The light atom constituents tend to form brittle phases. The braze seam should be narrow. The brittle phases can be removed by diffusion annealing.
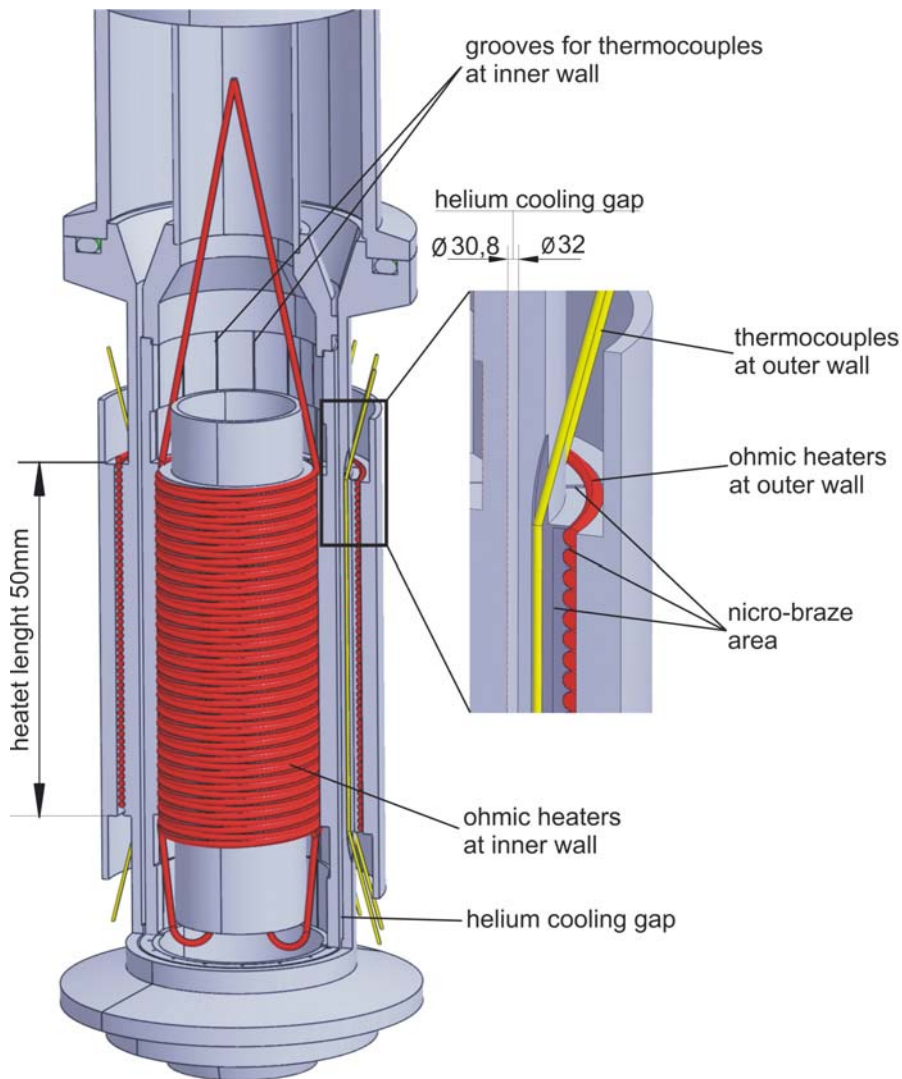
Fig. 8:   ITHEX annular test section.

Data for the filler material are (http://www.brazetec.de/brazetec/content/main.cfm):

BrazeTec (company name) 897-850-C2
Ni braze NI 107 according to DIN EN 1044 (L-Ni7 according to DIN 8513)
Composition in weight-%: Cr 14.0 %, P 10.1 %, rest nickel
Addition elements: Si 0.10, B 0.01, Fe 0.2, C 0.06
Max. impurities: Al 0.05, Co 0.10, S 0.02, Se 0.005, Ti 0.05, Zr 0.05

Melting range:	$\approx$ 890 °C (Din En 1044)
Brazing temperature	980 °C
Density of final material	7.9 g/cm^3
Density of paste	3.85 g/cm^3
Metal content	$\approx$ 85 weight-%

Experts in renowned laboratories were asked to braze the walls for the ITHEX test section. Though there existed some experiences in our laboratories with Nicrobraze joining, the 50 mm long narrow and complex gap (Fig. 8). was unusual.

The heat flux through a wall within a configuration like the ITHEX test section was simulated with PERMAS. The results showed, that interruptions of the braze material have to be less than 1 mm otherwise the failure is recognizable at the surface temperature distribution.
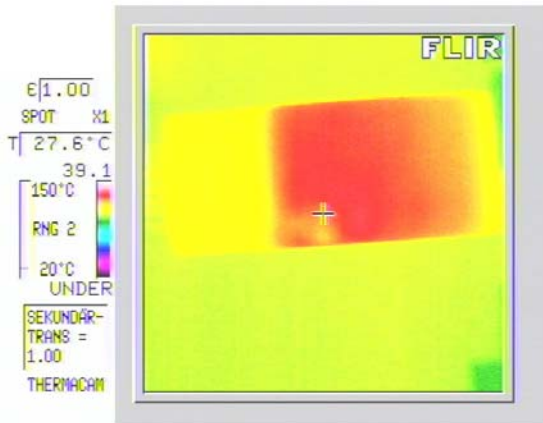
Fig. 9: Infrared picture of the ITHEX inner wall – only temperature deviations were detected.

Several failed tests caused a development in our laboratories. Fig. 9 shows a picture from an infrared camera of the inner ITHEX wall during heat up. Except a minor failure the braze joint provides a uniform heat transfer. The brazing procedure was done in a vacuum chamber with the following temperature ramps:

7 h   20 $\Rightarrow$ 600 °C

12 h   arrest temperature at 600 °C with gas release

5 h   600 °C $\Rightarrow$ 1000 °C with three shorted arrest point with gas release

24 h cooling down under vacuum

The whole procedure took 1 week.

The channel walls were heated up and the temperature measured with an infrared camera. The temperature distribution informs on the heat transfer or the completeness of the braze layer. As can be seen from Fig. 9, - for the best case - only minor temperature differences are visible.

Though the test were successful further development is necessary to transfer the procedure to the configuration of the HFTM capsules. Particularly brazing in smaller vacuum chambers or under inert gas is strived for.

A test piece with heater was brazed at 1000 °C (Fig. 10). The filler material was filled in the box into which the test piece was inserted. The atmosphere was a mixture of argon and hydrogen. The heater withstood the treatment. After cooling down the box was finally removed so that the braze seam is visible. The braze material followed the gap but gas pockets remained.

The braze tests have to be continued.
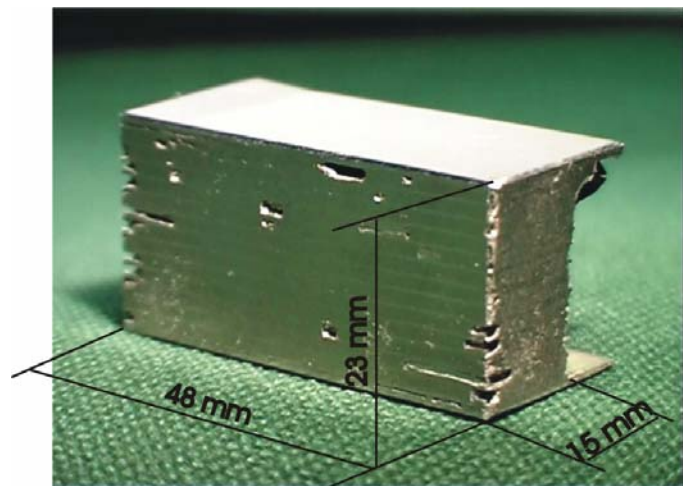
Fig. 10: Test piece with heater after brazing – the outer box was partially removed.

e) ITHEX Helium Loop

To control the temperature of the material specimen irradiated with neutrons in the IFMIF High Flux Test Module, a cooling helium flow is conducted on the outside surfaces of the rig containing the specimens; an additional segmented electrical heater is used to compensate the temperature gradient along the direction of flow. Since the volume of the HFTM is small, a primary design goal is to maximize the space used by specimens, and therefore reduce the space occupied by structural material (e.g. walls) and devices for temperature control such as heaters and temperature sensors. To keep the footprint small, the cooling channels gap width is reduced to 0.5mm on the narrow sides and 1.0mm on the wide sides of the rectangular rig cross section.

This design affects the conditions of the cooling helium flow:

- The entry pressure must be small in order to reduce the mechanical stress exerted by the gas on the thin walls of the rigs. The maximum entry pressure is 0.3MPa.

- The small cross section of the coolant ducts cause high helium velocities, when the massflow is chosen high enough in order to minimize the temperature rise in the gas. Mach numbers of 0.5 can be reached at the exit.

- Despite high velocities, the small hydraulic diameter of the coolant ducts leads to relatively low Reynolds numbers in the range Re < 10'000

- High velocities and the small hydraulic diameter cause a high pressure drop, which amounts to a considerable fraction of the entry pressure. This in addition to the temperature rise by heating reduces the density of the gas, thus accelerating the flow along the channel axis.

- The channels are short, so the flow is not in a fully developed state concerning the hydraulic and the thermal boundary layers on a relevant length. The shape of the entrance can be expected affect on the boundary layer.

This set of conditions characterizing the flow is poorly covered by experimental work. Recent studies of microchannel flow are concentrated on liquids, reporting contradictory results [5], [6], [7]. Strongly heated gas flows were investigated by McEligot [8] in 27mm diameter cylindrical tubes and by Bankston [9] in 3mm diameter cylindrical tubes. These studies do not include the hydraulic and thermal entry and do not report on the effect of the pressure gradient, which must considered in the HFTM cooling gas flow. Also, the hydraulic diameters in the reported experiments exceed the numbers characteristic for the HFTM cooling channels. In [Kakac], the value of d_h=2mm is given as a lower limit of validity for the thermohydraulic correlations compiled in that source. The hydraulic diameter is proportional to the ratio of the channel cross section to the wetted perimeter. In the range relevant for the IFMIF/HFTM cooling channel design with 1mm < d_h < 2mm, influences of the wall, like the effect of roughness or damping of the wall-normal turbulent fluctuations might therefore gain in importance over mechanisms effective in the free flow.

The thermal hydraulic layout depends on valid models to determine pressure loss in the channels and heat transfer from the rigs. It is especially important to know the function of the heat transfer coefficient in the thermally developing section, as this defines the pattern of segmentation of the electrical heaters and the position of the temperature sensors in the specimen. To obtain data which is significant to allow validation of the tools used in the HFTM design process, experiments meeting the conditions of the HFTM cooling channels have been initiated. These investigations have been termed IFMIF Thermal Hydraulic Experiment ITHEX.

The experiments are conducted with several test sections which are installed in a coolant gas circulating loop. The test sections are designed to reproduce the conditions of the HFTM channels at a lower massflow rate than the complete rig. The testsection in use is the annular duct shown in Fig. 11.
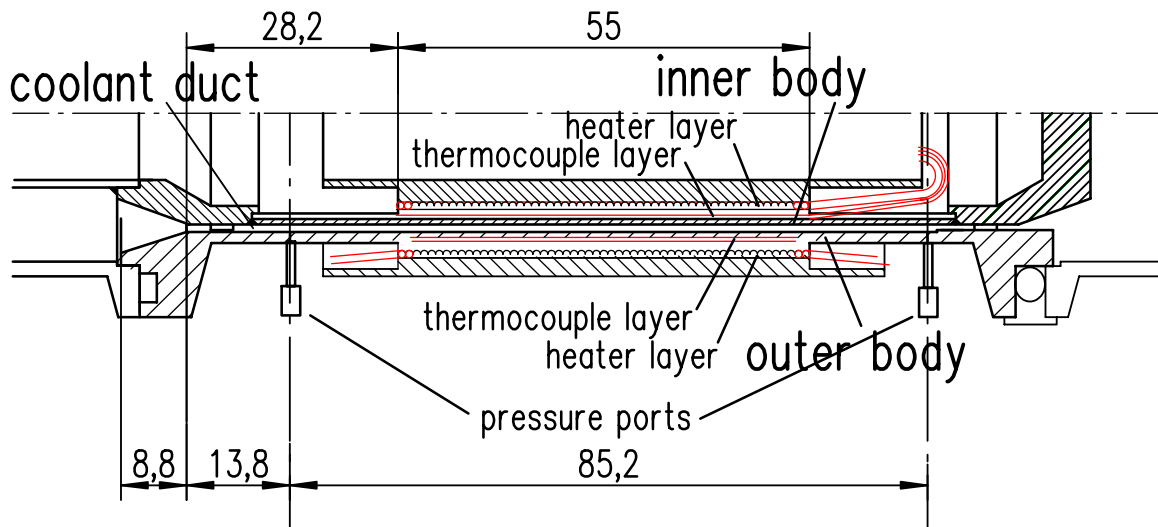
Fig. 11: ITHEX Annular testsection.

This test section allows the measurement of the temperature profile in the heated walls as well as the measurement of the pressure drop across the heated region. The hydraulic diameter of the annular duct is d_h=1.22mm.

The task of the coolant gas loop is to deliver the required massflow of coolant gas at the given conditions for pressure, temperature and gas composition at the test section entrance.

In a preliminary setup, the loop consisted of a frequency-invertor controlled 1.1kW double stage sidechannel compressor type Becker SV 5.190/2-50, a plate heat exchanger, the testsection, a coriolis massflow meter and a throttle valve. The loop could be evacuated with a diaphragm pump and then filled with helium from a pressure bottle. The pressure in the loop was kept close above the ambient level. Under these conditions, the compressor achieved a pressure rise of 400hPa for air and 240hPa for a helium-air mixture. This pressure rise could effect adiabatic flow in the testsection with Re < 2300 for helium and Re < 8000 for air.

The gas tightness of the compressor casing was improved by special sealing. Still, the gasket of the rotor shaft was tight only for pressure over the ambient level. Therefore, ambient air was drawn into the loop during the helium filling procedure. It was estimated that the resultant mixture contained approximately 10% of ambient air. Error estimation shows, that the uncertainty in the gas composition of 1% results in an uncertainty of the calculated friction factor of 10%. The reason for this influence is the difference between the properties of helium and air, especially M_{air}/M_{He}>7.

To construct a loop to deliver massflow rates to allow measurements with helium in the turbulent regime, and to ensure helium tight operation, a new compressor was installed.

The application in the ITHEX helium loop demands the following properties for the compressor unit:

- Helium tightness in vacuum as well as over-ambient pressure levels up to 0.42MPa
- Low pressure pulsations to ensure a continous massflow in the testsection.

- Possibility to control the massflow from verly low up to the maximum flow rate.

The design which is able to meet especially the demands of low pulsation and stable control is the sidechannel compressor. In comparison to a radial compressor, a higher pressure rise is effected per stage, and it features no instabilities as the "pumping" known from radial compressors. It is therefore possible to control the massflow by driving the motor using a frequency invertor. The selected model is a modified Becker SV 6.250/2 two stage compressor, which is designed to circulate CO2-laser gas and has therefore been designed completely gastight by encapsulation. The motor is water cooled. To effect a sufficient pressure rise, two compressors are arranged in a series linked by intercooling. This arrangement produces a pressure rise of 700hPa. The loop schematic can be seen from Fig. 12.
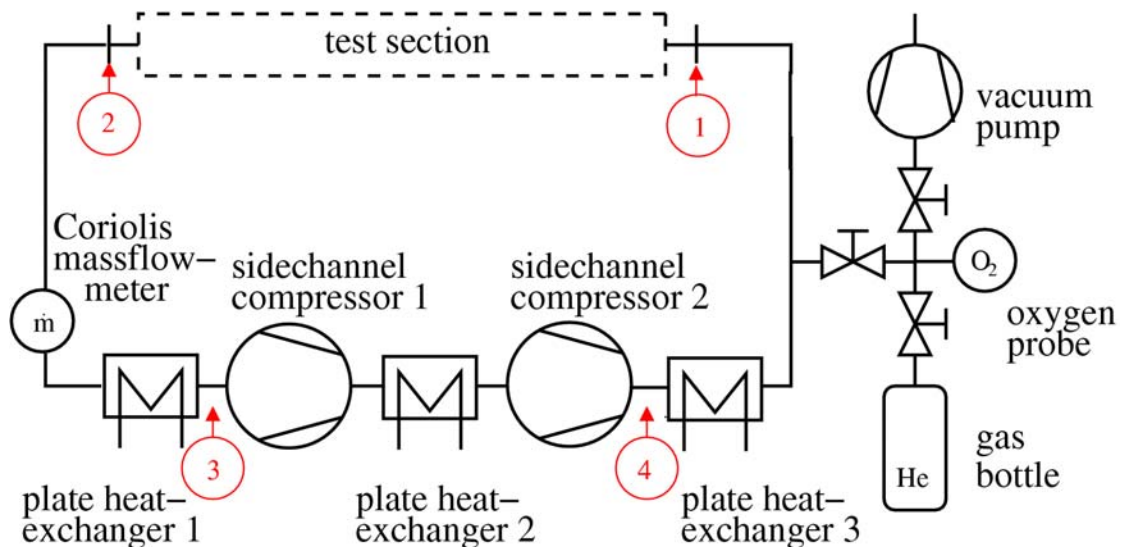
Fig. 12: ITHEX Loop with two sidechannel compressors

To reduce the uncertainty of the gas composition, a potentiometric ZrO_2 oxygen sensor has been installed. This type of sensor has the advantage that it can be installed in-situ (it was adapted for the use in up to 6bars) and does therefore not need a sampling system with pumps. The price marks the lower limit for all available oxygen probes. It also features a good accuracy also for small oxygen concentrations. To provide this good accuracy, the temperature of the probe has to be stabilized. Since the thermal conductivity of helium is much higher than for air, an additional heating jacket was fitted to the probe. The amount of ambient air in the cooling gas is calculated from the measured oxygen partial pressure.

The data acquisition is performed by a PC using a 16bit A/D converter card and a 64 channel multiplexer. The acquisition and logging is performed by a program written in the LabView environment. The data set comprises 36 thermocouple readings for the wall temperature profile, two Pt-100 sensors for the testsection entry and exit gas temperature, one absolute pressure and one differential pressure and the massflow determined directly with the coriolis massflow meter. Additional temperatures are measured at several positions on the loop.

The described setup of the loop has been used to measure adiabatic pressure drop factors as well as axial wall temperature profiles for differing wall heat fluxes. As coolant gases, air, nitrogen and helium have been used, the testsection entry pressure has been varied between 0.2 - 0.4MPa. The Reynolds numbers reached in the testsection range up to 14'000 with air or nitrogen, and 5'500 with helium.

The results shown in Fig. 13 for the friction factors indicate that an essentially laminar flow is sustained up to Reynolds numbers Re=6000. The turbulent level for wall friction is approached only for Re > 8000.
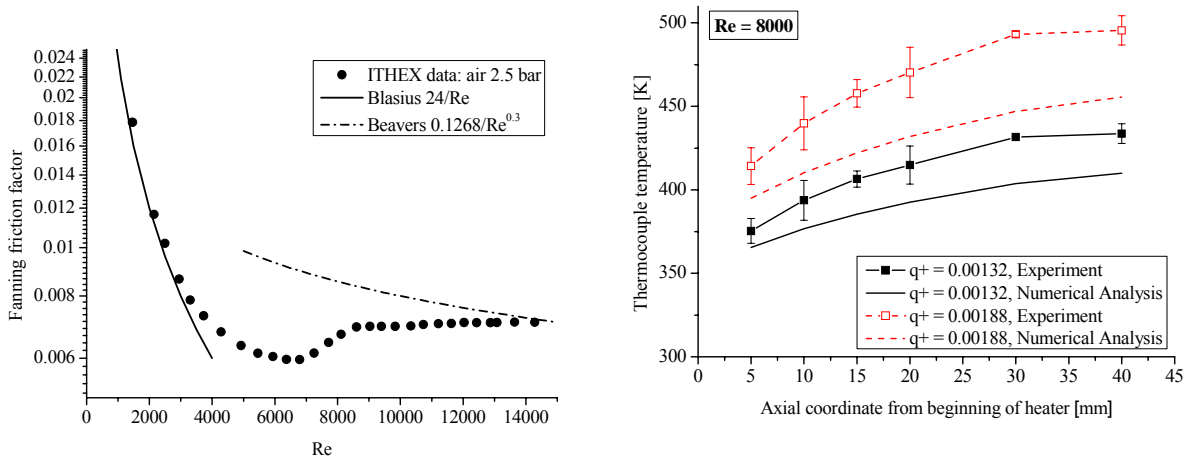
Fig. 13: Measured adiabatic friction factors and wall temperature profiles compared to results using recommended engineering correlations.

Since neither the bulk gas temperature nor the heat flux is measured in the minichannel, the local heat transfer coefficient can not be determined in a straight forward way. Instead, if a correlation or a model for the heat transfer is given beforehand, numerical methods can be employed to iteratively calculate coupled heat transfer and heat conduction in the solid walls. A solution is then obtained for the temperature field of the wall bodies, which can be compared to the measured temperatures in the wall. For this task, a dedicated code has been developed developed termed ITHEX Numerical Analysis (INA). This code treats the flow as a one-dimensional stream by applying given functions $f(x)$ and $Nu(x)$ to calculate pressure loss and heat transfer. The results shown in Fig.3 are obtained by applying the well known Gnielinski correlation, and accounting for the developing temperature boundary layer by a function given in [4]. It can be seen, that these recommended correlations overestimate the heat transfer, thus showing lower temperature levels. As it was observed with the adiabatic friction factor, also the heat transfer coefficient is found to be lower than for the fully turbulent flow. The case discussed is a flow of nitrogen at p_1=2.5bar, Re=8000. Two non-dimensional wall heat fluxes q^+=0.00132 and q+=0.00188 were investigated. These values of q^+ are smaller than the critical value of q^+=0.004 identified in the experiments by Bankston for flows of helium in tubes (d_h=3mm) as the low limit for reverse transition from turbulent to laminar flow. The reduced heat transfer observed indicates another source of laminarization, such as the acceleration by the pressure gradient, or the influence of the small hydraulic diameter.

Using the present configuration of the loop, further experiments are planned to be conducted using the annular testsection. The matrix of test conditions given in Tab. 1 allows to study the influence of acceleration by pressure loss, heating rate (q^+) and material properties, especially the Prandtl number.

Table 1: Matrix of measurement conditions for the ITHEX annular testsection.

		Re=1500	3000	4500	6000	7500	9000	10500	1200	q^+ Stufen
N2	2bar	X	X	X	X	X	X	X	X	4x
	3bar	X	X	X	X	X	X	X	X	4x
He	2bar	X	X	X						4x
	3bar	X	X	X						4x
Ne	2bar	X	X	X	X					4x

	3bar	X	X	X	X					*4x*
Ar	3bar		X	X	X		X		X	*1x*
CO2	3bar		X	X	X		X		X	*1x*

To study the effect of the hydraulic diameter, a flat duct testsection with adjustable gap width between 0.5 and 4mm will be used. This testsection is currently in production. Another flat testsection with optical acces is currently used in preliminary experiments to assess velocity profiles and turbulence parameters using Laser Doppler Velocimetry, which can be directly used to validate calculated flow fields with the software used in the layout of the IFMIF HFTM.

Staff:

O. Albrecht
F. Arbeiter
A. Brecht
B. Dolensky
U. Fischer
S. Gordeev
V. Heinzel
T. Kuhn
E. Kupper
K.H. Lang
I. Schwartz
S. Simakov
V. Slobodtchouk
E. Stratmans

Literature:

[1] S. Gordeev, et. al., Optimized Design and Thermal-Hydraulic Analysis of the IFMIF/HFTM Test Section, FZKA 6895, Okt. 2003

[2] A. Möslang, Presentation during the IFMIF User Meeting at Brasimone/Italy 1rst of Oct. 2004

[3] L. Dorn, et. al., Fügen und thermisches Trennen, Kontakt&Studium Band 121, S. 188

[4] S. Kakac, R.K. Shah, W. Aung, *"Handbook of Single-Phase Convective Heat Transfer"*, John Wiley & Sons, 1987.

[5] B. Agostini, B. Watel, A. Bontemps, B. Thonon, Liquid flow frictio factor and heat transfer coefficient in small channels: an experimental investigation, Experimental Thermal and Fluid Science Vol.28, 2003.

[6] S.M. Giaasiaan, T.S. Laker, *Turbulent forced convection in microtubes*, International Journal of Heat and Mass Transfer Vol 44, 2000.

[7] H.Y. Wu, Ping Cheng An experimental study of convective heat transfer in silicon microchannels with different surface conditions, International Journal of Heat and Mass Transfer Vol.46, 2003.

[8] A.M. Shehata, D.M. McEligot, *Mean structure in the viscous layer of strongly-heated internal gas flows. Measurements*, International Journal of Heat and Mass Transfer Vol.41 pp.4297-4313, 1998

[9] C.A. Bankston, *The Transition from Turbulent to Laminar Gas Flow in a Heated Pipe*, Journal of Heat Transfer Vol.92 pp.569-579, 1970.

TW4-TTMI-003 D9
Evaluation and Validation of D-Li Cross Sections

The objective of this sub-task was to improve the D-Li neutron source term calculation by updating the d+^{6,7}Li nuclear data evaluations and assessing the uncertainty of the neutron yields in IFMIF calculations with the McDeLicious Monte Carlo code [1, 2]. A first set of such cross-section data was evaluated previously in a collaboration between FZK and INPE Obninsk [3]. Updating of these evaluations was performed in the frame of TW4-TTMI-003, Deliverable 8 by IFIN-HH Bucharest mainly with regard to the deuteron elastic and inelastic scattering. Meanwhile new measurements of thin and thick lithium target yields by P. Bém et al. of NPI Řež (Czech Republic) at 16.3 and 17 MeV deuteron energy (TW3-TTMI-003, Deliverable 6 [4]) and by M. Baba et al. of the Tohoku University (Japan) [5] at 25 and 40 MeV deuteron energy became available. After processing of the updated evaluated d+^{6,7}Li reaction cross section data by the NJOY code, thick and thin lithium target neutron yields have been calculated using the McDeLicious code and compared with the available set of experimental data.

Experimental d-Li neutron yields for thick Lithium targets.

So far 11 independent experiments (Tab. 1) have been performed including the recent measurements by P. Bém et al. of NPI Řež (Czech Republic) at 16.3 and 17 MeV deuteron energy and M. Baba et al. of the Tohoku University (Japan) for 25 and 40 MeV deuteron energy. It is seen that these experimental data set cover the deuteron energy range from 5 to 40 MeV and thus are well suited for benchmarking the IFMIF d-Li source term.

Table 1: Parameters of the measurements of neutron angular (Q) and energy (above detector threshold E_{thr}) distributions from thick Li targets bombarded by deuterons (having the energy E_d).

No	First Author Year of Publ.	Laboratory, Country	Target	E_d, MeV	Θ, degrees	E_{thr}, MeV
1	V.K. Daruga 1968	Inst. of Physics & Power Eng., Russia	Li	22	0°	1.8
2	A.N. Weaver 1972	Livermore Laboratory, USA	Li	5, 9, 14, 16, 19	3.5°, 10°, 18°, 25°, 32°	2.5 1.6
3	A.N. Goland 1975	Naval Research Laboratory, USA	Li	13.4, 19, 25, 29, 34	0°, 5°, 10°, 15°, 20°	3
4	H.I. Amols 1976	Fermi National Laboratory, USA	Li	35	0°	5
5	C.E. Nelson 1977	Triangle University, USA	^{7}Li	8, 12, 15	0°, 10°, 20°, 30°, 45°	1
6	M.A. Lone 1977	Chalk River Laboratory, Canada	^{7}Li	14.8, 18, 23	0°, 10°, 20°, 30°, 40°	0.3
7	M.J. Saltmarsh 1977	Oak Ridge Laboratory, USA	Li	40	0°, 7°, 15°, 30°, 45°, 60°, 90°	2
8	D.L. Johnson 1979	University of California, USA	Li	35	0°, 4°, 8°, 12°, 20°, 30°, 45°, 70°, 105°, 150°	1
9	M. Sugimoto 1995	Japan Energy Research Institute, Japan	Li	32	0°,5°,10°,15°,20°,30°, 40°, 50°, 60°, 70°, 80°, 90°, 100°, 110°,120°, 130°, 140°, 150°	1
10	M. Baba 2003	Tohoku University, Japan	Li	25, 40	0°,5°,10°,15°,20°,25°,30°, 40°,45°,60°,90°, 110°	1
11	P. Bém 2003	Nuclear Physics Institute, Rez	Li	16.3, 17.0	0°	3

Validation of the d-Li source term against thick lithium target neutron yields.

The validation analyses comprised McDeLicious calculations with a detailed representation of the deuteron beam, target assembly, neutron detector and its surrounding. Comparisons have been also performed with calculation results obtained with the McDeLi and MCNPX codes using built-in analytical models for the Li(d,xn) reaction cross sections.

The analysis of the total and forward neutron yields from threshold up to 40 MeV deuteron energy (Fig. 1a, b) shows satisfactory agreement between McDeLicious calculations and experimental results. The McDeLi code, the pre-decessor of McDeLicious, shows worse agreement with the experimental neutron yields. The MCNPX code, on the other hand, underestimates the neutron yields by a factor 2 and thus fails to model this reaction with the required accuracy.
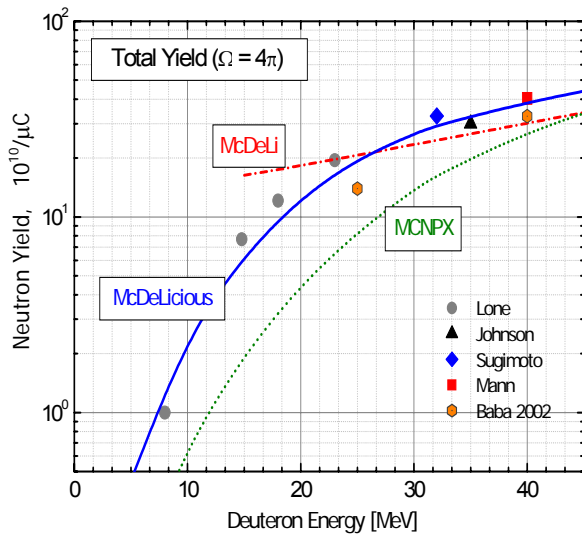
Fig. 1a: Thick Lithium target total neutron yield data   Fig. 1b: Thick Lithium target forward neutron yield data
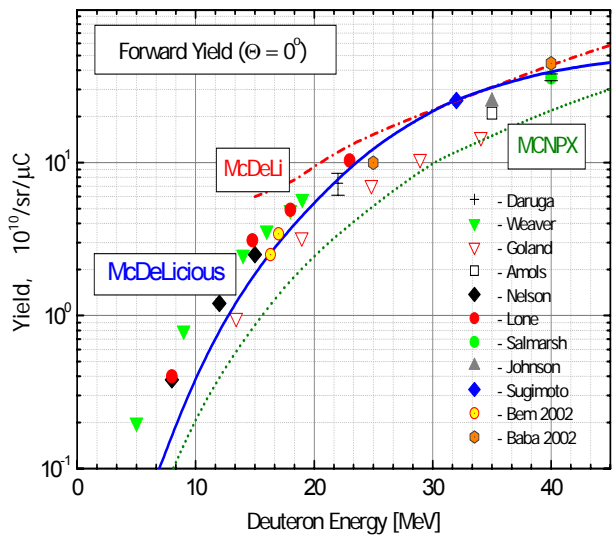
Neutron angular differential yields were measured at 15 to 40 MeV deuteron energy in several experiments, in most cases, however, only in the forward directed hemisphere (Table 1). The comparison of McDeLicious calculations with these data (Fig. 2) shows that the angular dependence can be satisfactorily predicted above 30 MeV deuteron energy. At lower energies the experimental data, in particular those of P. Bem et al., shows a higher angular forward directed anisotropy than McDeLicious does.

Testing of McDeLicious calculations against measured energy distributions (double differential thick target neutron yields) in general has shown good agreement with some inconsistencies in specific energy domains. As shown in Fig. 3, the new experimental data of M. Baba et al. at 25 and 40 MeV deuteron energies indicate that McDeLicious overestimates the production of neutrons with energies less than 5 MeV. This experiment as well as the measurements of P. Bem et al. point out that the spectral distribution of high energy neutrons resulting from the ^{7}Li(d,n) reaction needs further improvement. It is worthwhile to note that there is an inconsistency in the experimental energy differential thick target yields measured by different authors: the experimental results of Mann and Baba at 40 MeV essentially disagree in the high neutron energy domain.
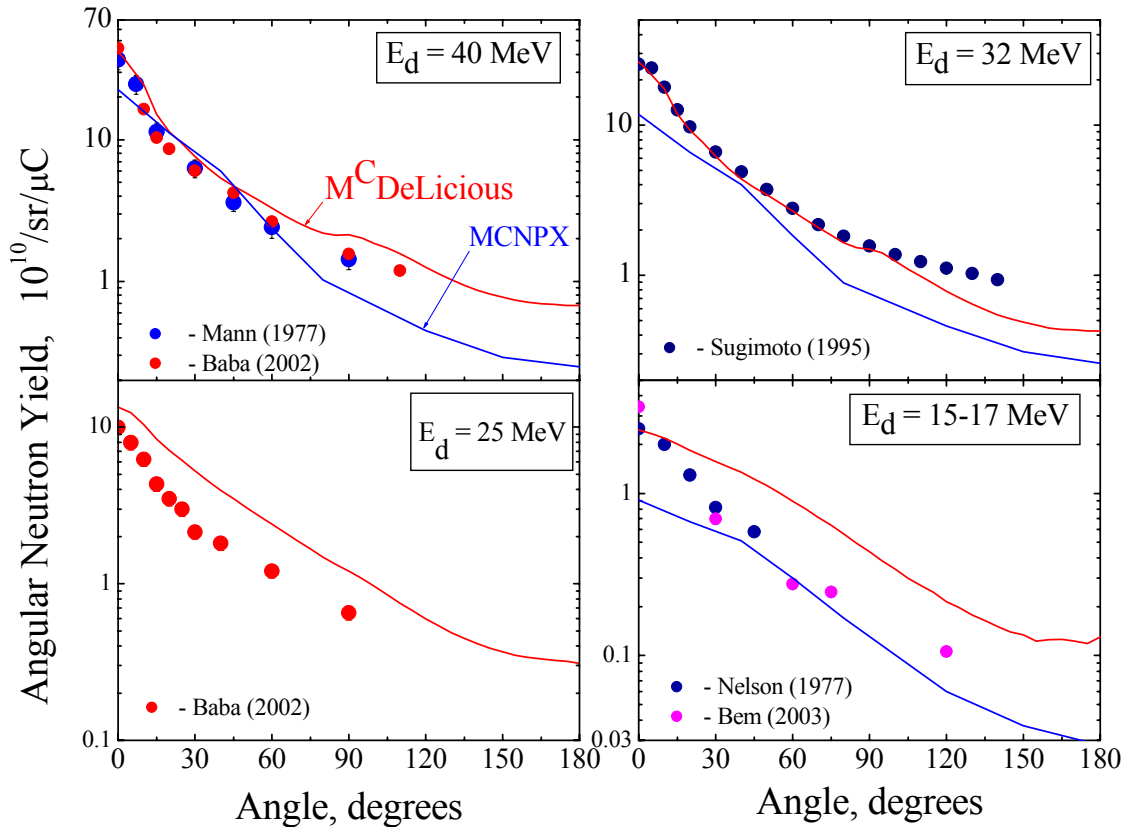
Fig. 2.   Angular neutron yields from thick Lithium target versus incident deuteron energy. Symbols – experimental data; solid curves – calculations with McDeLicious (red) and MCNPX (blue).

Testing of d-Li neutron data against thin Lithium target neutron yields.

The first measurements of neutron spectra from thin Lithium target become available only recently. They have been carried out at the Tohoku University at E_d = 40 MeV (M. Baba et al., private communication) and the Nuclear Physics Institute Řež at E_d = 17 MeV (P. Bem et al. TW0-TTMI-003, D13 [4]). Since the thickness of the Li target is relatively small (≈ 1 MeV) these data can interpreted as double-differential cross -sections (DDX) for the Li(d,xn) reaction. The excitation cross-sections for several states in the residual ^{8}Be nucleus have been previously measured by Azimov et al. [6] These data, folded with the spectrometer energy resolution function, are shown in Fig. 4 as solid curves.

The comparison shown in Fig. 4 indicates that the evaluated data underestimate the deuteron break-up peak in the measured Li(d,xn) cross-section at 40 MeV. The structure of the high energy tail of the emission spectrum, reflecting the excitation of the ground-, first- and higher states of the ^{8}Be* nucleus, cannot be reproduced either. For a better representation of the d-Li neutron source term with the McDeLicious code it is thus required to further improve the differential cross-sections of the ^{6,7}Li (d,xn)- reactions.
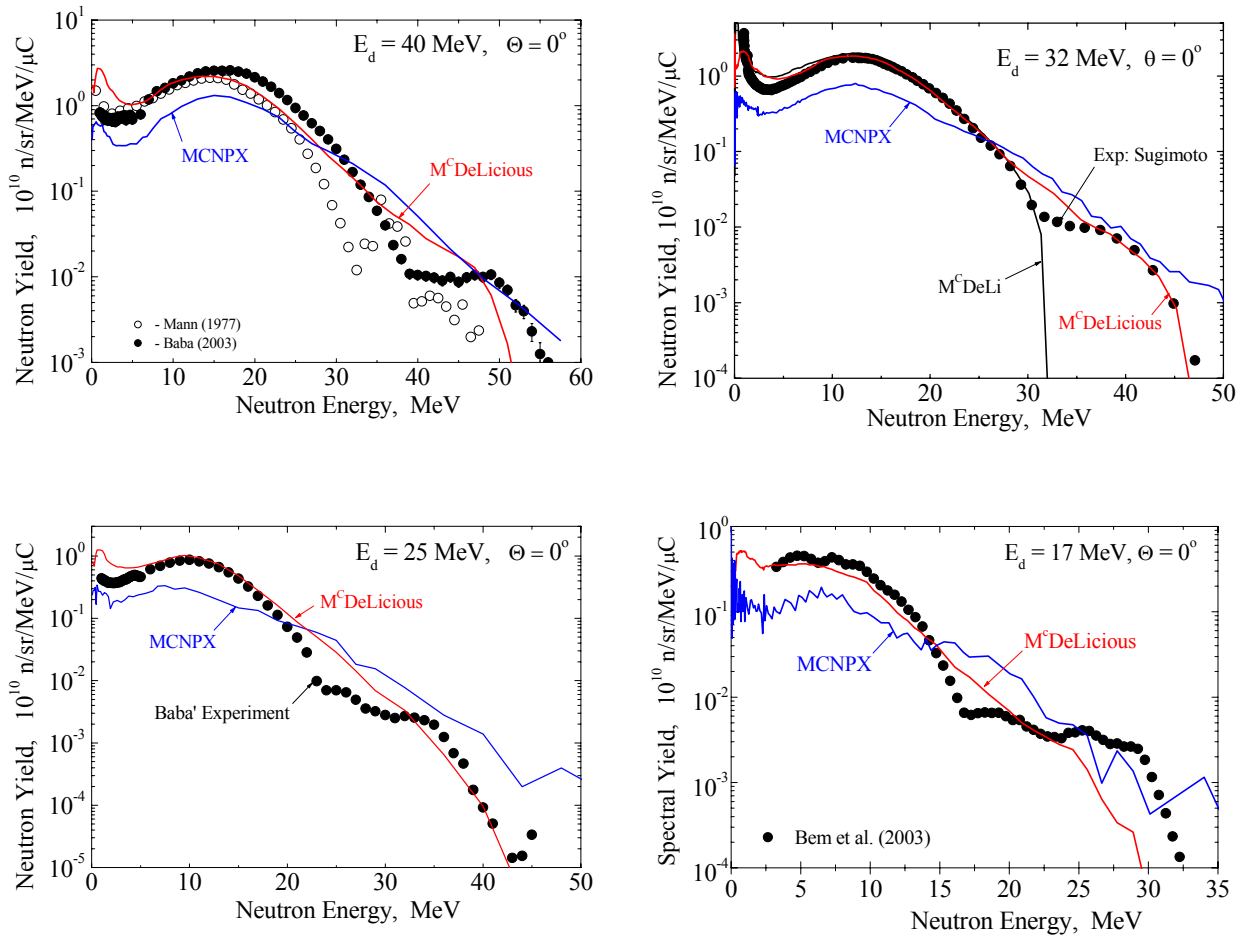
Fig. 3: Energy differential neutron yields from thick Lithium target versus neutron energy. Symbols – experimental data; solid curves – calculations with McDeLicious (red), McDeLi (black) and MCNPX (blue) codes.
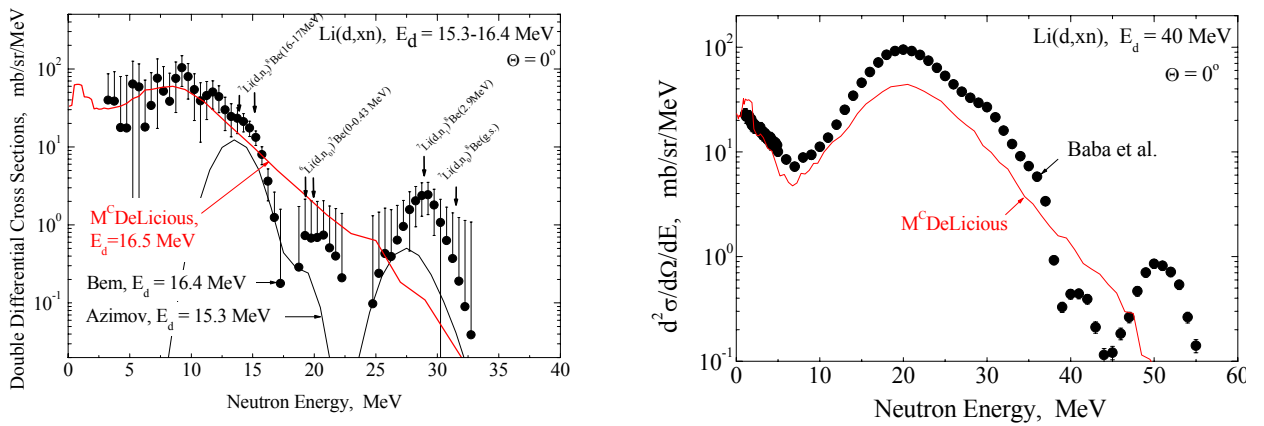
Fig. 4: Measured zero-degree double-differential cross-sections for the Li(d,xn) reaction at 15 MeV (Azimov et al., [6]), 17 MeV (Bem et. al., [4]) and 40 MeV (M. Baba et al) compared to McDeLicious calculations using d-Li evaluated data (red curve).

Staff:

U. Fischer
S.P. Simakov
P. Pereslavtev

Literature:

[1] U. Fischer, S. Simakov, U. v. Möllendorff, P. Pereslavtsev, P. Bem, A. Konobeev, P. Wilson: Validated Computational Tools and Data for IFMIF Neutronic Calculations, Proc. 6th Int. Meeting on Nuclear Applications of Accelerator Technology (AccApp'03), June 1-5, 2003, San Diego, 1000-1008.

[2] S.P. Simakov, U. Fischer, U. von Möllendorff, I. Schmuck, A.Yu. Konobeev, Yu. A. Korovin, P. Pereslavtsev, Advanced Monte Carlo procedure for the d-Li neutron source term based on evaluated cross sections files, J. Nucl. Mat. 307-311 (2002), 1710-1714

[3] A. Yu. Konobeyev, Yu. A. Korovin, P. E. Pereslavtsev, U. Fischer and U. von Möllendorff, Developments of methods for calculation of deuteron-lithium and neutron-lithium cross sections for energies up to 50 MeV, Nucl. Sci. Eng. 139 (2001) 1-23

[4] P. Bém, V. Burjan, M. Götz, U. Fischer, V. Kroha, U. v. Möllendorff, J. Novák, S. Simakov and E. Šimečková. "D-Li reaction source term: Experimental verification of neutron yield based on thick and thin Li-targets". Report NPI ASCR Řež EXP(EFDA)-05/2004.

[5] M. Baba, T. Aoki et al., J. Nucl. Mater. 307-311(2002) 1715.

[6] C.A. Azimov. U.R. Arifkhanov et al., Sov. Jour. of Nucl. Phys., 1975, p. 225

TTMI-004
IFMIF, Design Integration

TW4-TTMI-004 D3
Full 3D Analysis of the Shielding Performance of the IFMIF Test Cell by Making Use of a Computational Scheme Coupling 3D Monte Carlo and Deterministic (S_N) Transport Calculations

The objective of this sub-task was to assess the shielding performance of the test cell during IFMIF operation by means of an accurate calculation of the dose rate distribution in the neighbouring rooms.

A full 3D analysis of the shielding performance of the IFMIF Test Cell was performed by making use of a recently developed computational scheme for coupled Monte Carlo/deterministic (S_N) transport calculations [1]. To generate the S_N angular flux from the Monte Carlo particle tracks, a mapping approach has been developed [2] and implemented into a suitable interface programme. The resulting programme system makes use of the MCNP code for the Monte Carlo calculations and the three-dimensional S_N code TORT for the deterministic calculations (Fig. 1).
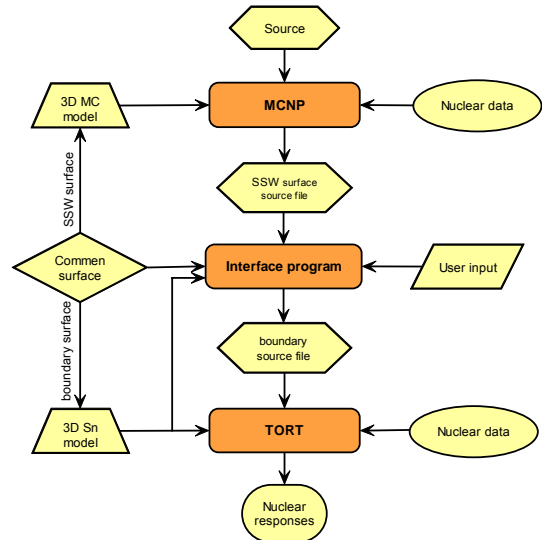
Fig. 1: Flow chart of the programme system for coupled Monte Carlo/S_N transport calculations.
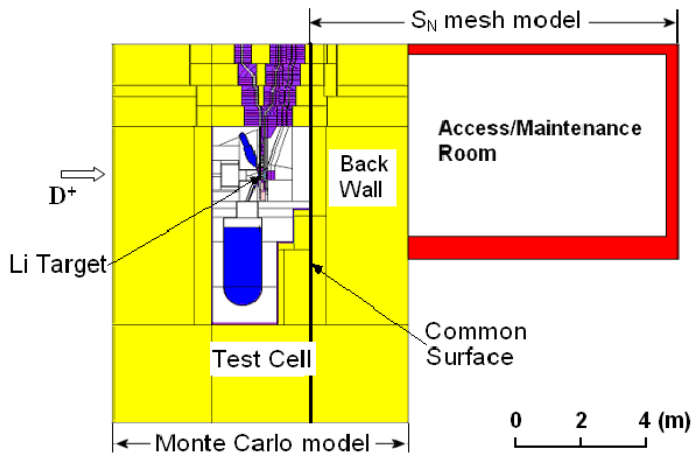
Fig. 2: Calculation model of the IFMIF Test Cell and the Acess / Maintenance Room (vertical cross section).

This approach enables the use of the detailed geometry model of the Test Cell in the Monte Carlo calculation as provided by TW4-TTMI-003, Deliverable 5(b), along with an accurate representation of the D-Li neutron source through the use of the McDeLicious Monte Carlo code with the associated d + Li cross-section data. The neutron transport through the thick concrete walls surrounding the Test Cell is described by means of 3D S_N calculations with the TORT code using the boundary source distribution calculated by McDeLicious at the inner surface of the Test Cell wall. The geometrical model for the coupled MC/S_N calculation comprises two parts: the Test Cell with the D-Li neutron source for the Monte Carlo simulation and the maintenance/access room for the S_N calculations (Fig. 2). The thick concrete wall between the Test Cell and the maintenance/access room is included in both the Monte Carlo and the S_N mesh model. The reference shielding material of the Test Cell walls was assumed to be heavy concrete.

The dose rate distribution was assessed across the 3m thick back wall of the Test Cell and in the maintenance/access room by calculating the neutron and photon flux distributions at IFMIF full power operation and multiplying them by the flux-to-dose rate conversion factors

according to the ICRP specifications. Fig. 3 shows the dose rates as a function of the distance from the inner surface of the back wall. It is seen that heavy concrete provides a significant better shielding performance than ordinary concrete. The dose rate attenuates across the back wall by about 9 orders of magnitude in the case of heavy concrete and about 8 orders of magnitude in the case of ordinary concrete. In the access/maintenance room the dose rate decreases by a factor of about 25 along the beam direction in both cases. It is also found that the dose rate is dominated by neutrons while photons contribute less than 15%.
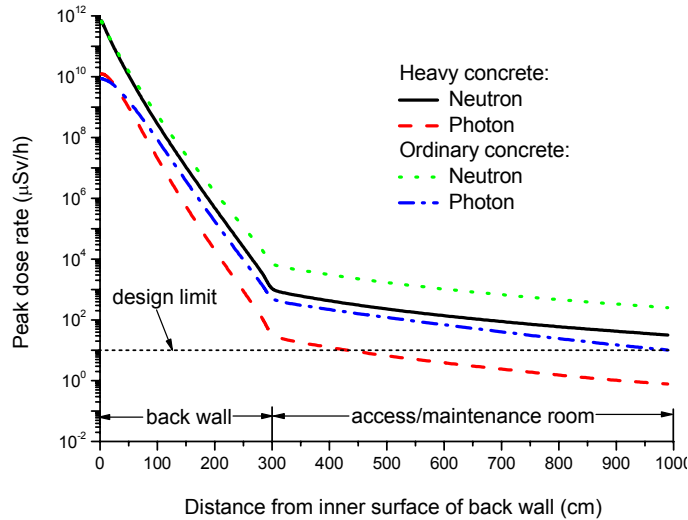
Fig. 3: Dose rate profile across the back wall of the Test Cell at IFMIF full power irradiation.

The peak dose rate in the access/maintenance room exceeds the design limit of 10µSv/h by about 3 orders of magnitude for ordinary concrete and by about 2 orders of magnitude for heavy concrete. To reduce the dose rate level in the room to the design limit, the thickness of the back wall would have to be increased to about 400 cm in the case of heavy concrete and to about 450 cm in the case of ordinary concrete. Figure 4 shows the 3-D dose rate distribution calculated for the access/maintenance room with heavy concrete as shielding material. It is noted that the profiles of the dose rates are still very similar to the incident beam profile.

Significant discrepancies were found when comparing the results of the coupled MC/S$_N$ calculation to those of previous IFMIF shielding calculations using an approximate neutron source representation and a simplified one-dimensional geometrical model. This indicates that the MC/S$_N$ coupling scheme can be a useful computational tool for the 3-D shielding analysis of IFMIF.

Staff:

U. Fischer
Y. Chen
S.P. Simakov
F. Wasastjerna (VTT Processes, Finland)

Fig. 4: Dose rate distribution in the access/maintenance cell at IFMIF full power irradiation.

Literature:

[1] Y. Chen, U. Fischer, S. P. Simakov, F. Wasastjerna, Three-dimensional shielding calculations of IFMIF based on a coupled Monte Carlo/deterministic computational approach, 10th International Conference on Radiation Shielding, Funchal, Madeira, May 9-14, 2004

[2] Y. Chen, Development of a coupled Monte Carlo/Deterministic scheme for three-dimensional shielding analysis, to be published

Fuel Cycle

GB8-VP 1
Cryopump Development and Testing: Effect of Strongly Sorbed Substances

1. Background and Objectives

The **T**est facility for **I**TER **mo**del pump (TIMO) is used to demonstrate the qualification of the ITER-torus cryopump which is recommended as the reference design for ITER. The test programme with the 1:2 model cryopump covered the simulated ITER conditions with respect to gas flow, gas composition, gas pressure, time periods for heating up and cooling down, temperature of the panels during pumping, partial regeneration and total regeneration.

One of the key points is the long term reliability of the cryopump. A major issue in this is the compatibility with high-boiling species which are still strongly bound to the cryosorbent at ambient temperatures, such as water and heavier hydrocarbons. Water is a specified component in the torus exhaust gas and may originate from water leaks, hydrocarbons may be formed in the torus by plasma wall interaction or at the charcoal under presence of atomic hydrogen or due to radiochemical reactions initiated by the tritium decay. The latter effect is investigated in a parallel task (TW3-TTFF-VP35).

Two questions have to be solved in this context, namely what conditions are needed to regenerate these substances (this topic is dealt with in the parallel task TW3-TI-VP31), and what is the impact on the pumping speed of the cryopump. The reduction in pumping speed for the standard exhaust gas components (hydrogens and helium) due to the presence of strongly sorbed substances on the cryosorbent is called poisoning. To investigate this, a parametric test programme has been conducted comprising water, and two very heavy hydrocarbons (n-hexane and i-octane). These two species have already been investigated several years ago in the component test facility TITAN and it was shown there that the poisoning effect starts to become critical with octane, whereas it is still weak for hexane. Any hydrocarbons with C content less than that of hexane are definitely less critical as being more volatile. From this point of view, octane is definitely a worst case species. To derive the poisoning effect quantitatively, ITER relevant pumping speed tests for deuterium were performed with the cryopanels being pre-loaded with a defined amount of poisoning species (water, hexane, octane).

2. Modification of the TIMO Test Facility

The TIMO facility includes a gas dosage system based on thermal mass flow meters. However, for injection of gases which are in the liquid state under ambient conditions, a special dosage device was developed. The aim is to preload the panel with defined amounts of the potentially poisoning substance. This species has to reach the panel to be fixed by sorption. Consequently, the loading has to be realised at ambient temperature, since all high molecular substances will immediately be frozen out at the entrance baffle under cold conditions. The technique shall be easy to perform, provide a small gas load that is built up homogeneously and uniform and not need too high calibration requirements so that the poisoning substance may be exchanged easily. To meet these requirements, the first solution was a bubble column, which allowed to moisturise a helium gas stream until saturation. This wet gas stream can then be injected into the facility so that the moisture adheres to the sorbent, see Fig. 1.

Fig. 1: Bubble column under operation with carrier gas He (at 1000 sccm) in water.

This methodology was already used at former tests in the TITAN facility and worked well [1]. Due to the transport via a carrier gas, it was no problem to load the panels very homogeneously. However, for the big gas loads needed in TIMO, the resulting helium pressure in the test vessel after the dosage step, was in the range of more than 200 mbar, which needed to be pumped down before the cooling of the cryopump could be initiated [2]. This pump out may lead to a pressure induced desorption of the tracer and thus affect quantitatively the remaining sorbed gas load, as found for some test runs. This was the reason why cross-checks have been made by direct evaporisation of a connected liquid volume. In this case, the gas balance (injected vs. released) could always be met, however, the uniformity of the pre-loading cannot be validated. However, as the pumping speed test results did not reveal any poisoning effects, the non-uniformity, if at all present, can be regarded as worst-case scenario. This procedure became the reference for the tracer test campaign, task TW1-TTF-VP13.

3. Results

Fig. 2 illustrates the achieved pumping speeds (related to the pumping charcoal-coated surface of 4 m²) for pumping deuterium at a surface-related gas flow of 2500 sccm/m², which corresponds to 130% of the ITER value. The amount of poisoning gas q, pre-loaded at the panels is also given related to the panel surface. Assuming an expected water/hydrocarbon content of about 1% in the exhaust gas (as specified roughly in the current ITER PID), the gas load of q=5 (mbar·l)/cm² would be accumulated after 20 consecutive pumping cycles without regeneration; for example for octane, the gas load of 2.5 (mbar·l)/cm² corresponds to a sorbed mass of 500 g. However, it is believed that the realistic contents are magnitudes below the 1% limit (the current task TW4-TTFD-TR42 aims at getting experimental values for this number from real machine data).

For all the deuterium pumping tests, the pumping speed was perfectly constant throughout the whole pumping time of 9 min. This indicates that there is no poisoning effect at all with respect to deuterium pumping, which is the reference pumping task. The measured speeds between 1.7 and 1.8 l/(s·cm²) are in very good agreement with the deuterium pumping speed values for a freshly reactivated charcoal, as measured at an early stage of TIMO operation.
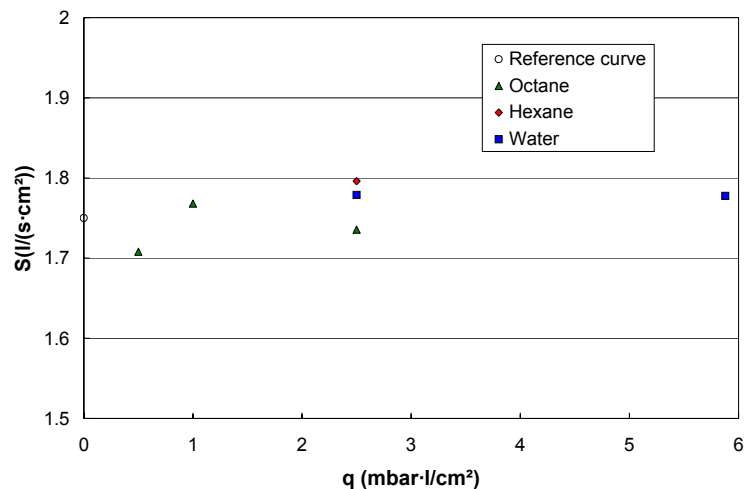
Fig. 2: Measured D_2 pumping speed tests at different pre-loadings of the cryosorbent with strongly sorbed substances.

As a conclusion to this, no critical issues due to any poisoning effect have been identified. The experimental programme has been finished and the task will be completed by comprehensive evaluation of the measured data, up to poisoning gas loads of 10 (mbar·l)/cm² .

Staff:

Chr. Day
A. Edinger
H. Haas
H. Jensen
A.Mack
P- Pfeil
R. Simon
H. Stump
J. Weinhold
D. Zimmerlin

Literature:

[1] Chr. Day, B. Kammerer and A. Mack, The influence of water on the performance of ITER cryosorption vacuum pumps, Fusion Engineering and Design 51-52 (2000) 229-235.

[2] H. Haas and Chr Day, Remaining test program for TIMO, Presentation at 7th ITER-FZK Interface Meeting, available at http://www.ITER.org/bl (ITER Technical Web Site, Pumping).

TW1-TTF/VP 11
Torus Exhaust Cryopump Development and Testing

After demonstration of the suitability of the ITER pump concept during extensive test series with the TIMO facility at FZK in the last years, the remaining task was to operate the pump in a fully automatic mode in the frame of multi-cycle tests. The accumulation of air-like impurities in the gas mixture to be pumped after many cycles with only partial regeneration in between was used as an illustrative example for the multi-cycle operation.

Each pump cycle comprises a pumping step and a regeneration step. For the ITER torus exhaust pump, both are equally long and last 600 s. The regeneration step itself can be subdivided in 6 stages, namely closing of the main valve, heating up the cryopanel system, desorption gas release, pump-out by means of the forepumping system to 10 Pa, cool-down, and opening the main valve to the torus. The valve actuation times are considered to take about 10 s each. The remaining time shall be distributed equally among the four different steps.

For the tests in TIMO, the complete cycling operation was programmed in automatic PLC control loops via the interface programme COROS [1]. Following this scheme, multi-cycle tests were performed. For the cycling tests the two ITER relevant gas mixtures "D_2–Base + 10% He" and "H_2–Base + 7% He" were examined over more than 20 cycles [2]. Both mixtures contain about 3.5% impurity fractions (CO, CO_2, CH_4 and O_2) besides hydrogen as major component. Within the regular regeneration, these impurities are not released and will therefore accumulate over the cycles. For composition analysis, a high resolution quadrupole mass spectrometer was used. Representative gas samples could be taken on-line during pumping from the test vessel and the cryopump inner volume, respectively, and from the exhaust gas collection buffer tank on demand. So composition information is available from the starting gas composition, the pumping cycles inside the model pump and the final check in the exhaust line.
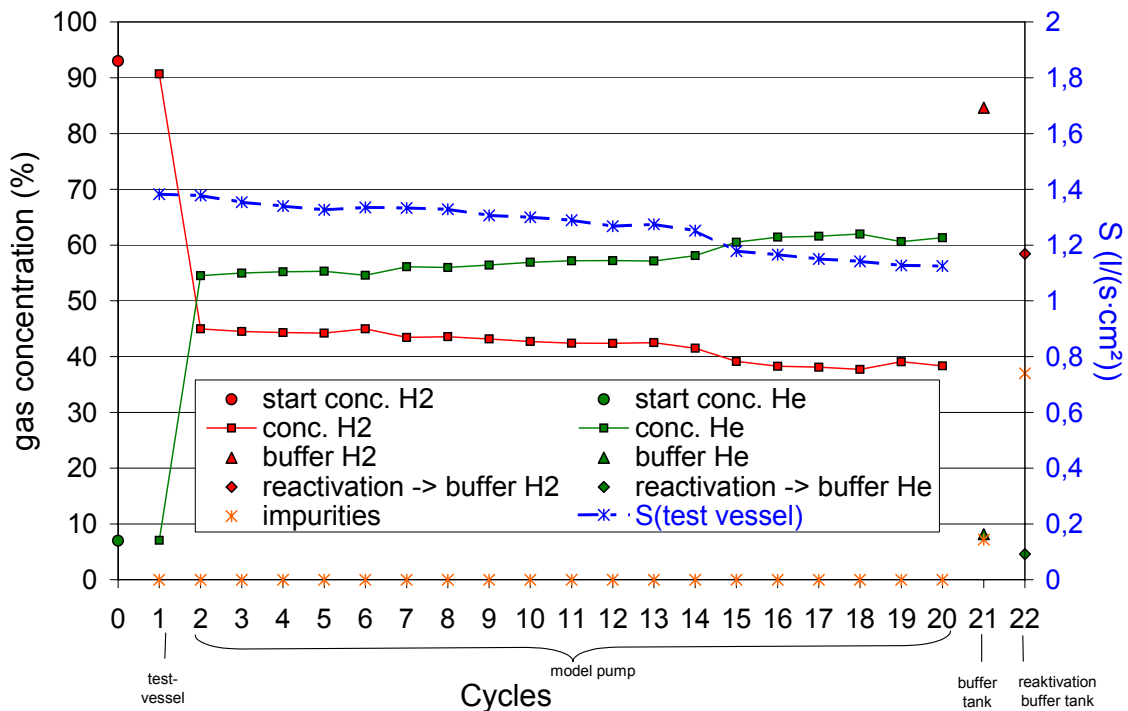
Fig. 1: Cycle tests with a protium-based exhaust gas mixture.

In Figs. 1 and 2 the summarized results of the cycling tests performed with the two gas mixtures are shown. It becomes obvious that the pumping speed values (blue curve) for the mixture with protium and helium do slightly decrease with increasing cycle number, whereas they stay pretty much constant for the (deuterium+helium) gas mixture. This result is in accordance with earlier measurements which showed that there is a competitive pumping situation for concurrent pumping of helium and protium, which is less pronounced for the combination of helium and deuterium. It holds for both combinations that the gas inside the pump is strongly enriched with helium, which is far more difficult to pump than hydrogen (difference by factor 4 to 5 in sticking coefficient). However, for both examined gas mixtures the ITER requirements concerning the pumping speed are fulfilled with S > 1.0 l/(s cm²).
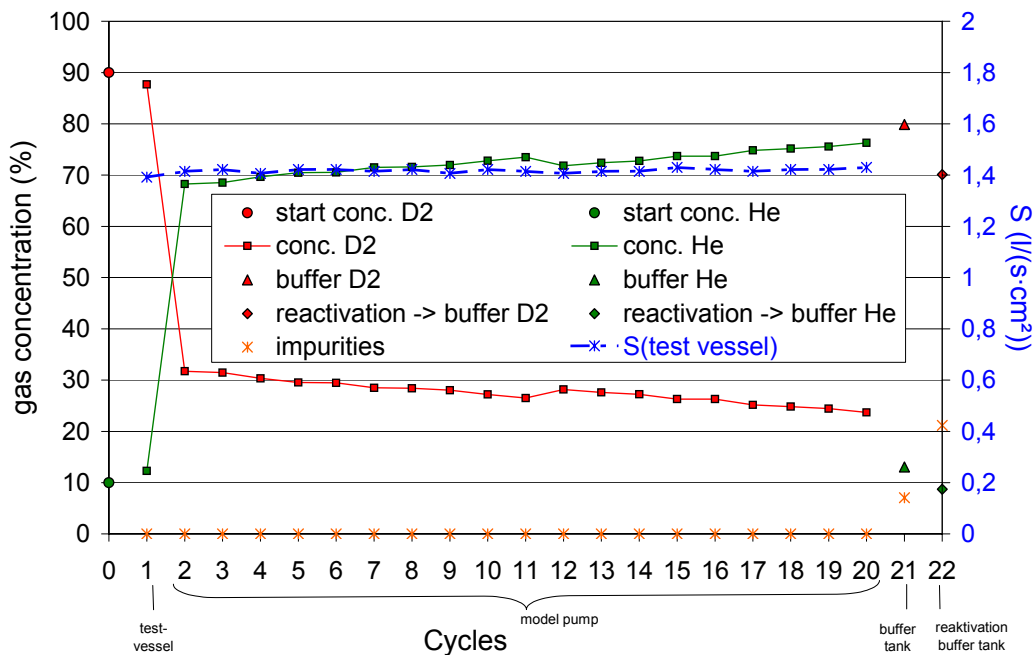
Fig. 2: Cycle tests with a deuterium-based exhaust gas mixture.

Staff:

Chr. Day,
A.Edinger,
<u>H. Haas,</u>
H. Jensen,
A.Mack,
P. Pfeil,
R. Simon,
H. Stump,
J. Weinhold,
D. Zimmerlin

Literature:

[1] H. Haas et al., Bericht zu den Aktivitäten der TIMO-Automatisierung, Internal Report # FE.5130.0046.0012/J, Forschungszentrum Karlsruhe, March 2004.

[2] H. Haas, TIMO progress, Actual Activities. Presentation at 6th ITER-FZK Interface Meeting, available at http://www.ITER.org/bl (ITER Technical Web Site, Pumping).

TW1-TTF/VP 12
Performance Evaluation of Roots Blower with Ferrofluidic Seal System

The objective of the task is the investigation into the application of ferrofluidic seals in Roots blowers to reduce the potential for cross-contamination between process gas and lubricant, thereby enhancing tritium compatibility. A Roots blower of a model relevant to the ITER roughing system design and equipped with ferrofluidic seals should be tested under representative cyclic pressure conditions.

By the beginning of the reporting period the first tritium compatible "Roots" vacuum pump has been delivered to FZK from UK Company Roots Systems Ltd. During the acceptance tests in the company, the internal helium leak rate between process chamber and both oil containing chambers was measured better that 10^{-8} mbar·l/s, the external leak tightness was better than 10^{-9} mbar·l/s.

Upon receipt of the pump, a test set-up has been completed for the performance testing of the seals. The stand could allow performance testing of the pump itself as well, but such tests were considered because the pump design was dedicated to allow a reliable testing of the seals. Before starting the tests a contamination of the pump chamber with ferrofluid was observed. The seals were overfilled during first installation at contractor's premises. The amount of liquid which was used exceeds many times the amount needed for sealing. Such an uncontrolled location of the liquid is unacceptable for the work with tritium.
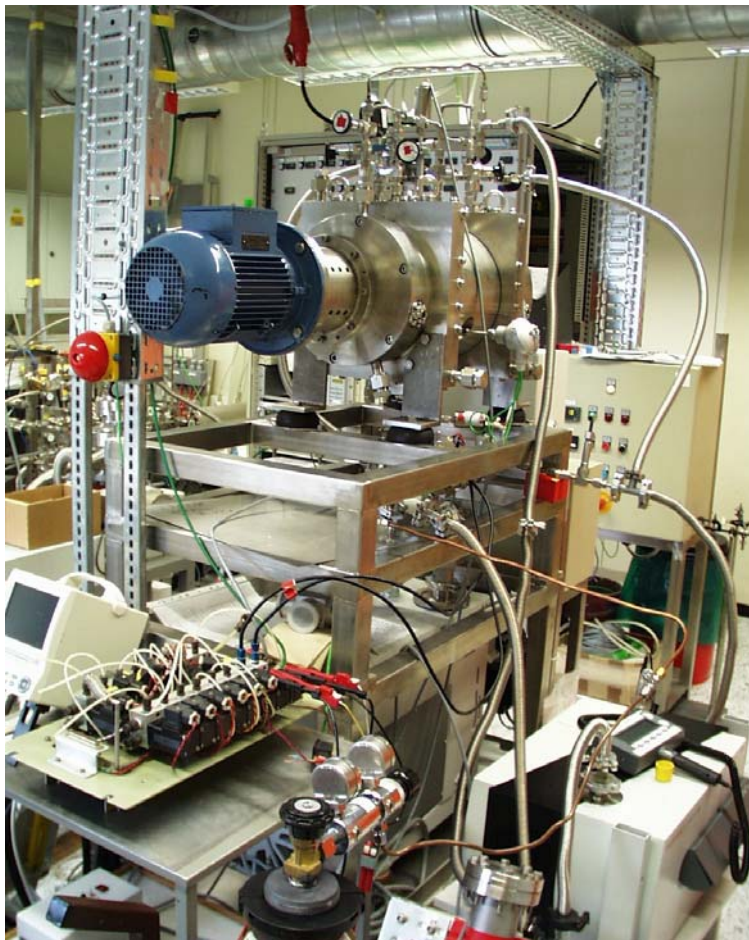
Fig. 1: 250 m^3/h Roots pump. Test set up.

After cleaning the pump chamber the tests without tritium were started. The final test set up is shown in Figure 1. In August 2004 the tests have been completed. In the first series of tests the helium leak was measured from the process chamber to the middle point of each of four seals. In the second series the leak was measured from the process chamber to the oil containing chambers. The helium pressure in the process chamber simulated the pressure variation of the ITER forepump inlet of the first stage (20 – 0.1 mbar every 2.5 min), and of the second stage (80 – 0.4 mbar every 2.5 min).

The reliability of the seals was demonstrated: None of them lost its integrity even after pressure runs of up to Δp=1 bar (a maximal design pressure difference is 0.5 bar). At the same time, upon more than one month of cycle testing with helium, the seals showed a degradation of their performance: The leak rate towards the gear end reached 3·10^{-7} mbar·l/s and fluctuated with pressure, the leak towards the drive end was stable at 3.5·10^{-8} mbar·l/s. One of the testing

curves is shown in Figure 2. The results do not match with the task requirements (<10^{-8} mbar·l/s).
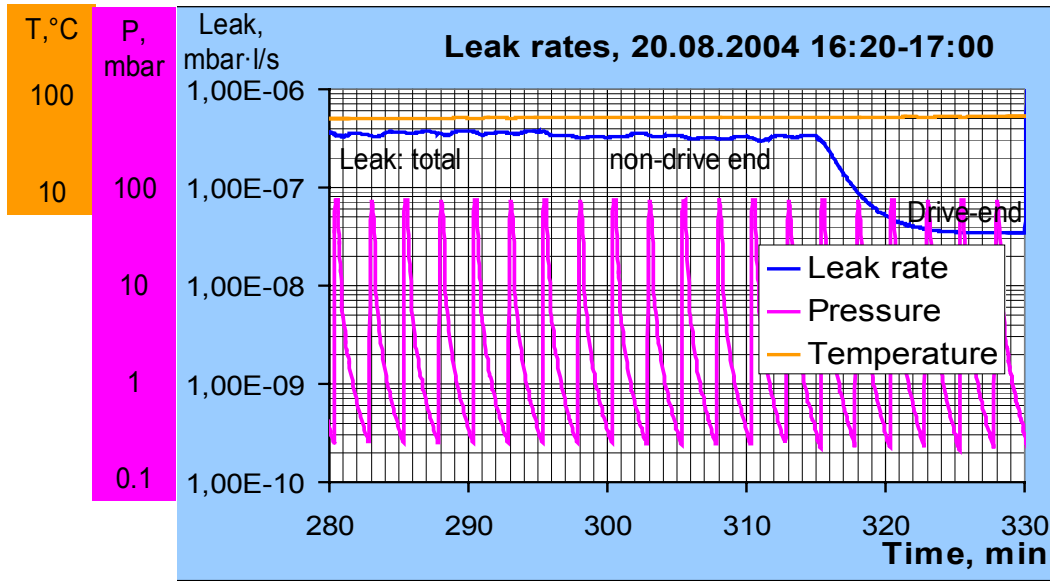
Fig. 2: 250 m^3/h experimental Roots pump for tritium.
Test results: leak rates through the shaft seals.

It was decided to modify the seals in cooperation with the company FerroTec and then repeat the tests. The seal modification is shown in Figure 3. In the initial design the magnetic liquid was directly applied to the shaft and it was not possible to provide its required distribution among the cells.
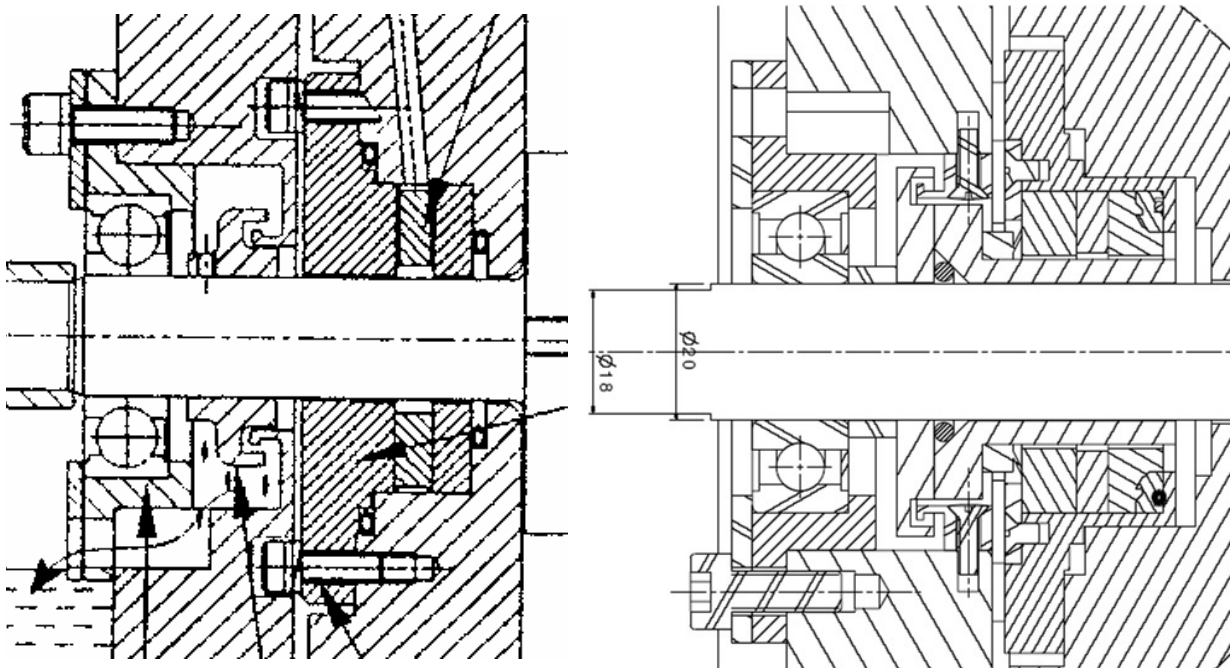
Fig. 3: Modification of the ferrofluidic seal:
left: original design of Roots Systems ltd., right: with integrated FerroTec cartridge.

Staff:

A. Antipenkov
R. Wagner
A. Mack
R. Simon

Literature:

[1] A. Antipenkov et.al., Large Forevacuum Pumping System for Tritium in a Nuclear Fusion Reactor, poster presentation for the 6th International Vacuum Congress, Venice, June-July 2004, Paper No. PS-WeP16

[2] A. Antipenkov et.al., Tritium Pumps for ITER Roughing System, proceedings of the 7th International Conference on Tritium Science and Technology, September 12-17, 2004, Baden-Baden, Paper No. A11-P3

[3] A. Antipenkov, A. Mack, Conventional Forepumping System, Final Report 2004, del. 1-3, EDFA task TW3-THHN-IITF1 "THE FIRST ITER NB INJECTOR AND THE ITER NB TEST FACILITY: DESIGN"

TW1-TTF/VP 13
Compatibility of Leak Localisation Tracers with Cryopanels

Background and Objectives

For ITER, a powerful and sensitive leak detection system is of utmost importance. Consequently, a multi-stage approach has been developed to meet the different leak detection requirements. One of the various strategies involved is for locating a leak in the cooling water circuits which is considered to be the most likely type of a leak into the vacuum vessel. Leak localisation will only be performed after a water leak has been noticed by poor plasma performance and confirmed.

A concept was proposed to add tracer substances at low concentrations which would be released in the gaseous phase in the event of a leak. These tracers would be pumped by the cryopumps and released during regeneration. They would then be detected by the global leak detection system located in the vacuum pump room which is connected to the torus roughing line and monitors the gases exhausted from the cryopumps. Due to the chemical species, the tracer substance will be released not after partial regeneration but after the less frequently performed regenerations at ambient temperature or high temperature (450-470 K). The use of the cryopump would ensure a high sensitivity even for very small leaks due to their accumulation effect over the pumping operational time in between the regenerations.

Any substance to be used as a tracer must be investigated for compatibility with the cryosorption pumping concept. It has to be quantified what amounts of tracers accumulated to the panels can be accepted without leading to charcoal poisoning which would result in a deterioration of pumping performance. Different tracers may be added to the different sub-loops so that one becomes able to pinpoint the leak down to the component level. Therefore, several tracers have been proposed, ranging from lighter hydrocarbons over alcohols to aromatics.

Needed changes to the test facility

The experimental tests to exclude poisoning effects and confirm the regeneration within the available 450 K conditions were performed in the TIMO facility. For the reactivation of the ITER model pump at temperatures up to 450 K, a new supply line for the helium gas flow at higher temperatures was needed. The high gas temperature was achieved by an electrical continuous-flow heater with a maximum electrical power of 10 kW. For defining the gas composition during the different process steps (metering, pumping, reactivation), a buffer tank in combination with a gas mass spectrometer were included into the model pump facility.

From the experimental point of view, there is a big difference between lighter and heavier hydrocarbons, because the first are in gaseous phase at ambient conditions, the latter are liquids and require totally different injection systems.

The hydrocarbons up to propane can be handled as fractions of the test gas mixture metered into the test facility during the pumping speed measurement. Their shares in the gas composition can be pre-defined. By a series of subsequent pumping speed tests, each of them comprising partial regeneration in the end, the amount of accumulated tracer can be increased cycle by cycle, as it will not be liberated within partial regeneration at 100 K.

To perform the poisoning tests with higher hydrocarbons, alcohols or heavier organics one has to handle substances that are in the liquid state at ambient conditions and can therefore not be processed by thermal mass flow controllers via the gas dome in the test facility. To cope with that, the direct evaporisation method of a connected volume was involved (cf Task GB8-VP1). Two injection positions were tried, see Fig. 1, and the agreement was satisfying [2].
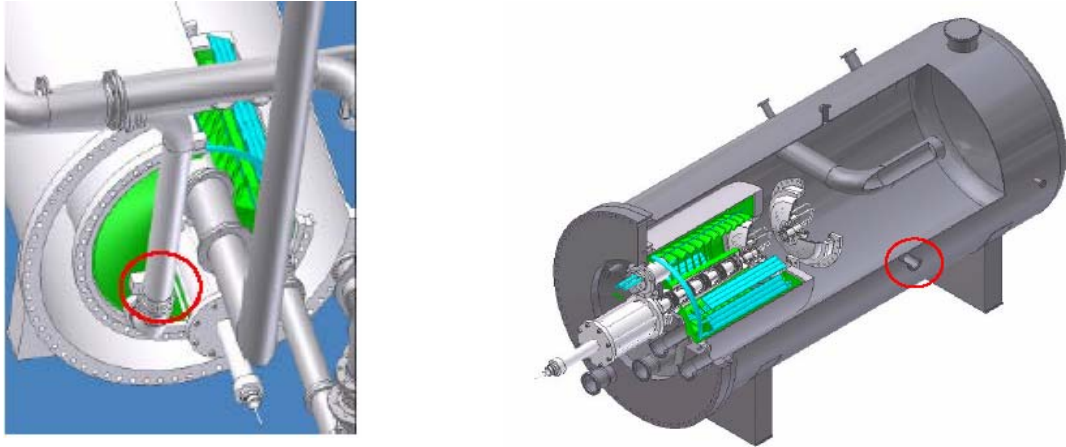
Fig. 1: The two injection points for the liquid water-solved tracers. Variant A (left) is dosing directly in the pump volume from backwards via the roughing pump line, variant B (right) is dosing via the test vessel.

The standard analytic tool in TIMO to monitor the release behaviour of the candidate tracer species is a quadrupole mass spectrometer (128 amu in standard resolution). For detailed investigations in low concentration ranges, a gas chromatograph-mass spectrometer (GC-MS) combination has been procured and set into operation (cf task TW0-T450), see Fig. 2.
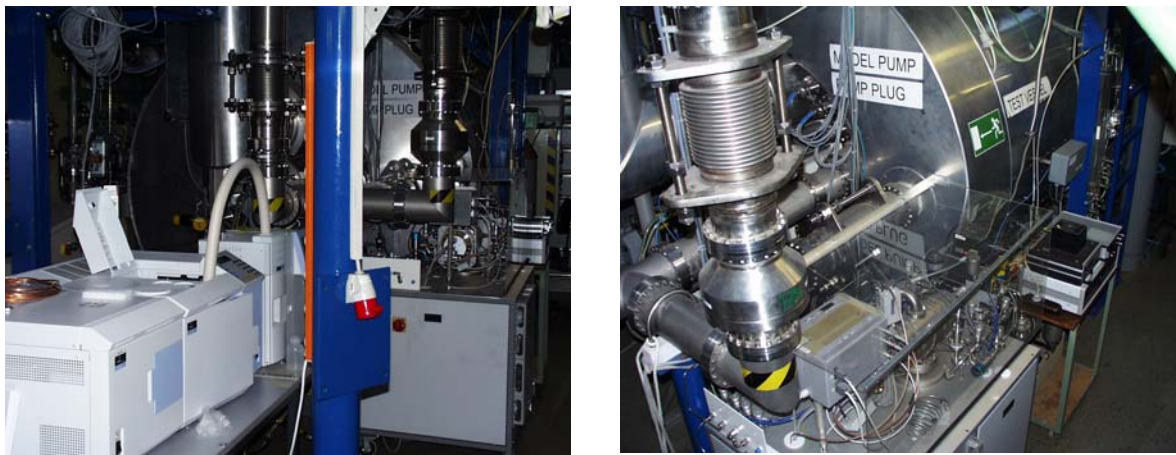
Fig. 2: The two analytical devices used for monitoring the tracer gas release behaviour: A GC-MS (left) and a stand-alone quadrupole MS (right).

Experimental results

The following candidate tracer substances have been investigated: Methane, ethane, propane, 1-butanol, 1-pentanol, 2-methyl-1-butanol, benzene, xylene, toluene.

Each test comprised a pumping speed test for deuterium with the panels being pre-loaded with the tracer, followed by a complete reactivation of the pump at temperatures up to 450 K. During reactivation, the release of the tracer was monitored as a function of panel temperature. After some tests, a pumping speed test for helium was carried through subsequent to the reactivation procedure, to identify any permanent degradation of the pump performance, as helium is the gas most difficult to pump.

For the tests with the gaseous light hydrocarbons, a fixed percentage was added to the ITER relevant gas mixture (D_2-Base gas mixture (96.2% of D_2, 1.4% CO; 1.2% CH_4, 0.7% CO_2, 0.5% O_2)), thus yielding a gas composition with 6% of methane and 4.5% of ethane or propane, respectively. By that, an ITER relevant gas load was pumped onto the panels. It was clearly found that these gases had no effect on the achievable pumping speed [1]. The re-

sults of the reactivation step are shown in Fig 3; the gas analysis was made with the regenerated gas in the closed cryopump, measured with the calibrated stand-alone mass spectrometer, at quasi isobaric conditions (several mbar). It is revealed that temperatures of about 360 to 400 K are needed to achieve a complete regeneration of methane, and the maximum temperature of 450 K for ethane, respectively. Propane is not released completely, even at the highest temperatures. However, by successive pump-down of the gas-filled cryopump volume, a complete regeneration could be achieved at pressures of about 1 Pa. Thus, combined pressure- and temperature induced desorption ensures a complete regeneration of the charcoal after contamination with light hydrocarbon tracers.
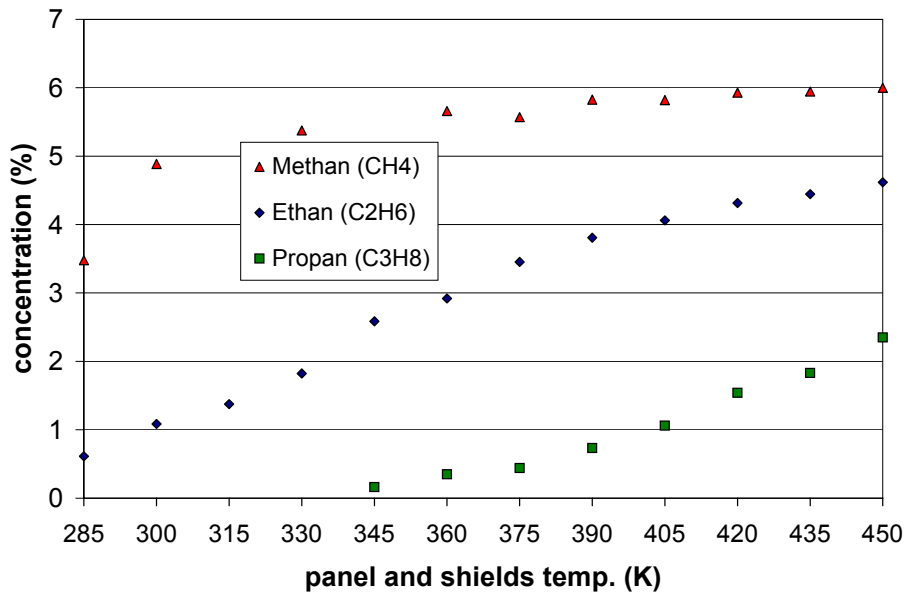
Fig. 3:   Release behaviour of the light hydrocarbons.

The liquid tracer substances were injected as pure substances or together with water. In the latter case, one has to consider that the solubility at ambient conditions in water is poor, so that the tracer with its high volatility will be evaporated very quickly compared to water. The deuterium pumping tests again did not reveal any deterioration.

For the reactivation tests, the GC-MS was applied together with the standard mass spectrometer. For each tracer substance, the individual GC-MS fingerprint could be determined and the qualitative release behaviour (in terms of ion currents) was monitored. A detailed evaluation of all test results will be made in the next reporting period for completion of this task.

Staff:

Chr. Caldwell-Nichols
Chr. Day
A. Edinger
H. Haas
J. Weinhold
D. Zimmerlin

Literature:

[1] H. Haas, TIMO progress, Actual Activities. Presentation at 6. ITER-FZK Interface Meeting, available at http://www.ITER.org/bl (ITER Technical Web Site, Pumping).

[2] H. Haas, New TIMO Test Results, Presentation at 8. ITER-FZK Interface Meeting, available at http://www.ITER.org/bl (ITER Technical Web Site, Pumping).

TW3-TTFF-VP 35
Study of Cryopump Compatibility with Carbon Erosion Products

1. Objectives

Predicting the amount and location of co-deposited hydrocarbon films is a major challenge for ITER. Recent studies have shown that only species with very small sticking probability may reach and stick along the inner surfaces of the pumping ducts [1]. When the inner surfaces are covered with a thin amorphous film, the hydrogen recombination coefficient may be significantly reduced so that atomic hydrogen and/or methane radicals could reach the cryopump region.

This task is dedicated to the analysis of the possible interaction between H atoms or CH_3 radicals and the activated charcoal sorbent in the cryopumps. It will investigate if the charcoal sorption properties will change due to the exposure to low sticking coefficient species and will identify the chemical species formed during such an exposure. The presence of any saturated hydrocarbon sorbed at the charcoal surface, which may act as promotor for a chemical reaction, will also be assessed. The saturated hydrocarbons, while not possible to get to the cryopump directly from the torus due to their high sticking coefficient, may be formed locally from radiochemical reactions in the presence of tritium, or originate from chemical reactions triggered by the radicals. Potential poisoning effects will also be analysed. Recommendations and conclusions with respect to any needs for changes in the design for the cryopump system will be given.

2. Experimental
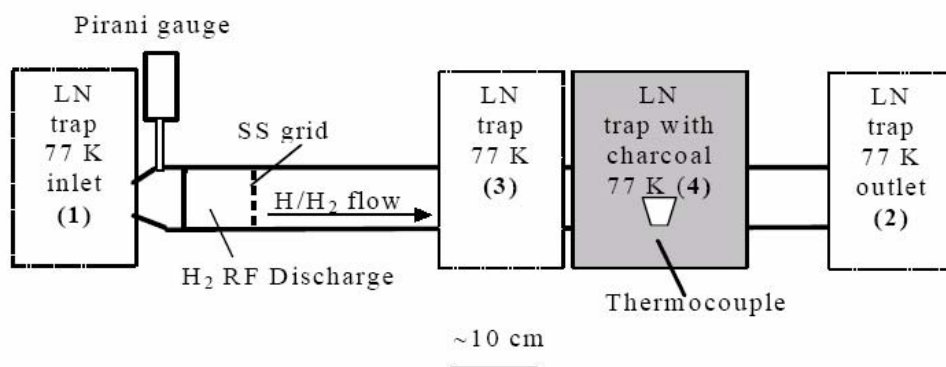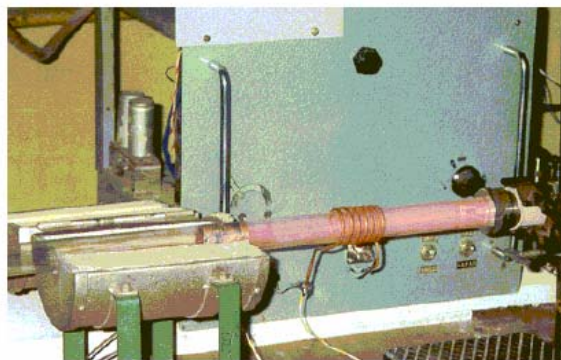
Fig. 1: Scheme of the quartz gas flow reactor with 1 cm radius and 100 cm length for experiments with charcoal in atomic/molecular mixture at 77 K. Gas flow controllers were installed at the tube inlet.

The experimental work with radicals will be performed in the Institute for Physical Chemistry of the Russian Academy of Sciences, Moscow. They involve a radio frequency plasma induced discharge in a hydrogen/hydrocarbon gas mixture as source for atoms, radicals and excited molecules. The varied parameters include gas pre-loading of the charcoal sample, exposure time and catalytic contact material (quartz, stainless steel). Within this reporting period, the tests with atomic hydrogen have been made. The interaction of thermal hydrogen molecules and atoms with charcoal has been analyzed by sorption measurements (based on the stream technique) at 77 K and thermodesorption (TD) experiments at 77-300 K and 300-700 K, respectively. The experimental set up is shown in Fig. 1.

A cylindrical quartz reactor of 100 cm length and 1 cm radius was the main part of the setup. The pressure difference between inlet and outlet of the tube did not exceed 2 Pa. The reactor was pumped out by a rotary pump. An H_2 RF inductive-coupled discharge (frequency 20 MHz, specific power 0.1 W/cm^3) in a flow of 6.9 sccm (3.1×10^{18} H_2/s) under a pressure of about 30 Pa has been utilized for production of atomic hydrogen. A plasma region of about 15 cm length was limited by a thin (100 μm) stainless steel grid. Hydrogen was used with a purity of 99.9999 vol.%.

Fig. 2: Hydrogen TD spectra for charcoal. The tests with molecular hydrogen were made after 30 min exposition in the gas flow, the H/H_2 exposure time was 3 h.

For determination of the flows and atomic hydrogen concentration at the various tube regions solid carbon films were used (H/C=0.4) deposited on silicon substrates. As the erosion coefficient of solid carbon films in the medium of atomic hydrogen is well known, measuring film areal densities before and after exposure in atomic hydrogen environment allowed to derive the erosion rate and, thus, the H atom thermal flow (~10^{16} H/cm^2 s) and concentration (~10^{11} H/cm^3) at the location of the charcoal. The atomic and molecular hydrogen ratio was about H/$H_2 \approx 10^{-4}$. The mass of the investigated ITER type charcoal samples was about 20 mg.

Each sample was first characterised via a sorption measurement and a TD run in a reference experiment with molecular hydrogen. The samples were then exposed to atomic hydrogen (77 K, 30 Pa, in the afterglow zone of the H_2/H RF discharge) over different time intervals, 0.5, 2, 3 and 4 hours, respectively. After that, the reference experiment was repeated to reveal the consequences of the exposure. Fig. 2 illustrates the changes in the hydrogen TDS spectra following a 3 hours exposure. From the adsorption-desorption experiments it is evident that irreversible hydrogen sorption takes place at charcoal exposure in the H/H_2 gas mixture, leading to smaller amounts of hydrogen sorbed. This experiment was repeated with methane, which did not cause any significant effect [2].

The sorption isotherms for nitrogen, measured after the different exposure times also show a pronounced decrease with increasing exposure time to atomic hydrogen, see Fig. 3. However, this effect may not be of ultimate importance to the cryosorbent application in ITER, which is characterized by the low pressure branch rather than by the asymptotic limit for

P/P$_0$>0.1. Furthermore, the ITER pumping concept does not rely on high saturation capacities of pumped gas amounts, but is defined by significant inventory limitation due to explosion safety hazards. Further tests are ongoing.

In a special experiment immediately after the exposure in the H/H$_2$ mixture and transfer through air the charcoal sample was analyzed in a mass-spectrometer with linear sample heating (20 K/min) up to 700 K directly in the equipment. The results are shown in Fig. 4.

In the temperature range 300-700 K hydrocarbon ions were found with masses of 41 (C$_3$H$_5$), 43 (C$_3$H$_7$), 55 (C$_4$H$_7$), 57 (C$_4$H$_9$), and others. These hydrocarbon species were not observed at all in a mass-spectrum of the initial charcoal. In this analysis the absolute quantities of hydrocarbons formed were not determined. However, the wide spectrum of the appeared heavy hydrocarbons seem to indicate intensive chemical interaction of atomic hydrogen with the charcoal surface at 77 K.

Fig. 3: Nitrogen adsorption isotherms for charcoal before and after exposure in the H/H$_2$ mixture (77 K, 30 Pa). The upper black curve is the reference curve measured at FZK for the untreated material.

This task will be continued with further quantification of the results obtained so far and by extension towards CH$_3$ radicals. The influence of contact materials on radicals will also be assessed [3]. Samples of the exposed material will be transferred to FZK and investigated in terms of sorption behaviour under ITER relevant conditions.

Staff:

Chr. Day

A.E. Gorodetsky
A.P. Zakharov
(Institute of Physical Chemistry RAS, Moscow)

Fig. 4: Temperature programmed desorption spectra (300 to 700 K) for charcoal before and after the H/H$_2 \approx 10^{-4}$ mixture exposure (77 K, 34 Pa, 1 hour).

Literature:

[1] G. Federici et al., Modeling of deposition of hydrocarbon films underneath the divertor and in the pumping ducts of ITER, Proc. 16th Int. Conf. on Plasma Surface Interactions in Controlled Fusion Devices, Portland Maine, USA, 2004 (in press).

[2] A. E. Gorodetsky et al., Interaction of atomic hydrogen with charcoal at 77 K, IAEA Fusion Energy Conference, Vilamoura, Portugal, Nov. 2004.

[3] A.E. Gorodetsky et al., Increased recombination of CH3 radicals on stainless steel, Proc. 16th Int. Conf. on Plasma Surface Interactions in Controlled Fusion Devices, Portland Maine, USA, 2004 (in press).

TW4-TTFF-VP 45
Performance Assessment of Mechanical Pumps in Tritium Plant

The Tritium Plant of ITER requires many pumps to move tritium and other gases within the plant and deliver gases to the torus and its subsystems. Several manufacturers produce mechanical pumps suitable for tritium operation and several models have been identified as candidates for the use in the Tritium Plant.

The manufacturer's data has been reviewed for the pumps currently planned for the ITER tritium plant. In particular the data has been converted to ISO units to conform with ITER design standards and allow direct comparison between pumps. The data for mass flow rate at the exhaust, exhaust gas velocity and Reynold's numbers has also been computed for these pumps. The last two parameters are important for control of mixtures and flow resistance calculations in long pipes. The test bed for the fast delivery getter bed will be used for testing these pumps as many of the required components are already installed, particularly a large buffer volume. Other pumps already in use at TLK will be tested either in their existing glove boxes or on the test bed.

A special pump from Thales, type PR-130, has been ordered as it can operate down to the low input pressure that will be required by some processes in the ITER Tritium Plant. This pump has a wobble plate driven by an eccentric rotor to provide the motion for pumping. The double bellows seal of the drive is an advantage for tritium operation as it provides warning of a bellows failure.

A major part of the assessment will be the lifetime, maintainability and long term availability of the various types of pumps proposed for ITER. None of the pumps are expected to survive the lifetime of ITER without requiring either maintenance or replacement so these are important factors in the choice of pumps, particularly as the pumps will be installed in glove boxes.

Staff:

C.J. Caldwell-Nichols
S. Welte
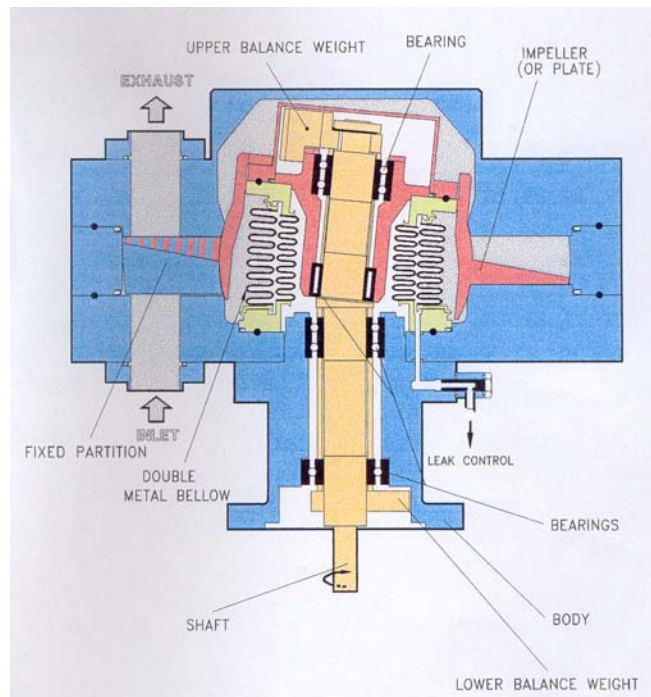
Thales PR-130 pump

EFDA/03-1095
Design of an ITER-Sized Mechanical Pump Train

The aim of this task is a detailed design of an ITER relevant, dry mechanical pump train as forepumping system for the cryopump systems of ITER. The tritium compatibility shall be realised with a ferrofluidic seal system, based on the results achieved in the R&D Task VP12, which is based on a modified roots blower. The design shall include other (dry) pump concepts for the pressure range not covered by roots blowers.

By the beginning of the reporting period the ITER operating requirements have been reviewed. The market of mechanical pumps has been surveyed. The task was started with selection of an optimal roughing train for ITER (consisting of two Roots stages: 6000 and 2000 m^3/h backed by a screw pump of 600 m^3/h pumping speed), but it practically could not be continued, because ITER operating requirements have been still developing. The new requirements were planned to be formulated by the middle of 2004. The ferrofluidic seal concept was not validated, pending on the test results of a pilot 250 m^3/h Roots blower with the ferrofluidic seal, and the survey of the market of fore-pumps, which should substitute reciprocating piston pump of Toyo Engineering, which is not produced any more.

In September 2004 ITER has issued a new Project Integration Document. The requirements to the roughing system have been specified. The torus cryopump volume has been revised (8.5 m^3 now). The torus cryopump regeneration scenario was not changed from 2003 (staggered mode with 2.5 min duration of each of four regeneration phases, 10 min duty cycle of each cryopump). The gas load was revised. One critical issue is the missing of pumping curves for explosive gases, especially hydrogen isotopes for commercially available pumps. For Roots pumps we have used the curves, obtained in Japan in 1994. For a screw pump a curve for helium with and without ballast gas (air) have been received from Leybold Vacuum and scaled up to protium, deuterium and tritium. The performance of these pumps for deuterium should be similar to helium. With the protium it will be much worse, as measured by Japanese home team. But one should notice that for ITER operation on protium, the requirements to the roughing system shall be much relaxed that for the operation on deuterium and tritium. Using an estimated performance of a train on helium (see diagram in Figure 1), and the code, allowing to take into account the gas temperature difference in the evacuated volume and at the entrance to the roughing pump, the pump down curve of a torus cryopump was calculated (see Figure 2), it confirms the train set up.
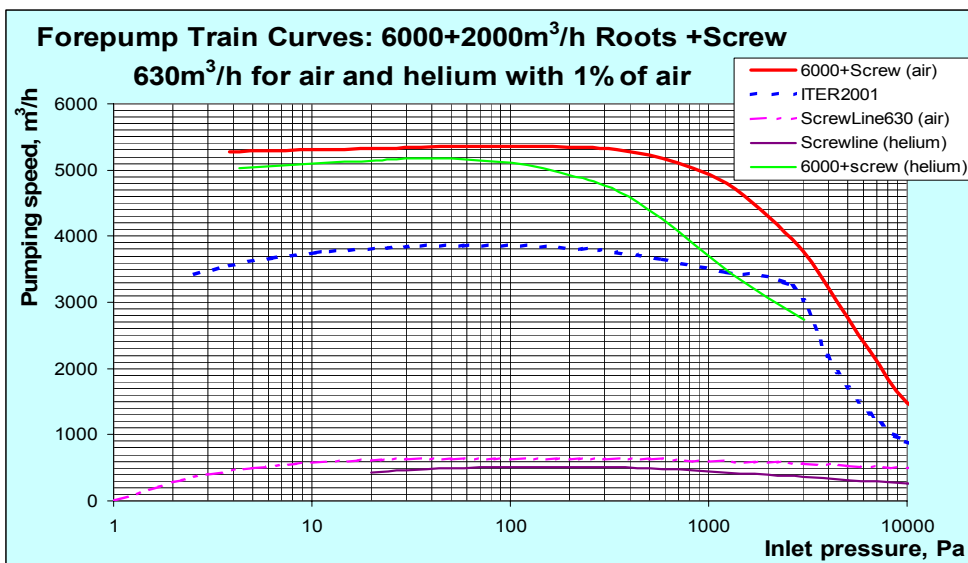
Fig. 1: Calculated Pumping curves of a train of 6000+2000m^3/h Roots and as screw pump SP630 for air and helium with 1% of air as a ballast gas.
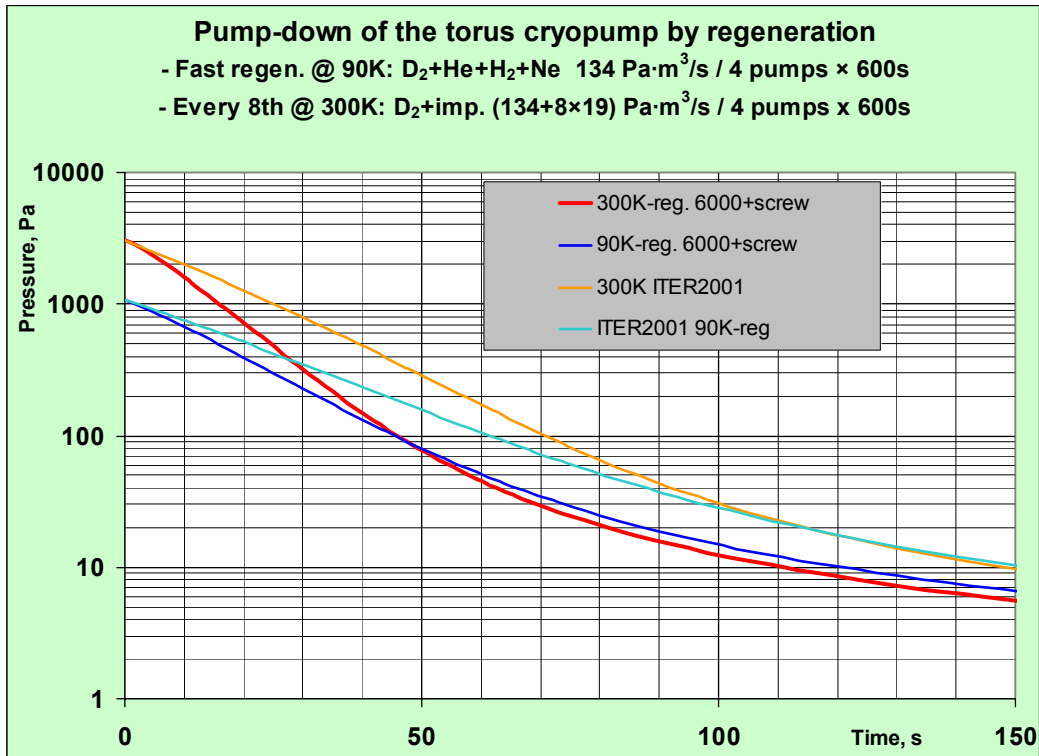
Fig. 2: Evacuation curves for torus cryopump regeneration.

The ITER requirement to the Neutral Beam vessel evacuation during its cryopump regeneration has revealed the first critical issue to complete the task: The requirements to the roughing pump are more challenging now, than for the torus cryopump (in opposite to 2003 concept). In PID-2004 regeneration mode is defined as isochronous, i.e. the vessel has to be evacuated down to 20 Pa during 337 s (960 s in FDR 2001). The calculations show that in this case the pumping speed of a roughing set of at least 9000 m^3/h is needed. We recommend not to select an unreasonably large forepump. The ITER requirements should be reconsidered.

The second critical issue to complete the task is absence of positive results with the ferrofluidic seal integration into the Roots pump in frame of VP12 subtask. The seal design of the UK company Roots Systems ltd. has not sustained the long term tests and is now due to be modified. The pump is planned to be reassembled in March 2005, then upon its successful tests with inactive gases, the recommendation for ITER relevant Roots design will be given. The third critical issue is that the ITER-2001 reference backing pump (the reciprocating piston pump of Toyo Engineering) is not produced any more. The research for an alternative on the pump market has revealed two types which can be used as a backing pump: a scroll pump with double bellows (NORMETEX) and a screw pump. The tritium pumps of required capacity are already manufactured by NORMETEX company, but the recommendation to use this type of pump for ITER is depending on the results of investigation of their failure at JET. The most compact solution is a screw pump either SP630 of Leybold, or SIHI-dry of Sterling-SIHI, but their modification toward tritium operation requires new efforts in addition to the activity with the Roots blower. Negotiations with these companies are on the way. As a back-up we keep in mind the multistage Roots with intermediate cooling or claw pump, but these options look less attractive and shall be considered only if two solutions above fail.

Staff:

A. Antipenkov
A. Mack
I. Meyer

Literature:

[1] A. Antipenkov et.al., Large Forevacuum Pumping System for Tritium in a Nuclear Fusion Reactor, poster presentation for the 6th International Vacuum Congress, Venice, June-July 2004, Paper No. PS-WeP16

[2] A. Antipenkov et.al., Tritium Pumps for ITER Roughing System, proceedings of the 7th International Conference on Tritium Science and Technology, September 12-17, 2004, Baden-Baden, Paper No. A11-P3

[3] A. Antipenkov, A. Mack, Conventional Forepumping System, Final Report 2004, del. 1-3, EDFA task TW3-THHN-IITF1 "THE FIRST ITER NB INJECTOR AND THE ITER NB TEST FACILITY: DESIGN"

EFDA/04-1141
ITERVAC Conductance Modelling of ITER Torus Exhaust Pumping Ducts: Development of ITERVAC Code

Background and Objectives

The reference design of the ITER exhaust pumping system is based on 8 cryopumps, connected via 4 ducts to the torus, each of them containing a pump in direct line of sight and a branched pump, see Fig. 1. For pulse lengths longer than 400 s, the pumps have to be operated in a staggered mode with 4 pumps pumping and 4 always in regeneration. Because the pumping speed of the branched pumps is less than that for the direct pumps, there must always be two branched pumps and two direct pumps pumping, otherwise there would be an oscillation in the pumping speed when a direct pump replaces a branched pump or vice versa. For short pulses (less than 400 s) all 8 pumps can pump from tritium inventory point of view [1].
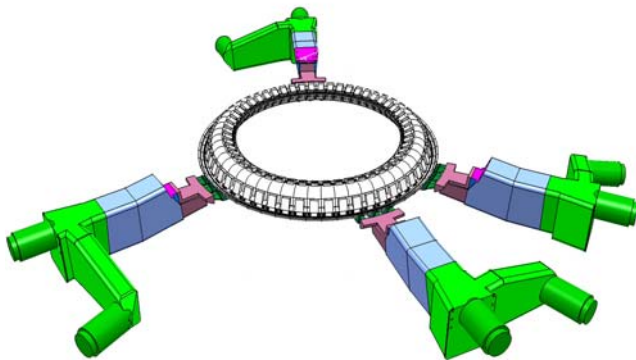
Fig. 1: Drawing of the ITER torus exhaust pumping system including the 4 pumping ducts and the connections to the 8 cryopumps.

The required ITER exhaust gas throughput is 153 (Pa·m³)/s (120 (Pa·m³)/s fuelling rate plus impurities) at specified divertor pressures between 1 and 10 Pa. The torus pumps themselves have a nominal pumping speed over 100 m³/s each. Consequently, the total throughput, theoretically achievable with four pumps, can be greater than 400 (Pa·m³)/s. However, the effective pumping speed on the divertor is much lower, caused by the conductance loss of the pumping ducts. Unfortunately, two of the four pumping cryopumps are in branch line connected to the main divertor duct, reducing the pumping speed additionally.

The gas passages through the divertor cassettes and torus exhaust vacuum pumping ducts on ITER form a complex network of poor conductances, cf Fig. 2. Several asymmetries in the system contribute to this complexity. Moreover, the gas flow regime is in the transitional range, which cannot be correctly described by just a combination of the boundary solutions for molecular and viscous flow. The correct assessment of this system requires a computer simulation programme to model the gas flow to the needed accuracy and to study the interaction of ducts of different types in this network.

Fig. 2: Detailed view of the individual divertor cassette and the three fingered connection to the duct, highlighting the pumping slot cross-section.

Basics of ITERVAC

Within this task, the numerical code ITERVAC was developed as a general tool to describe gas flows in the whole range from low to high Knudsen numbers with an excellent representation of the transitional flow range. The theoretical basis for ITERVAC is the calculation of the mass flow through a cylindrical pipe at isothermal conditions in a wide range of Knudsen numbers. Here, the flow can be described in dependence of the friction pressure loss in the pipe, the temperature and the molar mass of the gas. This concept was expanded to include

convex and prismatic channels. On this basis the dimensionless flow of every channel is calculated with 5 constants, describing the properties of the gas and the geometry of the channel.
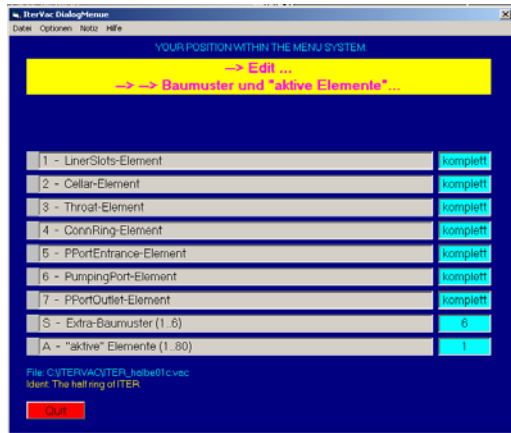
Fig. 3: Screenshot of the editing window to define the individual block cells.

For application to complex geometries, they have to be represented as a network of block cells with different properties and geometric features assigned to. Thus, a detailed geometrical description of the vacuum system, which usually is a big effort, is not needed. Simple block cells with a set of properties are sufficient, see Fig. 3. A model is completed, when all cells are wired and the gas properties are defined. A special feature is the application of the free flying length of particles in ITERVAC. This guarantees a smooth iteration between the single channels of a complex system.

Model generation

Within this task, calculations of the throughputs in the complex torus exhaust pumping ducts have been started [2]. Different models were generated for the different tests and calculations. Finally, a model of the half ITER ring was created; the flow system was represented via input, output and linking nodes, see Fig. 4. The global data sets for this model were set up for the gases helium, protium, deuterium and tritium. ITERVAC was applied to assess the conductance of the complicated ITER vacuum pumping duct geometry, which is characterised by low Knudsen numbers down to about 0.05 at the slots of the divertor cassettes (laminar and intermediate flow) and high Knudsen numbers of about 200 at the pump region (molecular flow). The main input parameters are the divertor pressure and the pumping speed of the cryopumps. The output is the maximum throughput from divertor into the pumps at isothermal conditions.
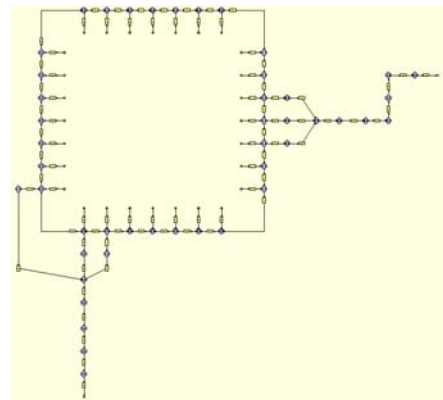
Fig. 4: ITERVAC simulation of the ITER torus exhaust duct and pumping system (half ITER ring).

In the last half year ITERVAC was tested intensively. Some bugs were found and were corrected. Since then, the program was working stable.

Results and first conclusions

The results of the throughput calculations, summarized in Fig. 5, showed that the achievable throughput starts to become independent on the attached pumping speed for values above 80 m³/s per pump. Consequently, this number shall be defined as reference pumping speed for the ITER torus pump, which is currently under detailed design.
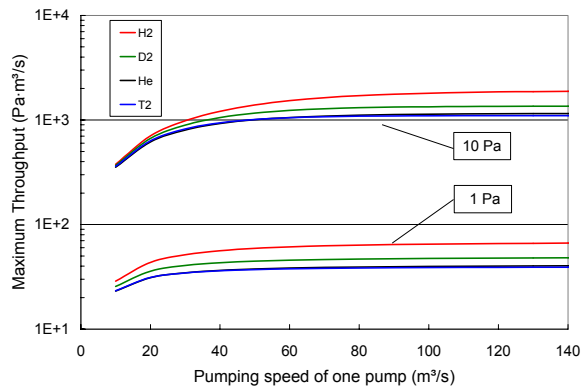
Fig. 5: Maximum achievable ITER throughput for 4 different gases at a divertor pressure of 1 and 10 Pa, respectively.

During parametric investigation, it was clearly found that there is a bottleneck of the gas flow coming from the three-fingered entrance section between the divertor cassettes and each pumping duct, see Fig. 2, limiting the throughput below its required value for pressures close to 1 Pa: The maximum throughput at 1 Pa is about 65 (Pa·m³)/s for H_2, and only 38 (Pa·m³)/s for T_2. A sensitivity study was therefore performed in which the divertor finger cross-section was step-wise increased in the ITERVAC model. It was found that it must be increased by 3 cm in both directions to allow for the required throughput at 2 Pa for all gas compositions; cf Fig. 6., which shows the results for tritium. Achievement of significantly lower pressures without remarkable changes to the divertor geometry would only be possible by introduction of additional pumping ports [3].
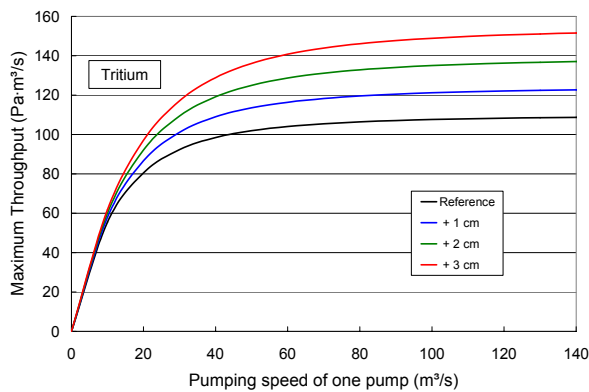
Fig. 6: Maximum achievable ITER throughput for a divertor pressure of 2 Pa and tritium. The curves highlight the impact of increased cross-sections at each of the three divertor fingers per duct (by 1/2/3 cm in both directions, see Fig. 2).

The modelling studies performed under this task will be continued to derive further optimised geometries and support the discussions currently initiated with the ITER team.

The code will be benchmarked against conductance calculations using existing methods, and with experimental results. However, as literature data are very scarce, especially for the transitional flow regime, an experimental EFDA task will be launched to produce a coherent and parametric data base which can be used for cross-check and validation. This is deemed to be necessary due to the important consequences of this modelling approach on the overall ITER vacuum pumping system design.

Staff:

Chr. Day
V. Hauer
A. Mack

Literature:

[1] M. Wykes, Minimisation of the hydrogenic inventory of the ITER neutral beamline and torus cryosorption pumps, Proc. TRITIUM 2004, Sept. 2004, Baden-Baden, Germany.

[2] V. Hauer, Chr. Day and A. Mack; ITERVAC - Development and Preparation of input data, Report on EFDA Task TW4-TTFF-VP47, Deliverable 1, September 2004.

[3] Chr. Day et al., Validated design of the ITER main vacuum pumping systems, Proc. IAEA Fusion Energy Conference, Nov. 2004, Vilamoura, Portugal.

TW0-T 450/01
Detection and Localisation of Leaks from Cooling Circuits

A method of locating leaks on ITER water cooling circuits is required which will be applied once a water leak into the torus has been confirmed. A proposed method is to add a tracer material into the water circuits and then analysing the exhaust from the ITER cryopumps for the tracer material. By isolating various parts of the cooling circuits and using several tracers it should be possible to locate any leak to a particular circuit and possibly to a sub-section of a circuit. The detector for this method is a gas chromatograph/mass spectrometer (GC/MS) combination which has been purchased and commissioned.

Software and hardware problems experienced with the GC/MS system purchased for this work have been mostly resolved, though the MS did have another failure that was fixed by the manufacturer. This particular recurring fault is likely to have been an original fault at manufacture and in general the equipment has not had a good reliability record.

However, the GC/MS equipment has been transferred to the TIMO facility at FzK and connected to the exhaust line of TIMO. A sample pump and buffer volume has been established to raise the pressure of the gas from TIMO after regeneration from 15 mbar to 1 bar required for the first stage of the GC/MS. 'Warm' runs on TIMO have been conducted where water /tracer mixtures have been injected into the TIMO vessel under vacuum but with the panels at ambient temperature. The panels were then progressively heated to examine the desorption characteristics from the charcoal coating. Two cryogenic runs have been undertaken where tracer solutions have been injected into TIMO with the panels later reduced to normal pumping temperature. The gases that evolved after regeneration at various temperatures were examined for the tracer materials. In both runs the tracers were detected so the technique has been proved in principle. It is clear that the GC/MS is considerably more sensitive that the existing MS on TIMO, however the GC/MS technique can only be used for compounds that condense at relatively high temperatures, i.e. not hydrogen, helium or normal air components. Further cryogenic test are planned which will be determined by the availability of cryogens, particularly helium, which are shared with other users at FzK.

A gas chromatograph scan from one of the cryogenic runs using benzene as a trace material is shown below:
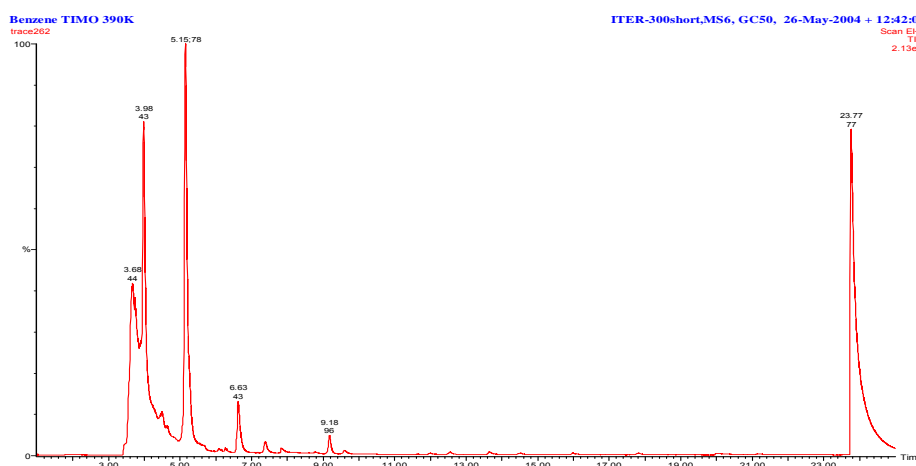
The mass spectrum of the peak at 5.15 minutes after background subtraction is shown below together with the fractionation pattern of benzene from a reference library of compounds.

Benzene TIMO 390K
trace262 828 (5.149) Cm (822:839-(753:802+871:957))

ITER-300short,MS6, GC50, 26-May-2004 + 12:42:05

F:854 Nist 30179: BENZENE
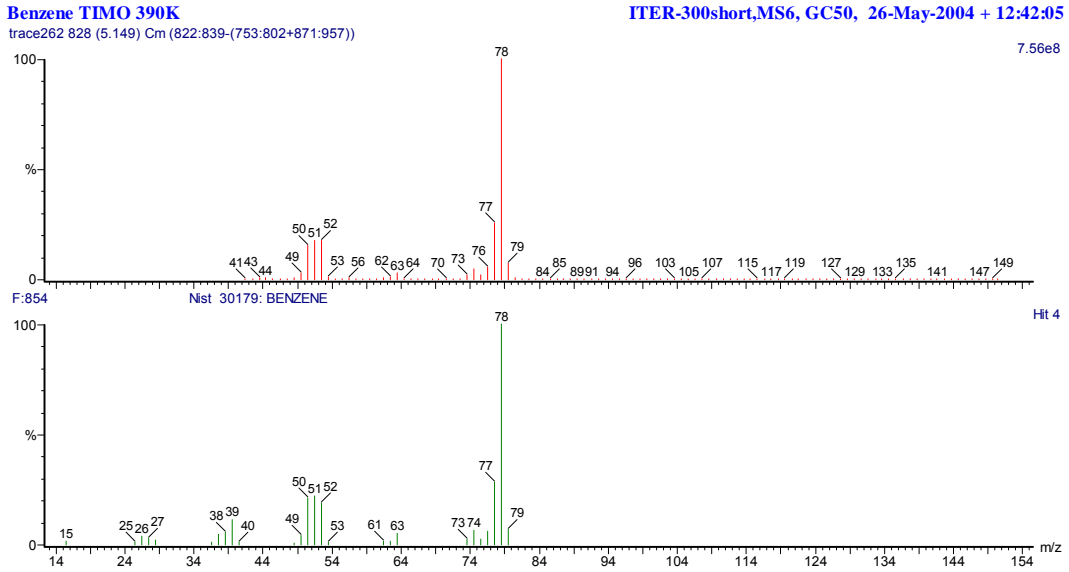
This identifies the peak as benzene and shows that after regeneration TIMO has released the benzene. Further tests are planned with other candidate tracer materials, dependent on the availability of TIMO. About 10 suitable tracers need to be identified for leak localisation on ITER as well as an estimate of the sensitivity of the method for each tracer, i.e. the minimum amount of tracer that can be detected after regeneration of a cryopump as this will determine some of the parameters of any search program on ITER to locate a leak. Of additional interest is the peak at 23.77 minutes in the gas chromatograph. Examination of the mass spectrum of this peak indicates that it is benzaldehyde and this suggests that some reactions may be taking place converting benzene to benzaldehyde, probably on the cryopanels. This phenomenon will be investigated as, in the presences of tritium, there is likely to be other species created by radiochemical reactions which may make positive identification of a tracer more difficult.

Staff:

C. J. Caldwell-Nichols
C. Day
D. Zimmerlin
J. Weinhold

EFDA/03-1097
Operation of the Tritium Laboratory Karlsruhe (TLK)

The Tritium Laboratory Karlsruhe (TLK) is a semi-technical facility which was founded with the aim to establish tritium handling techniques in Europe and to develop the technologies for the fuel cycle of future fusion reactors. Laboratory scale and technical scale experiments are conducted at TLK within the framework of the European Fusion Technology Program with realistic concentrations of tritium, tritiated gases and tritiated materials which are typical for future fusion devices.

The first license to use 10 g of tritium was granted in 1993. TLK was commissioned with a mixture of 1% tritium in deuterium in 1994 and tritium operation with gram amounts of tritium started in 1995. TLK is now licensed to hold 40 g of tritium and at present has approximately 23 g of tritium in use. A total glove box volume of 125 m³ is currently available within an area of 841 m² for experiments and 615 m² for infrastructure. In addition to the demonstration of the safe handling of tritium, the main purpose of the infrastructure is to supply the tritium necessary for technical experiments, take back the tritium after the experiments are finished and to process the returned gases for reuse. For this purpose TLK is equipped with a closed tritium loop. In general TLK has many similarities with the Tritium Plant of a fusion reactor like ITER, since it comprises a storage system, a plasma exhaust processing system for the recovery of tritium and an isotope separation system.
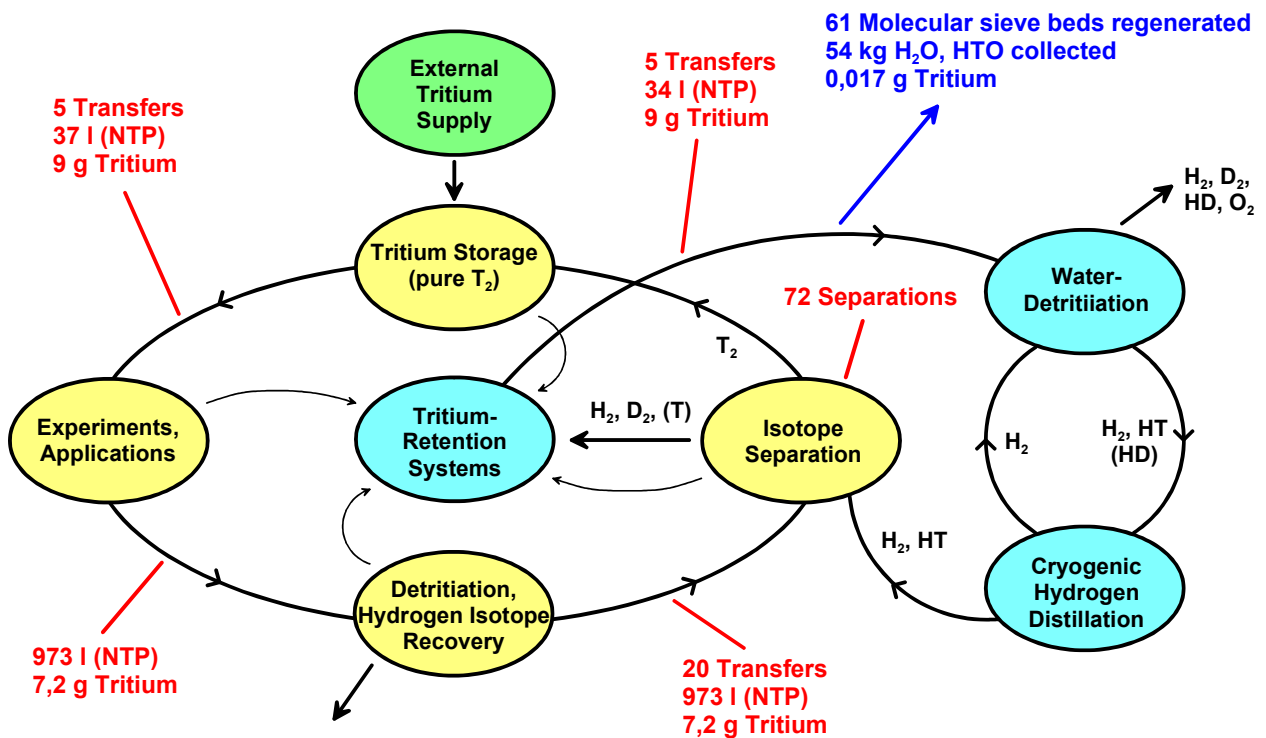
Fig. 1: Closed tritium loop at TLK.

The operation of the TLK is in itself an essential contribution to the fusion R&D work with tritium. In 2004 the laboratory has been extensively used for this program with the experimental facility CAPER. This involved round-the-clock operation of the TLK with frequent transfers of tritium and tritiated hydrogen isotopes between CAPER and the TLK infrastructure. As illustrated in figure 1, gram amounts of tritium have been transferred between the different facilities and 72 separation runs with the ISS have been carried out to separate tritium and deuterium for reuse in the CAPER facility. Tritium accountancy was carried out for each transfer by pVT-c measurements and calorimetry. The integrated operation of the CAPER facility with the infrastructure of the TLK also demonstrated the safe handling and transfer of tritium within a tritium plant.

In total 61 regenerations of molecular sieve beds from the different Tritium Retention Systems associated with glove boxes have been performed and 54 l tritiated water has been sent to the waste treatment department of FZK for disposal. Currently experimental work is on-going for the detritiation of such tritiated water, as shown on the right part of figure 1, so that the tritium from the HTO can be recovered.

After more than 10 years of operation some components and even complete equipment have reached their lifetime, failed or are no longer being used within the ongoing experimental program. Failed components of experimental facilities have been disconnected from the process and transferred to a repair box for inspection or repair. It has been proven that even components used with gram amounts of tritium can be repaired. During the last year the replacement of the hardware of the infrastructure process control system to ensure safe operation of the TLK for the future has been finished. With the migration of the visualization and operating software of the infrastructure process control system, TLK has now a new process control system which will allow safe operation of the infrastructure for the next 10 years.

<u>Staff:</u>

H-D. Adami
U. Besserer
<u>L. Dörr</u>
H. Dittrich
M. Göckel
G. Hellriegel
W. Hellriegel
F. Kramer
S. Krieger
K. Nolte
E. Porter
F. Rehlinghaus
P. Schäfer
P. Schuster
J. Wendel

Tokamak Exhaust Processing

TW1-TTF/TR 11
Gas Processing during in-situ Tritium Recovery from PFC's

TW4-TTFD/TR 41
Experimental Investigation of Undesired Side-reactions in PERMCAT

TW4-TTFD/TR 43
Comparison of Batch and Continuous Operation Modes for the Impurity Processing Stage of the Tokamak Exhaust Processing System

One of the key systems within the Tritium Plant of ITER is the Tokamak Exhaust Processing (TEP) system. However, exhaust gases from the vacuum vessel during D-D and D-T operation of ITER will certainly not be the only source for gaseous streams within the Tritium Plant from which deuterium and tritium need to be recovered. Besides the gases from other operational modes of the tokamak, such as deuterium or helium from Glow Discharge Cleaning (GDC) or the fluids from the retrieval of tritium from plasma facing components (PFC's) and co-deposits, various other sources within ITER will generate tritiated waste gases which have to be processed. Since ITER does not have a dedicated system for the treatment of gaseous wastes all the tritium needs to be recovered by the TEP system. Consequently the TEP system has many more duties than the name of this particular part of the ITER Tritium Plant may suggest.

The decontamination factor required for the TEP system which is only defined for a short pulse of the D-T burn phase of ITER, is based on the ratio of tritium-inlet to tritium-outlet flow rates, and is specified to be 10^8. Taking the gas composition and flow rates during the burn phase into account this decontamination factor can be translated into a target outlet concentration of $\leq 10^{-4}$ gm^{-3} (equivalent to≤ 1 Cim^{-3} or ≤ 0.4 ppm tritium). Off-gases from the TEP system shall be stacked via the Normal Vent Detritiation System (N-VDS) of ITER after intermittent storage for decay of γ-active species in dedicated tanks.

The removal of tritium down to levels below 1 ppm from D-T streams containing also tritiated impurities such as water or hydrocarbons can only be achieved by multistage processes. Figure 1 shows the principle of the three step CAPER process for the TEP system of ITER.
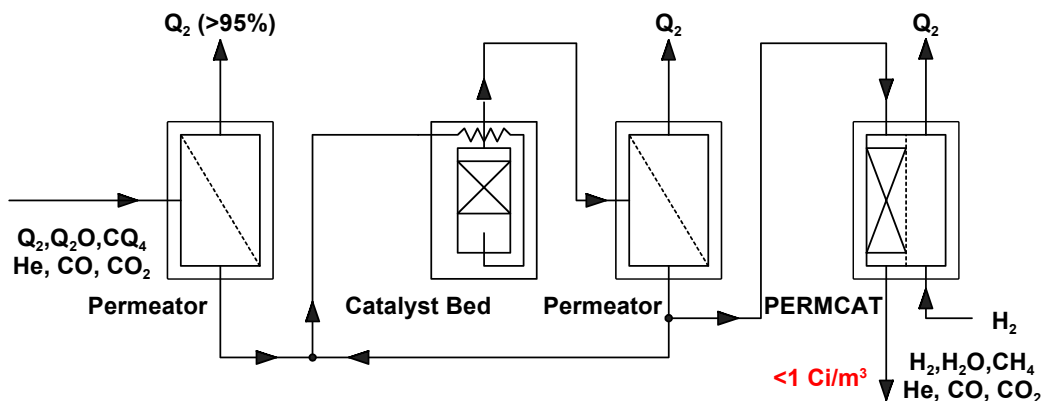
Fig. 1: Basic principles of the three step CAPER process for detritiation (Q=H, D, T).

The CAPER process employs a palladium / silver permeator as a first step ('impurity separation') to separate the bulk of un-burnt D-T fuel (tritium isotopomers) from the tritiated and non-tritiated impurities. The second step ('impurity processing') is carried out in a closed loop involving heterogeneously catalyzed cracking or conversion reactions combined with the permeation of hydrogen isotopes through another palladium / silver permeator to liberate and

recover tritium from tritiated hydrocarbons or tritiated water. The third step ('final clean-up') removes almost all of the residual tritium by counter current isotopic swamping and is based on a so called permeator catalyst (PERMCAT) reactor. The PERMCAT reactor is a direct combination of a palladium / silver permeation membrane and a catalyst bed and has been specifically developed for final clean-up of gases containing up to about 1% of tritium in different chemical forms such as water, hydrocarbons or molecular hydrogen isotopes.

To investigate the individual steps and to demonstrate the overall process in an integral manner the so-called CAPER facility is operated at the Tritium Laboratory Karlsruhe (TLK). CAPER is a versatile semi-technical test rig with a typical tritium inventory of about 3 to 5 g, and a team of about 4 persons is required for experiments; its modular set-up allows different routing of gases, and a large number of control loops along with the comprehensive instrumentation installed permit a proper characterization of the chemical processes and components. The latter is particularly important to scale the process to ITER throughputs. A mock-up section within the CAPER facility is available and employed for the preparation of gases with different compositions, particularly tritium and tritiated impurity contents, as they are expected to appear from the various modes of tokamak operation and from operation of all the systems of the ITER Tritium Plant. The CAPER facility is also an essential and central system within the closed tritium cycle of the TLK. All primary gaseous wastes arising from experiments at TLK are detritiated in CAPER. The integral tritium operation of the facility can therefore be considered as representative for the TEP system within the Tritium Plant of ITER.

The first step of the CAPER process was particularly investigated in view of the influence of different inert gas loads and the comprehensive results of the parametric study previously reported. In conjunction with the current tasks the recent experimental work was focused on the second and third stage.

The second CAPER process step being a closed loop with a catalyst reactor and a palladium / silver permeator can in principle be operated in two different modes. In the straightforward batch mode the loop is filled with the gas to be detritiated, is cycled for a certain period of time until the tritium level is sufficiently lowered, and then the loop is emptied for the next batch. Alternatively, gas to be detritiated is continuously fed into the closed loop upstream of the catalyst bed and permeator at a flow rate much lower than the loop circulation flow rate, and the loop pressure is kept constant by a continuous withdrawal of gas downstream of the two components. Such a mode is easy to control and in comparison to the batch mode may have a higher throughput and a reduced tritium inventory.

In principle, for continuous mode operation of the second CAPER step the decontamination factor (DF) is expected to be dependent upon the feed gas composition, the feed flow rate into the loop, the circulation flow rate inside the loop, the pressure inside the loop, the loop volume and the permeator pressure drop. In view of a complex relation-ship between these parameters a complete interpretation of experimental results may not in all cases be straightforward. Therefore, in a first attempt to measure the functional characteristics a number of experiments have been carried out to screen the parameter field.

Figure 2 shows an example of the tritium concentration given as ionization chamber current as a function of time with the feed flow rate into the loop as a parameter (loop volume ≈ 4 l, feed gas composition 230 kCim^{-3} CQ$_4$ (18%), 8.3 kCim^{-3} Q$_2$ (Q=H, D, T) in helium). As expected the activity inside the loop decreases with decreasing feed flow rates. Changing the feed flow rate leads to an instantaneous change of the activity, and a new steady state is reached within a few minutes. The measured curves have been analyzed with respect to the time constants using a simple, single exponential function. The time constants - within the experimental uncertainties - are independent of the activity level in the loop and found to be in the order of 7 min. This value is rather large and most likely due to the too low operation temperature of the permeator. The design temperature of 400°C could not be reached in this
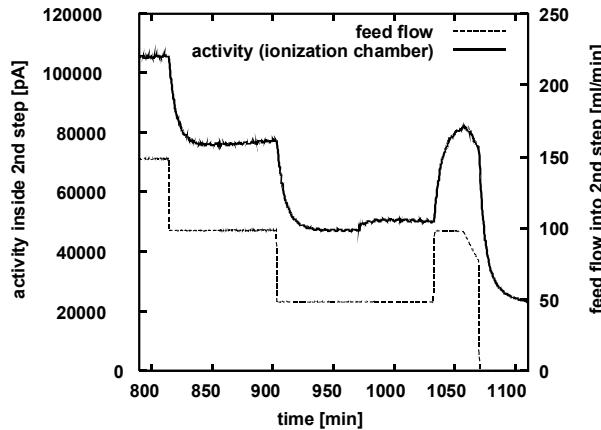
Fig. 2: Continuous mode operation of the second CAPER process stage.

campaign because part of the heaters failed (the permeator was only at about at 250°C). Since the DF achievable in the continuous mode is strongly dependent upon the time constant higher DF's will be obtained after replacement of the faulty permeator.

The essential components and instruments of the first and second stage of CAPER at TLK are now in tritium service for almost ten years, about twice the time originally projected for experiments with the facility. The extension is on one hand due to several changes of the TEP design requirements for ITER and the growing duties of this Tritium Plant system. On the other hand the successful operation of CAPER has given the facility a key role within the closed tritium loop of TLK, and in so-called waste runs tritiated off-gases from different sources are processed as they appear and independent upon their composition. This type of CAPER operation is considered to be particular relevant for ITER, since also the Tritium Plant TEP system will need to detritiate the gases from various sources, rather than being operated all the time with well defined gases. However, certain pumps and in particular the heaters of catalyst beds and palladium / silver permeators of the CAPER facility are used up and need to be replaced. The repair and replacement has led to significant down times of the different stages of CAPER and even to the facility as a whole. Quite a number of lessons have been learned, for example as far as the detailed design of heated components is concerned, and will be reflected in the corresponding work for ITER.

The third CAPER process stage has been tested under a variety of operational conditions. Gases of different composition have been fed into the PERMCAT, thereby varying major parameters such as impurity feed flow rate and impurity feed pressure, hydrogen purge flow rate and hydrogen outlet pressure. The main focus of these parametric studies has been set on achieving low tritium concentrations at the impurity outlet of the PERMCAT.

On the other hand, to understand the detailed characteristics of the PERMCAT the unit has to be operated beyond its limits. An impurity outlet tritium concentration which remains unchanged (within the margins of the technique employed to measure the tritium level) if varying a certain parameter does not disclose the functional dependence of the PERMCAT performance. Therefore in part of the experiments the PERMCAT unit was operated on purpose under conditions leading to tritium concentrations above the levels required by ITER (≤ 1 Cim^{-3}) and above the background level of the ionization chamber and the contamination level of its interconnecting pipe work.

A reliable and reproducible measurement of the residual tritium level at the impurity outlet of the PERMCAT turned out to be particularly difficult. Memory effects and in general different moisture levels in the impurity gas stream may cause systematical errors. Therefore a specific procedure based on grab sampling, oxidation of the sampled gas and liquid scintillation counting was developed. The method is commonly applicable to low level tritium measurement in gases and thus was published separately at the Tritium 2004 Conference in Baden-Baden in September 2004.
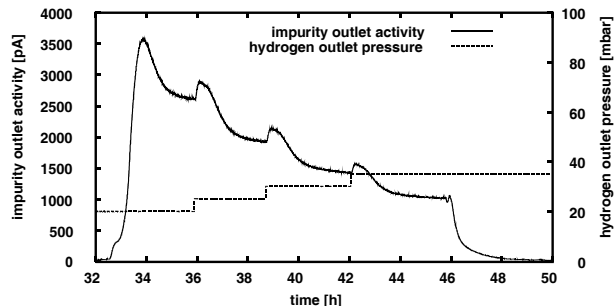
Fig. 3: Impurity outlet ionization chamber signal hydrogen outlet pressure during a parametric PERMCAT experiment.

In Figure 3 the results of a parametric test of the third step CAPER process are shown. The hydrogen pressure at the purge side was varied during this experiment.

The PERMCAT was operated with an impurity inlet activity concentration of 206 kCim^{-3} and an impurity flow rate of 0.00168 m^{3}h^{-3}, leading to an initial impurity outlet activity of about 6 Cim^{-3}, determined by grab sampling and subsequent scintillation measurements after passing the gas from the grab sample cylinder through an oxidation catalyst and a bubbler. Further details are given in Table 1.

Table 1: Experimental details of the PERMCAT test illustrated in Figure 3.

Gas composition [%]	8% Q$_2$, 6% CQ$_4$, He
Activity concentration (Impurity inlet)	Q$_2$: 84 kCim^{-3}, CQ$_4$: 88 kCim^{-3} Total: 206 kCim^{-3}, $\approx$ 9% T
Impurity feed pressure	0.12 MPa
Hydrogen outlet pressure	20 to 100 hPa
Impurity flow rate	0.00168 m^{3}h^{-3}
Hydrogen purge flow rate	0.00180 m^{3}h^{-3}
Activity concentration (Impurity outlet)	6 Cim^{-3} $\rightarrow$ 0.3 Cim^{-3}
Tritium concentration (H$_2$ purge outlet)	$\approx$ 9% T
Amount of tritium recovered during run	2 g

As expected from mathematical modeling a stepwise increase of the hydrogen outlet pressure reduces the impurity outlet tritium concentration. The observed time constant of about 40 min is typical for the PERMCAT unit and results in a steady state after about 200 min. At t = 46 h the system was switched to purging for several hours and then valved back to proceed the test. Finally, at a hydrogen outlet pressure of 10 kPa (not displayed in Fig. 3) a tritium concentration of 0.3 Cim^{-3} at the impurity outlet was reached. In total about 2 g tritium were recovered during this test.

The tritium experiments with the PERMCAT component currently installed in the CAPER facility have shown that the unit can be employed for final clean-up of tritiated gases with quite a variety of compositions. However, carbon oxides present in the feed gas are unavoidably converted to methane, and these unwanted side-reactions are reducing the throughput of the unit for a given decontamination performance. This should be taken into account when sizing the PERMCAT for the TEP system of ITER.

No reference process is chosen yet to recover tritium from flakes and co-deposits on PFC's. Most likely tritium will need to be recovered from highly tritiated water. Experiments with a single tube PERMCAT reactor have proven the concept to process water vapor at high partial pressures. The experiments will be continued with units having an improved mechanical design.

Staff:

B. Bornschein
C. Corneli
M. Glugla
K. Guenther
H. Kissel
T.L. Le
P. Schuster
K.H Simon

TW3-TTFD-TR 31
Improvements to the Mechanical Design of the PERMCAT Component

The third of the three stage CAPER process for detritiation and recovery of tritium from to-kamak exhaust streams and different gases appearing in the Tritium Plant of ITER is based on countercurrent isotopic swamping in a so-called PERMCAT, which combines heterogene-ously catalyzed isotopic exchange reactions with hydrogen permeation through palladium / silver membranes. The high efficiency of the technique has been shown in quite a number of experimental campaigns with single-tube and multi-tube membrane PERMCAT's, in which decontamination factors of 10^4 to 10^5 have been measured for gases containing tritiated methane, tritiated water or tritiated molecular hydrogen isotopes mixed with helium, nitrogen or carbon oxides. However, since palladium /silver membrane tubes show a significant dilata-tion upon uptake of hydrogen isotopes finger type tubes are employed so far, leading to a rather complicated mechanical design of the PERMCAT with three coaxial tubes.
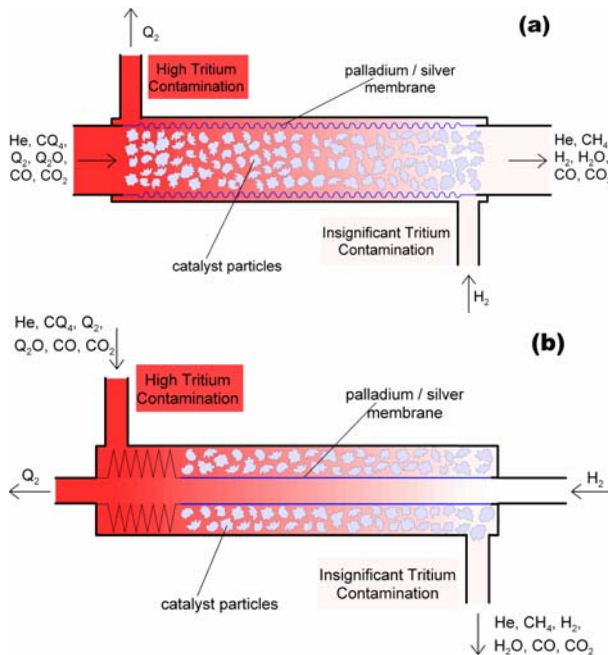
Fig. 1: Principle layout of two coaxial tube PERMCAT's.

In order to simplify the design and to achieve a two coaxial tube design bellows type palladium /silver tubes have been pro-cured. The process parameters to fabricate corrugated thin wall palladium / silver tubes with crack free convolutions and without axial cracks have been experimentally de-termined with a number of palladium / sil-ver tube samples annealed at different temperatures and times to produce a duc-tile material and to achieve a grain size distribution suitable for the corrugator tool. A sufficient number of bellows type palla-dium / silver tubes are now available for the manufacture of PERMCAT's with different design. The principle layouts are shown in Figure 1.

While the PERMCAT in Figure 1a is based on a palladium / silver bellows tube the design in Figure 1b shows a stainless steel bellow to cope with the varying length of the membrane tube.

Two type (a) units have already been pro-duced in the main workshop of the For-schungszentrum. A picture of the different parts just before final assembly and weld-ing is shown in Figure 2.

The permeability of the bellows type palla-dium / silver tube was experimentally tested and found to be within the expected range. The next tests will focus on the con-

Fig. 2: Picture of two coaxial tube PERMCAT parts before final assembly.

traction / expansion properties under hydrogen uptake at different temperatures to define the appropriate mechanical preloading (if necessary at all) of the bellows type palladium / silver tubes. This will eventually minimize the strain in the tube during operation in the PERMCAT of the final design. Performance tests with PERMCAT's of different designs will be carried out in parallel.

Staff:

S. Welte
M. Glugla
R. Wagner

TW1-TTF/TEP 13A
Self-assay, Fast Delivery Tritium Storage Bed

TW3-TTFD/TR 33
Determination of Isotopic Effect during Rapid Delivery from Storage Beds

In the present design of the Storage and Delivery System of the ITER Tritium Plant deuterium, tritium and their mixtures are stored in hydrogen storage beds with a storage capacity of 100 g. During plasma operation it is required that deuterium-tritium gases with well defined ratios of D/T are supplied by the different hydrogen storage beds. Due to isotope effects the composition of the hydrogen gas mixture supplied by the getter bed may be different from the one absorbed in the getter and may even change during unloading of the bed.

At the Forschungszentrum Karlsruhe a 1:1 prototype of ITER hydrogen storage bed with a capacity of 100 g tritium and a target supply rate of up to 200 Pam^3s^{-1} was designed and manufactured. The getter bed is currently filled with zirconium-cobalt and is installed in an experimental rig coupled with a micro gas chromatograph in order to perform tests under different operation conditions and to characterize the possible isotope effects.
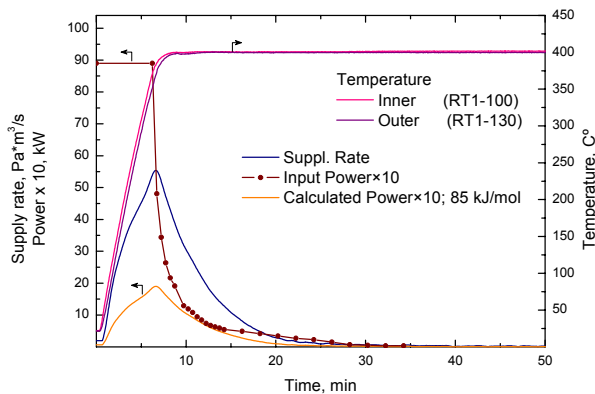
Fig. 1: Supply rate during rapid desorption.

Absorption- and desorption runs with hydrogen and hydrogen/deuterium mixtures were performed in order to investigate the supply rate during rapid delivery. Figure 1 shows an example of the results from a desorption experiment. Initially the zirconium cobalt getter bed was loaded with 18.2 moles of hydrogen as hydride $ZrCoH_{2.8}$. Desorption runs were performed by heating the bed from room temperature to 400ºC with the maximum available power (9.1 kW) of the four internal heaters. The blue line shows the gas supply rate by the storage bed. The maximum supply rate of 60 Pa m^3s^{-1} achieved applying a full heating power is significantly below the target value. Further investigations are necessary to validate the reason of the limited supply rate.

The disproportionation of zirconium-cobalt alloy is of concern if zirconium-cobalt storage beds are used in SDS of ITER. Even though conditions for disproportionation have been carefully avoided it was obtained that after 10 absorption-desorption cycles the zirconium-cobalt getter bed looses its ability to absorb hydrogen as shown in Figure 2.

Under dynamic conditions, such as fast desorption of isotope mixtures from hydrogen storage getter beds, significant kinetic isotope effects might superimpose the thermodynamic isotope effect in the metal hydride-hydrogen system, primarily depending on desorption temperature interval and isotopic composition
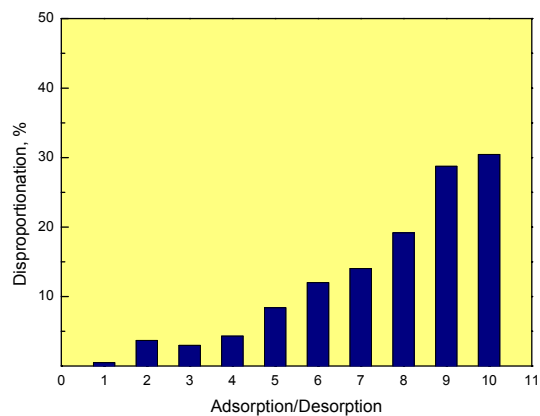
Fig. 2: Disproportionation of the ZrCo GB during 10 absorption/desorption runs.

in the metal hydride. Kinetic isotope effects may as well be of concern in the course of routine operation of the SDS. The composition of the hydrogen gas mixture supplied by the getter bed may be different from the one absorbed in the getter and may even change during

unloading of the bed. Figure 3 shows the variation of the hydrogen isotopes concentrations during the fast deloading of the stored equimolar hydrogen/deuterium gas mixture from the getter bed. At the beginning of desorption the deuterium concentration is higher than in the gas mixture loaded into the storage bed. After a certain time the deuterium concentration decreases below the initial value. Because the heavier isotopes are released preferably the zirconium-cobalt hydride/hydrogen system exhibits a negative apparent isotope effect. It can be seen in Figure 4 that H/D ratio varies up to 20% from the one initially absorbed in the getter bed. Such an isotope effect will have an impact on the final design of the control system of ITER SDS in order to supply deuterium/tritium mixtures of required composition during the plasma shots. Experiments at different heating rates and various gas H/D/T ratios in the gas mixture are necessary to investigate systematically the isotope effects during loading and unloading of the zirconium-cobalt getter bed.
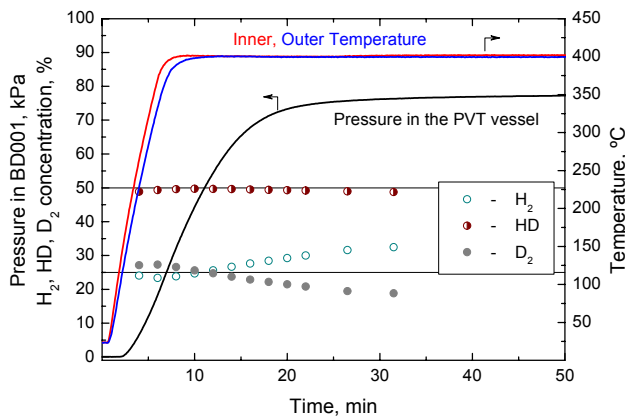
Fig. 3: Desorption of hydrogen/deuterium mixture from the storage bed.
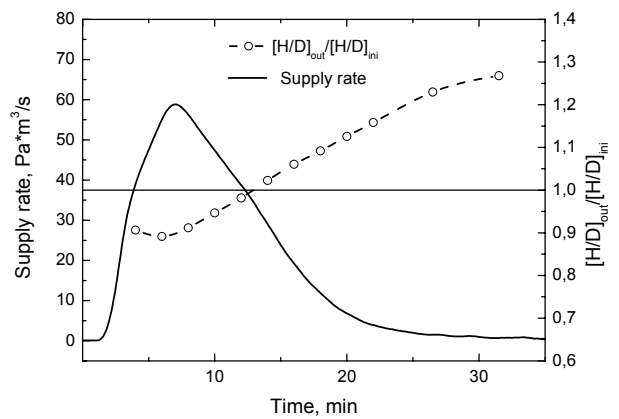
Fig. 4: H/D ratio in the outlet gas stream during fast deloading of the getter bed.

Staff:

S. Beloglazov
R. Wagner
E. Fanghänel
B. Kloppe

TW1-TTF/TR 16
Tritium Recovery from Ceramic Breeder Test Blanket Module

To validate design concepts of tritium breeding blankets as they are foreseen for the generation of fuel material in fusion machines, such as ITER and DEMO, experimental investigation and tests of these concepts are necessary.

In such designs the ceramic breeder materials such as lithium orthosilicate (Li_4SiO_4) will generate tritium by nuclear reaction involving the neutrons produced during the D-T fusion reaction and the lithium atoms of the breeder. The tritium generated in the breeder material has to be recovered by means of a tritium extraction system (TES) in which a helium purge gas is used, which contains up to 0.1% of hydrogen to assist the tritium release from the breeder, taking advantage of the isotopic exchange.

The TES foreseen for the ITER Helium Cooled Pebble Bed (HCPB) Test Blanket Module (TBM) will remove all tritiated species present in the He purge gas in a two-step process:

1) trapping water in a cryogenic Cold Trap (CT), and

2) adsorb all hydrogen isotopes (H_2, HT, T_2) as well as impurities (N_2, O_2) in a Cryogenic Molecular Sieve Bed (CMSB) operating at liquid nitrogen temperature.
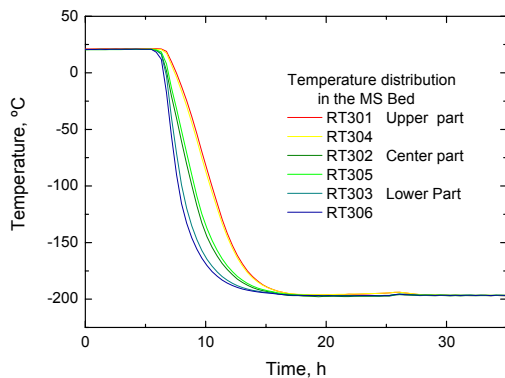
Fig. 1: Temperature distribution in the MS bed during adsorption.

In a first series of experiments the efficiency of a semi-technical scale cold trap (1/6 of the ITER operating conditions) with design features meeting the ITER requirements for water vapour trapping has already demonstrated its ability to remove efficiently water vapour from the He stream down to concentrations of less than 0.02 ppmv, even if the inlet water concentration is in the range of 300-650 ppmv or higher.

In order to validate the second part of the extraction process a tritium compatible cryogenic molecular sieve bed has been designed and manufactured at the Forschungszentrum Karlsruhe and is presently installed in the Tritium Laboratory Karlsruhe (TLK).

To comply with the ITER requirements and to economise on large amounts of He needed for the operation the CMSB has been implemented within a close loop allowing the He to be continuously circulated with flow rates up to 3 m^3 h^{-1}. Parametric studies with CMSB have been performed with flow rates between 2 m^3 h^{-1} and 3 m^3 h-1 and hydrogen inlet partial pressures of 100-200 Pa. Figure 1 shows the temperature distribution in the molecular sieve bed during the cooling of the bed from ambient temperature to 77K and during adsorption at 77K. The temperature profile was measured by set of a six Pt100 sensors placed inside the molecular sieve container. It was confirmed that the adsorbent is uniformly cooled during the adsorption. The pressure drop over the MS bed was less than 1000 Pa verifying the proper sizing of the molecular sieve container, filters and pipe work.

A typical breakthrough curve is shown in Figure 2. The flow rate of helium in this particularly run was 2 m^3h^{-1} and the partial pressure of H_2 was 110 Pa. The pressure in the CMSB was controlled at 1.2 MPa. In the example of the breakthrough curve a mass-transfer zone is represented as hatched area and fraction of the bed capacity used up to the break point as a shaded area. During the adsorption experiment the total amount of He passed through the CMSB was 211 m^3 and 211 l of hydrogen was adsorbed in the molecular sieve. The full ca-

pacity of the bed was calculated as full area above the breakthrough curve and found to be 9.4 moles or 4.7×10^{-4} mol/g. This value is in a good agreement with the adsorption capacity of MS-5A calculated from the adsorption isotherm. Figure 2 shows that the breakthrough curve is steep and has a typical "S" shape indicating a favorable isotherm of MS-5A. It was also found that the unused fraction of the bed is relatively small (12.5 %) allowing to scale up the CMSB to meet ITER requirements.

Fig. 2: Example of the breakthrough curve.
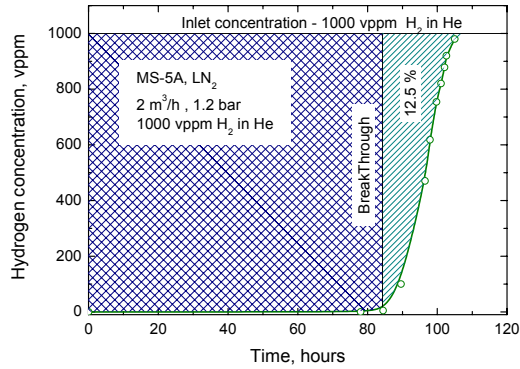
Staff:

S. Beloglazov
R. Wagner
E. Fanghänel
G. Hellriegel

TW4-TTFD-TR 46
Design, Experimental Plan and Procurement of Cryogenic Distillation System for Isotope Separation Tests for ITER

A cryogenic distillation facility will be installed at TLK with the aim to investigate the trade-off between the Water Detritiation System (WDS) and Cryogenic Distillation (CD) for ITER, to analyze the behaviour and the performances of different components and to validate the modelling software related to cryogenic distillation process. Design studies should commence establishing the concept definition of the cryogenic distillation facility that will allow developing the engineering design of all subsystems. A detailed design of main components such as cryogenic distillation column itself (including boiler, condenser and equilibrator), refrigeration unit for the column condenser, cold box layout and layout of enclosure for equipment operating at ambient temperature should be provided as well.

In Figure 1 the block diagram of the TRENTA4 facility is shown, which is under construction at the Tritium Laboratory Karlsruhe (TLK). TRENTA4 is a combination between WDS based on Combined Electrolysis Catalytic Exchange (CECE) and the CD process, allowing parametric studies for both combination and separately for each process. The configuration of the TRENTA4 facility is similar to the configuration of the proposed connection between the CD1 column and WDS from ITER.
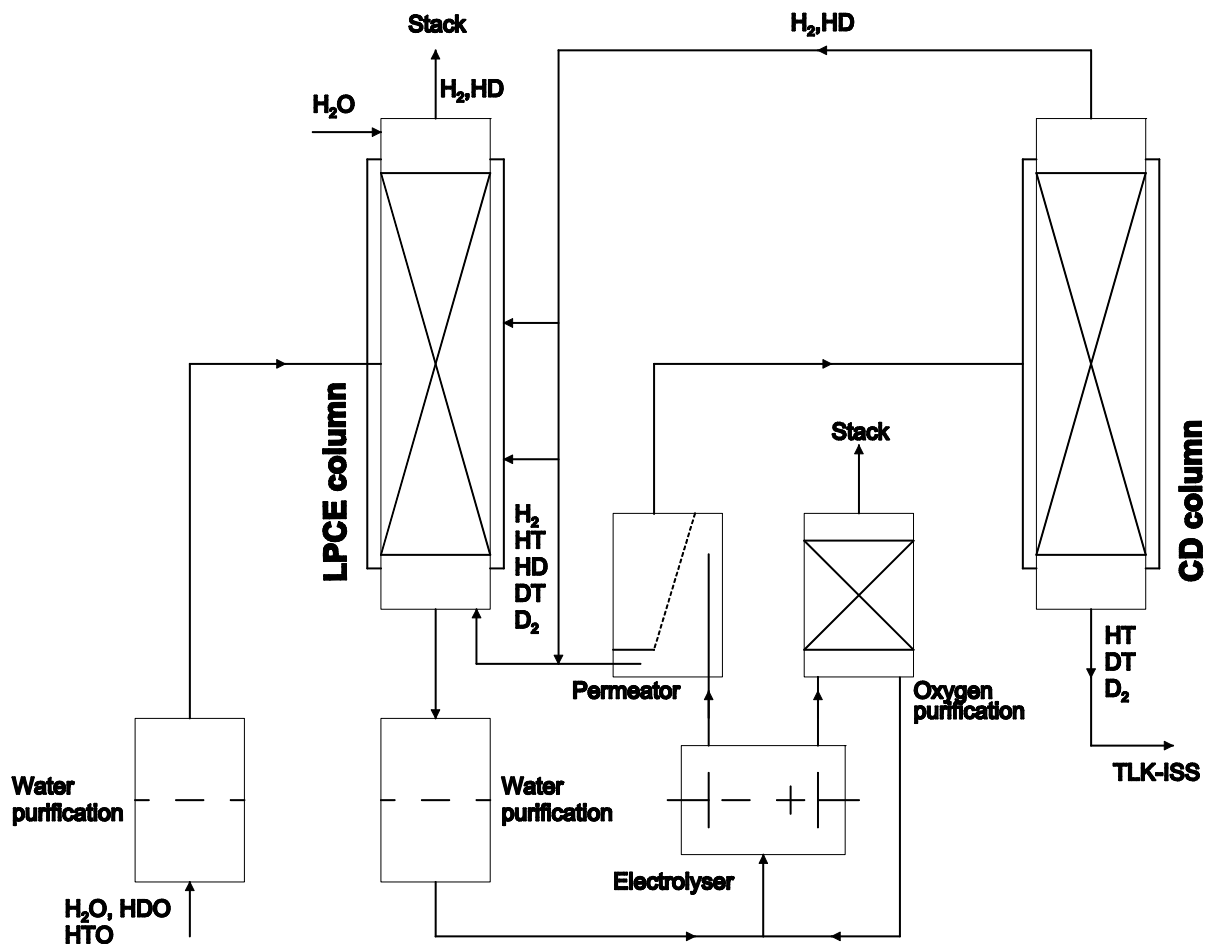
Fig. 1:   TRENTA 4 configuration; CECE-CD facility at TLK.

The necessary development related to the CECE process is covered in the additional task TW4 TTFD TR47. Related to the experimental program on the Cryogenic distillation facility devoted to ITER design, this will be based on two kinds of experiments:

1: Investigation of the separation performances of different packings in cryogenic distillation process and validation of the steady-state mathematical modeling of the process. The separation performances of the cryogenic distillation process at very low tritium concentrations in mixture with deuterium and hydrogen will be experimentally proven in similar working conditions as foreseen for the ITER-ISS CD1 from where the top product should be discharged into the LPCE column of WDS. For this first case, 150 W of cooling power is required at a temperature of the helium stream from the refrigeration unit in the range of 16-17 K.

2: Investigation and validation of the software for the cryogenic distillation process during thermal transitory regimes along the CD column. The data base obtained on the TLK cryogenic distillation facility will allow improving the dynamic modeling software taking into account the thermal fluctuations on different components. Therefore, the influence of thermal inertia of the column and other cryogenic components on separation performances of tritium, deuterium and hydrogen during transient regimes will be investigated in detail, namely regarded to the time response when rapid fluctuation in feed composition occurs.

For this second experiment, the behavior of the combination of the cryogenic distillation column with the refrigeration unit will be investigated for both isotopic and thermal transitory regimes. Therefore, about 250 W of cooling power at a helium stream temperature below 20 K is required. Besides the isotopic composition and temperature measurements along the cryogenic distillation column, measurements of flow-rates and temperatures in the refrigeration will be performed as well.

The general configuration of the refrigeration unit in combination with the CD column for hydrogen isotopes and its adjacent components is presented in Figure 2.
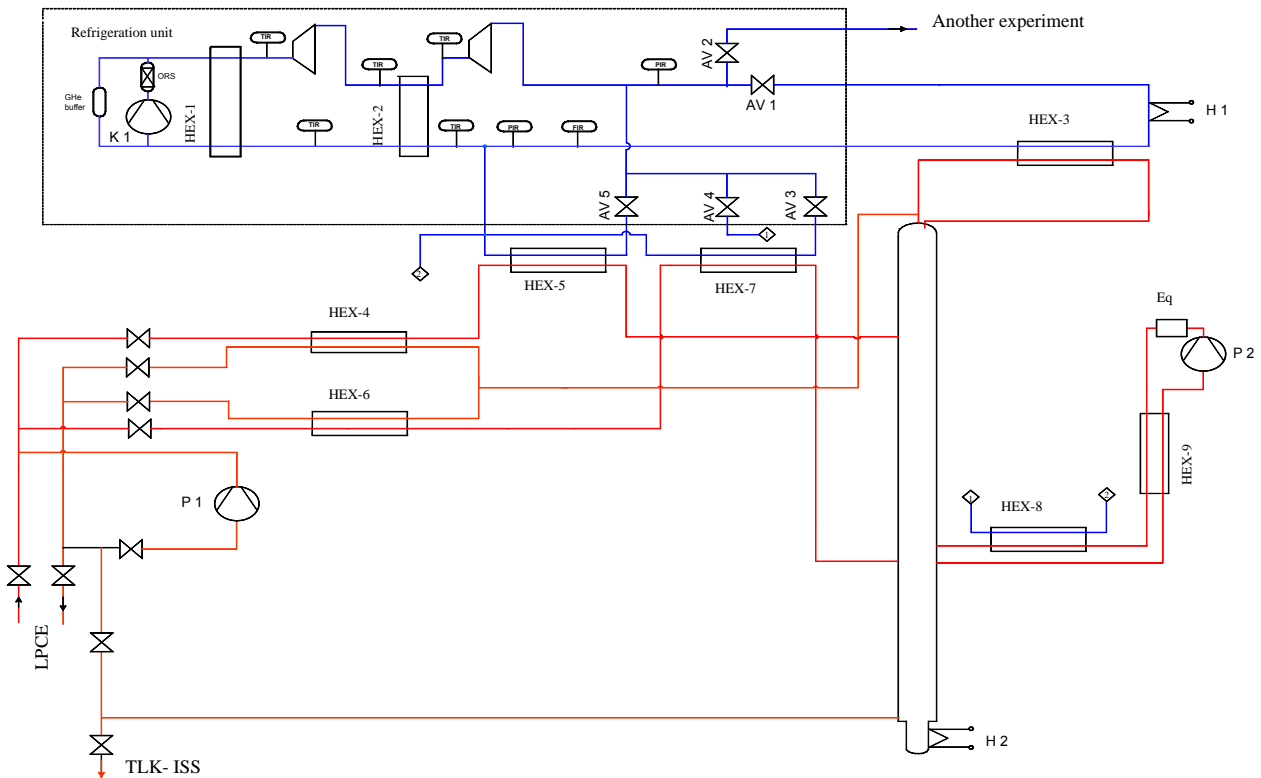
Fig. 2: Configuration of the CD system at TLK.

The refrigeration unit has to provide the cooling power necessary to cool down the condenser, the feed streams of the CD column and the hydrogen stream used in the chemical equilibrator loop.

The CD cold-box comprises the following main components:

- The CD column which for separation performances investigation may be filled with different types of packing. Several temperature sensors and sampling points located along the CD column will allow transitory regimes investigation.

- The boiler necessary to provide the vapor stream inside the CD column.

- The condenser necessary for condensation of uprising vapors, connected to the main helium stream of the refrigeration unit.

- Four heat exchangers needed to cool down or to liquefy the two feeding streams of the cryogenic distillation column.

- One circuit to investigate the influence of chemical equilibration of the vapors at a certain location in the CD column on tritium and deuterium profile along the cryogenic distillation column.

Based on the available capacity of the CECE unit at TLK of 90 $molh^{-1}$ (throughput of the electrolysers), it is envisaged that a fraction of 50%-75% from the electrolysed tritium and deuterium enriched hydrogen stream will be processed in the CD column. Hence, the feed flow in the CD is in the range of 45-65 $molh^{-1}$, with a design feed flow of 65 $molh^{-1}$.

The average tritium activity of the tritiated water to be processed at TLK should be in the range of 0.3×10^{10}-20×10^{10} $Bqkg^{-1}$. In order to investigate the simultaneous tritium and deuterium transfer, the hydrogen and deuterium content should be in the range of 10%-90% at. with T_2 in the range from $1*10^{-5}$ to $1*10^{-4}$ at. The tritium enriched hydrogen and deuterium from the bottom of the CD column of TRENTA4 is envisaged to be sent to the existing on displacement Gas Chromatography (GC) based Isotope Separation System at TLK for final tritium recovery. Therefore, the enrichment of tritium from the feed concentration up to $5*10^{-3}$-$1*10^{-2}$ at. is the duty of the enrichment section of the CD column. Related to the decontamination factor along the stripping section of the CD column, a depletion factor in the range of 10-100 is enough, as higher depletion factor have not significant influences in the separation performances of the LPCE column. Hence, the T_2 concentration in the top product of CD column should be in the range $1*10^{-7}$ -$5*10^{-8}$ at.

The characteristics of the TLK cryogenic distillation system are:

- Condensing power 150 W at 186 kPa;

- Two feed points located to divide the mass transfer part of the column into three equal sections and temperature measurements at each sampling point, necessary for investigations of the dynamic behavior of the CD column;

- An equilibrator loop with a flowrate up to 325 $molh^{-1}$ allowing testing the ITER equilibrators at relevant conditions (ratio vapor flowrate in CD column/equilibrator flowrate).

- Two inter-column liquid flow metering devices necessary for mathematical modeling validation, mainly on transient regimes.

As it can be seen from Figure 2, a conventional helium refrigeration cycle was chosen. The cycle has as active elements two turboexpanders. Two heat-exchangers assure the cold recovery. The standard configuration was modified in the sense that a part of the cold helium stream is used for the CD column condenser and a part is used to provide the cold necessary for the feed stream of the CD column and for the chemical equilibrator loop. The valves arrangement assures control of the refrigeration power delivered for the condenser and al-

lows operating the CD system under transient thermal regimes, as expected in the ITER-ISS. The experiments will permit to determine the influence of the transitory thermal regimes to the refrigeration system itself and to verify the ability of the refrigeration system to provide the necessary amount of refrigeration power for these regimes. A detailed description of the configuration and design of the refrigeration unit was provided.

Besides the conceptual design for the refrigeration unit and CD system, the detailed design of the facility have been done during 2004, consisting of:

- Process Flow Diagram and engineering description;

- Overpressure protection philosophy;

- Process and Instrumentation Diagram description;

- System interfaces have been defined;

- Lists of components have been provided (valves, pumps, temperature sensors, control loops, heat-exchangers, lines).

It is expected that the TLK tailored configuration refrigeration unit will be delivered until the end of 2005. Main components of the CD system (buffer vessels, CD column itself with boiler and condenser, cold-box) will also be manufactured in 2005. Commissioning of the TRENTA4 is expected in 2006.

The CECE system will be in operation in 2005 and will allow proving the achievement of the decontamination factor required for hydrogen that will be exhausted into the environment. During the trade-off studies between the CECE and CD process, as a support for ITER design, the decontamination factor along the LPCE column will be measured against thermal and isotopic fluctuations in the CD column. The influence of feeding location of the returned stream from the CD column into the LPCE for various tritium and deuterium concentrations will be investigated as well.

The combination between CECE and CD processes requires the development of dedicated software for un-steady-state operation. An extension of the existing TRIMO software (task TW3-TI-TR37) with the CECE process is under development and will be validated and improved using the experimental data from TRENTA4.

Staff:

Ion Cristescu
Ioana R. Cristescu

TW4-TTFD-TR 47
Upgrading of LPCE (Liquid Phase Catalytic Exchange) Column for Trade-off Studies between WDS and ISS

Development of a Water Detritiation System (WDS), i.e. configuration, design and perform-ance testing of critical components is essential for both JET and ITER. For JET, a WDS is needed to process tritiated water which was accumulated from operation and also the triti-ated water which will be generated during decommissioning. For ITER, the WDS is one of the key systems to control the tritium content in the effluent streams, to recover as much trit-ium as possible and consequently to minimize the impact to the environment. For both ITER and JET, the WDS is based on Combined Electrolysis Catalytic Exchange (CECE) process.

At the Tritium Laboratory Karlsruhe (TLK), a pilot WDS facility, shown schematically in Figure 1 is currently under design and installation to investigate the achievable decontamination factor and to characterize the behavior of the main components such as Liquid Phase Cata-lytic Exchange (LPCE) column and electrolyser at various experimental conditions.
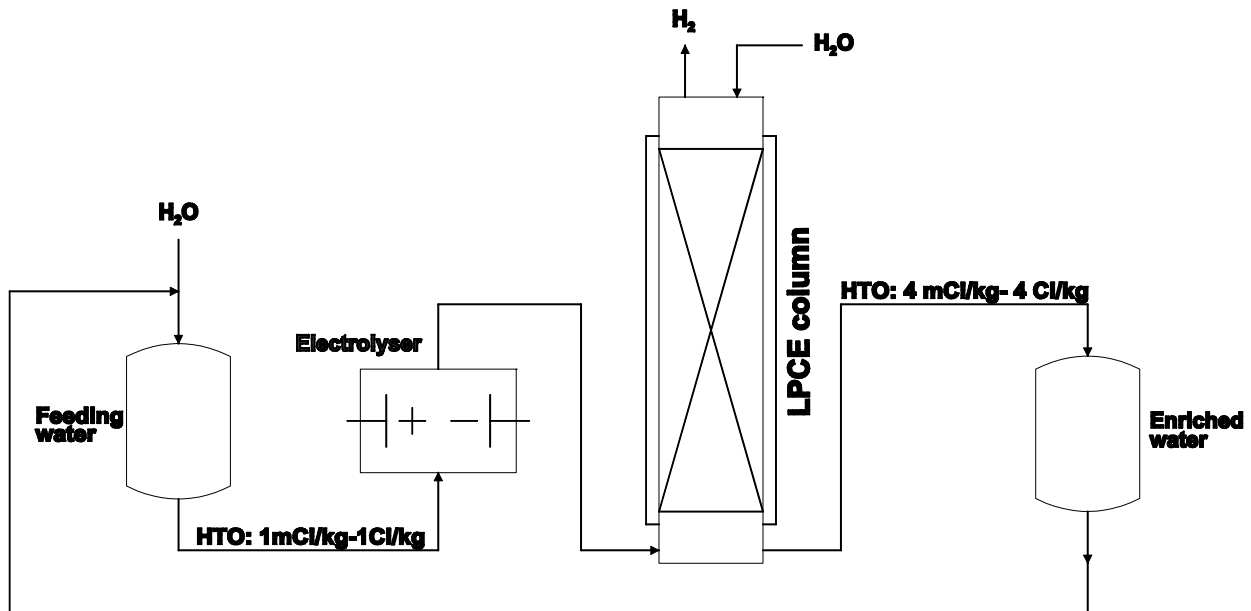
Fig. 1: Water detritiation facility at TLK.

The mechanical design for a LPCE subsystem consisting of a 8 m length column, boiler and condenser has to be developed. Several feeding points along the LPCE column are to be provided, to allow different options for connection with the Cryogenic Distillation (CD) column and further with the TLK existing Isotope Separation System (ISS) for final tritium recovery. A preparatory unit to feed the electrolyser and the LPCE column in closed or open loop have to be designed and commissioned. For the fraction of the gas provided by the electrolysers to be fed into the CD column, a hydrogen purification system based on a PdAg permeator has to be designed. A control and interlock system has to be developed and integrated into the TLK control system. Overpressure and overtemperature protection strategy will be defined and implemented. The new LPCE column (including packing and catalyst) and auxiliary equipment (including permeator, pumps, heat exchangers, hydrogen purification system, tanks, interconnecting tubing and control system) will be manufactured, installed and the sys-tem commissioned with hydrogen and deuterated hydrogen.

The Process Flow Diagrams (PFD) and Pipe and Instrumentation Diagrams (P&ID) of the TLK WDS have been produced.

Based on previous experimental data, a LPCE column of 8 m length was designed with the target of a decontamination factor of 10^4 for tritium. The tritium activity in the water to be processed should be in the range of 4×10^6 Bqkg^{-1} up to 4×10^{11} Bqkg^{-1}.

The mechanical design of all components has been completed and the main components such as the LPCE column itself, condenser, boiler, re-distributors have been manufactured.

The stripping column for the tritium contaminated oxygen stream from the electrolysers has been designed, manufactured and partially installed.

The control system for the LPCE column, oxygen stripping column and electrolyser unit was developed and is partially manufactured and commissioned.

The electrolysis unit consists of the two solid polymer electrolysers of 1 Nm^{3}h^{-1} each and is already installed in a ventilated enclosure as shown in Figure 2. The six vessels needed for closed loop operation of the CECE facility have been designed, manufactured and installed and can be seen in Figure 2.

Fig. 2: Ventilated enclosure for the electrolysis unit and feeding vessels.

The separation performances of the LPCE column will be investigated under different operation conditions. For several parameters (e.g. pressure, temperature, feed water composition) the experimental plans are under development. The plan for integrated testing of the two systems is currently under development in order to allow obtaining necessary experimental data for the decontamination factor achievable along the LPCE column when concentration fluctuations within the CD occur.

The previous measurements of mass transfer performances of different catalyst/packing mixtures investigated at TLK have shown dependence on deuterium presence in the LPCE process. The separation performances along the LPCE column will be measured against different operation conditions such as the feed composition, pressure and flow rates of gas, water and vapours along the column. The experimental results will be compared with the values predicted by a mathematical model developed at TLK.

Staff:

I. Cristescu
Ioana R. Cristescu
S. Welte
W. Wurster
P. Schäffer
G. Hellriegel
R. Wagner

TW4-TTFD-TR 42
Analysis of Gases from Fusion Devices with Carbon PFC's

A knowledge of the expected impurity species and their respective concentrations is of primary importance for the design of Fuel Cycle systems (especially the Torus Exhaust Cryopump and Torus Exhaust Processing systems (TEP)) and in defining the parameters for related R&D. Of particular relevance to cryopumping are data on higher hydrocarbons (-C7 and above), water and species with similar volatilities. This is also of utmost importance with respect to tritium inventory control, as these species may have a high tritium content due to isotope exchange of the hydrogen atoms [1]. For TEP, the presence of elements such as S, halogens and other components which might poison permeators and/or catalysts is critical. While data from other devices could differ from ITER, it will still be a valuable indication which should be assessed for its relevance and, where considered necessary, investigated experimentally.

The ITER design has recently seen a significant reduction in fuelling rate, however the impurity content as specified for the exhaust gas mixture remained the same in absolute numbers. So, in the current design this quantity (33 (Pa·m³)/s impurity plus 120 (Pa·m³)/s fuel) does not seem to be reasonable anymore. It is therefore essential to quantify the composition and the amount of impurities. This task will for the first time provide confirmed input to the data base for the reference composition of the ITER exhaust gas, mainly focussing on the impurity fractions, which may have a negative impact on the performance of the ITER Fuel cycle system.

To achieve this, it was intended to collect gas samples and analyse them with mass spectrometric and/or gas chromatographic methods. Machines such as ASDEX and TEXTOR will be used as sources of the gas samples. In the meetings with the operators, it turned out that getting a representative gas sample and having a reliable off-line analysis is quite a challenge and considered to be close to impossible, especially for the expected low contents of most of the interesting species. Consequently, it was agreed to go for an on-line mass spectrometer approach. For ASDEX, a wealth of mass spectrometric data (during shot and of the cryopump regenerated gas) is available (standard resolution), which is planned to be investigated. For TEXTOR, one pumping port will be equipped with a mass spectrometer to measure during the shots. Contacts with other machines are also under way (JT60-U and TORE SUPRA).

As an alternative procedure, it was proposed to set up a refrigerator-cooled device with a charcoal sample to simulate most neatly the ITER cryopump situation. Such a cryogen-free cryopump would be easy to operate and could take representative samples. The impurity species of interest do still stay sorbed at charcoal even under ambient temperatures. Thus, it would be no problem to transport the contaminated charcoal sample to an analytical lab for further analysis (most probably for Thermal Desorption Spectroscopy) without falsification. Possibilities to include such a device in ASDEX and TEXTOR are under preparation.

Staff:

Chr. Day

Literature:

[1] V. Philipps et al., Overview of recent work on carbon erosion, migration and long-term fuel retention in the EU fusion programme and conclusions for ITER, IAEA Fusion Energy Conference, Vilamoura, Portugal, Nov. 2004.

TW4-TTFD-TR 44
Inactive Tests of Selected SDS Control Loop Performance under Typical ITER Operating Conditions

ITER will require various gas mixtures to be delivered to the torus subsystems, i.e. Gas Injection Systems, Pellet Injectors and Neutral Beam. The ITER Tritium Plant is to supply various gas streams to these systems, both hydrogen isotopes and impurity gases. For neutral beams pure hydrogen or deuterium is required. For gas puffing and pellet injection gas mixtures are required and ITER will have gas valve boxes to produce and control the final mixtures required for plasma operations. 7 gas valve boxes are planned for gas puffing and 6 for pellet injection. The Tritium Plant will supply basic mixtures of hydrogen isotopes to the gas valve boxes.

As the final mixing of gases will be performed at the gas valve boxes, the interface between the gas valve boxes and the tritium plant in terms of gas composition, data exchange etc. is being examined to allow the parameters of control loops inside the Tritium plant to be defined. When this has been performed the experimental program will proceed.

Staff:

C. J. Caldwell-Nichols

EFDA/04-1142
Development of a Procedure for Global Fuel Cycle Tritium Inventory Determination

The objective of the task is to develop an adequate procedure of tritium accountancy in the ITER Fuel Cycle, to identify any aspects that require further investigation, and to assess the times needed to carry out each step of the accountancy process.

In ITER, the Fuel Cycle (FC), the Vacuum Vessel (VV) and the Hot Cell building will constitute a single tritium Material Balance Area (MBA). The global tritium inventory of this MBA at any selected time can be derived from the previous determination by measuring all tritium quantities entering and leaving the MBA and calculating the quantities of tritium created (by breeding) and consumed (by fusion reactions and decay) within it. This depends on the fact that reliable measurements and/or calculations of each of these source terms can be made.

The total MBA tritium inventory at any selected time (TT) can be derived from:

$$\mathbf{T_n = T_{n-1} - T_{Bu} - T_D - T_L - T_E + T_I + T_{Br}} \qquad (1)$$

Where: T_{n-1}- total tritium inventory at previous determination, T_{Bu} -tritium burned, T_D - tritium lost by decay, T_L -tritium leaving plant in effluent streams, $T_{I/E}$ - tritium imported/exported from plant, T_{Br} -tritium bred.

At this moment in time, only little information is available to the accuracy with which the amount of tritium burned can be measured (from plasma diagnostics), however this will have to be defined in the subsequent deliverables within the present task. Tritium lost by decay will be computed from total instantaneous inventory. Tritium leaving the plant in effluent streams will be continuously monitored at all potential discharge points. Tritium imported/exported from the plant will be accounted for by assaying the tritium batch and shipping container as received and after deloading by calorimetry. Tritium bred will be estimated from plasma diagnostics, breeder material and neutron multiplier, first wall and purge gas operating parameter records. Considerations about the accuracy of these methods to determine the tritium bred will have to be defined in a later stage but also within the present task.

In the considered MBA for ITER, the total tritium inventory can be divided into 4 categories:

$$T_n = M_{in} + T_{in} + M_{ex} + T_{ex} \qquad (2)$$

The method for global tritium inventory determination is based upon the idea that the gases in Fuel Cycle systems will be transferred to the self assay beds of the SDS. As these beds will only accept chemically pure hydrogens, gases containing impurities will be processed through Torus Exhaust Processing TEP and ISS. As a preliminary estimate, the tritium inventory determination procedure comprises a number of steps and will last several days.

A. Transfer mobile Fuel Cycle inventories to SDS.

As all the amount of tritium that can be withdrawn from other systems is fed in ISS, it is necessary to evaluate the tritium inventory contained in the Cryogenic Distillation columns by 'milking down' of tritium. A milking-down procedure of the ISS by replacing tritium with additional deuterium which has to be fed in the system is currently under development. Additionally the time required to milk down the ISS will be provided by dynamic modelling of the Fuel Cycle for ITER, TRIMO (task TW3 TI TR37).

B. Measure mobile inventory of the Fuel Cycle

In the specially designed beds of the SDS, calorimetric determinations of tritium are made by passing a helium stream of fixed mass flow rate through a closed circuit in each bed and measuring the temperature rise.

C. Recover in-vessel mobile inventory

In order to minimize the in-vessel inventory before restart of plasma operations and thereby maximize the operating time until the next inventory determination, the vessel walls should be conditioned and the torus exhaust cryopumps fully regenerated after the mobile ex-vessel tritium inventory determination has been made.

D. Measure mobile inventory of the in-vessel

A second inventory determination shall be made to determine the mobile in-vessel inventory and therefore also the effectiveness of the recovery procedures. This could be made by directing the gases released from in-vessel components, after processing, to a dedicated group of storage beds and repeating the inventory measurement.

Estimate trapped inventories

After performing steps A to D, the trapped tritium inventory in-vessel and ex-vessel can be computed from equation (2). The build up of tritium in specific components will be documented as operation of the ITER machine proceeds, to enable the evolution of these inventories to be correlated against operating parameters.

Considering the procedure for tritium inventory determination presented above, a logical flow chart with the necessary operations will be produced. The general approach will be to assess the extent to which the necessary steps can be carried out in parallel, together with an assessment of time for each step, resulting in overall time estimate (a generic time-schedule). This will be done in conjunction with the development of procedures to assess residual tritium inventories in process components after transfers to SDS.

Staff:

Ioana R. Cristescu
L. Dörr
Ch. Caldwell-Nichols

Safety Analysis and Environmental Impact

TW4-TSS-SEA 5.2
Dust Explosion Experiments in DUSTEX Facility

Objectives

For the characterization of dust explosion hazards in ITER, standard explosion parameters – so called explosion indices – of ITER-relevant dusts are to be measured in order to rank them among other industrial dusts. The measurements also provide an estimation of possible pressure loads in ITER in case of a dust explosion and an evaluation of the lower explosive concentrations and typical ignition energy necessary to explode the dust cloud which can be formed in case of LOCA or LOVA involving an air and/or steam ingress into the ITER vacuum vessel. One of the objectives of the work is to continue the standard tests of ITER-relevant dusts with focus on hydrogen containing atmospheres in ITER.

Another issue of the work is a result of the "Feasibility study for definition of large scale hydrogen and dust explosion experiments in FZK facilities A1, A3 and A6" (Subtask TW4-TSS-SEA 5.5), where it is shown that, in order to address the dust explosion hazard in ITER adequately, it is necessary to develop a computer code capable of modeling the combustion process under all possible conditions. An approach proposed there is to use an existing code for hydrogen combustion which uses a semi-empirical burning model with efficient burning rates in the combustible media. With this aim a new facility is designed and will be constructed in order to measure the efficient burning rates of the dusts in air using the method of an open-end combustion tube.

Background

A series of tests were performed in a standard apparatus with graphite and tungsten dusts and their mixtures to measure their explosion indices. A facility, called DUSTEX, was built up consisting of a standard 20-l sphere and supporting infrastructure: vacuum, gas filling, sphere cooling, test performance control and measurement systems. Three graphite dusts differing in characteristic particle size were tested. The tests were performed at standard conditions: the dust cloud was formed inside the sphere in air atmosphere at 1 bar initial pressure and room temperature and with strong chemical ignitors of several kJ energy release to explode the dust cloud. The maximum overpressures, rates of pressure rise, lower explosive concentrations and explosibility of the dusts were measured. It was shown that graphite dusts of some micron particle size could generate pressure loads which might cause heavy loads on some ITER VV components. The tests were continued with tungsten dust of one micron particle size, and its mixtures with four-micron graphite dusts. The same explosion indices were measured. One of the dust mixtures appeared to explode faster than its constituents.

An attempt was made to measure the laminar burning rates of the graphite dusts using a Bunsen burner method. The burner consisted of a vertical metal cylinder of 20 mm diameter and 200 mm length, where a continuous upward directed dust/air flow was arranged. A flame holder – a small metal ring heated electrically – was placed at the top to ignite the flow. If ignited, the flow would burn forming a flame cone; the laminar burning rate could be calculated from the cone angle and the upward flow velocity. For the tested dust-air mixtures the flows were not ignited up to the flame holder temperatures about 800 C. At higher temperatures the convection flows of ambient air induced by the holder destroyed the laminar dust/air flow, so the attempt failed.

Main results

In the year 2004 the main efforts were focused on developing a new method for measuring the efficient burning rates of ITER-relevant dusts, using an open-end combustion tube. The idea is to form a spatially homogeneous dust cloud in a tube with one end closed to keep the

cloud stable and the other end open to ambient atmosphere. After its formation the cloud is ignited at the open end of the tube and the flame propagates to the closed end with combustion products flowing away freely from the tube with no disturbance of the cloud in front of the flame. The observed flame propagation velocity is the efficient burning rate of the dust-air mixture. With this method it is possible to vary not only the dust concentration in air, but also the turbulence level in the cloud, which is known to be one of the most important influencing parameters on dust combustion.

The facility has been designed and manufactured in 2004. It consists of a plastic tube of 2 m length and 15 cm in diameter, connected with a dump tank of 0.5 m^3 volume to receive the combustion products.

To form a dust cloud, a layer of the tested dust is deposited on the tube bottom along the full tube length. At 10-15 mm height over the layer a metal pipe of 15 mm diameter is placed with a number of holes which are directed downwards to the dust layer. The pipe is connected via an electromagnetic valve to a pressure reservoir of 10 l volume filled with air at 20-25 bar. At test begin the valve is opened, providing strong air jets from the pipe holes to the dust layer, mobilizing the dust and forming the cloud. Before the test the tube is partly pre-evacuated to provide a specific initial pressure in the cloud. The tube is separated from the dump tank by a thin foil diaphragm. After the cloud is formed, the diaphragm is ruptured, and the cloud is ignited. As the tube is transparent, the process of flame propagation can be recorded by high-speed video. An ion-probe diagnostic technique is tested to measure the time-of-arrival of the flame front inside the tube.

The tests in DUSTEX facility are continued to study the dust explosion indices in hydrogen-containing atmosphere. They model a scenario of combined combustion of hydrogen and dust in ITER. In this case the dust is ignited not by a strong local ignition source like 2 kJ ignitors in previous tests, which might be unrealistic in ITER. Here the dust explosion can be initiated by a hydrogen combustion induced by a weak ignition source like an electric spark.

For these new experiments the gas filling system of the DUSTEX facility has been modified. Now it provides not only compressed air, but also hydrogen to fill the sphere, and nitrogen and oxygen separately to model different atmospheres possible in ITER. Furthermore, another ignition system was installed in the sphere. It provides an electric spark between two electrodes at the sphere center. The ignition voltage is 1-5 kV, applied to the electrodes at 1 to 3 kHz frequency. The spark circuit is fast at the test start with variable delay and cut-off after a variable time. In this way the spark voltage, duration and hence energy can be varied. The tests have been started with four micron graphite dusts; the experimental variables are dust concentration in air, hydrogen content in air, and ignition energy.

Summary

A new facility has been constructed to measure the efficient burning rates of ITER-relevant dusts with the open-end-tube method. The test tube is 2 m long and 15 cm in diameter. It allows cloud formation inside the tube by mobilizing a pre-deposited dust layer on the tube bottom by a row of air jets directed downwards to the dust layer. The experimental variables are dust concentration, initial pressures, and turbulence level. The DUSTEX facility has been modified to measure the dust explosion indices in hydrogen-containing atmospheres with electric spark as the ignition source. The tests are currently being performed.

Outlook

The tests with the open-end combustion tube will start next year with graphite and tungsten dusts to measure the efficient burning rates. The tests in the DUSTEX facility are planned to continue with CO_2 to investigate CO_2 - dilution as potential mitigation measure.

Staff:

K. Arheidt
S. Baur
A. Denkevits
B. Kaup
V. Krieger

Literature:

[1]   A. Denkevits, S. Dorofeev: Explosibility of fine graphite and tungsten dusts and their mixtures. 5th Internat. Conf. on Hazards, Prevention and Mitigation of Industrial Explosion (ISHPMIE), Krakow, PL, October 10-14, 2004

[2]   A. Denkevits, S. Dorofeev: Dust explosion experiments. Measurements of explosion indices of tungsten dusts and graphite-tungsten dust mixtures. Wissenschaftliche Berichte, FZKA-6987 (Mai 2004)

[3]   A. Denkevits, S. Dorofeev: Dust explosion hazard in ITER: explosion indices of fine graphite and tungsten dusts and their mixtures. 23rd Symp.on Fusion Technology (SOFT), Venezia, I, September 20-24, 2004

TSS-SEA 5.5
Validation of EU Safety Computer Codes and Models

TW4-TSS-SEA 5.5 D1 + D 4
Feasibility Study for Definition of Large Scale Hydrogen and Dust Explosion Experiments in FZK Facilities A1, A3 and A6

Objectives

Two combustible substances have been identified which can pose explosion hazards in ITER: (a) hydrogen produced from steam-metal reactions or desorbed from cryopumps, and (b) various dust species of first-wall materials (C, Be, W). The control of these combustible substances has received a high importance because explosions can act simultaneously as driving force for mobilization of the tritium inventory and as direct threat to the integrity of the vacuum vessel or interconnected systems. A strategy for addressing these safety issues has been proposed which involves setting of administrative tritium, hydrogen and dust limits for the ITER operation, monitoring of the respective inventories in the vacuum vessel during operation, removal of substances when the limits are approached, and limiting bulk Be-surface temperatures.

The major problem in the safety analysis of complex industrial installations like ITER is that many complicated accident scenarios can be envisioned which lead to a large variety of initial and boundary conditions for the combustion process. In general, the combustion regime and the resulting pressure load can react sensitively to some of the parameters, like for instance the geometry of the enclosure, obstacles, the initial fuel distribution (hydrogen or dust), initial temperature and pressure. Realistic and not too conservative predictions of the consequences of a combustion event can only be made with best estimate three-dimensional Computational Fluid Dynamics (CFD) codes which adequately model the governing physical processes. The term "best estimate" means here that not all of the physical length scales in the described problem can be resolved, but that the implemented model has been carefully validated against experimental data on various scales and that the validity domain of the model is well defined and proven.

Therefore the control of hydrogen and dust hazards in ITER requires the development and verification of new three-dimensional numerical tools for the mechanistic simulation of hydrogen and dust explosion under ITER-typical large scale conditions.

Main results

Large-scale experiments are proposed addressing the hydrogen and dust explosion hazard in ITER in case of LOCA or LOVA. The experiments are to study hydrogen-air combustion, dust mobilization, dust explosion, and combined hydrogen and dust explosions for ITER relevant scale and pressures. The experiments are planned to be performed in the HYDEX (HYdrogen and Dust EXplosion) facility at FZK, which is a combination of two large test vessels of about 150 m^3 total volume. ITER specific initial and boundary conditions can be simulated in these vessels.

An analysis strategy for modeling of hydrogen and dust explosion in case of severe accident in ITER is proposed, based on the experience gained in hydrogen safety studies for fission reactors. The strategy consists of four main steps: combustible mixture generation, evaluation of hazard potential, combustion process simulation, and consequence analysis. The main goal is to elaborate 3D computer codes capable to model accidental scenarios for ITER explosion hazards. Covering a wide variety of scenarios realistically without too conservative predictions of expected consequences can only be made with best estimate three-dimensional CFD codes which adequately model the governing physical processes. In

view of this goal, large scale experiments are an essential step to verify and validate the code models for ITER typical conditions.

For addressing the hydrogen phenomenology in ITER, research work has been done on the limiting conditions for fast deflagration and detonation regimes under the conditions typical for ITER. The possible regimes of hydrogen combustion in the ITER VV geometry with a typical initial hydrogen distribution have been analyzed. Now large-scale tests are necessary to validate the codes used to model hydrogen combustion under sub-atmospheric pressures. The general objectives of the tests are to evaluate flame acceleration and DDT criteria at larger scales, to study the hydrogen combustion regime for ITER relevant scale (100 m^3), initial pressure (below 1 bar), and typical gas compositions, and to evaluate realistic combustion loads. The results of large-scale tests will provide the database for adjusting the available hydrogen combustion models to ITER typical conditions.

The dust explosion issue for ITER is at the very beginning of its investigation. Though a large number of studies on dust explosions have been performed addressing safety issues in dust-dealing industries, their results are not applicable directly for the evaluation of possible loads in ITER. The ITER dust problem is specific: the dusts are of sub-micron particle size, have low content of volatiles, some might contain large amounts of hydrogen, the ITER atmosphere is at subatmospheric pressures, and it can contain hydrogen, which participates in the combustion process itself. Up to now, only small-scale tests have been performed giving a general impression on possible pressure loads from ITER-relevant dust explosions. The tests demonstrated the importance of the dust particle size, showed the necessity of a strong ignition source to explode the dusts, and measured the lower concentration explosion limits. Other important issues remain to be studied in medium-scale experiments (which are considered here as a part of the feasibility study for large-scale tests). Their objectives are to study the conditions of stable flame propagation in ITER-relevant dust/air mixtures, the limits/conditions for flame acceleration; conditions for detonation on-set and detonation propagation, dust cloud ignition by hydrogen combustion/ explosions, and efficient flame velocity measurements.

Conclusions

An strategy for modeling hydrogen and dust explosion in case of severe accident in ITER is proposed based on the experience gained in hydrogen safety studies for fission reactors.

The strategy consists of four main steps: combustible mixture generation, evaluation of hazard potential, combustion process simulation, and consequence analysis. The main goal is to elaborate 3D computer codes capable to model all possible severe accidents under concern for ITER explosion hazard.

Modeling of hydrogen explosions in ITER is possible using existing codes developed to address the hydrogen safety issues in fission reactors. To verify and validate the code models under ITER-typical condition, it is necessary to perform large-scale tests at sub-atmospheric pressures; the large-scale tests on hydrogen combustion can now be well defined.

Concerning the dust explosion problem, an approach is proposed to develop a code based on existing codes used to model hydrogen combustion. In this way several preliminary studies, both theoretical and experimental, have to be performed before the large-scale test conditions can be defined. They are to investigate the conditions on flame propagation in dust-air clouds, to measure the efficient burning velocities, and to implement the dust combustion model into the code.

A roadmap to develop a computer code for modeling hydrogen/dust explosion in ITER is proposed. It includes laboratory-scale experiments to measure the dust explosion indices

and efficient burning rates, and to study the limits of flame propagation; medium-scale tests to study the flame propagation and acceleration conditions; and large-scale tests to validate the modeling codes.

Outlook

Further analysis will be aimed at the techniques to suppress/mitigate the explosion hazard in ITER. The first issue will be a possibility of VV atmosphere dilution with CO_2 to reduce oxygen fraction and lower the flammability limits.

Staff:

W. Breitung
A. Denkevits
M. Kuznetsov
R. Redlinger

TW4-TSS-SEA 5.5 D3 + D6
Validation of EU Safety Computer Codes – Feasibility of Large Scale Experiments

At the present time, a reliable numerical simulation of high current busbar arcs is not possible as available arc models lack of accuracy and improvements are difficult as long as some principle items of busbar arc behaviour as propagation and destruction mechanisms are still not known in detail. For the licensing procedure, EFDA has to consider consequently a possible request for full scale arc experiments and asked for a feasibility study. It should be clarified if a controlled performance of such experiments is possible at all and which would be the suitable facilities to ask for their execution. Also a preliminary estimate of cost and manpower efforts was requested as a basis for future ITER/EFDA task and budget planning.

A completely realistic full scale experiment (in a cryostat under full magnet field conditions etc.) will get extremely expensive. Hence to check for possibilities which could limit costs without loosing relevance for ITER is a key issue for the preparation of such experiments. For the feasibility study, several scientific and commercial facilities were contacted, and for further information, in a few cases also visits to the sites were made. We learned that arc experiments often show a quite statistical behaviour which would reduce the relevance of a single experiment and consequently would enhance costs together with the number of required experiments. The study suggests that full scale busbar arc experiments should be possible in principle. The requirements to have certain experimental boundary conditions will have considerable impact to the choice of a site. E.g. the fact that the large ITER superconducting magnet coils use DC ruled out more or less commercial test labs as they usually do not have high power DC equipment available. But DC is preferable as it is not only more realistic, but also will help much for reproducibility because DC arcs are more stable than AC arcs. University labs could provide the required currents of about 50kA only for ms times. DC industrial applications as electrolysis or steelmaking could provide the required currents for long times, but do not achieve the required voltages of at least about 1kV. However, suitable large flywheel generators with DC equipment are available at most European tokamak fusion sites. Some boundary conditions might be less important but very expensive in realization as probably e.g. cryogenic temperatures. Magnet field surely has an impact to arc behaviour, but here rather direction but full strength may play a role. So one probably can avoid the efforts to have large superconducting coils to simulate a field of several tesla and use only some conductor loops. It would also be easier to perform the experiments in free air instead of looking for a suitable large vacuum vessel including a protection against overpressures. There is a large potential for cost reduction, but it has to be clarified in advance for each simplification step, that relevance for ITER does not get lost. This should be done in small and medium scale experiments where also experience of measurement, observation, design and execution for up to full scale large experiments can be collected.

As these experiments are not standard, they should be planned closely together with the executing site staff to be able to keep specifications and safety requirements of available equipment. Purchase of new equipment will be limited as high investment costs will be hard to justify for only a few experiments. Experience with similar experiments is a preferable point as own knowledge coming from preparing experiments will not reach up to that dimensions. Some preference for fusion sites might be that they are used to work with EFDA/ITER contracts on longer timescales. Specified feasibility studies including detailed technical and cost analysis from several candidate sites should be requested before a final decision for a cooperation is made

Staff:

V. Pasler

Literature:

[1] V. Pasler: First report on feasibility of medium and large scale arc experiments for ITER safety investigations, June 2004, TW4-TSS-SEA5.5/D3.

TW3-TSS-SEA 5.5 and
TW4-TSS-SEA 5.5 D7
Validation of EU Safety Computer Codes and Models

The EVITA condensation experiments at CEA in Cardarache (France) are part of a long-term validation program for several safety codes, which are intended to be prepared for a usage in the licensing procedure for ITER. MAGS-CRYOSTAT represents the FZK contribution. EVITA is a 0.22 m^3 stainless steel vessel that can be evacuated. A reservoir with an inlet system for steam and water injection and a nitrogen cooled cryogenic condensation plate are available for condensation experiments.

For the calculations of non-cryogenic EVITA experiments with MAGS-CRYOSTAT good results were received. However, the non-cryogenic experiments were difficult to analyze. After some changes to the experimental setup to optimize cooling and avoid unwanted heat barriers and flow effects, still no acceptable calculation results could be achieved without using completely unjustified assumptions.
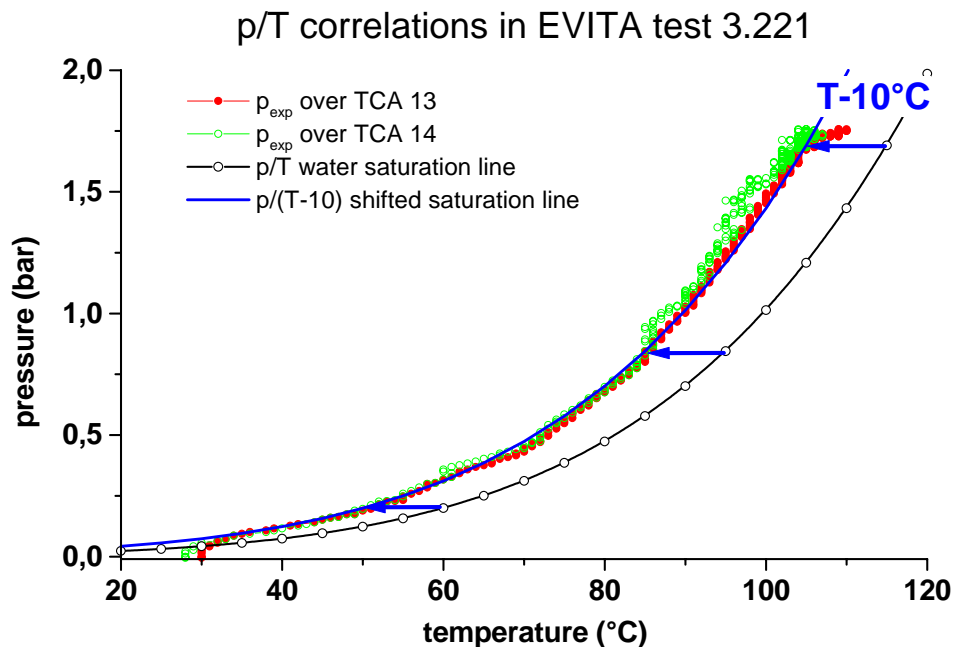
Fig. 1: Correlation of EVITA vessel pressure and temperatures on the cooling tube insulations below the protective lid in comparison to the water saturation line (black curve). The experimental data lay on a curve that is identical to the water saturation line shifted by 10K to the left (blue curve). The data were generated by a transformation ([p(ti),T(ti)], 0 < ti < tmax, -> p(T)) out of a graph similar to fig.2 with the time coordinate eliminated.

The origin of the modelling problems can be detected from a close analysis of the data: The obvious presence of an ice layer at a vessel pressure above the mbar range far away from the steam saturation line p(T) clearly indicates that nonequilibrium conditions are relevant during these experiments. Hence, the previously used equilibrium model is not expected to give reasonable results. Instead, a nonequilibrium condensation model is required. The data analysis allows for further conclusions. A correlation between EVITA vessel pressure and the temperature on the insulating tubes of the nitrogen cooling loop for the cryogenic plate was detected. The tubes are located under a metal cover, the so called protective lid, on the bottom of the EVITA vessel. This cover divides the vessel practically in two parts. The openings are large enough to guarantee pressure equilibrium in both parts, but temperatures in both parts are not necessarily equal. A very interesting result is that the observed correlation looks like a shifted saturation line, see fig. 1. This is a strong hint that

condensation on surfaces in the vicinity of the insulating tubes may be responsible for the vessel pressure with only little direct impact from the cryogenic plate. This is supported from the mass evaluation after the experiment. Here condensed water of unknown origin is found, which probably was condensed at these cold regions. Another quite obvious hint comes from a look on the almost identical experiments 5.51, 5.52 and 5.53. As the initial conditions were the same, the results may indicate the reproducibility of experiments. The reproducibility is not perfect which helps to learn about what is going on. In fig. 2 one can identify almost every detail in differences of pressure curves also for the insulation tube temperatures, however these correlations are not found for the thermometers on the cryogenic plate, see fig. 3. From this observation one may conclude that for a correct calculation of the pressure, an equilibrium model in the tube region could be applied. The cryogenic plate only has an indirect impact to the observed pressure by collecting some part of the incoming mass. From this data analysis it gets clear why equilibrium models based on the cryogenic plate alone had severe problems and worked, if at all, only with artificial assumptions.
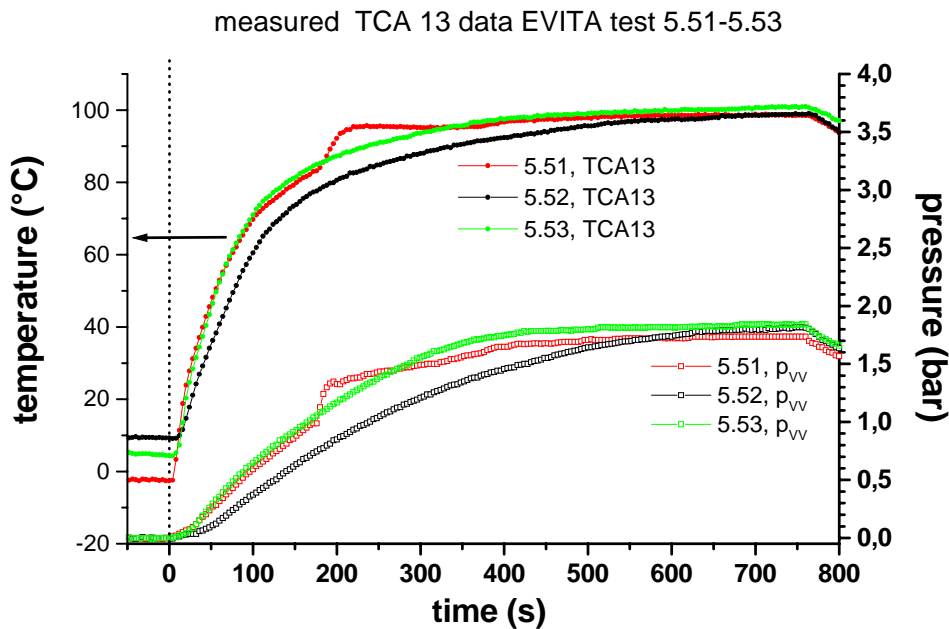
Fig. 2: EVITA vessel pressure and temperatures at thermocouple TCA13 on the cooling tube insulations below the protective lid for three similar runs. Details of differences clearly occur in both datasets. An identical graph could be generated for TCA14, the thermocouple on the second cooling tube insulation.

Two steps are necessary to adapt the calculation model to these findings: First, the vessel volume is split into two volumes with a possibility for mass exchange. This guarantees equal pressures, but allows for different temperatures in the two vessel parts. This step is possible with the present CRYOSTAT code simply from input modification.

The more demanding part is a description for the nonequilibrium condensation process at the cryogenic plate. Literature does not help here and one has to do the modelling more or less from scratch. Presently work is done on a code for the nonequilibrium cryogenic condensation process with a diffusion boundary layer model approach. Fig. 4 shows a first, preliminary result which indicates that this is probably the right way.
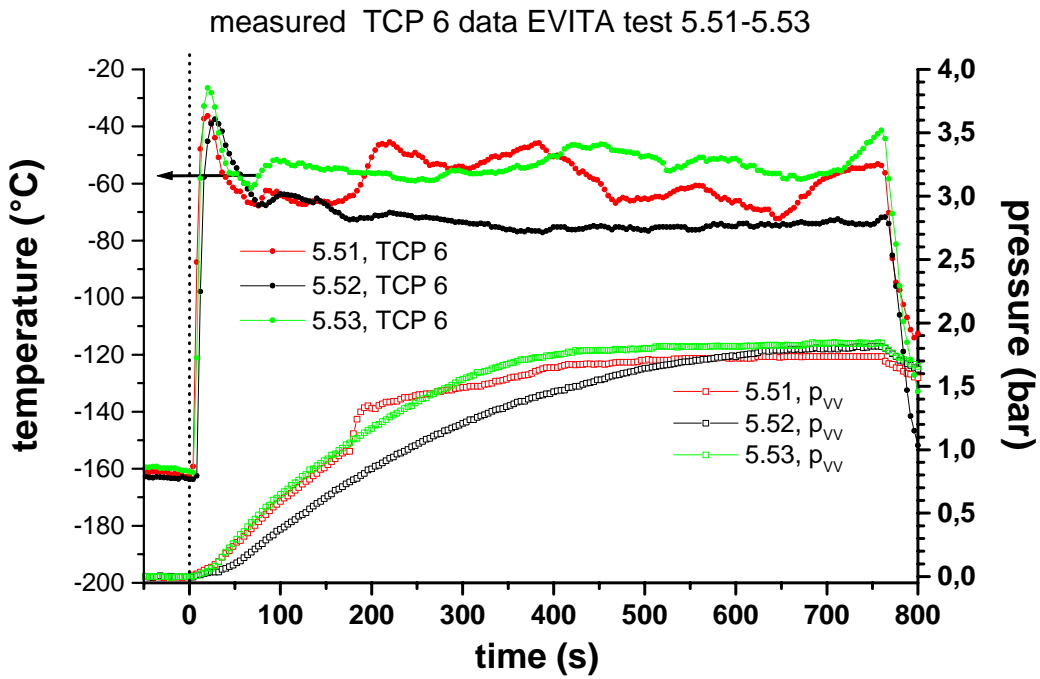
Fig. 3: EVITA vessel pressure and temperatures at thermocouple TCP6 on the cryogenic plate for the same experimental runs as in fig. 2. The correlation between datasets is much weaker than in fig. 2, it vanishes completely for most of the other 7 thermometers on the cryogenic plate not shown here.
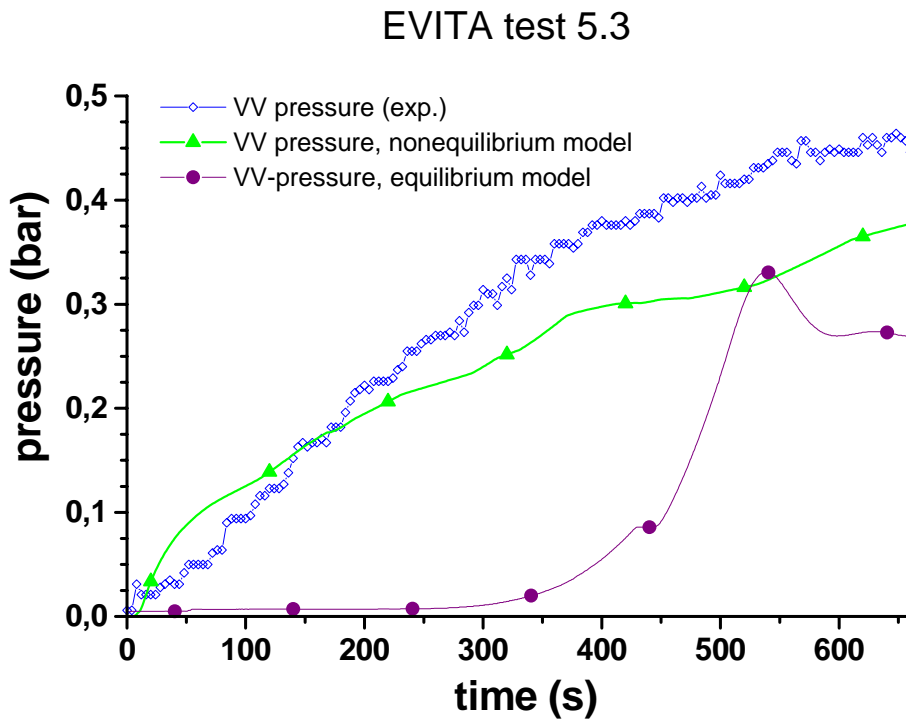
Fig. 4: EVITA vacuum vessel pressure during steam injection time for test 5.3. The first effort with the new model including nonequilibrium condensation and a model for the protective lid area already shows an obvious qualitative improvement of pressure results against the old model which was very successful only for non-cryogenic experiments.

Meanwhile the experimental EVITA campaign proceeded. Now nitrogen is present as an inert gas during condensation. Similarly as described above, a data analysis was done for some experiments. Nitrogen seems to accelerate condensation as final vessel pressures are lower compared to previous experiments with similar steam ingress but without nitrogen. The correlation between cold bottom vessel parts and steam partial pressure is still observed. So the work to match experiments including inert gas is expected to be restricted to modifications to the nonequilibrium cryogenic condensation model.

The principle modelling problems seem to be solved and the experiments under presence of nitrogen will be modelled as soon as the nonequilibrium model works properly for the non-nitrogen cases. It is intended to accompany the future course of the EVITA series with MAGS-CRYOSTAT calculations.

Staff:

G. Bönisch
Y. Ke
V. Pasler

Literature:

[1] G. Bönisch, Report on EVITA Experimental Recalculations and Documentation of MAGS-Module CRYOSTAT, June 2004, TW3-TSS-SEA5.5/D6A (ITER ITA 81-07).

TW3-TSS-SEA 5.4
Busbar Arcs Behaviour and Consequences

TW4-TSS-SEA 5.5 D8 + D9
Validation of EU Safety Computer Codes and Models

High power arcs at the ITER busbars are a possible threat for the cryostat wall which is part of the ITER containment. For licensing questions, this very improbable event must be investigated. Presently no suitable numerical models with reasonable accuracy are available. Model development turned out to be difficult due to low knowledge of arc propagation and destruction behaviour. Small experiments should clarify busbar arc behaviour with regard to model development and validation. Experience from experiments might also valuable for possible requests of full scale experiments from licensing authorities, if numerical efforts are not convincing.
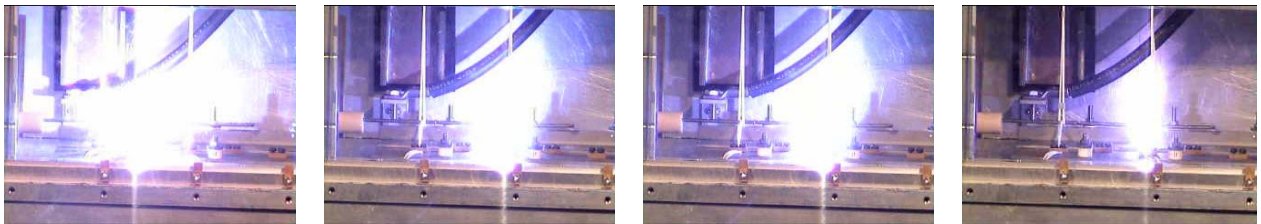
Fig. 1: Picture sequence taken during a pre-experiment.
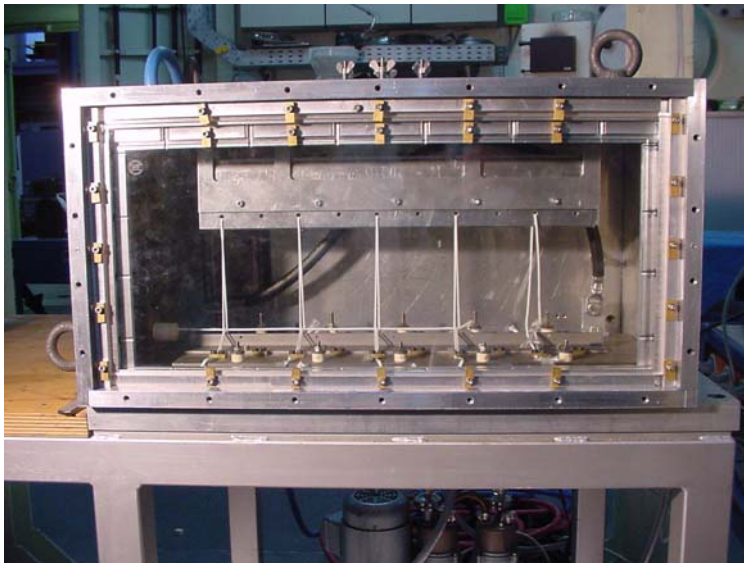
Fig. 2: Arc chamber after a pre-experiment.

The small arc experiments was delayed due to manpower reasons. During 2004 all parts for the arc device were manufactured, however technical problems during the outstanding experiments for insulation failure delayed the start of the arc chamber assembly. After the insulation failure experiments were finished successfully, the arc experiment was finally assembled. First test experiments are underway. Figs. 1-3 give a first documentation of the experimental work with arcs. As a consequence of this delay, also the work on numerical arc model development was postponed as the experiments were intended and required to provide a basis a for modelling.

Now that manpower problems on the experimental side are solved and the first experimental results look quite promising, there is a very good chance that the experimental and modelling work on busbar arcs will continue without further delay and the milestones will be reached.

Staff:

D. Klimenko
V. Pasler
G. Schmitz
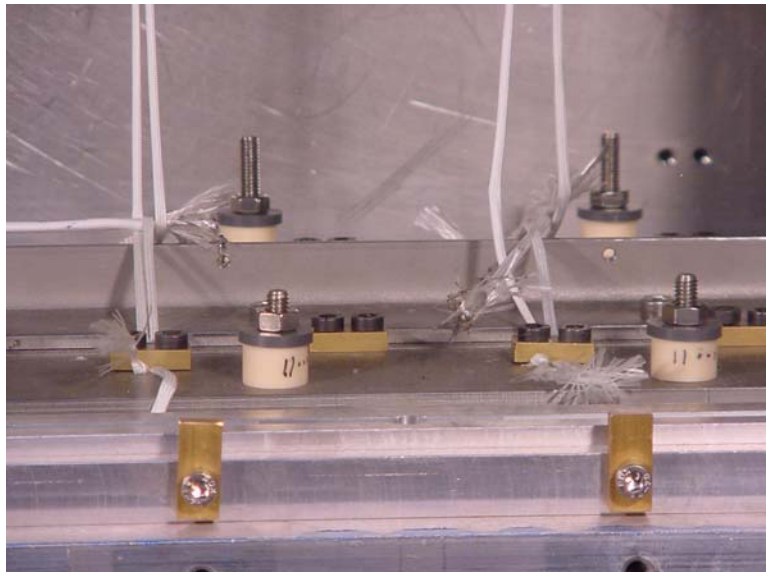
Fig. 3: Molten model conductor after a pre-experiment.

TW2-TSS-SEA 5.5
Safety Related Experiments to Investigate Air Inbreak Events in Cryopumps

Fusion reactor design includes cryopumps for evacuation of hydrogenic gas mixtures from the torus and neutral beam systems. The hydrogen inventory of the pumps themselves is limited such that under assumption of an air inbreak into these systems and assuming an explosion, the maximum explosion end pressure (deflagration case) will be 2 bar inside the pumps, and, thus, not be harmful to their mechanical design. However, the ITER vacuum vessel is not designed to such pressure levels. This is why a task has been launched to investigate such a scenario in detail.

The postulated event assumed as a basis for the experiments is a loss of vacuum (LOVA) through one vacuum vessel/cryostat penetration line. Air ingress causes pressurisation of the vessel and its extensions. Fusion power will be terminated by the air ingress, triggering a disruption. In the first phase, air will rapidly ingress into the vacuum vessel (plus all the connected peripheral components, such as the cryopumps (NBI and torus)), until the pressure inside the vacuum vessel and gallery are almost equal. After pressure equilibrium, the air inside is heated by hot plasma-facing component surfaces, and flows by natural convection, thereby stirring the air and the mobilized materials inside. This flow is regarded as a driving force for intense mass transfer between the cryopumps and the vacuum vessel. In order to model the formation of hydrogen/air-mixtures more accurately as done in past accident analysis, which was assuming instantaneous release of all hydrogen stored in the cryopumps at time zero of an accident, now the transient release shall be considered. However, an accurate modelling requires experimental release data, which shall be determined within this task exploiting the FZK test facility TIMO for of the ITER torus model cryopump.

The size for the air ingress area was postulated to be 0.02 m^2 as the reference case, since the minimum cross sectional area of every penetration line is required not to exceed this size. The pressure in the vacuum vessel is assumed to reach 800 mbar (the opening limit for the pressure suppression system) at 345 s after the LOVA initiation, which corresponds to an average pressurisation rate of about 2.3 mbar/s. As a parametric study, the air ingress area was varied up to 0.2 m^2. In this case, the pressure in the vacuum vessel rapidly increases to 800 mbar in 24 s after loss of vacuum initiation. This corresponds to an average rate of 33.3 mbar/s.
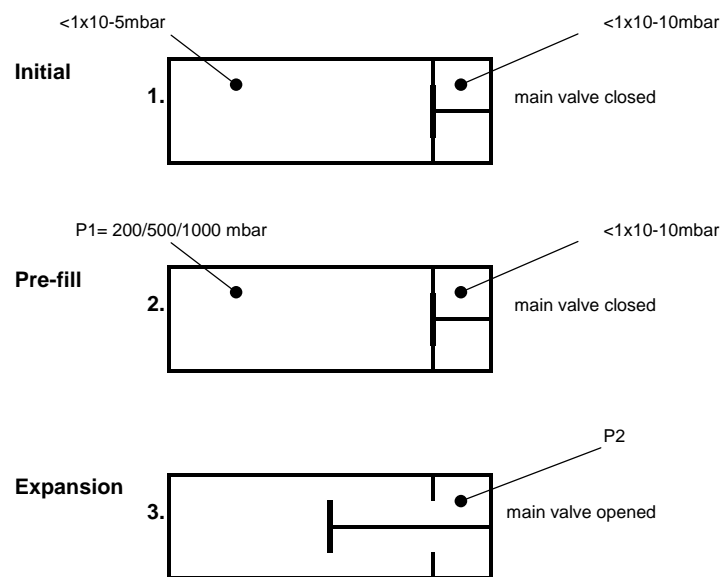
Fig. 1: Illustration of the expansion procedure used to realise very high pressurisation rates.

The release of hydrogen during normal regeneration conditions is well-known [1]. The experimental goal was therefore to measure the hydrogen release under rapid gas ingress conditions on TIMO. For safety reasons, pure nitrogen was used in all cases as model gas for air. Due to the fact that the available gas dosage system is not able to manage the required high gas flows, a new experimental concept was used to simulate an off-normal operation, see Fig. 1. The TIMO test vessel was filled with gas at a certain pressure (200, 500, 1000 mbar) with the pump main valve being closed. Then, the valve was opened so that the gas could

rapidly expand into the pump thus simulating the gas ingress coming from the vacuum vessel. During this expansion, the pressure and temperature evolution was measured. The achieved pressure increase rates covered a range from 800 to 130 mbar/s, depending on the pre-fill pressure of the test vessel. The disadvantage of this method is the fact that the gas inflow was quickly finished due to limitation of the gas inventory from the test vessel side. Smaller pressurisation rates (below 100 mbar/s) could not be achieved due to deficiencies of the valve control, which was of course not designed for such a task.

To achieve 2 mbar/s pressure increase rates, a special calibrated dosage system was used, which sent the gas in the vessel at a corresponding flowrate. For these tests, the pump valve was always fully open and the whole vessel was pressurised at such a rate. This is closest to the safety event scenario; however, due to continuous dosage and corresponding forced pressure increase, the additional pressure increase due to hydrogen gas release was somewhat masked.
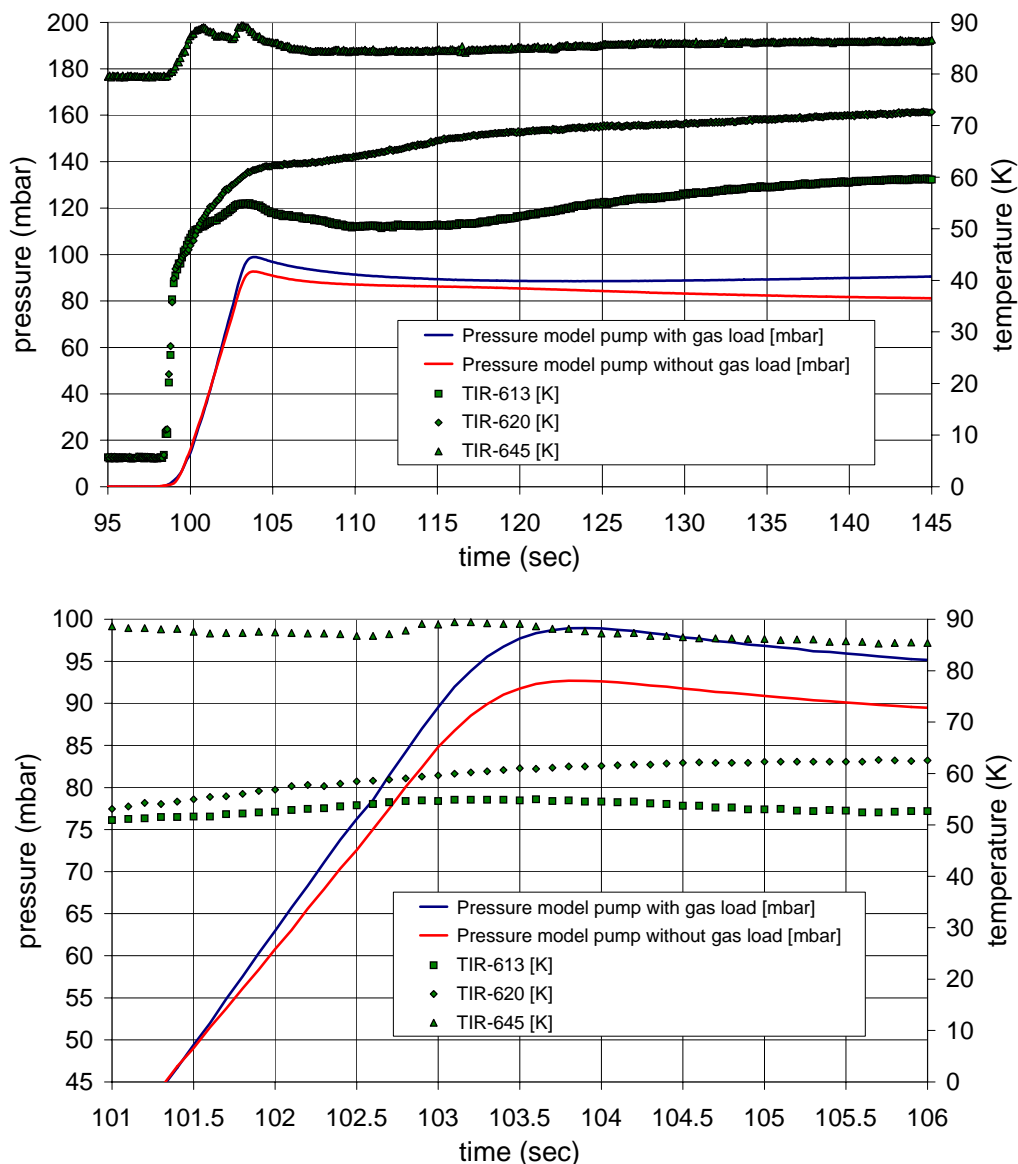
Fig. 2: Comparison of the pressure rise curves at 130 mbar/s for tests without and with gas load (H$_2$). *Bottom:* Zoom view to illustrate the release of the pumped gas.

All tests were performed at warm and cold conditions [2]. By comparison of the pressure evolutions measured at these two conditions the pumping capacity for nitrogen of the flooded but still cold pump was derived. The measured values of up to 50 (mbar·l)/cm² are a factor of

three higher than according to the sorption isotherms, which means that part of the pumped gas is condensed rather than sorbed [3].

The cold tests themselves were also performed twice, with and without pumped gas load (in the range of maximum surface-related ITER gas load) prior to the pressurisation step. By direct comparison of the two load cases, the transient hydrogen release curve could be derived. Two different gases (protium and deuterium) were used in the case of gas loaded pumps. However, the gas type did not show a significant effect on the release behaviour. It was also found that the released gas did not have a strong influence on the measured temperature distribution during the ingress event. This means that the effect of the released hydrogen is negligible compared with the inflowing gas. Altogether, 15 parametric tests were performed [4].

A typical example of the measurement results is given in Fig. 2, which compares the pressure rise curves of the cold pump at 130 mbar/s pressurisation rate for tests with and without gas load. It becomes very clear that between these two cases, there is practically no shift in the time needed to achieve the pressure peak. In the early phase of pressurisation (the firsts seconds), both curves are identical; in the second phase, the pumped gas is released and the pressure evolution starts to deviate; however, the peak is reached at very similar times. After completion of the release of the pumped gas, the pressure difference between both curves stays constant.

The measurements showed that the transient hydrogen release times have two contributions. At first the *delay time* t_D which is the time difference between initiation of the pressurisation and the time when the hydrogen starts to get released. Then the *actual release time* t_R interval along which the hydrogen release takes place until completion. Of course, any time lag of the pressurisation event in the vacuum vessel and in the cryopumps must be considered in addition to the delay time. Such a systematic time lag may be caused by a strong throughput limitation due to the small divertor slot geometry.

The gas release starts when the temperature of the panel system achieves values of about 50 to 55 K; the delay time is thermodynamically determined by the time need to achieve the desorption temperature on the charcoal panel surfaces. The measured delay times depend on the pressurisation rate and were in the seconds range.
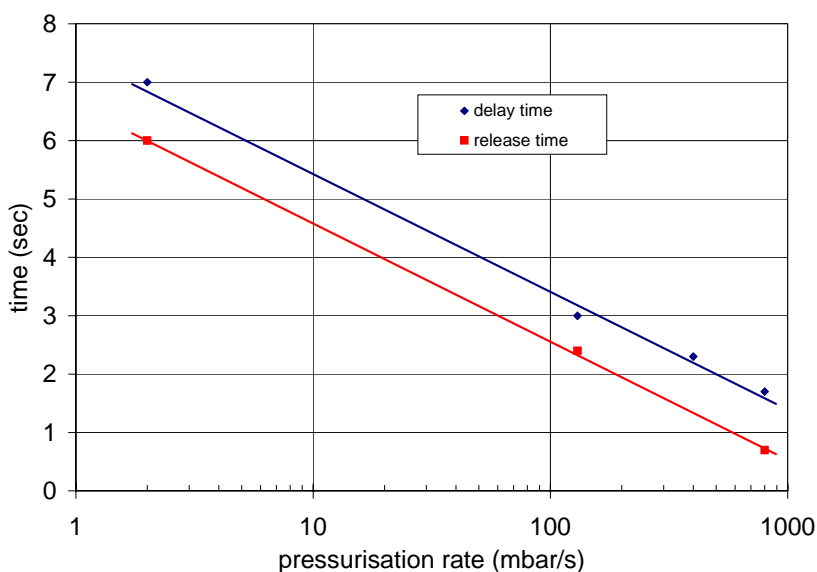
Fig. 3: Measured delay and release times vs. pressurisation rate.

As the gas release transient is clearly determined by the temperature distribution on the cryopanels, we tried a logarithmic plot of the measured times against the energy input expressed by the pressurisation rate, see Fig. 3. For estimation purposes, the following simplified model can be applied: The energy input is used mainly to heat up the cold cryopanel system (to increase its enthalpy), a part of it will be consumed by heat losses of the system. The solution of the energy conservation equation in this case yields that time will be proportional

to the logarithmic of pressurisation rate; the proportionality constant being linearly dependent on the temperature. Fig. 3 illustrates that a linear relationship is fulfilled with good accuracy. Due to the experimental and evaluation procedure, it must be pointed out that the uncertainty is at least ±0.2 s. Due to the very sharp pressure gradients upon pressurisation, any error in adjusting the zero times of the two experiments is of big influence.

It is shown that even for rapid air-ingress, the hydrogen release is determined by the temperature profile on the cryopanel system; the system behaviour is primarily governed by heat transfer effects.

This plot can be used as a tool for zeroth order interpolation predictions. Roughly both times are of the same magnitude. For the case which is closest to ITER (gas pressurisation rate of 2 mbar/s and continuing pump operation during this event) we found a delay time of seven seconds and a release time of 6 s. These times must be integrated in the safety case assessment and it must be investigated if the hitherto assumption of instantaneous release is compatible with this.

The pumping and release processes were checked for plausibility and it could be shown that during the air inbreak event, a combination of desorption and sublimation processes are taking place, however with an emphasis on the sorption part. This is why the start of the gas release agrees very well with the known desorption curve.

It could be demonstrated that the ITER model torus cryopump is robust enough to withstand a rapid air inbreak starting at ambient pressure directly in the cold pump. For the ITER reference accident scenario with a gas flow rate corresponding to a pressurisation rate of about 2 mbar/s, the pump can even continue pumping operation over a long period of time. This further prolongs the effective hydrogen release times. Thus, there is no need to implement any design changes to the torus exhaust cryopump design.

<u>Staff:</u>

<u>Chr. Day</u>
H. Haas
J. Weinhold
D. Zimmerlin

<u>Literature:</u>

[1] Chr. Day et al., R&D Progress for the ITER vacuum pumping system, Proc. 20th SOFE, pp. 465-461, IEEE, Piscataway, NJ, USA, 2004.

[2] H. Haas et al., Experiences from the operation tests with the ITER model pump, Int. Conf. Cryogenic Engng, Beijing, China, May 2004.

[3] Chr. Day and V. Hauer, A novel sorbent material test device at variable cryogenic temperatures, in: J. Waynert (ed.), Transactions ICMC, AIP Conference Proceedings 711, pp. 75-82, Melville, NY, USA, 2004.

[4] Chr. Day and H. Haas, Final report, Internal Report # FE.5130.0046.0012/O, Forschungszentrum Karlsruhe, July 2004.

TW4-TSS-SEP 2
Doses to the Public

Objectives

Volume IV "Normal Operation" of the ITER Generic Site Safety Report (GSSR) provides an assessment of the potential airborne and waterborne effluents and emissions from ITER. Volume VII "Analysis of Reference Events" and Volume VIII "Ultimate Safety Margins" include documentation of radioactive environmental source terms for the analysed representative accident sequences. Doses to the public due to these source terms are not given.

The objective of this task is to calculate in a consistent way these doses for realistic meteorological and siting conditions. In addition, parametric studies will be performed on request of the EFDA home team. Main computer codes to be used: UFOTRI, COSYMA, and NORMTRI.

Work performed

It is important to demonstrate, that potential releases from fusion power plant do not exceed internationally accepted intervention levels. In case of severe accidents, the radiological consequences have to be restricted to the vicinity of the plant and to times smaller than one year. Main safety targets for potential accidental releases to be compared with are European intervention levels for early (evacuation, sheltering) and late (relocation, food banning) actions and the regulations for European fission power plants. As the composition of realistic source terms is still open, a methodology has been developed to estimate the highest potential release which does not exceed the intervention levels. To this purpose, starting with the source terms as defined for the Power Plant Conceptual Study (PPCS) the contribution of each source term fraction to a particular dose target was calculated. Potential source term from future fusion power plants consists of mainly activated dust (AP), activated corrosion products (ACP) and tritium in form of HT and HTO. Performing calculations for unit releases, an equation has been derived which allows further scaling of all three fractions that the intervention level is not exceeded. This methodology has been developed in compliance with the European Utility Requirements.

As the number of calculations is large and the amount of data being processed and provided will be huge, and, as there is a certain possibility that the composition of a source term may change with time, a specific scoping tool was developed to allow an easy application for a particular case. This tool allows to

- load a particular scenario,

- load, modify or create a source term,

- and estimate the exhaust of the release targets for evacuation, sheltering, relocation and food banning.

The database of this tool contains nuclide specific doses and concentrations in food for the various release conditions. Each data set for one release condition includes information for all the four release targets. Only when a new release condition has to be investigated, additional calculations with UFOTRI and COSIMA would be necessary.

Microsoft EXCEL is used as basis for the tool. This allows an easy application as this software is widely distributed and a standard spreadsheet. Specific input forms will guide the user through the application function. The development of the first version of the tool is completed by the end of the year 2004. This includes a limited set of scenarios in the database.

Besides the application of the tool for actual source terms (Gulden 2004), parametric studies have been performed for source terms from the PPCS Model A. Areas and maximum distances of food banning zones for worst-case release scenarios for tritium (HT and HTO), dust (activated tungsten) and activated corrosion products (ACP) were performed. These calculations demonstrated, that the areas for food banning are limited when an internationally accepted dose criterion is applied. For releases of up to 100 g for each of the four source term fractions, the area did not exceed 10 km^2 for the first year and drops to zero in the second year.

Further work

The scoping tool, which is completed in a first version by end of 2004, considers dose criteria for the evacuation, sheltering and relocation. In addition, the concentration criteria for foodstuffs are implemented. A potential enhancement would be to consider also a dose criterion for the ingestion pathways in the scoping tool. To this purpose, the database has to be updated with additional calculations performed with COSYMA and UFOTRI, providing the necessary input for the dose criterion. If necessary, further release scenarios can be calculated on request.

Staff:

W. Raskob
F. Fischer
I. Hasemann

Literature:

[1] W. Gulden and W. Raskob, Environmental Release Targets for Fusion Power Plants. Presented at the 23rd Symposium on Fusion Technology, 20-24. September 2004, Venice, Italy.

Power Plant
Conceptual Study

TRP-001
PPCS He-cooled Divertor Concept

TW3-TRP-001 D4
Task Co-ordination

The objective of the task was the coordination of TW3-TRP-001. The activity was already concluded in 2003, however the final report was issued in 2004. In the following a summary of the final report is reported.

In the design of the Model B and C studied in the PPCS, He cooled divertors were chosen in the plant lay-out as alternative to a water cooled divertor of ITER derivation implicitly assumed in the past for a DEMO application. The main advantages of a He cooled divertor in this kind of reactors in comparison with a water cooled one are: i) to use the same coolant (or one of the coolants in case of model C) as the blanket system; ii) to allow coolant temperatures comparable or higher than the blanket system; this allows an efficient integration of the heat deposited in the divertor area (about 15 % of the total thermal power) into the power generation system contributing to increase the total efficiency of the reactor; iii) to avoid incompatibility with the breeder or multiplier that can produce concern for the safety. Typical example of this last issue is, for model B, the possible accidental reaction of water (steam) and Beryllium with hydrogen production that suggests to avoiding water cooled components inside the vacuum vessel for this class of reactor.
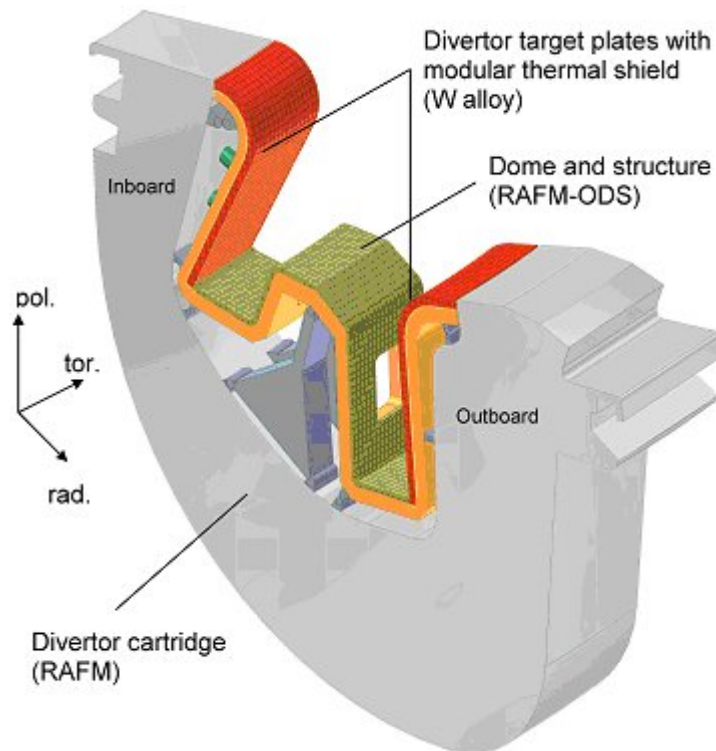
Fig. 1: Divertor concept for power plant B and C.

Based on preliminary studies about the feasibility of such a component, the task TW3-TRP-001 was launched with the objective to investigate some preliminary designs of this component that was used in the PPCS and to identify guidelines for the related R&D.

In the proposed concepts the divertor is divided into cassettes (Fig. 1) for easier handling and maintenance. It is essentially composed of the thermally highly loaded target plates, the dome that contains the opening for removing the particles by vacuum pumps, and the main structure or bulk which houses the manifolds for the coolant.

The design work has been concentrated on the target plate, which is the critical part of the design; in fact, incident heat fluxes not lower than 10 MW/m^2 are expected here. This very demanding requirement can be fulfilled if these two issues can be successfully addressed:

1) The identification of a heat transfer mechanism between Helium and plasma side structure able to reach heat transfer coefficient greater than 30 kW/m^{2}K (average).

2) The use of materials with very good thermal properties and a large operational temperature window that can be used as structural material (high pressure helium containment) for the high flux region at the plasma side.

The second item, together with reduced activation considerations, reduces the choice of materials drastically that at the present status of knowledge practically only W-alloys seem to have the potential to accomplish these requirements. Such a material qualified for fusion application doesn't exist at the present; objective of the task is also to define a list of minimum requirement for the development of fusion materials that will be addressed in the EU Material Programme.

The main objective of the TW3-TRP-001 is, however, to explore the item 1) and on the basis of the identified heat transfer mechanism, to propose conceptual designs (including the mechanical and thermo-hydraulic lay-out, fabrication technologies, etc.) for the target plates.

Taking into account a set of basic requirements, a lay-out for the target plates has been achieved based on the following principles:

−   modular design; the high flux surface is divided in small units (few cm^2) to reduce thermal stresses;

−   radial cooling: helium is fed in each unit from the vacuum vessel side, reaches the high flux surface and comes back; the units are fed almost in parallel to reduce the total pressure drops and the outlet helium temperature;

−   use of heat transfer promoters to reach high heat transfer coefficient (>30 kW/m^2K) at the plasma side of the coolant channels; helium reaches in this region high velocity (100-200 m/s) in small (1 mm or less as minimum dimension) and short channels;

−   use of W-alloy with structural functions for the whole containment of the high pressure helium (or part of them, e.g. caps or dome as shown later in the design description); the use of these materials envisages in the design high temperature for the coolant (at least greater than 600 °C) to provide margin against the increase of the DBTT under irradiation;

−   covering of the target plate with a sacrificial layer (tiles) to assure protection against plasma erosion; practically only W tiles with a thickness of about 5 mm are under discussion with an estimated lifetime of about 2 years.

ENEA and FZK have proposed two designs (Fig.2) for the high flux target based on two different heat transfer mechanisms between helium and high flux surface: the HETS (high efficiency thermal shield) and HEMP/HEMS (He-cooled modular divertor concept with integrated pin array / slot array), respectively. UKAEA has contributed to this task performing the thermal and structural assessment for the HETS concept. The main differences between of the two concepts are, as already mentioned, in the heat transfer mechanism used to reach the point 2), and on the different working point. Differences are also in the design of the target plates and in the proposed material especially for the structural part that should support the cups and provide the manifolds for the helium; however these later differences are less concept-depending and the results of the R&D can be mostly shared between the two proposed designs.

The studies carried out in the frame of the TW3-TRP-001 task of the PPCS have shown under which conditions a design of a He-cooled divertor for DEMO can be achieved. In particular two conceptual designs of the target plate have been presented based on the HETS and HEMP/HEMS heat transfer mechanisms; for these designs a mechanical and thermo-hydraulic lay-out has been proposed and assessed. Anticipated manufacturing technologies

and materials properties based on a reasonable extrapolation to DEMO of present knowledge have been assumed in the design.
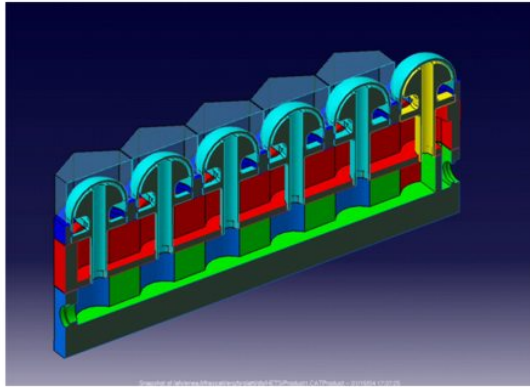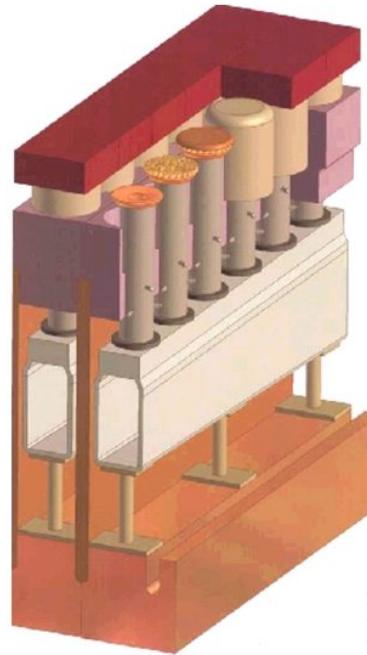
Fig. 2: Design of the target plates for the HETS (ENEA) and HEMP/HEMS (FZK) concepts.

Two important issues have been identified on which the successful completion of this work is depending: 1) the validation of the proposed heat transfer mechanisms with an appropriate experimental programme that should confirm the computational results, and 2) the qualification of fusion materials (especially W-alloy) and fabrication technologies (e.g. joint techniques for high temperature component).

The present studies will continue in the task TW4-TRP-001 in 2004 addressing the experimental validation of the HETS and HEMP/HEMS concepts (namely pressure drops and heat transfer coefficient); small mock-ups reproducing the finger units will be tested in helium facility in FZK and EFREMOV.

Staff:

L.V. Boccaccini

TW4-TRP-001 D2
Conceptual Design, Analysis and Tests

Introduction

The 2004 divertor work programme (TW4-TRP-001) focused on the optimisation of the concepts (design and analyses), preparation (layout and fabrication) of the experimental mock-ups, and execution of the experiments. The results and the status shall be reported.

Progress of the conceptual design

In the previous report [1, 2], a modular He-cooled divertor concept with integrated pin array and/or slot array (HEMP/S) was proposed and described in detail. Its main design principle is the use of small tiles made of tungsten as a thermal shield and sacrificial layer which is brazed to a finger-like (thimble) structure made of the tungsten alloy W-1%La$_2$O$_3$ (WL10) and forming a cooling finger unit. The pin and/or slot array with enlarged cooling surface is located on a flat plate which is brazed onto the bottom inside the thimble or cap and has the function of flow and heat transfer promoter. The cooling principle is convective heat transfer. In the first HEMP/S design, the modules have a nominal width of 16 mm. The W tiles are of quadratic shape with 5 mm thickness, whereas the thimbles are of cylindrical shape with an outer diameter of 14 mm and a wall thickness of 1 mm.

The advanced design HEMJ

In the course of 2004, an alternative concept, the so-called He-cooled divertor with multiple jet cooling (HEMJ) [3, 4], was introduced. It is based on direct jet-to-wall impinging cooling without flow promoter (Fig. 1). This cooling technology offers the advantage of a higher potential performance and easier design with more easily producible parts. The current HEMJ design employs small hexagonal tiles of tungsten with a width over flats of 18 mm. The tiles are brazed to a thimble of WL10 (Ø15 x 1.03 mm) that is dome-shaped at the top. A cartridge carrying the jet holes is placed concentrically inside the thimble. The number, size, and arrangement of the jet holes as well as the jet-to-wall spacing (i.e. gap clearance between the cartridge and the thimble bottom wall) are decisive parameters that need to be optimised.
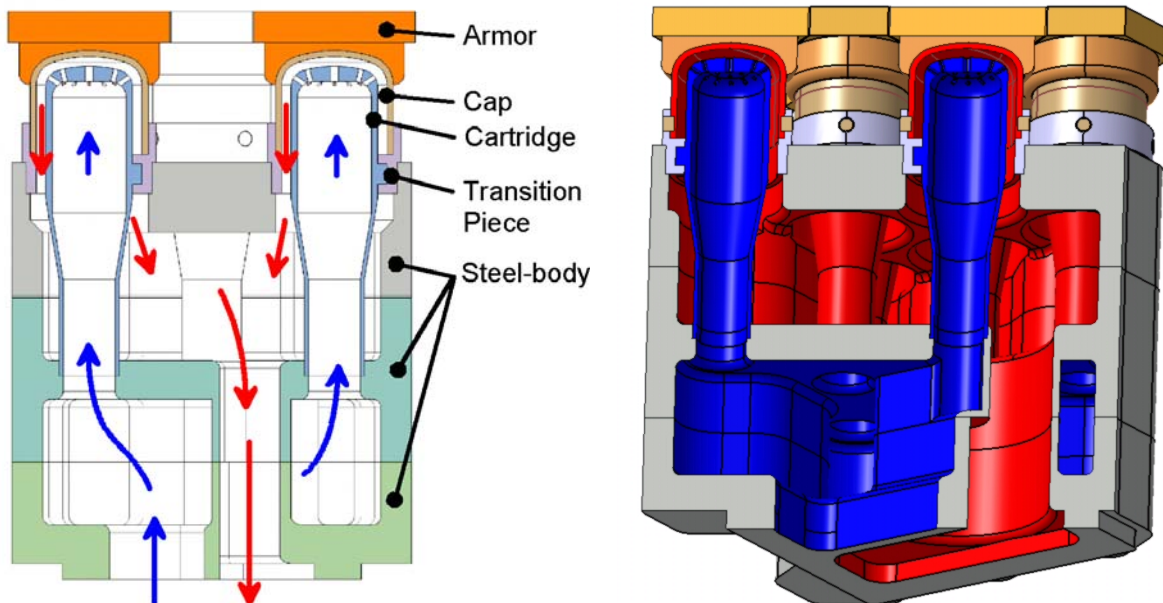
Fig. 1: Cross-section of the multiple cooling finger housing (left 2D, right 3D CAD).

For the reference load case of 10 MW/m^2, the nominal geometry for the multi-jet design was set to 27 holes (Ø 0.6 mm), jet-to-wall spacing 1.2 mm. A relatively large hole diameter of Ø0.6 mm was chosen, although a strong increase of the heat transfer coefficient can be expected at a smaller jet hole diameter, in particular at a size <0.5 mm. The reason is to avoid obstruction problems that are possibly caused by contaminated helium gas and reduce the cooling capacity. The divertor is cooled with high-pressure helium at 10 MPa, which is supplied by an inlet manifold. Helium enters the finger unit at a temperature of about 600°C and flows upwards to cool the plasma-facing wall at the top of the finger thimble. It is heated up to about 700°C before flowing back downwards to the He outlet manifold. The cooling finger units containing W tiles and WL10 thimbles are fixed to the supporting structure made of oxide dispersion-strengthened (ODS) steel (e.g. an advanced ODS EUROFER or a ferrite version of it) by means of e.g. brazing and/or mechanical interlock. This transition zone of two materials W and ODS with different thermal expansion coefficients requires a careful engineering design to avoid plasticising with temperature cyclic loads.

The HEMS design optimisation

To reduce the difficulties in fabricating the W pin array of the HEMP design, a similar concept HEMS with an alternative slot structure as flow promoter was analysed in 2003. It was found that the cooling performance of HEMS was at least as good as that of HEMP [1]. In 2004, the HEMS concept was then further optimised to increase its cooling performance and to reduce its pressure losses. As illustrated in Fig. 2, the helium coolant is directed through the inside of the steel cartridge and forced through an array of slots arranged on a W base plate. The same domed shape of the thimble as HEMJ has been chosen, as it offers more mechanical stability. The flow turn from radial to vertical direction is now achieved in a rounded section of the slots to reduce the pressure losses at the outlet of the slot array. In this connection, a diffuser-shaped slot outlet was designed, but the first mock-up fabrication by the EDM technique at Efremov revealed some difficulties in producing the exact angle of inclination.
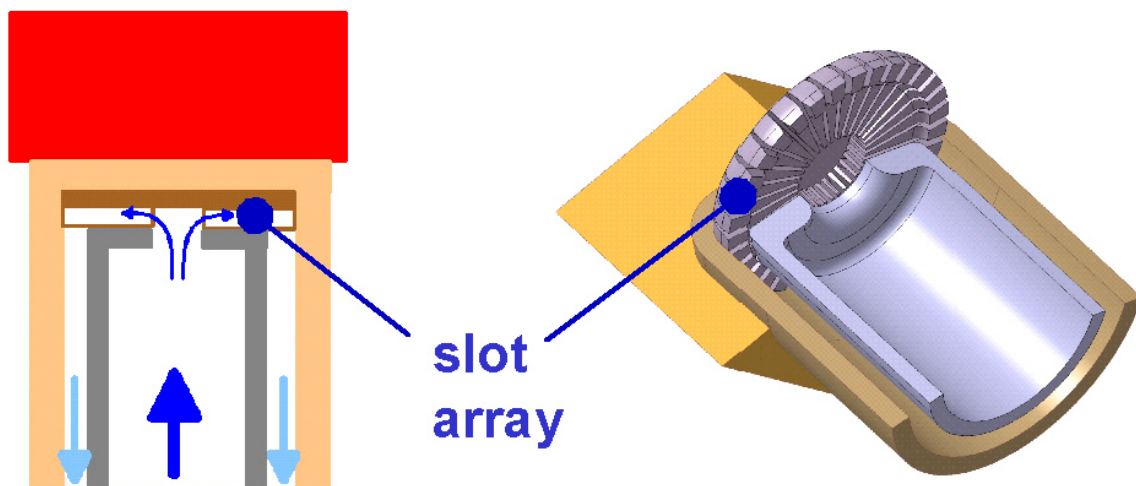
Fig. 2: Improved HEMS design with flow turn and diffuser-shaped slot outlet.

CFD and stress analyses

For the HEMJ design, CFD simulation calculations with the FLUENT code show that the above-mentioned reference HEMJ geometry can withstand 10 MW/m² as specified (Fig. 3). For a nominal mass flow rate of a cooling finger of 6.8 g/s, a value that allows keeping the He outlet temperature below the maximum allowable temperature of the steel structure of about 700°C, the maximum temperatures of the tungsten tile and the thimble amount to 1675°C (< ~2500°C allow.) and 1152°C (< 1300°C allow.), respectively. The mean HTC value amounts to 32 kW/m²K. The maximum He jet velocity was calculated to be about 300 m/s and the

resulting pressure loss amounts to about 0.14 MPa. The respective pumping power was estimated to be 57 MW for the whole divertor, which corresponds to 9.8% of the total divertor power (Table 1). With the same mass flow rate, the maximum thimble temperature could even be kept below the temperature limit for the W thimble of 1300°C under a heat flux of up to 12 MW/m^2. A smaller mass flow rate of 5.3 g/s would also fulfil this boundary condition at 10 MW/m^2 with lower pressure loss, if the operation temperature window of the steel structure material could be enhanced. Geometries adapted to a higher heat flux of up to 15 MW/m^2 are under investigation. The overall CFD results agree well with the values predicted by correlations. Accompanying stress analyses also show that all stresses are below the permissible (3-Sm) limit.
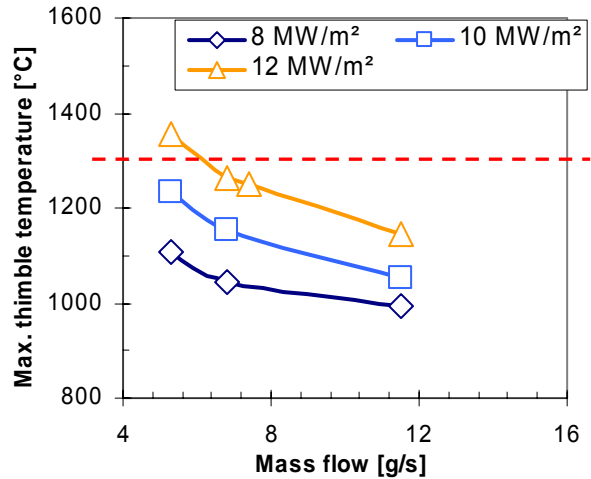
Fig. 3: Maximum thimble temperature (HEMJ-1a) as a function of He mass flow rate and heat flux.

Table 1: Total energy balance of the model C divertor in (MW).

	(A) Surface heat power $Q_\alpha + Q_H$	(B) Neutron heat power Q_n, (56%OB, 44%IB)			(A) + (B) $Q_{48\ cassettes}$	Values for one cassette $Q_{1cassette}$
		Targ. pl. [*)	Bulk	Sum		
Outboard	198.4	44.1	143.5	187.6	386	8.042
Inboard	49.6	34.7	112.7	147.4	197	4.104
Sum	248	78.8	256.2	335	583	12.146

*) volumetric power density of about 17 W/cm^3

Thermohydraulic experiments at Efremov

Prior to the He loop experiments with HHF tests, first thermohydraulics tests [5] in a gas puffing facility (GPF) were carried out at Efremov. These tests were based on a reversed heat flux method, i.e. hot helium (inlet/outlet temp. of 700°C/600°C) was pumped through the built-in CuCrZr and/or brass divertor mock-ups to estimate their thermohydraulic efficiency (pressure loss and HTC) when cooled by 100°C water coolant at the top of thimble. An experimental matrix for HEMJ and HEMS was set up for testing the influence of different parameters of the cooling system.

Mockup manufacturing at Efremov

For the first GPF test campaign, the HEMS and HEMJ mock-ups were fabricated from CuCrZr by means of EDM. The following test sequence was first applied to the HEMS mock-ups: pre-machining of thimble with cone shape, EDM fabrication of profile electrodes for use in the following EDM of the slots, and EDM of cylindrical slot part with tube electrodes. In a further process, the tile, thimble, and slot array of HEMS were combined in one unit and/or the tile and thimble of HEMJ were set up to form a cup element. For the second test campaign, brass L-63 (Russian grade) was chosen for both types of mock-ups (Fig. 4), as its thermal conductivity is closer to that of tungsten when compared with CuCrZr in the temperature range of RT-600°C. The remaining mock-ups for the improved HEMS design with different parameter variants are being manufactured. To simplify the manufacturing process,

tungsten plates (from rolled foil) with a thickness of 0.2 mm were used as electrode for EDM of slots of 0.3 mm width (for e.g. mock-up S1-c-0.3).

HEMS mockup

HEMJ cartridge
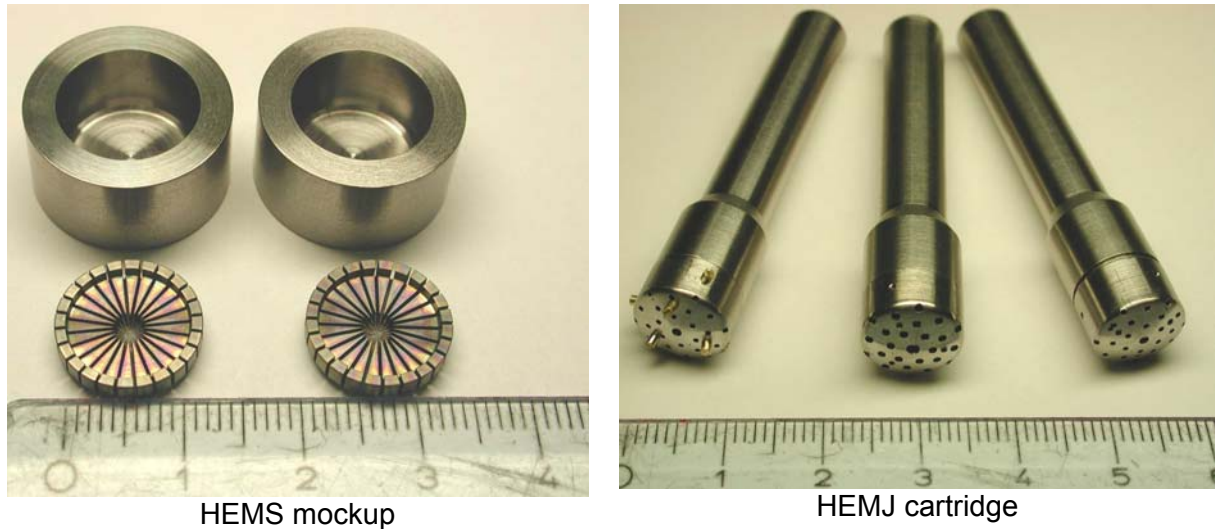
Fig. 4: HEMS and HEMJ mock-ups made of brass.
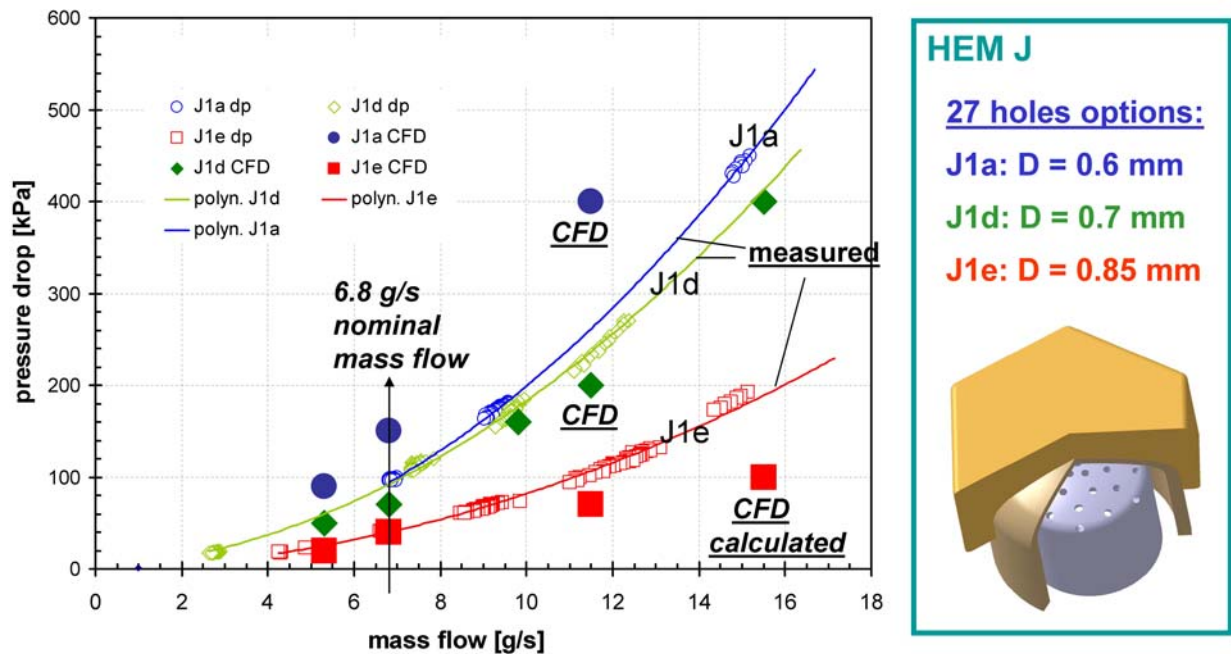
Fig. 5: Measured pressure losses and values calculated by CFD code Fluent.

First thermohydraulic test results

Fig. 5 shows first results of pressure loss measurements for the HEMJ design with varying jet hole diameters D (mm) / jet-to-wall distances h (mm): 0.6/1.2 (J1a), 0.7/0.9 (J1d), and 0.85/0.9 (J1e). The pressure losses calculated by the Fluent code are also plotted in this figure. These calculated pressure losses agree well with the measured values, with the exception of case J1a which shows a pessimistically large deviation e.g. at the nominal flow rate of 6.8 g/s. This is probably due to an inaccuracy of the drilling. The hole diameter was found to be increased by approx. 5% due to manufacturing. This will be verified later by the He loop experiments which will presumably begin in 2005.

Code validation experiments at HEBLO

Thermohydraulic experiments at the 'Helium Divertor & Blanket Test Loop' (HEBLO) are planned for CFD code validation using 10:1 mock-ups. This scaling allows for a detailed instrumentation to obtain reliable temperature and pressure data that may be used as a basis for the comparison with the calculation results. HEBLO consists of a main circuit with a He blower running at low temperature and a test circuit containing the test section with a higher temperature level. The test section (Fig. 6) is made of steel 15Mo3 and composed of a long inlet tube to ensure fully developed flow conditions. Mock-ups to be tested (e.g. HEMS, HEMJ) are mounted at its top and can be exchanged easily. An electrical heating plate is placed on top of the test section for a moderate heat flux simulation of up to 0.5 MW/m^2. The slot inlay for HEMS (one piece with the shroud) was produced by EDM using copper electrodes, while the pin array for the HEMP design was produced by cutting pins from a rod and brazing them onto a base plate. The quality of brazing was controlled by X-rays. First HEBLO experiments will presumably start at the beginning of 2005 for a HEMS mock-up with straight slots, followed by the HEMJ experiments. The design of the HEMJ mock-ups is under way.
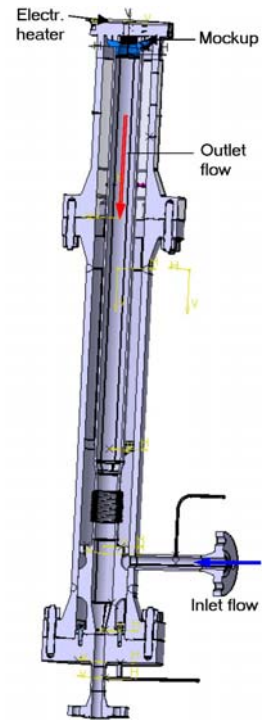
Fig. 6: HEBLO test section.

Progress made regarding the fabrication technology for W divertor components

Standard fabrication methods (e.g. milling) are not applicable to W or W alloys due to their high hardness and toughness. This particularly applies to microstructured parts of relatively high aspect ratios like pin and/or slot arrays. Promising methods for fabricating the flow pro-moter from tungsten are electric discharge machining (EDM), electrochemical milling (ECM), laser etching (LE), and powder injection moulding (PIM). Fabrication tests of W slot arrays by EDM in cooperation with Efremov showed that EDM can be applied to generate such shapes in principle. Both types of electrodes (graphite and copper) can be used to erode tungsten. The disadvantages of the EDM technology are the long processing time (> 24 hours for erod-ing 2 mm depth) and the relatively large wear of the tool. They render the technique unfa-vourable for mass production. For ECM of tungsten, efforts have been made to overcome surface passivation that suppresses current flow and stops local material removal. The re-sults obtained may help overcome the formation of short circuits which lead to failure in in-dustrial ECM processing of W. However, all other ECM equipment-typical parameters have to be adjusted also to W, similar to the job done in the past for high-alloyed Cr-Ni stainless steels. It was found in the first experiments that variation of chemical, physical, and important technical parameters (electrolyte composition, pH, temperature, convection, polarisation rou-tine) is favourable for W machining. Further investigations to optimise W shaping are under way. LE technology for fabricating W mock-ups with integrated slot arrays is being developed at Efremov. For PIM investigation, first sintering experiments with a suitable powder for feed-stock production yielded a relatively high final density of > 90% of theoretical density. Further sintering experiments are planned for improving final density without any contamination and for grain structure adjustment.

Investigation of the joining of W/W and W/steel components

High-temperature brazing tests for joining W/W components at Efremov revealed the best results for the filler materials 71KHCP (Co-based) and STEMET 1311 (Ni-based). The brazed joints withstood a cyclic thermal load of up to 14 and 16 MW/m^2 (Fig. 7), respectively. To join the W thimble and steel structure, different options of mechanical interlocking with

screws, bayonets, and pins have been investigated at Efremov. The latter is considered the easiest solution. Cold helium leak and pressure tests were carried out successfully.

W/W mock-up

Surface temperature at 16 MW/m^2
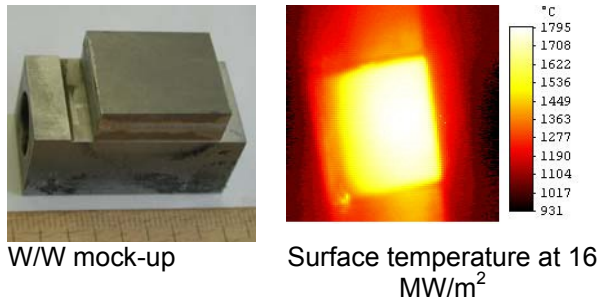
Fig. 7: W/W brazing and HHF tests with EB.

Conclusions and outlook

Work carried out in 2004 was aimed at demonstrating the performance of the design. Two design options HEMJ and HEMS with different heat transfer mechanisms were investigated in detail. First evaluation of the pressure loss and determination of the HTC within the limits of accuracy of the GPF experiments confirmed the tendency of validity of the design and simulation. Results of systematic investigations of the design variants showed that they meet a large variety of requirements, e.g. loading conditions (heat flux limit of 10 MW/m^2, 10 MPa He pressure) and materials and fabrication issues. The feasibility of fabrication and joining of divertor components of W was demonstrated by technological studies. First He experimental results from GPF show that both designs meet the performance requirement of 10 MW/m^2. The overall results of 2004 are reported in detail in [6]. Experimental programmes for HHF tests in the helium loop at EFREMOV have been worked out comprehensively for the next steps.

Staff:

T. Chehtov	V. Piotter
S. Gordeev	P. Norajitra
N. Holstein	R. Ruprecht
T. Ihli	J. Weggen
W. Krauss	B. Zeep
R. Kruessmann	K. Zinn

Literature:

[1] R. Krüssmann, P. Norajitra, L. V. Boccaccini, T. Chehtov, R. Giniyatulin, S. Gordeev, T. Ihli, G. Janeschitz, A. O. Komarov, W. Krauss, V. Kuznetsov, R. Lindau, I. Ovchinnikov, V. Piotter, M. Rieth, R. Ruprecht, Conceptual design of a He-cooled divertor with integrated flow and heat transfer promoters (PPCS Subtask TW3-TRP-001-D2), Part I (Summary) and Part II (Detailed Version), FZKA 6974 & 6975, 2004.

[2] P. Norajitra, L.V. Boccaccini, E. Diegele, V. Filatov, S. Gordeev, V. Heinzel, G. Janeschitz, J. Konys, W. Krauss, R. Kruessmann, S. Malang, I. Mazul, G. Reimann, M. Rieth, G. Rizzi, R. Ruprecht, V. Slobodtchouk, "State of the art: development of a helium-cooled divertor for DEMO", SOFE conference, San Diego, USA, October 2003.

[3] T. Ihli, P. Norajitra, G. Janeschitz, R. Kruessmann, R. Ruprecht, "Development of an advanced helium-jet-cooled divertor concept: cooling method and design", Jahrestagung der Kerntechnischen Gesellschaft Deutschland, Düsseldorf, 25th – 27th May 2004.

[4] T. Ihli, R. Kruessmann, I. Ovchinnikov, P. Norajitra, V. Kuznetsov, R. Giniyatulin, "An advanced He-cooled divertor concept", 23rd SOFT, Venice, Italy, 20.–24.9.2004.

[5] I. Ovchinnikov, R. Giniyatulin, T. Ihli, G. Janeschitz, A. Komarov, R. Kruessmann, V. Kuznetsov, S. Mikhailov, P. Norajitra, V. Smirnov, "Numerical and experimental study of DEMO He-cooled divertor target mock-ups", 23rd SOFT, Venice, Italy, 20.–24.9.2004.

[6] P. Norajitra, T. Chehtov, R. Giniyatulin, T. Ihli, R. Kruessmann, V. Kuznetsov, A.Makhankov, I. Ovchinnikov, J. Weggen, B. Zeep, Status of He-cooled divertor development (PPCS Subtask TW4-TRP-001-D2), to be published.

TRP-002
Conceptual Design of a HCLL Reactor

This task aimed at developing a PPCS (Power Plant Conceptual Study) reactor model based on the HCLL (Helium Cooled Lithium Lead) blanket concept for assessing its safety, environmental and economic performance in comparison to the previous PPCS models A (Water Cooled Lithium-Lead, WCLL), B (Helium Cooled Pebble Bed, HCPB), C (Dual Coolant Lithium-Lead, DCLL) and D (Self-Cooled Lithium-Lead, SCLL).

TW4-TRP-002 D2a
Neutronic Design Analyses

The objective of this task deliverable was to provide the neutronic data required for the conceptual design of PPCS reactor model AB based on the HCLL blanket concept.

A suitable MCNP power reactor model (torus sector of 20°) has been developed to this end following the HCLL blanket design specifications and the physics parameters of PPCS model AB. Vertical and horizontal cross-sections of the MCNP model are shown in Figs. 1a-c. The radial dimensions assumed for the breeder modules were 65.4 and 95.4 cm, inboard and outboard, with breeder zone thicknesses of 40 and 70 cm, respectively. The total thickness of blanket and shield amounted to 115 and 165 cm, inboard and outboard . A W protection layer of 2 mm thickness was assumed for the first wall.
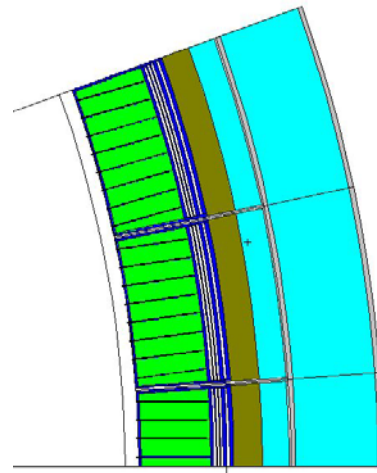
Fig. 1b: Horizontal cut at outboard mid-plane

Fig. 1a: Vertical cross-section
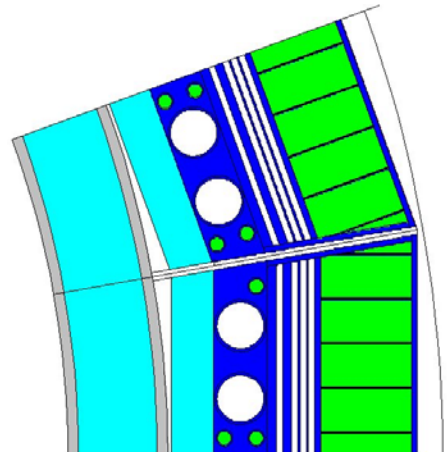
Fig. 1c: Horizontal cut at inboard mid-plane

Fig. 1:   MCNP 20° torus sector model of the PPCS reactor model AB (HCLL blanket).

A global TBR of 1.08 was achieved for the PPCS model AB employing the original design. This was considered not sufficient to compensate for uncertainties and a reduced breeding capability in the presence of blanket ports. The target TBR of 1.13 was achieved by increasing the breeder zone thickness to 80 cm at the outboard side (+ 10cm), to 45 cm at the inboard side (+ 5 cm) and adapting the top inboard module thickness to fit to the top outboard blanket module [1]. These modifications were adopted for the final HCLL reactor design ensuring thus a sufficient high Tritium breeding margin.

A nuclear power generation of 3760 MW was calculated for the complete PPCS reactor assuming a fusion power of 4000 MW and a unit net electrical power of 1500 MW. The resulting energy multiplication factor amounts to 1.175 which is very close to the values calculated previously for the PPCS models A and C [2]. The neutron wall loading distribution, the power density profiles in the torus mid-plane as well as the power produced in the single modules, their sub-components and materials were calculated to enable the proper thermal-hydraulic lay-out of the HCLL reactor.

With regard to the radiation shielding there are two essential requirements that must be fulfilled: first, the re-weldability of life-time components made of steel (such as the vacuum vessel, and, possibly, the high (HT) and low temperature (LT) shields), and, second, the sufficient protection of the super-conducting toroidal field (TF) coils. Based on existing data, the current assumption is that re-welding of stainless steel should be successful at He concentrations below 1 appm. The Helium production was shown to be below the limit of 1 appm only behind the low temperature shield assuming a 40 full power years operation [1]. Thus the HT shield cannot be designed as lifetime component of the HCLL reactor.

The shielding calculations performed for the original PPCS model AB showed that the design limits for the radiation loads to the super-conducting TF coil cannot be met even considering the use of tungsten carbide (WC) in the LT shield [1]. The shielding performance is deteriorated by the small dimension of the LT shield along with the rather large thickness of the HT shield region designed as collector block with large-sized He pipes. In addition, there is a rather strong neutron streaming through the 4 cm wide blanket segment gaps.

Table 1: Radiation loads to the inboard TF-coil.

	Design limits [ITER GDR]	HCLL (basic design)	HCLL (HTS-steel, LTS-0.65WC+0.1steel+0.25H_2O)	
			Void space at bottom of gap	Void space filled by SS-316
Integral radiation dose in insulator (Epoxy) [Gy]	$1.0 \cdot 10^7$	$1.19 \cdot 10^8$	$5.91 \cdot 10^7$	$3.32 \cdot 10^6$
Peak fast neutron fluence (E>0.1 MeV) to the Nb_3Sn Superconductor [cm^{-2}]	$1.0 \cdot 10^{19}$	$8.97 \cdot 10^{18}$	$4.53 \cdot 10^{18}$	$1.96 \cdot 10^{17}$
Peak displacement damage to copper stabilizer [dpa]	$5.00 \cdot 10^{-4}$	$6.83 \cdot 10^{-3}$	$3.4 \cdot 10^{-3}$	$1.11 \cdot 10^{-4}$
Peak nuclear heating in winding pack [W$\cdot$ cm^{-3}]	$1.0 \cdot 10^{-3}$	$4.05 \cdot 10^{-3}$	$1.87 \cdot 10^{-3}$	$2.73 \cdot 10^{-4}$

Supplementary shielding calculations were performed to investigate and optimise the shielding efficiency. First it was attempted to improve the shielding efficiency by increasing the LT shield by 5 cm at the expense of the breeding zone. No significant changes were observed, however, for the shielding efficiency in the inboard mid-plane. This behaviour suggested a significant impact of the neutron radiation streaming through the blanket segment gaps. Actually there is some void space at the bottom of the segment gap due to the fact that a toroidal curvature for the vacuum vessel is assumed while the blanket segments are designed

as straight planes in toroidal direction, see Fig. 1c. The attenuation of neutron radiation across the vacuum vessel was found to improve significantly when filling the void space by SS-316 steel. With this measure, all of the design limits of the radiation loads to the super-conducting TF-coil can be met (Table 1).

Staff:

U.Fischer
P. Pereslavtsev

Literature:

[1] U. Fischer, P. Pereslavtsev, Neutronics Results for PPCS Model AB: TBR, Power Generation and Shielding Efficiency, July 20, 2004, Forschungszentrum Karlsruhe.

[2] Y. Chen, U. Fischer, Y. Chen, P. Pereslavtsev, F. Wasastjerna, The EU Power Plant Conceptual Study - Neutronic design analyses for near term and advanced reactor models, Forschungszentrum Karlsruhe, Report FZKA-6763 (April 2003)

[3] U. Fischer, P. Pereslavtsev, Supplementary shielding calculations for the PPCS model AB, November 5, 2004, Forschungszentrum Karlsruhe.

TW4-TRP-002 D2b
MHD Analyses

Magnetohydrodynamic (MHD) flows in helium cooled lead lithium blankets for a future power reactor have been analyzed by combined asymptotic- numeric computations. The weak flow required for purification and tritium removal is driven by an applied pressure difference. The flow is considered in real 3D geometries. The global geometry is decomposed into main geometric elements. Of special concern are the connections between the circular access tubes with the breeder boxes through poloidal manifolds. The flow then enters the breeder box through narrow distributing gaps. The geometry used for MHD calculations is shown in Fig. 1.
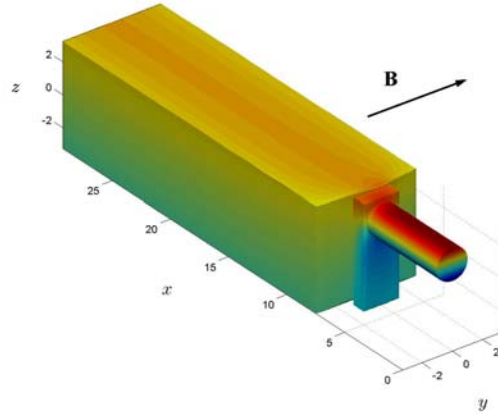
Fig. 1: Electric potential contours on the surface of the geometry
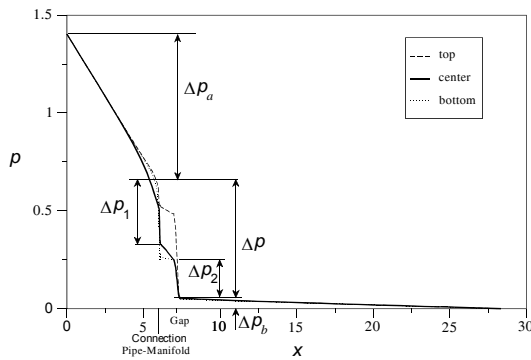
Fig. 2: Non-dimensional pressure along the flow path.

The distribution of induced electric potential is displayed in this figure by colored surface contours. The variation of non-dimensional pressure along the flow path (through the circular tube, poloidal manifold, distributing gap and breeder unit) is shown in Fig. 2. From this figure it is possible to identify individual contributions Δp_i which are used later to estimate the overall pressure drop of an assembly of 16 breeder units.

Another important geometric element is the region near the first wall, where the fluid has to pass another narrow gap. For that region the analysis results in additional non-dimensional pressure drop of Δp_3. The major fraction of total pressure drop Δp_m, however, arises in the poloidal manifold.

For applications to a power reactor, all contributions to pressure drop have been summarized as sketched in Fig. 3. As a result the total pressure drop reaches values as

$$\Delta p^* = \{16(\Delta p_a + \Delta p_1) + 2(\Delta p_2 + \Delta p_b) + \Delta p_3 + 8\Delta p_m\}\sigma v_0 B^2 L \ ,$$

where σ is the electric conductivity of the fluid PbLi, v_0 a typical velocity, B the magnetic flux density, and L is a length scale.

Using design relevant data, the total pressure drop can be estimated to $\Delta p^* = 0.27$MPa for an applied magnetic field of $B=5$T or $\Delta p^* = 1.1$MPa for $B=10$T. Such values seem acceptable for the current reactor design. Since the major contribution for pressure drop originates from the poloidal manifold, further improvements in the design should focus on this particular detail. For the final design the MHD flow in the supplying lines behind the blanket should be considered in addition.
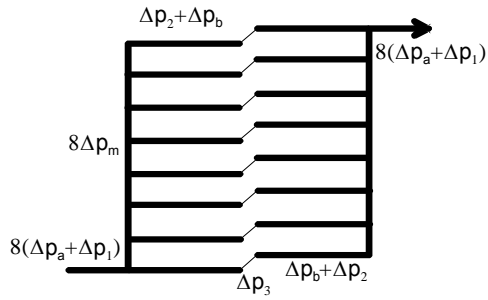
Fig. 3: Flow scheme for a HCLL blanket.

Some related results have been published at a conference (Bühler 2004). A final report on the subtask will appear as technical report FZKA 7069.

Staff:

L. Bühler

Literature:

[1] Bühler, L. 2004:, Magnetohydrodynamic pressure-driven flows in the HCLL blanket, 23rd Symposium on Fusion Technology, Venice, 20-24 September 2004.

[2] Bühler, L.:, Magnetohydrodynamic flow in the European HCLL blanket concept, *Forschungszentrum Karlsruhe,* Technical report, FZKA 7069

Tritium Inventory Control

TW3-TI-VP 31
High Temperature Regeneration Tests of the ITER Model Torus Cryopump

Task Objective

The regeneration of the cryopumps is a key issue for the tritium inventory control for ITER. To stay within the inventory limits, a multi-staged regeneration approach will be taken, comprising the regular regeneration stage at 100 K to release the hydrogen isotopes themselves, a second stage at ambient temperatures to release air-likes and light hydrocarbons, and a high temperature reactivation stage at 450-470 K to release any strongly sorbed substances such as water and heavy hydrocarbons. Especially the latter substances have a strong potential to build-up a high semi permanent tritium inventory in the cryopumps by isotope exchange. Although it could be shown that there will not result a significant poisoning effect from accumulated impurities (see tasks GB8-VP1 and TW1-TTF-VP13), from inventory limitation point of view it is essential to have an effective regeneration procedure available. The objective of this task was therefore to identify the temperature levels needed in order to release the accumulated impurities.

Test programme

Within the water tracer substances programme (task TW1-TTF-VP13), it was shown that methane, ethane and propane can be released completely, the latter by combination of temperature and pressure-induced desorption. Within the present task, water, n-hexane, and i-octane under conditions of high amounts of gas load were investigated quantitatively in the TIMO facility. The release pattern was monitored by high resolution quadrupole mass spectrometry. Each reactivation test started from ambient regeneration, with deuterium from the preceding pumping test filling the closed pump volume to about 5 mbar. From this starting point, the temperature of the cryopanel system was increased in steps of about 30 K, and the gas composition was analysed. After having reached 470 K at all inner pump parts, the pressure was reduced by means of the forepumping system down to 10^{-3} mbar in two steps with corresponding gas analysis to assess the effect of pressure reduction on gas release.
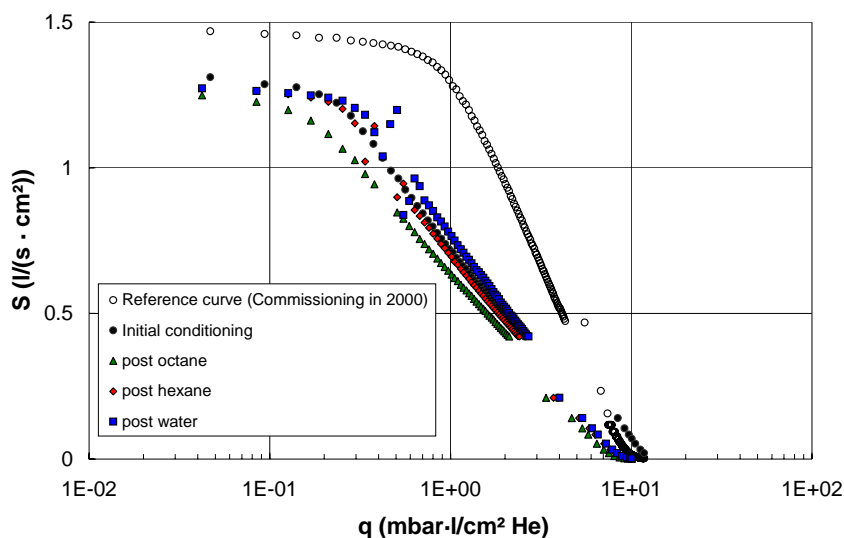
Fig. 1: Pumping speeds for helium, measured subsequent to reactivation after pumping high amounts of octane, hexane and water, respectively.

To further validate the effectiveness of the 450 K reactivation, pumping speed tests with helium, which is the most difficult gas to pump were performed afterwards, see Fig. 1. This figure shows the pumping speed measurements at ITER relevant conditions in terms of surface-related throughput and gas load.

The highest pumping speed curve was measured for the virgin charcoal, going back to the very first experimental campaign in 2000. The curve denoted ´initial conditioning´ was measured following a thorough bake-out and conditioning treatment in 2004, after first tests with tracer substances. It becomes clear that the helium pumping speed in 2004 was about 10 % below that measured for the very fresh pump, however, the ITER design requirements

are still met. For the measurements after the contamination with strongly sorbed substances, however, there is no big deviation and no further deterioration relative to the conditioning phase. This indicates clearly that even for the heavy hydrocarbon substances, the reactivation can be performed quite successfully.

The experimental programme is finished, but the gas analysis log files still have to be evaluated. However, it can already be claimed that water is significantly released at temperatures of about 100 °C, below the maximum ones of 450 K.

Staff:

Chr. Day
A, Edinger
H. Haas
H. Jensen
A. Mack
P. Pfeil
H. Stump
J. Weinhold
D. Zimmerlin

Literature:

[1] H. Haas, New TIMO test results, Presentation at 8th ITER-FZK Interface Meeting, available at http://www.ITER.org/bl (ITER Technical Web Site, Pumping).

EFDA/03-1096
Dynamic Modelling of Fuel Cycle Tritium Inventories

A tool for tritium inventory evaluation within each sub-system of the fuel cycle of ITER is vital, with respect to both the process of licensing ITER and also for operation. It is very likely that measurements of total tritium inventories may not be possible for all sub-systems, however tritium accounting may be achieved by modelling its hold-up within each sub-system and by validating these models in real-time against the monitored flows and tritium streams between the systems. To get reliable results, an accurate dynamic modelling of the tritium content in each sub-system is necessary. In order to optimize the configuration and operation of the ITER fuel cycle, a dynamic fuel cycle model CFTSIM was developed progressively in the decade up to 2000-2001. However, during extensive running of the CFTSIM code several inconsistencies in mass balance have been identified (e.g. mass imbalance in D_2, tritium inventory bound in impurities). During runs at various values for the input parameters some anomalies in the compositions of the streams from ISS also appeared. Corrections and an extensive upgrading are therefore necessary accompanied by documentation to facilitate its use.

A dynamic fuel cycle model was developed progressively to incorporate all the sub-systems of the fuel cycle. The code was initially developed in Java language, but in the frame of the present task the code was converted to Delphi Object Pascal, this new version of the code being nominated as TRIMO (Tritium Inventory Modeling). As the design for some sub-systems from the fuel cycle have substantially progressed meanwhile, TRIMO now incorporates these modifications.

The code operates by solving the mass balance around each sub-system from the fuel cycle of ITER, progressing in each time step through fuelling, torus, cryopumps, Tokamak Exhaust Processing (TEP), Water Detritiation System (WDS), Isotope Separation System (ISS) and finally fuel Storage and Delivery System (SDS). Two distinct operating modes depending on plasma burn time are considered: short pulse (450 s burn, 1350 s dwell) and long pulse (3000 s burn, 9000 s dwell).

Major improvements have been implemented in the code, related to the fuel handling strategy in the Storage and Delivery system; additionally, a model to account for the tritium inventory bound in impurities in the torus and vacuum pumping have been implemented.

Thorough checks in the original CFTSIM code on mass balance around each sub-system have been performed, proceeding from fuelling, through vacuum pumping, NB injection, TEP, ISS and SDS. At the same time, the procedure related to the storage system modelling has been debugged and necessary corrections have been implemented. The basic configuration for the ITER SDS is presented in Figure 1. SDS essentially contains four buffer tanks (D_2 for fuelling, high-quality D_2 for NB injection, DT and T_2) and three storage bed systems (D_2 (T), DT and T_2). At each timestep the amount of gas for fuelling is extracted from tanks as requested by the fuelling specification. Gas from the streams coming from ISS is added to the corresponding tanks. Gas from D_2 NB injection tank is added in the fuel D_2 tank if the inventory in this tank is lower than a minimum value. Additionally, D_2 can be added from bottles on-site. The minimum DT inventory in the DT tank is maintained by adding gas from the DT storage beds or by mixing T_2 and D_2 from the T_2 tank and fuel D_2 tank respectively. The minimum T_2 inventory in the T_2 tank is maintained by adding inventory from T_2 storage beds. If both T_2 tank and T_2 storage beds are drained out an Attention! flag is raised as the import of tritium into the main ITER Material Balance Area should be an operator controlled procedure. When DT or T_2 is in excess in the corresponding tanks (more than tank maximum inventory), DT and T_2 are stored in the corresponding storage beds.
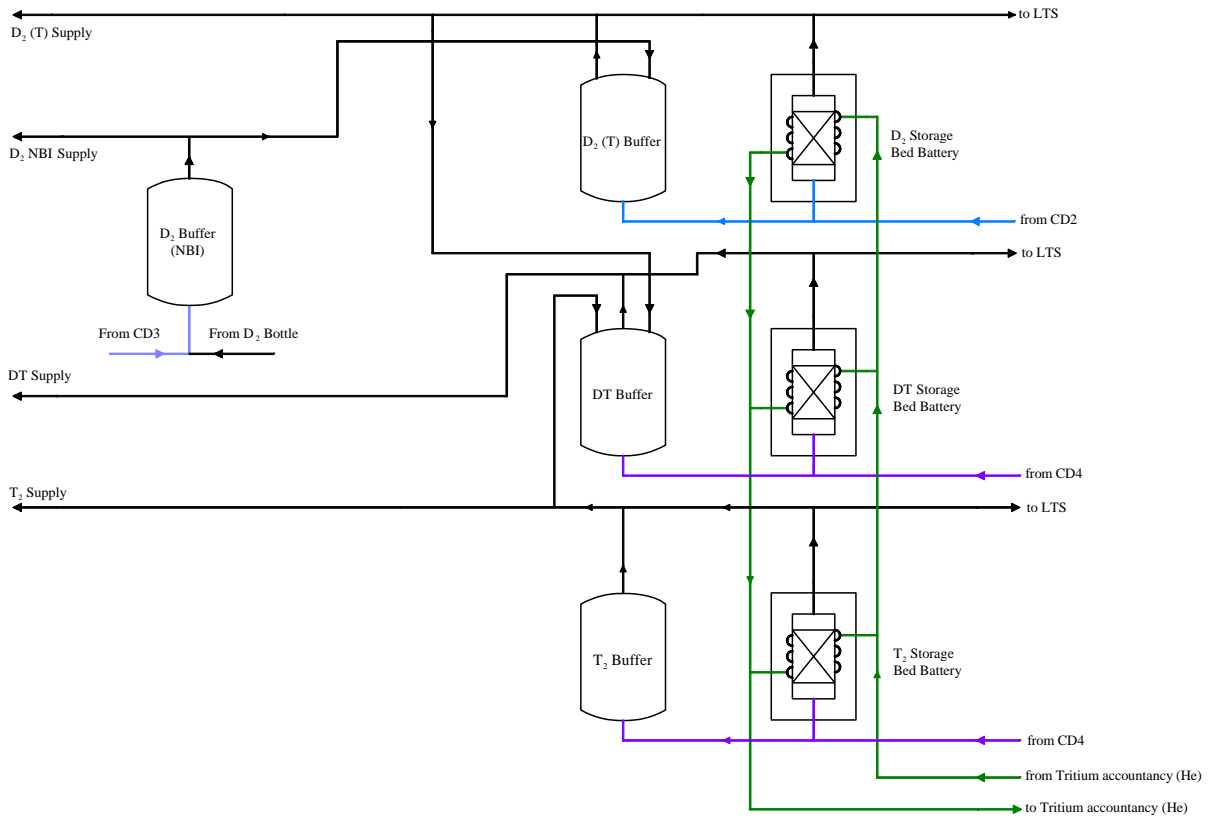
Fig.1: Simplified overall flow diagram of the Storage and Delivery system for ITER.

Several possible situations during fuel handling in the SDS, are presently uncovered by models in TRIMO, i.e.:

- The case when the inventory from D_2 NB injection tank and fuel D_2 tank exceeds the corresponding maximum inventory in the tanks; as the tritium concentration is 0.5%at. for D_2 fuel tank and 200 ppm at. for D_2 NBI tank, deuterium from these tanks can not be simply discharged; a strategy to handle this situation will have to be implemented.

- The case when the inventory in the DT tank is attaining the maximum value and DT storage beds system are loaded at full capacity; a procedure to return DT into the ISS for D_2 and T_2 separation will have to be implemented.

fuelling system respectively will need to be incorporated in the model. The important objective of modelling the fuel handling in SDS will be to keep inventories of hydrogen isotopes in the gaseous form to the minimum (for safety reasons), consistent with operational demands.

In Figures 2 and 3 the total deuterium (and correspondingly tritium) inventory for fuel cycle and for the main sub-systems are presented for long pulses.
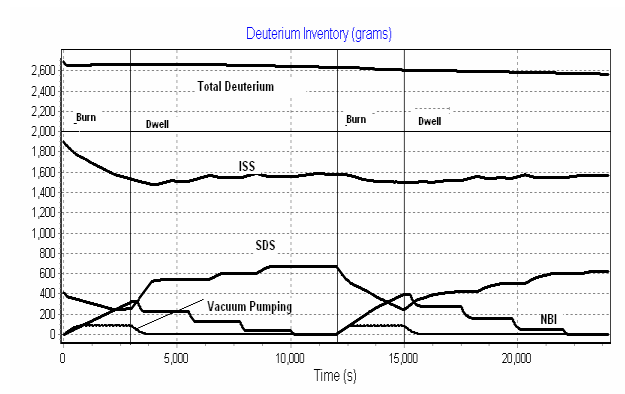
Fig. 2: Deuterium inventory in fuel cycle.
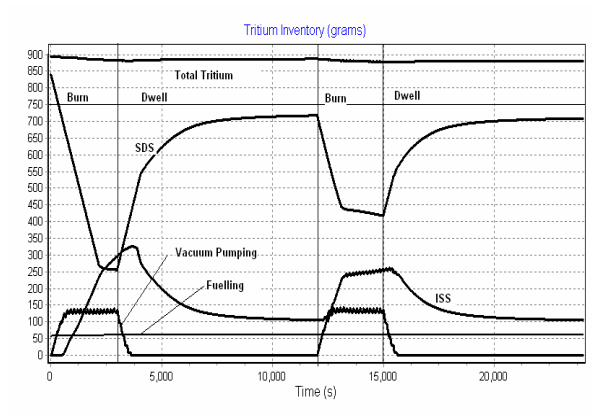
Fig. 3: Tritium inventory in fuel cycle.

The retention and permeation of tritium in ITER plasma facing components (PFC) have been widely studied. A sustained activity of modelling the tritium retention in the materials exposed to plasma and validation against experimental data is on-going in several research centers world-wide. Unfortunately, until now a consensus concerning a value of tritium inventory in plasma facing components from ITER has not yet been reached. Until a model with good predictions validated by experimental data will be available, a parametric model for the tritium retention in plasma facing materials is used in TRIMO. The tritium inventory trapped in the torus is considered as a fraction from the total fuelled tritium, the user having the possibility to modify this fraction.

Related to the residual inventory inside the Vacuum Pumping system, this is recovered during the high temperature regeneration at ambient temperature and at 450 K to release water-like species and higher hydrocarbons. The user specifies a value for the fraction from the fuelling rate that is transformed in tritiated methane and a value for the fraction from the fuelling rate that is transformed in tritiated water. Default values are available (consistent with the typical fusion exhaust gas composition as given in ITER Design Requirements Guidelines) and updated as R&D related to this subject proceeds. The residual tritium inventory as tritiated impurities in the vacuum pumping system is computed after each pulse as function of the total gas inventory in the pump. The tritium residual inventory in the vacuum pumping system in addition to the residual tritium in the torus constitutes the total residual tritium inventory. When the residual tritium inventory approaches the limitation of 450 g (specified-user input value) for in-vessel tritium inventory, tritium recovery from PFC and regeneration of the pumps at above ambient temperature is necessary.

Future work urgently needed to update TRIMO with the on-going design will have to comprise:

- Up-date the new regeneration scheme for the vacuum pumping system and NB injection.
- Development of a user friendly-graphical interface.
- Implement the water detritiation model, and establish the connection between the ISS and WDS.
- Improve the cryogenic distillation model and validate it against experimental data; special attention will be given not only to the accuracy with which the separation performances are modelled but also on the time response of a cryogenic distillation column at changes in the feed composition.

As TRIMO is intended to be used by different persons, the development of an accompanying documentation is of high priority. The documentation will have to comprise a user manual, to describe the way in which the program has to be used, a description manual where the basic physical assumption for each system and the numerical methods used will be presented and a collection file with the validation of the model on experimental data for various systems, where these data exists. If there is any intention to use the tool in the licensing process, to prove the accuracy of the program any modification implemented in the program will have to be documented.

Staff:

L. Dörr
Ioana R. Cristescu

EFDA/02-1019
Detailed Design of Water Detritiation Systems for JET

The Water Detritiation System (WDS) for JET is based on Combined Electrolysis Catalytic Exchange (CECE) process and is envisaged to work in combination with a new Cryogenic Distillation (CD) column with the aim to recover tritium contained in the processed tritiated water.

The main design requirements of JET-WDS are:

−   to process 10 tons of tritiated water with ~ 1 $Cikg^{-1}$ during one operation campaign of 2-3 months;

−   to achieve a decontamination factor of 10^4 along the stripping section of the LPCE column;

−   to deliver a tritium content in the bottom product of CD column in the range of 0.5-1% atomic ratio to allow further separation by the existing gas chromatography (GC) or CD systems of JET-AGHS.

The preliminary evaluation of the JET-WDS process options has shown that any increase of the deuterium content in the feeding water affects the required lengths of the LPCE column and the composition of the feed stream in to the cryogenic distillation column. Therefore, JET sampled twelve drums with tritiated water, and approximately 60 ml from each have been sent to TLK to measure the deuterium content. The device used for these measurements was an FT-IR, calibrated for deuterium content in water in the range of 0.1% HDO up to 2% HDO in mixture with H2O. The deuterium content was found to be between 0.3-0.9% HDO.

The compilation of the design input data and an overall process flow diagram (PFD) with flow sheets giving detailed information of the flow rates, physical conditions, and chemical and isotopic compositions for each main stream between the various components have been completed.

In addition, the evaluation of process options for JET WDS has been completed and the HAZOP study Level 2 was undertaken during a meeting with the representatives from JET and TLK. The use of solid polymer membrane (SPM) electrolyser has been agreed upon in the reference design.

The main components of the JET WDS are:

Front end and water purification system

The tritiated water at JET is stored in drums of 205 liters. It is desirable to have a constant tritium concentration in the feeding water of the WDS during one campaign, therefore a feeding vessel was envisaged to be used. Before being fed into the LPCE column, the tritiated water has to be purified to avoid contamination of the catalyst/packing mixture. The purification system consists of two units working alternatively. The purification system was chosen according to the chemical analysis of tritiated water provided by JET.

LPCE process

The LPCE columns have the aim to transfer tritium and deuterium from gas phase to liquid phase in the counter current mode. The most efficient transfer is obtained by employing three phases in the process: gas phase, vapour phase and liquid phase. For this multiphase system, deuterium and tritium transfer occurs in the following two steps:

- a chemical reaction between gas phase and vapour phase take place on a hydrophobic catalyst having as a result a higher concentration of deuterium and tritium in the vapour phase;

- between vapour phase and liquid phase an equilibration take place on packing separation as in the distillation process having as result an enrichment of heavier isotopes in the liquid phase;

Several combination catalyst-packing have been investigated at TLK. For the JET LPCE column, a combination based on SULZER structured packing and a hydrophobic catalyst developed at TLK is proposed to be used in a trickle bed exchange column.

In order to avoid hydrogen and tritium spilling from the LPCE columns, the flange connections between two sections of the LPCE columns have second containments, which allows both to detect and localize the leaks from the flanges and also to drain leaked water and to purge the area with nitrogen before dismantling the connections.

The LPCE columns have double walls, which allow thermal stability of the process by circulating heated water at the temperature of the streams within the column. Additional, the second wall can be considered as a second barrier against tritium migration from the LPCE process.

Electrolyser

In a WDS facility based on the CECE process, the electrolysis unit contains almost the entire inventory of tritium involved in the separation process. Usually the water hold-up of the electrolysis unit based on solid polymer electrolyte is three to five times larger than the water hold-up of the LPCE column. In the case of a KOH electrolyte, the water hold-up in the electrolysis unit is at least twenty five times larger than water hold-up of the LPCE column. The enrichment factor, defined as the atomic ratio between the tritium content in the water inside the electrolysis cell and the tritium content in the water fed into the electrolysis unit, together with the water hold-up in the electrolyser determine the tritium inventory contained in the electrolysis unit.

Similarly to the ITER design, for the JET-WDS an electrolyser based on solid polymer electrolyte has been chosen. This type was preferred instead of the classical one using KOH electrolyte due to the following main reasons:

- it avoids the K^+ ions transportation into the packing and catalyst material that fills the catalytic exchange column;

- it has a lower inventory of tritiated water;

- there is no generation of additional tritiated waste (KOH electrolyte).

Oxygen and nitrogen purification system

The oxygen purification system is needed to remove the hydrogen and tritiated water vapours from both oxygen and various nitrogen streams used to purge different subsystems of the WDS. The oxygen stream from the electrolysis cell is sent to a condenser, where is cooled down to ~5°C and the condensed tritiated water vapors are collected. Due to the fact that both the oxygen stream and the nitrogen stream coming from the outer containment of the electrolyser contain hydrogen, approximately in the range 1000-5000 ppm $H_2/H_2+O_2+N_2$, the oxygen stripping column is equipped at the bottom with a catalyst bed with the aim to convert to water the hydrogen contained in the oxygen-nitrogen stream. Essentially tritium free oxygen-nitrogen is released at the top of the oxygen stripping column and sent to stack. The stripping column is filled with structured packing of high efficiency, EX Sulzer type.

Permeator

A combination between CECE and CD processes is necessary because the tritium content in the deuterium-hydrogen mixture from the electrolysis cell is only of maximum tens of Curies and cannot be recovered at this level by the existing GC from AGHS at JET. In order to feed the tritiated mixture deuterium-hydrogen supplied by the electrolyser a purification system is compulsory in front of CD column. The permeation method is considered most suitable in order to achieve a very low oxygen concentration in the hydrogen-deuterium-tritium stream to be sent to CD column.

The WDS will be accommodated in a new building, as an extension of the Active Gas Handling Building from JET. The following main groups of components have to be properly combined to minimize the required area for installation:

− the LPCE and oxygen/nitrogen striping columns;

− the electrolyser;

− storage vessel, pumps and purification units.
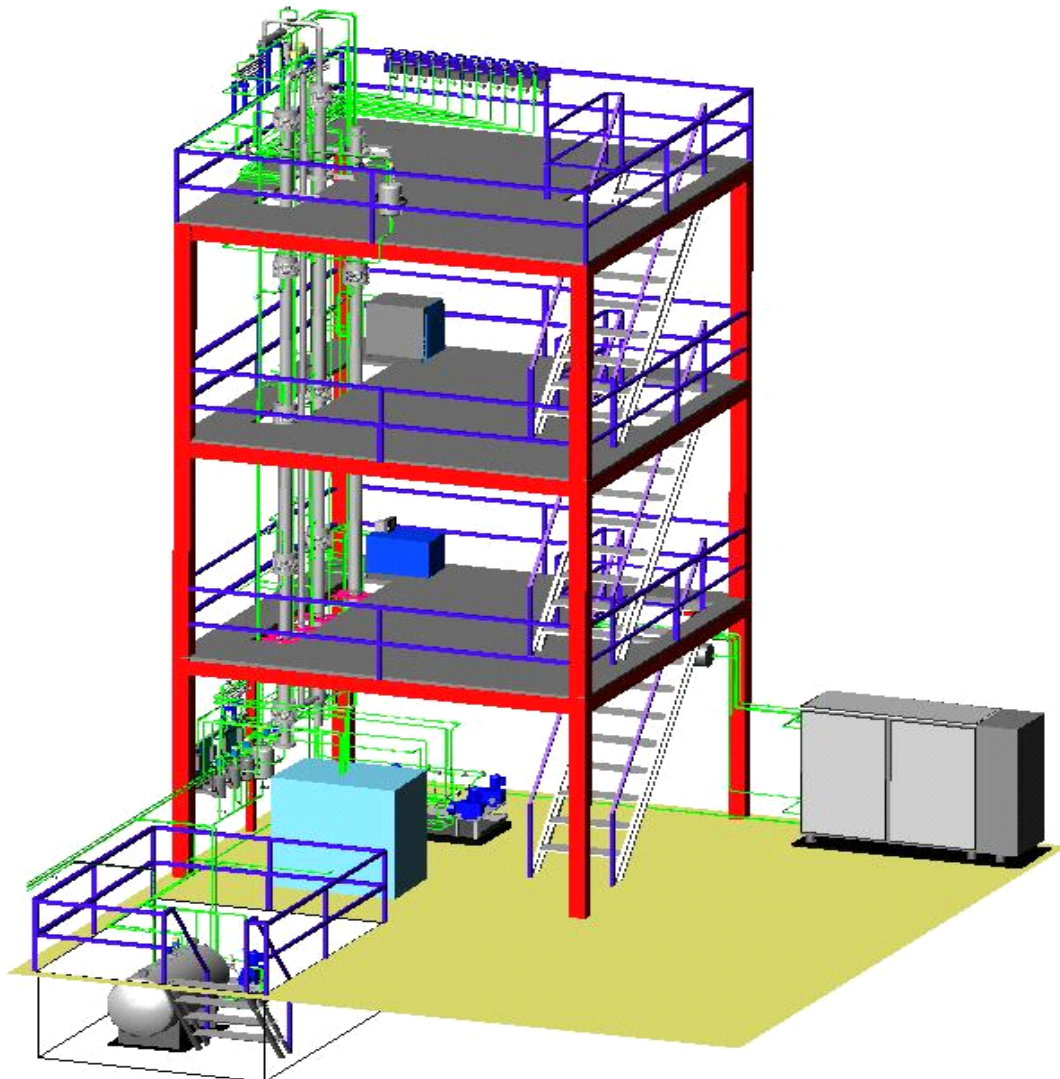
Fig. 1: 3D layout of WDS for JET.

Based on the size established for each component during the design, the 3D layout of JET-WDS have been produced and is shown in Figure 1.

The Water Detritiation System at JET has the following interfaces, which have been characterised:

–   the interface with the Cryogenic Distillation unit,

–   the interface with the building ventilation system,

–   the interface with the AGHS tritiated storage vessels.

The piping and instrumentation diagrams (P&ID), the mechanical design of all components of the facility, the general layout drawings showing equipment, piping and support location have been produced.

Staff:

Ion Cristescu
S. Welte
W. Wurster

Design Support and Procurement

EFDA/03-1100
Detailed Engineering and Manufacturing Studies of the ITER Magnet System:
Toroidal Field (TF) and Poloidal Field (PF) Coil Windings, Structure and Cold
Test Facility

The main objectives of the work is the review of the engineering design of critical areas, assessment of the manufacturing procedures and techniques, layout of the manufacturing facilities and test options, review of the fabrication schedule for the production of the ITER coils and their support structures. In particular, the subject of this study contract refers to three topics:

1. Contributions to the detailed review of the design of the termination areas and instrumentation of the Toroidal Field (TF) and Poloidal Field (PF) winding packs by giving support in the field of instrumentation and insulation;
2. Engineering and manufacturing studies of the Toroidal Field (TF) coil radial plates;
3. Development of the cold test procedures and proposals for the test facility design.

Point 1) is related to the support of other associations that ask for assistance in their review of the design of the termination area. Until now only a few requests have been placed which resulted in discussions with respect to high voltage insulation.

The main work of FZK is concentrated to point 2) and 3) and is discussed below.

Engineering and manufacturing studies of the Toroidal Field (TF) coil radial plates

FZK was requested to perform the work with industrial participation. In case of the engineering and manufacturing studies of the Toroidal Field (TF) coil radial plates the work is done in collaboration with Babcock Noell Nuclear.

The assessment was started with the comparison of manufacturing of raw material (hot rolled plates, forged sections) including

- Development and evaluation of fabrication procedures
- Assessment of machining and manufacturing tolerances
- Time estimations for fabrication procedures
- Basic layouts for fabrication processes
- Cost comparison of fabrication processes

Forged plates would allow a prefabrication of bent form and prefabrication of grooves with nearly no slicing. However, the manufacturing would be very complex. In case of hot rolled plates the big advantage is that standard dimensions are available on the market. On the other hand this may result in a lot of slices depending on the plate size. The fig. 1 shows two possible solutions with three slices only (left) or ten slices (right). In the case of only three slices only three welding connections are necessary and the overall tolerances could be achieved with no larger problems. On the other hand the large plates are not easy to fabricate, need large machines for milling and in this case heavy loads have to be handled. In the case of ten slices the dimensions of plates would be standard and the milling could be performed on standard machines. In addition only low loads have to be handled and using different fabricators the necessary fabrication time can be reduced. The disadvantage is to have many welding connections, the risk of distortion and it may be difficult to achieve the overall tolerances.
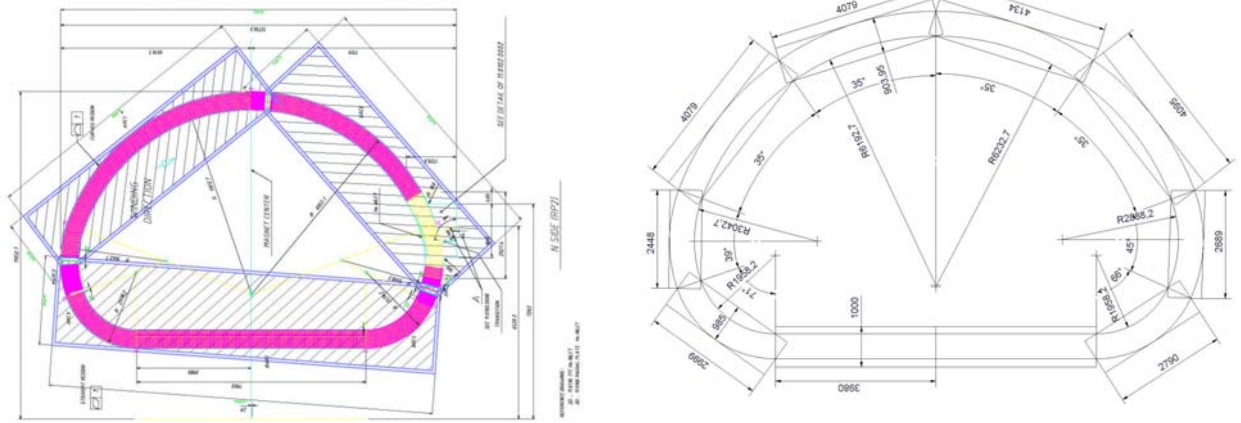
Fig. 1: Fabrication of radial plates from three slices (left) or ten slices (right).

In two concepts the fabrication of the radial plates has been assessed using 3 hot rolled plates or 3 forged plates. In principle the three slices could be welded and then machined on a large Gentry milling machine to form the radial plate (see fig.2). A special problem is the necessity to machine both sides of the radial plates. Therefore a special turning table has to be foreseen.
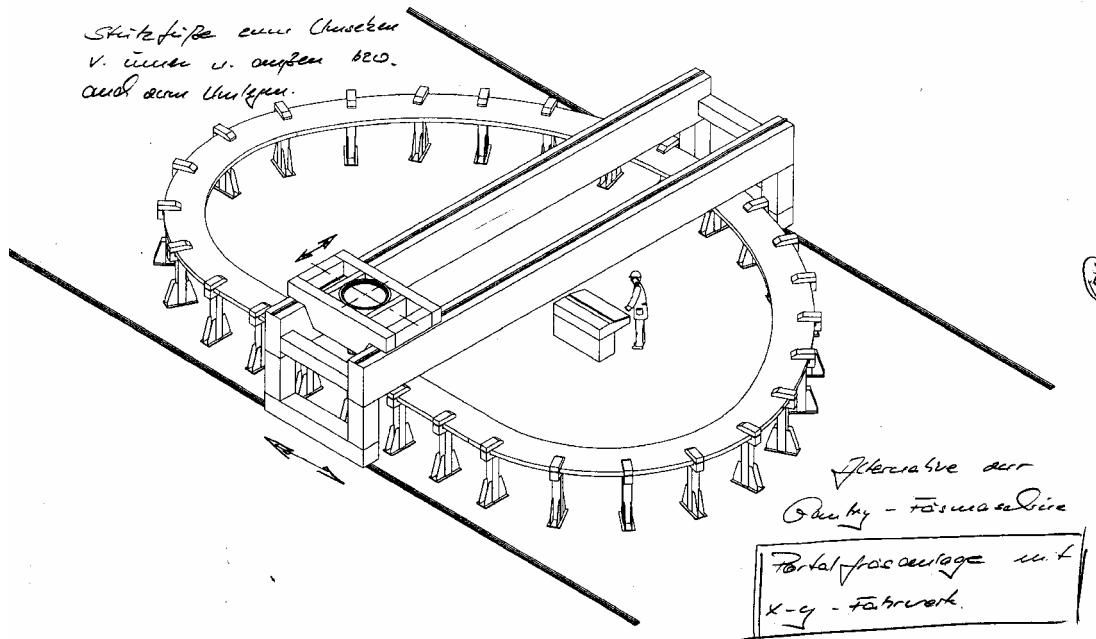
Fig. 2: Milling of a radial plate on a large Gentry milling machine.

Another idea is to prepare the slices by individual milling but exclude the welding area (see fig. 3). Each slice can be prepared individually which allows the distribution of the fabrication process to a large number of suppliers. The prepared slices can then be fixed on a turning table to perform the welding with a local electron beam welding and milling machine. In this case a special problem is the precise alignment of the slices before welding.
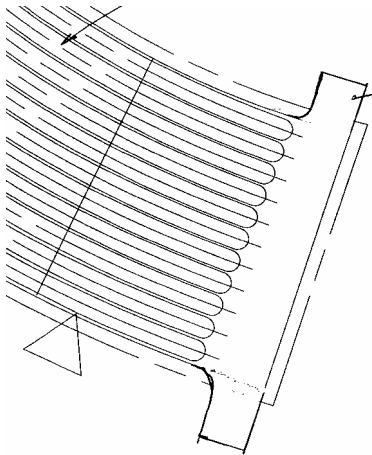
Fig. 3: Pre-fabricated slice with special end section for electron beam welding.

First estimations about milling time with machine and tool suppliers shows that the area that has to be milled is 51,922 mm², the length of milling is 34,283 mm and the average machining volume speed is 233 cm³/min. This results in an average milling time of 127 h for a radial plate.

When the time for heat treatment and intermediate transport is included a total time for the fabrication of a radial plate of 500 h can be estimated.

Development of the cold test procedures and proposals for the test facility design

At the moment a cold test of ITER coils is not foreseen in the ITER schedule. However, problems with the coil system could cause:

- a disassembly of the almost completed machine
- an extreme time delay
- tremendous additional costs
- risk for the entire project!

In other large scale experiments like W7-X or LHC all coils are tested, and they <u>do</u> find problems in spite of all QA!

First it has to be considered which tests should be performed:

- Leak tests
- High voltage tests (incl. Paschen tests at room temperature)
- Mass flow distribution and pressure drop in pancakes and casing
- Current tests to determine joint resistances
- Test of all sensors.

Some of these tests (e.g. leak tests and high voltage tests) have to be performed during fabrication at room temperature. However, cryogenic conditions at 4.5 K are indispensable to find cold leaks that open below 77 K, to determine the He-mass flow distribution and pressure drop and to determine joint resistances with moderate current. In addition sensor tests can ensure functioning at operating conditions of 4.5 K. The necessity of these tests can be demonstrated with the following arguments:

- Cold leaks can exist that reproducibly open/close at a certain temperature, e.g. at 20 K!

- Vacuum breakdown will cause a safety discharge of the coils, naturally. As a consequence under undefined vacuum conditions voltages above several hundred volts or several kV will occur, which may cause arcing and the destruction of coil and surrounding! Only a Paschen test can show to be safe against such a scenario.

- Blocked He channels that are penetrated by manufacturing remnants have been found in the past beside all QA! He-mass flow distribution and pressure drop has to be measured!

- Even when joints are fabricated under reproducible conditions, joint resistances beyond the allowable limits have been found. Joint resistances can only be measured in the superconducting state!

As a consequence, a cold test is indispensable and the risk of a coil failure cannot be accepted comparing the investment volume and the costs for a cold test of the coils. The costs of a 4.5 K cold test of the coils have to be compared to the investment costs of the complete ITER because the machine depends 100% on functioning coils. A simple cost / risk analysis shows that spending some % of ITER costs on an ITER coil test is a good choice! The test should include leak tests, high voltage tests (incl. Paschen tests), thermo hydraulic tests, low current tests (e.g. joint resistance) and instrumentation tests. Testing of single pancakes and the complete winding pack can be performed during fabrication (probably at room temperature). However, the complete TF coil has to be tested at 4.5 K. Within the EFDA cold test task it is still under discussion if tests should be performed under rated current, too.

The coil may be tested at manufacturer site with the advantage that a repair is possible without additional shipping. The disadvantage in this case is that the investment costs for test facility have to be spent without synergy effects (refrigerator, buildings, power supply ...) and have to be possibly invested twice (EU and Japan).

A test at the ITER site has the disadvantage that in case of a defect the coil must be shipped - a disadvantage that does not exist in the case of an on-site fabrication of the ITER coils. The advantages are the possible synergy effects

− use of refrigerator, buildings, power supply foreseen for ITER. Details have to be discussed.
− staff can be trained on refrigerator and power supply
− same test conditions for EU and Japanese coils.

As a consequence the test at ITER site is the favored solution, even more in case of on-site fabrication.

In addition a cold test offers the possibility to test

• current leads with respect to He consumption and heat load
• ITER current feeder system
• cold He circulation pumps
• control strategy of the ITER cooling system
• heat load cycling to simulate the plasma pulsing
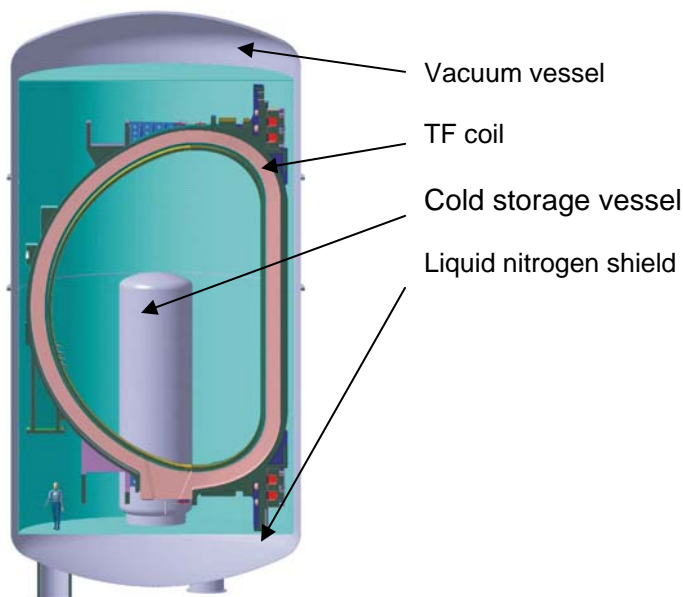
		Single Test	Twin Test
Diameter	=	10 m	12 m
Height	=	20 m	20 m

Fig. 4: Proposal for vertical installation of TF coils for cold test. In case of a single coil or a double coil test a diameter of 10 m or 12 m is necessary with a height of 20 m.

A proposal for the vertical installation of TF coils is made as shown in fig. 4. Alternatively a parallel installation of two coils is under discussion to save cool down and warm up time during the cold test.

The complete cold test facility may have the layout shown in fig. 5. Near an assembly area the vacuum vessel is found where the coil can be placed with a crane. The lid of the vacuum vessel can be split in two halves to reduce the necessary height of the building.
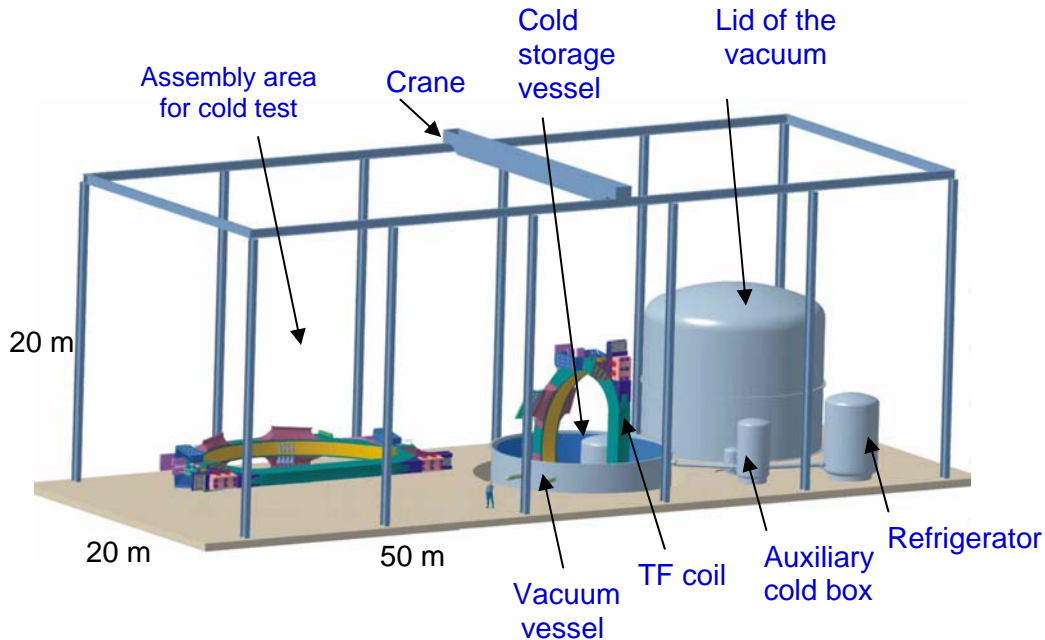
Fig. 5:   Proposal for the layout of the cold test facility.

In case of an on-site coil fabrication synergy effects may be used to optimize the financial effort.

The cold test facility is expensive because aside from the cryostat, the refrigerator and the power supply investments for a building, an assembly area and a 400 t crane is needed. These things are necessary for an on-site fabrication, too. To integrate the assembly, the storage of coils and the test facility is an obvious solution and offers possibilities to reuse tools. As an example the 400 t crane may be discussed. A single crane of 400 t is non standard and thus expensive. Instead of a single crane it would be possible to use two cranes with two lifting gears of 150 t, each. These lifting gears for 150 t are standard and thus cheap. As a consequence we have

- 4 lifting gears for 150 t (pair wise coupled at one of the two cranes)
- 2 lifting gears for 280 t (using connection piece to couple two 150 t gears)
- 1 lifting gear for 450 t (with a connection piece to couple the two cranes).

These tools can be used for assembly area, storage area and cold test. Because in most cases in the assembly not the full weight of the complete coil has to be lifted, for routine operation two or more cranes are available.

From these considerations it is clear that in the case of an on-site assembly of the ITER coils the areas for assembly, storage and cold test should be merged in one building with shared cranes. Fig. 6 gives a sketch of such a facility.

2 cranes, each with
2 standard lifting gears of 150 t

Cold test area

Storage area
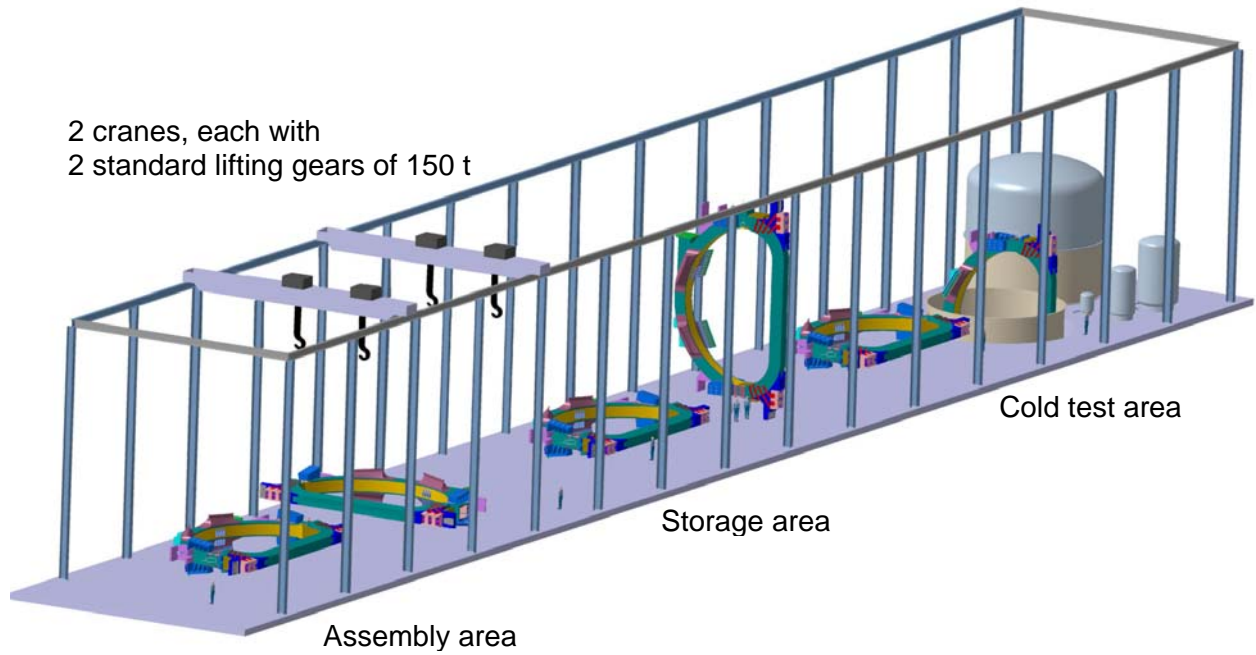
Assembly area

Fig. 6:   Building for joint assembly, storage and cold test.

The task is still in progress but as a short conclusion a cost/risk analysis clearly shows that a cold test is indispensable. In case of an on-side assembly the areas for assembly, storage and cold test should be merged together.

Staff:

W.H. Fietz
G. Zahn
S. Fink

JET Technology

JW2-FT-2.9
Tritium Removal from JET Tiles

All present-day tokamaks, such as JET, JT-60, TEXTOR or ASDEX upgrade, use tiles of graphite and carbon fibre composite (CFC) as a first wall material. Major merits of carbon are its low Z, neutron compatibility, good mechanical properties and especially its high heat conductivity which make CFC the material of choice for the divertor strike points as it does not melt during disruptions or Edge Localised Modes (ELM´s).

However, carbon has a major drawback related to its relatively high erosion rate producing large amounts of eroded material which, associated with hydrogen isotopes, leads to the production of the so-called co-deposited layers. These layers, after several erosion-deposition cycles, are enriched with all available hydrogen isotopes and they are eventually deposited in the gaps between the tiles, in the shadowed part of the tiles and/or in the colder parts of the vacuum vessel, i.e. in locations where they are no longer in line-of-sight of the plasma. As a consequence, substantial amounts of fuel material (deuterium/tritium) are immobilised in inaccessible parts of the fusion machine and hence increasing the total tritium inventory of the machine.

At JET, based on preliminary measurements on flake material, it was estimated that after the first Deuterium-Tritium Experiment (DTE1), 6.2 g tritium did not return to the Active Gas Handling System (AGHS). After the clean-up campaign 3.2 g were recovered but about 3.0 g still remain in the machine after the end DTE1. It was assumed that the missing tritium was probably attached to flakes and dust that has accumulated on water-cooled louvres or in the sub-divertor region of the machine as well as into the inner divertor tiles.

Therefore, once carbon tiles are retrieved from a machine and prior to their conditioning for disposal in a repository, a careful estimation of their total tritium inventory and their efficient detritiation is mandatory in order to permit their classification into one of the accepted waste disposal categories.

With this aim inductive heating using Radio-Frequency (RF) was tested at TLK to treat complete tiles using the Tritium Decontamination Experimental facility (TIDE), which basically exploits very rapid heating of carbon tile surfaces using the RF induction heating.

The detritiation technique was assessed after measuring the total tritium inventory of a whole tile by calorimetry prior to and after the RF treatment. With this non-destructive technique very low detection limits can be achieved for the measurement of total tritium in the sample regardless of its chemical form. The selected tile heated by RF was the one which, according combustion measurements, exhibited the higher tritium content on the surface and the bulk i.e. tile 1BN4, retrieved at 1998 from the JET inner divertor (type MKIIA) after the DTE1 campaign. The tile was cut in two pieces (part a and b) in order to fit in the tile holder installed inside the metallic container used in TIDE.

By calorimetry it was measured that the total tritium content for tile 1BN4 is 95.9 GBq or 2.59 Ci. For the first part of tile 1BN4-a, two series of RF heating experiments were performed. The first series consisted of heating the tile at an average temperature of 435°C (25 cycles) while during the second series 15 cycles were used at an average temperature of 490°C. Figure 1 illustrates three representative cycles from the first series of 25 cycles.

During the RF heating process the carbon tile is moved in front of an induction coil. One back and forth movement of the tile is counted as one cycle. When the tile is at its lowest position its distance to the coil is the closest and this is illustrated in Fig.1 by the highest temperature. Starting from the lower position of the tile (1) and moving the tile up, its temperature decreases sharply (Fig.1). Reaching the co-deposited layer (2) (see also Fig.2) the temperature slope changes as the thermal conductivity of this layer is much lower than the corresponding

one to the bare tile and also probably because the interconnection between the co-deposit and the substrate is very poor.
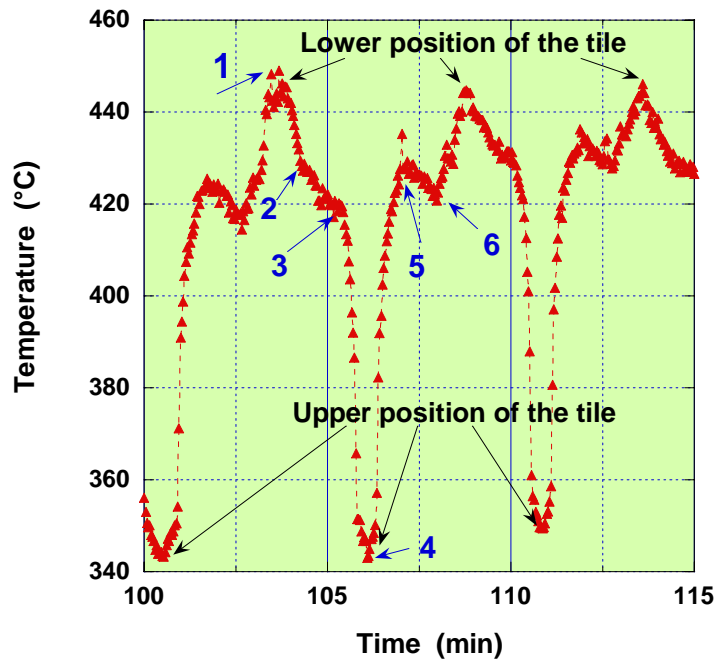
Fig. 1: Temperature excursion during three consecutive cycles, for tile 1BN4-a.

After having crossed the co-deposited layer (3) the temperature slope shows the same behaviour as before (sharp decrease) up to point (4) corresponding to the upper position of the tile (Fig.2). Moving the tile from its upper position (4) and going back to (1), the inverse phenomenon is observed. Here, the tile is coming gradually again closer to the coil and its temperature increases at the same rate as before. However, once the tile reaches the co-deposited layer (5) the temperature slope changes again. What is surprising is that this part of the curve is not inverted as would have been expected. It is assumed that this is due to the poor interconnection between the tile and the co-deposited layer mentioned above.

Indeed, the heat induced in the bulk of the tile is not efficiently conducted up to the co-deposited layer present in the surface which remains "colder". After crossing the co-deposited layer the temperature of the tile increases again up to its maximum value (1).

After the two series of thermal heating experiment, autoradiography has shown that a Decontamination Factor (DF) of 116 has been achieved indicating that more than 99% of the tritium has been released.

Conclusions

Radio-frequency heating was successfully used as an ex-situ technique for the detritiation of entire tiles retrieved from JET. Autoradiography showed that using the RF technique more than 99% of total tritium inventory can be efficiently removed from a tile by several heating cycles at an average temperature of 490°C

Compared to the heating process involving an open flame the RF tech-

Fig. 2: Tile 1BN4-a. The black and red arrows illustrate one back and forth movement of the tile versus the induction coil which corresponds to one heating cycle. (see also Fig 1.).

nique has the advantage of heating the co-deposited layer from the reverse side. Indeed, during the open flame treatment the heat is provided to the tile from the surface and therefore the tritium liberated from the tritiated layer co-deposited in the plasma exposed surface of the tile can diffuse to the bulk of the tile (redistribution).

On the other hand, during the RF treatment the temperature gradient is inverted as the heat is generated in the bulk of the tile and is conducted toward the surface, heating the co-deposit from behind. This avoids redistribution of the tritium in the bulk of the tile.

Staff:

N. Bekris
U. Berndt
U. Besserer
H. Dittrich
L. Doerr
B. Kloppe

JW3-FT-2.13
Studies about the Performances and Required Improvements to use a Solid Polymer Electrolyser in a CECE Process for Water Detritiation

In a Water Detritiation facility based on the Combined Electrolysis Catalytic Exchange (CECE) process (see task JW4 TTFD TR47), the electrolysis unit contains almost the entire amount of tritium involved in the separation process. Usually the water hold-up of the electrolysis unit based on solid polymer membrane (SPM) electrolyte is three to five times larger than the water hold-up of the Liquid Phase Catalytic Exchange (LPCE) column.

The tritium enrichment factor, defined as the atomic ratio between the tritium content in the water inside the electrolysis cell and the tritium content in the water fed into the electrolysis unit, together with the water hold-up in the electrolyser determine the tritium inventory in the electrolysis unit.

A method to decrease the tritium inventory of an SPM electrolyser was developed during this task. Basically, the components with large water hold-up and consequently large tritium inventory have been identified and redesigned. Also the standard configuration of a SPM electrolyser was improved based on specific working conditions for the combination of the SPM electrolyser and the LPCE column. The method was proven by measurements of the deuterium enrichment factor against different water hold-up in a SPM electrolyser. Three types of configurations have been tested and the enrichment factors have been measured for different deuterium content in the feeding water and found to be in the range 1.9 - 2.6, lower at smaller water hold-ups.
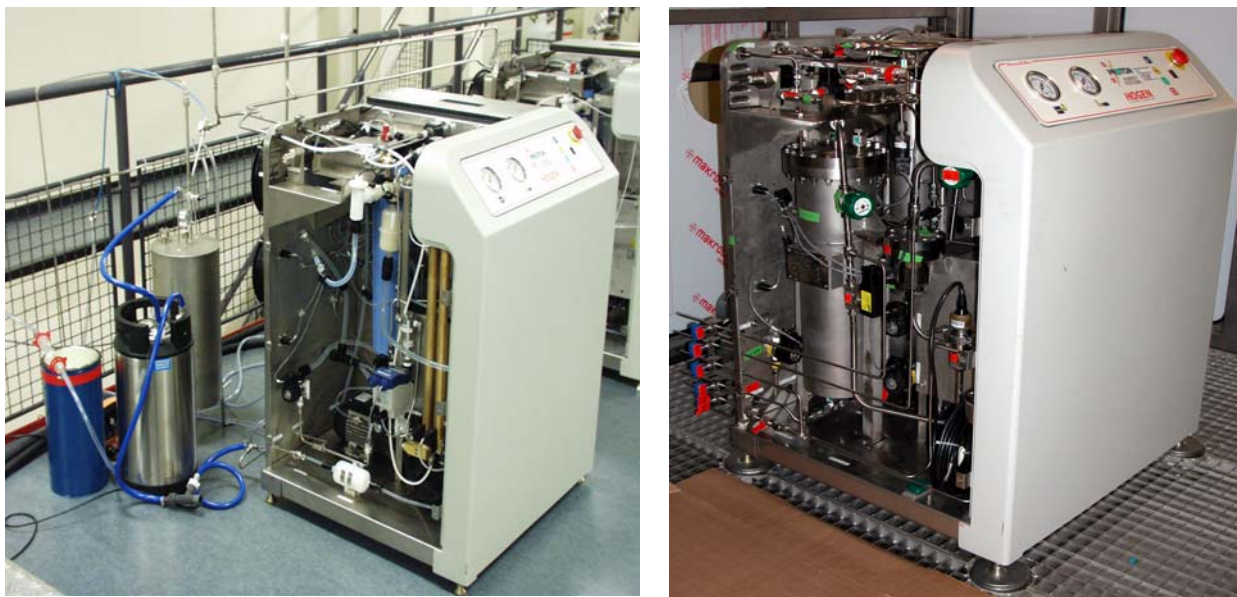
Fig. 1: Solid Polymer Electrolyser before and after the improvements.

At the Tritium Laboratory Karlsruhe (TLK), two SPM electrolysers commercially available have been improved to allow operation with tritium in accordance to TLK safety requirements. In the commercial configuration the electrolysers are equipped with several dryers on the hydrogen stream in order to remove most of the moisture coming from the electrolysis cell. Since the electrolysers are used in a CECE facility, where it is necessary to saturate the hydrogen with water vapor the in-build dryers have been removed. From the safety point of view this is of advantage since the in-build dryers contain plastic components. In addition, all plastic components have been replaced by stainless steel components. The modifications were agreed with the electrolyser manufacturer and the configuration of an HOGEN 40 electrolyser before and after the improvements is shown in Figure 1. For the tritium concentration

envisaged to be used in the experiments at TLK, a helium leak rate less than 10^{-5} mbarls^{-1} was established as a target value for the enhanced electrolysers.

A method for purification of the oxygen stream produced by electrolyser unit with the aim to remove the tritiated hydrogen and moisture has been developed during this task. The method is based on a striping process between the tritiated vapors and water flowing in countercurrent mode. The oxygen stream saturated with tritiated vapors flows in countercurrent with tritium free demineralized water supplied in at the top of the striping column. Tritium is transferred from tritiated vapors into demineralized water and the tritium enriched water will be collected and removed from the bottom of the stripping column. To support the isotopic exchange reaction the stripping column should be filled with material having high exchange surface. In view of the fact that the stripping column for the oxygen stream has to be incorporated in the WDS facility and in particular its connection with the SPM electrolyser is required, only packings manufactured by stainless steel have been considered. The decontamination factor along a striping column of 2 m length and 55 mm in diameter (Figure 2) was determined against the following parameters:

- The saturation temperature of vapors in nitrogen stream fed into the stripping column (5°-10°);
- Ratio between the amount of water fed in at the top of stripping column and the amount of water carried by nitrogen stream (0.88-10);
- Velocity of nitrogen stream within striping column (0.11-0.55 ms^{-1}).

The stripping process is proposed to be used for oxygen purification which is coming from the electrolyser and which contains highly tritiated water from the bottom of the LPCE column.

Fig. 2: Oxygen stripping column at TLK.

The tritiated water withdrawn from the bottom of the stripping column will be sent back to the electrolyser. From the efficiency point of view of the entire CECE process, the amount of demineralized water fed in at the top of the stripping column has to be as low as possible but having a reasonable length of the striping column. For the striping column envisaged to be used for JET-WDS, the proposed ratio between the demineralized water fed in at the top of the stripping column and the amount of vapors carried by oxygen stream is 1.5. The value has to be validated by measurements for tritium decontamination factor with TRENTA3 facility (task JW4 TTFD TR47).

D3. One of the key issues related to the SPM electrolyser is the lifetime under tritiated water processing. In order to investigate the behavior of the SPM under tritium exposure, a stand alone small electrolysis cell was operated with tritiated water of 4×10^{10} Bqkg^{-1}. Its behavior,

functioning characteristics and chemical composition of processed water over six months continuous operation have been investigated.

An experimental rig with the aim to investigate the behavior of a small electrolysis cell based on SPM has been developed at TLK and is presented in Figure 3. The process was conceived in order to allow operation of tritiated water in a closed loop. Therefore, in addition to the electrolysis cell, which produces tritiated hydrogen and oxygen, a catalyst bed was inserted along the process with the aim to convert the products of the electrolysis cell to water. Several buffer vessels are in the experimental rig in order to allow feed and emptying the process. After commissioning, the experimental rig was accommodated during the entire period of investigation inside of a glove box. The chemical composition of the water from the electrolysis cell was measured on a regularly basis, considering that fluorine may be released in the process water by the damage of the PTFE support. The solid polymer membrane used during the investigations at TLK was of NAFION type.

Fig. 3: The experimental rig to test the SPM lifetime.

In order to have a comparison of the cell current behavior, in an additional experimental set-up an electrolyser cell of the same size was in function with demineralized water but in opened loop. For the electrolysis cell where tritiated water was processed, the cell current decreased after 220 days down to 64 % from the starting value. For the electrolysis cell which processed demineralized water a decreasing down to 79 % from the initial value was noticed after 150 days. During six months continuous operation, the cell current decreased quit fast during the first two months and later some fluctuations occurred. The decrease of the cell current during operation when the voltage drop between the electrodes is kept constant is a normal behavior for such kind of electrolyser. The common practice in order to keep a constant throughput of the electrolyser is to slightly increase the voltage applied to the electrodes.

The mechanical properties such as tensile strength and elongation of the membranes used at TLK during the investigation of the two small electrolysis cell in operation with tritiated and demineralized water have been measured. Therefore, the SPM used in the electrolysis cell which processed tritiated water was decontaminated in order to allow to perform the mechanical measurements in the monitored area of TLK but not in a dedicated enclosure.

For mechanical properties comparison, in addition to the two SPM used in electrolysis process with tritiated and demineralized water, a virgin SPM was measured as well. The comparison of the tensile strengths and elongation of the two membrane used in operation with tritiated water and respectively demineralized water did not show a clearly differences that can be considered as a contribution of tritium decay.

The task is completed, however due to interest of the ITER-IT related to the issue of SPM life-time, long-term test to SPM behaviour under tritium exposure at higher tritiated water concentration will still be carried out in 2005.

<u>Staff:</u>

<u>Ion Cristescu</u>
S. Welte
D. Adami

JW4-FT-2.19

Endurance Test for the Catalyst-Packing Mixture Proposed for Water Detritiation System at JET with FZK Mixture

The aim of the endurance test is to measure and compare both the separation performances of the catalyst/packing mixture and the chemical composition of tritiated water after different exposure times (3,6 and 9 months) in similar conditions as foreseen for the JET Water Detritiation System WDS.

A column of 2 m length and 55 mm in diameter filled with the catalyst/packing mixture developed at Tritium Laboratory Karlsruhe (TLK) is used for this endurance test. The catalyst/packing mixture is based on hydrophobic catalyst, having platinum as active element, and structured Sulzer packing. Having in view the tritium profile along the Liquid Phase Catalytic Exchange (LPCE) column envisaged to be built at JET, respectively from 1×10^{12} Bqkg^{-1}-5×10^{12} Bqkg^{-1} in the bottom of the column down to 2×10^{5} Bqkg^{-1} at the top of the column, an endurance test using tritiated water of 4×10^{10} Bqkg^{-1} is proposed.

The catalyst-packing mixture is exposed to tritiated water at the operation temperature to be used, and at each three months, the separation performance for both deuterium and tritium is envisaged to be measured. The performances of the catalyst - packing mixture is to be determined after two different exposure modes: catalyst-packing immersed in tritiated water and catalyst-packing mixture exposed to water-vapour as in a total reflux distillation process. Beside the separation performances measurements, the quality of water drained from the column after each exposure will be measured as well.
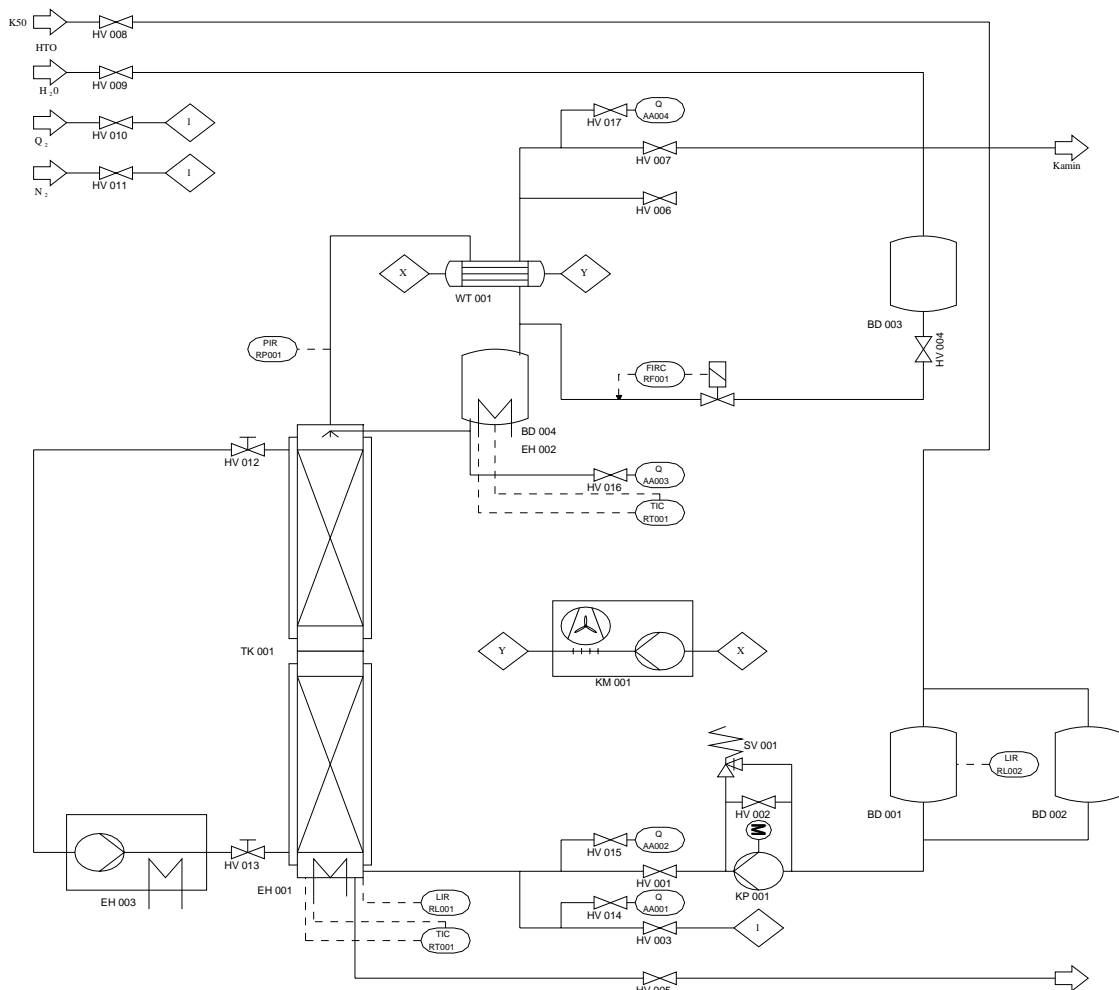
Fig. 1: Process flow diagram of the facility for the endurance tests.

A double wall column with 2 m length was installed in the experimental rig connected to TLK water detritiation facility, and is schematically shown in Figure 1. One electrolyser of 1 Nm^3h^{-1} hydrogen throughput was enhanced to allow processing of tritiated water. In the new configuration, the electrolyser was commissioned with demineralised water and the working parameters are similar with those before modifications (task JW3 FT2.13). Two types of hydrogen sensors for the electrolyser oxygen stream have been tested and incorporated in the interlock system of the electrolyser. Two ionization chambers have been installed, one for feed gas and another for exhausted gas of the LPCE column.

The CECE system employing the two electrolysers, one already modified to be tritium compatible, and the LPCE column with the catalyst/packing for endurance test has been commissioned with demineralised water.

The lower part of the experimental rig (LPCE column, boiler, pumps and IR spectrometer) is shown in Figure 2.

Fig. 2:   Experimental rig for catalyst/packing endurance test.

Since mid 2004, the LPCE column at TLK was continuously in operation for the endurance test. The exposure of catalyst to tritiated streams followed the agreed endurance test procedure.

The tritiated water of 1 $Cikg^{-1}$ used during the first three month of endurance test was sampled and the chemical analysis is already available.

The separation performances of catalyst/packing mixture using tritiated and deuteriated hydrogen as feed gas in the LPCE column will start before end 2004. The separation performances will be measured by employing the existing analytical systems: Omegatron mass spectrometer for deuterium measurements, ionisation chamber for tritium measurements and LSC and FT-IR spectrometer for tritium and respectively deuterium in the liquid phase.

The separation performances after long time functioning in water distillation mode will be measured as well.

The separation performances after 3, 6 and 9 months operation with tritiated water will be measured. The quality of water drained from the column after each exposure will be measured as well.

Based on the experience gained during the development of catalyst and packing, a regeneration procedure for the catalyst-packing mixture will be enhanced and tested, if necessary.

Staff:

Ion Cristescu
Ioana R. Cristescu
S. Welte
W. Wurster
L. Dörr
G. Hellriegel
H. Dietrich

JW3-FT-5.6
CAD Interface for MCNP

JW4-FT-5.15
Fully Automated Interface to Convert CATIA Files into MCNP Geometry Surfaces and Cells

Objectives

The overall objective of Tasks JW3-FT-5.6 and JW4-FT-5.15 was to develop an interface programme between a Computer Aided Design (CAD) system and a Monte Carlo (MC) particle transport code for accessing the geometric and topological data of CAD systems and then construct a geometry representation appropriate for MC particle transport calculations.

The specific goal of Task JW3-FT-5.6 was to test and demonstrate the capability of the interface programme for the automated processing of CAD data describing a JET octant and the conversion into surface data as required by the MCNP Monte Carlo code. The aim of Task JW4-FT-5.15 was to further develop the interface programme to enable the automatic generation of MCNP geometry cells.

Methodology

The geometry needed for the MC particle transport simulation is a decomposition of the problem space into a finite collection of disjoint regions (cells) whose union is the problem space. It is usually represented as a Boolean form of primitive solids or algebraic half-spaces. Most commercial CAD systems use the boundary representation (B-rep) method to store geometric models of solids. A solid is assumed to be a compact and regular point set whose boundary is composed of closed oriented manifolds. The difference in the representation schemes makes a conversion necessary. The geometric and topological data of a B-rep solid from a CAD system can be used to construct its semi-algebraic representation as employed in MC codes. The two main steps involved in this approach are the access to the CAD data and the conversion process itself. Access to the data of a CAD system can be provided through the data export in neutral format. The conversion proceeds in two steps. After the traversal of the B-rep data structure of a solid and extraction of the boundary supports, the first step is to determine the definability of the solid by the available boundary support set. If this is not the case the set is enlarged until definability is achieved. In the second step, a cell construction is performed by a sign constant decomposition of the solid by the boundary supports. The algorithms required for the automatic generation of the MCNP geometry cells have been implemented and integrated to the interface programme as part of Task JW4-FT-5.15.

Application to JET Torus Sector

Starting from available design models, a suitable CAD model of JET octant 3 was generated at the JET drawing office using CATIA V5. Several iteration steps were required to optimise the CAD model for the conversion and the use with MCNP. Free form surfaces (B-Splines) e. g. can neither be treated by the interface nor used in MCNP calculations and had to be replaced by algebraic surfaces. The original model also included lots of details which are unsuitable for neutronic calculations and had to be discarded. The simplification of the CAD model was performed in collaboration with the JET drawing office. Date files in STEP API-214 format were used to exchange the geometry data between the CATIA system and the interface programme.

The final CAD model as used for the conversion is shown in Fig. 1. It consists of 83 solids with 696 surfaces (517 planes, 140 cylinders, 31 cones and 7 tori). The converted MCNP model of the JET torus sector is shown in Fig. 2. It is composed of 210 geometry cells with

1386 surfaces (1116 planes, 214 cylinders, 36 cones and 20 tori) generated automatically by the interface programme.
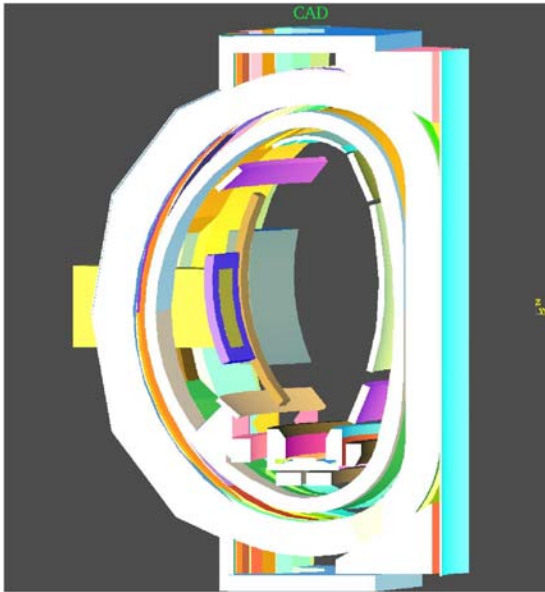
Fig. 1: CAD model of JET octant 3:
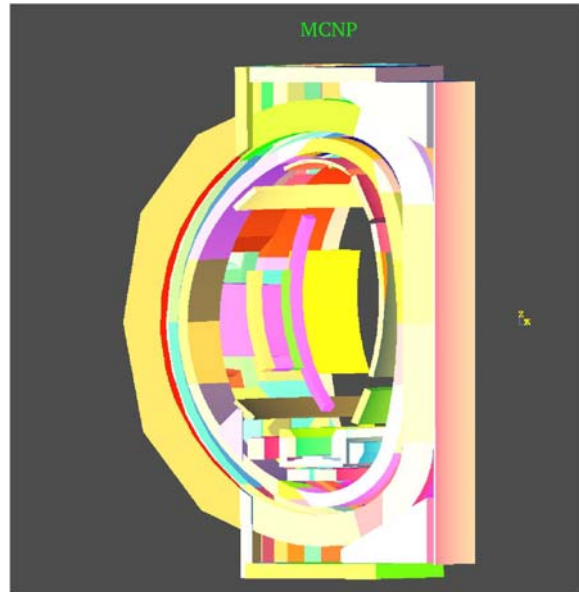
Fig. 2: Converted MCNP model:

For validating the converted geometry model, volume calculations of parts were performed with MCNP. Since the CAD model does not describe the complete geometry model including voids and contacts as required by MCNP, the calculations were performed for single components. Very satisfactory agreement was achieved for the volumes as compared to the CATIA data. It was thus concluded that the automatic conversion process reproduces the CAD geometry properly.

As indicated above, the converted MCNP model contains solids grouped together to parts with no voids included. To have a full computational model for MCNP transport calculations it is necessary to include voids and discard interferences among parts which are actually present in the CAD model. A significant effort was therefore dedicated to enable the automatic calculation of voids and to detect and correct interferences. Suitable algorithms for these purposes were developed and integrated to the interface programme. First successful tests have been performed. The application to the JET torus sector model is currently underway.

Staff:

U. Fischer
H. Tsige-Tamirat

Literature:

[1] H. Tsige-Tamirat, U. Fischer, P. Carman, M. Loughlin, Automatic Generation of a JET 3D Neutronics Model from CAD Geometry Data for Monte Carlo Calculations, 23rd Symposium on Fusion Technology (SOFT), 20-24 September 2004, Venice, Italy

[2] H. Tsige-Tamirat, U. Fischer, CAD Based Geometry Generation for Monte Carlo Particle Transport Codes, ANS Winter Meeting, November 14-18, 2004, Washington DC, USA

JW3-FT-5.8
Validation of Shutdown Dose Rate Calculations

The objective is to validate the computational methods for shutdown dose rate calculations through the comparison with experimental dose rates available at JET. Such data were recorded by the JET Health Physics team as part of the regular monitoring programme during the DTE1 experimental campaign in 1997/98.

Two different computational schemes have been recently developed, both of them relying on the Monte Carlo technique for the transport simulation. The rigorous 2-step (R2S) method [1] makes use of the Monte Carlo code MCNP [2] for the transport calculations (neutron and decay photons) and the FISPACT inventory code [3] for the activation calculations with a suitable coupling scheme for the automated routing of decay photon source distributions and neutron flux spectra. The direct 1-step (D1S) method [4] is based on the assumption that a radioactive nuclide generated during irradiation spontaneously emits the associated decay photons. Neutron and decay photon transport then can be treated in one single Monte Carlo calculation run. When calculating the dose rate, correction factors are applied to account for the proper decay rate of a radioactive nuclide. The D1S approach uses a modified version of the MCNP code together with special, ad hoc generated nuclear cross-section data

The two approaches have been successfully applied to dose rate analyses of ITER and the JET (Joint European Torus) tokamak revealing, however, some inherent discrepancies. Good agreement was found for a benchmark experiment performed on a ITER shield blanket mock-up at the Frascati 14 MeV neutron generator (FNG). Further benchmarking was considered necessary by utilizing, as much as possible, a real fusion device with a plasma volume source such as the JET tokamak. First benchmark tests on JET were conducted in the framework of Task JW2-FT-5.5 by means of comparison calculations for a 3D torus sector model of the JET device. The shut-down dose rates were calculated for different positions inside and outside the vessel and in the torus hall assuming a representative irradiation scenario. The R2S and D1S results of this calculational benchmark showed agreement within ± 25 % [5]. This was considered satisfactory taking into account the very different approaches.

A more realistic benchmark exercise on JET was the subject of Task JW3-FT-5.8. The real irradiation history of D-T and D-D campaigns conducted at JET during the years 1997-98 were used to calculate the shut-down doses at four different locations (positions 1 – 4:) and four different irradiation histories with different decay times labelled #1, 9, 15 and 16 in Fig. 1.
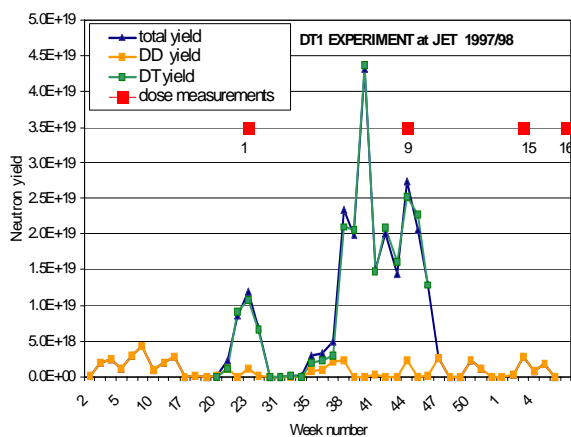
Fig. 1: JET DTE 1 neutron yields and dose measurements as function of time. Times at which the dose measurements have been taken are shown as red squares.
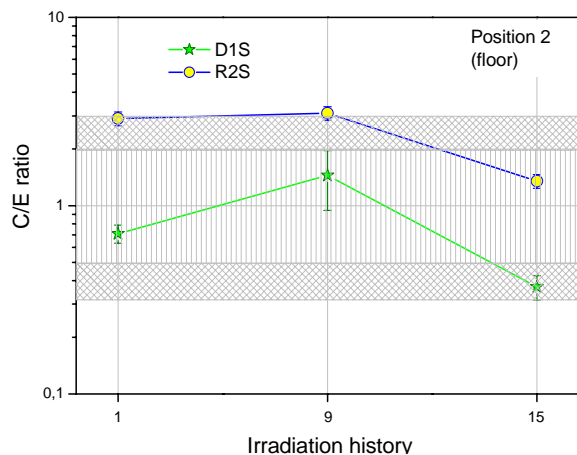
Fig. 2: C/E ratio of calculated (C) and experimental (E) dose rates for JET position 2 at different irradiation histories.

The two computational procedures gave results that in general agree with the available measurements within a factor 2 to 3 except for position 3, measurement 15 (R2S) and posi-

tion 4, measurement 9 (R2S and D1S). Figs. 2 - 4 show the corresponding graphical comparisons of calculated (C) and experimental (E) shut-down dose rates for the positions 2 – 4 on the torus hall floor, in contact with the upper coil and in contact with the machine structure, respectively. Inside the machine (position 1) there was only one measurement available (irradiation history #16). The C/E ratios for the dose measurement at this location amounts to 1.67 and 1.73 for the R2S and the D1S approach, respectively.
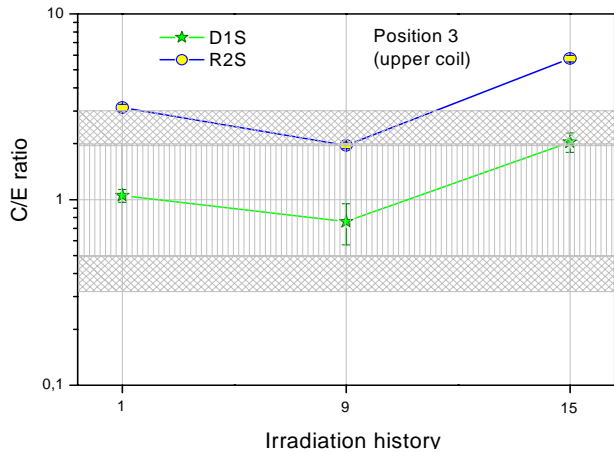
Fig. 3: C/E ratio of calculated (C) and experimental (E) dose rates for JET position 3 at different irradiation histories.
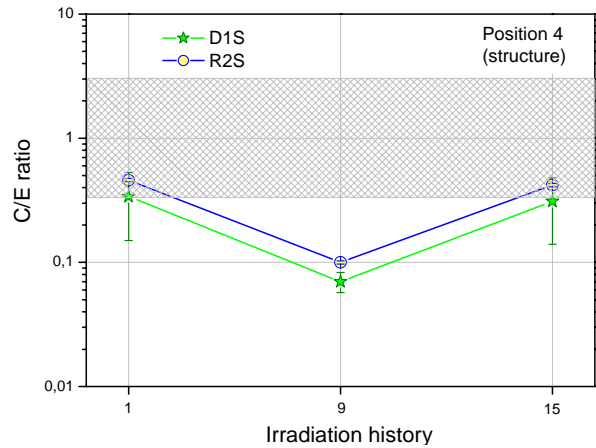
Fig. 4: C/E ratio of calculated (C) and experimental (E) dose rates for JET position 4 at different irradiation histories

The comparison between calculational and experimental JET dose rate results was constrained, however, by the rather high uncertainties associated with the available measurements. These data were recorded by the JET Health Physics team as part of the regular monitoring programme under not well defined conditions and were judged to be not accurate enough to validate computational results. In addition it was not ensured that the available JET model did adequately represent the geometry and material distribution around the locations where the doses were recorded during the DTE1 experimental campaign in 1997/98.

It was therefore concluded that a dedicated experiment on JET need to be conducted for the benchmarking of R2S and D1S shut-down dose rate calculations. This is planned as part of the experimental programme during the D-D operation of JET in 2005.

Staff:

U. Fischer
P. Pereslavtsev
P. Batistoni (ENEA Frascati)
M. Loughlin (UKAEA Culham)
L. Petrizzi (ENEA Frascati)
R. Villari (ENEA Frascati)

Literature:

[1] Y. Chen, U. Fischer, "Rigorous MCNP based shutdown dose rate calculations: Computational scheme, verification calculations and applications to ITER", Fus. Eng. Des. 63-64 (2002), 107-114.

[2] J.F. Briesmeister (ed.), "MCNP - A General Monte Carlo N-Particle Transport Code, Version 4C", Los Alamos National Laboratory, Report LA-13709-M, April 2000.

[3] R. A. Forrest, J-Ch. Sublet, "FISPACT 99: User Manual", UKAEA Fusion, Report UKAEA FUS 407, December 1998

[4] H. Iida, D. Valenza, R. Plenteda, R. T. Santoro and J. Dietz "Radiation Shielding for ITER to allow for Hands-on Maintenance inside the Cryostat", J. Nucl. Sci. Techn,. Sup. 1 (March 2000) 235-242

[5] L. Petrizzi, P. Batistoni, U. Fischer, M. Loughlin, P. Pereslavtsev, R. Villari, "Benchmarking of Monte Carlo based shutdown dose rate calculations for applications to JET", 10th Int. Conf. Reactor Shielding (ICRS-10), Madeira, Portugal, 9-14 May 2004

JW4-FT-5.17
Simulation of Tritium Spreading in Controlled Areas after a Tritium Release Considering Inner Obstacles

The knowledge on tritium distribution in a confined area in case of a tritium spill, and the knowledge of tritium removal rate is useful to determine the removal time for existing ventilation conditions in a tritium handling room, to design suitable detritiation systems and to identify effective monitor locations in a facility. A mathematical model to simulate tritium behaviour after a release into a confined ventilated volume has been developed at the Forschungszentrum Karlsruhe. The model assumes that for the investigated cases, tritium behaviour can be characterized by solving the dynamic equations of motion (the Navier-Stokes equations) coupled with the classical k-ε turbulence model to simulate the ventilation in the room and mass diffusion for tritium spreading. The GASFLOW-II fluid dynamics field code, developed through a Los Alamos National Laboratory (LANL) – FZK co-operation, was used as the computational tool to solve the equations that describe the processes. The numerical results have been validated with experimental data collected on the experimental facility (Caisson) at the Tritium Process Laboratory (TPL) Japan.
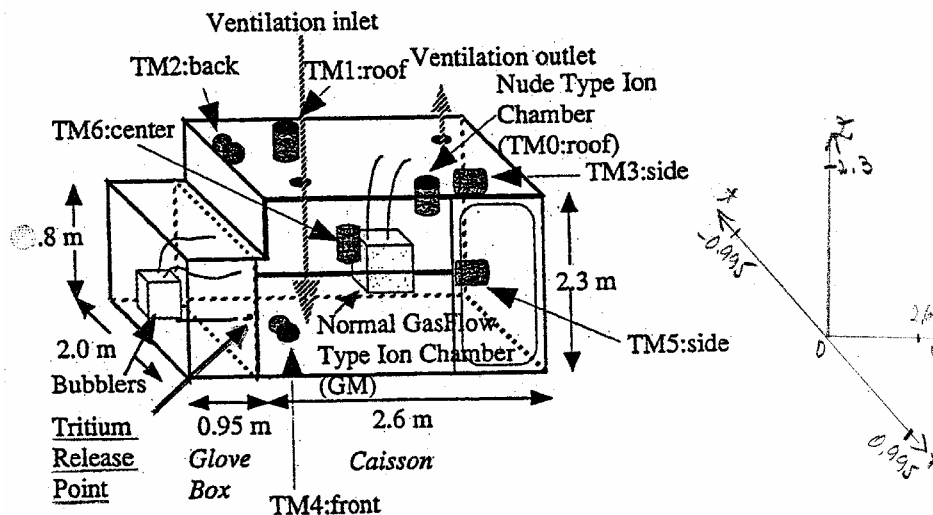
Fig. 1: Structure of the CATS and location of tritium monitors and tritium release point.

The Caisson is a 12 m^3 stainless steel leak-tight box that is connected to a glove box housing the equipment to release tritium into the Caisson. The Caisson is connected to a membrane detritiation system with 4 volume exchanges per hour. The connection between the Caisson and the ventilation system is realized through a supply duct and an exhaust duct located at 0.09 m below the ceiling. Seven ionisation chambers, designated TM0 to TM6 were installed in the Caisson for tritium concentration monitoring (Figure 1).

Five different cases with different obstacles and/or tritium release point locations have been investigated:

Case 1: Caisson without obstacles, tritium release point on the back wall.

Case 2: Caisson with 2 obstacles of approx. half-height, one under the supply duct, one under the exhaust duct; tritium release point - on the back wall

Case 3: Caisson with 2 obstacles of approx. half-height, one under the supply duct, one under the exhaust duct; tritium release point from one of the obstacles, simulating an release from a glove-box (Figure 2.a).
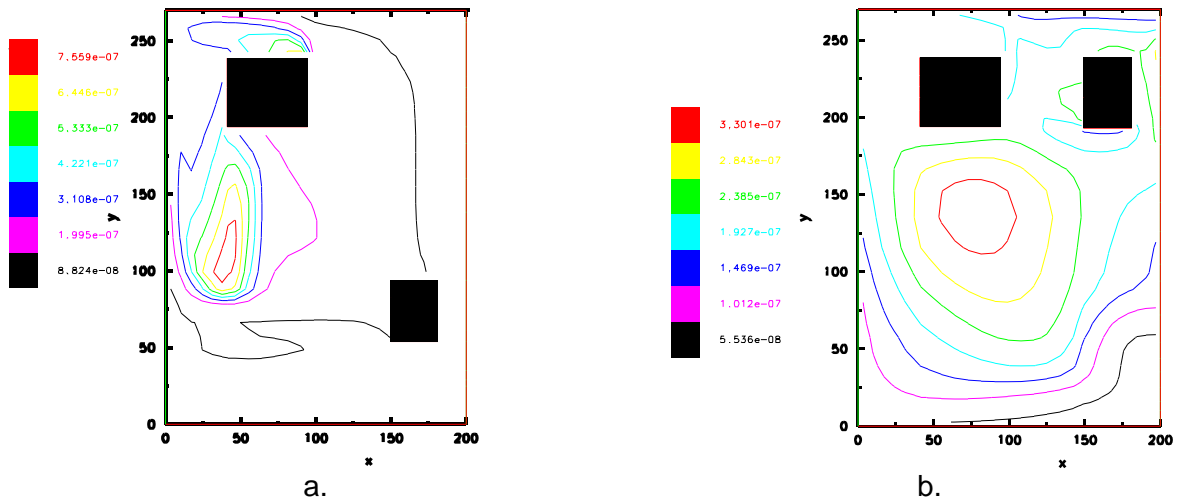
Fig. 2: Geometries investigated, obstacles location and/or tritium release points.

Case 4: Caisson with 2 obstacles of approx. half-height; one under the supply duct, one in parallel; tritium release point from 2-nd obstacle, simulating an release from a glove-box, in opposite direction compared with case 3. (Figure 2.b).

Case5: Caisson with 4 obstacles of approx. half-height, one under the supply duct, one in parallel, one under the exhaust duct, one in parallel; tritium release point – on the back wall.

For all five investigated cases, the exchange rate was 4 Caisson volumes/hour, and the value of the initial tritium release was 444 GBq. In case of a perfect mixing this will give an average tritium concentration of 37GBqm^{-3}.

GASFLOW output capabilities used for tritium spreading analyses include concentration plots in user-specified sections and velocity field plots in user-specified sections, both at specified moments of time; time-history plots of concentration and velocity at specified locations. In the locations where the tritium monitors have been placed during the experiments, the tritium concentration as computed by GASFLOW was plotted and is presented in Figures 3 a and b.
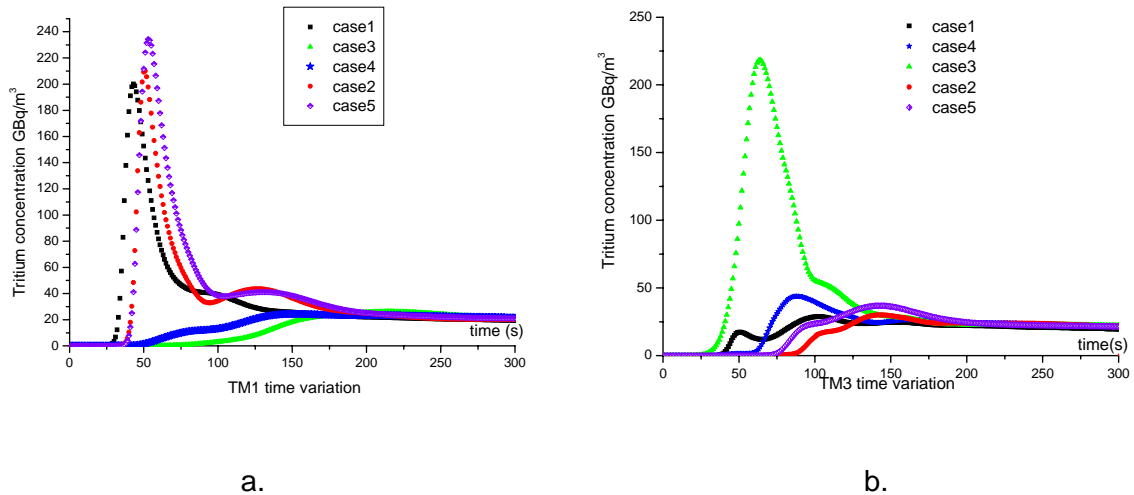
Fig. 3: Time variation of tritium concentration at location TM1 (a) and TM3 (b).

As already pointed out, the release location is the key for the initial tritium behaviour. In the investigated case when tritium release point is located in the back wall, due to the location of the inlet duct, tritium is quickly carried up by the strong flow near the wall, as it can be seen in Figure 4.

At this moment in time the work can be concluded as follows:

- At high ventilation rates the time when a tritium monitor detects a maximum amount of tritium depends strongly on the tritium release point location and only weakly on the existence of inner obstacles;

- As the differences between indications in various investigated locations of the Caisson is strongly dependent on the tritium release point location, it is necessary to determine possible locations (e.g.

Fig. 4: Velocity field in a section through the tritium release point back wall.

inlet duct, release duct) where this dependence is not so strong. This is of particular importance for the ITER tritium monitoring system location, as this triggers the shut-down of the normal ventilation system and the switch to the emergency ventilation system. As it can be seen from Figure 3, a tritium monitor location in the neighborhood of the tritium release point can indicate tritium concentrations one order of magnitude higher than an averaged concentration.

In the next future lower ventilation rates (max. 1 volume exchange/hour as HVAC foreseen for ITER) will be investigated. A uniform ventilation appears of highest importance; a better ventilation distribution (several inlet ducts) at ITER relevant ventilation rate will be investigated and outlined in the final report.

Staff:

Ioana -R. Cristescu
J. Travis (IKET)

JW1-FT-6.1
Impact of Tritium on the Performance of a Prototype Cryosorption Pumping Panel

1. Objectives

This task is an essential complement to the parallel assessment of the pump performance of the ITER torus model cryopump in FZK, where the tritium fractions have been replaced by deuterium. The central objective of this task, which will be performed within the Task Force Fusion Technology at JET [1], is to study the interaction of tritium and tritiated gas mixtures with the panel, in terms of pumping performance, desorption characteristics and structural influences. The existing knowledge in this field is limited to qualitative results gained in other fusion devices and only one small scale phenomenological experiment. Together with the existing data for protium and deuterium, a sound assessment of any isotopic effect is aimed at. The understanding of the pumping mechanism of tritiated gases, which is expected from this experiment, is needed to develop advanced regeneration procedures for cryosorption panels. This experiment is a benchmark test which would reveal any showstoppers to the ITER cryopumping concept arising from tritium interaction, which is the only field not having been fully covered yet.

2. Experimental results from operation during the JET Trace Tritium Experiment

Within this task, a Prototype Cryosorption Pump (PCP) was designed, manufactured and installed into an existing cryogenic forevacuum (CF) module of the Active Gas Handling System (AGHS) at JET. With respect to the outer dimensions, the PCP is a complete copy of the existing ACP pump, which will be re-installed in the CF module after completion of the task. However, the interior parts are designed completely different to provide for a cryosorption pumping effect, whereas the ACP is working on cryocondensation. The existing cryosupply was upgraded for higher flowrates of liquid helium (LHe). To achieve ITER relevant temperatures of 4.2 K, a separate transfer line from a LHe dewar was installed, different from the normal JET cryosupply conditions with sub-atmospheric LHe at about 3.4 K. This temperature difference is very relevant since too low temperatures may completely change the pumping mechanism from sorption (at higher temperatures) to condensation (at lower temperatures).

The internal module pipework had to be adapted, which was prepared prior to the installation procedure, such that the incoming gas can be taken from two sources. This is to reflect the two-stage strategy foreseen for testing the pump. In the first stage, the PCP will be operated within the JET trace tritium campaign (TTE) directly on the main torus volume under direct processing of tritiated gases to pump tritium-rich gas from the neutral beam injector box and trace tritium gas from the torus.

CF is typically operated in a batch-wise manner. This means, a portion of gas released from the divertor or NIB cryopumps under regeneration is rapidly expanded into the pump volume, typically over night. This causes a sudden temperature increase (up to 40 K to 50 K) and a pumping effect during the following cool down. Due to the presence of charcoal in the PCP, this operational procedure ensures that any pump effect is definitely caused by cryosorption and not by condensation, because adsorption starts to become active at much higher temperatures.

The PCP was running without problems and according to specification. The pump performance was very supportive of AGHS operation due to the fact that sorption pumping of hydrogens begins at much higher temperatures than condensation. The cumulative amount of pumped tritium was approximately 1 bar·l (0.3 g T_2). The highest gas amount pumped in one batch was under non active conditions 140 bar·l of D_2. Related to the charcoal-coated pump-

ing surface of 4000 cm², this yields a gas load of about 2.3 (Pa·m³)/cm². This is higher than ever measured before and by a factor 10 larger than what is required for ITER.

3. Experimental results from parametric testing

The second experimental stage was the investigation of the pump performance under a more structured and parametric variation of the influential properties. The PCP parametric tests are characterised by the supply gas being fed externally at pre-defined composition from an external reservoir. The reservoir volume could be fed with standard gases and with tritium from the U-beds. The maximum tritium inventory was limited to 5 g in the system. This corresponds to a filling pressure of 200 mbar in the 100 l reservoir (at room temperature). To have a defined flowrate from the reservoir into the PCP, a JET certified tritium compatible valve equipped with a defined orifice was installed in the dosage line. An orifice diameter of 0.3 mm was found to be sufficient to ensure choked flow conditions (which means throughput becoming directly proportional to the reservoir pressure) and to generate cryopanel surface related flowrates and gas loads in the range comparable with the ones in ITER. The final set-up (valve+orifice+filter) was calibrated at FZK prior to the experiments.

This campaign was most relevant to obtain the underlying data needed to design the regeneration and pumping parameters for tritium operation of the ITER torus cryopump. The tests involved two basic categories: Pumping tests (i.e. measurement of PCP pressure evolution under defined inflow of gas) and Thermal Desorption Spectroscopy experiments (TDS, i.e. measurement of PCP pressure evolution with active forepumping during regeneration heating).

To have a sound data-base which allows for cross-checks with literature data, a series of non-active reference gases was started with: N_2, D_2, H_2, He and a D_2-based gas mixture (denoted D2-base, containing 3.7% fusion typical impurities (CO, CO_2, O_2, CH_4)) with 10% He. These runs were complemented with pure tritium, an equimolar D_2+T_2 mixture (close to equilibrium when being pumped: 30% D_2, 40% DT, 30% T_2) and a three-component mixture with 10% He [2]. Fig. 1 illustrates the results obtained for the fusion relevant isotopes D_2, T_2 and DT as well as for He, in terms of the sticking coefficient vs. the gas load being pumped. The big scatter of the derived data results from insufficient smoothing of the reservoir pressure sensor signals used to calculate the throughput and the limited bandwidth in transfer of the PCP vacuum gauge output voltages. The first 100 s of each run could not be evaluated because the measured pressures were significantly falsified by the transient build-up of the steady-state pressure profile along the connection pipe to the vacuum gauge.
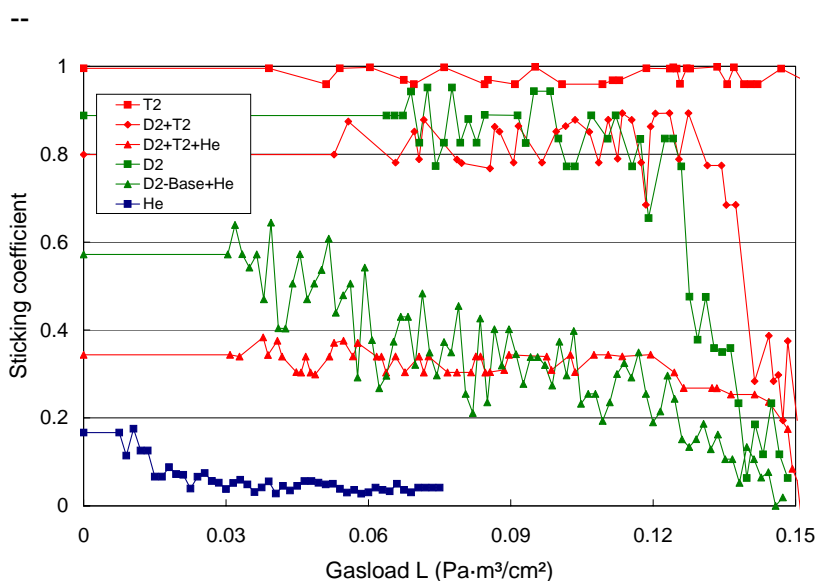
Fig. 1: Measured sticking coefficients for fusion relevant gases.

It becomes obvious that hydrogen isotopes are pumped very well with tritium being close to ideality (sticking coefficient unity). Moreover, tritium is the only gas which behaves almost constant over the increasing gas load. This behaviour was validated within a special long-term test with a final gas load of 0.25 (Pa·m³/cm²) of tritium, which is a clear indication that tritium is pumped by resublimation rather than by

sorption. It is known from the TIMO tests that H2 is pumped by sorption exclusively, D2 is pumped by combined sorption and resublimation. Table 1 compares the measured initial sticking coefficients with literature data. For He and H2 which are known to show a strong temperature dependency of the sticking coefficient, the measured values are smaller than reported elsewhere. This is probably due to the fact that the temperature of the upper cryopanel was not below 9 K. It is also revealed that the pump performance of a 10% helium in hydrogen mixture is governed by the helium content due to its low sticking coefficient.

Table 1:   Comparison of initial sticking coefficients.

	He	H_2	D_2	T_2
This work	0.1	0.4	0.88	1.0
Lit [3]	0.15	0.6	0.90	-

The absolute values of the pumping speeds for the hydrogen isotopes (D_2, T_2, DT) were in the range of 6.5 m³/s. In this experimental campaign, the PCP has pumped an integral amount of 4.8 g of T_2 and 1.3 g of DT. To assess any permanent effect of tritium on the pump performance for other gases, a comparison before and after the tritium runs has been made, using the 90% D2-base + 10% He-mixture, which did not show any significant effect.

The second central issue in performing these tests was to clarify the pumping mechanism of tritiated gases. The advantage of using a cryosorbent is that the DT fusion ash helium can be pumped effectively. Earlier investigations have shown that, under the conditions of a cryosorption pump at 4.5 K, protium is predominantly pumped by sorption (as helium) in the charcoal pores, and deuterium is pumped by combined sorption and resublimation, governed by sorption at small gas loads (as for the experiments described in this paper) to resublimation at high gas loads. From the extrapolation of the saturation pressure curve, one would expect tritium to be pumped predominantly by resublimation (formation of ice layers) on top of the charcoal. However, the decay heat and existence of ß particles may change the energy distribution on the surface of the charcoal and thus lead to different results. One goal of the test campaign is therefore to identify the pumping mechanism of tritium.

The constant sticking coefficient for tritium shown in Fig. 1 was already one indication for condensation pumping. Fig. 2 shows the result of a TDS experiment for the two gases D_2 and T_2, i.e. the pressure evolution curve when the panels get heated for regeneration. The pressure peak for tritium, which has no correspondence for deuterium, is interpreted by sublimation of tritium, which is then re-adsorbed from the gaseous phase, because the sorption efficiency of charcoal is still quite high at temperatures above sublimation. After this step, all condensed particles end up at the charcoal again, but bound at a different energy. So, in the temperature range above sublimation, thermodynamics of classical desorption are valid. The actual desorption regeneration starts quantitatively not before 40 K at the charcoal.

An important consequence of condensation pumping of T_2 is the potential risk of blocking the charcoal pores by formation of an ice layer on top. In this case the pumping speed for the species which have to be pumped by sorption, especially He, may drastically diminish. It has been agreed that a second experimental campaign will be started to better characterize and quantify this competing pumping situation.
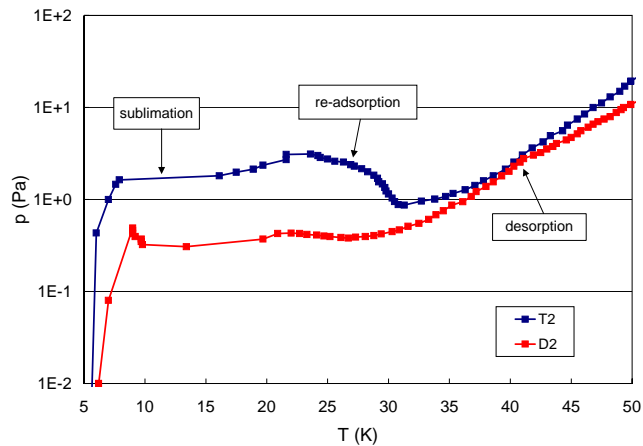
Fig. 2:   TDS test for resublimated T_2 and sorbed D_2.

Staff:

Chr. Day
H. Jensen
P. Pfeil
R. Simon

D. Brennan (UKAEA)
P. Camp (UKAEA)
S. Knipe (UKAEA)

Literature:

[1] C. Grisolia et al., JET contributions to the ITER technology issues, Symp. On Fusion Technology, Venice, Italy, Sept. 2004.

[2] Chr. Day et al., Performance of ITER relevant cryopump panels for tritiated gases, Int. Conf. On Tritium Science and Technology, Baden-Baden, Germany, Sept. 2004.

[3] Chr. Day, The Use of Porous Materials for Cryopumping, in: H.S. Nalwa (ed.), Handbook of Surfaces and Interfaces of Materials, Chapter 8, Academic Press, San Diego (2001).

Heating Systems Technology Project

TW3-THHE-CCGDS1 D1 and D2
ITER ECRF Advanced Source Development
– Coaxial Cavity Gyrotron –

In cooperation with European Associations (CRPP Lausanne, TEKES Helsinki) and with Thales Electron Devices, Velizy, France (TED) as industrial partner a general design of a prototype of a 2 MW, CW coaxial cavity gyrotron operated at 170 GHz has been finished and the manufacturing of this prototype started in July 2004. The work is based mainly on results obtained at FZK in the past years. During the manufacturing phase the Associations will support TED. In particular, the design and the specifications of the different components will be done by the Associations.

A facility for testing of the 2 MW 170 GHz prototype gyrotron up to CW operation is under preparation at CRPP Lausanne. The gyrotron is expected to be delivered beginning of 2006.

In parallel to the contributions to the work on the industrial prototype the experimental 165 GHz coaxial cavity gyrotron at FZK has been modified for operation at 170 GHz in order to verify the design of critical components (cavity, RF output system, electron gun) of the prototype. The modified tube has been brought into operation and experimental investigations are under way.

2 MW, CW 170 GHz prototype of a coaxial cavity gyrotron for ITER

A contract has been placed in July 2004 by EFDA at TED for manufacturing of a prototype of a coaxial cavity gyrotron with an RF output power of 2 MW, CW at 170 GHz. The development work on the 2 MW, CW coaxial cavity gyrotron is done in cooperation between European Associations (CRPP Lausanne, FZK Karlsruhe and HUT Helsinki) with TED as industrial partner. Within this cooperation the responsibility of the Associations is to provide the specifications and the physical design of the gyrotron components. The fabrication of the prototype as well as all problems related to that are within the responsibility of TED. The delivery of the prototype is expected for beginning of 2006. A suitable superconducting (SC) magnet has already been specified and ordered. The main parameters of the gyrotron are summarised in Tab. 1.

Table 1: Nominal operating parameters of the gyrotron and some design specifications

operating mode:	$TE_{34,19}$
frequency, f	170 GHz
accelerating voltage, U_{acc}	90 kV
beam current, I_b	75 A
RF output power, P_{out}	2 MW
RF output efficiency, η_{out}	$\geq 45\ \%$
magnetic field in the cavity, B_{cav}	6.86 T
Ohmic losses (twice the losses of ideal copper at 273 K; P_{RF} = 2.2 MW):	
peak wall loading at outer wall p_{cav}	2 kW/cm²
peak wall loading at coaxial insert p_{ins}	0.2 kW/cm²
power dissipated in the collector - nominal operation:	≤ 2.4 MW
with modulated RF output power (0.6 - 2 MW):	≤ 3.1 MW

The design of all components have been practically finished in the reporting period. The $TE_{34,19}$ mode has been selected as operating cavity mode. In order to reduce the diffraction losses at the launcher cut, and thus to decrease the amount of microwave stray losses inside

the gyrotron tube, a quasi optical (q.o.) RF output system with a dimpled wall launcher and three mirrors has been designed. A single-disk CVD-diamond window with a thickness of 1.852 mm = $5\lambda/2$ (at 170 GHz) can be used for transmission of 2 MW microwave power at 170 GHz. At a loss tangent of 2×10^{-5} (state of the art) 880 W power will be absorbed in the disc. Edge cooling of the CVD diamond disc with water is sufficient for removing the heat load. A single-stage depressed collector with the collector at ground potential will be used. Under nominal operating conditions about 2.4 MW beam power has to be dissipated in the collector. In operation with the microwave power modulated between about 0.6 MW and 2 MW the power dissipated in the collector increases to about 3 MW.
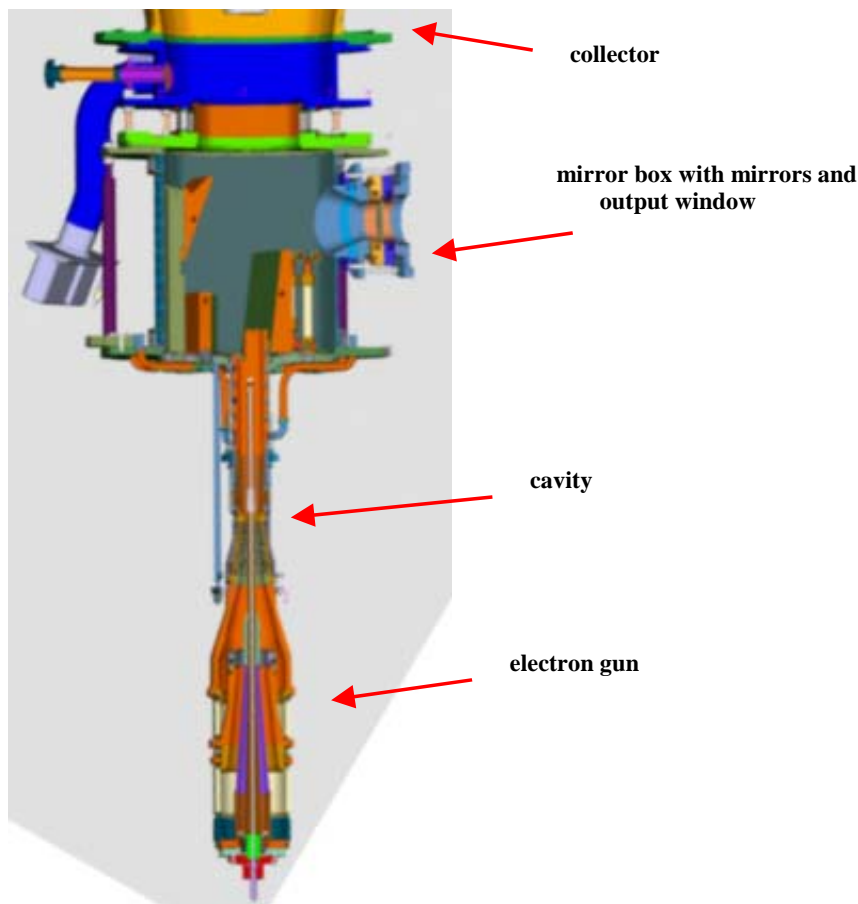
Fig. 1: Schematic view of the prototype of the 170 GHz coaxial cavity gyrotron.

170 GHz short-pulse coaxial cavity gyrotron (pre-prototype)

In parallel to the work on the industrial prototype, the $TE_{31,17}$ short pulse gyrotron at 165 GHz used previously for the performing the basic investigations at FZK has been modified for operation in the $TE_{34,19}$ mode at 170 GHz. The modified tube, which can be considered as a pre-prototype of the industrial tube, will be used to verify the design of the main gyrotron components as electron gun, cavity and the quasi-optical RF output system under relevant conditions. The cavity dimensions and the geometry of the RF output system are the same in the prototype as in the pre-prototype tube. The geometry of the electron gun, mainly of the anode, differs slightly from the gun of the industrial prototype because of the different magnetic field distribution and different anode voltage. However, the main features are equal. Since the SC-magnet used for the short pulse experiments delivers only a magnetic field up to about 6.68 T, the beam voltage has to be reduced to values below 80 kV in order to be able to excite the $TE_{34,19}$ mode at 170 GHz. The operation at the lower voltage results in

comparison to the prototype in a reduced value of the RF output power depending on the finally obtained magnetic field.

Experimental results

The experimental operation started with some delay in May 2004 due to late delivery of the electron gun. When starting the operation strong parasitic low frequency (LF) oscillations have been observed at beam currents $I_b \geq 10$ A and accelerating voltages $U_c \geq 40$ kV. The amplitude of these oscillations could become very large thus preventing a stable gyrotron operation. The spectrum of the LF oscillations consisted of up to 3 different frequencies as shown in Fig. 2. The appearance of those LF oscillations was unexpected, in particular because no such oscillations appeared in the previous 165 GHz coaxial gyrotron with very similar geometrical dimensions (relevant for the wavelength of the LF frequencies). In addition, the external assembly including the cabling has not been modified either. Extended search for causes became necessary until the parasitic LF oscillations have been suppressed and a stable operation has been obtained over a wide range of parameters.
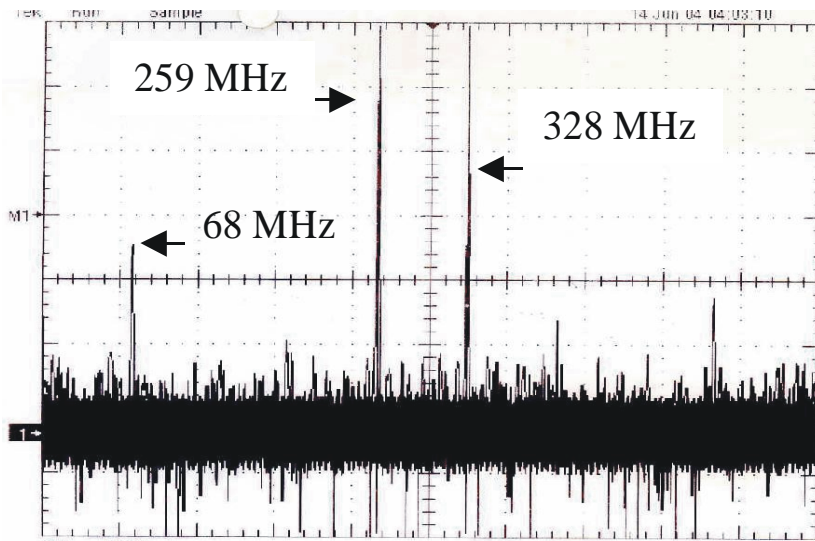
Fig. 2: Spectrum of the parasitic LF oscillations.

After suppressing the LF oscillations, measurements in the gyrotron mode have started. The inner conductor and the outer cavity wall have been radially aligned with respect to the electron beam within $\pm$ 0.1 mm. Until now following results have been obtained:

(1) The electron gun and the electron beam behave satisfactorily and fulfil the requirements as needed for the prototype tube. A stable operation up to $I_b \approx 80$ A and $U_c \approx 80$ kV has been observed without any instabilities and LF oscillations. An extension of the pulse length up to 100 ms / 40 ms at $I_b \approx 1$A / 17 A did not show any indications of occurrence of a Penning discharge inside the gun.

(2) The nominal $TE_{34,19}$ mode at 170 GHz has been excited stably over a reasonable parameter range. As an example Fig. 3 shows the RF output power measured in dependence of the applied accelerating voltage U_c. Besides the $TE_{34,19}$ mode two neighboured modes have been identified, the $TE_{33,19}$ and the $TE_{32,19}$ mode. The observed mode sequence is not in agreement with results of numerical simulations. A maximum RF output power of $P_{out} \cong 1.15$ MW has been measured with an output efficiency of about 20 %. This value corresponds to about 2/3 of the value expected from the design calculations. The main reason for the discrepancy is thought to be due to the fact that the oscillation range of the nominal mode occurs at beam voltages lower than expected from calculations. The reasons for that are under investigation.

(3) The distribution of the RF output beam outside the gyrotron has been measured with an infrared camera. Unfortunately it has been found that the measured pattern is only in poor agreement with the results of design calculations. However, a reasonable good agreement has been found with results of low power measurements. Further on, the amount of stray radiation inside the gyrotron tube has been measured to be about 8 % in comparison to a design value of 5 to 6 %. As a consequence of the results a further improvement of the RF

output system is needed. For that a new RF output system is under design with an improved launcher which will be optimized with a new more accurate code.
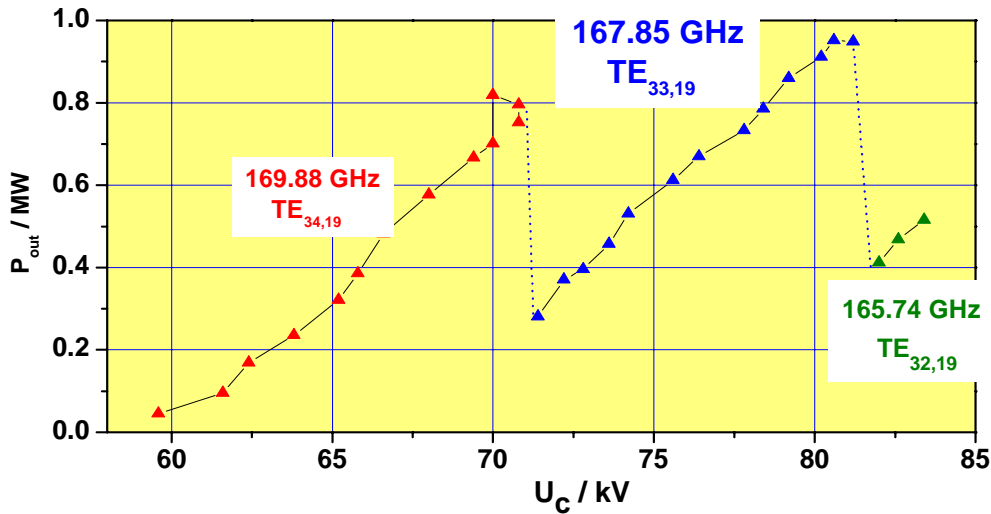
Fig. 3: RF output power vs. U_c. B_{cav} = 6.68 T, $I_b \cong$ 51 A at U_c = 70 kV.

Summary and outlook

The work on the industrial prototype of the 2 MW, CW coaxial cavity gyrotron is in progress. The information and data required by TED has been delivered in time. The experimental work on the pre-prototype tube started in May 2004. Parasitic LF oscillations have been successfully suppressed and stable gyrotron operation has been obtained over a wide parameter range. The nominal $TE_{34,19}$ mode at 170 GHz can be excited stable in single mode operation. Detailed investigations of the gyrotron oscillating characteristic are under way. The performance of the RF output beam is not in agreement with the design calculations and the amount of stray radiation has been measured to be about 8%. In order to increase the Gaussian content in the RF output beam and to reduce the microwave stray losses an improved RF output system is under design. Measurements of absorption of the stray losses by internal loads have been prepared and will be performed next.

Staff:

A. Arnold (Uni Karlsruhe)
H. Budig
G. Dammertz
S. Illy
J. Jin
K. Koppenburg
W. Leonhardt
M.V. Kartikeyan (guest scientist)
H.R. Kunkel
D. Mellein
B. Piosczyk
T. Rzesnicki
M. Schmid
W. Spiess
J. Szczesny
M. Thumm
R. Vincon
X. Yang

Literature:

([5] to [9] are some selected contributions to conferences):

[1] PIOSCZYK, B.; DAMMERTZ, G.; DUMBRAJS, O.; DRUMM, O.; ILLY, S.; JIN, J.; THUMM, M.; "165-GHz coaxial cavity gyrotron.", IEEE Trans. on Plasma Science, 32(2004) pp.853-60.

[2] PIOSCZYK, B.; DAMMERTZ, G.; DUMBRAJS, O.; DRUMM, O.; ILLY, S.; JIN, J.; THUMM, M.; "A 2 MW, 170 GHz coaxial cavity gyrotron", IEEE Trans. on Plasma Science, 32(2004) pp. 413-17.

[3] DUMBRAJS, O.; IDEHARA, T.; WATANABE, S.; KIMURA, A.; SASAGAWA, H.; AGUSU, L.; "Reflections in gyrotrons with axial output." IEEE Trans. on Plasma Science, 32(2004) pp. 899-902

[4] DUMBRAJS, O.; Nusinovich, G.S.; PIOSCZYK, B.; "Reflections in gyrotrons with radial output. Consequences for the ITER gyrotron." Physics of Plasmas, Vol. 11, No.12, December 2004, pp. 5423-5429

[5] AVRAMIDES, K.A.; VOMVORIDIS, J.L.; PIOSCZYK, B.; IATROU, C.T.; "Second-harmonic operation of coaxial gyrotrons. Towards a proof-of-principle experiment.", 29th Internat. Conf. on Infrared and Millimetre Waves, Karlsruhe, September 27 - October 1, 2004, pp. 627-28

[6] PIOSCZYK, B.; RZESNICKI, T.; ARNOLD, A.; BUDIG, H.; DAMMERTZ, G.; DUMBRAJS, O.; ILLY, S.; JIN, J.; KOPPENBURG, K.; LEONHARDT, W.; MICHEL, G.; SCHMID, M.; THUMM, M.; YANG, X.; " Progress in the development of the 170 GHz coaxial cavity gyrotron.", 29th Internat. Conf. on Infrared and Millimeter Waves, Karlsruhe, September 27 - October 1, 2004.

[7] THUMM, M.; ARNOLD, A.; BORIE, E.; DAMMERTZ, G.; HEIDINGER, R.; ILLY, S.; JIN, J ; KOPPENBURG, K.; MICHEL, G.; PIOSCZYK, B.; RZESNICKI, T.; WAGNER, D.; YANG, X.; "Advanced high power gyrotrons for EC H&CD applications in fusion plasmas"; 31st IEEE Internat. Conf. on Plasma Science (ICOPS 2004), Baltimore, Md., June 28 - July 1, 2004.

[8] TRAN, M.Q.; ARNOLD, A.; BARIOU, D.; BORIE, E.; DAMMERTZ, G.; DARBOS, C.; DUMBRAJS, O.; GANTENBEIN, G.; GIGUET, E.; HEIDINGER, R.; HOGGE, J.P.; ILLY, S.; KASPAREK, W.; LIEVIN, C.; MAGNE, R.; MICHEL, G.; PIOSCZYK, B.; THUMM, M.; YOVCHEV, I.; "Development of high power gyrotrons for fusion plasma applications in the EU.", 29th Internat. Conf. on Infrared and Millimeter Waves, Karlsruhe, September 27 - October 1, 2004

[9] ILLY, S.; PIOSCZYK, B.; RAFF, S., "Numerical simulation of the single-stage depressed collector for the 2 MW, CW, 170 GHz coaxial cavity gyrotron."; Proc. of the 10th Triennial ITG-Conf., Garmisch-Partenkirchen, May 3-4, 2004

EFDA/03-1048
The First ITER NB Injector and the ITER NB Test Facility: Design

Background and Objectives

The design of the Neutral Beam (NB) system to be used in ITER and the results of the relevant R&D are described in the documents, which were produced at the end of ITER-EDA (July 2001). FZK is now reviewing the design of the cryopump for the first ITER NB Injector. Starting from the final report of the task TW1-TTF/D465-3, dated February 2002 FZK is working further on the technical assessment of the cryopumps [1] and the mechanical forepumping system.

Table 1: Design parameters.

Power delivered to the plasma per injector	16.5 MW
Beam Energy	1 MeV
Ion Species	D^-
Accelerated ion current	40 A
Average accelerated ion current density	200 A/m^2
Current density uniformity over the extraction area	±10 %
Source filling pressure	0.3 Pa
Hydrogen source gas flow (max. flow)	1.73 Pa·m^3/s
Hydrogen gas flow from neutralizer	31.6 Pa·m^3/s
Hydrogen gas flow to Residual Ion Dump (RID)	3 Pa m^3/s
Required pumping velocity for hydrogen	3800 m^3/s
Required pumping velocity for deuterium	2600 m^3/s
Pulse lengths	≤ 3600 sec.

The key NB design parameters and required pressures by given gas flows are summarized in table 1.

Cryopump Design Concepts

The cryopump has a cylindrical shape and can be separated into six submodules. In each of these submodules there are in the present design 28 cryopanels installed. 14 of them are in a serial connection. The distribution of the cryosupply starts at the inlet on the top of the cryopump and is then split up in two parts for each side of the cryopump. Each of these sides has a parallel connection of the six halves of the submodules, (see Fig. 1).

Cooling Principles

The cryoplant design proposed by CEA Cadarache has foreseen a cooling of the cryopanels with a forced flow of ScHe at about 4.5 K inlet temperature and 6.5 K outlet temperature at 4 bar. The cryopanels are only on one side coated with charcoal, to reduce the heatload. The front side of the cryopanels, which is faced to the blackened chevron baffle is therefore electropolished.
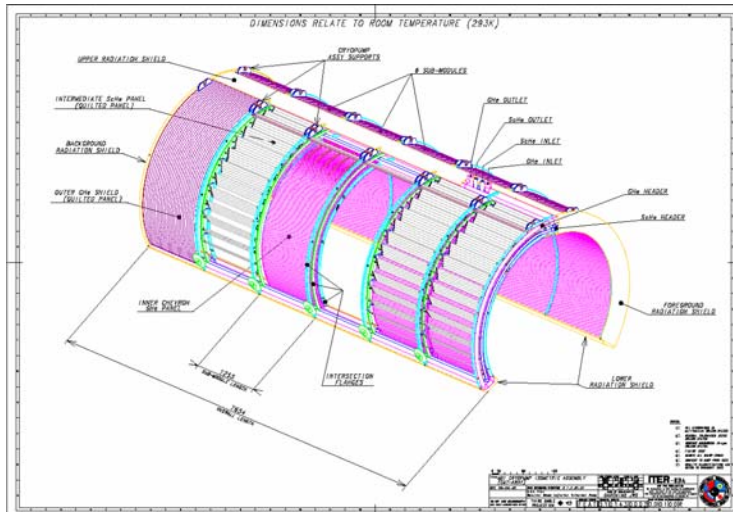
Fig. 1: ITER reference design of the NB cryopump.

The radiation shield consists of a closed radiation wall to the vessel and a chevron baffle facing to the inner vessel of the beam line, were the beam line components are installed. Closed stainless steel plates that are cooled passively by heat conduction realize front endings and bottom openings. The shieldings are cooled by a forced flow of GHe.

Pump Performance

To assess the pump performance the design of the chevron baffle

was improved to increase the transmission coefficient through it and in this way also the pumping speed. In the case of one side coated cryopanels the pumping probability is reduced compared to both side coated cryopanels. The resulting assessed pump velocity just fulfils the requirement given in DRG1. The pump capacities of this design are for both chambers high enough to handle the gas load occurring after a pulse length of 3600 s without any problems.

Cryopump design for the first ITER NB Injector
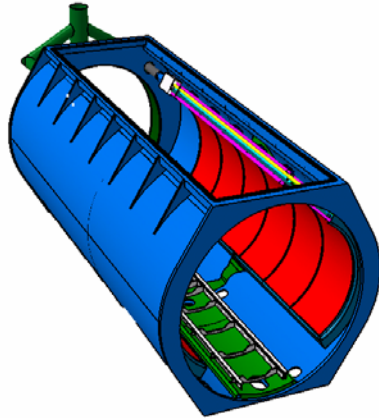
Fig. 2: Elliptical beam line vessel of the ITER NB test facility with one half of the split cylindrical cryopump on the right side.

For the ITER NB Test Facility more flexibility for the maintenance of the NB components is wanted and therefore a proposal about a mixing of the two alternative vertical and horizontal maintenance schemes was made. This is realized using an elliptical vessel with a large upper flange for vertical access (see figure 2). The use of such a vessel concerns the design of the cryopump, because the ITER reference design with a closed cylindrical shape around the beam line cannot be used. To come closest to the ITER relevant cryopump it is foreseen to split the pump into two halves and install them to the left and the right of the vessel along the beam line (see figure 3). This conserves the conditions for the cryopanels behind the shielding very well and makes only changes to the shielding and the supply manifolds of the cryopump.

Thermal loads onto the cryogenic cycles

For the different design options and all operation scenarios, calculations about the thermal loads have been performed. The distinguished operation modes can be described with beam line off (no pulse), pulse operation and the regeneration of the cryopump not considering the transient modes like cooldown and warm up. The resulting thermal load onto the shielding if no pulse is extracted is about 16 kW increasing to about 20 kW during pulse operation. During the 100 K regeneration of the cryopump the thermal load increases to 25 kW for the testbed design and to 32 kW for the ITER reference design.

For both cryopump designs the heat load onto the 4.5K cryopanel structure is 40 W without pulse operation and 160 W during pulse operation of the beam line.

Hydrogen Safety of the Cryopump
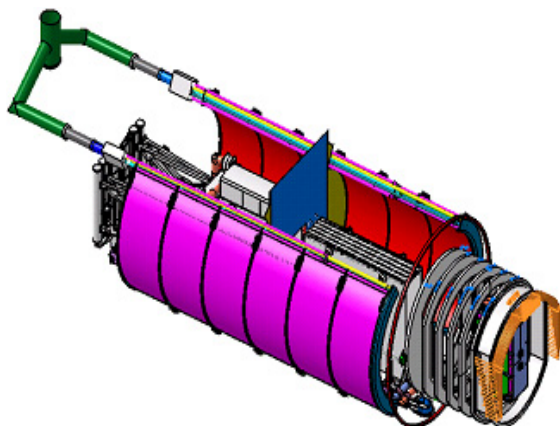
Fig. 3: Cryopump with beam line components.

In case of hydrogen safety the former considered air leak scenario has been expanded to a scenario with an additional water leak. This is the most likely scenario, because all the beam line components are water-cooled. Finally, it is assured that with the long pulse operation of 1 hour the hydrogen safety limit of 1.7% will not be exceeded. This inspection assumed a homogeneously distribution of the gas in the vessel what is probably not given. Nevertheless, even if an ignition of the hydrogen air/mixture occurs the arising pressure due to the deflagration would not

exceed 100 kPa. It has been shown that an additional water steam in the vessel reduces the possibility of an ignition compared to a pure air/hydrogen.

Conventional Forepumping System

For the NB Test Facility a commercial forepumping system shall be used. Its main task is to provide the pumpdown of the vessel after 100 K regeneration in sufficient time to allow for a 3600 s pulse every 4 h. The cross-over pressure between mechanical and cryogenic pumping system shall be 10 Pa, according to ITER requirements.

As first step, a market survey was performed for large dry forepumping units with high pumping speeds for hydrogen. Several options were worked out. Finally FZK recommended a standard combination of a roots and a screw pump, see Fig. 4.
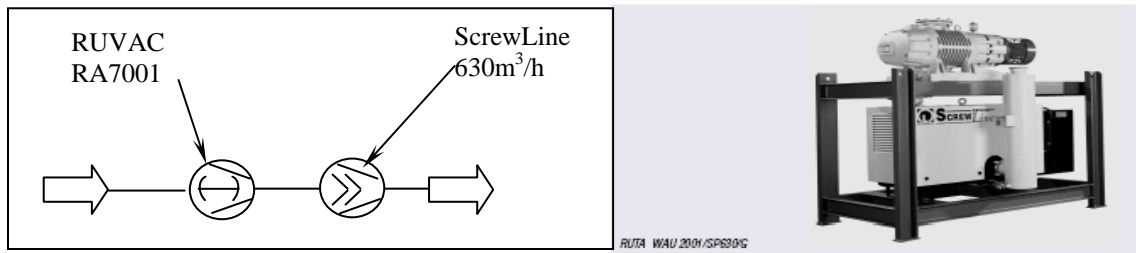
Fig. 4: Nominal 7000 m³/h roots pump backed by a 630 m³/h screw pump.

This pump-set was calculated to do the pump down after a regular 100 K regeneration subsequent to a 3600 s pulse in about 1000 s.

It was agreed that in the lay-out of the NB Test Facility space is provided to be able to connect and test the 1:1 ITER tritium-compatible forepump train, which is developed under the parallel task TW3-TTFF-VP34.

Further Activities

Based on the final reports of the task TW3-THHN-IITF1 [2, 3] FZK starts the detailed design of the cryopump and to complement this design work by Monte Carlo simulations and FEM analysis, as required. In the following task (TW4-THHN-IITF2) FZK is going on with the design of the fixations and rail systems to adapt them to the split cryopump design. In addition FZK is going to analyse and improve the mechanical stiffness of the ITER NB cryopump and the cryopump halves used for the first ITER NB Injector by finite element calculations and will carry out mechanical and thermal stress analyses. Moreover, FZK starts to calculate the gas distribution for the complete injector considering molecular, intermediate and viscous flow regime by Monte Carlo simulations.

In the field of forepumping, the effect of gas ballasting to achieve sufficient hydrogen pumping speed will be investigated in more detail. Moreover, a turbomolecular pump system will be designed for conditioning and leak test purposes.

Staff:

A. Antipenkov
Chr. Day
M. Dremel
A. Mack
R. Simon

Literature:

[1] M. Dremel et al., Design and manufacturing of cryosorption pumps for testbeds of ITER relevant neutral beam injectors, Proc. ICEC, Beijing, China, May 2004.

[2] M. Dremel, Final report about: The first ITER NB Injector and the ITER NB test facility: Design, EFDA Reference:TW3-THHN-IITF1, Cryo Pumping System, Available on: http://efdasql.ipp.mpg.de/EUHandCD/NBI/.

[3] A. Antipenkov, and A. Mack, Final report about: The first ITER NB Injector and the ITER NB test facility: Design, EFDA Reference: TW3-THHN-IITF1, Conventional fore-pumping system, Available on: http://efdasql.ipp.mpg.de/EUHandCD/NBI/.

TW3-THHN-NB-RFS
Cryopumps for the NBI-Testbed at IPP Garching

Background and Objectives

IPP Garching is developing a powerful negative ion source for the ITER Neutral Beam Injection System. It is planned to use the existing NBI testbed MANITU at IPP for this development work. However, with respect to pulse length, an upgrading of vacuum pumping is required. It has therefore been decided to replace the existing small capacity titanium sublimation pumps by a cryopump system to be connected with the ASDEX cryosupply. FZK is responsible for this upgrade.

Table 1:   Technical Specifications for the cryopumps

Gas throughput:	≤ 3 Pa m^3 / s (H$_2$)
Pumping speed:	≥ 700 m^3 / s (H$_2$)
Pulse length of gas load:	3600 s
Pumping capacity:	10^5 Pa•m^3
Operating pressure:	Several 10^{-5} mbar
Max. leak rate (per pump)	1×10^{-7} Pa m^3 / s
Cryogenic media:	Liquid helium at 4.45K, 1.25 bar Liquid nitrogen at 80K, 1.3bar
Dimensions:	ca. 4400 x 1500 x 260mm (h x w x l)

The scope of the work was the development and manufacturing of a system of two cryopumps including the required cryo-, valve and intermediate storage systems for connection with the existing ASDEX cryoplant according to technical specifications given in table 1 [1].
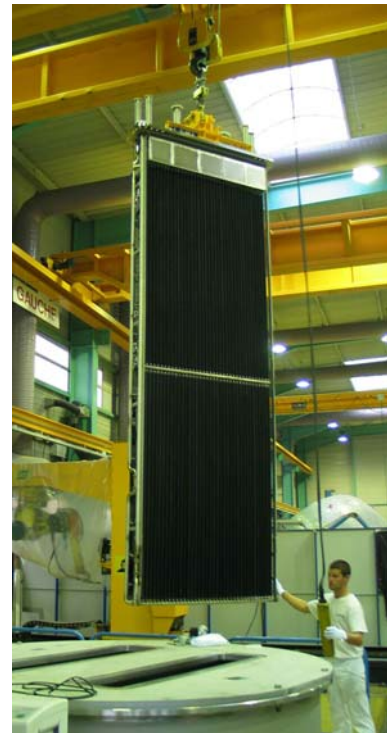
Fig. 1:   IPP Cryopump when mounting into the test vessel.

Development work for the cryopumps

The detailed design of the cryopumps has been finalised and the manufacturing drawings were generated to tender the fabrication of the cryopumps. Based on the thermodynamic and vacuum technological design of the cryopumps, the necessary cryogenic needs to fulfil the cooling requirements during all operation scenarios of the cryopumps have been identified. Thus the design of the cryosupply system for the independent operation of both cryopumps has been finalised, tendered and an order was placed. The cryosupply system consists of the liquid helium cryostat, the valve box and the transfer lines for the cryogenic liquids and off gas systems. For all these components FZK supervised the manufacturing and is carrying out the quality control prior to start the integration into the cryoplant of the ASDEX UPGRADE.

Manufacturing of the cryopumps and the cryosupply

The manufacturing of the cryopanels has been started in 2003 and was successfully finished with the charcoal coating of the panels in the FZK facilities. The second long delivery items have been the components for the chevron baffle consisting of 154 brazed chevrons, which have been all blackened by plasma spray coating with Al$_2$O$_3$/TiO$_2$. All these long delivery items and many other additional special components like Johnston Couplings and bellows were delivered to the main assembly contractor of the cryopumps in January and February 2004 to start the fabrication.

All components of the cryosupply system have been manufactured in 2004. The first acceptance tests of the cryostat and the valve box at the manufacturer's premises were carried out in November 2004 and the components will be delivered to IPP during December, to be integrated in the cryosupply system of ASDEX UPGRADE.

Testing and Delivery of the cryopumps

Both cryopumps have been manufactured in parallel and the possibility to use a cryostat at the premises of the fabricator was taken to make the first cold tests at 77 K before the delivery of the cryopumps to IPP. These cold tests and even the pressure tests for the certification of the cryopumps were successful and both pumps have been delivered to IPP. With the final acceptance tests including a cold test and leak testing at 77 K the contract with the fabricator of the cryopump could be finished.

Further Activities

FZK is going on to supervise the commissioning and quality control of the cryosupply. In close co-work with the staff at IPP Garching the installation and the integration of the cryosupply components will be managed. Additional tasks like the integration of an electrical break in the liquid helium transfer line and some changes in the run of the line has been taken over by FZK

Fig. 2: Cryostat with valve box for the supply of the cryopumps.

and will be supervised until the final acceptance tests. After the successful integration into the ASDEX UPGRADE cryo-system and the first operation of the cryopumps in the neutral beam test facility at IPP Garching the total unit will be handed over to IPP.

Staff:

Chr. Day
M. Dremel
H. Jensen
A Mack
P. Pfeil
R. Simon
D. Zimmerlin

Literature:

[1] M. Dremel et al., Design of cryosorption pumps for testbeds of ITER relevant Neutral Beam Injectors, Proc. SOFT, Venice, Italy, Sept. 2004.

Physics Integration

ECR Heating and Current Drive – Step-Tunable Gyrotron Development

1. Introduction

Magnetohydrodynamic (MHD) instabilities are one of the main reasons for the limiting confinement of plasmas. The stability is to a large extent determined by the distribution of plasma currents and driving localized currents in a plasma is a very important tool to suppress current-driven instabilities and thus to optimize the performance of tokamaks. The suppression of plasma pressure limiting MHD instabilities (so called 'Neoclassical Tearing Modes') has been demonstrated successfully by localized electron cyclotron current drive (ECCD) at ASDEX-Upgrade, DIII-D and JT-60U.

The absorption of RF-waves with the angular frequency ω is dependent on the resonance condition $\omega - k_z v_z = \omega_c$. Thus, the driving currents can be counteracted by an external current drive at different localizations either by changing the injection angle or the RF-frequency.

For plasma stabilization, multi-frequency tunable 1 MW long pulse gyrotrons are highly needed by ASDEX-Upgrade at IPP Garching for advanced ECRH and ECCD experiments [1-3]. Four gyrotrons will be or were already ordered by IPP Garching at the "Institute of Applied Physics (IAP)" in Nizhny Novgorod. Two of them operating as two frequency gyrotrons at 105 GHz and 140 GHz , two of them will be multi-frequency gyrotrons operating at different frequencies between 105 GHz and 140 GHz. The $TE_{22,8}$ mode was chosen as cavity mode at 140 GHz [4,5], 105 GHz corresponds to the $TE_{17,6}$ mode in this gyrotron. However, multi-frequency gyrotrons have to be equipped with a matched window in order to avoid reflections. That is either a Brewster angle window or a tunable double-disk window, both from synthetic diamond.

2. Gyrotron cavity

To compare with results from the IAP, the $TE_{22,6}$ gyrotron existing at FZK has been modified to operate in the $TE_{22,8}$ mode. This gyrotron had been used very successfully concerning fast step-tunability for which tuning within 1 s was proven. Beam tunnel, collector and the superconducting magnet system of the $TE_{22,6}$ gyrotron are used in the new experiment, the resonator, quasi-optical mode converter and window will be changed and optimized for operation at different frequencies. A new electron gun was manufactured and delivered by IAP, Nizhny Novgorod. The acceptance tests at FZK showed a very good performance of this new gun.

The resonator with uptaper was redesigned and was manufactured. It was optimized for a series of modes from $TE_{17,6}$ to $TE_{23,8}$ corresponding to 105 to 143GHz with respect to broadband operation. Some additional modes from $TE_{24,8}$ to $TE_{25,10}$ for even higher frequencies can also be excited.

3. Quasi-optical mode converter

The quasi-optical mode converter of the gyrotron consists of a dimpled-wall antenna and a beam-forming mirror system optimized for nine modes from $TE_{17,6}$ to $TE_{23,8}$ [6-8]. The first mirror is a large quasi-elliptical one, the second and third are phase correcting mirrors with a non-quadratic function of surface contour. The two phase correcting mirrors (Fig.1) have been optimized and redesigned for broadband operation with the new Brewster window system. This new quasi-optical mode converter will be tested in our low power measurement test bed.
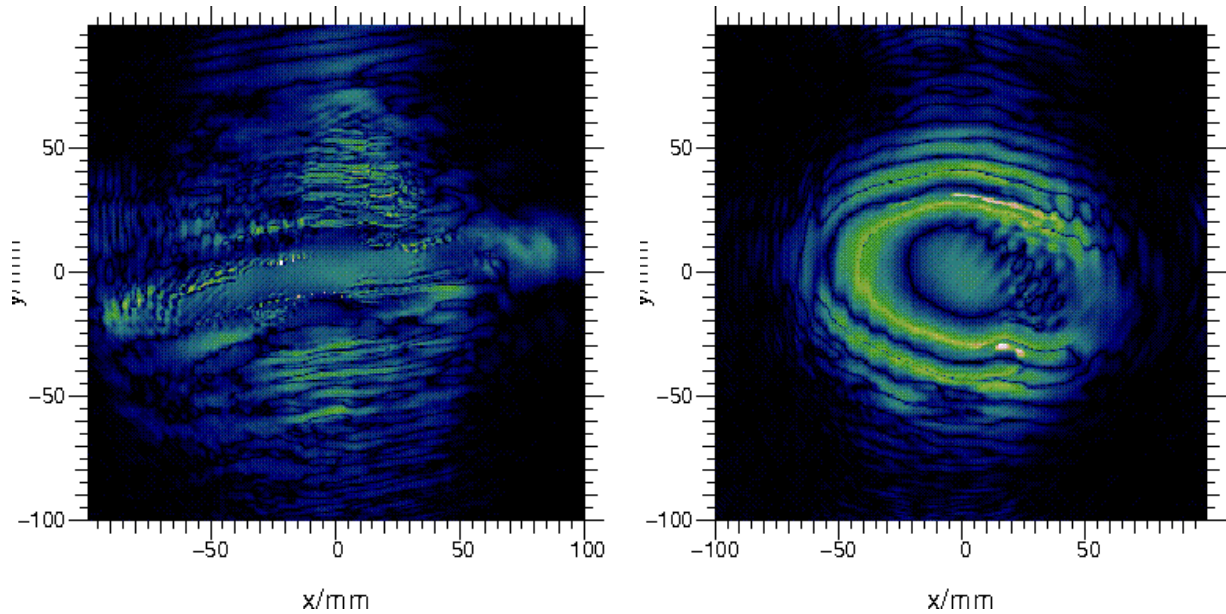
Fig. 1: Phase correcting surface amplitude of mirror 2 (left) and 3 (right).

4. CVD-diamond Brewster window

Efficient operation for the large number of operating modes at different frequencies is possible by using a broadband diamond Brewster window fabricated by chemical vapor deposition (CVD) [9-12]. Due to the large Brewster angle, the diameter of the disk has also to be rather large in order to have sufficient aperture for the RF beam. One disk with a thickness of 1.7 mm and a diameter of 140 mm was developed by Element Six (formerly DeBeers) and already delivered. Unfortunately this disk has two cracks at the edge but nevertheless there is a suitable elliptic area with a very low value of the loss tangent, which can be used for the elliptic shape of a Brewster window with an effective aperture of 50mm (Fig. 2). The next step for the Brewster window development will be the brazing of the disk. Finite element stress calculations for the brazing process and for gyrotron operation have already been performed. The CVD-diamond Brewster window will be ready for operation in the middle of 2005.
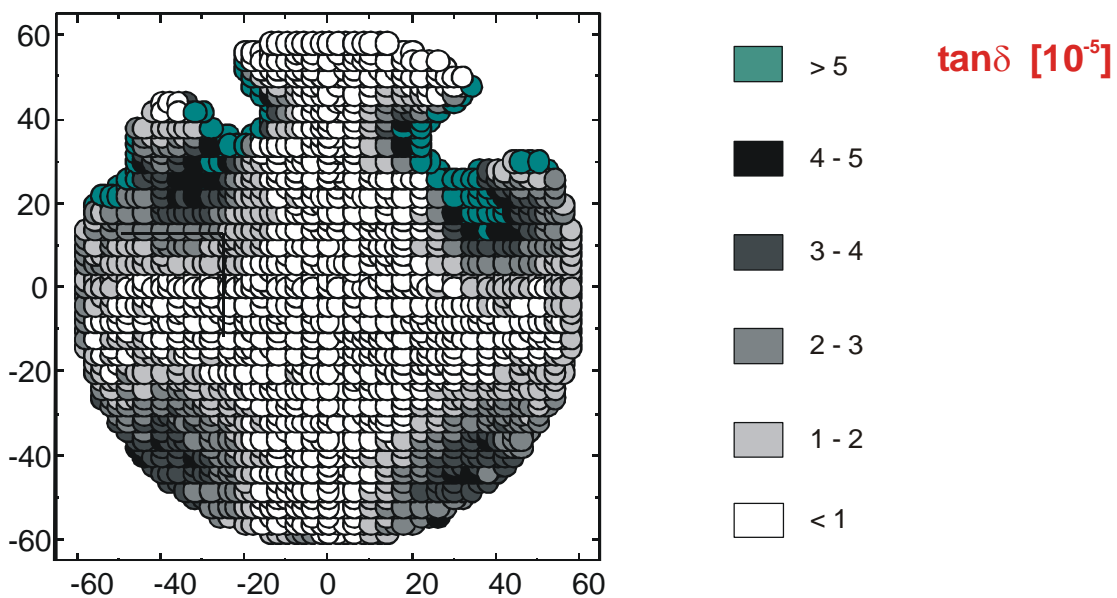
Fig. 2: Dielectric loss of the CVD-diamond disk with 140mm diameter mapped over 120mm inner diameter.

As the diamond window will not be available during the next experimental phase (spring 2005) the gyrotron will be equipped with a quartz glas Brewster window with the same dimensions as the diamond Brewster window. This quartz glass Brewster window is now under manufacturing.

To achieve a better performance and to cover the whole frequency band of the step-tunable gyrotron a new real-time frequency measurement system with an increased bandwidth of 100-175GHz was built up and installed [13]. It replaces the previous system with a bandwidth of 130-165GHz. The sensitivity was enhanced by more than 15dB.

Staff:

A. Arnold (Uni Karlsruhe)
E. Borie
H. Budig
G. Dammertz
R. Heidinger (IMF I)
S. Illy
K. Koppenburg
H.-R. Kunkel
W. Leonhardt
D. Mellein
B. Piosczyk
O. Prinz
M. Schmid
W. Spieß
M. Thumm
X. Yang

Literature:

[1] Leuterer, F., Grünwald, F. Monaco, M. Münich, H. Schütz, F. Ryter, D. Wagner, R. Wilhelm, H. Zohm, T. Franke, G. Dammertz, R. Heidinger, K. Koppenburg, M. Thumm, W. Kasparek, G. Gantenbein, H. Hailer, G.G. Denisov, A. Litvak, V. Zapevalov: Status of the new ECRH system for ASDEX Upgrade, 13th Joint Workshop on Electron Cyclotron Emission and Electron Cyclotron Resonance Heating (EC 13), Nizhny Novgorod, Russia, May 17-20, 2004.

[2] Leuterer, F., G. Grünwald, F. Monaco, M. Münich, H. Schütz, F. Ryter, D. Wagner, H. Zohm, T. Franke, W. Kasparek, G. Gantenbein, H. Hailer, G. Dammertz, R. Heidinger, K. Koppenburg, M. Thumm, X. Yang, G. Denisov, V. Nichiporenko, V. Miasnikov, V. Zapevalov: Status of the new ECRH system for ASDEX upgrade, 23rd Symp. on Fusion Technology (SOFT), Venice, Italy, September 20-24, 2004.

[3] Leuterer, F., G. Grünwald, F. Monaco, M. Münich, F. Ryter, H. Schütz, D. Wagner, H. Zohm, T. Franke, G. Dammertz, R. Heidinger, K. Koppenburg, M. Thumm, W. Kasparek, G. Gantenbein, G.G. Denisov, A.G. Litvak, V.E. Zapevalov: Progress in the new ECRH system for ASDEX Upgrade, Conf. Digest Joint 29th Int. Conf. on Infrared and Millimeter Waves and 12th Int. Conf. on Terahertz Electronics, 2004, Karlsruhe, Germany, pp. 219-220.

[4] Koppenburg, K., Arnold, A., Borie, E., Dammertz, G., Drumm, O., Kartikeyan, M.V., Piosczyk, B. Thumm, M. Yang, X.: Recent results of the multifrequency high power gyrotron development at FZK, Proc. 28th Int. Conf. on Infrared and Millimeter Waves, Otsu, Japan, 2003, pp.125-126.

[5] Koppenburg, K., A. Arnold, E. Borie, G. Dammertz, O. Drumm, M.V. Kartikeyan, B. Piosczyk, M. Thumm, X. Yang: Design of a step-tunable 105-140 GHz, 1 MW gyrotron at FZK, Proc. 10th Int. Conf. on Displays and Vacuum Electronics, Garmisch-Partenkirchen, ITG-Fachbericht 183, 2004, pp. 55-59, Invited Paper.

[6] Yang, X, O. Drumm, A. Arnold, E. Borie, G. Dammertz, K. Koppenburg, B. Piosczyk, D. Wagner, M. Thumm: Design of a quasi optical mode converter for a frequency step tunable gyrotron, Proc. 28th Int. Conf. on Infrared and Millimeter Waves, Otsu, Japan, 2003, 353-354

[7] Yang, X., G. Dammertz, R. Heidinger, K. Koppenburg, F. Leuterer, B. Piosczyk, D. Wagner, M. Thumm: Design of an ultra-broadband single-disk output window for a frequency step-tunable 1 MW gyrotron, 23rd Symp. on Fusion Technology (SOFT), Venice, Italy, September 20-24, 2004.

[8] Yang, X., A. Arnold, E. Borie, G. Dammertz, O. Drumm, K. Koppenburg, B. Piosczyk, D. Wagner, M. Thumm: Investigation of a broadband quasi optical mode converter for a multi-frequency 1 MW gyrotron, Conf. Digest Joint 29th Int. Conf. on Infrared and Millimeter Waves and 12th Int. Conf. on Terahertz Electronics, 2004, Karlsruhe, Germany, pp. 485-486.

[9] Piosczyk, B., A. Arnold, E. Borie, G. Dammertz, O. Dumbrajs, R. Heidinger, S. Illy, J. Jin, K. Koppenburg, G. Michel, T. Rzesnicki, M. Thumm, D. Wagner, X. Yang: Development of advanced high power gyrotrons for EC H&CD applications in fusion plasmas, 13th Joint Workshop on Electron Cyclotron Emission and Electron Cyclotron Resonance Heating (EC 13), Nizhny Novgorod, Russia, May 17-20, 2004.

[10] Thumm, M., A. Arnold, E. Borie, G. Dammertz, R. Heidinger, S. Illy, J. Jin, K. Koppenburg, G. Michel, B. Piosczyk, T. Rzesnicki, D. Wagner, X. Yang: Advanced high power gyrotrons for EC H&CD applications in fusion plasmas, Conference Record-Abstracts 31st IEEE Int. Conf. on Plasma Science (ICOPS 2004), Baltimore, Maryland, 2004, p. 265.

[11] Piosczyk, B., A. Arnold, G. Dammertz, O. Dumbrajs, R. Heidinger, S. Illy, J. Jin, K. Koppenburg, G. Michel, T. Rzesnicki, M. Thumm, X. Yang: Research on advanced high power gyrotrons at FZK, 15th Int. Conf. on High-Power Particle Beams (BEAMS'2004), St. Petersburg, Russia, 2004, p. 129.

[12] Dammertz, G., R. Heidinger, K. Koppenburg, B. Piosczyk, M. Thumm: ECRH-development at Forschungszentrum Karlsruhe, US/Japan/EU RF Technology Workshop, Amsterdam, Netherlands, October 4-5, 2004.

[13] Prinz, H. O.: Aufbau eines breitbandigen Echtzeit-Frequenzmesssystems für mm-Wellen Hochleistungsgyrotrons, Diplomarbeit, Universität Karlsruhe, FZKA 7020, 2004

Microwave Heating for Wendelstein 7-X

Introduction

Electron Cyclotron Resonance Heating (ECRH) has an inherent capability for plasma start up, localized heating and current drive and is of particular importance for stellarators. ECRH is thus foreseen as a basic heating system in the first operation stage of W7-X with 10 MW heating power at 140 GHz in continuous wave (CW) operation [1]. The complete ECRH-system for W7-X will be provided by FZK, which has established the 'Projekt Mikrowellenheizung für W7-X (PMW) in 1998 to run the project. The responsibility covers the design, development, construction, installation and integrated tests of all components required for stationary plasma heating on site at IPP Greifswald. PMW coordinates the contributions from IPF Stuttgart, which is responsible for the microwave transmission system and part of the HV-system, and from the team at IPP Greifswald, which is responsible for the in-vessel components and for the in-house auxiliary systems. In particular a European collaboration has been established between the Forschungszentrum Karlsruhe, Centre de Recherche de Physique des Plasmas (CRPP) Lausanne, Institut für Plasmaforschung (IPF) of the University Stuttgart, Commissariat à l´Energie Atomique (CEA) in Cadarache and Thales Electon Devices (TED) in Vélizy, to develop and build a prototype gyrotron for W7-X with an output power of 1 MW for CW operation at 140 GHz.

Development of Gyrotrons

The major problems of high power, high frequency gyrotrons are given by the Ohmic heating of the cavity surface, by the dielectric losses in the output window, by the power capability of the collector and by the amount of stray radiation absorbed inside the gyrotron. The technical limit of the power density on the resonator surface is assumed to be 2 kW/cm² for CW operation. For this reason high power gyrotrons are operated in high order volume modes with a large cavity [2].

A major breakthrough for a CW compatible source is the use of a diamond window fabricated by chemical vapor deposition (CVD), which allows the design and the operation of a CW tube at the 1 MW power level. The single-stage depressed collector brings the overall efficiency of the gyrotron in the 50% range and at the same time significantly reduces the thermal loading on the collector.

A contract between European Institutes (CRPP Lausanne, IPP Garching / Greifswald, IPF Stuttgart and FZK Karlsruhe) and Thales Electron Devices (TED), Vélizy, had been settled to develop continuously operated gyrotrons at an output power of 1 MW.

The pre-prototype "Maquette" had been tested successfully at the Forschungszentrum Karlsruhe. The pulse-length limitations were mainly due to a pressure increase inside the tube. This tube was subjected to a visual inspection of internal parts. After reassembly, the tube was sent to IPP Greifswald and taken into operation. In short pulse experiments of 10 ms, an output power of 850 kW with an efficiency of about 27% has been achieved. Before further optimizing the magnetic field distribution to achieve higher output powers, long pulse operation has been started and at 600 kW a pulse length of 10 s could be achieved without any problems. Difficulties had only arisen due to arcing inside the long-pulse load which has to be modified now similar to the one used at FZK for long pulse operation. To perform long pulses with gyrotrons, sweeping of the electron beam along the collector surface is indispensable in order to reduce the power loss density at the surface of the collector. This is done by normal conducting coils surrounding the collector and changing the axial fields. Unfortunately, the expansion of the pulse lengths was not possible due to a failure in the power supplies of the normal conducting magnets. The HV-systems and the gyrotron protection system (crowbar) could be operated without any problems.

In addition to the European development of 1 MW, 140 GHz CW gyrotron (see below), a development at "Communication and Power Industries (CPI)" in the United States has been accomplished. After the successful tests of the CPI-gyrotron at the company in short pulse operation, the gyrotron and the superconducting magnet from ACCEL were delivered to IPP Greifswald and integrated into the system. The water cooling system, the vacuum connections, the RF-shielding tubes and the lead shielding for reduction of X-rays and some other were installed. During the first tests, arcing at the crowbar-system delayed the operation. To achieve 500 kW with a pulse length of 3 minutes was rather fast. Conditioning of the tube at high power for long pulses turned out to be rather time-consuming. To increase the output power by a few tens of kilowatts needed a complete new conditioning procedure. 700 kW with a pulse length of 40 s and at 800 kW a few 100 ms could be achieved. Further conditioning is necessary. During these measurements, localized heat-up in the beam duct was detected. By installing some additional absorbers and water loads these effects were avoided.

Table 1: Results and pulse-length limitation at different output powers for the prototype gyrotron.

Pulse length	Power (kW)	Current (A)	Efficiency	Energy (kJ)	limitation
3^m	890	41	0.41	160	power supply
15^{m}37^s	537	24	0.42	505	pressure
21^{m}40^s	257	26		350	pressure

The prototype gyrotron of TED had been built with some improvements concerning the water cooling of the mirror box and had also been tested successfully. The results though already reported in the last "Annual Report" are shortly summarized in Table 1.

Two problems were faced: the limitation at 890 kW in output power and the limitation in pulse length to 16 minutes at even reduced output power of 540 kW [3-5]. (The design value is 1 MW for 30 minutes.)

The reasons for these two effects are known and it was decided to finish the development phase and to order the series gyrotrons. The prototype was sent back to TED for a visual inspection. The reason for the limitation in power clearly could be seen: The electron emitter ring showed different regions with different surface quality, that means different surface roughness.
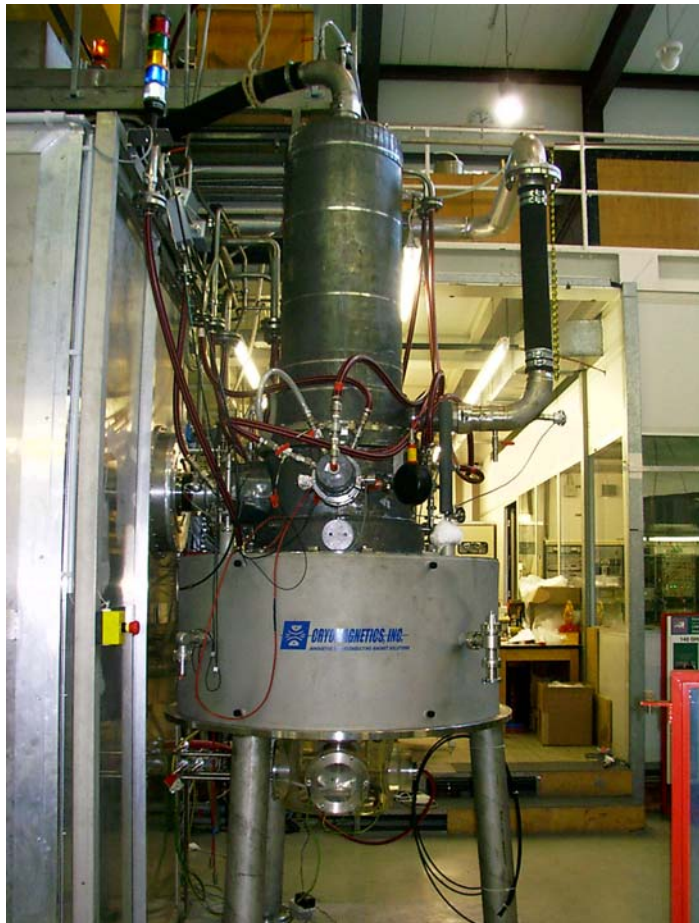

Fig. 1: The reassembled prototype with improved emitter ring inside the new superconducting magnet.

The second problem is related to the internal ion getter pumps. An infrared measurement through the diamond window clearly indicated a strong temperature rise of these components.

Distribution measurements of the RF- beam were performed. These measurements showed a slight shift (a few mm) with respect to the window axis. In low power measurements it was shown that this effect is due to a very small misalignment of the first quasi-elliptic mirror of the optical mode converter system [6,7].

During the visual inspection, no severe damage or overheating (except in some parts of the collector where it could be expected) was found.

The prototype tube was reassembled with a better emitter ring (from optical point of view) and sent back to Forschungszentrum Karlsruhe. It is now placed inside the new superconducting magnet (Fig. 1) and will be measured very soon.

Series Gyrotrons

Seven series gyrotrons have been ordered at TED. Including the pre-prototype tube, the prototype tube and the CPI-tube now operated at IPP Greifswald, ten gyrotrons will be operated at Wendelstein 7-X. To be able to operate these gyrotrons, eight more superconducting magnetic systems are necessary and have been ordered at Cryomagnetics, Oak Ridge, USA.

The series tubes avoid the above mentioned difficulties concerning the output power and the pulse length limitation. The emitter rings undergo a better optical quality assurance before they are installed inside the gyrotron. The ion getter pumps which were located inside the gyrotron in the prototype tubes are now placed outside the gyrotron. This proves a better shielding of the internal parts of the ion getter pump against RF radiation and heating. Further, the mirror box mostly exposed to RF has got a double wall structure for better cooling. Stainless steel parts with poor cooling are coated with copper to reduce the RF absorption. The first series gyrotron had been expected to be delivered to FZK during September 2004. Unfortunately, the first mirror box was strongly deformed during the final welding process and could not be used. The new one was delivered to TED in November 2004 and is now being installed into the gyrotron. This is expected to be delivered in February 2005.

Fig .2:   Final work on the second series magnet.

The eight necessary superconducting magnets are ordered from Cryomagnetics. Despite the successful tests of the superconducting coils at the design value of 5.56T in the factory dewar, the delivery was delayed by quenches after installing the coils in the cryostat. Despite continuous conditioning, the level of slightly below 6 T (8% higher than the design field, but 2% lower than the specified field) could not be overcome. The system was accepted and sent to Forschungszentrum. During the transport, a severe damage in the vacuum system had occurred. A leak to the vacuum vessel had developed. The magnet was sent back to the factory for repair. The second transport with added transport bars was more successful. The magnet was tested at Forschungszentrum with respect to the specifications. A small leak of $3 \cdot 10^{-3}$ mbar l/s was detected, but this will not cause any problems in the future. The deviation between the specified field and the measured distribution on axis is less than 3%. The field distribution at the gun and at the cavity can be adjusted to the design values by separated main and gun coils, the deviation is at about half the distance between gun and cavity and can be tolerated.

The alignment of the system was very successful. Within a short time the magnetic axis could be aligned with respect to the geometrical axis to better than ± 0.1 mm. Though the system quenched at rather low values, at the second try a field 5% higher than the design field could be achieved. The prototype has been installed now into this magnet (Fig. 1). The first short pulse tests were made in December 2004: an output power of about 1100 kW were measured at 40 A with an output efficiency of about 50%.

The second series magnet has almost been finished (Fig. 2) and is expected to be delivered to IPP Greifswald in January 2005.

Transmission line
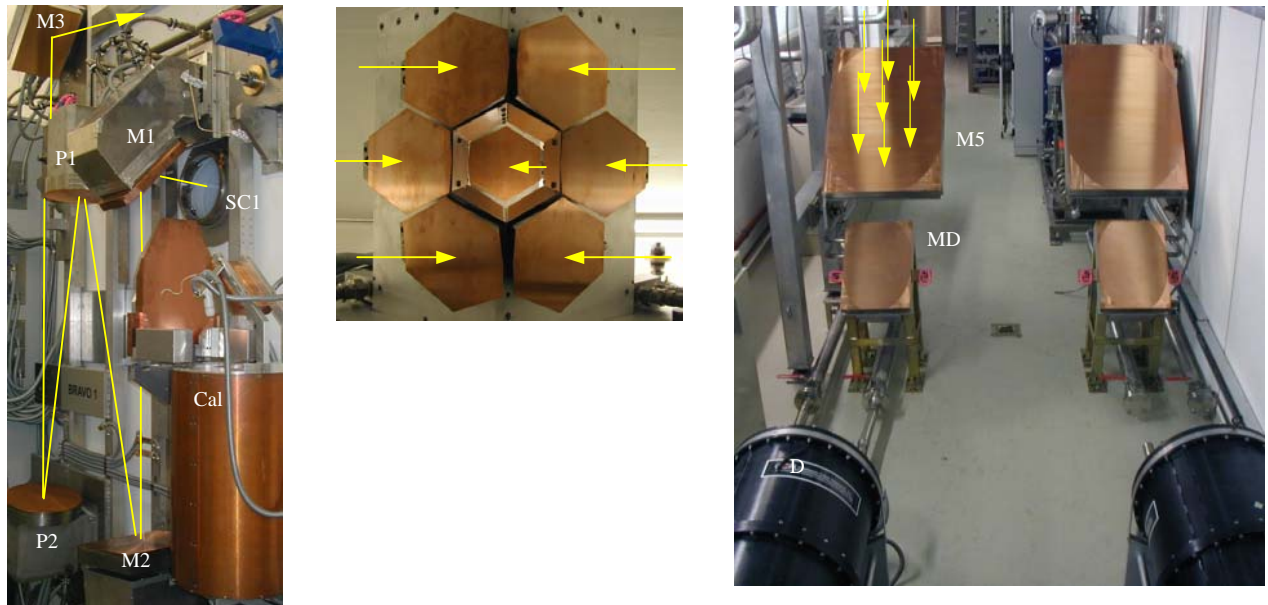
Fig. 3: View into the transmission duct of the ECRH system on W7-X. a) The left picture shows matching optics M1, M2, and polarizers P1, P2, as well as M3, switch mirror SC1 and short-pulse calorimeter Cal for one gyrotron. b) In the middle, the beam combining optics (BCO) as seen from the first MBWG mirror M5 is displayed. Individual beams coming from M3 are impinging on the plane mirrors from left and right and are directed onto M5 of the MBWG system. c) The right picture shows a view into the beam duct with two large multi-beam mirrors M5 and the mirrors MD which can focus one selected beam into one of the CCR dummy loads D seen in the foreground.

The transmission line [8,9] consists of single-beam waveguide (SBWG) and multi-beam waveguide (MBWG) elements (Fig. 3). For each gyrotron, a beam conditioning assembly of five single-beam mirrors is used. Two of these mirrors (M1, M2) match the gyrotron output to a Gaussian beam with the correct beam parameters, two others (P1, P2) are used to set the appropriate polarization needed for optimum absorption of the radiation in the plasma. A fifth mirror (M3) directs the beam to a plane mirror array (BCO), which is situated at the input plane of a multi-beam wave guide (Fig. 3). This MBWG is designed to transmit up to seven beams (five 140 GHz beams, one 70 GHz beam plus an additional spare channel) from the gyrotron area (entrance plane) to the stellarator hall (exit plane). It consists of four focusing mirrors with optimized surfaces in a confocal arrangement in square configuration to get low mode conversion. Additional plane mirrors are installed to fit the transmission lines into the building. At the output plane of the MBWG, a mirror array separates the beams again and distributes them via CVD-diamond vacuum barrier windows to individually movable antennas in the torus. To transmit the power of all gyrotrons, two symmetrically arranged MBWGs are used.

The mirrors M1-M3, the polarization mirrors P1, P2, the BCOs, the MBWG mirrors and switching mirrors for calorimeters are completely installed. The fabrication of the mirrors SD is almost completed.

Due to the delay of the W7-X it is not possible to install the mirrors inside the torus hall. To test the beam line, retro-reflector mirrors are necessary in order to test the complete beam line at transmission powers of 1 MW. The RF beam will be reflected at the end of the beam duct (before entering the torus hall) towards the RF loads inside the beam duct. The supporting structures for the retro-reflector mirrors were designed. The design for the mirror supports (towers in the torus hall) for the mirrors inside the torus hall has been started.

Short-pulse calorimeters will be installed in order to detect the output power of each gyrotron. The initial problems with the manufacturing of the ceramic cylinders were solved. One calorimeter has been fabricated and is installed at IPP Greifswald for the measurements on the Maquette. The others are ordered.

The tubes for the absorption of stray radiation inside the gyrotron hall (between gyrotron and beam duct) have been fabricated and were delivered to IPP Greifswald. The operation on the tube "Maquette" was successful.

HV-systems

After some initial problems during the operation with the "Maquette" tube, the pre-prototype version of a regulator-modulator for the acceleration voltage control (energy recovery with single-stage depressed collector) in combination with a pre-prototype version of the fast crowbar for gyrotron protection worked satisfactorily. Tests of the new system for gyrotron power control and protection were successful.

The concept of a safety system for personal HV protection has been installed and showed its effectiveness during operation with the tubes.

The fabrication of the series modulators (including emitter heating and tube protection system) by IPF Stuttgart is on the way. Most parts of the systems have been ordered. The first series modulator will be sent to Greifswald at the beginning of 2005.

In-vessel components

Different possibilities for movable launcher mirrors were investigated. The problem is, that the mechanics for the movement and the connections for cooling water have to be integrated in very small space. The most reliable solution seems to be a push-pull rod in which the water cooling is integrated. The design and of a motor driven prototype launcher has been finished, the fabrication is under way.

The fabrication of the torus window units (diamond disk with cupper cuffs and stainless steel housing) has been started at TED. Two of them have been fabricated and have been already delivered. Their microwave properties were measured by the Institut für Materialforschung at the Forschungszentrum Karlsruhe.

The microwave chamber for testing the in-vessel-components with RF-radiation has successfully taken into operation at IPP Garching. This chamber is also foreseen as the test-bed for the prototype launcher.

Auxiliary systems

The water cooling systems for individual components as the RF-shielding tubes and by-passes for the gyrotron collectors were installed and successfully tested. The soft-ware to operate the system has been installed.

The short pulse calorimeters were connected to the water cooling system, and the same holds for the second long-pulse RF-load.

The water cooling for the CPI-gyrotron has been fabricated and was tested in combination with the gyrotron. The cathode cooling (with air at CPI) was modified in order to be able to operate the tube with oil cooling. This was necessary due to the high amount of stray radiation at the gun region of the CPI gyrotron. Further the tube has to be run with oxygen-free water (in contradiction to the other tubes from TED). The removal of oxygen was prepared and operates successfully. The three water circuits are now equipped with de-ionizers.

For all these installations, the controlling system and the visualization has been designed and installed. The visualization for the gyrotron operation has been improved and was integrated into the operation- and interlock system of IPP Greifswald.

The supply and interlock system for the superconducting magnet from ACCEL (to operate the CPI-gyrotron) was changed to be operational at IPP Greifswald as well.

<u>Staff:</u>

IHM / FZK	IPF (University of Stuttgart)	IPP (Greifswald/Garching)
A. Arnold (Uni KA)	H. Babilon	H. Braune
<u>G. Dammertz</u>	P. Brand	V. Erckmann (PMW)
A. Götz	G. Gantenbein	H. Hofner
P. Grundel	M. Grünert	F. Hollmann
R. Heidinger (IMF I)	H. Hailer	L. Jonitz
S. Illy	W. Kasparek	H. Laqua
H. Kunkel	M. Krämer	G. Michel
K. Koppenburg	R. Munk	F. Noke
W. Leonhardt	G. Müller	F. Purps
R. Lukits	P. Salzmann	T. Schulz
D. Mellein	H. Schlüter	M. Weißgerber
G. Neffe	K. Schwörer	
B. Piosczyk	R. Wacker	
M. Schmid		
W. Spiess		
J. Szczesny		
<u>M. Thumm</u>		

<u>Literature:</u>

[1] T. C. Luce, "Applications of High-Power Millimeterwaves in Fusion Energy Research," IEEE Trans. Plasma Science 30 (2002) 734-754

[2] B. Piosczyk, G. Dammertz, O. Dumbrajs, M. V. Kartikeyan, M. K. Thumm, and X. Yang, "165 GHZ Coaxial Cavity Gyrotron", IEEE Trans. Plasma Science 32 (2004) 853-860 [2]

[3] G. Dammertz, S. Alberti, A. Arnold, E. Borie, V. Erckmann, G. Gantenbein, E. Giguet, R. Heidinger, J. P. Hogge, S. Illy, W. Kasparek, K. Koppenburg, M. Kuntze, H. P. Laqua, G. LeCloarec, F. Legrand, Y. LeGoff, W. Leonhardt, C. Liévin, R, Magne, G, Michel, G. Müller, G. Neffe, B. Piosczyk, T. Rzesnicki, M. Schmid, M. K. Thumm, and M. Q. Tran, "Development of multimegawatt gyrotrons for fusion plasma heating and current drive", 5th IEEE Internat. Vacuum Electronics Conf, (IVEC 2004), Monterey, California, April 27-29, 2004, pp. 28-29

[4] G. Dammertz, H. Braune, V. Erckmann, G. Gantenbein, W. Kasparek, H. P. Laqua, W. Leonhardt, G. Michel, G. Müller, G. Neffe, B. Piosczyk, M. Schmid, M. K. Thumm, "Progress in the 10 MW ECRH system for the Stellarator W7-X, IEEE Trans. on Plasma Science 32, (2004) pp. 144-151

[5] G. Dammertz, S. Alberti, A. Arnold, E. Borie, P. Brand, H. Braune, V. Erckmann, G. Gantenbein, E. Giguet, R. Heidinger, J. P. Hogge, S. Illy, W. Kasparek, K. Koppenburg, M. Kuntze, H. P. Laqua, G. LeCloarec, F.

Legrand, W. Leonhardt, C. Liévin, R, Magne, G, Michel, G. Müller, G. Neffe, B. Piosczyk, T. Rzesnicki, M. Schmid, M. K. Thumm, and M. Q. Tran, "Status of the 1 MW, CW gyrotrons for the Stellarator W7-X", Conf. Dig. of the Joint 29th Internat. Conf. on Infrared and Millimeter Waves and 12th Internat. Conf. on Terahertz Electronics, Karlsruhe, Sept. 27-Oct. 1, 2004, pp. 113-114

[6] A. Arnold, G. Dammertz, X. Yang. K. Koppenburg, M. K. Thumm , and D. Wagner, "Low power measurements on the output beam of a 140 GHz, TE28,8 gyrotron", Proc. of the 10th Triennial ITG Conf., Garmisch-Partenkirchen, May 3-4, 2004, pp.379-384

[7] A. Arnold, G. Dammertz, M. K. Thumm, „Performance measurements on high order gyrotron mode generators",Conf. Dig. of the Joint 29th Internat. Conf. on Infrared and Millimeter Waves and 12th Internat. Conf. on Terahertz Electronics, Karlsruhe, Sept. 27-Oct. 1, 2004, pp. 565-566

[8] W. Kasparek, H. Braune, G. Dammertz, V. Erckmann, G. Gantenbein, F. Hollmann, M. Grünert, H. Kumric, L. Jonitz, H. P. Laqua, W. Leonhardt, G. Michel, F. Noke, B. Plaum, M. Schmid, T. Schulz, K. Schwörer, M. K. Thumm, and M. Weissgerber, "Status of the 140 GHz/10 MW CW Transmission System for ECRH on the Stellarator W7-X", 23rd Symp. On Fusion Technology (SOFT), Venezia, Sept. 20-24, 2004

[9] W. Kasparek, "High Power CW Transmission Lines and Launchers", 13th Joint Workshop on Electron Cyclotron Emission and Electron Cyclotron Resonance Heating (EC13), Nizhny-Novgorod, Russia, Section IV, May 17-20, 2004

Underlying Technology

Underlying Technology

Operation and Upgrade of the Fusion Materials Laboratory

The Fusion Materials Laboratory provides the infrastructure for the performance of R&D tasks defined in the EFDA workprogramme related to the characterisation and testing of irradiated and non-irradiated materials. The equipment of the lab allows optical and electron microscopy, tritium adsorption and desorption measurements, He pycnometry and Hg porosimetry as well as mechanical testing of materials e.g. crush load, micro hardness, creep, charpy impact and tensile.

Results and consecutive analysis of the measurements performed in the Fusion Materials Laboratory are reported in more detail the respective chapters of this report. In the following only some important results are highlighted.

The Post Irradiation Examination (PIE) of the samples irradiated in the HFR Phase IB Programme was completed. Different OPTIFER and F82H mod materials had been irradiated up to 2.4 dpa at different temperatures by thermal neutrons. The specimens under investigation represented different materials, heat treatment procedures and welding techniques. The main results of the charpy impact tests on OPTIFER steels were

- less radiation-induced embrittlement compared to former materials
- reduced low-temperature irradiation damage
- no irradiation influence on the differences of heat treatment procedures.

Fig. 1: Glove Box with Tritium and Helium Desorption Measurement Devices at Fusion Materials Laboratory.

With the F82H mod materials we found comparable radiation induced embrittlement both in the base material and the welding zone, where the TIG weldings seem to provide better properties before and after irradiation than EB weldings. Another aim of the investigations was to study the irradiation effects in the light of the structural properties of these materials. For this purpose the broken samples were also investigated by light optical microscopy, SEM and TEM.

The investigation of blanket functional materials was continued with the characterisation of different batches of unirradiated lithium orthosilicate material. The influence of the parameters of the fabrication process on the mechanical and structural properties was subject of these investigations. Tritium adsorption and desorption of beryllium pebbles was compared for different surface treatments. Fig. 1 depicts the facility used. A BeO surface layer turned out to delay the tritium release especially at lower temperatures. Investigations of metal pebbles from uniaxially stressed pebble beds yielded coordination numbers and the elastic and plastic deformation as input parameters for model calculations of the pebble bed behaviour.

Out of JET and TFTR carbon tiles further samples were prepared for the investigation of tritium retention and tritium release of these materials. The samples were analyzed in the TLK.

The upgrading of the Fusion Materials Laboratory plant was continued with the build-up of two small lead-shielded hot cells. They are specially suited to the requirements of the fusion materials examinations and serve as replacements of two old large hot cells which are now subject of a decommissioning task.

Staff:

P. Bariè	W. Nägele
E. Damm	D. Reichmann
A. Erbe	H. Ries
M. Gilpert	R. Rolli
M. Holzer	O. Romer
H. Jackisch	G. Rösch
S. Lautensack	R. Schmidt
P. Lauterbach	H. Steinle
J. Ludat	A. Veit
G. Mangei	

Literature:

[1] G. Piazza, A. Erbe, R. Rolli, O. Romer, "Post-irradiation examinations of Li_4SiO_4 pebbles irradiated in the EXOTIC-8 experiment", Journal of Nuclear Materials 329 – 333 (2004) 1260 – 1265

[2] N. Bekris, C. H. Skinner, U. Berndt, C. A. Gentile, M. Glugla, A. Erbe, W. Pilz, "Assessment of the heating technique as a possible ex situ detritiation method for carbon wall materials from fusion machines", Journal of Nuclear Materials 329-333 (2004) 814 – 819

[3] Y. Torikai, M. Matsuyama, N. Bekris, M. Glugla, P. Coad, W. Nägele, A. Erbe, N. Noda,

[4] V. Philipps, and K. Watanabe, "Tritium distribution in JET mark IIA type divertor tiles analyzed by BIXS", 16th International Conference on Plasma Surface Interactions, Portland, Maine, USA, May 24th –28th , 2004

[5] N. Bekris, J. P. Coad, R. – D. Penzhorn, S. Knipe, L. Doerr, R. Rolli, W. Nägele, "Characterisation of flakes generated in carbon fusion machines after DD and DT plasma operations", 16th International Conference on Plasma Surface Interactions, Portland, Maine, USA, May 24th –28th , 2004

[6] H.–C. Schneider, B. Dafferner, H. Ries, S. Lautensack, O. Romer, „Bestrahlungsprogramm HFR Phase IB – Ergebnisse der Kerbschlagbiegeversuche mit den bis 2,4 dpa bestrahlten Werkstoffen", FZKA 6976, April 2004

Appendix I: FZK Departments Contributing to the Fusion Programme

FZK Department	FZK Institut/Abteilung	Director	Ext.
Institute for Materials Research	Institut für Materialforschung (IMF)	I. Prof. Dr. K.-H. Zum Gahr	3897
		II. Prof. Dr. O. Kraft	4815
		III. Prof. Dr. H. Haußelt	2518
Institute for Pulsed Power and Microwave Technology	Institut für Hochleistungsimpuls- und Mikrowellentechnik (IHM)	Prof. Dr. M. Thumm	2440
Institute for Nuclear and Energy Technology	Institut für Kern- und Energietechnik (IKET)	Prof. Dr. T. Schulenberg	3450
Institute for Reactor Safety	Institut für Reaktorsicherheit (IRS)	Prof. Dr. D. Cacuci	2550
Institute for Technical Physics	Institut für Technische Physik (ITP)	Prof. Dr. P. Komarek	3500
Institute for Micro Process Engineering	Institut für Mikroverfahrenstechnik (IMVT)	Dr. K. Schubert	3114
- Tritium Laboratory Karlsruhe	- Tritiumlabor Karlsruhe (TLK)	Dr. M. Glugla	3226
Institute for Data Processing and Electronics	Institut für Prozessdatenverarbeitung und Elektronik (IPE)	Prof. Dr. H. Gemmeke	5635

Contributing:

Institute for Nuclear and Particle Physics, Technical University Dresden	Institut für Kern- und Teilchenphysik Technischen Universität Dresden	Prof. Dr. H. Freiesleben	+49 351/4635461
Max-Planck-Institute for Plasma Physics Berlin	Max-Planck-Institut für Plasmaphysik Berlin	Prof. Dr. G. Fussmann	+49 30/20366130
Institute for Applied Physics University Frankfurt	Institut für Angewandte Physik J.W. Goethe-Universität Frankfurt	Prof. Dr. H. Klein	+49 69/7982 3489

Appendix II: Fusion Programme Management Staff

Head of the Research Unit	Dr. G. Janeschitz	ext. 5460 e-mail: guenter.janeschitz@fusion.fzk.de
Assistant:	Mrs. M. Winkelmann	ext. 5461 e-mail: miriam.winkelmann@fusion.fzk.de
Secretariat:	Mrs. C. Hermsmeyer	ext. 5466 e-mail: carmen.hermsmeyer@fusion.fzk.de
Program Budget, Administration, Reports, EU-Affairs	BW. M. Henn	ext. 5547 e-mail: michael.henn@fusion.fzk.de
	Mrs. V. Lallemand	ext. 6461 e-mail: vera.lallemand@fusion.fzk.de
	Mrs. I. Pleli	ext. 8292 e-mail: ingrid.pleli@fusion.fzk.de
Blanket and Divertor Development, Neutron Source, Reactor Studies, Public Relations	DI. W. Bahm	ext. 5465 e-mail: werner.bahm@fusion.fzk.de
Fuel Cycle, Structural Materials, Irradiations, Superconducting Magnets	DI. S. Gross	ext. 5468 e-mail: sigurd.gross@fusion.fzk.de
Quality Management, Resource Loaded Planning, Plasma Heating Technology, Physics, Safety Studies, Neutronics	Dr. K. Hesch	ext. 5462 e-mail: klaus.hesch@fusion.fzk.de

<u>**Address:**</u>   **Forschungszentrum Karlsruhe GmbH**
Nuclear Fusion Programme Management

Post Office Box 3640, D - 76021 Karlsruhe / Germany

<u>**Telephone No:**</u>   **07247-82- Extensions .....**

<u>**Telefax No:**</u>   **07247-82-5467**

<u>**world wide web:**</u>   **http://www.fzk.de/fusion**

Appendix III: Glossary

AC	Alternating Current
ACP	Actived Corrosion Products
ADC	Analog Digital Converter
AGHS	Active Gas Handling System
ALARA	As Low As Reasonably Achievable
ANFIBE	Analysis of Fusion Irradiated Beryllium
AP	Activated Particles
ARBOR	Associated Reactor Irradiation in BOR 60
ASDEX	Axial-symmetrisches Divertor-Experiment
CAD	Computer Aided Design
CCD	Charge Coupled Device
CD	Cryogenic Distillation
CDM	Current Distribution Measurements
CEA	Commissariat à l'Energy Atomique
CECE	Combined Electrolysis and Catalytic Exchange
CF	Cryogenic Forevacuum
CFC	Carbon Fibre Composite
CFD	Computational Fluid Dynamics
CICC	Cable in Conduit Conductor
CMSB	Cryogenic Molecular Sieve Bed
CPI	Communication and Power Industries
CRPP-EPFL	Centre de Recherches en Physique des Plasmas Ecole Polytechnique Fédérale de Lausanne
CT	Cold Trap
CVD	Chemical Vapor Deposition
CW	Continuous Wave
DBTT	Ductile Brittle Transition Temperature
DC	Direct Current
DCLL	Dual Coolant Lithium-Lead
DEMO	Demonstration Power Station
DTL	Drift Tube Linear, accelerator structure
EAF	European Activation File
EASY	European Activation System
EB	Electron Beam
ECCD	Electron Cyclotron Current Drive
ECH&CD	Electron Cyclotron Heating and Current Drive

ECM	Electrochemical Milling
EC(R)H	Electron Cyclotron (Resonance) Heating
ECW	Electron Cyclotron Waves
EDA	Engineering Design Activity
EDM	Electro Discharge Method
EDX	Energy Dispersive X-Ray
EFDA	European Fusion Development Agreement
EFF	European Fusion File
ELM	Edge Localized Mode
ENEA	Italian National Agency for New Technologies, Energy and the Environment
ESIS	European Structural Integrity Society
ESRF Grenoble	European Synchrotron Radiation Facility
EVEDA	Engineering Validation/Engineering Design Activities
EVITA	Experimental Vacuum Ingress Test Apparatus
FBI	Force-magnetic field current
FDR	Final Design Report
FE	Finite Element
FEM	Finite Element Method
FM	Ferritic-martensitic
FMI	Fractographic and Microstructural Investigations
FML	Fusion Materials Laboratory
FNG	Frascati Neutron Generator
FRP	Fiber Reinforced Polymer
FT-IR	Fourier Transform – Infra Red
FTP	File Transfer Protocol
FW	First Wall
GDC	Glow Discharge Cleaning
GPF	Gas Puffing Facility
GSSR	Generic Site Safety Report
HAZ	Heat Affected Zone
HAZOP	Hazard and Operability
HAADF	High Angle Annular Dark Field Detector
HCLL	Helium Cooled Lithium-Lead
HCPB	Helium Cooled Pebble Bed
HEBLO	Helium Divertor and Blanket Test Loop
HEMJ	He-cooled Divertor with Multiple Jet Cooling
HEMP	Helium Cooled Modular Divertor Concept with Pin Array

HEMS	Helium Cooled Modular Divertor Concept with Slot Array
HETS	High Efficiency Thermal Shield
HFR	High Flux Reactor at Petten
HFTM	High Flux Test Module
HHF	High Heat Flux
HIP	Hot Isostatic Pressing
HTM	High Flux Test Module
HTS	High Temperature Superconducting
HTS-CL	High Temperature Superconducting – Current Lead
IEAF	Intermediate Energy Activation File
IFMIF	International Fusion Materials Irradiation Facility
IFP	Institut für Plasmaforschung, Universität Stuttgart
IPP	Max-Planck-Institut für Plasmaphysik
ISO	International Standard Organization
ISS	Isotope Separation System
ITER	International Thermonuclear Experimental Reactor
ITHEX	Teststrecke für thermohydraulische Experimente zur IFMIF-Hochflusszelle
JAERI	Japan Atomic Energy Research Institute
JET	Joint European Torus
JETT	J Evaluation on Tensile Test
KONUS	Kombinierte Nullgrad-Struktur
LAFM	Low Acitivating Ferritic Martensitic
LANL	Los Alamos National Laboratory
LCF	Low Cycle Fatigue
LE	Laser Etching
LEBT	Low Energy Beam Transport
LF	Low Frequency
LHC	Large Helical Coil
LLRM	Linear-Low-Reynolds-Model
LOCA	Loss of Coolant Accident
LOVA	Loss of Vacuum Accicent
LPCE	Liquid Phase Catalytic Exchange
LSC	Liquid Scintillation Counting
MAGS	Magnet Safety (software module)
MC	Monte Carlo
MCNP	Monte Carlo Neutron Particle
MEBT	Medium Energy Beam Transport

MEKKA	Magneto-hydrodynamic Experiments in Sodium and Potassium Karlsruhe
MFTM	Medium Flux Test Module
MHD	Magneto Hydrodynamics
MOU	Morror Optical Unit
MPACVD	Microwave Plasma Assisted Chemical Vapour Deposition
NB	Neutral Beam
NBI	Neutral Beam Injection
NRG	Netherlands Energy Reserarch Foundation, Petten
N-VDS	Normal Vent Detritiation System
ODS	Oxide Dispersion Strengthened
OFHC	Oxygen Free High Conductivity (copper)
PBA	Pebble Bed Assembly
PCP	Prototype Cryosorption Pump
PERMCAT	Permeator Catalyst
PFC	Plasma Facing Components
PHT	Powder HIP Technology
PID	Project Integration Document
PIE	Post Irradiation Examination
PIM	Power Injection Moulding
PLC	Programmable Logical Controller
PPCS	Power Plant Conceptual Study
QA	Quality Assurance
RAFM	Reduced Activation Ferritic Martensitic
RF	Radio Frequency
RFQ	Radio Frequency Quadrupol, accelerator structure
RSU	Remote Steering Unit
RT	Room Temperature
SAD	Secondary Angular Distributions
SBWG	Single Beam Ware Guide
SCK-CEN	Studiecentrum voor Kernenergie, Mol / Belgium
SCLL	SiC Lithium Lead
SDC	Structural Design Criteria
SDS	Storage and Delivery System
SEM	Scanning Electron Microscope
SPICE	Sample Holder for Irradiation of Miniaturised Steel Specimens Simultaneously at Different Temperatures
SPM	Solid Polymer Membrane

TBM	Test Blanket Module
TD	Thermodesorption
TDS	Thermal Desorption Spectroscopy
TED	Thales Electron Devices, Velizy
TEM	Transmission Electron Microscope
TEP	Tokamak Exhaust Processing
TES	Trtitium Extraction System
TF	Toroïdal Field
TFMC	Toroïdal Field Model Coil
TFTR	Tokamak Fusion Test Reactor
THELMA	Thermo-Hydraulic Electro-Magnetic Analysis
TIDE	Tritium Decontamination Facility
TIG	Tungsten Inert Gas
TIMO	Test Facility for ITER Model Pump
TITAN	Tieftemperaturadsorption
TLK	Tritium Laboratory Karlsruhe
TOSKA	Torusspulen Testanordnung Karlsruhe
TRIMO	Tritium Inventory Modeling
TRM	Tritium Release Model
TTE	Trace Tritium Experiment
TUD	Technische Universität Dresden
U-DW	Uniaxial Diffusion Welding
UKAEA	United Kingdom Atomic Energy Authority
UNR	Universidad Nacional de Rosario
UPP	Upper Port Plug
USE	Upper Shelf Energy
WCLL	Water Cooled Lithium-lead Blanket
WDS	Water Detritiation System
WTZ	Wissenschaftlich-Technische Zusammenarbeit